Wet-Based Glaciation on Mars

Thesis

WET-BASED GLACIATION ON MARS

Frances Eleanor Grace Butcher

BA (Hons), MA (Cantab)

A thesis submitted to The Open University for the degree of Doctor of Philosophy in Planetary Science

School of Physical Sciences

The Open University

February 2019

DECLARATION

I confirm that this thesis is my own work, and that I have indicated where data or information has been derived from other sources.

Frances Butcher

February 2019

ABSTRACT

Mars is a glacial planet. It hosts water ice in large polar ice caps, and in thousands of 'viscous flow features' in its mid latitudes that are thought to be debris-covered water ice glaciers. These ice deposits range between a few million to ~1 billion years in age and formed during Mars' most recent epoch, the late Amazonian. The late Amazonian was characterised by extremely cold and arid climate conditions that are not conducive to melting of ice. Consequently, late-Amazonian glaciation has been dominated by cold-based glacier thermal regimes. However, the recent discovery of an esker (a ridge of sediment deposited by meltwater flowing through a tunnel within or beneath glacial ice) associated with a viscous flow feature in the Phlegra Montes region of Mars' northern mid latitudes provided the first indicative evidence that wet-based glaciation occurred in at least one location during the late Amazonian.

In this thesis, I present the discovery of a second candidate esker associated with a viscous flow feature, in the NW Tempe Terra region of Mars' northern mid latitudes. I argue that the remarkably similar geologic settings of the NW Tempe Terra and Phlegra Montes candidate eskers (both within tectonic rift/graben valleys) suggests that geothermal heating, possibly with an additional component of viscous strain heating within the basal ice, was a prerequisite for basal melting under cold climate conditions. I then characterise the 2D and 3D morphometries of these candidate eskers, undertake comparisons with the morphometries of ancient putative eskers on Mars and eskers on Earth, and develop conceptual models for the dynamics of esker formation in NW Tempe Terra. Finally, I present a geomorphic map of Chukhung crater, Mars, which hosts esker-like sinuous ridges associated with viscous flow features and provides a case study of the ongoing challenges for esker identification on Mars.

ACKNOWLEDGEMENTS

There are many people without whom this thesis would not have been possible. I am indebted to my supervisors, whose encouragement and commitment have made every moment of my doctoral research a pleasure. I am grateful to Matt for his steadfast mentorship, for trusting and allowing me to make this project my own, and for taking time to listen whenever I needed support. I am thankful to Susan for helping me to turn my planetary ambitions into a reality, for teaching me the tools of the trade, and for encouraging me to make the most of every opportunity. I have thoroughly enjoyed working with Neil, who has shared new Martian endeavours with enthusiasm and dedication, and has helped me to keep one foot firmly grounded on Earth. I am also grateful to Stephen for his diligent feedback and climatological insight, and to Axel for his gems of geophysical and grammatical wisdom.

I am also thankful to fellow esker enthusiasts Colman, Rob, and Andrew: to Colman for going beyond the call of duty at every turn to support me in my research, and for his hospitality during a thoroughly enjoyable tour of the eskers of Ireland; and to Rob and Andrew for their generous permission to analyse their terrestrial data in order to satisfy my interplanetary curiosity. I am particularly grateful to Colman and Rob for their insightful feedback on this thesis. I also thank Joel for countless valuable discussions, and Lori-Ann for her meticulous and efficient proofreading.

On a personal note, I am appreciative of many friends. I would like to thank Natalie, James, Sam, and Rioghnach, for their friendship and encouragement throughout my undergraduate years and beyond. Rhian, Stacy, and Lauren have been dependable comrades in hours of need. My housemates Costanza, Matt, Eleni, Kerry, Carrie, Melissa, Pegg, Chris, and David have made the time spent away from my thesis thoroughly enjoyable. Thoughtful gestures

from Peter, Leanne and Rachael helped me over the finish line. Alex, Candice, Paul, Robert, Zoe, Laura, Kaspar, Becca, Emma, and Zoë have been kind and considerate officemates.

I am also grateful to Jenny and Mark for welcoming me into their home when I needed a break, and to Lily and Rose for making me smile.

I wrote this thesis alongside a person I am fortunate to call my best friend. To Jack, thank you for your reassurance and companionship along the way, and for giving me so many reasons to laugh each and every day. I look forward to sharing many more adventures together.

Finally, this thesis is testament to the unfailing support of my family, to my parents' selfless commitment to providing a nurturing environment for my education, and to Peter for always having my back. This is our achievement, and I hope it makes you all proud.

TABLE OF CONTENTS

LIST OF FIGURES

LIST OF TABLES

LIST OF EQUATIONS

List of Abbreviations

AD	Ablation-Dominant
cal kyr BP	Calibrated Kilo-years Before Present
CCF	Concentric Crater Fill
CTX	Context Camera
D	Diameter
DEM	Digital Elevation Model
ESRI	Environmental Systems Research Institute
Ga	Giga-annum (billion years ago)
GLF	Glacier-Like Form
Gyr	Giga-year (billion years)
HiRISE	High Resolution Imaging Science Experiment
HRSC	High Resolution Stereo Camera
IR	Infrared
ISIS3	Integrated Software for Imagers and Spectrometers 3
ISSM	Ice Sheet System Model
kyr	Kilo-years (thousand years)
LDA	Lobate Debris Apron
LDM	Latitude-Dependent Mantle
LiDAR	Light Detection and Ranging
LVF	Lineated Valley Fill
M2CND	Mean Second Closest Neighbour Distance
Ma	Mega-annum (million years ago)
MARSIS	Mars Advanced Radar for Subsurface and Ionosphere Sounding
MOLA	Mars Orbiter Laser Altimeter
MRO	Mars Reconnaissance Orbiter

Myr	Mega-year (million years)
NASA	National Aeronautics and Space Administration
SHARAD	Shallow Radar
TAR	Transverse Aeolian Ridge
THEMIS	Thermal Emission Imaging System
VFF	Viscous Flow Feature

CHAPTER 1

INTRODUCTION

1.1. Introduction

During recent decades, data returned to Earth from robotic spacecraft have revealed that glaciation is a process that operates on many planetary bodies throughout the solar system, including Mars (e.g., Leighton et al., 1969), Mercury (e.g., Butler et al., 1993; Fastook et al., 2019), and Pluto (Stern et al., 2015).

In the present day, the planet Mars (Figure 1.1) hosts water ice within ~3.5 km thick polar ice caps (Figure 1.2; Zuber et al., 1998; Smith et al., 2001; Plaut et al., 2007), extensive high-latitude ground ice and ice-rich mantling deposits (e.g., Fanale, 1976; Mustard et al., 2001), and thousands of mid-latitude viscous flow features (VFFs) that are thought to be debris-covered water ice glaciers (e.g., Levy et al., 2014; Souness et al., 2012; Petersen et al., 2018).

In this thesis, I explore the role of liquid water in glaciation on Mars, with a specific focus upon the past production of meltwater by existing VFFs in Mars' mid latitudes. While I apply these insights primarily to advance understanding of the recent history of liquid water and environmental change on Mars, such research is of significant cross-disciplinary interest, including for the search for past and present life beyond Earth (e.g., Skidmore et al., 2000); and for the identification of potential scientific targets within the exploration zones of future crewed missions to Mars, which will depend upon water extracted from nearby, in-situ, non-polar water ice reservoirs (e.g., Hoffman et al., 2017).

Mars' present climate conditions are extremely cold and hyper-arid, and its low surface atmospheric pressure means that liquid water is unstable at the planet's surface (e.g., Haberle et al., 2001). Such environmental conditions are thought to have prevailed throughout the Amazonian period of Mars' geological history (e.g., Carr and Head, 2010), which spans the period from ~3 billion years (Gyr) ago to the present day (Hartmann and Neukum, 2001). Thus, until recently, it was widely thought that existing glaciers in Mars' mid latitudes,

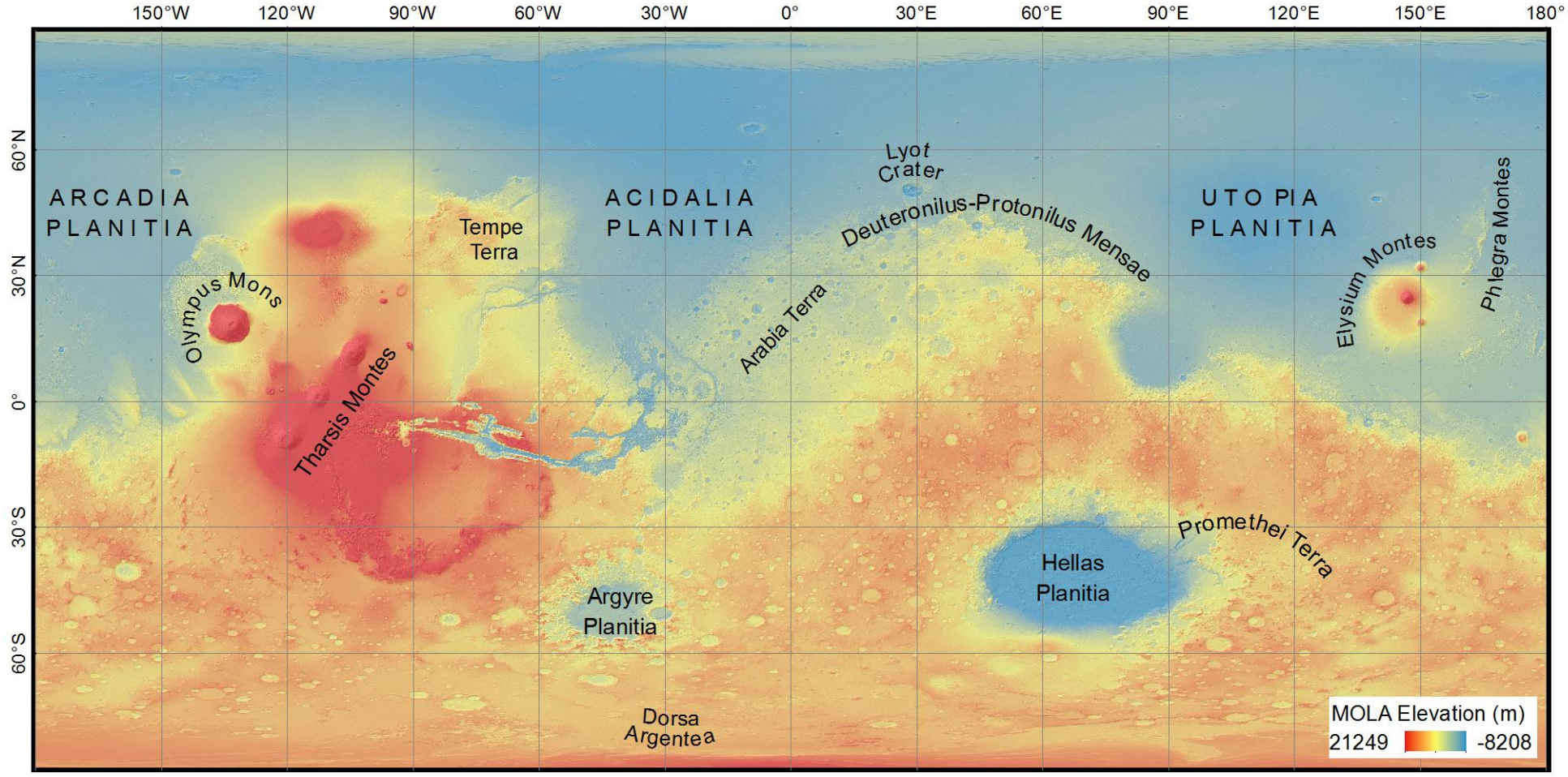

Figure 1.1. Global elevation map of Mars. Mars Orbiter Laser Altimeter (MOLA; Smith et al., 2001) elevation map (see Table 1.1) in an equirectangular projection overlain on a shaded relief basemap, with key regions that are discussed in this thesis labelled. Mars' equatorial to northern mid-latitude regions host the global topographic dichotomy boundary between the high-elevation southern highlands and the low-elevation northern lowlands. Mars' equatorial circumference is 21,344 km. Maps of Mars' polar regions are displayed in Figure 1.2.

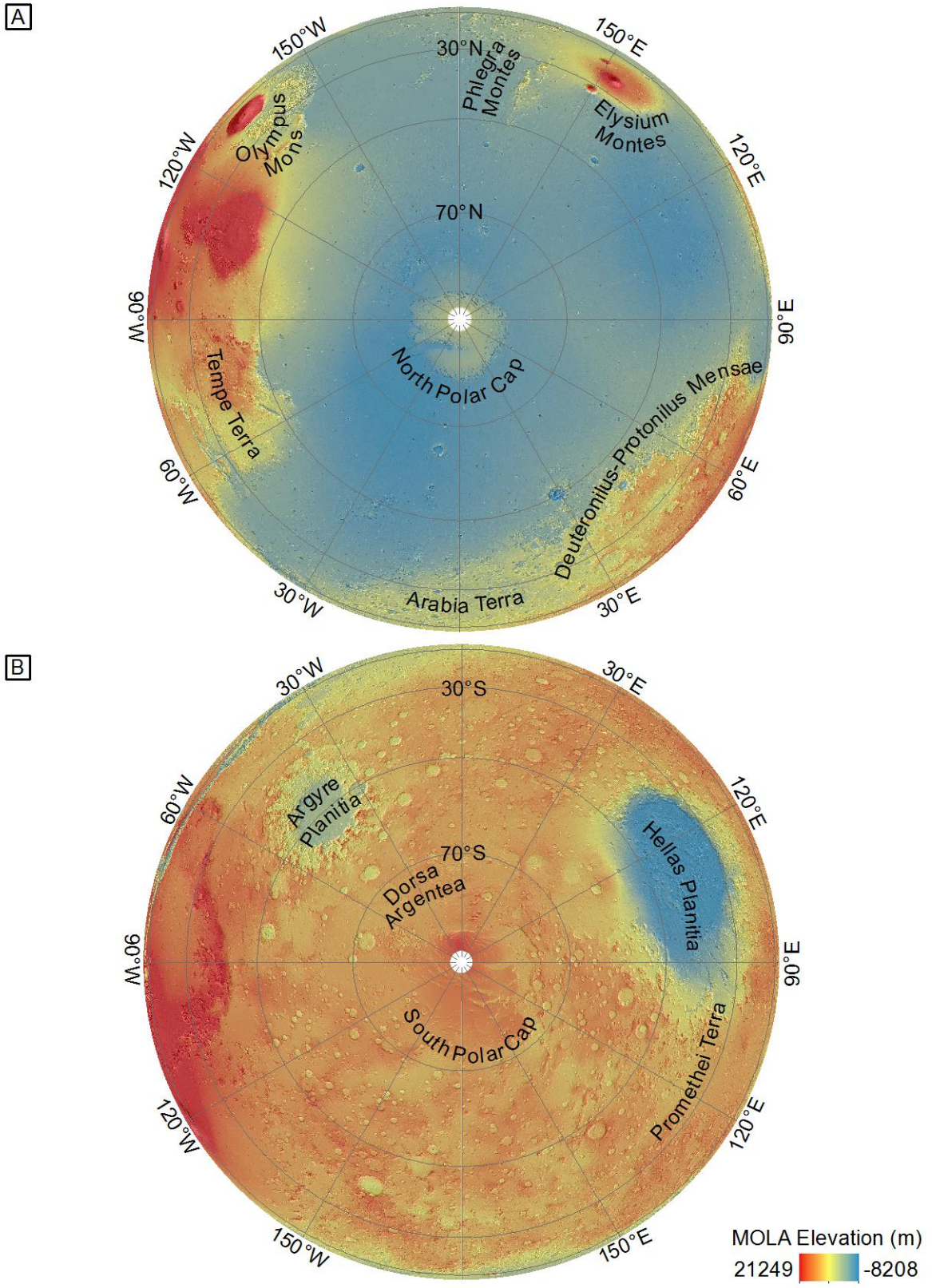

Figure 1.2. Elevation maps of Mars' northern and southern hemispheres. MOLA elevation maps (Table 1.1) overlain on shaded relief maps in polar orthographic projections centred on (A) Mars' north pole, and (B) Mars' south pole. Key regions that are discussed in this thesis are labelled. Mars' equatorial diameter is 6779 km.

which formed millions to hundreds of millions of years (Myr) ago (e.g., Hepburn et al., 2018; Arfstrom and Hartmann, 2005; Hartmann et al., 2014; Gallagher and Balme, 2015; Baker and Carter, 2019a), have always been cold-based (e.g., Hubbard et al., 2014; Levy et al., 2016) and have not produced liquid water at their beds.

However, recent discoveries have highlighted the requirement to reconsider the hypothesis that existing glaciers on Mars have always been ubiquitously cold-based (Hubbard et al., 2011; Gallagher and Balme, 2015; Orosei et al., 2018). Gallagher and Balme (2015) discovered a complex of eskers (Figure 1.3A) associated with an existing ~150 Myr old VFF in the Phlegra Montes region of Mars' northern mid latitudes (Figure 1.1). Eskers are sinuous sedimentary ridges deposited by glacial meltwater flowing through meltwater conduits, typically within or beneath glacial ice (Shreve, 1985a; Brennand, 2000). They can comprise single ridges or multi-ridged networks, and are commonly characterised by sharp-, round-, or multiple-crested morphologies (Figure 1.3B; e.g., Shreve, 1985a; Perkins et al., 2016). The discovery of the glacier-linked esker in Phlegra Montes provided the first indicative evidence for past basal melting of an extant glacier anywhere on Mars. Prior to this, ambiguous evidence for wet-based glaciation, in the form of streamlined glacial bedforms similar to those produced by wet-based glaciers on Earth, had been identified only for a single VFF in Greg crater in the Promethei Terra region of Mars' southern hemisphere (Figure 1.1; Hubbard et al., 2011). Since this time, orbital radar sounding techniques have revealed evidence for a possible present-day subglacial lake or water-saturated sediments beneath Mars' south polar ice cap (Orosei et al., 2018; see Section 3.6.1). This discovery provides the first evidence for the existence of a standing body of water and for the occurrence of wet-based glaciation anywhere on Mars in the present day.

Glaciers are typically warmer at their beds than at their surfaces because they trap heat from the planetary interior (geothermal heat), and heat generated by friction within and beneath flowing ice (strain heating). Mixing of ice with impurities (e.g., salts) and, to a lesser degree, pressure of overlying ice can depress the melting point of ice to permit basal melting at temperatures below 273 K. Consequently, glaciers can undergo basal melting despite sub-freezing temperatures at their surfaces. Such mechanisms could explain the occurrence of wet-based glaciation despite extremely cold climate conditions of the late Amazonian, albeit in extremely rare, localised cases (Gallagher and Balme, 2015; Orosei et al., 2018).

In this thesis, I present analyses of newly-identified esker-like sinuous ridges emerging from extant, mid- to late-Amazonian-aged glaciers in the Tempe Terra region of Mars' northern mid latitudes (Butcher et al., 2017, 2018). I propose that a glacier-linked sinuous ridge within

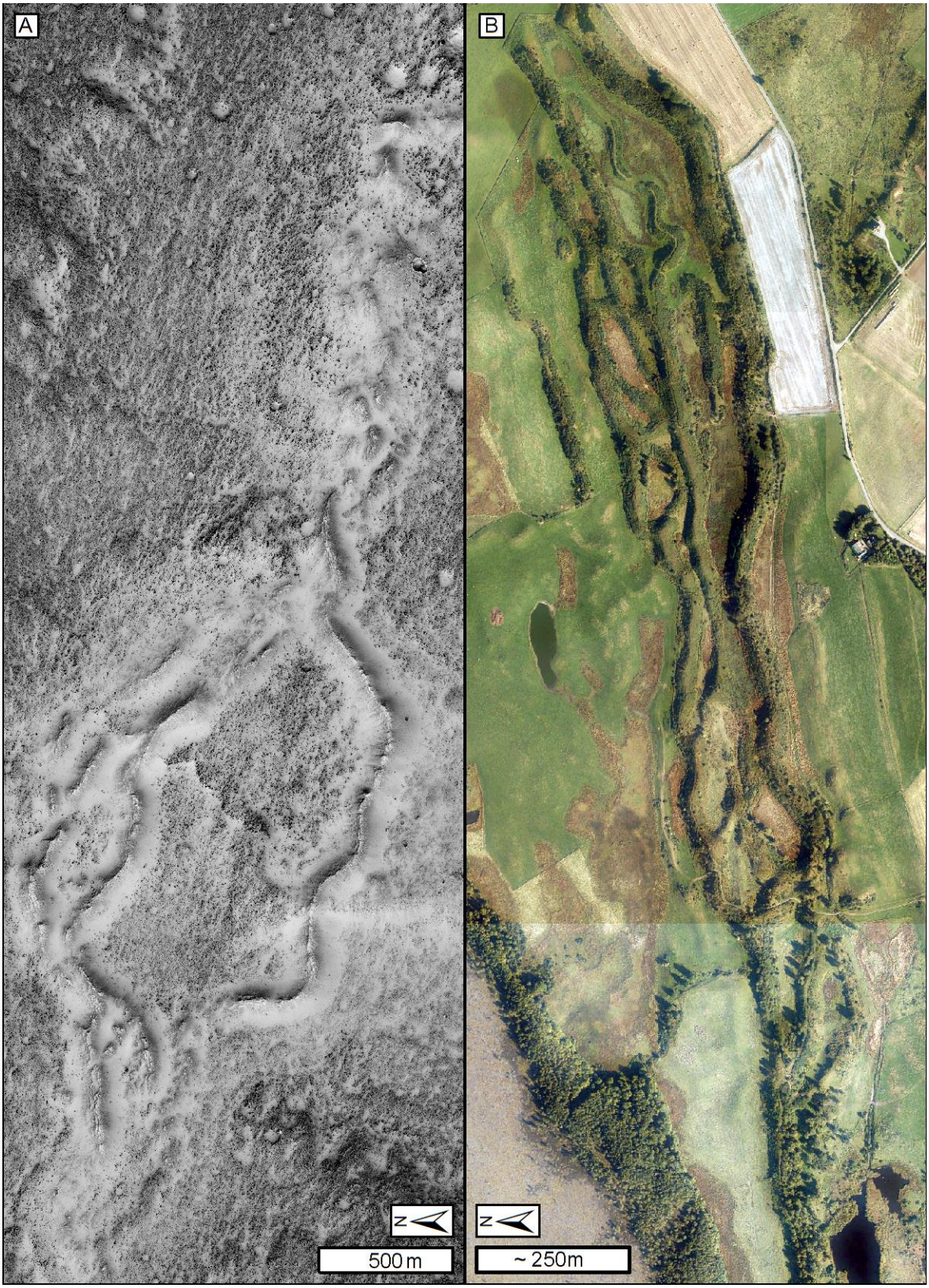

Figure 1.3. Eskers on Earth and Mars. (A) High Resolution Imaging Science Experiment image (McEwen et al., 2007) ESP_044316_2130 of the glacier-linked esker complex identified by Gallagher and Balme (2015) in Phlegra Montes, Mars. Image centred on 162.97°E, 32.68°N. (B) High Resolution (25 cm/pixel) Vertical Aerial Imagery of the Flemington eskers near Nairn, Scotland, Earth. Image centred on 57.55°N, 3.93°W. Image tiles nh8553, nh8453, and nh8353 [JPG geospatial data], Getmapping, from: EDINA Aerial Digimap Service, https://digimap.edina.ac.uk, updated 5 November 2017, downloaded: 2019-01-21 14:55:07.866, © Getmapping Plc. Illumination is from the right in both panels.

a tectonic rift valley in NW Tempe Terra is an esker formed by geologically-recent wet-based glaciation, while the origins of esker-like glacier-linked sinuous ridges in Chukhung crater, central Tempe Terra are more ambiguous.

As depositional relicts of glacial drainage systems, eskers are key geomorphic tools for reconstructing the former extent, dynamics, and environmental drivers of wet-based glaciation on Earth (e.g., Boulton et al., 2001; Kleman et al., 1997; Stroeven et al., 2016; Scanlon et al., 2018), and have similar applications on Mars (e.g., Fastook et al., 2012; Bernhardt et al., 2013; Scanlon et al., 2018). To date, such reconstructions for Mars have been limited to high-latitude eskers that formed in Mars' ancient history (3.5–3.6 billion years ago, Ga; e.g., Bernhardt et al., 2013; Fastook et al., 2012; Kress and Head, 2015; Scanlon et al., 2018), of which parent glaciers have long since retreated. Global reconstructions of Mars' ancient climate conditions have relied heavily upon insights from the Dorsa Argentea eskers which record basal melting of a large, ancient south polar ice sheet (e.g., Fastook et al., 2012; Scanlon et al., 2018).

1.2. Aims

This thesis exploits opportunities afforded by the younger (hundreds of Myr old) glacier-linked eskers in Phlegra Montes and NW Tempe Terra to advance understanding of the distribution, dynamics and possible environmental drivers of more recent basal melting of existing, late-Amazonian-aged mid-latitude VFFs on Mars. I also better characterise the geometries and morphologies of these eskers (their morphometries), and their inter-relationships, in order to aid future identification of eskers elsewhere on Mars. Additionally, I explore the possible origins and palaeoenvironmental implications of the glacier-linked sinuous ridges of ambiguous origin in Chukhung crater, central Tempe Terra. In doing so, I develop a case study of the ongoing challenges for the identification of eskers on Mars.

1.3. Objectives

In order to achieve the aims outlined in Section 1.2, I define the following objectives:

- *Objective (1):* Produce a geomorphic map of the landsystem comprising the new candidate glacier-linked esker in NW Tempe Terra, and use the map along with high-resolution observations of landforms to: (a) explore alternative explanations for the origins of the ridge, and (b) develop a conceptual model to explain formation of the full suite of observed landforms. Use observations of the broader geologic setting of the candidate esker to identify possible explanations for the generation of esker-forming basal meltwater in this location.

- *Objective (2):* Obtain high-resolution (metre-scale) measurements of the planform and 3D geometries of the glacier-linked esker in NW Tempe Terra, and use relationships between its geometry and morphology to develop a conceptual model for the spatiotemporal variations in the sediment-discharge dynamics of esker-forming meltwater drainage.
- *Objective (3):* Obtain similar high-resolution measurements for the esker complex in Phlegra Montes and compare them with the measurements of the NW Tempe Terra esker to identify possible relationships between esker morphology and morphometry that could be used to aid identification of eskers elsewhere on Mars.
- *Objective (4):* Assimilate the new morphometric measurements of the mid-latitude glacier-linked eskers with my previous measurements of the ancient south polar Dorsa Argentea eskers (Butcher et al., 2016), and compare them with similar measurements of eskers on Earth (Storrar et al., 2013; Storrar and Jones, unpublished) to constrain the range of morphometries of known eskers on Mars, and provide insight into how they compare with analogous landform on Earth.
- *Objective (5):* Produce a geomorphic map of landforms in Chukhung crater and use the map to develop arguments for and against the hypothesis that sinuous ridges emerging from extant glaciers in the crater are eskers. Use observations of sinuous ridges in Chukhung crater to demonstrate the challenges posed by convergence of form between eskers and sinuous ridges of non-glacial origin on Mars, and outline the potential applications of morphometric studies such as those completed by objectives 2–4 for overcoming these challenges.

1.4. Methodology

Reconstructing the geological histories of other planetary bodies in the solar system is reliant upon data returned to Earth from un-crewed robotic spacecraft, including flyby probes, orbital satellites, stationary surface platforms (landers), and mobile surface rovers. To date, five landers (Viking 1, Viking 2, Phoenix, Mars Pathfinder, and InSight) and four rovers (Sojourner; Mars Exploration Rover A, 'Spirit'; Mars Exploration Rover B, 'Opportunity'; and Mars Science Laboratory, 'Curiosity') have operated successfully on the surface of Mars. Landers and rovers provide exceptionally detailed views of Mars' surface but, at the time of writing, the greatest distance travelled by a rover on Mars was by the Opportunity rover, which had covered 45.16 km (28.06 miles) at last contact (10th June 2018). Consequently, our understanding of the majority of Mars' surface relies upon geomorphological analyses of images and elevation data returned from instrument suites on orbital satellites, which provide more extensive coverage of the planet's surface, albeit at

lower spatial and temporal resolutions than landers and rovers. At the time of writing, the Context Camera (CTX) instrument (Malin et al., 2007) on board Mars Reconnaissance Orbiter (MRO) had imaged > 99% of the surface of Mars' surface at 6 m/pixel resolution. By January 29th 2019, the High Resolution Imaging Science Experiment (HiRISE) camera (McEwen et al., 2007) on the same spacecraft had provided coverage of ~3.42% of Mars' surface (including repeat observations) at ~25–50 cm/pixel resolution. Repeat imaging from different viewing angles (stereo pair imaging) by these instruments in some locations allows the production of digital elevation models (DEMs) of Mars surface with spatial resolutions ~3–4 times lower than those of the original images (e.g., Kirk et al., 2008). These data allow detailed 3D analyses of the form of Mars' surface.

In this thesis, I employ a geomorphological approach utilising images and DEMs from the HiRISE and CTX instruments in combination with lower-resolution image and elevation datasets from instruments on board other orbital spacecraft, including: (1) the High Resolution Stereo Camera (HRSC; DEMs from stereo pair imagery; Neukum et al., 2004b; Jaumann et al., 2007) instrument on board Mars Express, (2) the Thermal Emission Imaging System (THEMIS; Christensen et al., 2004; Edwards et al., 2011) instrument on board Mars Odyssey, and (3) the Mars Orbiter Laser Altimeter (MOLA; Gridded DEMs derived from laser shot points with ~300 m spacing; Smith et al., 2001) instrument on board Mars Global Surveyor (Table 1.1).

Geomorphology involves the study of landforms and their spatial relationships on a planetary surface to make inferences about the processes that formed them. A lack of ground truth in all but a handful of locations on Mars, which have been explored by ground-based robotic missions, means that all geomorphic interpretations are accompanied by the unavoidable caveat that those interpretations could be erroneous (Baker, 1996, 2014). A particular challenge for planetary geomorphology is the problem of convergence of form, whereby different processes can produce landforms with similar morphologies (e.g., Baker, 2014). However, by drawing together multiple techniques, it is often possible to converge upon one or more most likely working hypotheses for the origin of a given landform. Without the near-term prospect of ground-based observations of the majority of Mars' surface, it is necessary to use these working hypotheses as tools that advance understanding of Mars' geological and environmental history, recognising that they are but the most apt subset of those hypotheses that might explain the observations (Baker, 1996). For the sake of brevity, in this thesis, I refer to features for which I am confident of an esker origin as 'eskers'.

Table 1.1. Specifications of instruments onboard Mars orbital spacecraft from which data were analysed for this thesis. Names and sources of individual data products, secondary datasets and products from airborne remote sensing of Earth are detailed within the relevant chapters.

Spacecraft	Instrument	Abbreviation	Band	Pixel size	Footprint width (m)	Notes	Source
Thermal data products							
Mars Odyssey	Thermal Emission Imaging System	THEMIS	9	100 m	8.4 km, global mosaic	Infrared day and night time	[1]
Visible data products							
Mars Reconnaissance Orbiter	Context Camera	CTX	Panchromatic	6 m	26.5 km		[2]
	High Resolution Imaging Science Experiment	HiRISE	Red	0.25–50 m	5 km		[3]
Topographic data products							
Mars Global Surveyor	Mars Orbiter Laser Altimeter	MOLA		463 m	Gridded global mosaic		[1]
Mars Express	High Resolution Stereo Camera	HRSC	Stereo 1 and 2	50–100 m	50–80 km		[4]
Mars Reconnaissance Orbiter	Context Camera	CTX		24 m	5 km		[5]
	High Resolution Imaging Science Experiment	HiRISE		1–2 m	5 km		[6]

[1] United States Geological Survey Planetary GIS Web Server: http://webgis.wr.usgs.gov/pigwad/down/mars_dl.htm
[2] Arizona State University http://viewer.mars.asu.edu/viewer/ctx#T=0
[3] The University of Arizona https://hirise.lpl.arizona.edu/
[4] Freie Universität Berlin: http://maps.planet.fu-berlin.de/
[5] Mayer and Kite (2016), personal communication
[6] Various, see sources listed in specific chapters.

However, I emphasise that new insights from future data returns could provide alternative explanations for their origins that overturn the esker hypothesis.

The objectives defined in Section 1.3 draw together four key techniques in planetary geomorphology: geomorphic mapping, quantitative morphometric analyses, terrestrial analogue comparisons, and surface age estimations from measurements of the size-frequency distributions of impact craters.

Geomorphic mapping is a technique that consolidates observations of the contextual landscape within which a landform exists. Geomorphic maps can be used to understand the distributions of different landforms and surface morphologies, their spatial relationships, and the sequence in which they formed. If a map reveals that a landform (e.g., a candidate esker) exists within a landscape that hosts an assemblage of consilient landforms (e.g., glaciers and/or moraines) and is contextually consistent with the past and/or present occurrence of the inferred formation mechanism, this can bolster confidence in hypotheses of landform origins (Baker, 1996, 2014). These insights can be consolidated into conceptual models (called landsystem models; e.g., Eyles, 1983) of the spatiotemporal dynamics of landscape evolution.

Similarities between martian landforms and landforms thought to share a common origin on Earth, and their contextual landsystems, can also improve confidence in formation hypotheses for martian landforms (Baker, 2014). It is also possible to make broad inferences about the formation dynamics of landforms on Mars based on observations of relationships between the morphometry, composition, and internal structure of analogous landforms on Earth. However, terrestrial analogue comparisons are accompanied by the caveat that there are fundamental differences in key parameters (such as surface gravity and atmospheric pressure) that influence surface processes between Earth and Mars. Thus, it is also important to undertake inter-comparisons of landforms that are thought to share common origins on Mars, since it is conceivable that the same processes operating on Mars and Earth could produce landforms with different morphometries (e.g., Sharp, 1980).

The ages of landforms can be used to contextualise inferences about the processes that formed them within the conceptual framework of Mars' broader geological history (Carr and Head, 2010). Currently, the only samples of martian rocks for which precise dates are known are for martian meteorites that have fallen to Earth (e.g., Nyquist et al., 2001), and the specific source regions for these meteorites are unknown. Measurement of size-frequency distributions of impact craters is a widely-employed proxy technique for dating of planetary

surfaces. It is based on the assumption that an older surface, or one that has been exposed for longer, will have accumulated a greater number of impact craters with larger radii, provided that there has been minimal post-impact modification of that surface (e.g., Hartmann, 1977; Hartmann and Neukum, 2001; Ivanov, 2001; Hartmann, 2005). In practise, the measured size-frequency distribution of impact craters on a given surface is compared to isochrons that have been calculated on the basis of theoretical impact crater production functions scaled from cratering rates at the Moon (Ivanov, 2001; Hartmann and Neukum, 2001; Hartmann, 2005). Although impact crater size-frequency distributions are extremely valuable for reconstructing broad chronologies of Mars' surface evolution, they must be employed with caution, particularly for studies of small landforms with young ages (Hartmann, 2005; Warner et al., 2015). Impact crater statistics for small count areas (i.e., small sample sizes) can be unreliable (Warner et al., 2015), and impact crater populations with small diameters may include secondary impact craters formed by fall-out of material ejected from a primary impact centre, which have the effect of erroneously increasing modelled surface ages by producing multiple impact craters for a single primary impact event (Hartmann, 2005; Michael et al., 2012). Impact crater size frequency distributions can also be affected by surface modification processes that obliterate impact craters (e.g., erosion and resurfacing; Michael and Neukum, 2010), or processes that inhibit their accumulation (e.g., protection of surfaces by glaciers, or burn-up of bolides in the atmosphere; Hartmann, 2005). These processes can result in underestimation of surface ages from impact crater size-frequency distributions.

1.5. Thesis Structure

In Chapter 2, I review the history of liquid water on Mars, and outline current theory pertaining to the cycling of water and ice on Mars, both in the present day and during the most recent geological epoch. In Chapter 3, I review the configuration of non-polar ice reservoirs on Mars and outline the state of knowledge on their formation and the involvement of liquid water in their evolution, before setting out the research questions explored by this thesis.

In Chapters 4–8, I present the results of this thesis, which satisfy the objectives outlined above (Section 1.3). In Chapter 4, I present the discovery of the glacier-linked esker in NW Tempe Terra, develop a landsystem model to explain its formation, and explore the implications of its geologic setting for the hypothesis that elevated geothermal heat flux was a prerequisite for wet-based glaciation during the late Amazonian (Gallagher and Balme, 2015). In Chapters 5–7, I present the first systematic metre-scale characterisation of the

planform and 3D morphometries of candidate eskers on Mars. Chapter 5 describes my approach to measuring 3D morphometries of the NW Tempe Terra and Phlegra Montes eskers, and describes secondary datasets of the 2D and 3D morphometries of eskers on Earth (Storrar et al., 2014a; Storrar and Jones, unpublished), to which I compare the martian eskers in Chapter 7. In Chapter 6, I present the morphometries of the esker in NW Tempe Terra and use a novel morphometric approach to develop a conceptual model for spatiotemporal variations in the sediment-discharge dynamics of the esker-forming drainage episode(s). In Chapter 7, I compare the morphometries of the candidate glacier-linked esker in NW Tempe Terra with those of the Phlegra Montes esker complex to explore possible morphometric relationships that could be used to aid identification of eskers elsewhere on Mars. I compare these measurements to existing measurements (Butcher et al., 2016) of the ancient south polar Dorsa Argentea eskers on Mars, and to measurements of eskers on Earth (Storrar et al., 2014a; Storrar and Jones, unpublished), including the first large database of 3D morphometries of eskers on Earth (from SW Finland), which was obtained by Storrar and Jones (unpublished) in parallel with the preparation of this thesis and is used here with their kind permission. In Chapter 8, I explore the possibility that VFFs within Chukhung crater, Tempe Terra, also underwent basal melting during the Amazonian. I present a geomorphic map of Chukhung crater and analyse esker-like sinuous ridges associated with extant VFFs within the crater. I present these analyses as a case study illustrating the challenges that remain for the identification of eskers on Mars, and thus for reconstructing the history of wet-based glaciation on the planet. I explore the possible applications of morphometric studies such as those presented in Chapters 5–7 for overcoming these challenges. In Chapter 9, I present a synthesis of my observations in the context of the broader history of liquid water and environmental change on Mars. Finally, in Chapter 10, I summarise the overarching conclusions of this thesis, and identify opportunities for future research.

1.6. Attribution of Published Work and Secondary Data Sources

Chapters in this thesis that contain or are based on published work, or include analyses of secondary datasets, are stated below. I also note the relevant sources in the 'Attribution' section at the start of the relevant chapter.

1.6.1. Portions Included from or Based on First Author Publications

The majority of Chapter 4 is published as a peer-reviewed journal article in the *Journal of Geophysical Research: Planets* (Butcher et al., 2017). The published article includes additional 1D modelling experiments which were contributed by N. S. Arnold. I do not include these experiments in Chapter 4, and instead discuss them in the overall context of

my observations in Chapter 9. The section of the article pertaining to previous studies of eskers on Mars has been removed from Chapter 4 and is instead included in background discussion of eskers on Mars in Chapter 3.

The method for obtaining new measurements of esker morphometries that I describe in Chapter 5 is published in a peer-reviewed journal article in *Icarus* (Butcher et al., 2016). This article was based on work submitted to a previous degree, but I include a description of the method here for clarity.

1.6.2. Sections Based on my Contributions to Publications as a Co-Author

Small portions of this thesis are based on my contributions as co-author to published works.

Sections 3.4 and 3.5 of the background discussion in Chapter 3 are based on my contributions as co-author to the peer-reviewed book chapter *'The Hydrology of Mars Including a Potential Cryosphere'* (Lasue et al., 2019).

In Section 9.4, I discuss my observations in the context of the results of a journal article published in *Geomorphology* (Conway et al., 2018a), of which I am the second author. I also briefly discuss my results in the context of the findings of an article in *Geological Society of London Special Publication 467* (de Haas et al., 2017), of which I am third author.

1.6.3. Secondary Data included in this Thesis

Chapter 5 includes analyses of two datasets comprising blind repeat measurements obtained by R.D. Storrar and A. Jones. These blind repeat measurements are for a method validation exercise that necessarily required data collection by independent workers.

Chapter 7 includes the datasets of 2D and 3D morphometries of the Dorsa Argentea eskers that I previously published in *Icarus* based on work submitted to a previous degree. These data are included for the purposes of new comparative analyses with the new morphometric datasets for the Phlegra Montes and NW Tempe Terra eskers collected during preparation of this thesis.

Chapter 7 also contains comparisons to previously unpublished data for the morphometries of eskers in SW Finland, which were collected by R.D. Storrar and A. Jones in parallel with the preparation of this thesis and are used here with their kind permission.

I also use pre-existing DEMs kindly provided by Mayer and Kite (2016; Chapter 8) and S. J. Conway (Chapter 4).

CHAPTER 2

WATER ON MARS

2.1. Liquid Water on Mars: A Brief History

The geological history of Mars is divided into three main periods: the Noachian (~4.1–3.7 Ga), Hesperian (~3.7–3.0 Ga), and Amazonian (~3.0 Ga to present) periods (Figure 2.1; Ivanov, 2001; Hartmann and Neukum, 2001; Hartmann, 2005; Michael, 2013). The divisions between these periods correspond approximately with significant shifts in the volume, distribution, and geologic influence of liquid water on Mars, towards the hyper-arid environment of the present-day (Figure 2.1). In this chapter, I briefly review the history of water on Mars within this chronological framework.

2.1.1. The Noachian Period

Formation of the ~1700 km diameter Hellas impact basin is generally considered to define the base of the Noachian (~4.1 Ga; Frey, 2003; Carr and Head, 2010). During this period, relatively frequent large impacts (e.g., Segura et al., 2002) and widespread volcanism (Carr, 1973; Werner, 2009) are likely to have liberated carbon dioxide and water vapour to Mars' atmosphere, resulting in atmospheric pressures that were higher than the present day, and in the stability of liquid water at the surface (e.g., Phillips et al., 2001; Segura et al., 2002; Grott et al., 2011). Stability of liquid water permitted formation of abundant fluvial landforms observed on Mars' surface, including fluvially-modified impact craters (Craddock et al., 1997; Craddock and Howard, 2002), extensive highland valley networks (e.g., Masursky et al., 1977; Hynek et al., 2010) and palaeolake basins (e.g., Fassett and Head, 2008a; Goudge et al., 2016). Many of the highland valley networks are continuous with topographically inverted palaeochannels (channel-fill deposits that have been exhumed to form ridges; Davis et al., 2016) and/or sedimentary fans (e.g., Moore and Howard, 2005), which provide evidence for aggradation of fluvial sediments under prolonged or recurrent fluvial activity (e.g., Malin and Edgett, 2003; Davis et al., 2016). In several locations along the hemispheric

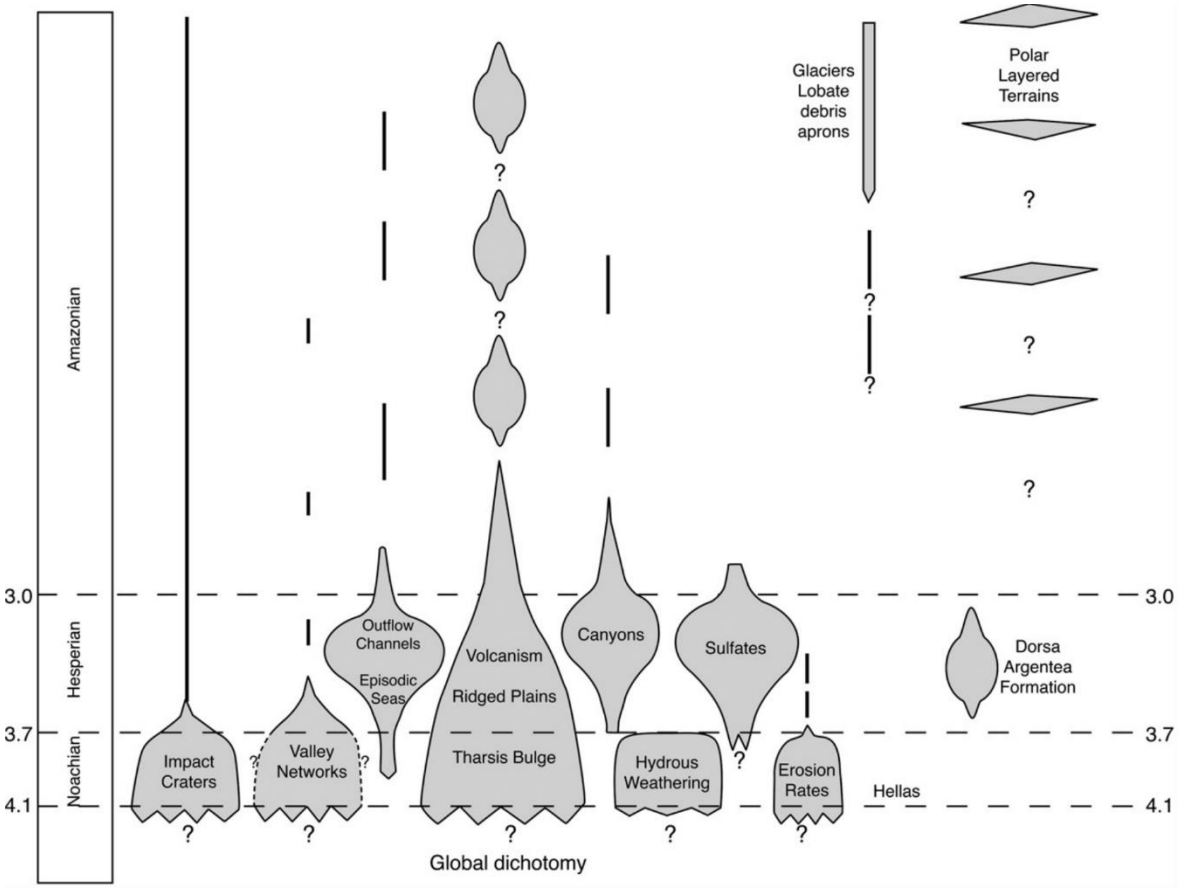

Figure 2.1. The geological history of Mars. The left hand column shows the three major geological periods and their time divisions in Gyr (Hartmann and Neukum, 2001). The balloons show the time periods during which various major geological processes are thought to have occurred. Width variations along balloons are schematic representations of the relative rates of these processes over time. Modified from Carr and Head (2010).

dichotomy boundary, which forms the topographic boundary between Mars' southern highlands and the northern lowlands (Figure 1.1), valley networks terminate in deltas that may have formed along the coastline of an ancient ocean in the northern lowlands (e.g., Parker et al., 1989; Di Achille and Hynek, 2010; Rodriguez et al., 2016; Fawdon et al., 2018). Widespread hydrous alteration of volcanic and igneous rocks resulted in formation of clay minerals over large areas of the planet (e.g., Bibring et al., 2005; Ehlmann et al., 2011).

In combination, these observations have prompted many workers to suggest that, during the Noachian, Mars' atmospheric pressure approached (or exceeded) 1 bar, and supported a sustained or episodic hydrological cycle with a significant component of precipitation and overland flow of liquid water (e.g., Masursky et al., 1977; Parker et al., 1989; Phillips et al., 2001; Segura et al., 2002; Craddock and Howard, 2002; Malin and Edgett, 2003; Moore and Howard, 2005; Hynek et al., 2010; Di Achille and Hynek, 2010; Grott et al., 2011; Goudge et al., 2016; Davis et al., 2016).

There are several complications for a 'warm and wet' Noachian climate scenario, however, which have lead many workers to support an alternative 'cold and dry' scenario (e.g., Carr and Head, 2010; Ehlmann et al., 2011; Niles et al., 2013; Wordsworth et al., 2013, 2015; Wordsworth, 2016). The first complication is that a significantly warmer climate than the present day violates the assumed effect of the faint young Sun; ~3–4 Ga, the Sun's luminosity was 20–30% weaker than in the present day (Read et al., 2015), and may have inhibited warming of Mars' climate to temperatures that could sustain a prolonged hydrological cycle. A second complication is that carbonate deposits, which would be expected to form under a warm and wet climate (e.g., Pollack et al., 1987), are scarcely observed by remote sensing techniques (e.g., Niles et al., 2013). Those that have been observed, including by landed missions, are more consistent with localised formation by subsurface fluid-rock interactions (e.g., Niles et al., 2013). Consequently, post-Noachian loss of a 1 bar carbon dioxide atmosphere cannot be reconciled with storage volumes in observable present-day atmospheric and surface reservoirs (e.g., minerals and polar caps) and a realistic rate of exospheric loss to space (Bibring et al., 2005). Thirdly, global climate modelling experiments that simulate a thicker (1 bar) atmosphere and warmer surface temperatures, fail to reproduce a spatial distribution of precipitation consistent with the distribution of valley networks (e.g., Wordsworth et al., 2013, 2015). However, recent high-resolution mapping by Davis et al. (2016) identified extensive relicts of ancient valley networks in the form of topographically inverted palaeochannels, in the Arabia Terra region. This was a key region in which the global climate models (Wordsworth et al., 2015) predicted precipitation but previous identifications of valley networks were scarce. Hence, it is possible that further high resolution observations in other regions will help to reconcile global climate models with evidence for a warm and wet ancient climate in Mars' geologic record (Davis et al., 2016).

Under the 'cold and dry' Noachian climate scenario, fluvial landforms on Mars' surface were formed by short-lived, episodic flows of liquid water supplied by groundwater seepage (e.g., Goldspiel and Squyres, 2000) and/or transient melting of snow or ice deposits (e.g., Wordsworth et al., 2013, 2015), and widespread clays were formed by subsurface water-rock interactions rather than alteration in subaerial systems (Ehlmann et al., 2011). Transient meltwater production was driven by episodic warming events triggered by volcanism, impacts, variations in planetary obliquity and/or radiative forcing by atmospheric dust (Wordsworth et al., 2015).

Debate regarding the relative merits and caveats of the 'warm and wet' and 'cold and dry' scenarios is ongoing, but recent assessments suggest that the true state of Mars' Noachian climate may have approximated a middle-ground between these end-member hypotheses, with a generally cold and dry climate having been modulated by multiple warmer and wetter periods (Wordsworth, 2016).

2.1.2. The Hesperian Period

Impacts, volcanism and fluvial activity continued into the Hesperian period (~3.7–3.0 Ga), but at lower rates than during the Noachian. Climate cooling and drying during the Hesperian drove a precipitous drop in clay formation, and the products of water-rock interactions were instead dominated by hydrated sulfates, consistent with cold-climate alteration by frost or cold, acidic water (Bibring et al., 2005; Ehlmann et al., 2011). Particularly intense periods of valley network incision and fluvial modification of impact craters (Craddock et al., 1997; Howard et al., 2005; Irwin et al., 2005) have been attributed to the transition between the late Noachian and early Hesperian, but rates of valley network formation declined thereafter (Fassett and Head, 2008b; Hynek et al., 2010).

As Mars' climate cooled and its geothermal heat flux waned during the Hesperian, a substantial proportion of its ancient unbound water inventory was incorporated into ground-ice reservoirs (Clifford, 1991; Squyres et al., 1992; Rossbacher and Judson, 1981; Clifford et al., 2010; Carr and Head, 2015; Weiss and Head, 2017), while loss of atmospheric water to space also contributed to planet-wide drying (e.g., Carr and Head, 2015). Hesperian fluvial activity was focussed in the southern highlands, but was different in nature to that of the Noachian, most notably in its formation of a small number of large (thousands of kilometres long) outflow channels via catastrophic groundwater outburst floods (e.g., Masursky et al., 1977; Komar, 1979). Such catastrophic outbursts may have occurred as a result of hydrofracture through ground ice in a growing global cryosphere (Section 2.3; Carr and Head, 2010). Under cold climates, outflow channels may have terminated in open-basin lakes and seas which rapidly froze (e.g., Carr, 2007; Hynek et al., 2010). Observations of smaller systems of Hesperian-aged valleys, palaeolakes, and deltas suggest that more prolonged (on the order of hundreds to thousands of years), albeit rare occurrences of subaerial fluvial activity (either fed by precipitation, snowmelt, or local melting of ground ice) did occur in some locations after the Hesperian-Noachian transition (e.g., Mangold and Ansan, 2006; Hauber et al., 2013; Wilson et al., 2016).

The south circumpolar Dorsa Argentea Formation is thought to comprise deposits emplaced by a large ancient south polar ice sheet that accumulated during the late Noachian and retreated during the early Hesperian (Head and Pratt, 2001; Ghatan and Head, 2004; Kress and Head, 2015; Fastook and Head, 2015; Scanlon et al., 2018). The Dorsa Argentea Formation hosts extensive networks of sinuous ridges (the 'Dorsa Argentea') that are widely interpreted as eskers (Howard, 1981; Tanaka and Scott, 1987; Ruff and Greeley, 1990; Metzger, 1992; Kargel and Strom, 1992; Kargel, 1993; Head, 2000a, 2000b; Head and Hallet, 2001a, 2001b; Tanaka and Kolb, 2001; Head and Pratt, 2001; Tanaka et al., 2014a; Kress and Head, 2015; Butcher et al., 2016). The Dorsa Argentea record extensive basal melting of the south polar ice sheet during the Hesperian (e.g., Head and Pratt, 2001; Fastook and Head, 2015; Scanlon et al., 2018). Early modelling experiments, which relied upon climate model inputs scaled from present-day conditions, suggested that basal melting of a south polar ice sheet could be achieved under cold global climate conditions, considering reconstructions of geothermal heat flux during the Noachian-Hesperian transition (Fastook et al., 2012). However, more recent modelling experiments, which make use of a new global climate model for ancient Mars, suggest that 20–30°C of atmospheric warming, in addition to greenhouse warming provided by a 1 bar carbon dioxide atmosphere, would be required to permit basal melting of a south polar ice sheet in the Dorsa Argentea Formation (Scanlon et al., 2018). Thus, Scanlon et al. (2018) suggest that the Dorsa Argentea eskers formed during a warm episode that occurred during the Noachian-Hesperian transition. Similar sinuous ridges in southern Argyre Planitia have also been interpreted as Hesperian-aged eskers (Hiesinger and Head, 2002; Banks et al., 2009; Bernhardt et al., 2013), suggesting that basal melting of ice deposits occurred beyond the south polar ice sheet during the Hesperian.

2.1.3. The Amazonian Period

Geologic activity on Mars, including impacts, volcanism and tectonism slowed further towards the Hesperian/Amazonian boundary (~3.0 Ga), and geomorphic evidence for the involvement of liquid water in Mars' surface evolution thereafter is extremely rare. Volcanism became isolated to the Tharsis and Elysium volcanic provinces, but persisted in some locations until ~100 Ma (e.g., Neukum et al., 2004b; Werner, 2009; Hauber et al., 2011). Rare fluvial valley network formation (accounting for just 3% of valley networks on Mars; Hynek et al., 2010), which occurred predominantly in the early Amazonian, became restricted to the flanks of volcanoes (Gulick and Baker, 1990; Fassett and Head, 2008b; Hynek et al., 2010), parts of Valles Marineris (Mangold et al., 2004b), and the interiors and

ejecta of young impact craters (Dickson et al., 2009; Jones et al., 2011; El-Maarry et al., 2013; Peel and Fassett, 2013).

As a freezing front continued to propagate downwards through the regolith under cooling climate conditions and waning geothermal heat flux, a majority of Mars' remaining inventory of unbound water in surface, subsurface (i.e., groundwater), and atmospheric reservoirs was incorporated into the global cryosphere (e.g., Lasue et al., 2013), both as ground ice and as massive ice deposits such as polar ice caps. Formation of the late-Amazonian-aged Athabasca Vallis outflow channel has been attributed to catastrophic outflow of water, possibly in a single event, from a subsurface aquifer within the Cerberus Fossae fault system that subsequently resealed via freezing (Plescia, 2003).

The production of valley-forming flows of liquid water during the Amazonian has largely been attributed to melting of ground ice or snowpacks by geological heat sources (e.g., Fassett and Head, 2008b, 2008b; Hynek et al., 2010; Jones et al., 2011; El-Maarry et al., 2013), but in some locations, it has been attributed to precipitation or melting of snow or ice under locally-elevated atmospheric temperatures (e.g., Gulick and Baker, 1990; Mangold et al., 2004b; Dickson et al., 2009; Peel and Fassett, 2013).

Under present mean atmospheric conditions on Mars, pure liquid water is unstable with respect to evaporation at the surface (Haberle et al., 2001). Despite this, late-Amazonian-aged gully landforms, which comprise a source alcove, transportation channel, and depositional apron, and occur on steep slopes (Malin and Edgett, 2000), have been identified across Mars' mid latitudes (e.g., Malin and Edgett, 2000; Balme et al., 2006; Kneissl et al., 2010; Harrison et al., 2015). Present-day sediment transport within gullies is probably driven by sublimation of carbon dioxide frost (e.g., Dundas et al., 2010), but the long-term evolution of gullies that incise bedrock has been widely attributed to the flow of liquid water (e.g., Christensen, 2003; Head et al., 2008; Schon et al., 2009; K. E. Williams et al., 2009; Conway and Balme, 2014). Debate regarding the relative influences of liquid water and carbon dioxide (e.g., Pilorget and Forget, 2016) in gully formation is ongoing, but it seems likely that both have influenced their evolution during Mars' recent history (see Conway et al., 2018b, and references therein). However, the scale of gully landforms (less than a few kilometres long) illustrates that, under present conditions, small amounts of liquid water–if present–can have geomorphic impact only over small runout distances.

Recent observations have suggested seasonally recurrent liquid water flows on Mars' surface in the present day, in the form of recurring slope lineae (McEwen et al., 2011; Grimm et al.,

2014; Stillman et al., 2014; Ojha et al., 2015; Stillman et al., 2016). Recurring slope lineae are elongate (0.5–5 m wide), low-albedo features that have been observed to extend down steep, equator-facing slopes during warm seasons and fade during colder seasons (McEwen et al., 2011). Subsurface aquifers of briny liquid water have been invoked as a possible source for liquid water to form recurring slope lineae (McEwen et al., 2011; Ojha et al., 2015; Stillman et al., 2016), but recent analyses have also supported dry granular flow origins, with limited or no involvement of liquid water (Dundas et al., 2017; Schmidt et al., 2017). Thus, the existence of liquid water on the surface of Mars in the present day and during its recent geological history remains a topic of significant debate. This thesis contributes to this debate by presenting evidence for past meltwater production by Amazonian-aged glaciers in Mars' northern mid latitudes.

2.2. Seasonal Cycling of Ices on Mars in the Present Epoch

2.2.1. The Martian Atmosphere

In the present day, Mars has an average atmospheric pressure of ~6 mbar at the surface, which is ~0.6% of that at sea level on Earth, and below the triple point of water (6.1 mbar). The triple point represents the pressure and temperature at which a substance can exist in solid, liquid and gas phases. At temperatures and pressures below the triple point, liquid is unstable with respect to the atmosphere, and ice transitions directly to a gas and vice versa. Carbon dioxide accounts for 96% of Mars' atmosphere by volume, while water vapour exists only as a trace gas, having a globally-integrated volume equivalent of just ~1–2 km^3 of ice (Jakosky and Haberle, 1992). This contrasts with the 13,000 km^3 ice-equivalent volume of water vapour in Earth's atmosphere (Zurek et al., 1992), of which water vapour comprises, on average, ~0.4% by volume (Read et al., 2015).

Water vapour and other gases, such as carbon dioxide and methane, contribute significantly to greenhouse warming of Earth's surface, cumulatively raising its surface temperature by ~30 K (Read et al., 2015). Although Mars' atmosphere has a column mass of carbon dioxide that is 38 times that of Earth, the small volumes and concentrations of additional greenhouse gases result in a relatively weak greenhouse effect, which elevates Mars' surface temperature by just ~6 K (Read et al., 2015).

As a result of Mars' distance from the Sun, its thin atmosphere, and a relatively weak greenhouse effect, temperatures at its surface reach far below the minimum temperature recorded on Earth, ranging down to < 150 K at the winter pole (Leighton and Murray, 1966; Mellon and Phillips, 2001; Longhi, 2006). Mean annual surface temperatures of ~220 K at

Mars' equator (Leighton and Murray, 1966) are comparable to the coldest recorded temperatures on the surface of the Earth (< 225 K), in the interior regions of the East Antarctic Ice Sheet (Lenaerts et al., 2016).

2.2.2. The Seasonal Carbon Dioxide Cycle

Carbon dioxide can exist in solid and gas phases under the low pressures and temperatures of Mars' atmosphere. Seasonal temperature variations result in exchange of large volumes of carbon dioxide between atmospheric and surface reservoirs, mobilising > 30% of the average mass of Mars' atmosphere seasonally (James et al., 1992). In the winter hemisphere on Mars, temperatures fall below the frost point of carbon dioxide in the atmosphere (~145 K; James et al., 1992). The frost point is the temperature at which a gas, present in a given concentration, under a given atmospheric pressure, becomes saturated with respect to the bulk atmosphere and precipitates as frost, without transitioning via the liquid phase. Increases in temperature above the frost point drive sublimation of ice at temperatures below the melting point. When temperatures in Mars' atmosphere fall below the frost point of carbon dioxide, atmospheric carbon dioxide condenses to form polar hood clouds (Hayne et al., 2012; Read et al., 2015), and extensive carbon dioxide frost deposits at the surface (Leighton and Murray, 1966; Kieffer, 1970; Jakosky, 1983; James et al., 1992). At the highest latitudes, precipitation from the polar hood clouds also contributes to carbon dioxide ice deposition (Read et al., 2015). The contiguous seasonal polar frost deposits are termed the seasonal polar caps. The seasonal polar caps are deposited atop the kilometres-thick, perennial residual polar caps (see Section 2.3), extending far beyond the margins of the residual polar caps (located at ± ~85°) to latitudes of ~45–55° in the winter hemisphere (Leighton and Murray, 1966; James et al., 1992; Piqueux et al., 2015).

In the northern hemisphere, the seasonal carbon dioxide frost sublimates entirely during northern spring, completely exposing water ice in the perennial residual ice cap. In contrast, at the south polar cap (which is at higher elevation than the north polar cap, and at least ~20 K colder), seasonal sublimation of carbon dioxide is insufficient to excavate the underlying water ice cap, and a layer of solid carbon dioxide ice (<10 m thick) remains at the surface throughout the year (James et al., 1992; Byrne and Ingersoll, 2003; Bibring et al., 2004, 2005).

2.2.3. The Seasonal Water Cycle

Despite its low abundance, water vapour is close to saturation in the low temperature environment of Mars' atmosphere (Zurek et al., 1992). Seasonal surface temperatures vary

about the frost point of water (190-200 K; Hess et al., 1977; Farmer and Doms, 1979; Haberle et al., 2001; Longhi, 2006), encouraging transfer of water between surface and atmospheric reservoirs.

As atmospheric temperatures fall during late summer, water ice clouds form in Mars' atmosphere (Whiteway et al., 2009). The light detection and ranging (LiDAR) instrument on the Phoenix lander (located at 68°N) observed snowfall from these clouds that reached the ground and deposited as a seasonal water ice frost (Whiteway et al., 2009). Additionally, carbon dioxide ice encourages direct deposition of small fractions of water ice frost onto the seasonal polar caps by cold trapping atmospheric water vapour that makes direct contact with their surfaces (Kieffer, 1970; Jakosky, 1983; Jakosky and Haberle, 1992; Appéré et al., 2011).

Sublimation of seasonal water ice deposits during spring and summer is strongly controlled by the duration for which carbon dioxide ice persists at the surface. Water ice frost at a given location within the seasonal polar caps begins to sublimate following removal of the major fraction of carbon dioxide frost (Leighton and Murray, 1966; Kieffer, 1970; Jakosky, 1983; Bibring et al., 2005; Langevin et al., 2005). Carbon dioxide ice in the northern hemisphere sublimates entirely during northern summer, exposing bulk water ice within the northern residual polar cap, and allowing water ice to sublimate from its surface (e.g., Bibring et al., 2005). In contrast, lower summer surface temperatures in the southern hemisphere (owing to its higher elevation) allow persistence of a perennial slab of carbon dioxide atop the south polar cap, which inhibits sublimation of underlying bulk water ice during southern hemisphere summer (Bibring et al., 2005). As a result, the peak atmospheric water vapour concentration during southern hemisphere summer is up to six times lower than during northern hemisphere summer (James et al., 1992).

Measured seasonal increases in atmospheric water vapour are significantly greater than those that can be accounted for by sublimation from the seasonal and perennial polar caps alone (e.g., Leovy, 1973; Farmer and Doms, 1979). This suggests that seasonal storage and release of water vapour from voluminous non-polar reservoirs of water ice is also an important component of Mars' hydrological cycle. In the following section, I review the theoretical configuration of water ice reservoirs on Mars.

2.3. The Theoretical Distribution of Ice in Mars' Cryosphere

Mars' cryosphere is defined as the layer of the crust and the portions of its surface where temperatures are permanently below the melting point (e.g., Rossbacher and Judson, 1981;

Clifford et al., 2010). In the present day, the only locations where water ice is perennially stable at the surface are at the poles. The perennial residual polar caps are ~3.5 km thick and extend to latitudes of ± ~85° (Zuber et al., 1998; Smith et al., 2001; Plaut et al., 2007). The south polar residual cap has a total volume of 1.6×10^6 km^3 (Smith et al., 2001; Plaut et al., 2007). Large areas of its surface are covered by a perennial slab of carbon dioxide ice. However, geomorphic and spectral observations suggest that this layer is < 10 m thick and is underlain by a larger ice cap comprising bulk water ice (Byrne and Ingersoll, 2003; Bibring et al., 2004, 2005). The north polar cap comprises ~$1.2–1.7 \times 10^6$ km^3 water ice (Paige et al., 1994; Zuber et al., 1998; Smith et al., 2001). Thus, the northern and southern residual ice caps contain a combined volume of water ice that is approximately equal to the volume of the Greenland ice sheet on Earth (Bamber et al., 2013).

Water ice is also stored in Mars' subsurface cryosphere over timescales that are dependent upon the seasonal-to-interannual stability of ice in the near-subsurface at a given latitude (Figure 2.2; Farmer and Doms, 1979; Squyres et al., 1992). The temperature of the regolith is determined by the average surface temperature and the geothermal heat flux, and the base of the cryosphere is defined as the depth to the melting isotherm (Rossbacher and Judson, 1981; Squyres et al., 1992). Between the equator and the poles, the melting isotherm deepens, and the cryosphere thickens as a result of the general poleward decline of average surface temperatures (Figure 2.2). Estimates of the thickness of Mars' cryosphere range between 1–4.7 km at the equator, and between 3–22 km at the poles (Sharp, 1973a; Rossbacher and Judson, 1981; Clifford, 1993; Clifford and Parker, 2001; Clifford et al., 2010).

The cryosphere does not necessarily contain ice. The presence of ice is dependent upon two conditions: (1) the inventory of water available to freeze into the cryosphere during past epochs, and (2) the stability of near-surface ground ice with respect to sublimation to the atmosphere in the present epoch. Uncertainty over Mars' climatic history (Section 2.1.1) has prompted debate over the volume of water that was available to freeze into the cryosphere in past epochs (Clifford and Parker, 2001; Carr and Head, 2015). Under warm and wet scenarios for Mars' early climate conditions (see Section 2.1.1), the volume of water stored in Mars' subsurface in the present day may exceed the capacity of the cryosphere, resulting in complete filling of the cryosphere with ice, and storage of excess water in a sub-permafrost reservoir of liquid water (Rossbacher and Judson, 1981; Clifford, 1993; Clifford et al., 2010). In contrast, under cold and dry scenarios for Mars' early climate conditions (see Section 2.1.1), the present inventory of water on Mars may not be sufficient to fill the cryosphere (as

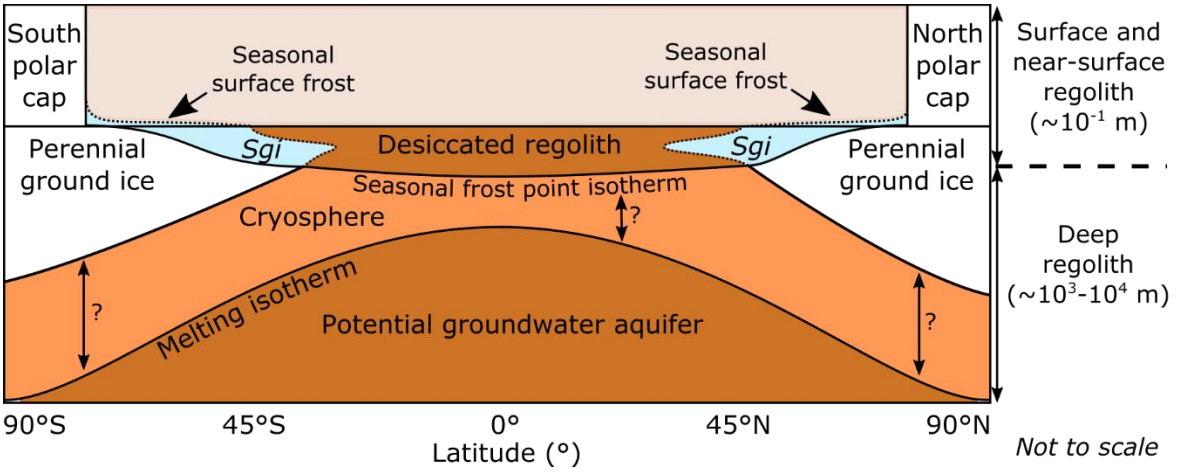

Figure 2.2. Schematic showing the theoretical distribution of ice reservoirs on Mars in the present epoch. Schematic representation (not to scale) of the theoretical distribution of seasonal and perennial water ice within surface and subsurface reservoirs on Mars, assuming strong diffusive coupling between the atmosphere and the regolith. See text for explanation of reservoirs. The heavy dashed line (right) indicates a discontinuity in the vertical scale of the diagram; the vertical scale of the zone above this line is on the order of tens of centimetres, whereas the vertical scale of the zone below this line is on the order of kilometres. The dotted lines show the approximate maximum seasonal extents of seasonal ground ice (Sgi; Farmer and Doms, 1979), and the seasonal surface frosts of which water ice constitutes a minor component. The lower boundary of the perennial ground ice reservoir is based upon a scenario where the cryosphere is not filled with ice (i.e., the volume of ice in Mars' cryosphere is supply limited). Hence, there are portions of the cryosphere in this schematic that are free of ice. The region below the melting isotherm represents a zone in which groundwater could be stored if the lower boundary of the perennial ice extends to the melting isotherm (i.e., the cryosphere is filled). The seasonal frost point isotherm represents the maximum seasonal depth at which the temperature of the regolith exceeds the frost point. Perennial ice cannot exist at depths shallower than the seasonal frost point isotherm unless isolated from the atmosphere by overlying materials. Based upon Fanale (1976), Farmer and Doms (1979), Rossbacher and Judson (1981), and Schorghorger and Aharonson (2005).

in Figure 2.2), and in some regions, the cryosphere may be desiccated (Rossbacher and Judson, 1981).

The second condition for the presence of ice at a given point in Mars' cryosphere is the stability of near-surface ground ice with respect to sublimation to the atmosphere under past and present environmental conditions. In this sense, the minimum depth at which perennial ice can be stored in the cryosphere is defined by the penetration depth of the seasonal frost point isotherm (Figure 2.2). Field observations of impact craters on Earth, and the seismic properties of the lunar regolith suggest that impacts into Mars' surface probably generated a highly porous regolith comprising a thick blanket of impact debris overlying heavily fractured bedrock. As a result, Mars' bulk regolith is thought to be strongly coupled to the atmosphere by gaseous diffusion (Squyres et al., 1992), such that ice cannot exist in long-term stability (i.e., as permafrost) where seasonal temperatures exceed the frost point of water vapour (190–200 K) unless protected by relatively non-porous materials (e.g., fine-

grained dust) that deviate from the generalised model of Mars' bulk regolith (Fanale, 1976; Farmer and Doms, 1979; Squyres et al., 1992).

According to a theoretical latitude-depth profile of ice stability in the upper metre of Mars' regolith derived by Farmer and Doms (1979), each hemisphere can be divided into three latitudinal provinces based on the temporal scale of ice stability: equatorial, mid-latitude and polar provinces. In the equatorial province (35°S–46°N), diurnal temperatures exceed the frost point throughout the year and ice in the cryosphere is unstable with respect to sublimation to the atmosphere (Farmer and Doms, 1979). Long-term diffusion has resulted in desiccation of the equatorial regolith to depths on the order of hundreds of metres (Fanale, 1976; Squyres et al., 1992).

In the mid latitudes, (35–85°S, 46–85°N), surface temperatures exceed the frost point during summer. The seasonal warm wave penetrates to greater depths towards lower latitudes, resulting in deepening of the upper interface of the permafrost zone towards the low-latitude margins of the mid-latitude provinces. In winter, mid-latitude temperatures fall below the frost point, and the interface of ice stability migrates up towards the surface, creating a layer in which seasonal ground ice (termed tempofrost by Farmer and Doms, 1979) can accumulate (Farmer and Doms, 1979; Rossbacher and Judson, 1981; Squyres et al., 1992). This 'tempofrost' zone serves as a significant seasonal reservoir for water ice in Mars' water cycle (Farmer and Doms, 1979). The margins of the residual polar ice caps mark the intersection of the tempofrost-permafrost boundary with the planet's surface, and define the boundary between the mid-latitude and polar provinces described by Farmer and Doms (1979). In the polar provinces (>85°N and S), the seasonal warm wave does not penetrate beyond the near-surface layers of the polar ice caps, resulting in perennial stability of bulk ice in the polar caps, and of ground ice that likely extends to great depths in the underlying cryosphere.

However, it should be noted that the theoretical distribution of ice described above considers only latitudinal variations in insolation as a control upon the distribution of ground ice reservoirs on Mars. The regional distribution of ground ice can be modified by several factors, including: (1) local slope effects upon insolation of the surface (e.g., Schorghofer and Aharonson, 2005), (2) spatial variations in regolith temperatures arising from differences in the thermal inertia of materials at the surface (Mellon and Jakosky, 1993), and (3) variations in the diffusive properties of the regolith (e.g., Fanale, 1976; Farmer and Doms, 1979; Squyres et al., 1992). Isolation of near-surface ice from the atmosphere by a protective layer of relatively non-porous material could prevent sublimation loss of ground ice where

seasonal surface temperatures exceed the frost point of water (Fanale, 1976; Farmer and Doms, 1979; Squyres et al., 1992). Thus, as I will discuss in Chapter 3, the true distribution of water ice reservoirs on Mars may vary from the theoretical distribution described above and illustrated in Figure 2.2.

2.4. Migration of Water Ice on Mars during Past Epochs

At present, Mars' spin-axis obliquity (defined as the tilt of its spin axis relative to the Sun) is ~25°, similar to that of Earth (23.3°). Statistical reconstructions of orbital and spin-axis parameters (including orbital eccentricity, longitude of perihelion, and spin-axis obliquity) for the most recent 20 Myr of Mars' history (Figure 2.3; Laskar et al., 2004) show that they have varied in ways that are likely to have changed the distribution of stable ice reservoirs on Mars, driving changes in climate, and cycles of glaciation and deglaciation of Mars' polar, mid-latitude, and equatorial provinces (e.g., Head et al., 2003). Similar reconstructions prior to 20 Ma have non-unique solutions (Laskar et al., 2004), but it is likely that variations in Mars' axial tilt also influenced the distribution of ice on Mars prior to the late Amazonian. Climate changes induced by orbital and spin-axis variations and their possible effects upon the redistribution of ice over Mars' surface are important for understanding the nature and configuration of ice reservoirs on the planet in the present day. Thus, I briefly review the theoretical effects of variations in orbital and spin-axis parameters upon the distribution of stable water ice reservoirs on Mars before I review the geomorphic evidence for the distribution of ice reservoirs on Mars in Chapter 3.

The stabilising effect of the Moon means that variations in Earth's obliquity are relatively muted, varying by ± 1.3° about a mean obliquity of 23.3° (Laskar et al., 1993). Within the last 20 Myr, the extremes of Mars' spin axis obliquity have been significantly greater than those of Earth, varying between ~20° and ~45° due to a lack of gravitational stabilisation by its small moons Phobos and Deimos (Laskar et al., 2004). Towards the upper extremes of Mars' recent spin axis obliquity variations, insolation quantities at the poles would increase above those at non-polar latitudes such that ice would become more stable in non-polar regions than at the poles and any ice within polar reservoirs would be mobilised equatorward (e.g., Levrard et al., 2007; Madeleine et al., 2009). As a result, variations in Mars' spin-axis obliquity have the opposite effect upon cycles of obliquity-driven glaciation and deglaciation to those that occurred on Earth during the early Pleistocene (~2.58–0.9 Ma). Cycles of glaciation on Earth that occurred after this time (i.e., the late Pleistocene, 0.9 Ma–11.7 ka) were less strongly controlled by obliquity-driven forcing (Ruddiman et al., 1989; Imbrie et al., 1992; Maslin et al., 2001). During the early Pleistocene glacial cycles on Earth,

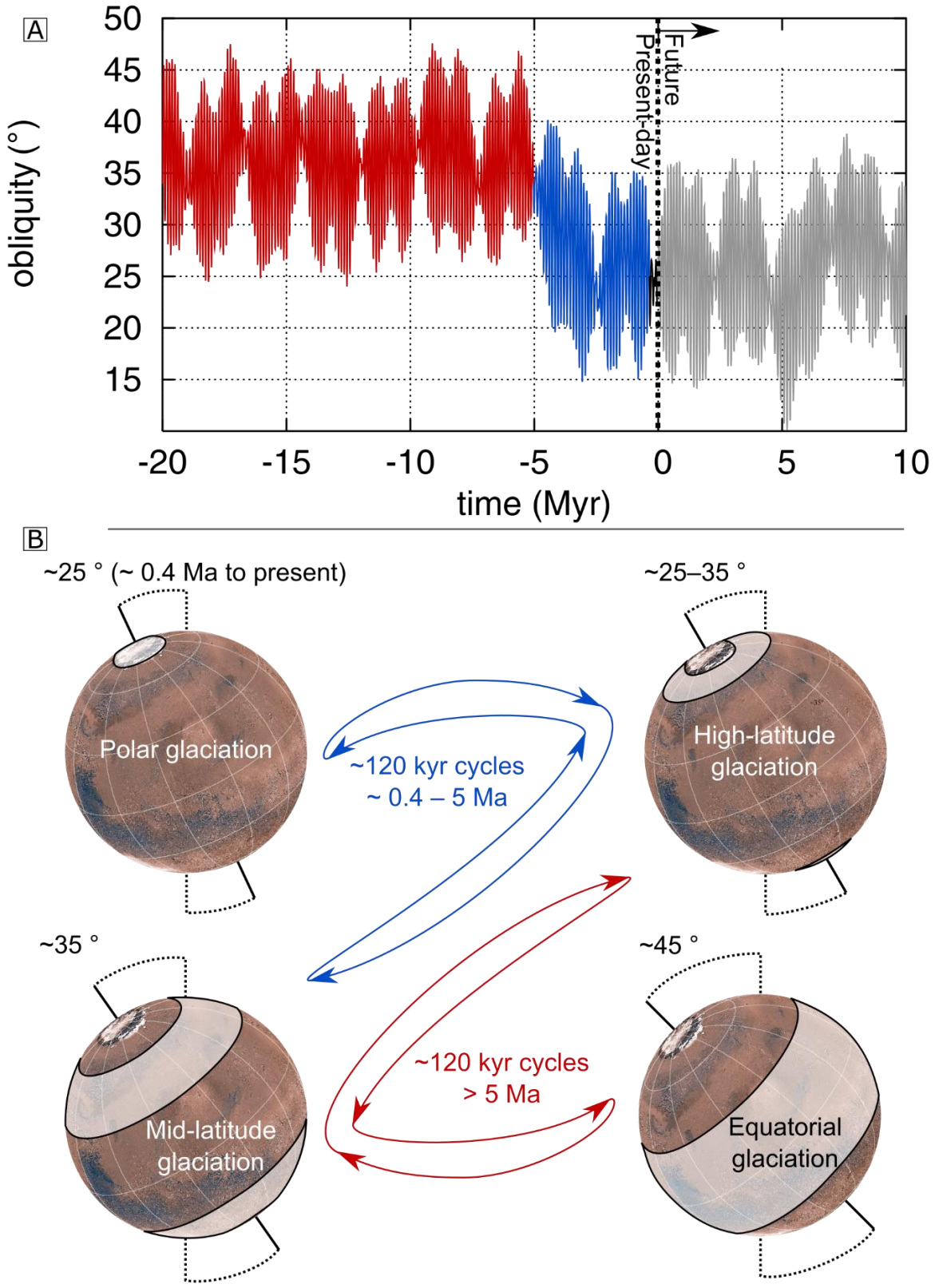

Figure 2.3. Variations in Mars' spin-axis obliquity (-20 to +10 Myr), and theoretical effects on the latitudinal distribution of stable surface ice reservoirs. (A) Mars' orbital spin-axis obliquity (°) between 20 Ma and 10 Myr in the future, coloured according to the major mean obliquity states described in the text (mean obliquity ~35° in red, mean obliquity ~25° in blue, relatively stable ~25° obliquity in black, and future obliquity in grey). Modified from Laskar et al. (2004). (B) Schematic of the theoretical effect of cyclic obliquity variations (arrow loops) upon the latitudinal distribution of stable surface ice reservoirs (white regions) on Mars ~0.4–5 Ma (blue arrows) and >5 Ma (red arrows). Mars' spin axis obliquity has been approximately ~25° for the last ~0.4 Ma. Basemaps are Viking orbiter image mosaics.

periodic excursions to low obliquity reduced total summer insolation at high latitudes, but excursions to higher obliquity did not result in increases in polar solar insolation quantities above those at mid latitudes (Ruddiman et al., 1989; Imbrie et al., 1992; Maslin et al., 2001). Solar forcing induced by initial reductions in Earth's obliquity were amplified by complex feedbacks within Earth's atmosphere, cryosphere, oceans and biosphere, and drove dramatic climate shifts that permitted widespread net annual ice accumulation and advance of ice sheets into the mid latitudes. Thus, non-polar glacial maxima on Earth have been associated with decreases in planetary spin-axis obliquity, whereas non-polar glacial maxima on Mars are thought to have been driven by increases in the planet's spin-axis obliquity. Correspondingly, 'interglacials' on Mars have been associated with transitions to low obliquity and the redistribution of ice deposits from the middle and/or low latitudes towards the poles.

Figure 2.4 shows variations in summer solstice insolation at Mars' north pole over the last 10 Myr, calculated by Levrard et al. (2007) based upon reconstructions of Mars' orbital eccentricity, longitude of perihelion, and spin-axis obliquity (Laskar et al., 2004). According to this model, variations in north polar insolation for Mars have been influenced predominantly by ~120 kyr-period oscillations in planetary spin-axis obliquity of ± 15°. These oscillations are modulated by a longer cycle with a ~2.4 Myr period. In the 2.4 Ma cycle, the magnitude of obliquity oscillations varies. During periods when they become muted (varying over a range of < 5°, e.g., 2.4 Ma and 0.5 Ma–present), variations in polar insolation are instead dominated by the relatively weak solar forcing effect of the 51 kyr orbital precession cycle (Laskar et al., 2004; Levrard et al., 2007). A major step-change from high mean obliquity (~35° ± 15°) to low mean obliquity (~25° ± 10°) occurred between ~4 and 6 Ma (Laskar et al., 2004).

Prior to the shift in Mars' mean spin-axis obliquity ~4–6 Ma, mean solar insolation at the northern pole was above the threshold for ice stability at the polar cap. Under this configuration, the average condition was one of ice instability at the poles, and any ice within a northern polar cap would have been exhausted rapidly and transferred to non-polar reservoirs. At high (45°) obliquity, ice would preferentially accumulate at low latitudes (Levrard et al., 2007). Global climate simulations by Madeleine et al. (2009) indicate that at intermediate obliquities of ~35°, ice would accumulate in mid-latitude reservoirs. At obliquities between ~35–25°, ice would accumulate in high-latitude reservoirs (Levrard et al., 2004), while at present (~25°) surface ice is stable only in polar reservoirs (Levrard et al., 2007). Brief excursions in spin-axis obliquity below the threshold of north polar cap

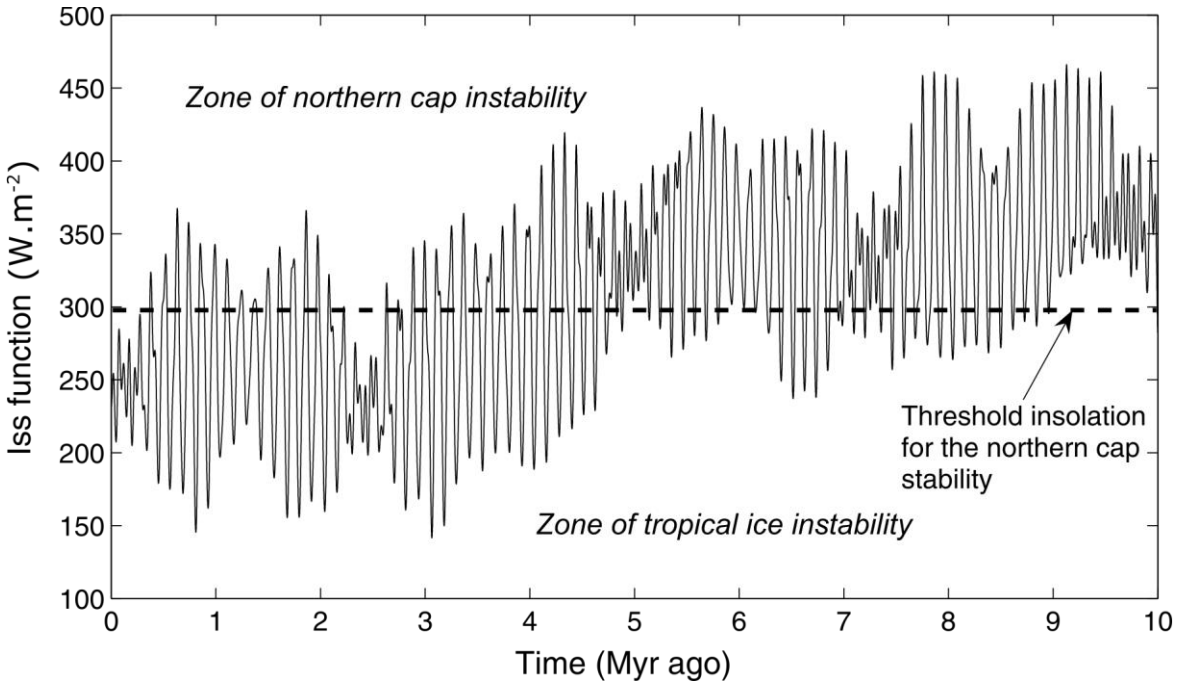

Figure 2.4. Orbitally-induced variations in Mars' summer solstice insolation for the last 10 Myr. Levrard et al. (2007) calculated diurnally-averaged summer solstice insolation (Iss in W m^{-2}) based on reconstructions by Laskar et al. (2004) of Mars' orbital eccentricity, longitude of perihelion, obliquity, and orbital velocity at summer solstice. The horizontal dashed line represents the summer solstice insolation above which a north polar cap would become unstable with respect to sublimation to the atmosphere. Modified from Levrard et al. (2007).

stability, which punctuated the ~5–10 Myr period, could also have permitted short-term accumulation of ice within polar reservoirs (Levrard et al., 2007).

The step-like transition to lower mean obliquity that occurred ~4–6 Ma is thought to have initiated long-term transfer of ice to the existing polar caps, at the expense of ice reservoirs that accumulated in the mid and low latitudes during the preceding period (Levrard et al., 2007). The 2.4 Ma modulating cycle resulted in muted obliquity oscillations for the last 0.4 Myr, permitting long-term, possibly continuous accumulation of the polar caps, and prolonged removal of ice from reservoirs at lower latitudes (Laskar et al., 2004; Levrard et al., 2007; Mellon and Jakosky, 1995). A similar period dominated by polar cap accumulation is also likely to have occurred ~2.4 Ma (Levrard et al., 2007).

During the intervening periods since the 4–6 Myr transition (i.e., 0.4–2.1 Ma and 2.9–4 Ma), when insolation quantities were dominated by the effects of spin-axis obliquity variations, Mars underwent ~30 short, periodic excursions to intermediate obliquity, up to a maximum of ~35° (Head et al., 2003; Laskar et al., 2004). These excursions may have allowed temporary transport of ice towards non-polar reservoirs at the expense of polar cap accumulation, but were relatively short and minor compared to those that occurred > ~5 Ma (Head et al., 2003; Levrard et al., 2007). Therefore, the major transition in mean planetary

obliquity ~4–6 Ma may be considered as the termination of the 'Last Martian Glacial Maximum' (Souness and Hubbard, 2013; Brough et al., 2016). It is thought that accumulation of ice within surface reservoirs on Mars has been dominated by growth of the polar ice caps since this time. Layering interfaces within the north polar residual cap that were detected by the Shallow Radar (SHARAD) sounder on board MRO correlate (Smith et al., 2016) with the theoretical time divisions in the evolution of the north polar residual cap (Levrard et al., 2007) described above. These observations suggest that the upper 300 m of the north polar residual cap (equivalent to a ~55 cm thick global ice layer) accumulated since ~0.4 Ma, and that a majority of its thickness accumulated since ~4 Ma (Smith et al., 2016).

In the following chapter, I review the geomorphic manifestation of water ice reservoirs on Mars outside the polar regions, including evidence for variations from the theoretical distribution of existing ice reservoirs, and geomorphic evidence for the past redistribution of water ice between polar, mid-latitude and equatorial reservoirs described in Section 2.4. As predicted by Laskar (2004), this geomorphic evidence suggests that obliquity-driven variations in the distribution of stable ice reservoirs like those discussed in Section 2.4 occurred for at least hundreds of millions of years prior to the most recent ~20 Myr of Mars' geological history for which orbital solutions are well-constrained. I then explore extremely rare evidence for the involvement of liquid water in the evolution of Mars' existing glacial deposits, and hypotheses for the environmental controls upon this melt before setting out the research questions to be explored by the remainder of this thesis.

CHAPTER 3

AMAZONIAN-AGED GLACIAL LANDSCAPES ON MARS

3.1. Attribution

Sections 3.4 and 3.5 of this chapter are based upon my contributions (as co-author) to the book chapter 'The Hydrology of Mars Including a Potential Cryosphere' (Lasue et al., 2019). Section 3.7.2 is based on a portion of the discussion in a published article in *Journal of Geophysical Research: Planets* (Butcher et al., 2017).

3.2. Non-Polar Ice Deposits on Mars

In this chapter, I review the inferred present-day distribution of non-polar ice deposits on Mars based on observations from orbital and landed missions (Figure 3.1). I describe current models for the formation of these ice deposits in the context of the theoretical obliquity-driven changes in the latitudinal distribution of stable ice reservoirs during the Amazonian, which I outlined in Chapter 2. I then review evidence for the nature of past and present thermal regimes of existing glaciers on Mars, and thus our present understanding of the role of liquid water in the evolution of Mars' existing glaciers.

3.2.1. Ground Ice

Observations of Mars' surface by orbital and landed missions have identified evidence for the presence of ground ice in Mars' mid- to high-latitude near-surface regolith, consistent with theoretical predictions (see Chapter 2). Small-scale polygonal landforms (metres to tens of metres width; Mutch et al., 1977) form polygonal patterned ground that occurs over extensive portions of Mars' surface in the ± ~40°–70° latitude bands (Figures 3.1 and 3.2A), and has been attributed to thermal contraction cracking processes associated with the presence of shallow (less than a few tens of metres deep) ground ice (e.g., Malin and Edgett, 2000; Seibert and Kargel, 2001; Mangold et al., 2004a; Levy et al., 2010b). The distribution

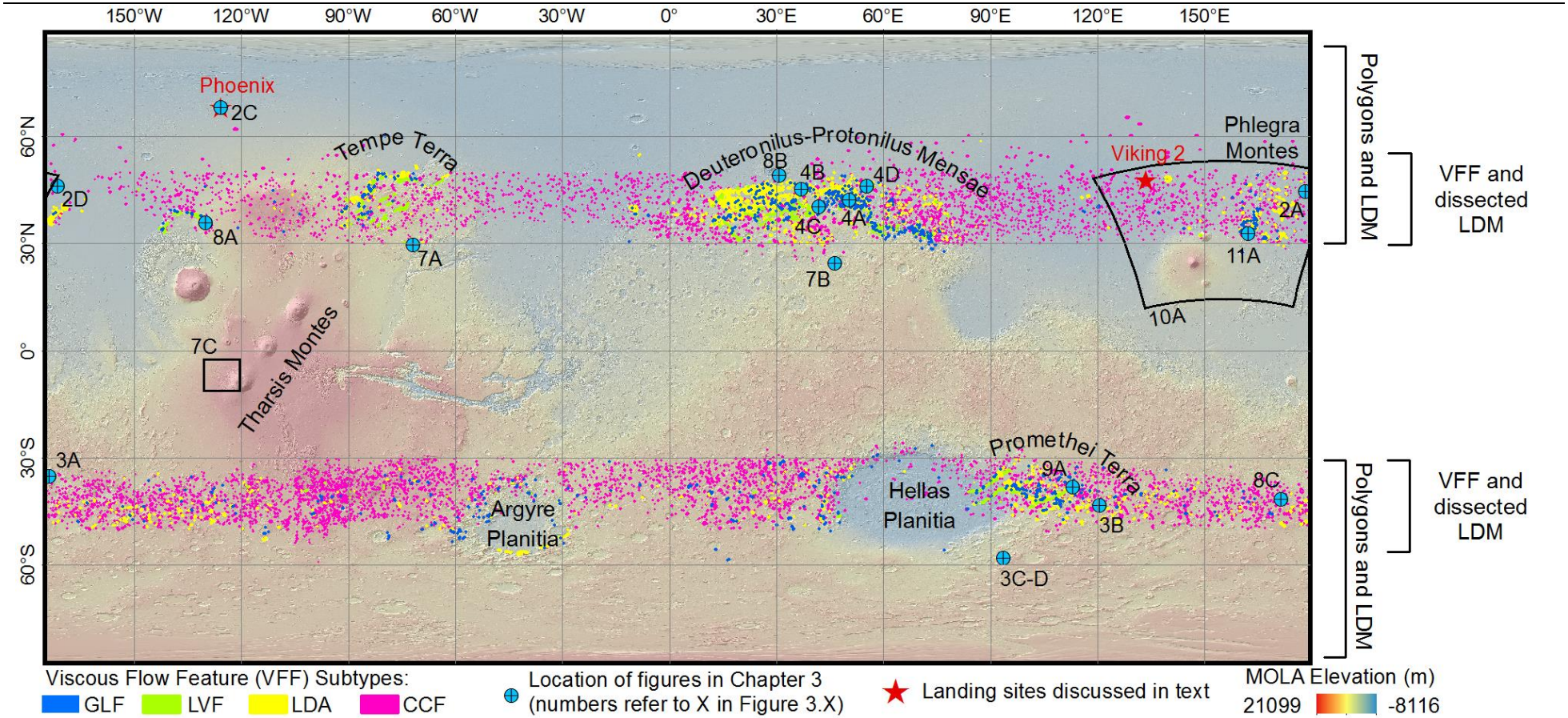

Figure 3.1. Global map of present-day non-polar ice reservoirs on Mars and related landforms discussed in Chapter 3. MOLA elevation map overlain on MOLA hillshade map, showing the distribution of lineated valley fill (LVF), lobate debris apron (LDA), and concentric crater fill (CCF) type viscous flow features (VFF; Section 3.4;) mapped by Levy et al. (2014), and glacier-like forms (GLF) mapped by Souness et al. (2012). Brackets on right show the approximate latitudinal distributions of the latitude-dependent mantle (LDM; Section 3.3) and ground ice-related polygons (Section 3.2.1). The extents of Figures 3.7C and 3.10A are outlined in black, and blue crossed points show locations of other figures in Chapter 3. Redrawn and adapted from Lasue et al. (2019). See Table 3.1 for data products.

Table 3.1. List of data products used in Chapter 3. Sources of figures taken or modified from published works are noted in the relevant figure captions and are not included here.

Instrument or Source	Image/Product ID	Figure
Mars Orbiter Laser Altimeter[1]	Global Elevation Model 463 m (MEGDR)[2]	3.1, 3.7C, 3.10A–D, 3.13
High Resolution Imaging Science Experiment[3]	PSP_001737_2250[4]	3.2A
	ESP_011494_2265 Merged RGB[4]	3.2D
	ESP_011365_1365[4]	3.3B
	ESP_040772_1215 Merged RGB[4]	3.3C–D
	ESP_019258_2225[4]	3.4A
	PSP_003243_1415[4]	3.9B–D
	ESP_044804_2130 (orthorectified)[5]	3.11B
Context Camera[6]	P08_003992_1469_XN_33S174W[7]	3.3A
	F13_040772_1217_XN_58S226W[7]	3.3C
	G02_018857_2226_XI_42N309W[7]	3.4A
	Mosaic[3] generated from images: F02_036382_2259_XN_45N322W and P17_007544_2247_XN_44N323W[7]	3.4B
	B17_016286_2204_XI_40N318W[7]	3.4C
	Mosaic[5] generated from images: G01_018448_2251_XI_45N303W, P19_008308_2265_XN_46N304W, B16_015969_2293_XI_49N304W[7]	3.4D
	B01_010185_2099_XN_29N071W[7]	3.7A
	G04_019622_2034_XN_23N313W[7]	3.7B
	P03_002289_1729_XI_07S123W[7]	3.7D
	P02_001933_2174_XN_37N130W[7]	3.8A

Table 3.1 continues on next page

Table 3.1 continued from previous page

Instrument or Source	Image/Product ID	Figure
Context Camera (continued)	B17_016339_2293_XN_49N329W[7]	3.8B
	P15_006933_1393_XN_40S188W[7]	3.8C
	G12_022745_1415_XN_38S246W[7]	3.9A
	Mosaic[5] generated from images: B05_011706_2116_XN_31N198W, G20_026224_2116_XN_31N196W, G23_027279_2132_XN_33N198W, P18_007935_2132_XN_33N197W, P22_009583_2132_XN_33N197W, P22_009794_2155_XI_35N198W[7]	3.11A–F
	P15_006730_1237_XI_56S043W	3.13D
	B11_013745_1037_XN_76S045W	3.13E
	Mosaic[5] generated from images: P17_007814_1773_XI_02S129W and P21_009251_1771_XI_02S128W[7]	3.14
Thermal Emission Imaging System[8–9]	THEMIS-IR Day Global Mosaic 100m v12[2]	3.10B, 3.10D
Levy et al. (2014)	Supplementary GIS dataset[10]	3.1
Souness et al. (2012)	Supplementary GLF database[11]	3.1
Personal communication	Crestline shapefile of the Dorsa Argentea eskers[12]	
	Crestline map of putative eskers in Argyre Planitia[13]	

[1] (Smith et al., 2001)
[2] United States Geological Survey Planetary GIS Web Server: http://webgis.wr.usgs.gov/pigwad/down/mars_dl.htm
[3] (McEwen et al., 2007)
[4] The University of Arizona https://hirise.lpl.arizona.edu/
[5] Generated by F. E. G. Butcher; [6] (Malin et al., 2007)
[7] Arizona State University http://viewer.mars.asu.edu/viewer/ctx#T=0
[8] (Christensen et al., 2004)
[9] (Edwards et al., 2011)
[10] Accessed on 10/08/2018 at: https://agupubs.onlinelibrary.wiley.com/doi/full/10.1002/2014JE004685
[11] Accessed on 10/05/2016 at: https://www.sciencedirect.com/science/article/pii/S0019103511004131#m0005
[12] Butcher et al. (2016); data available from the author
[13] Bernhardt et al. (2013); data provided by H. Bernhardt

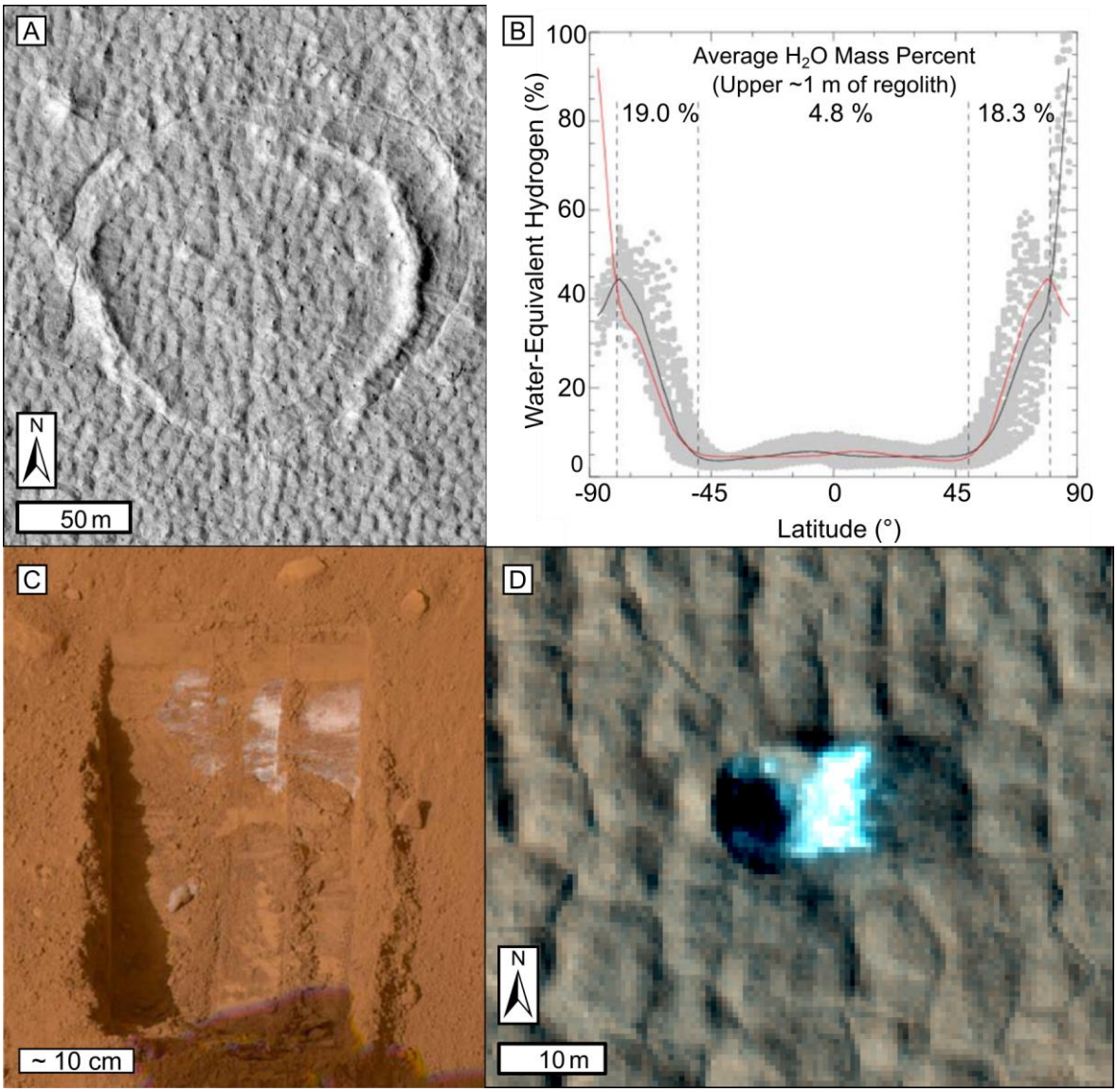

Figure 3.2. Evidence for near-surface ground ice in Mars' mid to high latitudes. (A) HiRISE image of thermal contraction crack polygons within a deposit that drapes topography (including an impact crater) in Arcadia Planitia. (B) Plot from Feldman et al. (2004) of latitudinal variations in the percentage of water-equivalent hydrogen in the upper ~1 m of Mars' regolith from Mars Odyssey Neutron Spectrometer epithermal neutron count rates. Grey points are derived for equal areas equivalent to 2° × 2° squares at the equator. The black line is the zonal average of points and the red line is the same curve flipped at the equator. Percentage values separated by grey dashed lines are the average mass percentage of water in the upper ~1 m of the regolith for the equatorial-to-mid-latitude and high-latitude regions. Non-polar deposits of bulk subsurface ice (see Sections 3.3 and 3.4) are deeper than the ~1 m detection depth for the instrument. (C) Excess near-surface water ice within a trench excavated by the Phoenix Lander. Adapted from Mellon et al. (2009). (D) HiRISE false colour image of water ice exhumed by a fresh ~0.4 m deep impact into polygonised terrain. Identified by Byrne et al. (2009; Site 5). See Figure 3.1 for locations and Table 3.1 for data products.

of polygonal patterned ground is well correlated with detections of hydrogen in the upper 1 m of Mars' regolith by the Mars Odyssey Neutron and Gamma-Ray Spectrometers (Mangold et al., 2004a), which have been interpreted as indicating the presence of extensive ground ice (Figure 3.2B; Boynton et al., 2002; Feldman et al., 2004). Additionally, Byrne et al. (2009) identified surface exposures of ground ice in the ejecta of small, fresh impact craters within polygonal patterned ground, which sublimated over the course of a few months following the impact event (Figure 3.2D). The Phoenix lander also made direct observations of ice-cemented soils and segregated ice lenses within shallow (~5 cm) trenches (Figure 3.2C) excavated into polygonal patterned ground at its landing site in the northern lowlands (68°N, 126°W; Mellon et al., 2009).

3.2.2. Massive Ice Deposits

Observations of Mars' surface via orbital remote sensing have also revealed the presence of massive non-polar water ice deposits in the near subsurface in Mars' mid to high latitudes (Figure 3.1). Massive ice deposits that far exceed the pore volume of the regolith cannot be explained by the same process of vapour diffusion that might have permitted formation of ground ice deposits (e.g., Boynton et al., 2002); hence their formation has been widely attributed to deposition from the atmosphere (e.g., as snowfall or frost) during excursions in Mars' spin-axis obliquity (Chapter 2), and subsequent burial by dust and/or debris (e.g., Mustard et al., 2001; Kreslavsky and Head, 2002; Head et al., 2003; Milliken et al., 2003; Head et al., 2006; Schon et al., 2009).

Extant non-polar ice-rich deposits on Mars can be broadly divided into two morphological categories associated with the two distinct configurations of mean planetary obliquity that have occurred in the last 20 Myr (Chapter 2): (1) a young (< 5 Ma), metres to hundreds of metres-thick (e.g., Conway and Balme, 2014; Dundas et al., 2018), ice-rich latitude-dependent mantle (LDM) in Mars' mid to high latitudes (30–70°N and 25–65°S; Mustard et al., 2001; Head et al., 2003), and older (> 5 Ma) viscous flow features (VFFs) that are morphologically similar to terrestrial glaciers (e.g., Milliken et al., 2003; Head et al., 2010; Souness et al., 2012) and occur exclusively in Mars' mid latitudes (± 30–60°; e.g., Squyres, 1979; Dickson et al., 2012; Souness et al., 2012; Levy et al., 2014)

3.3. Latitude-Dependent Mantle

The latitude-dependent mantle comprises smooth deposits with thicknesses of up to tens (e.g., Mouginot et al., 2010; Conway and Balme, 2014) to hundreds (e.g., Dundas et al., 2018) of metres that drape topography in Mars' high-latitude regions (Figures 3.1 and 3.3).

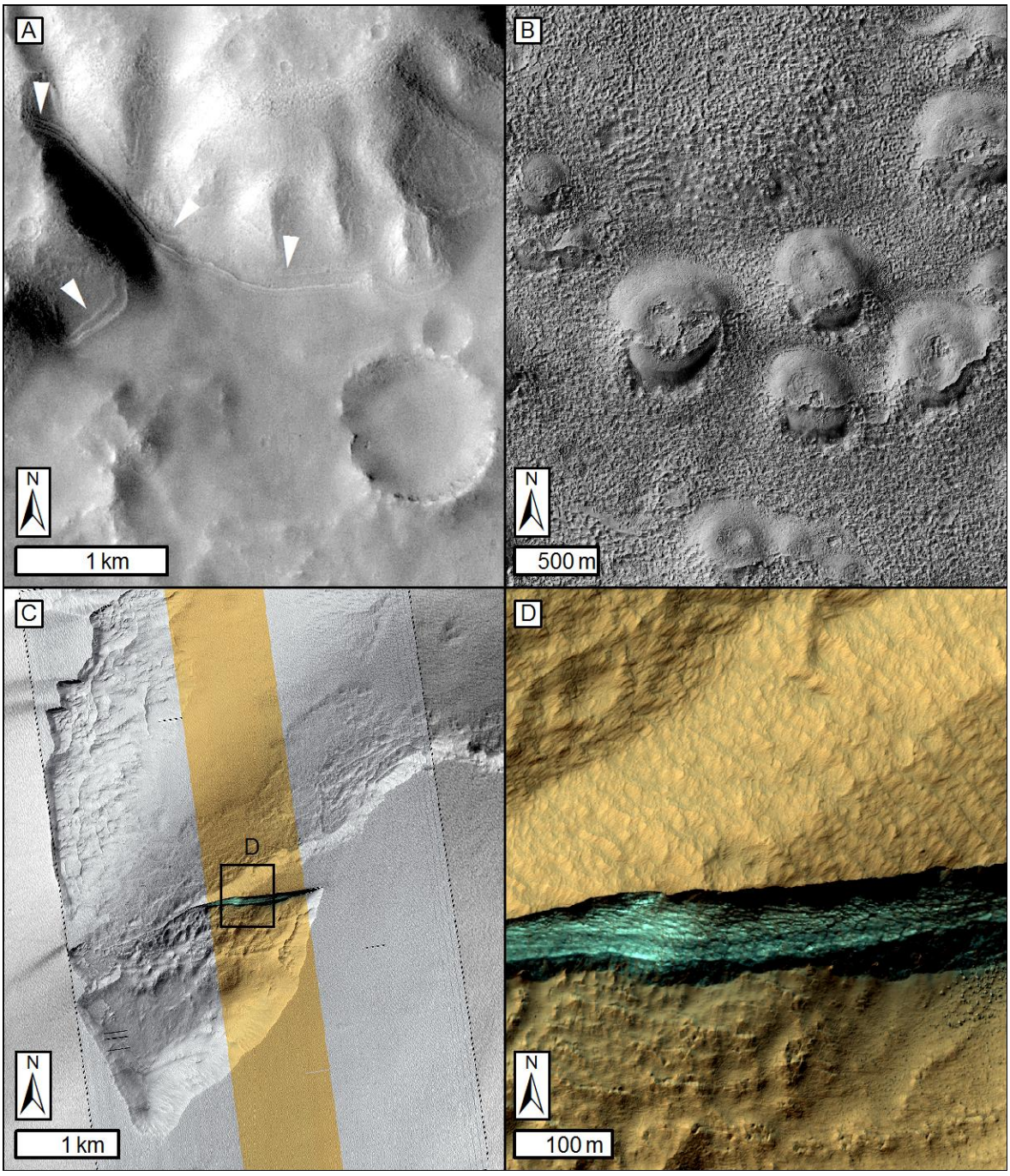

Figure 3.3. Features of the latitude-dependent mantle. (A) CTX image of layers (white arrows) in the margins of discontinuous latitude-dependent mantle in Terra Sirenum (35.1°S). The deposit drapes topography, including impact craters. (B) HiRISE image of dissected and pitted latitude-dependent mantle draping mounds in Promethei Terra (43.3°S). (C) CTX and HiRISE (including false colour) images showing exposed water ice (teal) within a scarp at the margins of a smooth mantle deposit in Promethei Terra (58.1°S). Black box shows extent of panel D, a closer view of the exposed ice (teal) within the scarp. Panels A and B are based on Head et al. (2003). Panels C and D are based on Dundas et al. (2018). See Figure 3.1 for figure locations, and Table 3.1 for data products.

The LDM provides near-continuous coverage at latitudes > ± ~55°, becomes increasingly thin and discontinuous in the mid latitudes (Figure 3.3A–B; ± ~25–55°), and is absent in equatorial regions (Figure 3.1; e.g., Mustard et al., 2001; Head et al., 2003). It covers approximately 23% of the surface of Mars (Kreslavsky and Head, 2002).

3.3.1. Ice Content of the LDM

Subsurface radar reflectors detected by the Mars Advanced Radar for Subsurface and Ionosphere Sounding (MARSIS) instrument onboard the Mars Express spacecraft indicate that the LDM comprises subsurface ice in volume fractions of 50–100%, covered by a surface layer of desiccated regolith that decreases in thickness (from metres to sub-metres thick) towards the poles (Mouginot et al., 2010). For example, recent radar sounding found evidence for an extensive (375,000 km^2), 80–170 m thick subsurface deposit that comprises ~50–80% water ice by volume (equating to 8400–14,300 km^3 ice) in western Utopia Planitia (centred on ~45°N). A similar deposit was discovered by Bramson et al. (2015) to extend between latitudes of 38–52°N in Arcadia Planitia.

Orbital observations have identified spectral evidence for exposures of massive ice within the LDM within mid-latitude ice cliffs with heights of ~100 m at the margins of LDM deposits (Figure 3.3C–D; Dundas et al., 2018). Dundas et al. (2018) suggest that the liberation of rocks from the ice cliffs indicates that they are actively receding at rates of a few millimetres per year. Typical estimates for the globally-integrated ice content of the LDM are ~3.6–3.9 × 10^5 km^3, equivalent to a ~2.5 m deep global layer of water (Levy et al., 2010b; Conway and Balme, 2014). Evidence for voluminous excess ice within the LDM supports its deposition via precipitation, as opposed to atmospheric vapour diffusion into the regolith (e.g., Head et al., 2003; Bramson et al., 2015; Stuurman et al., 2016).

3.3.2. Modelled Ages and Formation of the LDM

Modelled age determinations from impact crater size-frequency statistics (Kostama et al., 2006; Schon et al., 2012) support formation of large portions of the LDM between 0.1–2 Ma. This is consistent with the theorised mobilisation of ice from polar and/or equatorial reservoirs and its deposition at mid to high latitudes during multiple brief excursions to spin axis obliquities of 30–35° that occurred ~0.4–2.1 Ma (Figure 2.3; Chapter 2; Head et al., 2003; Levrard et al., 2007). Observations of the margins of LDM deposits revealed that it comprises multiple metres-thick layers (Figure 3.3A) that are consistent with such episodic LDM deposition events (Head et al., 2003; Schon et al., 2009).

Morphologies indicative of sublimation of ice contained within the LDM (e.g., pits, hummocks, and evidence for dissection of the deposit; see Figure 3.3B–C and e.g., Head et al., 2003; Malin and Edgett, 2000; Mustard et al., 2001; Schon et al., 2009) in the lower latitudes of its distribution (± ~30–55°; e.g., Mustard et al., 2001) indicate that at present spin-axis obliquity, the LDM is undergoing episodic latitude-dependent degradation (Head et al., 2003). During the low-obliquity intervals (~15–25°) that punctuated intermediate-obliquity (30–35°) excursions ~0.4–2.1 Ma, similar desiccation by sublimation of ice is likely to have occurred. Accumulation of a sublimation lag derived from dust in the LDM likely retarded, and possibly even halted, prolonged ice removal such that some of the initial ice content was preserved into each successive intermediate-obliquity accumulation episode. This process can explain the layered nature of the LDM (Schon et al., 2009). Formation of a low-porosity dust lag deposit atop the uppermost LDM deposits, and a relatively large accumulated ice volume, can explain why remnants of the LDM are observed equatorward of the lowest latitude of theorised perennial near-surface ice stability (~45°) in the present day. It is possible that insufficient time has passed to allow complete removal of ice from the LDM by diffusion, or that a low-porosity fine-grained dust lag could result in diffusive isolation of the deposit from the atmosphere (Head et al., 2003).

3.4. Mid-Latitude Glaciation

Mars' mid latitudes (± ~25–60°) host abundant landforms with morphologies that are consistent with extensive, present-day, topographically-controlled (i.e., valley-style) and piedmont-style glaciers (Figure 3.1; e.g., Sharp, 1973b; Carr and Schaber, 1977; Squyres, 1978, 1979; Lucchitta, 1981, 1984; Squyres and Carr, 1986; Pierce and Crown, 2003; Arfstrom and Hartmann, 2005; Head et al., 2010; Hubbard et al., 2011; Souness et al., 2012). The collective term for glacier-like landforms in Mars' mid latitudes is viscous flow features (Figure 3.4; Milliken et al., 2003; Head et al., 2010). In the present day, ice is seasonally or perennially unstable at the surface in Mars' mid latitudes (Chapter 2), so the presence of extant glacial ice necessitates the existence of lithic (i.e., fine-grained dust or debris) mantling deposits on the surfaces of VFFs that inhibit sublimation of ice to the atmosphere. Hence, it is widely thought that the closest terrestrial analogues for VFFs are debris-covered glaciers (Section 3.4.4; e.g., Holt et al., 2008; Plaut et al., 2009; Head et al., 2010; Petersen et al., 2018).

3.4.1. Morphology of Viscous Flow Features

VFFs occupy topographic lows and have surface morphologies (including parallel arcuate ridges and longitudinal ridges which divert around topography) that are suggestive of past

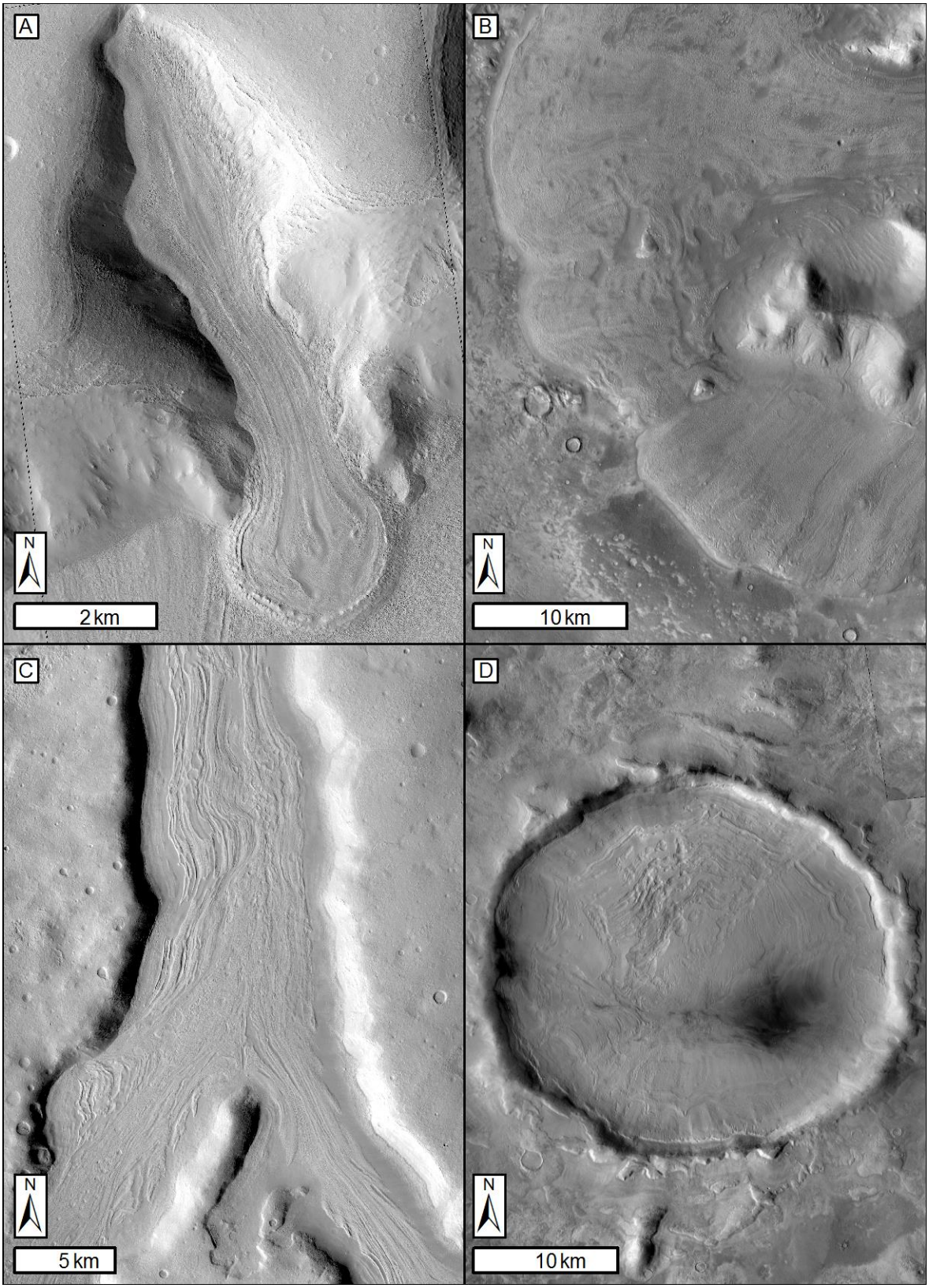

Figure 3.4. Viscous flow features and their morphological subtypes. (A) HiRISE image of a glacier-like form (GLF) in Protonilus Mensae. (B) Context Camera image mosaic of a lobate debris apron (LDA) complex extending from a mesa in Protonilus Mensae. (C) Context Camera image of lineated valley fill (LVF) in Deuteronilus Mensae. (D) Context Camera image of concentric crater fill (CCF) in Protonilus Mensae. See Figure 3.1 for image locations, and Table 3.1 for data products.

flow (e.g., Head et al., 2010). Common surface morphologies that support ice-rich compositions of VFFs include: (1) small (metre-scale) pits suggestive of ice loss and collapse of overlying debris-cover via sublimation, (2) polygons that suggest cryotic modification of ice-rich materials (Levy et al., 2009), and (3) impact craters with ring-mold morphologies, which have been attributed to impact penetration of subsurface interfaces between an upper layer of desiccated regolith and an underlying layer of near-pure water ice (Kress and Head, 2008).

VFFs have been categorised into four morphological subtypes (Figure 3.4): glacier-like forms (GLF; Milliken et al., 2003; Arfstrom and Hartmann, 2005; Souness et al., 2012) , lobate debris aprons (LDA; e.g., Squyres, 1979; Lucchitta, 1981, 1984; Pierce and Crown, 2003), lineated valley fill (LVF; e.g., Squyres, 1978, 1979; Kochel and Peake, 1984; Carr, 2001; Head et al., 2006), and concentric crater fill (CCF; Squyres, 1979; Head et al., 2005; Dickson et al., 2010, 2012).

3.4.1.1. Glacier-Like Forms

Glacier-like forms (Figure 3.4A) are elongate (typically < ~10 km long and < ~2 km wide; Souness et al., 2012), tongue-shaped features that commonly extend from theatre-headed alcoves on moderate to steep slopes. Typically, they are bounded by high topography at their headward and lateral margins, and by raised arcuate ridges at their termini that are morphologically similar to terminal moraine ridges (comprising material ploughed and/or deformed by the flow of glacial ice) on Earth (Milliken et al., 2003; Arfstrom and Hartmann, 2005; Hubbard et al., 2011; Souness et al., 2012).

3.4.1.2. Lobate Debris Aprons

Lobate debris aprons (Figure 3.4B) are unconstrained by lateral topography. They extend tens of kilometres across low-lying plains from the base of escarpments, and commonly surround isolated massifs and mesas, forming radial apron complexes (Squyres, 1979; Pierce and Crown, 2003). They have large width-height ratios, surface areas up to thousands of square kilometres, and thicknesses of up to hundreds of metres (Crown et al., 2002; Holt et al., 2008; Plaut et al., 2009; Parsons et al., 2011).

3.4.1.3. Lineated Valley Fill

Lineated valley fill (Figure 3.4C) occupies the floors of large (tens of kilometres wide and hundreds of kilometres long) valleys and troughs in Mars' mid latitudes. LVF surfaces host several morphologies that suggest past flow was dominated by down-valley (as opposed to valley-transverse; see Squyres, 1978, 1979; Carr, 2001) flow, including: (1) valley-parallel

lineations (Kochel and Peake, 1984), (2) valley-transverse arcuate ridges that point down-valley, (3) evidence for down-valley deflection of surface materials derived from mass wasting of confining valley walls, and (4) a lack of evidence for lateral flow deflection of trunk LVF where they cross the mouths of tributary valleys containing contributory valley fill (Lucchitta, 1984).

3.4.1.4. Concentric Crater Fill

Concentric crater fill (Figure 3.4D) is found on the floors of mid-latitude impact craters (e.g., Levy et al., 2010a; Dickson et al., 2012). At latitudes of ± ~45–60°, CCF commonly provides complete coverage of impact crater floors. In these regions, concentric ridges on CCF surfaces suggest past flow of material from all portions of the rims to the centres of their host craters. At lower mid latitudes (± ~25–45°), CCF deposits predominantly extend towards the interiors of their host impact craters only from their pole-facing walls, having similar appearances to lobate debris aprons (see Section 3.4.1.2; Dickson et al., 2012).

3.4.2. Distribution of Viscous Flow Features

Cumulatively, VFFs cover ~0.5% of Mars' surface area (Levy et al., 2014; Brough et al., 2019), and are concentrated almost exclusively at latitudes ~± 25–60° (Figure 3.1; Dickson et al., 2012; Souness et al., 2012; Levy et al., 2014). Concentric crater fill occurs throughout these latitude bands (Dickson et al., 2012; Levy et al., 2014), whereas glacier-like forms, lobate debris aprons and lineated valley fill cluster zonally in Deuteronilus Mensae, Protonilus Mensae, Tempe Terra, and Phlegra Montes of the northern hemisphere, and in the Promethei Terra and Charitum Montes regions of the southern hemisphere (Sharp, 1973a; Carr and Schaber, 1977; Squyres, 1978, 1979; Kochel and Peake, 1984; Milliken et al., 2003; Souness et al., 2012; Levy et al., 2014). In many locations, the morphological subtypes of VFFs co-exist and form integrated glacial landsystems (Head et al., 2010).

3.4.3. Modelled Ages of Viscous Flow Features

Estimates of the ages of VFFs from impact crater size-frequency statistics suggest that glacier-like forms have impact crater retention ages of a few million years (Hepburn et al., 2018) to tens of millions of years (Arfstrom and Hartmann, 2005; Hartmann et al., 2014), while the other VFF subtypes (lobate debris aprons, lineated valley fill and concentric crater fill) have older impact crater retention ages between hundreds of millions of years and ~1 Gyr (Levy et al., 2007; Berman et al., 2012; Baker and Head, 2015; Gallagher and Balme, 2015; Butcher et al., 2017; Baker and Carter, 2019a). Such age differences are supported by morphological evidence for superposition of glacier-like forms upon other VFF subtypes

downslope in many locations (e.g., Levy et al., 2007; Baker et al., 2010; Brough et al., 2015; Hepburn et al., 2018).

Impact crater retention ages for small, young (or recently modified) features on Mars rely on small impact crater count areas (and hence the statistics of small numbers; Warner et al., 2015), and on population statistics for small-diameter impact craters that commonly represent secondary impacts (Hartmann, 2005). These factors, combined with evidence for flow deformation and mantling of the surfaces of VFFs (and hence potential destruction of older craters; Baker and Carter, 2019a) introduce significant uncertainty into age determinations; secondary craters would return older modelled ages than the true age, while reliance on small count areas that may have been deformed or mantled would return younger modelled ages than the true age (Hartmann, 2005; Warner et al., 2015; Baker and Carter, 2019a). However, consistent ages (within a few tens to hundreds of millions of years) between independent studies of VFFs in multiple locations on Mars give confidence in their origins during the mid to late Amazonian (Hartmann, 2005; Tanaka et al., 2014a).

3.4.4. Composition and Formation of Viscous Flow Features

Early hypotheses developed from Mariner 9 and Viking orbiter images proposed that VFFs formed by creep of ice-rich regolith, and that pore ice in volumes < 30% was emplaced by atmospheric vapour diffusion (rock glacier model; Squyres, 1979, 1978; Squyres and Carr, 1986; Pierce and Crown, 2003). Since this time, numerous studies employing metre- to sub-metre resolution image and elevation data, and orbital radar sounding instruments, have found substantial evidence to corroborate an alternative debris-covered glacier model (e.g., Head et al., 2006; Holt et al., 2008; Plaut et al., 2009; Head et al., 2010; Baker et al., 2010; Dickson et al., 2010; Hubbard et al., 2011; Petersen et al., 2018) that was first considered by Luchitta (1984). Subsurface radar reflection and power loss data from SHARAD indicate the presence of nearly pure (~80–90%) water ice within lobate debris aprons throughout Deuteronilus Mensae (Plaut et al., 2009; Petersen et al., 2018), and the small number of lobate debris aprons in Promethei Terra for which radar data have been analysed (Holt et al., 2008). Reflectors representing the interface between bulk water ice and lithic mantling deposits, which are required to allow stability of ice at these latitudes, have not been detected by radar sounding techniques; thus, it is thought that the thickness of the debris cover atop VFFs is similar to or less than the 10 m vertical resolution of the SHARAD instrument (Holt et al., 2008; Plaut et al., 2009; Petersen et al., 2018).

It should be noted that, while the debris-covered glacier model is widely accepted, some workers consider ice-assisted mobilisation of the regolith under the rock glacier model to be

a plausible explanation for the formation of VFFs (van Gasselt et al., 2011, 2010). They cite difficulties in explaining the transport of a ubiquitous debris cover over VFF surfaces, and alternative wall-rock mass-wasting or aeolian deposition mechanisms by which observed surface morphologies could form (van Gasselt et al., 2010, 2011). However, they do not dispute radar evidence (Holt et al., 2008; Plaut et al., 2009) for the presence of massive buried ice, and recent expansion of the number of features within which massive subsurface ice has been detected (Petersen et al., 2018) refutes their suggestion that features containing massive buried ice deposits could be rare exceptions within a population dominated by rock glaciers (van Gasselt et al., 2011). Considering the abundance of evidence that has accumulated in support of the debris-covered glacier model, and new evidence for glacial landforms associated with VFFs identified in the present thesis (see also Butcher et al., 2017), I consider the debris-covered glacier model to be the stronger working hypothesis.

Assuming 90% ice content for VFFs, Levy et al. (2014) estimate that lobate debris apron, lineated valley fill and concentric crater fill comprise a globally-integrated ice volume of 3.74×10^5 km^3, and Brough et al. (2019) estimate that the smaller glacier-like forms comprise a globally-integrated ice volume of 1.57 km^3. This equates to mid-latitude glacial ice volumes ~10% of the combined volume of Mars' polar caps (Levy et al., 2014). According to these estimates, mid-latitude glaciers on Mars may contain ice volumes that exceed the cumulative volume of all glaciers on Earth, excluding the Greenland and Antarctic ice sheets (Levy et al., 2014).

The observations of the morphologies, dielectric properties, distributions, and impact crater retention ages of VFFs, summarised above, are consistent with theoretical models concerning the redistribution of water ice to non-polar reservoirs under recent obliquity-driven climate changes on Mars (Section 2.4; see also Madeleine et al., 2009). Substantial evidence exists for mid-latitude VFFs having bulk water ice compositions, which in turn suggests that they formed by precipitation-driven accumulation of ice, and that lithic mantling deposits were inherited after the major phase of ice accumulation due to: (a) rock falls from the valley walls, (b) release of debris from sublimating ice, and/or (c) atmospheric dust deposition (Section 3.4.5; Baker and Head, 2015). The observed latitudinal and zonal distributions of VFFs (Figure 3.1; Souness et al., 2012; Levy et al., 2014) provide a good match to modelled regions of net ice accumulation under intermediate (~35°) spin-axis obliquities (Madeleine et al., 2009), and impact crater retention ages are consistent with their formation prior to the shift in mean obliquity (from ~35° to ~25°) ~4–6 Ma (see Section 2.4; Laskar et al., 2004). Younger ages of glacier-like forms (~tens of millions of years)

compared to other VFF subtypes (hundreds of millions of years) suggests that they represent late-stage ice advance shortly before the termination of major ice accumulation in Mars' mid latitudes (Baker et al., 2010; Brough et al., 2015; Hepburn et al., 2018; Jawin et al., 2018). Inferred mantling of VFFs by lithic deposits permits preservation of massive glacial ice in Mars' mid latitudes in the present day, despite instability of ice at the surface arising from the present low spin-axis obliquity (e.g., Farmer and Doms, 1979; Fanale et al., 1986; Squyres et al., 1992).

3.4.5. Ice-Rich Mantling of Viscous Flow Features

The latitudinal distributions of VFFs (mid latitudes; Figure 3.1) and the latitude-dependent mantle (mid to high latitudes; Figure 3.1) overlap (e.g., Mustard et al., 2001; Head et al., 2003; Levy et al., 2014). As such, the inferred stratigraphy of VFFs in the higher latitudes of their distribution (Figure 3.5) is somewhat more complex than the simple two-layer debris-covered glacier model described above. Where the LDM is relatively continuous (> ± ~55°), it is thought to provide near-ubiquitous coverage of older VFFs to depths of up to a few metres.

At latitudes equatorward of ~± 55°, dissection of the LDM reveals portions underlying VFFs. Previous workers have identified evidence for older (hundreds Myr old), decametres-thick, layered ice-rich mantling deposits (termed upper plains) that superpose VFFs at latitudes ~40–45°N in Deuteronilus Mensae (Carr, 2001; Mangold, 2003; Baker and Head, 2015; Baker and Carter, 2019b). The upper plains are thought to comprise ice-rich dust deposited via airfall during high-obliquity excursions following accumulation of VFFs during the mid to late Amazonian (Baker and Head, 2015; Baker and Carter, 2019b). The upper plains provide evidence that latitude-dependent deposition of ice-rich mantles has occurred throughout the mid to late Amazonian, and that the < 10 Myr old latitude-dependent mantle represents only the most recent (and possibly shorter) cycles of such mantle deposition (Baker and Head, 2015; Baker and Carter, 2019b).

It is thought fractures, ridges and furrows in upper plains materials were inherited from flow lineations on the surfaces of underlying VFFs via settling, fracturing, and a limited amount of ice creep within the mantling deposit (Mangold, 2003; Baker and Head, 2015; Baker and Carter, 2019a, 2019b). It should be noted that it is not yet known whether the upper plains unit occurs on the surfaces of VFFs beyond the Deuteronilus Mensae region.

Surface thermal inertia measurements and high-resolution observations of exposed, boulder-rich flow lines on VFFs equatorward of ~45°N in Deuteronilus Mensae are interpreted as

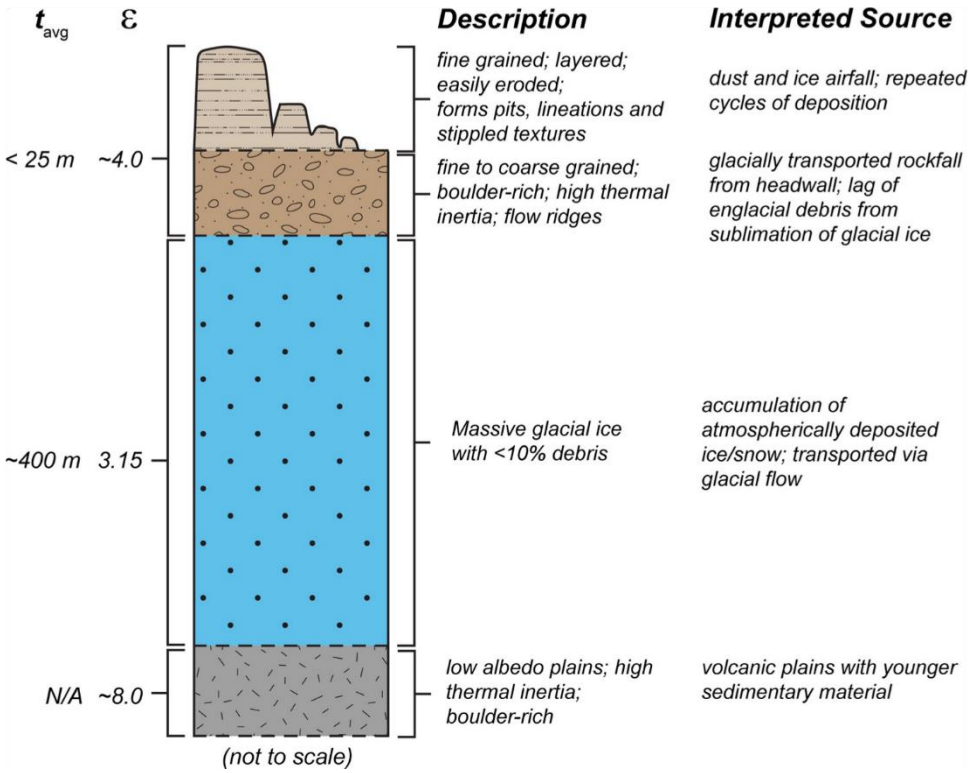

Figure 3.5. Schematic of the internal stratigraphy of viscous flow features in Deuteronilus Mensae, Mars. The uppermost layer represents hundreds Myr old upper plains mantle that superposes VFF in the Deuteronilus Mensae region. It is not known whether this unit superposes VFF in other regions, and it may be absent for VFF with younger ages than those in Deuteronilus Mensae. In some locations the upper plains mantle is superposed by younger, typically thinner latitude-dependent mantle with a similar origin (Baker and Carter, 2019b). In the lowest latitudes of VFF distributions in Deuteronilus Mensae the upper plains unit is absent. t_{avg} is average inferred layer thickness, and ε is dielectric permittivity. From Baker and Carter (2019b).

evidence that ice-rich mantling deposits, including the upper plains and latitude-dependent mantle, are < 1 m thick, or absent towards the lower latitudes (~25–45°N) of VFF distributions in the northern hemisphere (Baker and Carter, 2019b). In these zones, rockfall and sublimation-derived lithic debris that protects glacial ice within VFFs is exposed at the surface.

3.4.6. Viscous Flow Features as Remnants of Mid-Latitude Ice Sheets?

Morphological evidence of deflation and retreat of VFFs (e.g., trimlines, sequences of recessional moraine-like ridges, sublimation pits, evidence for flow reversals, and perched VFFs; Levy et al., 2009; Brough et al., 2016; Dickson et al., 2008, 2010) indicates that, while debris-cover has slowed ice loss under recent low obliquity conditions, VFFs have undergone significant sublimation-driven degradation since glacial maximum, particularly in the lowest latitudes of their distributions (Brough et al., 2016).

Debate surrounding the former extent and thickness of mid-latitude glaciers on Mars at glacial maximum can be summarised by three hypotheses. Briefly, the first hypothesis is that

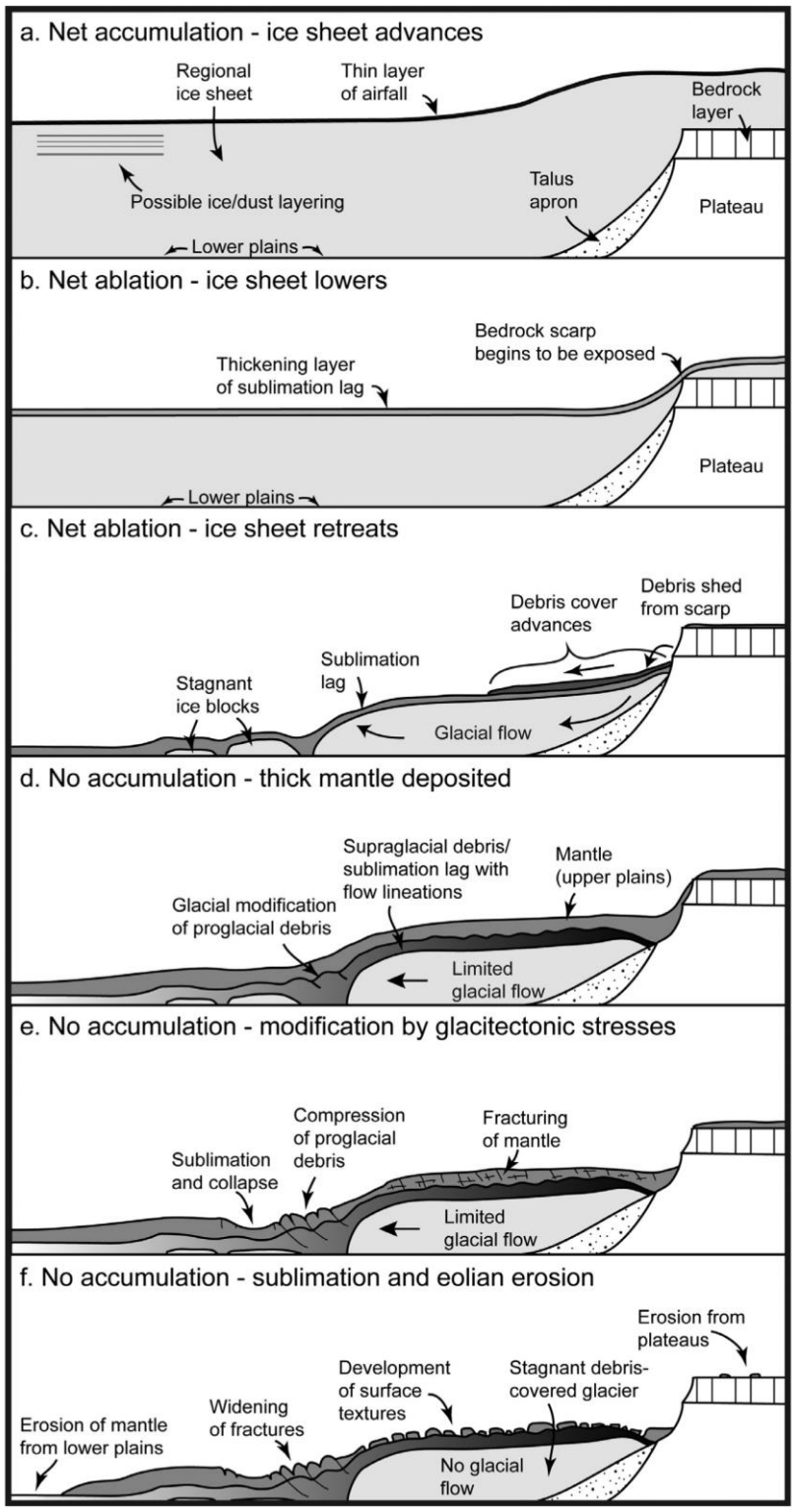

Figure 3.6. Schematic of the collapsed ice sheet model for the formation of viscous flow features. The final stratigraphy (panel F) is the same as that in Figure 3.5. The model is based upon lobate debris aprons in Deuteronilus Mensae. (A) A regional ice sheet covers topography and small amounts of debris are deposited on its surface via airfall. (B) Sublimation of the ice sheet liberates small amounts of internal debris, forming a thin sublimation lag. (C) The ice sheet surface lowers to below the elevation of bedrock plateaus. Rockfall delivers debris to glacier surfaces. Local topography controls glacier flow and flow textures develop within the debris layer. (D) The upper plains mantle unit is deposited via airfall of ice and dust. (E) Glacier flow encourages fracturing and glaciotectonism of the mantle and debris cover layers. (F). Glacier flow ceases and sublimation drives mantle erosion, widening surface fractures. From Baker and Head (2015).

mid-latitude glacial maximum was characterised by topographically-controlled valley- and crater-style glaciation similar to the configuration of VFFs observed today (Baker et al., 2010; Parsons et al., 2011; Brough et al., 2016). The second hypothesis is that mid-latitude glaciation maximum was characterised by unconfined, ice sheet and plateau glaciation, and that subsequent thinning and retreat isolated individual VFFs. Newly isolated VFFs then inherited debris cover as down-wasting ice exposed high terrain, and flowed under the influence of local topography (Figure 3.6; Dickson et al., 2008; Madeleine et al., 2009; Dickson et al., 2010; Fastook et al., 2014; Baker and Head, 2015).

The third hypothesis involves a latitudinal transition from valley- and crater-style glaciation in the ± ~25–45° latitude bands, to more extensive ice sheet style glaciation in the ± ~45–60° latitude bands (Dickson et al., 2012). This hypothesis is intermediate between the two end-member hypotheses described above, and can explain the latitudinal transition between crater-filling and pole-facing concentric crater fill morphologies identified by Dickson et al. (2012). This hypothesis can also account for observations in higher mid-latitude regions of evidence for deflation-driven flow reversals of VFFs (Dickson et al., 2008), and past overtopping of confining topography by glacial ice (Dickson et al., 2010). Dickson et al. (2008, 2010) suggest that such morphologies require the former presence of kilometre-thick ice deposits in these regions.

3.5. Equatorial Glaciation during the Amazonian Period

Prior to the step-change at ~4–6 Ma (Chapter 2), Mars' mean spin-axis obliquity was 35°, with excursions of about ± 15° (Laskar et al., 2004). Global climate modelling experiments find that, given spin-axis obliquities of ~45°, ice would preferentially accumulate in Mars' equatorial regions (~30°N–30°S ; Forget et al., 2006). Consistent with these predictions, geomorphic observations suggest that glaciation of Mars' equatorial regions has occurred during the Amazonian period.

In some locations, equatorial glaciation was similar in nature to that recorded by mid-latitude VFFs. Shean (2010) identified relict deposits within steep-sided craters in Sinus Sabaeus (~5–11°S) that are morphologically similar to concentric crater fill-type VFFs in Mars' mid-latitudes (Figure 3.7B). Similarly, Hauber et al. (2008) identified moat-like features that surround mesas and trace the base of escarpments in Kasei Vallis (~25–30°N; Figure 3.7A). They interpreted these moats as negative-relief imprints of former lobate debris aprons that retreated when, or after, Amazonian lava flows came into contact with their outer margins ~1 Ga (Hauber et al., 2008).

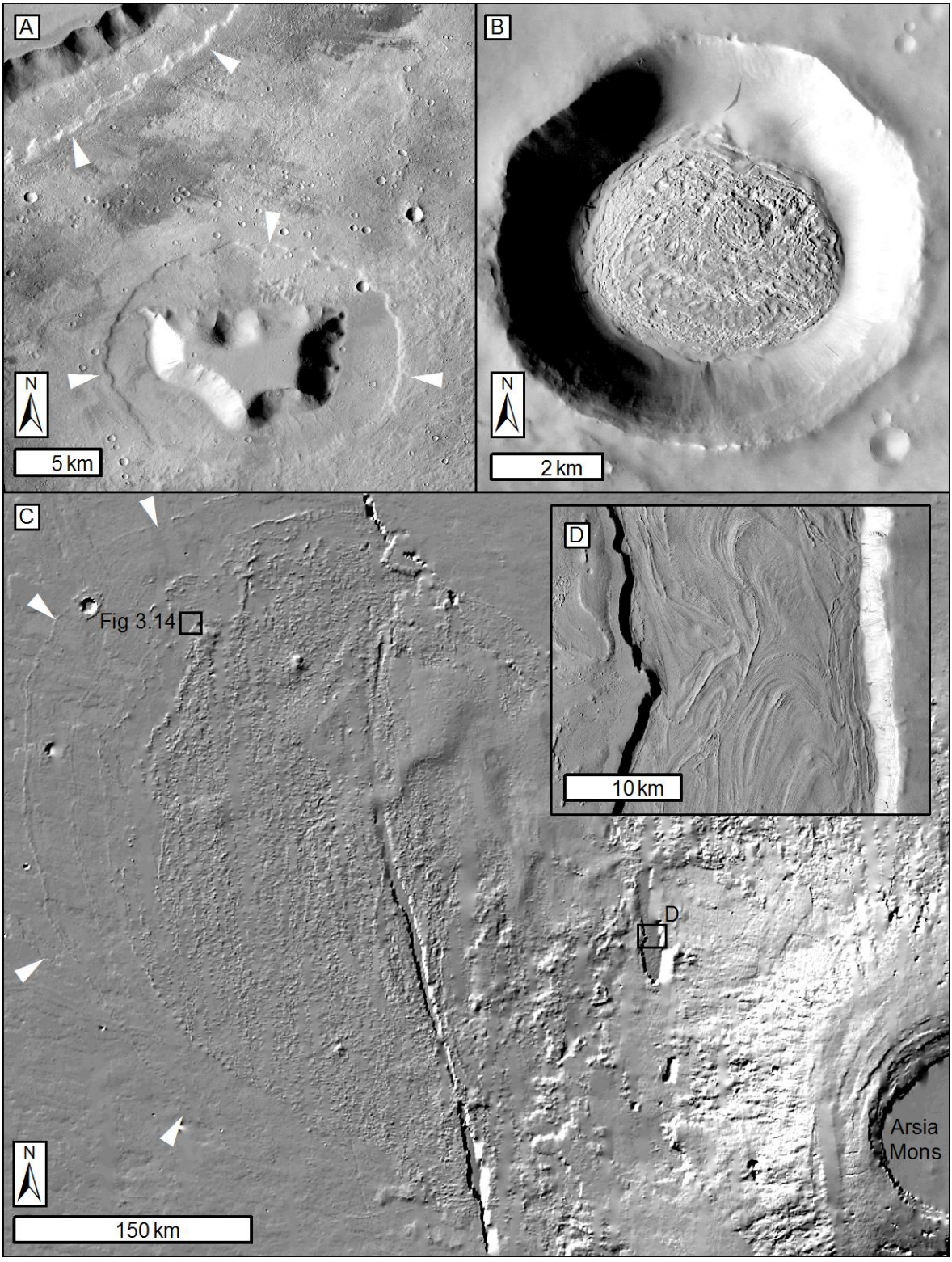

Figure 3.7. Evidence for glaciation of Mars' equatorial regions during the mid to late Amazonian. (A) CTX image of depressions (white arrows) at the base of mesas and scarps in northern Kasei Valles (29.6°N), which Hauber et al. (2008) interpret as imprints of former (~1 Ga) lobate debris aprons. (B) CTX image of relict concentric crater fill-like deposits identified by Shean (2010) in eastern Arabia Terra (24.5°N). (C) MOLA hillshade map of a fan-shaped deposit (6.6°S) on the NW flank of Arsia Mons. White arrows indicate outermost concentric ridges which formed ~725 Ma (Kadish et al., 2014). Black box shows extent of (D), a CTX image of ~65 Myr old graben fill interpreted as glacial in origin by Shean et al. (2007). See Figure 3.1 for image locations, and Table 3.1 for data products.

However, it is thought that perhaps the most substantial accumulations of glacial ice in Mars' equatorial regions during the Amazonian occurred on the flanks of large equatorial volcanoes, including the Tharsis Montes (Forget et al., 2006). Extensive (up to 166,000 km^2 per deposit) fan-shaped deposits, which comprise prominent concentric ridges, extend from the NW flanks of Olympus Mons, Ascraeus Mons (Figure 3.7C), Pavonis Mons, and Arsia Mons (Head and Marchant, 2003; Head et al., 2005; Shean et al., 2005, 2007; Kadish et al., 2008; Scanlon et al., 2014, 2015). Geomorphic interpretations of these deposits as drop moraines deposited by large, cold-based, ~1.6–2.4 km thick piedmont-style glaciers are consistent with global climate modelling experiments, which predict foci of ice accumulation in these locations due to orographic forcing of air flow, and atmospheric condensation and precipitation under high (45°) obliquity conditions (Head and Marchant, 2003; Head et al., 2005; Shean et al., 2005; Forget et al., 2006; Shean et al., 2007; Kadish et al., 2008; Fastook et al., 2008). Estimates of former ice thicknesses suggest that the parent glaciers of the fan-shaped deposits on the Tharsis Montes had a combined volume equivalent to ~13–19% of Mars' present polar caps (Shean et al., 2005). Smooth, lobate landforms that appear to be restricted to high-altitude zones within the fan-shaped deposits (Figure 3.7D) have been posited as evidence for the continued presence of small volumes of extant ice in these regions (Shean et al., 2007).

Age determinations from impact crater size-frequency distributions on the Tharsis Montes fan-shaped deposits suggest that glaciation of the equatorial volcanoes occurred during the mid to late Amazonian. The major phases of glaciation are thought to have occurred ~725–130 Ma (Shean et al., 2005; Kadish et al., 2008, 2014); the last phase of small-scale ice advance at high altitudes within these regions occurred ~65 Ma (Shean et al., 2007). Thus, the equatorial fan-shaped deposits may represent the locations of former ice reservoirs from which ice within extant VFFs (Section 3.4) was sourced during cyclical fluctuations from high- to intermediate-spin-axis obliquity (Madeleine et al., 2009).

3.6. Glacier Thermal Regimes during the Amazonian

3.6.1. A Present-Day Subglacial Lake beneath Mars' South Polar Ice Cap?

New insights from the MARSIS instrument revealed evidence for bright basal reflectors beneath Mars' south polar ice cap that have been interpreted as consistent with the presence of a > 1 m deep subglacial lake or water-saturated sediments over a ~20 km wide area of the bed (193°E, 81°S; Orosei et al., 2018). Production of meltwater at the bed of the south polar ice cap, which is thought to have a basal temperature (~205 K) far below the melting point of pure water requires depression of the melting point in the presence of salts (Orosei et al.,

2018). This is the only location in which possible evidence for present-day liquid water has been observed in association with glacial ice on Mars.

3.6.2. Cold-Based Glaciation during the Amazonian

Given extremely cold climate conditions on Mars in the present day, it is widely accepted that existing non-polar ice deposits on Mars, which are significantly thinner than the south polar cap discussed above, are cold-based, i.e., that they are perennially frozen to their beds and do not produce meltwater (e.g., Hubbard et al., 2014). Given that climatic conditions throughout the Amazonian are thought to have been similarly cold to the present day, it is also thought that the vast majority of Amazonian glaciers, including extant VFFs, have always had cold-based thermal regimes (e.g., Levy et al., 2016).

In the absence of basal meltwater, and associated lubrication-enhanced basal sliding and/or meltwater-driven basal pressure fluctuations, cold-based glaciers on Earth have limited capabilities to erode and modify the landscapes over which they advance. Average rates of cold-based glacier erosion are ~1–3 m Myr^{-1} (Cuffey et al., 2000). In contrast, wet-based glaciers (which produce meltwater via melting of basal ice) mobilise sediment at rates on the order of 10–1000 m Myr^{-1}, which exceed those measured for other erosional processes over similar timescales (Hallet et al., 1996). Wet-based glaciers commonly produce suites of streamlined and/or flow transverse landforms such as drumlins and glacial lineations formed by deformation and/or erosion of the glacier bed (see Benn and Evans, 2010 for a comprehensive review).

Levy et al. (2016) quantified erosion rates associated with lobate debris apron, lineated valley fill, and concentric crater fill-type VFFs in Mars' mid-latitudes by comparing: (1) the volume of debris cover over the surfaces of these features (assuming ubiquitous, 10 m thick debris cover over the surface areas of the features; see Section 3.4.4), (2) the erodible surface area of scarps surrounding them, and (3) the maximum and minimum durations of mid-latitude glaciation predicted by impact crater counting (Fassett et al., 2014) and climate modelling studies (Fastook et al., 2014). They found that average erosion rates associated with these VFF subtypes are on the order of 10^{-2}–10^{1} m Myr^{-1}, and are therefore comparable to typical erosion rates associated with cold-based glaciation on Earth (Levy et al., 2016). In combination with a lack of observed streamlined landforms in the forelands of lobate debris apron, lineated valley fill and concentric crater fill deposits, this provides support for the prevailing view that mid- to late-Amazonian glaciation on Mars has been dominated by cold-based glacier thermal regimes.

3.6.3. Wet-Based Glaciation during the Amazonian

Despite extremely cold Amazonian climate conditions and low average planetary geothermal heat flux, there are a handful of locations in which landforms associated with mid-latitude VFFs on Mars appear to record extremely rare, localised meltwater production by existing glaciers, either by supraglacial runoff (which can occur atop cold-based glaciers), or by subglacial melting under wet-based glacial regimes.

3.6.3.1. Supraglacial and Proglacial Fluvial Valleys

Fassett et al. (2010) provided evidence (in the form of small fluvial valleys with widths of tens to hundreds of metres and lengths < 10 km) for the past flow of small volumes of meltwater over the surfaces (Figure 3.8A) and into the forelands of some VFFs, but attributed meltwater generation to focussing of insolation onto the surfaces of VFFs by adjacent valley walls, rather than basal melting under wet-based glacier thermal regimes. Similar small (i.e., a few kilometres long) fluvial valleys (Figure 3.8C), and associated fan-shaped deposits (alluvial fans or deltas), were also identified by Adeli et al. (2016) in Terra Cimmeria (38°S, 175°E), in association with small patches of material that they interpret as being ice-rich. They attribute valley and fan formation to melting of these hypothesised ice deposits ~0.51–1.8 Ga, and consider climatic, geothermal and/or volcanic heat sources to be possible drivers of valley-forming meltwater production. They favour transient, possibly catastrophic drainage (on the order of days to thousands of days) to explain formation of these features (Adeli et al., 2016). However, it is not known if the hypothesised ice-rich deposits are remnants of past glaciers, and therefore if valley formation in Terra Cimmeria resulted from ground ice melting, snowpack melting, supraglacial runoff, and/or wet-based glaciation.

Dickson et al. (2009) identified fluvial valleys that extend from extant lobate debris apron-type VFFs and associated ice-rich mantle deposits within the Amazonian-aged (3.3–1.6 Gyr old) Lyot impact crater (Figure 3.8B). The floor of Lyot crater is the lowest elevation location in Mars' northern hemisphere and maximum annual surface pressures (>10 mbar) exceed the triple point of water in the present day (Haberle et al., 2001). Thus, Dickson et al. (2009) attribute fluvial valley formation to melting, either of the extant lobate debris aprons, or of older (~1.5 Gyr old) ice rich mantling deposits, under unique Amazonian microclimates afforded by Lyot crater's low altitude and high surface pressure. Formation of proglacial valleys in Lyot crater, however, does not necessitate past wet-based glaciation in this location. Melting within ice-rich mantling deposits superposed by the lobate debris aprons, or supraglacial runoff from the lobate debris aprons could explain valley formation

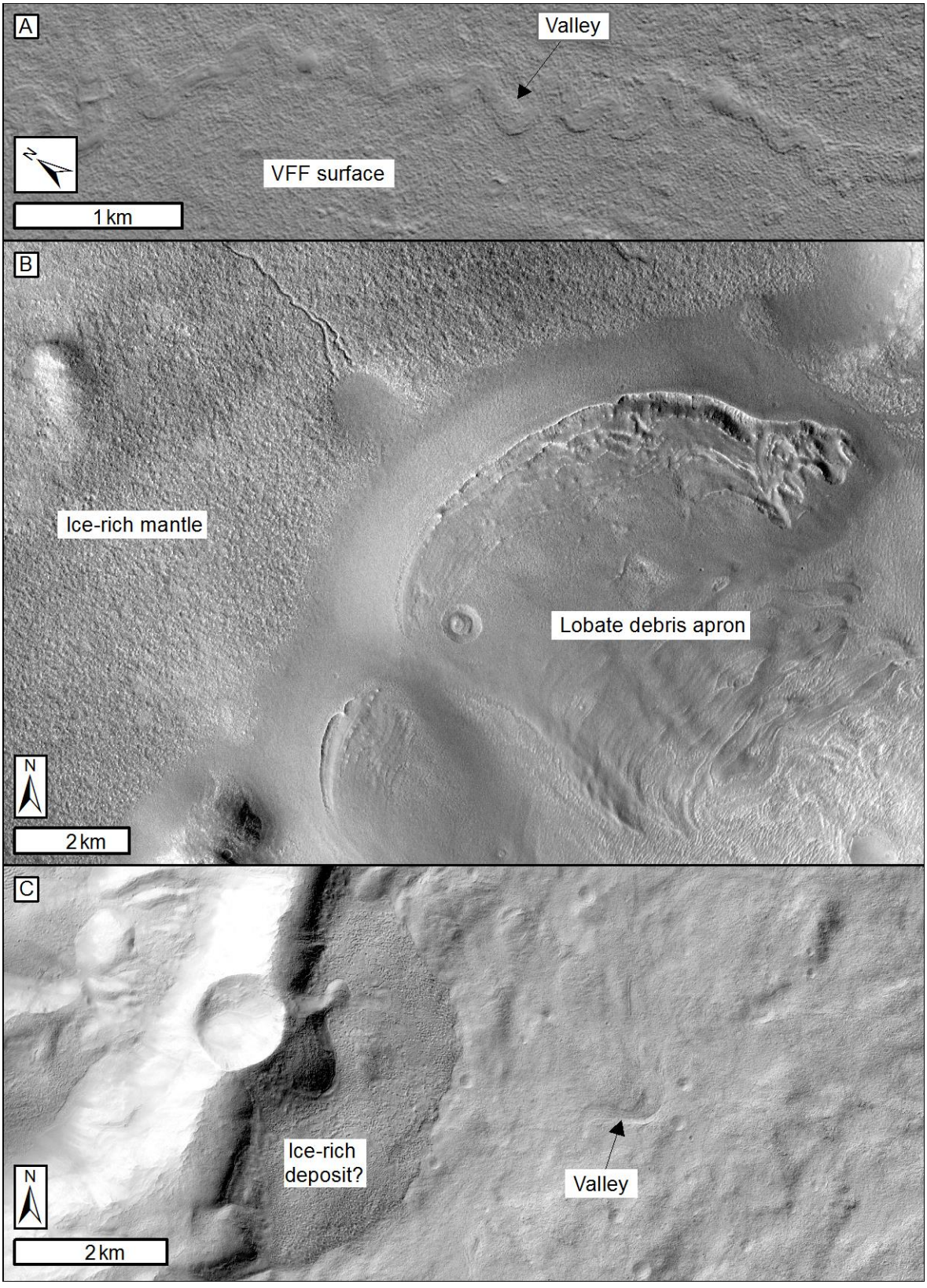

Figure 3.8. Small valleys associated with extant ice-rich deposits in Mars' mid latitudes. (A) CTX image of a valley identified by Fassett et al. (2010) on the surface of lineated valley fill in Archeron Fossae. (B) CTX image of valleys identified by Dickson et al. (2009) within a 1.5 Gyr old ice-rich mantle deposits in the proglacial zone of a lobate debris apron in Lyot crater. (C) CTX image of a small valley proximal to a deposit in Terra Cimmeria interpreted by Adeli et al. (2016) as being ice rich. See Figure 3.1 for image locations and Table 3.1 for data products.

in Lyot crater without the requirement to invoke wet-based glaciation. Hence, it is possible that the microclimate-induced, meltwater-generating warm wave(s) did not penetrate to the base of the lobate debris aprons in Lyot crater, and that these glaciers remained cold-based throughout valley formation.

The case studies described above highlight some challenges for using fluvial valleys to assess the involvement of meltwater in glaciation on Mars. Fluvial valleys and associated landforms (e.g., alluvial fans and deltas) can be formed by flows from non-glacial water sources (including precipitation, groundwater floods, and melting of ground ice or snowpacks), and by supraglacial meltwater flowing over cold-based ice. They do not necessitate the past occurrence of wet-based glaciation. Fluvial valleys incised into the surfaces of extant glaciers (Fassett et al., 2010) provide strong evidence for past meltwater production by mid-latitude VFFs on Mars, but only in small volumes derived from localised portions of the surface. Fluvial valleys that emerge from beneath extant glaciers (Dickson et al., 2009; Fassett et al., 2010) or remnant patches of hypothesised ice deposits (Adeli et al., 2016) could represent past meltwater discharge from wet-based glacial ice, but could also be explained by pre-glacial flows of liquid water derived from other sources (Dickson et al., 2009; Adeli et al., 2016).

3.6.3.2. Streamlined Glacial Landforms

As noted above, at the scale of 6 m/pixel resolution CTX images, streamlined glacial landforms produced by wet-based glaciers on Earth are notably absent in the vicinity of lobate debris apron, lineated valley fill, and concentric crater fill deposits. However, using HiRISE images, Hubbard et al. (2011) identified a suite of streamlined landforms associated with a single glacier-like form-type VFF in Greg crater, which they suggest could represent past deformation of bed sediments by wet-based ice. The streamlined landforms are located upslope of a pronounced tongue-shaped ridge complex interpreted as terminal moraine deposits (Figure 3.9A), and downslope of polygonised deposits interpreted as relict debris-covered glacial ice (Figure 3.9B). The landforms include subparallel ridges (Figure 3.9C) interpreted as megascale glacial lineations, and mound-and-tail terrains (Figure 3.9D) whose closest analogues on Earth could be drumlins (Hubbard et al., 2011). On Earth, both landforms require wet-based glaciation to form, though they are typically larger in scale than the landforms in Greg crater. Thus, this glacier-like form hosts promising evidence for wet-based glaciation beneath a glacier-like form in a single location on Mars (Hubbard et al., 2011), but issues of landform scale remain. Expansion of observations to glacier-like forms elsewhere, and further scrutiny of the streamlined landforms is required to assess the

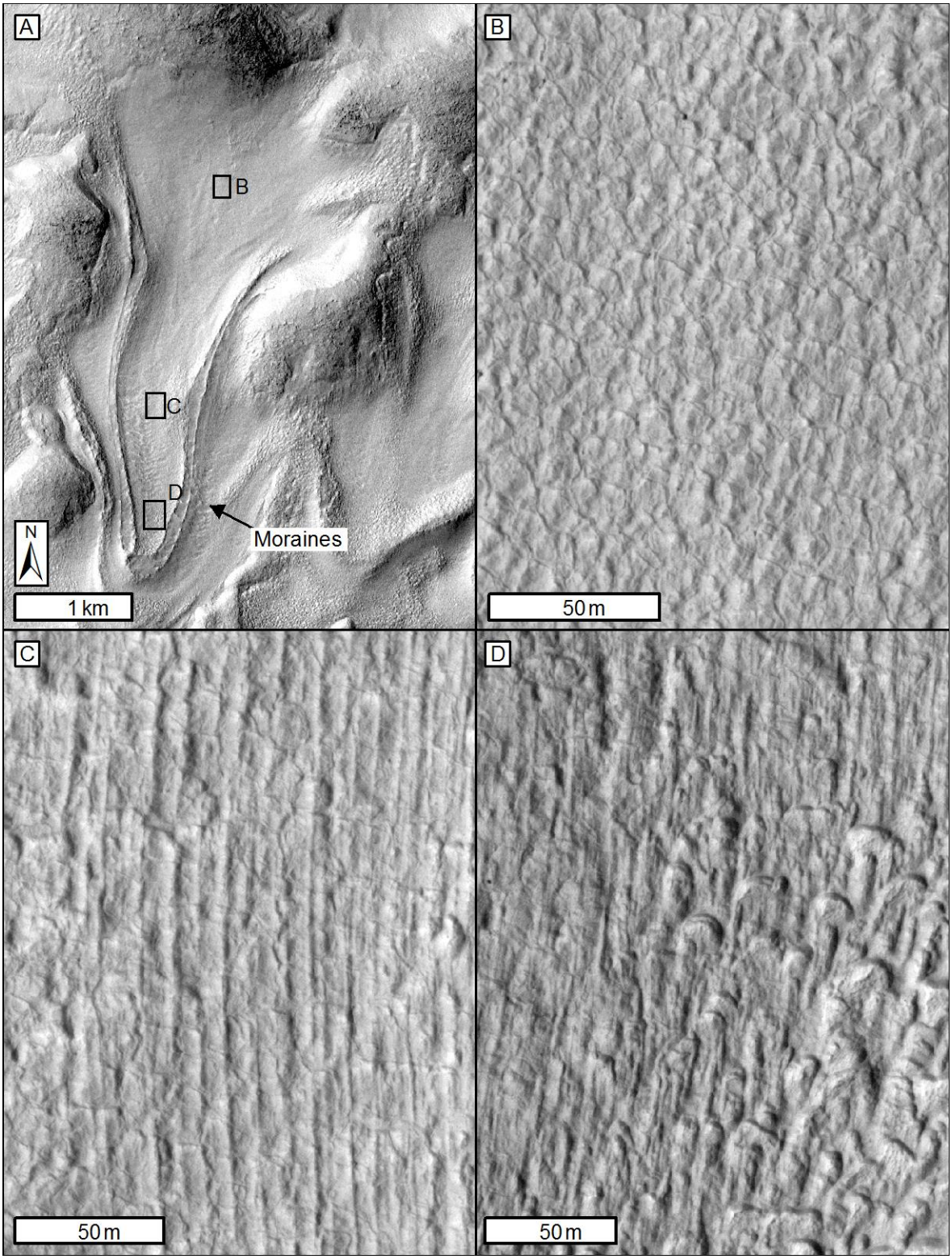

Figure 3.9. Streamlined landforms on the partially-exposed bed of a glacier-like form in Greg crater (A) CTX image of the glacier-like form in Greg crater mapped by Hubbard et al (2011). Black boxes show extents of panels B–D. See Figure 3.1 for location. (B) Polygonal thermal contract cracks within material interpreted by Hubbard et al. (2011) as hosting relict glacial ice. (C) Streamlined landforms interpreted by Hubbard et al (2011) as megascale glacial lineations on the exposed portion of the former glacier bed between the relict glacier and the terminal moraine complex (see panel A). (D) Mound and tail terrain interpreted by Hubbard et al. (2011) as possible drumlins on the exposed portion of the former glacier bed. Panels B–D are HiRISE images. See Table 3.1 for data products.

potential role of wet-based glaciation, and alternative, non-glacial mechanisms (foremost aeolian and mass wasting processes), in their formation.

3.6.3.3. Eskers Associated with a Viscous Flow Feature in Phlegra Montes

Perhaps the most compelling evidence for the past occurrence of basal melting of an existing mid-latitude glacier on Mars was presented by Gallagher and Balme (2015) using 6 m/pixel CTX images, for a VFF in the Phlegra Montes region of Mars' northern mid latitudes (Figure 3.10). They discovered an esker complex (located at 162.1°E, 32.8°N) located ~36 km ESE of the present terminus of a lineated valley fill-type VFF (Figure 3.11) that occupies a WNW–ESE oriented graben (Figure 3.10B) within the southern uplands of the Phlegra Montes massif (Figure 3.10C). Phlegra Montes is an ~80–180 km wide, ~1350 km long massif with its long-axis oriented approximately SSW–NNE (Figure 3.10).

Gallagher and Balme (2015) demonstrated that the foreland between the terminus of the VFF and the esker complex hosts geomorphic evidence for glaciation with a component of meltwater activity (Figure 3.11). This evidence includes: (1) channel-like furrows reminiscent of outwash streams, which divert around an isolated mass of pitted hummocky terrain consistent with dead ice topography (Figure 3.11C), and originate at a zone of scoop-shaped depressions within disrupted lobate flow deposits (Figure 3.11D); (2) heavily pitted (i.e., possibly ice-rich) valley-filling deposits in the glacier foreland (Figure 3.11E); (3) re-entrant valleys and breaches within arcuate deposits ~6.5 km E of the terminus of the VFF that are consistent with down-cutting and breach of a topographic barrier by glacial meltwater (Figure 3.11E); and (4) two valley-transverse pitted arcuate ridge complexes extending across the entire valley width proximal to the present glacier terminus, which Gallagher and Balme (2015) interpret as recessional moraines (Figure 3.11F). Thus, Gallagher and Balme (2015) provide comprehensive evidence for an integrated system of landforms, generated in the presence of glacial meltwater, which connects the esker complex to the VFF to the WNW. This provides robust evidence that the VFF likely represents the parent glacier of the esker, implying terminus retreat over the intervening foreland since esker deposition. The impact crater retention model age of the surface of the VFF implies that its last major activity was ~150 Ma (late Amazonian; Gallagher and Balme, 2015), providing a minimum estimate of the age of the esker complex.

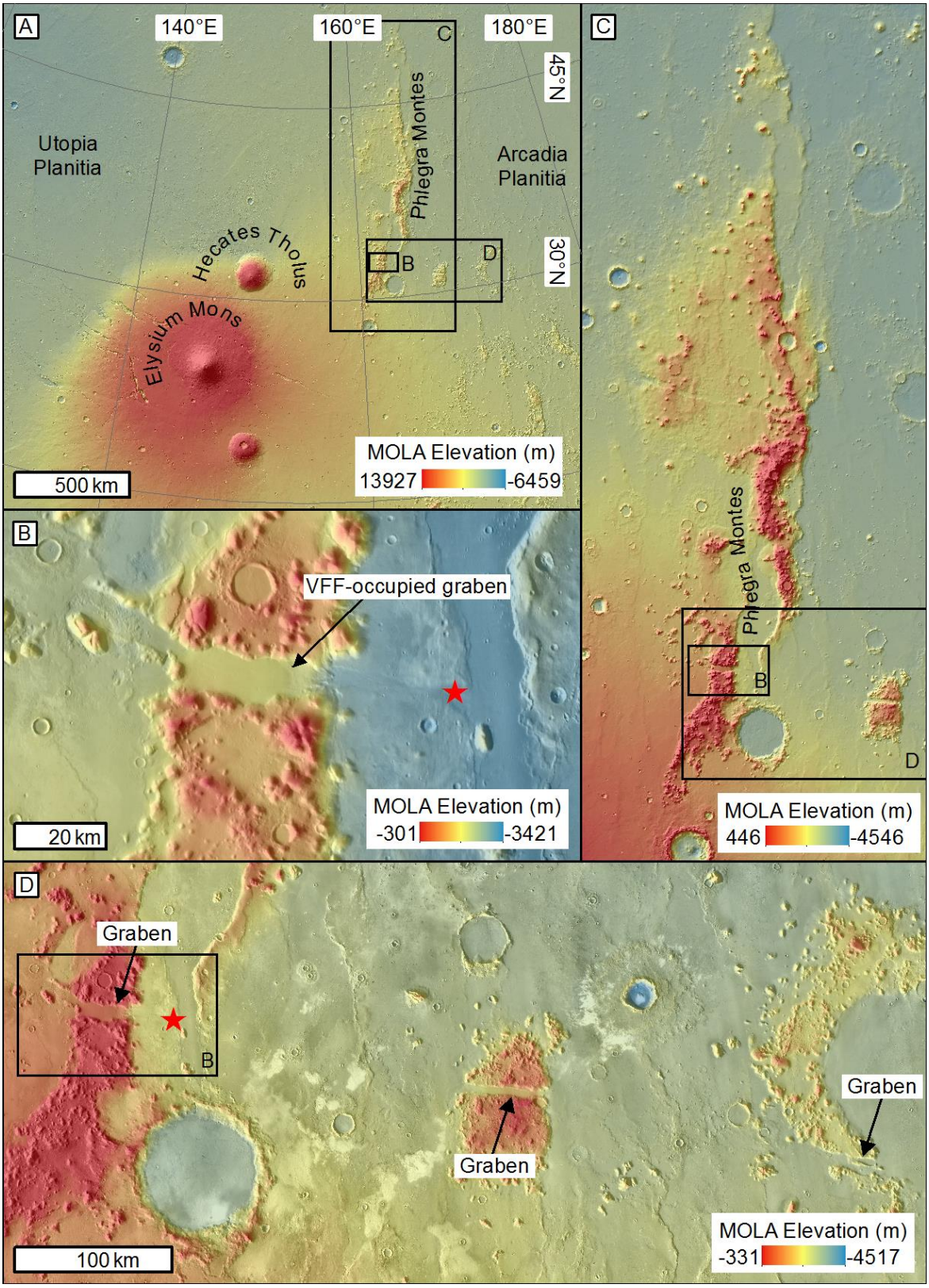

Figure 3.10. Location of the glacier-linked esker in Phlegra Montes identified by Gallagher and Balme (2015) MOLA elevation maps underlain by MOLA hillshade (panels A and C) or THEMIS daytime infrared images (panels B and D). (A) Phlegra Montes and the Elysium volcanic province showing locations of subsequent panels. (B) The graben hosting the parent VFF of the Phlegra Montes esker complex (esker location shown by red star). (C) Closer view of the Phlegra Montes massif showing locations of panels B and D. (D) The relationship between the graben hosting the parent glacier of the esker (esker location shown by red star) and similarly-oriented graben within massifs ESE of Phlegra Montes. See Table 3.1 for data products.

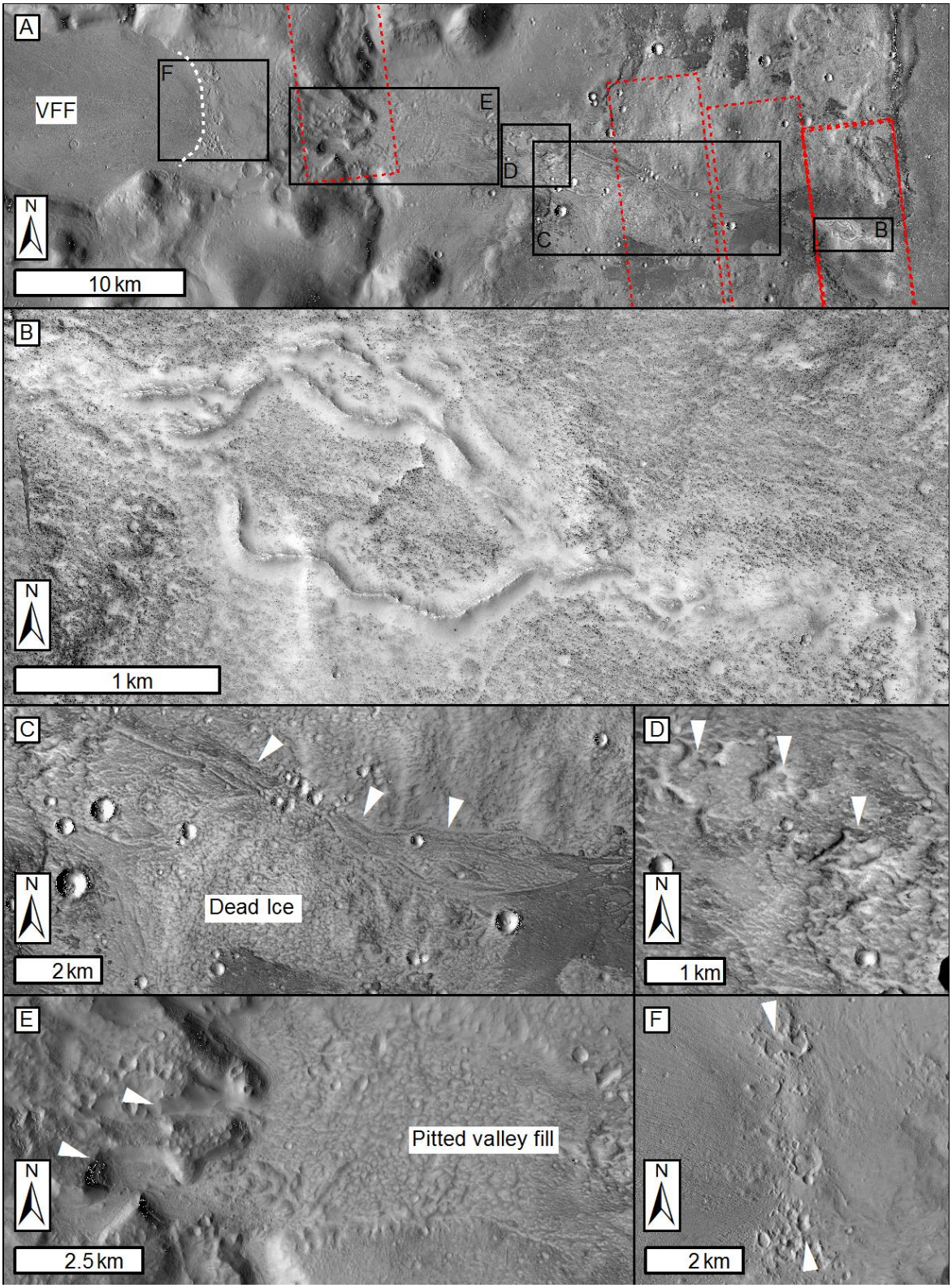

Figure 3.11. Esker associated with a viscous flow feature in Phlegra Montes, and associated landforms consistent with past wet-based glaciation. (A) CTX image mosaic of the glacial landsystem studied by Gallagher and Balme (2015), including VFF (white dashed line is present terminus), footprints of HiRISE images released since their study (red boxes), and extents of panels B–F. Location in Figure 3.1. (B) HiRISE image of the Phlegra Montes esker complex released after the Gallagher and Balme (2015) study. (C) Channel-like furrows (white arrows) and hummocky topography. (D) Scoop-shaped depressions (white arrows) at the head of the channel-like furrows in panel C. (E) Pitted proglacial valley fill and re-entrant valleys (white arrows). (F) Valley-transverse moraine-like ridge. Panels C–F are CTX images. See Table 3.1 for data products.

3.6.4. Geothermal Heating as a Driver of Recent Wet-Based Glaciation?

Evidence for spatially-restricted wet-based glaciation during the Amazonian, and particularly as recently as the late Amazonian, is difficult to reconcile with the prevailing understanding that climatic conditions during the Amazonian have been similarly cold and dry to the present day (Carr and Head, 2010). Thus, it is necessary to appeal to other heat sources that could either complement or act independently of atmospheric warming to induce wet-based glaciation, and hence esker formation in Phlegra Montes.

The VFF associated with the esker identified by Gallagher and Balme (2015) occupies a ~10 km wide, WNW–ESE oriented graben that dissects the southern portion of the Phlegra Montes massif (Figure 3.10B). Grabens are fault-bounded valleys formed in extensional tectonic settings. On Earth, they are commonly associated with elevated geothermal heat flux, either as a result of ascent of magma or hydrothermal circulation (Fernàndez and Banda, 1990; Jordan et al., 2010). Thus, Gallagher and Balme (2015) argue that geothermal heat flux could have been an essential driver of basal melting of the VFF in southern Phlegra Montes under cold Amazonian climatic conditions.

Mars' geothermal heat flux has waned significantly over the course of its geological history (Figure 3.12; Montési and Zuber, 2003; McGovern et al., 2004; Solomon et al., 2005). It is thought that Mars' globally-averaged geothermal heat flux declined rapidly from ~65 mW m^{-2} to ~45 mW m^{-2} during the Noachian and Hesperian (Montési and Zuber, 2003; McGovern et al., 2004), and declined more gradually thereafter, towards a present-day global average of 23–27 mW m^{-2} (Plesa et al., 2016). Thus, Mars' recent geothermal heat flux has been significantly lower than the 60–105 mW m^{-2} average for Earth (the lower value for Earth corresponds to continental crust and the higher value to oceanic crust; Plesa et al., 2016). However, existing estimates for Mars past and present geothermal heat flux are largely derived from numerical models that use orbital gravity measurements, greatly simplified planetary topography, and assume globally uniform distributions of heat-producing radiogenic elements in the crust (e.g., McGovern et al., 2002; Montési and Zuber, 2003; McGovern et al., 2004; Plesa et al., 2016). Therefore, they do not resolve spatiotemporal variations in geothermal heat flux at spatial scales that are comparable to those of individual glaciers or glaciated regions, or over timescales that are comparable to those of glacial cycles. Reconstructions of past geothermal heat flux for the largest volcanic provinces on Mars suggests that their formation increased geothermal heat flux in their vicinity far above the global average, including during the Amazonian (McGovern et al., 2004). The maximum estimated present-day geothermal heat flux values of ~50 mW m^{-2}

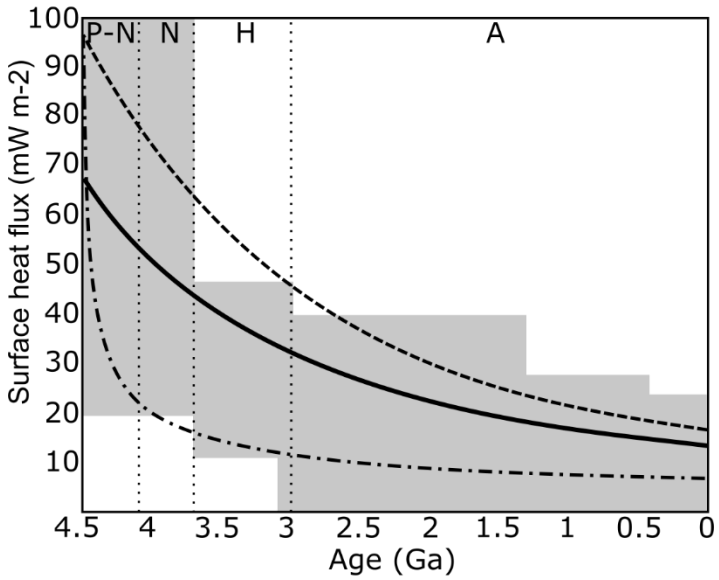

Figure 3.12. Modelled evolution Mars' surface geothermal heat flux. Lines are estimates of global geothermal heat flux from heat production (solid and dashed lines) and lithospheric cooling (dash dot line) models plotted by Montési and Zuber (2003). Grey regions are estimates of geothermal heat flux based upon relationships between gravity and topography for key regions (e.g., the Tharsis volcanoes, Valles Marineris, the Hellas impact basin, and the southern highlands) from McGovern et al. (2002), combined with heat flux estimates from mechanical models based on the spacing of compressional tectonic features (wrinkle ridges) in Solis and Lunae Plana by Montési and Zuber (2003). Time periods covered by these estimates are based on the surface age of the region. It should be noted that corrected calculations from McGovern et al. (2004) provide upper Amazonian geothermal heat flux estimates for Pavonis and Ascraeus Mons that exceed 65 mW m^{-2}; however, best-fit models for these regions are not significantly dissimilar from the scenario shown by the grey regions here. Vertical dotted lines are boundaries of the major geological periods (P-N, pre-Noachian; N, Noachian; H, Hesperian; and A, Amazonian) from Hartmann and Neukum (2001). Redrawn and adapted from Montési and Zuber (2003) and Solomon et al. (2005).

are centred on these provinces, with heat flux anomaly radii of < ~815 km (Plesa et al., 2016). It is possible that processes operating on smaller spatial and temporal timescales (e.g., Hauber et al., 2011) have caused local variations in Mars' recent geothermal heat flux that are not considered in province or planetary-scale models.

The glacierised graben in southern Phlegra Montes is ~110 km long but, based on similarities in strike and geometry to two grabens that manifest within isolated massifs centred ~280 km and 550 km to the ESE (Figure 3.10D), Gallagher and Balme (2015) argue that it is a portion of a more regionally-extensive graben system. The strike of this graben system is also consistent with fault systems that extend across the Elysium volcanic province to the west of Phlegra Montes, and into Utopia Planitia (Gallagher and Balme, 2015). The Elysium volcanic province has a protracted history of volcanism; Elysium Mons (centred ~900 km SW of the Phlegra Montes graben) formed ~3.5 Ga (Werner, 2009), while late stage caldera-forming activity at Hecates Tholus (centred ~590 km WSW of the Phlegra Montes graben) occurred 350 Ma (Hauber et al., 2005). Thus, Gallagher and Balme (2015) argue that

geothermal heat flux in the glacierised graben in southern Phlegra Montes could conceivably have been elevated above the global average by late-stage tectonic and/or magmatic activity along the fault system which coincided with late-Amazonian glaciation in Phlegra Montes, or pre-dated glaciation on timescales of ~10 Myr.

3.7. Eskers beyond Mars' Mid-Latitude Regions

The Phlegra Montes esker complex is the first of its kind to be identified in association with an extant parent glacier anywhere on Mars, including mid-latitude VFFs. It provides the most convincing evidence presented to date for former wet-based conditions beneath at least one existing mid-latitude glacier on Mars during the late Amazonian (Gallagher and Balme, 2015). Putative eskers in a handful of locations beyond Mars' mid latitudes (Figure 3.13), which I summarise below, formed during earlier epochs, and their parent glaciers have long since retreated.

3.7.1. The Dorsa Argentea and Southern Argyre Planitia Eskers

Previous studies have identified putative candidate eskers Mars' southern high latitudes, both in southern Argyre Planitia (Figure 3.13B; Ruff and Greeley, 1990; Kargel and Strom, 1992; Metzger, 1992; Kargel, 1993; Banks et al., 2009; Bernhardt et al., 2013) and in the south polar Dorsa Argentea Formation (Figure 3.13C; Howard, 1981; Ruff and Greeley, 1990; Kargel and Strom, 1992; Kargel, 1993; Head, 2000b; Head and Hallet, 2001a; Head and Pratt, 2001; Head and Hallet, 2001b; Kress and Head, 2015; Butcher et al., 2016). The esker hypothesis has withstood decades of debate pertaining to the origins of the Dorsa Argentea, including statistical tests for morphometric relationships predicted by terrestrial esker theory (e.g., Parker et al., 1986; Tanaka and Scott, 1987; Ruff and Greeley, 1990; Kargel, 1993; Head and Pratt, 2001; Tanaka and Kolb, 2001; Tanaka et al., 2014a; Butcher et al., 2016). The Dorsa Argentea and Argyre Planitia eskers do not conform to the paths of steepest topographic slope, and ascend local topographic undulations in many locations (e.g., Banks et al., 2009; Butcher et al., 2016). This is consistent with their formation within pressurised subglacial meltwater channels. Unlike water flow in sub-aerial channels, which invariably follows the steepest topographic gradient under gravity, routing of subglacial meltwater is modified by the pressure exerted by the overlying ice (e.g., Shreve, 1972). Consequently, eskers on Earth commonly cross topographic undulations (e.g., Shreve, 1985a; Perkins et al., 2016). Banks et al. (2009) and Butcher et al. (2016) identified relationships between the heights and bedslopes of the Argyre Planitia and Dorsa Argentea eskers, respectively, that were predicted by Shreve (1985a) for eskers as they cross topographic undulations.

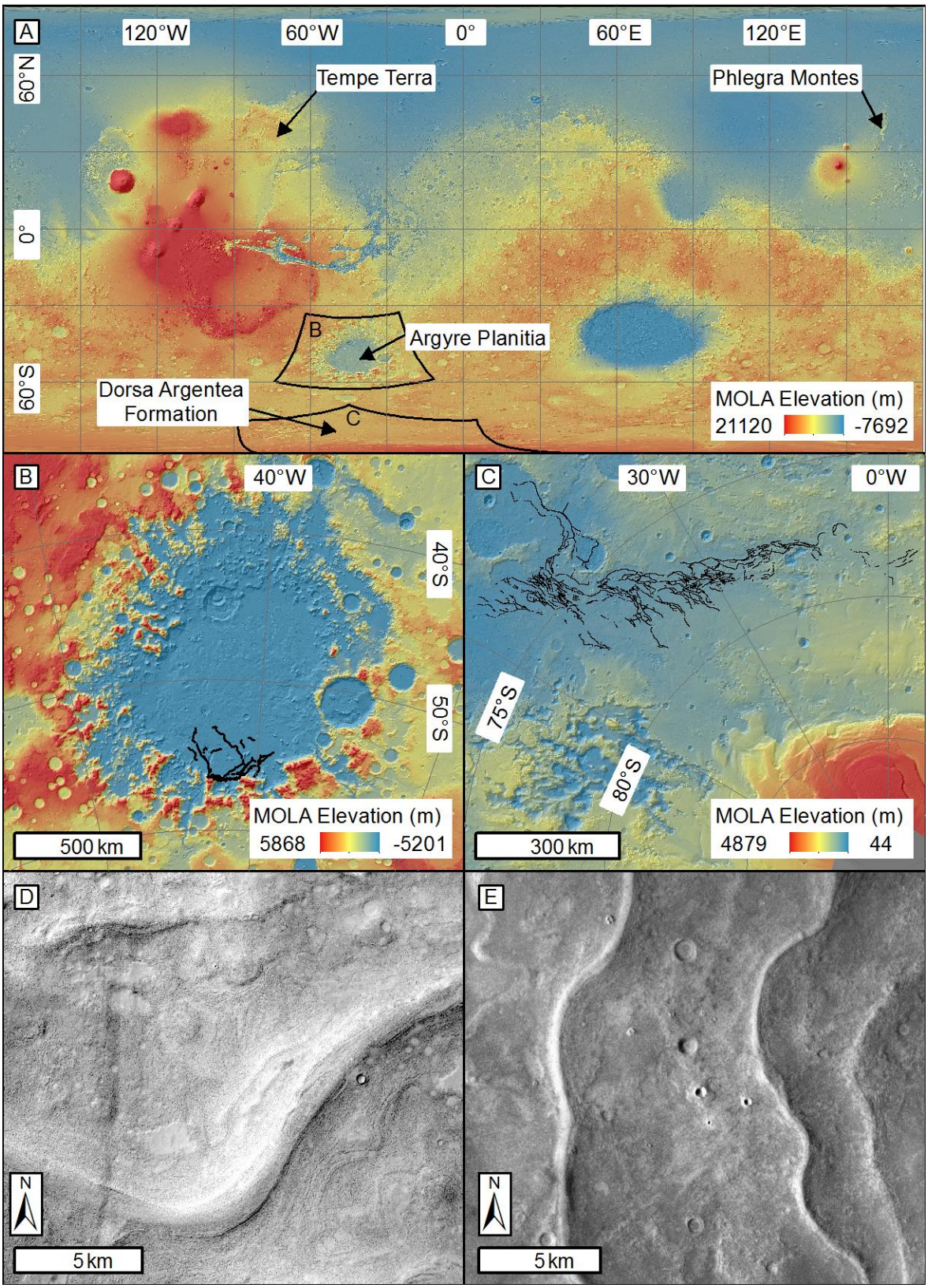

Figure 3.13. Ancient putative eskers in Mars' southern high latitudes. (A) Global MOLA elevation map overlain on MOLA hillshade map showing locations of eskers (black lines in panels B–C are esker crestlines) in: (B) Argyre Planitia (Bernhardt et al., 2013), and (C) the Dorsa Argentea Formation (Butcher et al., 2016). (D) CTX image of a portion of an esker in Argyre Planitia. (E) CTX image of portions of three subparallel Dorsa Argentea eskers. See Table 3.1 for data products.

Foremost among alternative hypotheses proposed for the origins of the Dorsa Argentea is that they represent former subaerial valleys that have become topographically inverted by differential erosion, forming ridges called inverted palaeochannels (Kargel, 1993; Ruff and Greeley, 1990; Tanaka and Kolb, 2001; Tanaka and Scott, 1987; Tanaka et al., 2014a). I discuss the 'esker vs. inverted channel' debate further in Chapter 8.

Detailed 3D morphometric studies of the southern Argyre Planitia (Banks et al., 2009; Bernhardt et al., 2013) and Dorsa Argentea (Butcher et al., 2016) eskers have been limited to the largest ridges within the complexes, owing to reliance upon digital elevation model (DEM) products from MOLA with resolutions of hundreds of metres. Banks et al. (2009) performed metre-scale 3D analyses of small portions of Cleia Dorsum, a candidate esker in southern Argyre Planitia, using HiRISE stereo-pair-derived DEMs. However, owing to sparse HiRISE coverage, these analyses were limited to a handful of topographic profiles. The Dorsa Argentea and southern Argyre Planitia eskers are comparable in size to the largest eskers on Earth (Banks et al., 2009; Bernhardt et al., 2013; Butcher et al., 2016), being up to ~200–300 km long (e.g., Kargel and Strom, 1991, 1992; Butcher et al., 2016), ~10-160 m high (e.g., Kargel and Strom, 1991, 1992; Butcher et al., 2016), and 0.3–6 km wide (Kargel and Strom, 1992; Butcher et al., 2016).

Impact crater size-frequency distributions within the Dorsa Argentea and Argyre Planitia esker complexes indicate that they formed in the early Hesperian, ~3.6 Ga (Bernhardt et al., 2013) and ~3.48 Ga (Kress and Head, 2015), respectively. The spatially extensive basal melting required to form eskers as large as the Dorsa Argentea has been attributed to their formation under warmer climate conditions (Scanlon et al., 2018) and higher global average geothermal heat flux shortly after the Noachian-Hesperian transition (Fastook et al., 2012). Considering the similarity of age between the Argyre Planitia and Dorsa Argentea eskers, it is likely that their formation occurred under similar environmental conditions.

3.7.2. An Equatorial Esker Complex?

An esker interpretation of a ridge within late-Amazonian-aged (~210 Ma; Kadish et al., 2014) portions of the fan-shaped deposits on the NW flank of the equatorial Arsia Mons volcano (Section 3.5; Head and Marchant, 2003; Shean et al., 2005; Forget et al., 2006) has been proposed (Scanlon et al., 2014, 2015). This candidate esker is interpreted by Scanlon et al. (2014, 2015) to have formed under transient, localised wet-based conditions induced by a late-Amazonian volcanic eruption beneath a glacier that has since completely ablated.

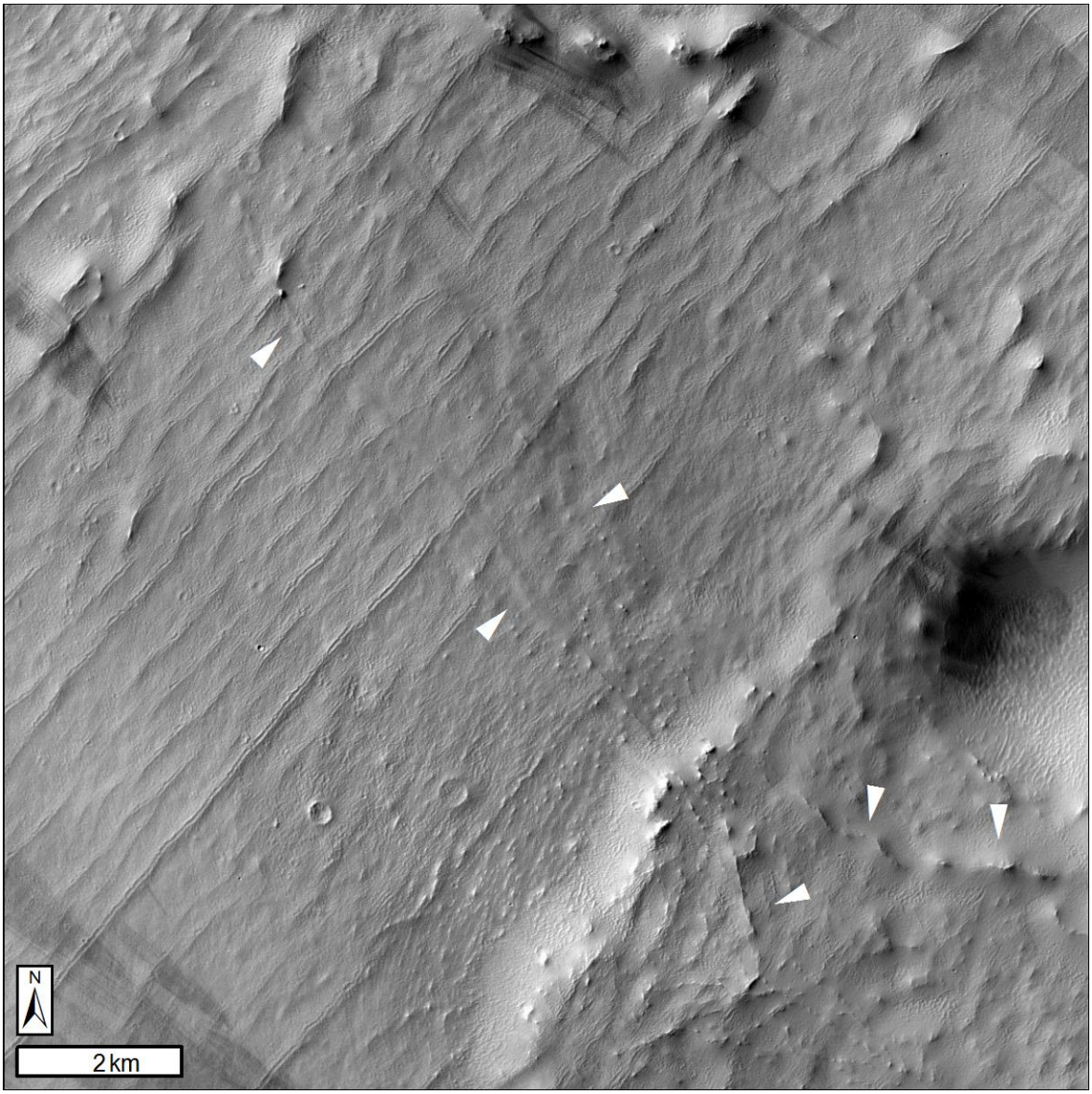

Figure 3.14. Possible mid-Amazonian-aged esker within the Arsia Mons fan-shaped deposit. CTX images showing the ridges (white arrows) interpreted to be an esker by Scanlon et al. (2014, 2015). Curvilinear ridges transverse to these features are widely interpreted as drop moraines formed by a cold-based glacier. Extent shown in Figure 3.7C. See Table 3.1 for image products.

Unlike the mid-latitude Phlegra Montes esker complex, the candidate esker at Arsia Mons lacks a preserved parent glacier, although the evidence of a glacial origin for the landforms here is well explored at a broad scale (Head and Marchant, 2003; Forget et al., 2006; Kadish et al., 2014; Scanlon et al., 2014, 2015). Absence of a clear association with an existing parent glacier does, however, reduce confidence in interpretations of sinuous ridges as eskers and further tests are required to corroborate or disprove the esker hypothesis for these ridges given their indistinct manifestation in available CTX images, and the clear abundance of alternative ridge-forming processes that have operated in this location (Figure 3.14).

As discussed in Section 3.5, Amazonian glaciation of the low latitudes is widely thought to have occurred during periods of high (>45°) planetary obliquity that were climatically distinct from the periods of intermediate (~35°) obliquity during which mid-latitude glaciers advanced (Madeleine et al., 2009; Fastook et al., 2008). Thus, while broadly similar in age (hundreds of Myr) the palaeoenvironmental implications of possible wet-based glaciation on Arsia Mons (Scanlon et al., 2014, 2015) are different to those of the mid-latitude wet-based glaciation recorded by the Phlegra Montes esker complex (Gallagher and Balme, 2015). Nonetheless, the subglacial volcanic eruption hypothesis advanced by Scanlon et al. (e.g., Scanlon et al., 2014, 2015) to explain the formation of an esker at Arsia Mons is broadly consistent with the requirement for warming of basal ice by subsurface heat sources that was proposed by Gallagher and Balme (2015) to explain wet-based glaciation in Phlegra Montes during the late Amazonian (Section 3.6.4).

3.8. New Opportunities for Studies of Eskers on Mars

The study by Gallagher and Balme (2015) was limited to qualitative descriptions from a single 6 m/pixel CTX image that was available at that time. In this thesis, I exploit opportunities for metre-scale 3D analyses of mid-latitude glacier-linked eskers afforded by HiRISE stereo-pair images available for the Phlegra Montes esker complex. These images were released after the publication of Gallagher and Balme (2015; Figure 3.11A–B), and for a glacier-linked sinuous ridge in NW Tempe Terra, which I propose is a second, newly-identified mid-latitude glacier-linked esker (Butcher et al., 2017). I also combine HiRISE and CTX image and elevation data to explore the origins of esker-like glacier-linked sinuous ridges in Chukhung crater, central Tempe Terra, for which the possibility of esker origins has previously been informally discussed[1], but for which the esker hypothesis has not been analysed in detail. Thus, this thesis provides the first characterisation of a martian glacier-linked esker outside of the Phlegra Montes region; the first systematic metre-scale characterisation of eskers anywhere on Mars; and the first formal analyses of sinuous ridges in Chukhung crater, for which evidence of esker origins is more ambiguous.

[1] The esker hypothesis for sinuous ridges in Chukhung crater was discussed by E. Lakdawalla in two online blog posts for the Planetary Society available at: http://www.planetary.org/blogs/emily-lakdawalla/2010/2822.html and http://www.planetary.org/blogs/emily-lakdawalla/2011/2879.html (last accessed 24/01/2019).

3.9. Research Questions

As outlined in Chapter 1, this thesis develops upon the discovery by Gallagher and Balme (2015) of the glacier-linked esker complex in Phlegra Montes by advancing the following overarching research questions. The specific objectives identified to answer these questions are stated in Chapter 1.

- Did existing debris-covered glaciers elsewhere in Mars' mid latitudes undergo basal melting, and if so, what were the likely environmental drivers of meltwater production?
- What do the morphometries of glacier-linked eskers in Mars' mid latitudes imply about the spatiotemporal dynamics of esker forming meltwater drainage?
- How do the planform and 3D morphometries of glacier-linked eskers in Mars' mid latitudes compare to the Dorsa Argentea and to eskers on Earth, and how could these morphometries be used to aid the identification of eskers elsewhere on Mars?

CHAPTER 4

RECENT BASAL MELTING OF A MID-LATITUDE GLACIER IN NW TEMPE TERRA, MARS.

4.1. Attribution

The majority of this chapter has been published as a peer-reviewed paper in the *Journal of Geophysical Research: Planets* (Butcher et al., 2017). The published article includes additional 1D numerical modelling experiments, which were performed by N. S. Arnold. These sections have been removed and are described in Chapter 9. Slight amendments including modification of the title; conversion from US to UK English; alterations to figures; updates to references; and the addition of Figure 4.9 and the accompanying description, have been made for consistency with the thesis. A section of the discussion on 'Eskers on Mars' has also been moved to background discussion in Chapter 3. The DEM of the tectonic fault described in Section 4.5.6 was generated by S. J. Conway.

4.2. Background

Mars' mid latitudes host abundant water ice within young (late-Amazonian-aged; 40 Ma–1 Ga; e.g., Berman et al., 2012; Hartmann et al., 2014) viscous flow features (VFFs; e.g., Squyres, 1979; Levy et al., 2014). Morphological (e.g., Head et al., 2010), geophysical (e.g., Holt et al., 2008; Plaut et al., 2009; Petersen et al., 2018) and modelling (e.g., Parsons et al., 2011) evidence suggest that they are debris-covered glaciers.

Morphologies indicative of basal melting of mid-latitude VFFs are extremely rare. Therefore, it is widely thought that they have been perennially frozen to their beds in cold-based thermal regimes (e.g., Levy et al., 2016). Here I identify a sinuous ridge (46.17°N, 83.06°W) emerging from a VFF within a tectonic rift (Hauber et al., 2010) in northwest

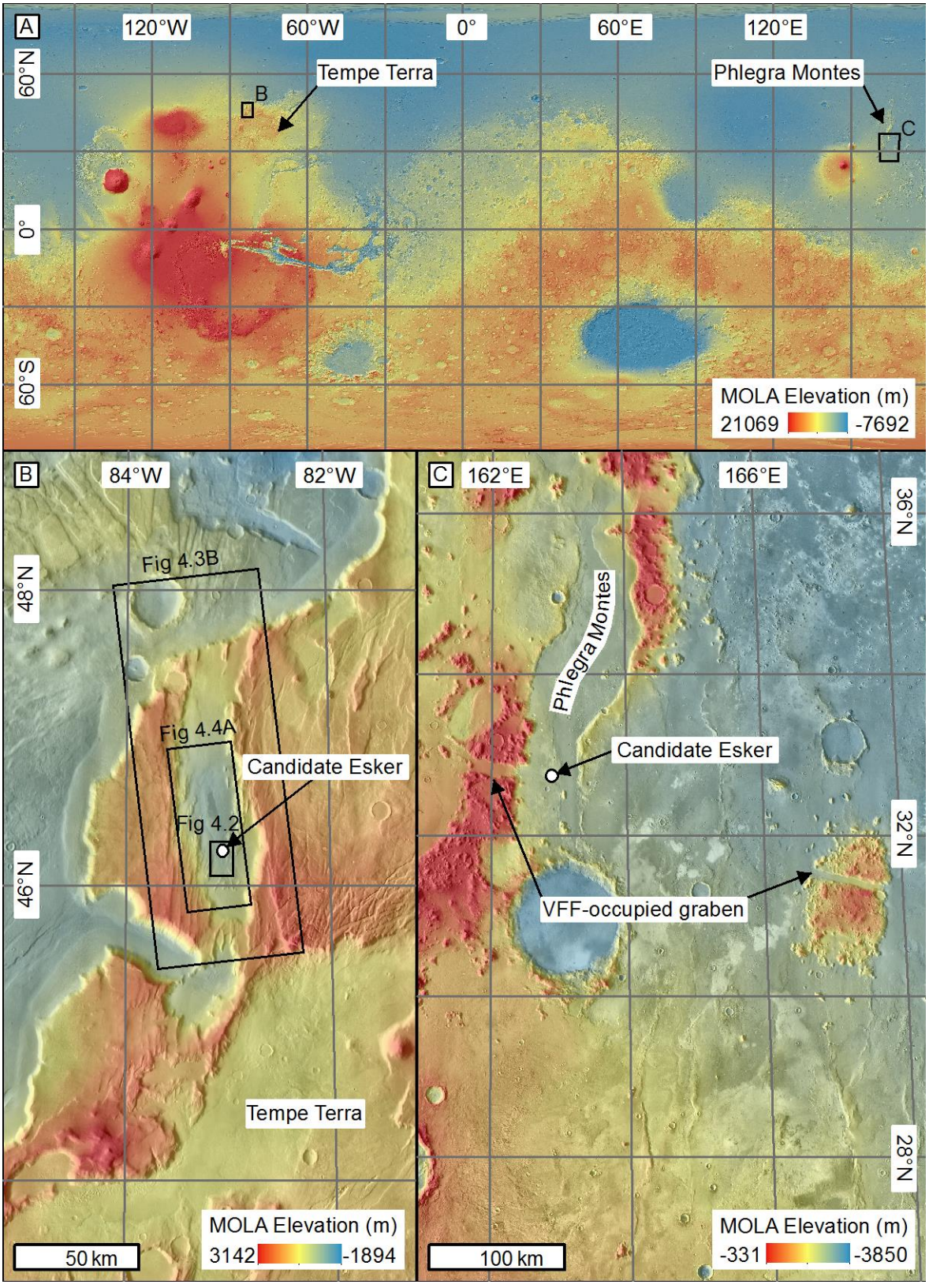

Figure 4.1. Locations of candidate glacier-linked eskers on Mars. (A) Global MOLA elevation context map showing locations of: (B) the present study, and (C) the candidate esker identified by Gallagher and Balme (2015). Panels (B) and (C) are THEMIS daytime infrared images overlain by MOLA elevation maps. See Table 4.1 for list of data products. Modified from Butcher et al. (2017).

Figure 4.2. The candidate esker in NW Tempe Terra. Context Camera image (Table 4.1). The white arrow shows the first trace in the VFF's surface. Extent in Figure 4.1B. Modified from Butcher et al. (2017).

Tempe Terra, northeast of the Tharsis volcanic province (Figure 4.1A and B). I interpret the sinuous ridge (Figure 4.2) as an esker formed by deposition of sediment in an ice-walled and ice-roofed subglacial meltwater conduit. Thus, I present a rare, localised example of recent basal melting of a mid-latitude glacier on Mars.

To my knowledge, one other example of an esker associated with a late-Amazonian-aged (~150 Ma) mid-latitude VFF has been documented to date, in a graben in Phlegra Montes, northeast of the Elysium volcanic province (Chapter 3; Gallagher and Balme, 2015). These young, mid-latitude, VFF-linked candidate eskers are distinct from other candidate eskers on Mars (see Chapter 3) in their age, mid-latitude location, and association with an extant parent glacier.

In this chapter, I present a geomorphic map of landforms in the NW Tempe Terra rift and develop a landsystem model to explain their formation. I analyse the metre-scale three-dimensional morphology of the candidate esker and compare it to terrestrial analogues as a precursor to more detailed morphometric analyses performed in Chapter 6. I highlight that the rift setting of the newly identified candidate esker in Tempe Terra is similar to the graben in which the Phlegra Montes candidate VFF-linked esker is located (Figure 4.1C; Gallagher and Balme, 2015). Terrestrial grabens/rifts are commonly associated with elevated geothermal heat flux (e.g., Fernàndez and Banda, 1990; Jordan et al., 2010). Additionally, strong glacier flow convergence in these steep-sided troughs could drive significant viscous strain heating of glacial ice. That both candidate mid-latitude VFF-linked eskers found to date occur within grabens/rifts suggests a genetic link between the setting and the landform. The broad lack of identified evidence for basal melting of modern VFFs elsewhere in Mars' mid latitudes implies that cyclic (~120 Myr period) obliquity-induced climate changes (e.g., Schorghofer, 2008; Madeleine et al., 2009) alone were insufficient to permit widespread basal melting of VFFs without an additional heat source. Thus, I explore qualitatively the possibility that late-Amazonian magmato-tectonic processes (e.g., Tanaka, 1990; Neukum et al., 2004a; Hauber et al., 2011), possibly supplemented by viscous strain heating, could have induced positive geothermal anomalies in the vicinity of these ancient rifts (Hauber et al., 2010) that facilitated glacial melt (Gallagher and Balme, 2015). Numerical modelling experiments undertaken by N. S. Arnold in parallel with the preparation of thesis, which provide quantitative constraints on the requisite conditions for basal melting, are discussed in Chapter 9.

4.3. Data and Methods

4.3.1. Observations and Mapping

I mapped the landforms in the rift (Figures 4.3 and 4.4) by analysing ~6 m/pixel CTX images (Malin et al., 2007) and ~100 m/pixel day and night infrared (IR) THEMIS image mosaics (Table 4.1; Christensen et al., 2004; Edwards et al., 2011). I digitised the map in Environmental Systems Research Institute (ESRI) ArcGIS 10.1 using a sinusoidal projection centred on the long axis of the rift valley (83.5°W) to minimise cartographic distortion.

Following the method of Kirk et al. (2008), I generated a 2 m/pixel digital elevation model (DEM) and 50 cm/pixel orthorectified images of the sinuous ridge from 50 cm/pixel High Resolution Imaging Science Experiment (HiRISE; McEwen et al., 2007) images ESP_049573_2265 and ESP_049639_2265 using U.S. Geological Survey Integrated Software for Images and Spectrometers 3 (ISIS3) and BAE Systems SOCET SET 5.6.0[2].

4.3.2. Estimation of Impact Crater Retention Age of VFFs

I measured the size-frequency distribution of impact craters on the surface of the VFFs within the rift to determine the minimum age of the termination of the last major VFF-surface modification phase. I measured impact craters using the *CraterTools* add-in for ArcGIS (Kneissl et al., 2011), following the method of Gallagher and Balme (2015). Complete CTX image coverage permitted inclusion of all undeformed crater-like circular features of diameter (D) $\geq$ 50 m. Pitting and lineation of the VFF surfaces prevented reliable identification of impact craters of D < 50 m.

4.4. Observations

The Tempe Terra rift is ~110 km long, ~24.5 km wide, and up to ~2300 m deep, and is bounded to the east and west by normal fault scarps (Figure 4.5; see also Figure 2b in Hauber et al., 2010). Its northern and southern margins rise ~1550 m above the rift floor, forming a closed basin (Figure 4.5). Pitted and lineated lobes, consistent with the lobate debris apron (LDA) subtype of martian VFFs (e.g., Squyres, 1979; Head et al., 2010), extend ~15 km down into its centre from all marginal walls (Figures 4.3B, 4.4A-C, 4.5). They converge laterally, and their termini confine a ~225 km^2 region of the rift floor. Their upper margins are gradational with highland mantle that drapes topography and infills topographic lows (Figures 4.3B, 4.4A, 4.5), similar to that described by van Gasselt et al. (2011).

[2] I followed the workflow guide generated by the U.S. Geological Survey, available at: ftp://pdsimage2.wr.usgs.gov/pub/pigpen/tutorials/SS4HIRISE_JULY2015/HiRISE_StereoProcessing_Tutorial_July_2015.pdf (last accessed 02/02/2019).

Table 4.1. Instrument and product IDs for data used in Chapter 4.

Instrument	Image/Product ID	Figures
Mars Orbiter Laser Altimeter[1]	Global Elevation Model 463m (MEGDR)[2]	4.3A 4.1A and C 4.10E (Inset)
Thermal Emission Imaging System[3-4]	THEMIS-IR Day Global Mosaic 100m v12[2]	4.3A 4.1B and C 4.10A
	THEMIS-IR Night 60N60S Mosaic 100m v14[2]	4.4F (Inset)
High Resolution Stereo Camera[5-6]	h3316_0001.da4.50[7]	4.5
Context Camera[8]	Mosaic[10] generated from images: B21_017807_2262_XN_46N083W P05_002907_2258_XN_45N083W P15_007021_2276_XN_47N082W P18_008168_2279_XI_47N082W[11]	4.2 4.3B 4.4A–H 4.5 (Inset) 4.7A
	P16_007166_2283_XN_48N082W[11]	4.10D
	P17_007843_1927_XN_12N203W[11]	4.10E
High Resolution Imaging Science Experiment[9]	Digital elevation model[10] generated from images: ESP_049573_2265 and ESP_049639_2265	4.6
	ESP_049573_2265 (orthorectified)[10]	4.7B–K
	ESP_049639_2265 (orthorectified)[10]	-
	ESP_052553_2260[12]	4.10D (Inset)
	ESP_052065_2260[12]	-
	Digital elevation model[13] generated from images: ESP_052553_2260 and ESP_052065_2260	-

[1] (Smith et al., 2001)
[2] United States Geological Survey Planetary GIS Web Server: http://webgis.wr.usgs.gov/pigwad/down/mars_dl.htm
[3] (Christensen et al., 2004)
[4] (Edwards et al., 2011)
[5] (Neukum et al., 2004b)
[6] (Jaumann et al., 2007)
[7] Freie Universität Berlin: http://maps.planet.fu-berlin.de/
[8] (Malin et al., 2007)
[9] (McEwen et al., 2007)
[10] Generated by F. E. G. Butcher
[11] Arizona State University http://viewer.mars.asu.edu/viewer/ctx#T=0
[12] The University of Arizona https://hirise.lpl.arizona.edu/
[13] Generated by S. J. Conway

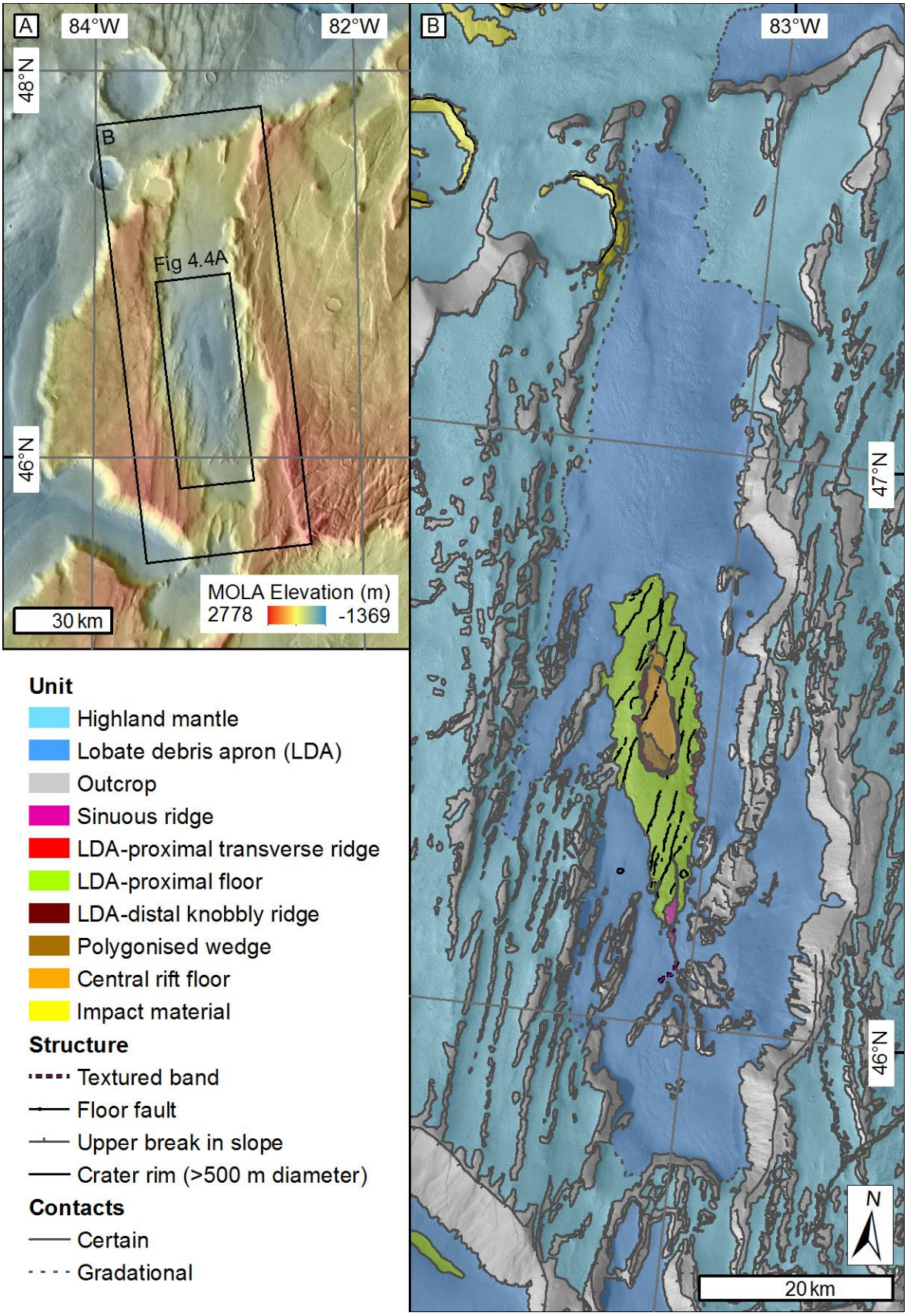

Figure 4.3. Full extent of the geomorphic map of the NW Tempe Terra rift. (A) MOLA elevation map of the Tempe Terra rift overlain on THEMIS daytime infrared images showing the extent of the map displayed in panel B and Figure 4.4. (B) The full extent of the geomorphic map of the Tempe Terra rift, overlain on a mosaic of Context Camera images (Table 4.1). Modified from Butcher et al. (2017).

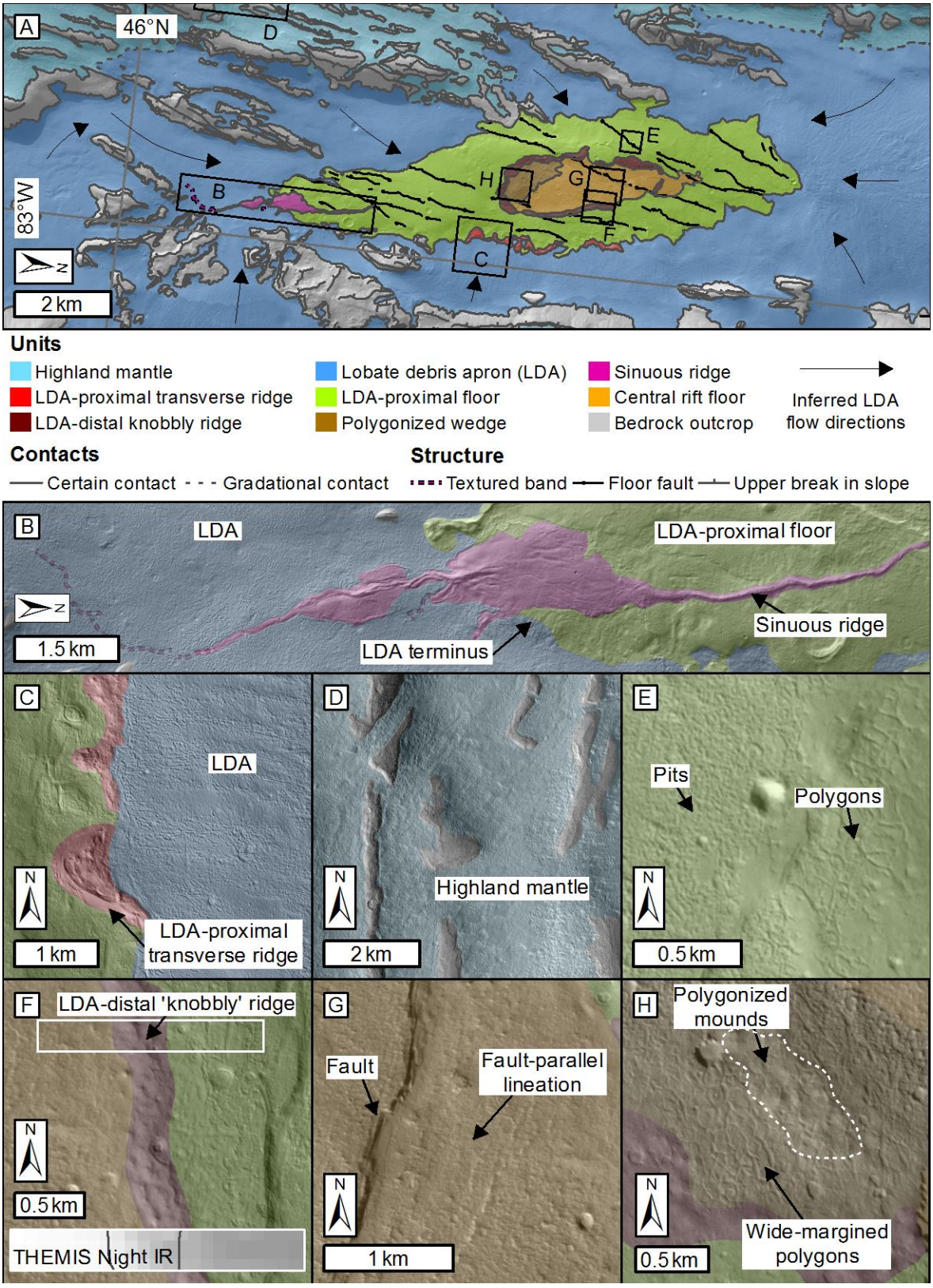

Figure 4.4. Geomorphic map of the central portion of the Tempe Terra rift, and constituent units. All panels have CTX image basemaps (see Table 4.1). (A) Central portion of the rift (extent in Figure 4.1 and Figure 4.3) showing extents of panels B-H. (B) Sinuous ridge. (C) LDA-proximal transverse ridges. (D) Highland mantle. (E) LDA-proximal floor. (F) LDA-distal knobbly ridge (the white box shows the extent of THEMIS night IR inset, in which bright areas have higher surface temperatures relative to darker areas). (G) Central rift floor. (H) Polygonised wedge with dashed line delineating polygonised mounds. Modified from Butcher et al. (2017).

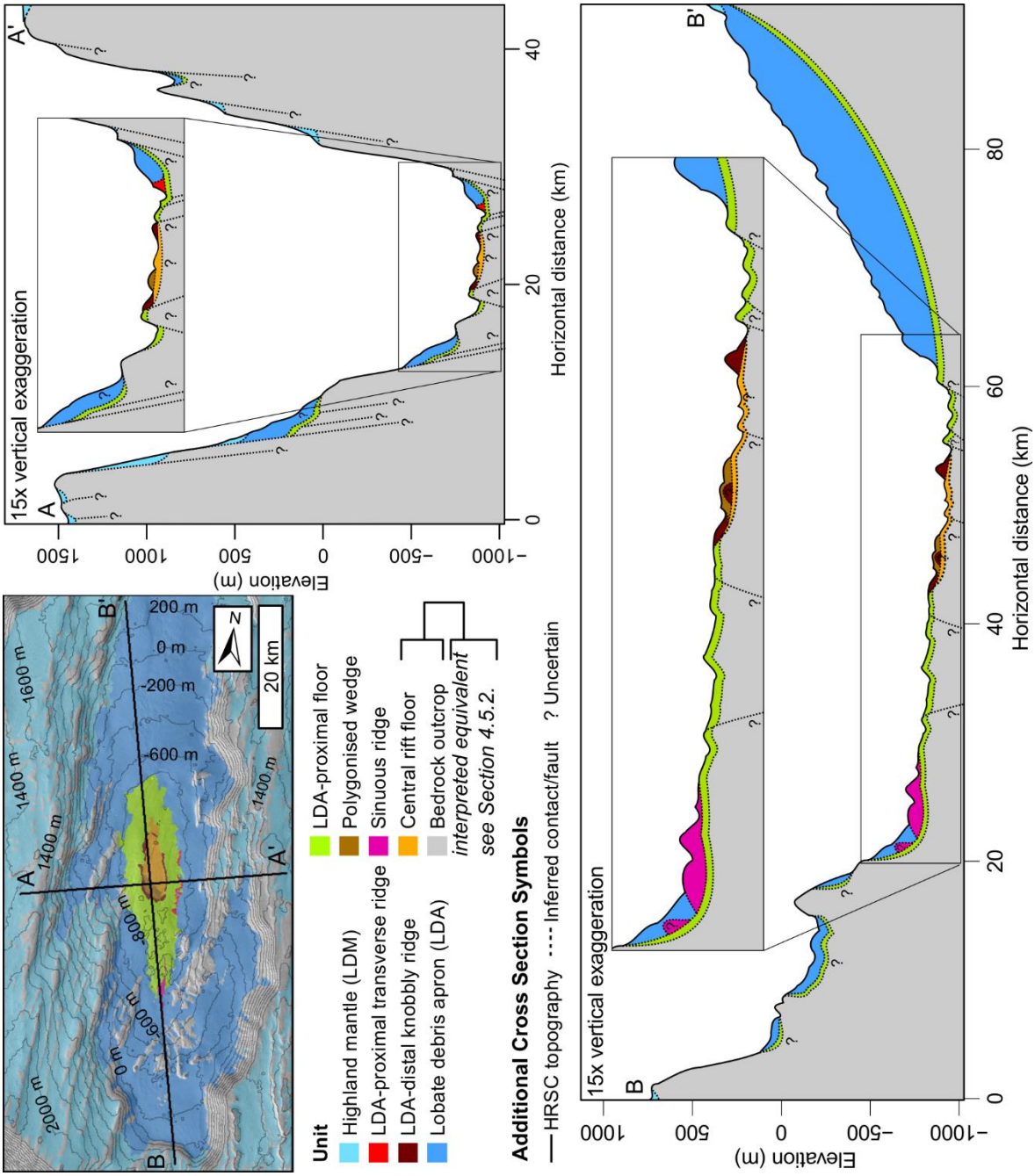

Figure 4.5. Schematic cross-sections showing inferred stratigraphic relationships between mapped units in the NW Tempe Terra rift. The locations of profiles A–A' and B–B' are shown in the inset map. The upper solid line in each cross section is HRSC topography (Table 4.1; Neukum et al., 2004b; Jaumann et al., 2007) and all contacts below this line have inferred depths and profiles. Modified from Butcher et al. (2017). Note that in the original publication, bedrock outcrop and central rift floor units were represented as equivalent units in the cross-sections. For clarity and consistency with unit representations in the geomorphic map, these units are represented individually in the profiles presented here, but the interpretation that they are equivalent remains unchanged (see Section 4.5.2).

4.4.1. Sinuous Ridge

A south-north-oriented sinuous ridge (Figures 4.2–4.4B and 4.5–4.7) emerges from the terminus of the southern LDA at 46.17°N, 83.06°W. It originates ~8 km into the LDA tongue and extends a further ~9 km north into the foreland. I identify four morphological zones[3] along the ridge (Figures 4.6 and 4.7A).

The sinuous ridge originates as an 80–150 m-wide textural band in the LDA surface (zone I, 0–5 km), ~700 m from its lateral margin. It transitions between 60–160 m wide ridges and troughs (sub-DEM resolution; Figure 4.7B). The ridge crest becomes topographically distinct from the LDA surface towards the end of this zone (Figure 4.6).

In zone II (5–7.6 km), the ridge transitions into a ~150 m wide, ~5–10 m high multi-crested ridge with two sharp, parallel crests, atop a broader, round-crested, ~500–1.5 km wide, ~30 m high topographic rise (Figures 4.6 and 4.7C). The central ~500–800 m wide portion of the topographic rise is exposed above the LDA surface. Its margins are dissected by several steep-sided troughs (~20 m wide, ~25–150 m long, ~3–5 m deep; Figure 4.7D). The flanks of the topographic rise in zone II are superposed by LDA materials. This limits scrutiny of whether this topographic rise represents an emergent undulation of the bed upon which the central multi-crested ridge is superposed, or a lateral continuation of the ridge that has been incompletely exposed from the basal ice. I favour the latter on the basis of its elongation along the axis of the ridge (Figure 4.6).

As it emerges from the LDA terminus, the main ridge widens into a broad (up to 1300 m wide), round-crested, ~10–55 m high, diamond-shaped plateau (zone III, 7.6–10.7 km; Figures 4.6 and 4.7A). In zone III, the flanks of the ridge are fractured sub-parallel to its long axis (Figure 4.7E). Its surface hosts shallow ~10 m diameter pits and ~15–30 m diameter polygonal fractures (Figure 4.7F) which cut through impact craters (Figure 4.7G). At the northernmost end of zone III, the ridge is superposed by a complex of ~5 m high, ~30–100 m wide ridges oriented transverse to the sinuous ridge (Figure 4.7A and H). The transverse ridge complex originates at the terminus of the LDA ~1 km east of the sinuous ridge and crosses its crest in zone III, before tracking southwest along its northwest-facing margin.

At the northernmost end of zone III, 2 km beyond the LDA terminus, the sinuous ridge transitions to a narrow (150–200 m-wide), ~5–15 m high, sharp-crested ridge (zone IV, 10.7–17 km; Figure 4.6). Pits are densely clustered along its crest (Figure 4.7I). The ridge

[3] I originally defined these zones as ‘subzones’ (Butcher et al., 2017). I update the nomenclature here based on the new analyses presented in Chapter 6.

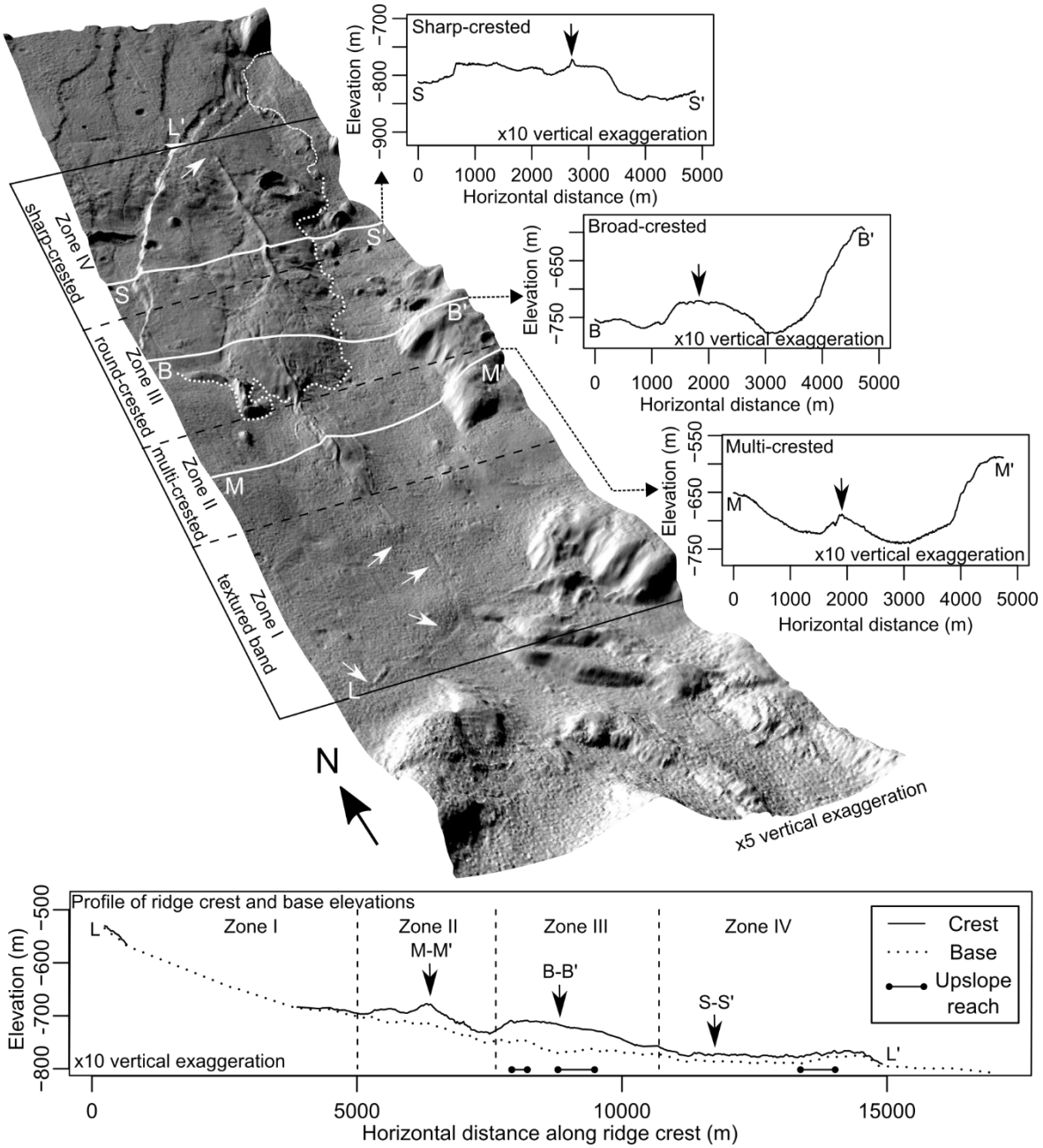

Figure 4.6. Oblique view towards sinuous ridge. View across hillshade map draped on HiRISE DEM (Table 4.1), looking downhill from the region in the top left of Figure 4.4A. The white dashed line is the LDA terminus. The white solid lines show locations of cross-sectional topographic profiles M–M', B–B', and S–S'. Profile L–L' shows the ridge crest and base elevations every ~20 m along the ridge. I analyse the 3D morphometries further in Chapter 6. Three minor ridge segments that are separated from the main ridge by gaps extend a further ~2 km beyond the northern end of the major ridge shown here (see Chapter 6). The profile follows the sinuous crest of the ridge from its origin at L to its termination at L'. Base elevations calculated as average of left and right base points (see Chapter 5). Modified from Butcher et al. (2017).

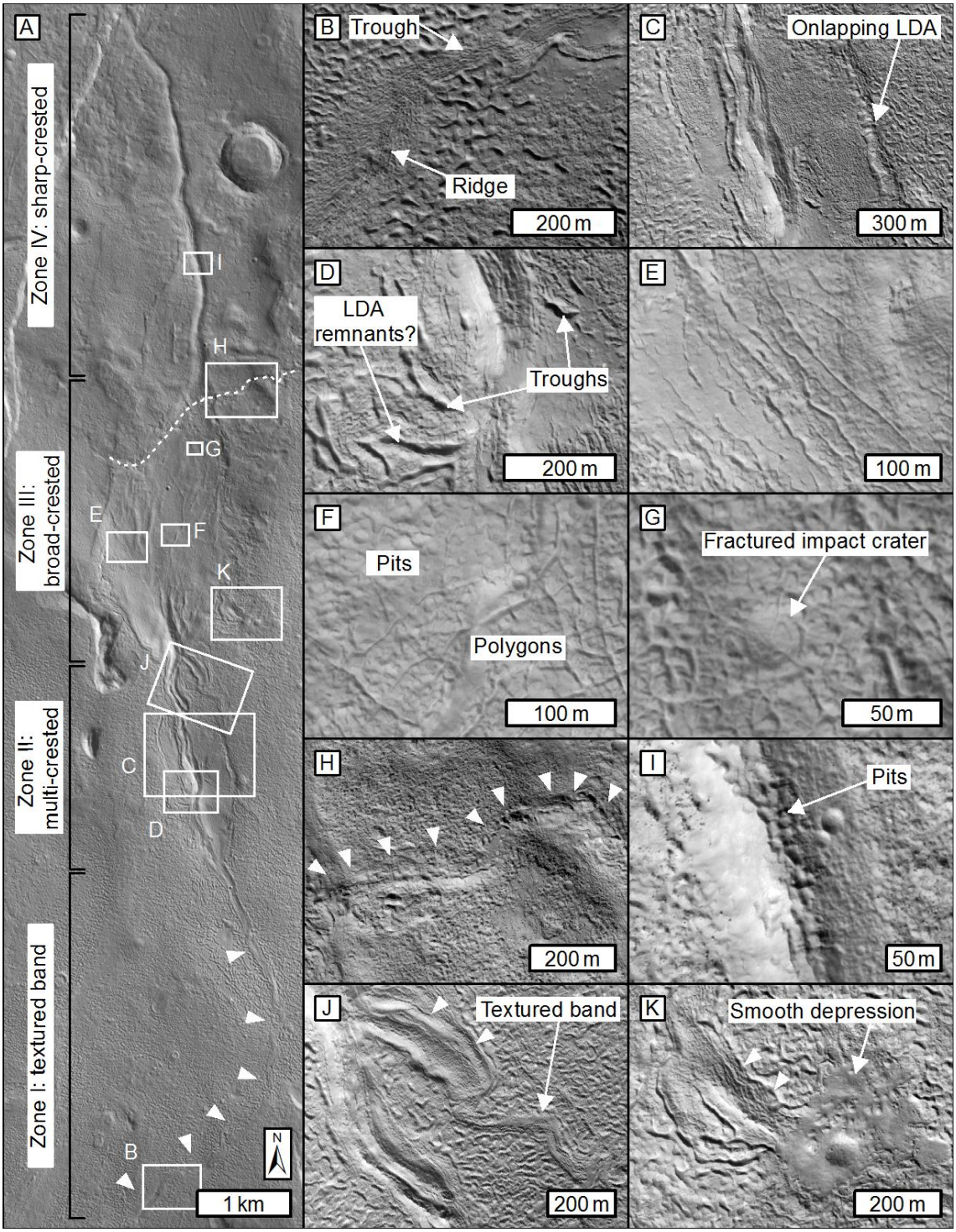

Figure 4.7. Morphology of sinuous ridge from HiRISE. (A) CTX image (Table 4.1) of the sinuous ridge (the white arrows indicate the textured band) showing locations of panels B–K. The white dotted line indicates the transverse ridge shown in panel H. (B) Ridge and trough within textured band (zone I). (C) Multi-crested ridge atop LDA-mantled topographic rise (zone II). (D) Steep-sided flank troughs (zone II). (E) Longitudinal flank fractures (zone III). (F) Pits and polygons (zone III). (G) Polygonally fractured impact crater (zone III). (H) Transverse ridge (white arrows) that crosses the sinuous ridge (subzone III, track shown by white dotted line in Figure 4.7A. (I) Pits on the ridge crest (zone IV). (J) Tributary A (white arrows) with textured band. (K) Tributary B (white arrows) with smooth depression at head. Panels B-K are HiRISE images (see Table 4.1). Modified from Butcher et al. (2017).

becomes topographically indistinct from the LDA-proximal floor at the northernmost end of zone IV.

Two minor ridge segments (~400 m long, 150–200 m wide, ~5–10 m high) merge with the eastern flank of the sinuous ridge ~7 km (tributary A) and ~7.8 km (tributary B) along its track (Figure 4.4B). Tributary A (Figure 4.7J) merges with the main ridge as it crosses the LDA terminus, at the northernmost end of zone II. It originates at the terminus of a textured band with negative topographic expression in the LDA surface, which resembles that in zone I of the sinuous ridge. Tributary B (Figure 4.7K) merges with the eastern flank of the round-crested plateau in zone III. It originates at the margin of a ~400 m diameter smooth-bottomed depression in the LDA surface, which I interpret as an exposure of the LDA bed.

4.4.2. Rift Floor Units and Landforms

At its emergence from the LDA terminus, the sinuous ridge crosses into the LDA-proximal floor unit (Figure 4.4E), which forms the LDA foreland. The LDA-proximal floor comprises smoothed, pitted and fractured materials (Figure 4.4E). Fractures commonly intersect to form ~100 m diameter polygons. This unit extends 2–10 km from the LDA termini towards the centre of the rift, separating the LDA termini from an annulus of LDA-distal 'knobbly' ridges (Figure 4.4F). The LDA-distal knobbly ridges are oriented oblique to the SSW–NNE-oriented floor fault scarps, which cut through them, but correlate well with the termini of the surrounding LDAs, being subparallel to them. A distinct population of arcuate LDA-proximal transverse ridges (Figure 4.4C) bounds the termini of portions of the eastern LDA that are marked by longitudinal ridges and troughs.

The central rift floor has a distinct bright (night) and dark (day) THEMIS IR signature relative to the LDA-proximal floor and LDAs (Figure 4.4F, inset), indicating a higher thermal inertia. The LDA-distal knobbly ridges conform near-continuously to its boundary with the LDA-proximal floor unit. Poorly expressed lineations in the central floor unit are subparallel to the SSW–NNE-oriented floor fault scarps (Figure 4.4G). A polygonised wedge extends into this central floor zone from beneath the southern knobbly ridge (Figure 4.4H). Its THEMIS IR signature is intermediate between those units. The ~100 m diameter polygons on the surface of the polygonised wedge have wider (tens of metres) marginal troughs than those within the LDA-proximal floor unit. They superpose a chain of mounds that is morphologically similar to the parallel LDA-distal knobbly ridge to the south.

4.4.3. VFF Impact Crater Retention Age

I counted 795 impact craters over all LDAs within the rift (1.51×10^3 km^2; Figure 4.8). *D*(50–80 m) impact craters (n = 311) follow the 30 ± 1 Ma isochron and *D*(130–350 m) impact craters (n = 104) follow the 110 ± 10 Ma isochron. *D*(450–700 m) impact craters, consistently proximal to LDA margins and infilled by the LDA surface materials, may record the age of an older underlying surface (~170–570 Ma). However, owing to the small sample size of craters in this diameter range (n = 5), I do not treat this result as significant. Unavoidable dependence upon small impact craters could result in a factor of ten uncertainty in these model ages (Hartmann, 2005). Age estimates at the upper extreme of this uncertainty are ~300 Ma for *D*(50–80 m) impact craters, and 1.1 Ga for *D*(130–150 m) impact craters.

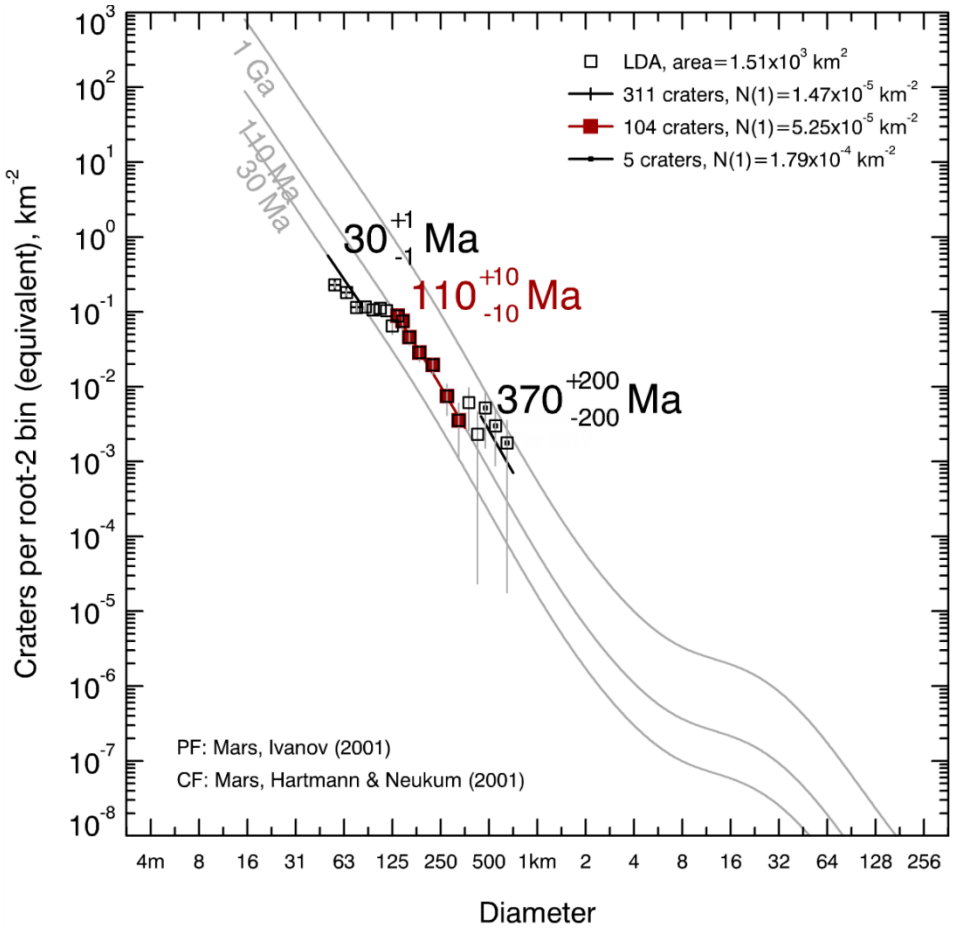

Figure 4.8. Impact crater size-frequency distribution for all LDA within the NW Tempe Terra rift. Log incremental plots (Hartmann, 2005) showing best fit ages along three isochrons. Statistics are based on the Ivanov (2001) production function and Hartmann and Neukum (2001) chronology function. Note that the 370 Ma best-fit age is deemed statistically insignificant due to a small sample (n=5). From Butcher et al. (2017).

4.5. Discussion

4.5.1. Origin of the Sinuous Ridge

Given the glacierised tectonic setting of the sinuous ridge in Tempe Terra, I consider four possible origins: (i) an esker, (ii) an ice-confined subglacial lava flow, (iii) a medial moraine ridge, or (iv) a topographically inverted fluvial palaeochannel, later buried and partially re-exposed by LDA emplacement and degradation. The production of liquid water by Amazonian melt of the LDA is implicit in the first two hypotheses; channelised meltwater drainage is a prerequisite for formation of eskers and esker-like lava flows (e.g., Mathews, 1958), and meltwater is an inevitable by-product of subglacial volcanism. Meltwater is not required for medial moraine formation via supraglacial accumulation of rockfall debris. Liquid water is required for hypothesis (iv), but in this case water could have occurred much earlier in Mars' history, divorced temporally from the glacial landscape described here.

4.5.1.1. Esker Hypothesis

The sinuous ridge emerges from the terminus of an LDA, which leads me to consider a genetic link between these landforms. The sinuous ridge is similar in mean length to terrestrial esker systems in Canada (5932 measured, mean length 15.6 km; Storrar et al., 2014a). The longitudinal transitions in crest morphology between zones I and IV are remarkably similar, in both morphometry and sequence, to those observed along North American eskers that formed within pressurised water-filled subglacial conduits (Shreve, 1985a; Perkins et al., 2016). Sharp- to round-crested elements of these eskers (analogous to zone IV, 5–15 m high, 150–200 m wide) are typically ~3–50 m high and ~150 m wide (e.g., Shreve, 1985a; Perkins et al., 2016). Broad-crested elements of the Katahdin esker, Maine, USA (analogous to zone III, 10–55 m high, 1300 m wide) are typically ~10 m high and 2 km wide (Shreve, 1985a). Multi-crested reaches of North American eskers (analogous to zone II, 5–10 m high, 150 m wide, atop ~30 m high, 500 m–1.5 km-wide topographic rise) have typical heights of 10–15 m (Shreve, 1985a; Perkins et al., 2016), and widths ranging from hundreds of metres (Perkins et al., 2016) to kilometres (Shreve, 1985a).

The sequence of morphological transitions between zones II and IV of the sinuous ridge is the same as those identified along the Katahdin esker system by Shreve (1985a; Figure 4.9). Shreve attributed these transitions to changes in the shape of the meltwater conduit due to bed slope and ice pressure gradient-controlled modification of melt dynamics at the conduit roofs and walls. Under this model, sharp-crested elements form on flat or downslope reaches where meltwater has sufficient energy to melt the conduit roof. In contrast, round-crested elements form on upslope reaches, where the requirement for the meltwater to warm to the

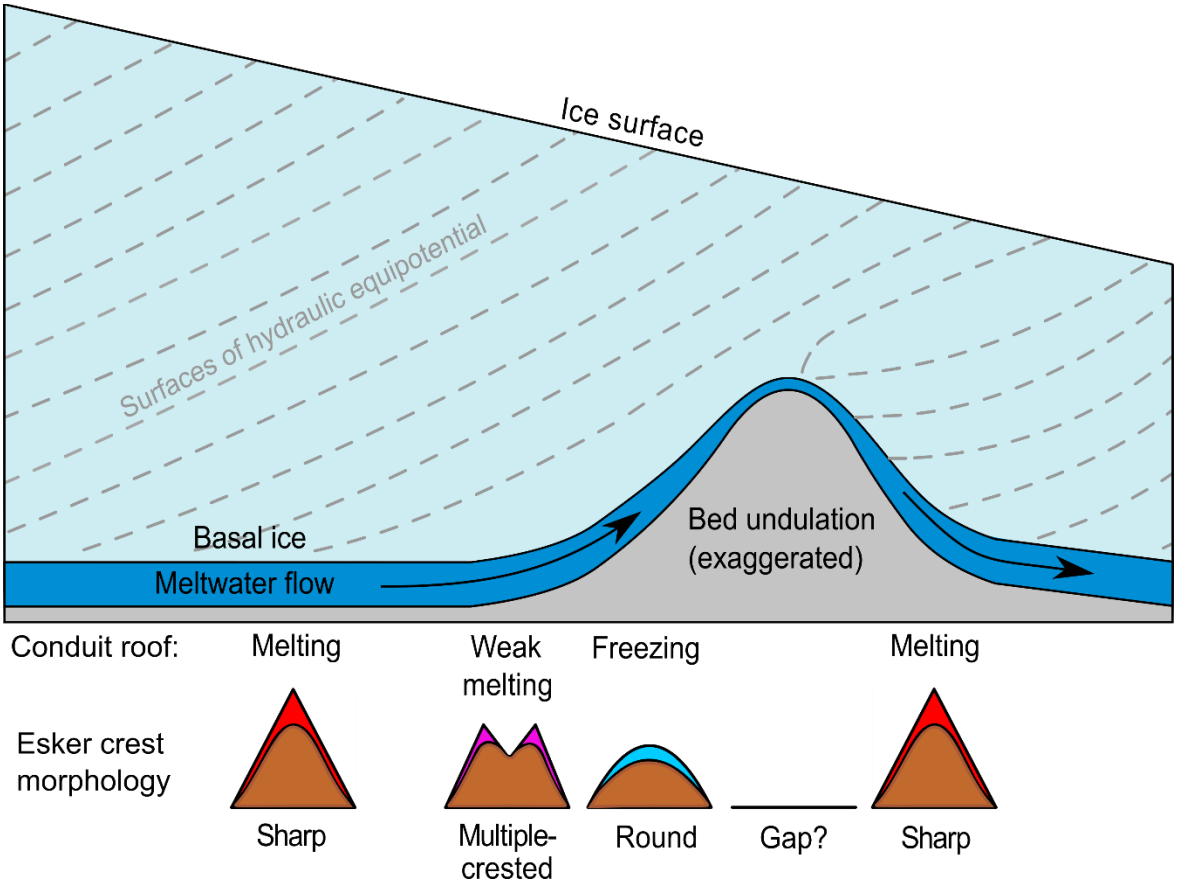

Figure 4.9. The Shreve (1985) model for bed slope-controlled transitions in esker crest morphology. Schematic representation (not to scale) of the transitions predicted by Shreve (1985) from sharp- to multi- to round-crested esker crest morphology as the esker-forming subglacial meltwater conduit approaches and ascends a bed undulation, and the transition back to a sharp-crested morphology in the lee of the undulation. Shreve attributed these crest morphology transitions to reductions in the energy available to melt the conduit roof on ascending bed slopes, and increases on descending bed slopes. 'Pinching' of contours of hydraulic equipotential at the peak of the bedrock undulation can increase meltwater flow power and encourage a transition to a regime of non-deposition (or even erosion) here. If this occurs, a gap between esker segments can result. A gap is not observed along the sinuous ridge in NW Tempe Terra, but I discuss this mechanism further in Chapter 6. Redrawn from Butcher et al. (2016) based on Shreve (1985), and Anderson and Anderson (2010).

raised pressure melting point as it passes into thinner ice means that it has less energy to melt the conduit roof and can even begin to freeze on to the roof. Multi-crested reaches occur on intermediate positive bed slopes between sharp- and round-crested elements (Shreve, 1985a). Eskers are aggradational landforms, and the greater height of the round-crested section in zone III compared to the sharp-crested section in zone IV could be explained by progressive vertical migration of a low, round-roofed conduit over aggrading zone III sediments in response to increases in hydraulic pressure resulting from sedimentation-driven decreases in accommodation space (e.g., Burke et al., 2015). I discuss detailed models that could explain the formation of observed morphological transitions under the esker hypothesis in Chapter 6. Obscuration of the LDA bed by existing LDA deposits prevents detailed tests for such topographic relationships; however, the round-crested zone (III) does

cross upslope reaches of the LDA-proximal floor and transitions back to a sharp-crested morphology downslope (Figure 4.6), as predicted under the Shreve (1985a) model. As is also predicted by the Shreve (1985a) model, the sharp-crested ridge in zone IV progressively reduces in height as it ascends a gentle upslope reach of the bed at its VFF-distal end (Figure 4.6).

Under the esker hypothesis, an alternative explanation for the broad, round-crested morphology in zone III is that it represents an outwash fan which was deposited over a central esker ridge following retreat of the LDA terminus to its present position. Such outwash fans overlie the central ridge of the Vars-Winchester esker in Canada (Cummings et al., 2011). However, outwash fans typically form subaqueously in proglacial lakes, for which I identify no strong evidence within the rift. Continuous meltwater production throughout retreat of the LDA terminus to its present position would be expected to form a continuous sequence of onlapping fans (Cummings et al., 2011) from the northernmost margin of the sinuous ridge to the present LDA terminus, but this is not observed. Therefore, fan formation at this position along the sinuous ridge would require a second discrete phase of meltwater production to that which formed the sinuous ridge in zone IV. I consider this to be less likely than formation of all zones during the same phase of meltwater production. Finally, the margins of the ridge in zone III progressively narrow towards zone IV. This is more readily explained by a narrowing subglacial meltwater conduit towards zone IV than by narrowing of an outwash fan in its ice-distal reaches.

Tributary ridges merging with the main ridge are consistent with capture of minor subglacial drainage by a major meltwater conduit (Shreve, 1972). Disruption of the LDA surface at the heads of the tributaries, and troughs in zone I of the main ridge, are consistent with collapse of the LDA surface under conduit enlargement and evacuation (see Benn et al., 2017). The textural band at the head of tributary A could indicate an underlying (possibly collapsed or infilled) subglacial conduit. This conduit may have formed by lateral escape of over-pressurised meltwater from the central conduit, a process that drives formation of anastomosing branches along terrestrial eskers (Gorrell and Shaw, 1991). The broad depression at the head of tributary B is more consistent with capture of water from a subglacial pond or cavity. Alternatively, this depression could have been excavated by the impact event that formed the impact crater at its centre.

Several smaller-scale features of the sinuous ridge can also be readily explained under the esker hypothesis. Pits in its surface can be explained by collapse into void spaces evacuated by sublimation of ice that was trapped during esker deposition. Subsequent exposure from

the LDA could have triggered destabilisation and sublimation of ice to the atmosphere. Similarly, steep-sided troughs (zone II) could be explained by sublimation of dead ice that was trapped within the esker surface and subsequently sublimated upon exposure from the LDA.

Polygonal fractures cross-cutting impact craters superposed upon zone III of the sinuous ridge provide strong evidence that fractures are not primary structures associated with ridge formation but formed due to secondary modification of its surface. They can be explained by thermal contraction cracking of ice-rich sediments. Their size and morphology are consistent with contraction crack polygons observed in ice-rich terrains elsewhere on Mars and on Earth (see Chapter 3 and e.g., Mangold et al., 2004a; Levy et al., 2010b). Longitudinal fractures along the flanks of the ridge in zone III can be explained by relaxation of the ridge flanks following loss of lateral support by confining walls of a meltwater conduit (Burke et al., 2008, 2012a).

I interpret the small transverse ridge complex that crosses the crest of the sinuous ridge at the northern end of zone III (Figure 4.7A and H) to be a moraine ridge formed by transient ice margin fluctuation following exposure of zone IV by LDA retreat, similar to < 5 m high transverse ridges crossing eskers on the floors of fjords in Spitsbergen, Earth (Dowdeswell and Ottesen, 2016).

4.5.1.2. Ice-Confined Subglacial Lava Flow Hypothesis

Given its glacierised tectonic setting, I consider whether an ice-confined subglacial lava flow could form a viable alternative origin for the sinuous ridge. I find that my observations are inconsistent with such an origin. Terrestrial examples of "esker-like" lava flow ridges have been associated with eruptions of mafic lava into subglacial environments (Mathews, 1958; Smellie and Skilling, 1994; Lescinsky and Fink, 2000; Hungerford et al., 2014). Their esker-like morphologies have been attributed to exploitation of pre-existing subglacial meltwater channels by lava flows. Thus, they may adopt very similar planforms to eskers.

The surfaces of subglacial lava flows are typically characterised by fractures forming columnar joints arising from rapid quenching of lava flow margins upon contact with ice (Lescinsky and Fink, 2000). While polygonal fractures are observed on the surface of the sinuous ridge in Tempe Terra, they have diameters 1 to 2 orders of magnitude greater than those within terrestrial ice-contact lava flows (tens of centimetres to 1 m) (Lescinsky and Fink, 2000; Hungerford et al., 2014). Furthermore, I assert that the observed polygonal fractures cannot be explained by rapid cooling because they cross-cut superposed impact

craters which postdate ridge formation (Figure 4.7G). Thus, fracture formation was not coincident with ridge emplacement but occurred due to secondary modification of ridge surface materials. Thermal contraction of ice-rich sediments under the esker hypothesis can more adequately explain both the scale and relative time of formation of the polygonal fractures.

Furthermore, there exists insufficient evidence to invoke a subglacial volcanic eruption to explain the origin of the sinuous ridge. While it is conceivable that a subglacial volcanic eruption could occur in such an extensional tectonic setting, no large-scale disruption of the LDA surface indicative of an underlying eruptive edifice, such as an ice cauldron, is observed, and no lava flows or volcanic edifices are identified in the surrounding region. Moreover, origination of tributary B from a distinct point to the main ridge and tributary A is better explained by scavenging of water over wide areas of the glacier bed than by the origin of tributary B from a distinct volcanic edifice. Thus, I argue that a subglacial volcanic eruption is inconsistent with the geomorphic evidence documented here.

4.5.1.3. Medial Moraine Hypothesis

Medial moraines are bands of debris oriented parallel to glacier flow direction, and positioned distal from the lateral margins of a glacier. The insulating effect of supraglacial medial debris bands can promote differential ablation of the glacier surface, resulting in preservation of a debris-covered ice core as a ridge within the ablation zone, and occasionally the proglacial zone. These characteristics lead me to consider a medial moraine as a third alternative explanation for the origin of the sinuous ridge.

Whereas the morphological transitions along the sinuous ridge can be readily reconciled with a subglacial esker origin, I find that they are harder to explain under a medial moraine origin. Medial moraines typically have a relatively simple planform morphology. Where they can be traced to their source, medial moraines originate as broad debris accumulations, becoming concentrated into narrow, low-sinuosity ridges down-glacier (e.g., Eyles and Rogerson, 1978; Vere and Benn, 1989; Goodsell et al., 2005). They rarely undergo abrupt variations in width but may spread laterally towards the glacier terminus. Lateral expansion of medial moraines is typically accompanied by an overall lowering of ridge height (e.g., Eyles and Rogerson, 1978; Vere and Benn, 1989). This contrasts with the abrupt variations in width observed along the sinuous ridge, and the apparent increase in height that accompanies ridge widenings in some locations.

Medial moraines can form via ice-stream interaction, avalanche-type, or ablation-dominant mechanisms, as described by Eyles and Rogerson (1978). Ice-stream interaction-type medial moraines form by the convergence of two lateral moraines at a glacier confluence (Eyles and Rogerson, 1978). I exclude such an origin for the sinuous ridge, since the textural band in zone I is not spatially associated with a longitudinal confluence between VFF lobes. The sinuous ridge is clearly superposed by the LDA and emerges from beneath LDA materials in zones I and II. Based on this superposition relationship, I can also exclude an origin as an avalanche-type medial moraine: rare, often transient bands of debris transported supraglacially away from a subaerial debris source such as a rockfall or avalanche at a headwall or nunatak (Eyles and Rogerson, 1978).

Ablation dominant (AD) medial moraine formation involves entrainment of subaerially-derived debris into englacial transport paths and its re-exposure downglacier by ablation of overlying ice (Eyles and Rogerson, 1978). Eyles and Rogerson (1978) identified three subtypes (AD1, AD2, and AD3) based on the mechanism of debris entrainment, which I now consider in sequence. Debris comprising AD1 medial moraines is entrained into shallow englacial transport paths via crevasses below the firn line (Eyles and Rogerson, 1978). A lack of visible crevasses or crevasse traces on the VFF surface leads me to exclude this mechanism for formation of the sinuous ridge.

Debris comprising AD2 medial moraines is entrained into englacial transport paths via burial by snowfall or avalanches above the firn line (Eyles and Rogerson, 1978). Ice flow patterns within terrestrial glaciers commonly dictate that supraglacial debris deposited at the foot of the headwall is transported along englacial flow paths that are close to the bed (Benn and Evans, 2010). During an earlier phase of glaciation within the rift, the bedrock outcrops to the south-east of the sinuous ridge were likely overridden by the LDA to form subglacial bedrock knobs, as evidenced by their rounded, planed, and smoothed morphologies. This would likely have resulted in direct ice flow from the southern rift wall to the LDA terminus. Under this configuration, the bedrock knobs could have formed a topographic obstruction to near-bed englacial transport of a debris septum sourced at the southern rift wall. If englacial debris had been transported along a flow path above the bedrock knobs, evidence for let-down of a moraine ridge over the present-day bedrock outcrops would also be expected, but is not observed. Thus, I find insufficient evidence that the sinuous ridge is an AD2 medial moraine sourced from the southern rift wall.

The AD3 formation mechanism for medial moraines is rarer than the AD1 and AD2 subtypes. Under this mechanism, debris is derived directly from subglacial bedrock knobs

(Eyles and Rogerson, 1978; Vere and Benn, 1989). As discussed above, the bedrock outcrops to the south-east of the sinuous ridge may have formed subglacial bedrock knobs during an earlier stage of glaciation. In the absence of data for the bed topography of the LDA, including the continuation of the bedrock outcrop beneath the LDA, I am unable to exclude conclusively the possibility that these bedrock knobs could have provided a debris source to the sinuous ridge. However, the orientation of the sinuous ridge, lateral to the nearest bedrock outcrop ~700 m to the south-east, seems inconsistent with debris supply from this location. Meltwater is typically required as an agent for erosion and entrainment of such large volumes of subglacial bedrock material into glacial ice.

4.5.1.4. Topographically Inverted Fluvial Palaeochannel Hypothesis

It is possible that the sinuous ridge originated as an ancient subaerial fluvial palaeochannel which was topographically inverted by extensive erosion of the surrounding rift floor and subsequently buried by and re-exposed from later LDA deposits. However, the sinuous ridge does not follow the steepest topographic gradient, and ascends ~5–10 m high topographic undulations in some reaches (Figure 4.6). In the absence of evidence for bedslope modification by differential erosion of the LDA-proximal floor unit, this is inconsistent with subaerial gravity-driven flow, but it can be explained by flow under hydraulic pressure in a subglacial meltwater conduit according to the esker hypothesis (Shreve, 1972). Second, I identify no other evidence for subaerial fluvial erosion within the rift, or inversion of topography in the broader region. I exclude an inverted floodplain for the origin of the broad portion of the ridge in zone III. The upper surface of zone III is tilted, and its crest is higher in elevation than the adjacent portions of the sinuous ridge, which is inconsistent with an origin as a sediment sink. I also observe no evidence for meanders or scroll bars anywhere along the ridge, as are commonly observed along inverted palaeochannels and within inverted floodplains in Aeolis Planum (e.g., Burr et al., 2009). Third, evidence for disruption of the LDA surface (zone I; Figure 4.7B) is more consistent with ridge formation via a process that actively influenced the structure of the overlying LDA (i.e., opening and subsequent evacuation of a meltwater conduit) than with passive advance and retreat of LDA over a pre-existing inverted palaeochannel. Finally, the inverted fluvial palaeochannel hypothesis invokes multiple unrelated processes: aggradation of sediment in a fluvial channel, armouring of channel deposits, differential erosion of surrounding plains, then burial and subsequent exposure by a cold-based glacier. This contrasts with the simpler process explanation under the esker hypothesis, which invokes a genetic relationship between the sinuous ridge and the existing VFF from which it emerges.

4.5.1.5. Working Hypothesis

Of the four hypotheses considered here, I find a subglacial esker origin to be most consistent with my observations of the sinuous ridge on the basis of (1) its association with an existing putative debris-covered glacier, (2) crossing of topography and longitudinal transitions in cross-sectional morphology that are strikingly similar to those of terrestrial eskers formed under hydraulic pressure in subglacial meltwater conduits, and (3) metre-scale morphologies indicative of a volatile-rich composition and formation within an ice-confined subglacial environment.

4.5.2. Origin of Pro-LDA Landforms and Units

I interpret the LDA-proximal transverse ridges as moraines based on their similarity to other moraine-like ridges on Mars (e.g., Arfstrom and Hartmann, 2005; Hubbard et al., 2011). The oblique orientation of the LDA-distal knobbly ridges to structural faults on the rift floor is inconsistent with tectonic control. I interpret them as moraines based on their correlation in orientation to adjacent LDA fronts. Their knobbly appearance and muted topographic expression could imply derivation from supraglacial or englacial debris released from a glacier terminus, similar to marginal aprons at the termini of cold-based glaciers in the Antarctic Dry Valleys (Cuffey et al., 2000).

The high thermal inertia signature of the central rift floor is consistent with a consolidated lithology of the surface materials relative to the LDA-proximal floor (Putzig and Mellon, 2007). The coherence in strike of the lineations here with local faults suggests that they are structural features of the faulted bedrock, rather than streamlined glacial landforms. I therefore interpret the central rift floor as an unglaciated surface, possibly comprising bedrock which also outcrops in the rift-marginal fault scarps (Figure 4.5). The lower thermal inertia of the LDA-proximal floor is consistent with the presence of deposits of less-consolidated (e.g., glacigenic) material (Putzig and Mellon, 2007). Loss of an ice component of the material can explain the pitted textures, while thermal contraction cracking of an ice-rich sedimentary substrate (Levy et al., 2010b) can explain the observed polygonal fracturing. I therefore interpret the LDA-proximal floor unit as a glaciated zone across which the LDAs retreated from the terminal knobbly ridges. The lack of evidence for glacial scour, streamlined forms, or channels implies that the LDAs were cold-based as they crossed this unit. A low sediment supply under such a regime explains the apparent lack of thick sedimentary accumulations in the LDA-proximal floor unit, and the muted topographic expression of the LDA-distal knobbly ridges.

I interpret the polygonised wedge as a relict deposit of an older, slightly more extensive glacial advance within the rift because (1) it is superposed by the knobbly ridge complex but superposes a chain of mounds that is morphologically similar to it (Figure 4.7H), implying stratigraphically-separated episodes of terminal apron deposition, (2) wider polygon-marginal troughs than those within the LDA-proximal floor unit are consistent with more advanced disruption of the surface by thermal-contraction cracking, and (3) intermediate thermal inertia between the central rift floor and LDA-proximal floor units could result from induration of older glacigenic sediments.

4.5.3. Impact Crater Retention Ages

My modelled surface ages from impact crater size-frequency distributions (Figure 4.8) are in agreement with those by van Gasselt et al. (2011) who identify two dominant crater retention ages in their analyses of LDAs in Tempe Terra. They interpret older crater retention ages (up to ~200 Ma) as early traces of modification of LDA surfaces, and younger (10–50 Ma) isochrons to represent episodes of emplacement and modification of an ice-rich mantle on top of the LDAs. My best estimate for the minimum age of the LDAs in the Tempe Terra rift (~110 Ma) places their minimum age of stagnation, and thus formation of the candidate esker, during the late Amazonian (Hartmann and Neukum, 2001), at a similar time to the VFF-linked candidate esker in Phlegra Montes (~150 Ma; Gallagher and Balme, 2015). My upper estimate of 1.1 Ga for the age of the bulk LDA—which considers the potential for a factor of 10 uncertainty (see Section 4.4.3)—is consistent with the 100 Ma–1 Ga age range estimates of Berman et al. (2012) for LDAs in Deuteronilus Mensae and East Hellas. VFFs are generally interpreted to have formed during cyclic (~120 kyr) excursions to intermediate (~35°) planetary spin-axis obliquity during the late Amazonian (Laskar et al., 2004), which permitted prolonged ice accumulation in Mars' mid latitudes (Madeleine et al., 2009).

Similar to van Gasselt et al. (2011), I invoke deposition of an ice-rich mantle deposit superposing the LDAs to explain the younger ~30 Ma isochron in the impact crater size-frequency distribution. This can explain the gradational nature of the contact between the upper margins of the LDAs and the highland mantle unit. The origin of this mantle can most readily be explained by the tens of metres-thick (Conway and Balme, 2014) latitude-dependent mantle (LDM) identified throughout Mars' mid to high latitudes (see Chapter 3; e.g., Mustard et al., 2001). LDM deposition is generally attributed to more recent (0.4–2.1 Ma) (Head et al., 2003; Schon et al., 2012) increases in spin-axis obliquity than those during which LDAs formed. It is possible that the LDA-proximal transverse ridges are

moraines formed by minor, localised, late-stage readvance of small lobes within the VFF in this location.

4.5.4. Landsystem Model

The candidate esker is the only landform within the mapped assemblage that is indicative of glacial meltwater production. All other landforms within the rift can be explained without invoking glacial melting. Hence, I propose that the candidate esker probably represents a phase of meltwater production resulting from a transient perturbation of a longer-term cold-based regime. The position of the sinuous ridge relative to terminal moraine deposits (knobbly ridges) and the parent LDA implies that it formed during partial deglaciation of the rift according to the following landsystem model.

First, LDAs advanced across the LDA-proximal floor unit towards a period of glacial maximum, merging laterally. They advanced under cold-based regimes, which precluded significant reworking of the bed. Thus, terminal deposits (LDA-distal knobbly ridges), fed primarily by supraglacial debris, were poorly developed, and the proglacial zone (central rift floor) was unmodified. Transient basal melting, perhaps associated with the onset of deglaciation, permitted esker formation beneath the southern LDA. Following esker deposition, the parent LDA returned to a cold-based thermal regime and stagnated ~110 Ma, but minor readvance of small lobes within the VFF on the eastern floor of the rift may have occurred since this time, forming the LDA-proximal transverse ridges. The esker was preserved in the basal ice and was partially exhumed from the LDA tongue by sublimation. The upper reaches of the esker remain buried within the LDA and may extend further into the LDA than the visible textural band in zone I. The highlands surrounding the rift and the LDA were subsequently mantled by a thin ice-rich deposit ~30 Myr ago (or periodically deposited and ablated since LDA stagnation, resulting in a model crater retention age of ~30 Ma).

4.5.5. A Newly-Identified Glacier-Linked Esker on Mars

As discussed in Chapter 3, one other example of a late-Amazonian-aged (~150 Ma) mid-latitude VFF-linked esker has been documented to date, in a graben in Phlegra Montes, NE of the Elysium volcanic province (Gallagher and Balme, 2015). The VFF-linked sinuous ridge in NW Tempe Terra identified in the present study, which I interpret as an esker, provides a second location in which an existing mid-latitude VFF underwent wet-based mid-latitude glaciation during the late-Amazonian. Sinuous ridges interpreted as eskers in the south circumpolar Dorsa Argentea Formation (Head and Pratt, 2001; Kress and Head, 2015;

Butcher et al., 2016) and southern Argyre Planitia (Banks et al., 2009; Bernhardt et al., 2013) are early-Hesperian in age (>3.4 Ga; Bernhardt et al., 2013; Kress and Head, 2015). Their formation has been attributed to basal melting of ancient high-latitude ice sheets under warmer climates (Scanlon et al., 2018) and higher global average geothermal heat flux of the late Noachian and early Hesperian (Fastook et al., 2012). The parent ice sheets of these candidate eskers have long since retreated. Thus, these candidate eskers are distinct from the mid-latitude VFF-linked eskers discussed here in their ancient ages, high-latitude locations, and lack of preservation of their parent glaciers.

Similarly, a possible esker complex within fan-shaped deposits on the NW flanks of the equatorial Arsia Mons volcano, which are thought to have been deposited by cold-based glaciers (e.g., Head and Marchant, 2003; Shean et al., 2005; Kadish et al., 2014), could represent a transient episode of wet-based glaciation induced by subglacial volcanism during mid to late-Amazonian glaciation of the equatorial regions (see Chapter 3; Scanlon et al., 2014, 2015) under high planetary spin-axis obliquity (>45°) conditions that were distinct to those that prevailed (~35°) during formation of existing glaciers in the mid latitudes. Like the ancient Dorsa Argentea and Argyre Planitia eskers, this candidate esker complex lacks a preserved parent glacier.

Hence, while there is some evidence for a handful of other candidate eskers on Mars at a range of latitudes, thus far, the only two documented examples of eskers emerging from existing parent glaciers are seen at mid latitudes, and are of late-Amazonian age.

4.5.6. Geologic Setting and Environmental Controls on Melting

As discussed in Chapter 3, Gallagher and Balme (2015) suggest an enhanced geothermal heat flux in the rift setting of the candidate esker in Phlegra Montes to explain its formation. Hence, I now consider the influence of geologic setting on basal meltwater production by mid-latitude VFFs.

Terrestrial grabens/rifts are commonly associated with elevated geothermal heat flux, for example due to heating from intrusive magma bodies (e.g., dikes), volcanic plutons, and/or hydrothermal circulation (e.g., Fernàndez and Banda, 1990). Enhanced geothermal heat flux within terrestrial grabens/rifts can influence the production of basal meltwater by glaciers which occupy them (e.g., Jordan et al., 2010; Schroeder et al., 2014). Identification of mid-latitude VFF-linked candidate eskers within grabens/rifts in Phlegra Montes and now Tempe Terra leads me to consider whether a genetic link exists between the setting and the landform. Thus far, a lack of evidence for basal melting of existing VFFs elsewhere in Mars' mid

latitudes implies that broad-scale, cyclic (~120 kyr), obliquity-induced mid-latitude climate warming (e.g., Madeleine et al., 2009) alone was insufficient to melt basal ice during the Amazonian. Hence, mid-latitude Amazonian glaciation was broadly cold-based. A regional warm climate anomaly would have to persist over long timescales in order to induce and maintain temperate conditions at the glacier bed. The lack of morphological evidence for prolonged supraglacial or subglacial melting (e.g., fans, and streamlined bedforms) leads me to exclude such a regional climate anomaly as the sole driver of wet-based glaciation in the Tempe Terra rift. Thus, while I do not exclude climate warming as a possible contributing factor in inducing wet-based glaciation, I argue that perturbation of basal ice temperatures by a geothermal heat flux anomaly (Gallagher and Balme, 2015) is more consistent with the tectonic setting and my geomorphic observations.

While primary geothermal anomalies associated with the formation of the ancient rift in NW Tempe Terra (Hauber et al., 2010) are unlikely to have persisted into the Amazonian, magmato-tectonic processes could have exploited pre-existing structural weaknesses in their vicinity to induce geothermal anomalies coincident with recent glaciation. Given uncertainties over the precise ages of features on planetary surfaces, and the current lack of available ground-truth for global geothermal heat flux models, reliable identification of a specific syn-glacial source of geothermal heat to the rift cannot be achieved with confidence. Therefore, I do not aim to identify a specific geothermal source event. Instead, I highlight evidence that magmato-tectonic activity in NW Tempe Terra is unlikely to have ceased at the termination of the last major phase of faulting. Thus, I argue that a recent phase of above-average geothermal heat flux in the vicinity of the rift cannot be excluded as a possible heat source for wet-based glaciation.

Multiple generations of Hesperian- to Amazonian-aged grabens dissect the region surrounding the NW Tempe Terra rift (e.g., Scott and Dohm, 1990a, 1990b; Tanaka, 1990). Giant magmatic dike swarms emanating from the Tharsis volcanic province have been posited as a driver for their initial formation (Mège and Masson, 1996). I identify evidence for recent, localised reactivation of portions of these faults proximal to the rift in NW Tempe Terra.

A ~3000 km-long graben system originating in Tractus Catena (SW) and terminating in Acidalia Planitia (NE) passes directly through the centre of the rift (Figure 4.10A). Portions of this system have been associated with mid- to late-Amazonian (~0.25–0.7 Ga) reactivation of early-Hesperian to mid-Amazonian-aged (~0.7–3.8 Ga) faults by magmatism at Ascraeus Mons (Tanaka, 1990). Small, fresh, cross-cutting faults in the rift-marginal fault

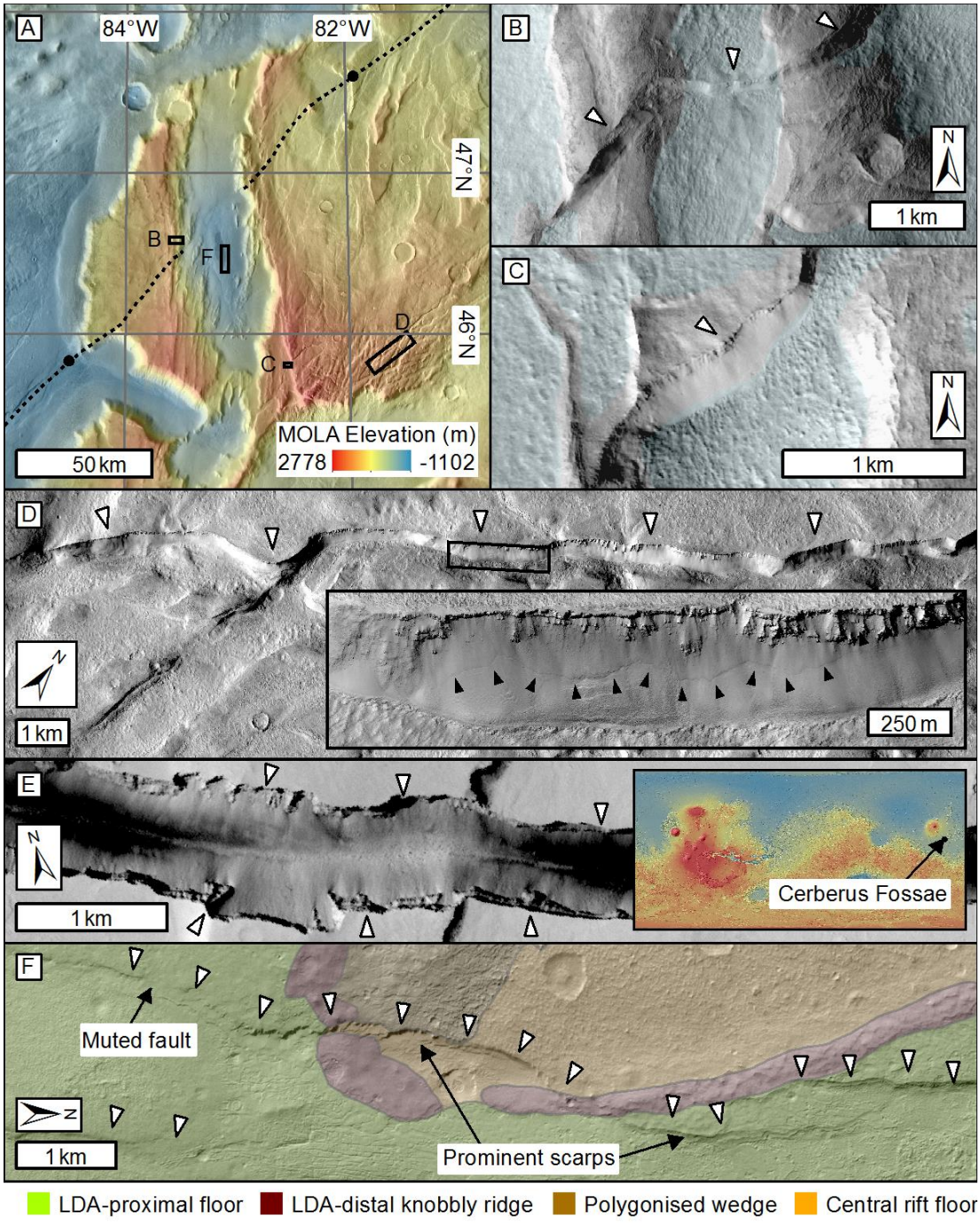

Figure 4.10. Examples of morphologically fresh (i.e., recently active?) fault scarps in and around the NW Tempe Terra rift, and comparison to young fault scarps in Cerberus Fossae. White arrows indicate fault scarps. (A) MOLA elevation on THEMIS daytime infrared context map (Table 4.1) showing major rift-crossing Hesperian- to Amazonian-aged fault system (dashed line) and locations of panels B–D and F. (B and C) Morphologically fresh fault scarps cutting rift-marginal fault blocks (grey) and possibly cutting young LDM (blue). (D) Morphologically fresh fault scarp east of the mapping area. The black box shows the extent of the inset HiRISE image (Table 4.1) which shows a laterally extensive slope failure (black arrows) on the uncratered fault scarp. (E) Late-Amazonian-aged fault scarp in Cerberus Fossae (image centred 10.32°N, 156.73°E; location in inset MOLA elevation map) showing similar morphological freshness to scarps in panels B–D. (F) Variable expression of fault scarps within LDA-proximal floor, LDA-distal knobbly ridge, polygonised wedge, and central floor map units. Panels B–F are CTX images (Table 4.1). Modified from Butcher et al. (2017).

blocks, and possibly even in the latitude-dependent mantle, support recent localised reactivation of portions of the fault system proximal to and within the rift (Figure 4.10B and C). Additional (up to ~40 km long) fault scarps (e.g., Figure 4.10D) ~10 km southeast of therift, which are subparallel to those within the rift-marginal fault blocks (i.e., possibly related to the same stress field), are comparable in morphological freshness to some of the youngest graben scarps on Mars, such as Cerberus Fossae (Figure 4.9E; e.g., Taylor et al., 2013). Using standard techniques in NASA Ames Stereo Pipeline (Shean et al., 2016), a 5 m/pixel DEM of the fault scarp in Figure 4.10D was generated[4] from HiRISE images ESP_052553_2260 and ESP_052065_2260, vertically aligned to HRSC image H1528_0000. Average slopes on the fault scarp range from 30° to 55°. Such steep slopes, above the angle of repose, could be attributed to recent formation of the fault scarp, and the resulting short timescales available for scarp degradation and lowering of slopes. Furthermore, the young latitude-dependent mantle, which blankets adjacent surfaces and faults, is absent on the fresh fault scarps, possibly implying faulting since emplacement of mantle materials. A continuous sheet of material appears to have been mobilised downslope along a ~1.5 km long portion of the fault scarp in Figure 4.10D (inset, black arrows). I consider it unlikely that local slope instabilities within individual alcoves along the scarp could mobilise a continuous lobe with such a large lateral extent. Therefore, I tentatively propose that seismicity associated with recent fault movements could be a more plausible mechanism for initiating such slope failures.

Such spatially restricted fault reactivation is more likely to have been induced by local tectonism than distal activity in the source regions of the grabens (i.e., the Tharsis volcanoes). Impact crater size-frequency distributions for lava flows within the Tempe Volcanic Province indicate very recent (100–800 Ma) volcanism ~500 km SSW of the rift (Plescia, 1981; Hauber et al., 2011). While the scale of, and distance to, the Tempe Volcanic Province likely excludes it as a direct cause of rift-proximal fault reactivation, or a source of geothermal heat to the rift, this highlights that very recent volcanism, probably derived from shallow melt sources (Plescia, 1981), has occurred within the Tempe Terra region. Non-eruptive magmatism, which could manifest at the surface as reactivated faults, probably persisted into more recent times than eruptive volcanism. However, identifying a specific mechanism for the origin of the fresh fault scarps would involve significant unknowns, so I do not speculate further.

[4] DEM generated by S. J. Conway.

If my interpretations of the LDA-distal knobbly ridges as terminal moraines and/or my interpretation of the polygonised wedge as older glacial sediments are correct, faults that cut through them (Figure 4.10F) could imply syn-glacial tectonism within the rift. The polygons within the polygonised wedge appear to exert a structural control upon the morphology of the scarp that passes though it and the overlying knobbly ridge. Thus, it is also plausible that the fault predates the most recent glacial advance within the rift and that its apparently morphologically "fresh" expression within these units can be attributed to modification of scarp degradation processes by the polygonised wedge, and associated disruption of the overlying knobbly ridge. These faults also manifest, with variable scarp morphology, within the LDA-proximal floor unit, which I interpret as a glacier foreland across which the LDA retreated. In some locations (predominantly in the northern portion of the unit where surficial sedimentary deposits appear thinner), they have prominent scarps, while in others (predominantly in the southern portion of the unit where LDA-proximal floor materials appear slightly thicker), they are muted. Such muted expressions could result from faulting within unconsolidated (e.g., glacigenic) sediment (syn-glacial faulting), or deposition over a pre-existing scarp (preglacial faulting). Thus, it is difficult to determine whether they predate or postdate emplacement of this unit. No faults manifest within LDA surfaces, but this does not refute small-scale syn-glacial faulting, particularly given the small vertical expression of the rift floor faults, since viscous relaxation, ice flow, and mantling processes would be expected to erase small fault traces on short timescales.

All three examples of relatively fresh fault scarp populations discussed here were unmapped in Viking-era studies, which concluded that formation of the major grabens in this region was largely, yet not entirely, complete by the mid to late Amazonian (e.g., Scott and Dohm, 1990a, 1990b; Tanaka, 1990). It is therefore conceivable that small-scale tectonism might have continued into the late Amazonian. Thus, the existence of positive geothermal anomalies in the vicinity of the rift (for example due to magmatic dike propagation into the near subsurface), in the period during which the VFFs formed, is plausible.

In addition to potential subglacial geothermal heat sources, I also consider the possibility that viscous strain heating within the basal ice could have contributed to warming of the glacier bed to the melting point. The candidate esker I identify here is located in an area of potential topographic flow convergence. The configuration of the remnant LDA suggests that ice flow converged horizontally from the western and eastern flanks of the rift at the time of esker formation (Figure 4.3 and Figure 4.4A). Additionally, the along-profile slope of the parent glacier decreases markedly in the location of the candidate esker (Figure 4.5).

This glacier configuration seems conducive to production of higher shear stresses and locally thicker ice in the vicinity of the candidate esker, hence encouraging warming of the basal ice. Strain heating is highly sensitive to ice temperature; thus, strain heating would have been particularly important if geothermal heat flux was also elevated. Colder basal temperatures towards the glacier margin arising from thinning of the parent LDA towards its terminus would not preclude esker formation, as channelised meltwater has been observed to penetrate through cold margins of polythermal glaciers on Earth (Bingham et al., 2008, 2005; Kavanaugh and Clarke, 2001).

4.6. Conclusions

In this chapter, I have documented a geomorphic assemblage associated with a late-Amazonian-aged debris covered glacier within a tectonic rift in NW Tempe Terra, in Mars' mid latitudes. I interpret a sinuous ridge emerging from the glacier as an esker formed by deposition of sediment in a pressurised subglacial meltwater channel during a transient phase of wet-based glaciation. For brevity, I hereafter refer to the VFF-linked sinuous ridge in NW Tempe Terra as a glacier-linked esker, but emphasise that the unavoidable caveats of uncertainty in geomorphic interpretations of planetary surfaces (see Chapter 1) remain. To my knowledge, the glacier-linked eskers in NW Tempe Terra (this study) and Phlegra Montes (Gallagher and Balme, 2015) are the only documented examples that emerge from parent VFFs in Mars' mid latitudes. Their parent VFFs both occupy graben-like rifts within which late-Amazonian Tharsis/Tempe Terra and Elysium magmatism could plausibly have enhanced geothermal heat flux. Small, fresh faults in Tempe Terra could be a surface manifestation of such late-stage magmatism. A lack of documented evidence (thus far) for widespread basal melting of mid-latitude VFFs is widely interpreted to indicate that atmospheric warming alone was insufficient for wet-based glaciation. Therefore, enhanced geothermal heat flux, possibly supplemented by internal strain heating, might have been a prerequisite for basal melting. I predict that eskers are most likely to be found in association with VFFs within faulted zones close to recently active volcanic regions.

The discussion above considers the qualitative evidence for environmental controls upon basal melting, and hence esker formation in the tectonic rift in NW Tempe Terra. I discuss the results of quantitative models that constrain the environmental requirements for basal melting, which were undertaken by N. S. Arnold in parallel with the preparation of this thesis, in Chapter 9.

CHAPTER 5

METHODS FOR MEASUREMENT OF ESKER MORPHOMETRIES

5.1. Attribution

The core morphometric methods presented in this chapter are published in a peer-reviewed journal article in *Icarus* (Butcher et al., 2016). This article was based on work submitted to a previous degree, but I re-describe the method here for clarity. The method by which I generated the DEM for the NW Tempe Terra site is published in a peer-reviewed journal article in the *Journal of Geophysical Research: Planets* (Butcher et al., 2017). I also briefly describe the methods used by Storrar et al. (2014a) and Storrar and Jones (unpublished) to obtain the datasets of the morphometries of eskers in Canada and SW Finland, respectively, with which I compare the morphometries of the martian eskers. In Section 5.7.2, I describe method validation undertaken in collaboration with R. D Storrar and A. Jones, which necessitated blind repeat measurements to be obtained by independent workers. In these experiments, I obtained manual measurements and Storrar and Jones obtained semi-automated measurements.

5.2. Background

In this chapter, I describe the methods used to obtain measurements of the 2D and 3D morphometries of the NW Tempe Terra and Phlegra Montes eskers presented in Chapters 6 and 7 respectively, and the secondary datasets with which I compare these measurements in Chapter 7. The term '2D esker morphometries' refers to the geometric properties of eskers when viewed from above, including their lengths, the degree to which they deviate from a straight-line path (sinuosity), and the degree of fragmentation along their paths (continuity). The term '3D esker morphometries' refers to geometric properties of eskers in topographic profile, including their heights, widths, width-height ratios, and cross-sectional slopes.

5.3. Basemap Data

5.3.1. Phlegra Montes, Mars

The basemap data from which I obtained 2D and 3D morphometries of the esker complex in Phlegra Montes comprised a 1 m/pixel DEM with a vertical precision of ± 0.252 m, and two 25 cm/pixel orthorectified images, which I generated from 25 cm/pixel HiRISE stereo pair images ESP_044316_2130 and ESP_044804_2130 (Table 5.1) using U.S. Geological Survey ISIS3 and BAE Systems SOCET SET 5.6.0 software, according to the method of Kirk et al. (2008)[5].

I imported these data into ESRI ArcGIS 10.1 software in a sinusoidal projection that was centred on 162.5°E (i.e., the centre of the glacier foreland) to minimise cartographic distortion. Using standard tools in ArcGIS, I derived three accompanying raster products from the DEM to aid visual inspection and interpretation of the 3D surface: (1) a slope map colourised according to the slope of a plane fitted to the elevation values of each pixel and the eight pixels that surround it, (2) an aspect map colourised according to the compass direction faced by that plane, and (3) a shaded relief (hillshade) model of the surface that replicates the illumination of the surface by a light source with a given azimuth and altitude.

This basemap represents an improvement upon that used by Gallagher and Balme (2015), who were limited to a 6 m/pixel CTX image (Image ID: G20_026224_2116_XN_31N196W), with no DEM of sufficient resolution available for 3D characterisation of the esker complex.

5.3.2. North West Tempe Terra, Mars

Using the same approach as for the Phlegra Montes esker complex (Section 5.3.1), I generated a DEM with 2 m horizontal resolution (and ± 0.492 m vertical precision), and two orthorectified images, of the glacier-linked esker in NW Tempe Terra using 50 cm/pixel HiRISE images (ESP_049573_2265 and ESP_049639_2265; Table 5.1; Chapter 4, this thesis; Butcher et al., 2017). This is the same DEM as I used in Chapter 4. I imported these data into ArcGIS in a sinusoidal projection centred on 276.5°W (the centre of the rift valley hosting the esker) and produced accompanying slope, hillshade, and aspect maps from the DEM, to form the integrated image and topographic basemap from which I obtained measurements of the 2D and 3D morphometries of the NW Tempe Terra esker.

[5] I followed the workflow guide generated by the U.S. Geological Survey, available at: ftp://pdsimage2.wr.usgs.gov/pub/pigpen/tutorials/SS4HIRISE_JULY2015/HiRISE_StereoProcessing_Tutorial_July_2015.pdf (last accessed 02/02/2019).

5.4. Measurement

I performed all measurements within ArcGIS 10.1 software, and all statistical analyses within the statistical computing package R (R Development Core Team, 2008).

5.4.1. 2D Morphometries

I obtained planform morphometries of the Phlegra Montes (Gallagher and Balme, 2015) and NW Tempe Terra (Chapter 4, this thesis; Butcher et al., 2017) eskers following the method of Storrar et al. (2014a) and Butcher et al. (2016). First, I digitised the crests of individual, unbroken ridge *segments* as lines onto the integrated basemaps (Section 5.3) in ArcGIS. I grouped these segments into ridge *systems* comprising aligned, discontinuous chains of individual segments. I digitised segments or systems that formed branches of larger esker *networks* individually; where segments or systems joined at a junction, I used ridge orientation and morphological similarity to distinguish the primary ridge (i.e., the system or segment that is continuous across a junction) from a tributary or distributary ridge.

I then extracted five types of length measurement from the digitised crestlines (Figure 5.1): (1) individual segment lengths (L_s); (2) the combined lengths of all individual segments within a given ridge system (mapped length, L_m); (3) the combined length of all segments within the system plus the straight-line distance between successive segments (interpolated system length, L_i); (4) the straight-line distance between the start and end points of individual segments (segment path length, P_s); and (5) the straight-line distance between the start and end points of each ridge system (system path length, P_i).

Following Storrar et al. (2014a) and Butcher et al. (2016), I then quantified the *continuity* (*C*; i.e., the degree of fragmentation) of each ridge system, according to:

$$C = \frac{L_m}{L_i} \quad \textbf{5.1}$$

where $C = 1$ indicates a continuous system with no gaps, and, for example, $C = 0.5$ indicates a system where gaps comprise 50% of the system length.

I also calculated the degree to which segments deviated from a linear path (segment *sinuosity*, S_s) as:

$$S_s = \frac{L_s}{P_s} \quad \textbf{5.2}$$

and the degree to which systems deviated from a linear path (system sinuosity, S_i) as:

$$S_i = \frac{L_i}{P_i} \quad \textbf{5.3}$$

(Butcher et al., 2016; Storrar et al., 2014a).

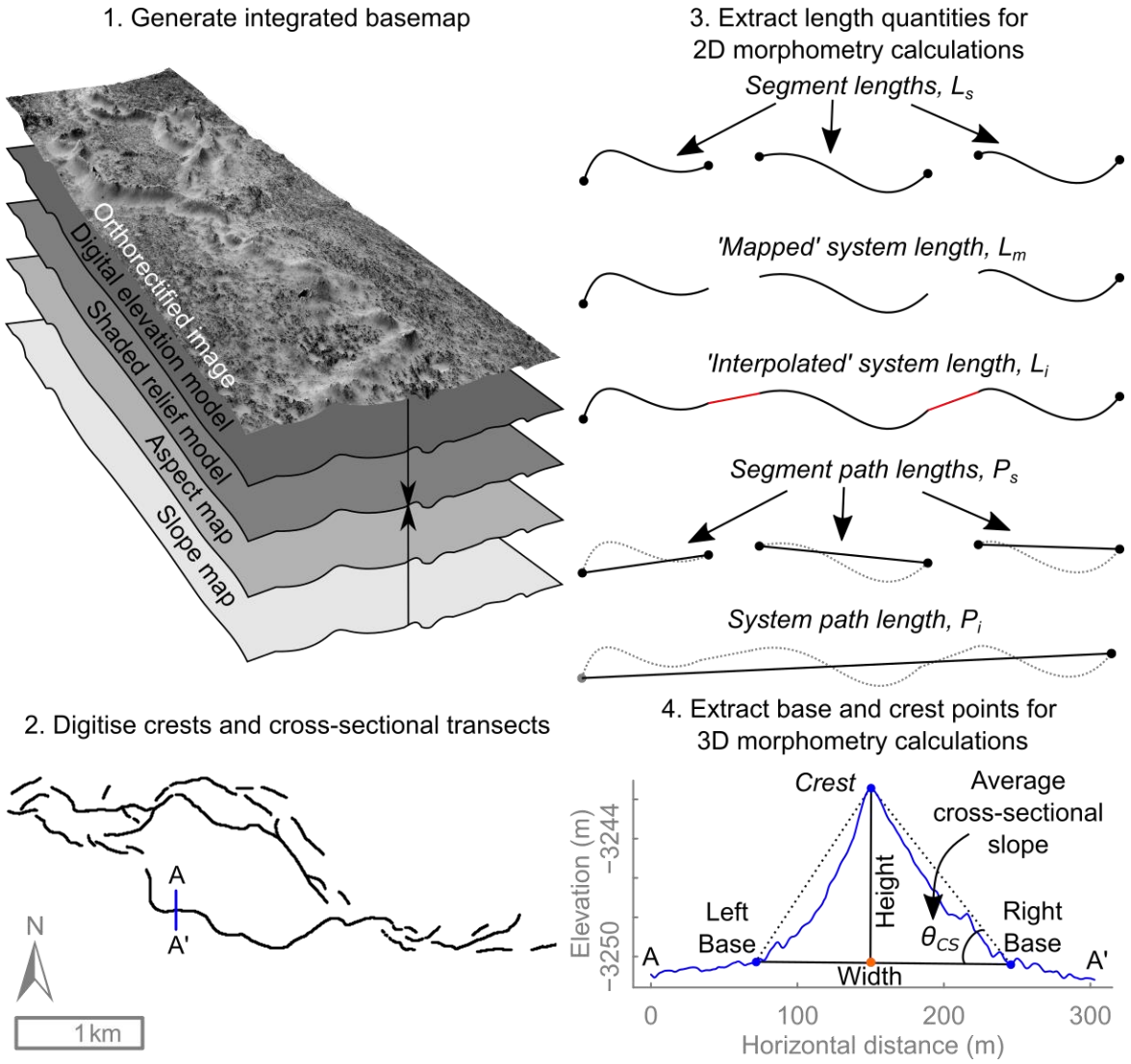

Figure 5.1. Schematic showing approach to measuring the 2D and 3D morphometries of eskers on Mars. Stage 1: Preparation of integrated basemap for each site (oblique view of orthorectified HiRISE image for Phlegra Montes esker complex shown, see Table 5.1). Stage 2: Digitisation of ridge crestlines onto the integrated basemap (crestline map of Phlegra Montes esker complex shown) and construction of cross-sectional transects perpendicular to digitised crestlines (for clarity, only a single example transect A–A' is shown here by the blue line; see Figure 5.2 for sample locations). Stage 3: Extraction of segment length, mapped system length, interpolated system length, segment path length, and system path length. I used these values to calculate system continuity, segment sinuosity, and system sinuosity. Black dots represent the start and end points of the measurements for each length quantity, and solid lines represent the measured length. Red lines represent linear interpolation across gaps between associated segments comprising a ridge system. Adapted from Butcher et al (2016). Stage 4: Viewing of cross-sectional transects in topographic profile (location of example transect A–A' shown by blue line on crestline map) and identification of ridge crest, left base and right base points. I used these points to approximate the elevation of the base of the ridge (shown by the orange point), and to calculate ridge width and height for each transect. I then calculated width-height ratios and average cross-sectional slopes (θ_{CS}) from these values.

Table 5.1 List of data products used in Chapter 5.

Instrument or Source	Image/Product ID or Description	Figure
Mars Orbiter Laser Altimeter[1]	Gridded South Polar Elevation Model, 256 pixel/degree (MEGDR)[2]	5.4
	Hillshade generated from MEGDR[2]	5.4
Context Camera[3]	Mosaic[4] generated from images: B05_011706_2116_XN_31N198W, G20_026224_2116_XN_31N196W, G23_027279_2132_XN_33N198W, P18_007935_2132_XN_33N197W, P22_009583_2132_XN_33N197W, P22_009794_2155_XI_35N198W[5]	5.2A
	Mosaic[4] generated from images: B21_017807_2262_XN_46N083W, P05_002907_2258_XN_45N083W, P15_007021_2276_XN_47N082W, P18_008168_2279_XI_47N082W[5]	5.2B
High Resolution Imaging Science Experiment[6]	ESP_044804_2130 (orthorectified)[4]	5.1, 5.3A, 5.8A
	ESP_044316_2130 (orthorectified)[4]	-
	ESP_049573_2265 (orthorectified)[4]	5.3E and I
	ESP_044105_2130 (orthorectified)[4]	5.2A
	Digital elevation model[4] (PM DEM) generated from images ESP_044316_2130[7] and ESP_044804_2130[7]	5.8A, D
	Figure of Merit for PM DEM[4]	-
	Slope map generated from PM DEM[4]	5.8A (Inset)
	Hillshade map generated from PM DEM[4]	5.3B
	Aspect map generated from PM DEM[4]	-
	Smoothed PM DEM[4]	-
	Hillshade map of smoothed PM DEM[4]	5.3C

Table 5.1 continues on next page

Table 5.1 continued from previous page

Instrument or Source	Image/Product ID or Description	Figure
High Resolution Imaging Science Experiment (continued)	Map of elevation difference between raw and smoothed PM DEM[4]	5.3D
	Digital elevation model[4] (NWTT DEM) generated from images ESP_049573_2265[7] and ESP_49639_2265[7]	-
	Slope map generated from NWTT DEM[4]	-
	Hillshade map generated from NWTT DEM[4]	5.3F and J
	Aspect map generated from NWTT DEM[4]	-
	Smoothed NWTT DEM[4]	-
	Hillshade map of smoothed NWTT DEM[4]	5.3G and K
	Map of elevation difference between raw and smoothed NWTT DEM [4]	5.3H and L
Storrar et al. (2013)	Canadian eskers shapefile[8]	5.5
Natural Earth[9]	1:10 million physical vector shapefiles	5.5, 5.6A
	1:10 million cultural vector shapefiles	5.5, 5.6A
National Land Service of Finland[10]	1:800,000 scale Background Map Series	5.6B
	Light Detection and Ranging DEM mosaic[11] generated from 8 x 8 grid 6 x 6 km tiles. Tile codes for corners of grid: L4224B, L4242H, L4213A, L4231G[10]	5.6A, C, 5.7A
	Hillshade model generated from LiDAR DEM[11]	5.6A, C, 5.7A
	Slope map generated from LiDAR DEM[11]	5.7B
Stroeven et al. (2016)	Deglaciation reconstruction isochrones shapefile[12]	5.6C
Personal communication	Crestline shapefile of the Dorsa Argentea eskers[13]	5.4
	2D and 3D morphometries of the Dorsa Argentea eskers[13]	-

Table 5.1 continues on next page

Table 5.1 continued from previous page

Instrument or Source	Image/Product ID or Description	Figure
Personal communication (continued)	2D morphometry dataset for eskers in Canada[14]	-
	Crestline shapefile of eskers in Fennoscandia[15]	5.6
	Crestline shapefile of eskers in SW Finland[14]	5.6C
	2D and 3D morphometries of eskers in SW Finland[14]	
	Blind repeat measurements of an esker in SW Finland obtained via semi-automated method[15]	5.7
	Blind repeat measurements of an esker in SW Finland obtained via manual method[4]	5.7
	Blind repeat measurements of the Phlegra Montes esker complex obtained via semi-automated method[14]	5.8
	Blind repeat measurements of the Phlegra Montes esker complex obtained via manual method[4]	5.8

[1] (Smith et al., 2001)
[2] United States Geological Survey Planetary GIS Web Server: http://webgis.wr.usgs.gov/pigwad/down/mars_dl.htm
[3] (Malin et al., 2007)
[4] Generated by F. E. G. Butcher, this thesis
[5] Arizona State University http://viewer.mars.asu.edu/viewer/ctx#T=0
[6] (McEwen et al., 2007)
[7] The University of Arizona https://hirise.lpl.arizona.edu/
[8] Accessed on 25/10/2018 at: www.researchgate.net/publication/284715993_Canadian_eskers_shapefile
[9] Available at: www.naturalearthdata.com, accessed 12/07/2018.
[10] Available at https://tiedostopalvelu.maanmittauslaitos.fi/tp/kartta?lang=en, accessed 12/07/2018.
[11] Generated by R. D. Storrar
[12] Accessed on 01/11/2018 at: www.sciencedirect.com/science/article/pii/S0277379115301141#ec2
[13] Butcher et al. (2016); data available from the author
[14] Storrar and Jones (unpublished); data provided by R.D. Storrar and processed by F. E. G. Butcher
[15] Stroeven et al. (2016); data provided by C. Hättestrand

5.4.2. 3D Morphometry

I obtained measurements of esker height, width, and width-height ratio using the manual 3D point classification method of Butcher et al. (2016) as follows.

In ArcGIS, I converted the segment crestlines, from which I measured 2D morphometries (see Section 5.4.1), to equidistant points. Taking into consideration the lengths of the eskers, the resolution of their respective basemaps, and the labour intensity of the manual measurement approach, I used sample spacing of 10 m for the Phlegra Montes esker, and 20 m for the NW Tempe Terra esker (i.e., 10 times the horizontal resolutions of the DEMs).

I then manually digitised cross-sectional transects, which intersected each sample point perpendicular to the ridge crest and extended across the full width of the ridge and into surrounding terrain. Some sampling gaps (Figure 5.2) occurred around tight bends. I converted the cross-sectional transects to equidistant (~1 m spaced) points and extracted elevation values from the DEMs for each point. I then viewed the cross-sectional transect points, both in topographic profile (with 10 x vertical exaggeration to aid identification of the major breaks in slope) and in planform, against the integrated basemap to classify the crest, left base and right base points of the ridges. I identified the left base and right base points as the major break in slopes either side of the ridge, and the crest as the point of maximum elevation between these points. Cross-referencing the topographic profiles with planform views of the transects on the integrated basemap ensured that adjacent topographic features did not affect my classification of the ridge base points. I used the crest, left base and right base points to calculate the height, width, width-height ratio, and average cross-sectional slope for each cross-sectional transect according to the following equations.

Following Butcher et al. (2016), I calculated ridge height (H) for each cross-sectional transect as the difference in elevation between the crest of the ridge (Z_{crest}) and the bed (Z_{base}):

$$H = Z_{crest} - Z_{base} \quad \textbf{5.4}$$

where Z_{base} is approximated from the elevations of the left base point (Z_{left}) and the right base point (Z_{right}) according to:

$$Z_{base} = \frac{Z_{left} + Z_{right}}{2} \quad \textbf{5.5}$$

I calculated ridge width (W) for each cross-sectional transect as the horizontal distance between the right base point and the left base point according to:

$$W = M_{right} - M_{left} \quad \textbf{5.6}$$

where M_{right} and M_{left} are the along-transect distances (from the leftmost end of the transect) of the right base and left base points, respectively.

I then calculated the width-height ratios according to:

$$A_{W:H} = \frac{W}{H} \quad \textbf{5.7}$$

where W is ridge width from Equation 5.6 and H is ridge height from Equation 5.4.

Following Storrar et al. (2015) and Butcher et al. (2016), I also approximated the average slope (Figure 5.1) across each cross-sectional transect, according to:

$$\theta_{CS} = \tan^{-1}\frac{H}{0.5W} \quad \textbf{5.8}$$

5.4.3. Sampling

The sample locations for the 2D and 3D morphometries of the Phlegra Montes and NW Tempe Terra eskers are shown in Figure 5.2.

I measured the 2D morphometries of all visible ridges in the Phlegra Montes esker complex. Owing to uncertainties in their origin, I excluded the two short (~400 m long) ridges that merge with the eastern flank (Figure 5.2B, white arrows) of the NW Tempe Terra esker from subsequent analyses. While I tentatively interpreted these ridges as tributaries to the main trunk esker in Chapter 4, their near-complete burial by remnant materials of the parent viscous flow feature prevents conclusive identification of these ridges as tributaries.

For measurements of 3D morphometries, I excluded cross-sectional transects from both samples if: (1) they crossed ridge intersections, (2) their bases were obscured by adjacent ridges, (3) they had been visibly modified by secondary processes such as impact cratering, and (4) if they were within 40 m of the tapering ends of the ridge segment. The 40 m exclusion distance from ridge ends was an empirical criterion based on the typical distance over which the ridges tapered. Additionally, I excluded systems covered by fewer than 15 transects from the 3D analyses for Phlegra Montes, since the short lengths of these segments approached the typical widths of ridges within the complex. I did not extract 3D measurements in zone I of the NW Tempe Terra esker (the textured band; see Chapter 4), owing to near-complete obscuration of its topography by superposing material of its parent viscous flow feature. Sample locations are shown in Figure 5.2. The raw dataset comprises 582 transects for the Phlegra Montes esker complex and 457 transects for the NW Tempe Terra esker.

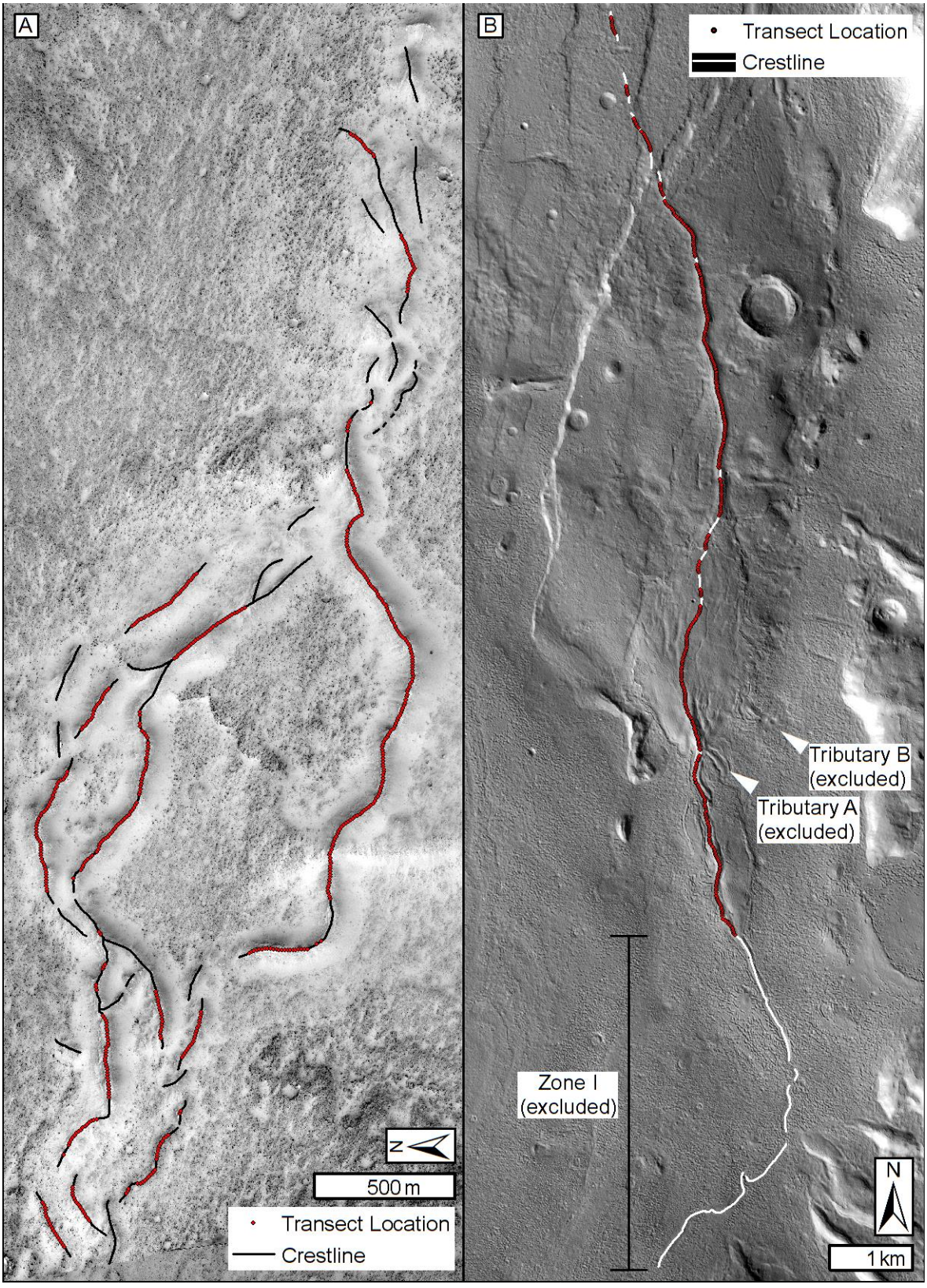

Figure 5.2. Sampling locations for 2D and 3D morphometry measurements of glacier-linked eskers in Phlegra Montes and NW Tempe Terra. Crestline maps (lines) from which 2D morphometries were obtained, with red points indicating where cross-sectional transects for 3D measurements intersected these lines for: (A) the Phlegra Montes esker complex (orthorectified HiRISE image), with a sample spacing of ~10 m for 3D measurements; and (B) the NW Tempe Terra esker, excluding two possible tributaries (CTX image mosaic), with a sample spacing of ~20 m for 3D measurements. See Table 5.1 for a list of data products.

5.5. Measurement Uncertainties

5.5.1. Uncertainties in Measured Quantities

My approach to calculations of uncertainties for measured quantities for the NW Tempe Terra and Phlegra Montes sites is described in Appendix A. These uncertainties are displayed in Table 5.2.

Here, I describe the uncertainties associated with the map projections used for both sites, and those arising from both the vertical precision of the DEMs and the vertical magnitude of noise within them. Where relevant, these uncertainties are incorporated into the uncertainties for measured quantities in Table 5.2 (see Appendix A).

It should be noted that the flanks of zone II of the NW Tempe Terra esker (see Chapter 4) are partially mantled by remnant LDA materials. It is likely that this results in underestimation of ridge height, and overestimation of ridge width in zone II, possibly with uncertainties on the order of tens of metres. Owing to a lack of known bed topography, it is not possible to quantify the magnitude of this uncertainty with confidence, but the significant break in slope visible at the classified base of the zone II ridge suggests that the material that mantles the lower ridge flank in zone II is relatively thin; thick ice or ice-rich debris would be expected to equilibrate this break in slope over time via relaxation.

Table 5.2. Uncertainties in 2D and 3D geometries of eskers in Phlegra Montes and NW Tempe Terra.

	Phlegra Montes	**NW Tempe Terra**
2D geometries		
Segment length (m)	±1.27	±5.48
Mapped length (m)	±3.11	±15.50
System length (m)	±3.11	±15.50
Path length (m)	±1.23	±1.55
Segment sinuosity	±0.13	±0.04
System sinuosity	±0.03	±0.01
Continuity	±0.01	±0.001
3D geometries		
Height (m)	±1.09	±1.65
Width (m)	±1.41	±2.83
Width-height ratio	±3.19	±4.97
Average cross-sectional slope (°)	±1.45	±3.43

5.5.2. Uncertainties Resulting from Map Projection

Following Butcher et al. (2016), I quantified the uncertainties in measurements due to projection distortion by comparing geodetic and projected lengths of horizontal lines generated at 0.01° intervals of longitude across the full width of the DEMs for each of the study sites. I found the uncertainty in measurements due to projection distortion to be insignificant ($\ll$ 0.001 m) for both study sites.

5.5.3. Uncertainties Resulting from Vertical Precision of DEMs

I estimated the vertical precision of the DEMs according to the method of Kirk et al. (2008) and Okubo (2010), and using the equation stated by Davis (2017):

$$EP = \frac{(RMS \times IFOV)}{\tan(e)} \quad \textbf{5.9}$$

where *EP* is vertical precision, *RMS* is the error in pixel correlation (in pixels) between stereo images (which, following Okubo (2010), I assume to be 1/5th of a pixel), *IFOV* is instantaneous field of view (m/pixel) of the input image (which I conservatively take to be the same as that of the lower resolution image in each stereo pair), and *e* is the difference in emission angle (i.e., stereo convergence angle, in degrees) between the input images (Kirk et al., 2008; Okubo, 2010; Davis, 2017). I found the vertical precision of the DEMs to be ± 0.252 m for the Phlegra Montes site (1 m horizontal resolution), and ± 0.492 m for the NW Tempe Terra site (2 m horizontal resolution).

5.5.4. Uncertainties Resulting from Noise within DEMs

The uncertainties arising from the vertical precisions of the DEMs (Section 5.5.3) are smaller than the uncertainties introduced by the vertical magnitude of noise in the DEMs. I quantified the vertical magnitude of DEM noise by generating smoothed reference surfaces from regions of the DEMs with representative levels of noise and subtracting them from the same regions of the original, unsmoothed DEMs. To make the reference surfaces, I removed pixels where the quality of pixel correlation during the SOCET SET stereo matching process was classified as moderate-to-poor[6], then performed several iterations of DEM smoothing based on the mean elevation value within rectangular moving windows in ArcGIS, until all visible artefacts within shaded relief maps of 50 × 50 m sample areas of representative noise were smoothed. Selected sample areas were areas with no visible topographic undulations within

[6]I assessed pixel correlation quality using the Figure of Merit raster output by the DEM generation workflow in BAE Systems SOCET SET software. The Figure of Merit is a raster dataset replicating the configuration of pixels in the DEM, in which pixels are assigned values according to the quality of pixel correlation during the stereo matching process. I included only DEM pixels with corresponding Figure of Merit pixel values of 60–99, which correspond to 'good correlation'.

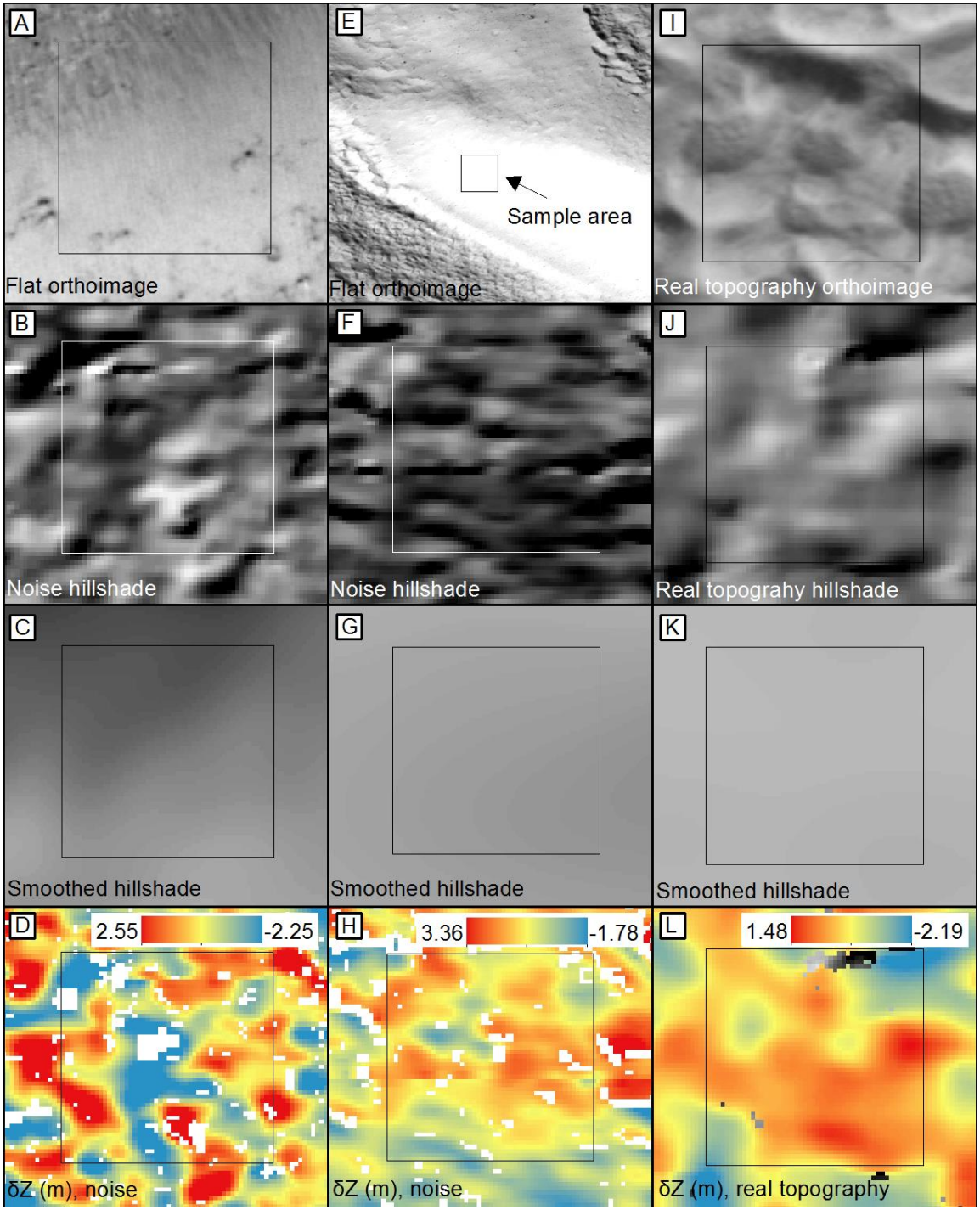

Figure 5.3. Illustration of process for quantifying vertical magnitude of DEM noise. Boxes show examples of 50 × 50 m sample areas from which I quantified DEM noise for the Phlegra Montes (column 1) and NW Tempe Terra (column 2) sites, and the magnitude of pervasive real surface topography (see Section 5.5.4.2) for the NW Tempe Terra site (column 3). Row 1 shows orthorectified HiRISE images. Panels A and E are visually smooth, so undulations in hillshade models of the DEMs (panels B and F) are noise. Panel J shows real metre- to decametre-scale topography visible in the orthoimage (panel I). Row 3 shows smoothed hillshade models. Panels C and G approximate the real, smooth surfaces in panels A and E, respectively, while panel K is a hypothetical smooth surface, with real topography removed as if it was noise. Row 4 shows maps of elevation difference (δZ) between the original (row 2) and smoothed (row 3) DEMs, from which I calculated the vertical magnitude of DEM noise. White pixels are those excluded from smoothing calculations due to poor pixel correlation quality (see Section 5.5.4). See Table 5.1 for data products.

the orthorectified images, but where artefacts were observed within the DEMs. I avoided areas with real metre-scale topographic undulations. I then subtracted the original DEM surfaces from their respective reference surfaces to produce raster maps showing the elevation differences between them caused by noise. I used these difference maps to extract statistics for the minimum (i.e., negative; δZ_{min}) and maximum (i.e., δZ_{max}) deviations of the original surfaces from the smoothed surfaces for each of the sample areas. This gave two deviation values for each sample area. I then calculated the mean vertical magnitude of noise within each DEM (δZ_{DEM}) as:

$$\delta Z_{DEM} = \frac{\sum_{i=1}^{n}\left(\left|\delta Z_{min_i}\right| + \delta Z_{max_i}\right)}{2n} \quad \textbf{5.10}$$

where n is the number of sample areas.

5.5.4.1. Phlegra Montes Site

Estimates of δZ_{DEM} for the Phlegra Montes site were based on ten sample areas of representative noise. The plains surrounding the Phlegra Montes esker hosted high densities of metre-scale boulders, and the majority of areas of representative noise with minimal real metre-scale undulations were located on the ridge flanks. Consequently, the use of sample areas with some degree of real surface curvature was unavoidable, but I avoided areas (such as ridge bends) where curvature was multi-dimensional. I performed five iterations of smoothing in total. The first three iterations used a 9 × 9 m rectangular moving window to smooth the smallest artefacts, and the final two iterations used a 15 × 15 m rectangular moving window to smooth the coarsest artefacts. I calculated δZ_{DEM} as ± 0.889 m for the Phlegra Montes site.

5.5.4.2. NW Tempe Terra Site

My approach to estimating δZ_{DEM} for the NW Tempe Terra site deviated somewhat from the process outlined in Section 5.5.4 because the DEM contained pervasive metre-scale undulations representing true features visible within the orthorectified images. Inspection of the orthorectified images revealed that truly flat sample areas suitable for quantifying real noise were scarce. I identified only a single truly flat 50 × 50 m sample area for which a smoothed reference surface could be produced. Therefore, I modified the above process and compared the magnitude of the single sample of true noise within this area with the vertical scale of true topographic undulations in eight other sample areas containing real metre-scale topography. I measured the scale of undulations within the sample areas of real topography using the same smoothing approach as above, treating the true undulations as if they were noise. I performed seven iterations of smoothing for NW Tempe Terra site. The first three

iterations used a 9 × 9 m rectangular moving window to remove the smallest undulations. The next two iterations used a 15 × 15 m rectangular moving window to smooth intermediate scale undulations. The final two iterations used a 30 × 30 m rectangular moving window to smooth coarse-scale undulations.

$\delta Z_{DEM}$was greater for the regions of true topography (±1.343 m) than for the single region of real noise (± 1.002 m), suggesting very high DEM quality. However, I took a conservative approach and adopted the value derived from the large sample of true undulations as a conservative estimate of DEM noise for the NW Tempe Terra site: ±1.343 m.

5.6. Comparisons with the Dorsa Argentea Eskers, Mars

In Chapter 7, I compare the morphometries of the glacier-linked eskers in Phlegra Montes and NW Tempe Terra with the 2D and 3D morphometries of the ancient Dorsa Argentea eskers, which were measured by Butcher et al. (2016). The 2D morphometry dataset comprises all Dorsa Argentea ridge systems > 10 km in length, while the 3D morphometry dataset covers only four of the largest ridge systems in the population (Figure 5.4).

Butcher et al. (2016) extracted 2D morphometries for the Dorsa Argentea from crestlines that they digitised onto an integrated basemap comprising 6 m/pixel CTX images, ~11–20 m/pixel HRSC images, and 115 and 230 m/pixel gridded MOLA DEMs. They calculated 2D morphometries according to the same equations used for the present study (Section 5.4.1). They sampled 3D morphometries according to the 3D point classification method described in Section 5.4.2. Given the lower resolution of the available DEM compared to those available for the present study and the larger typical widths of the Dorsa Argentea (up to 6 km wide), they generated cross-sectional transects at approximate ~1 km intervals along four of the longest ridges in the population, excluding portions of the ridge in which the DEM was derived from a low density of raw MOLA laser shot points (< 5 within a 0.5 km buffer zone from the desired sampling location). They sampled 3D morphometries only in the regions covered by the 115 m/pixel DEM. They calculated ridge heights, widths, and width-height ratios according to the same equations used for the present study (Section 5.4.2). For the purposes of the present study, I calculated the average cross-sectional slope from these quantities according to Equation 5.8.

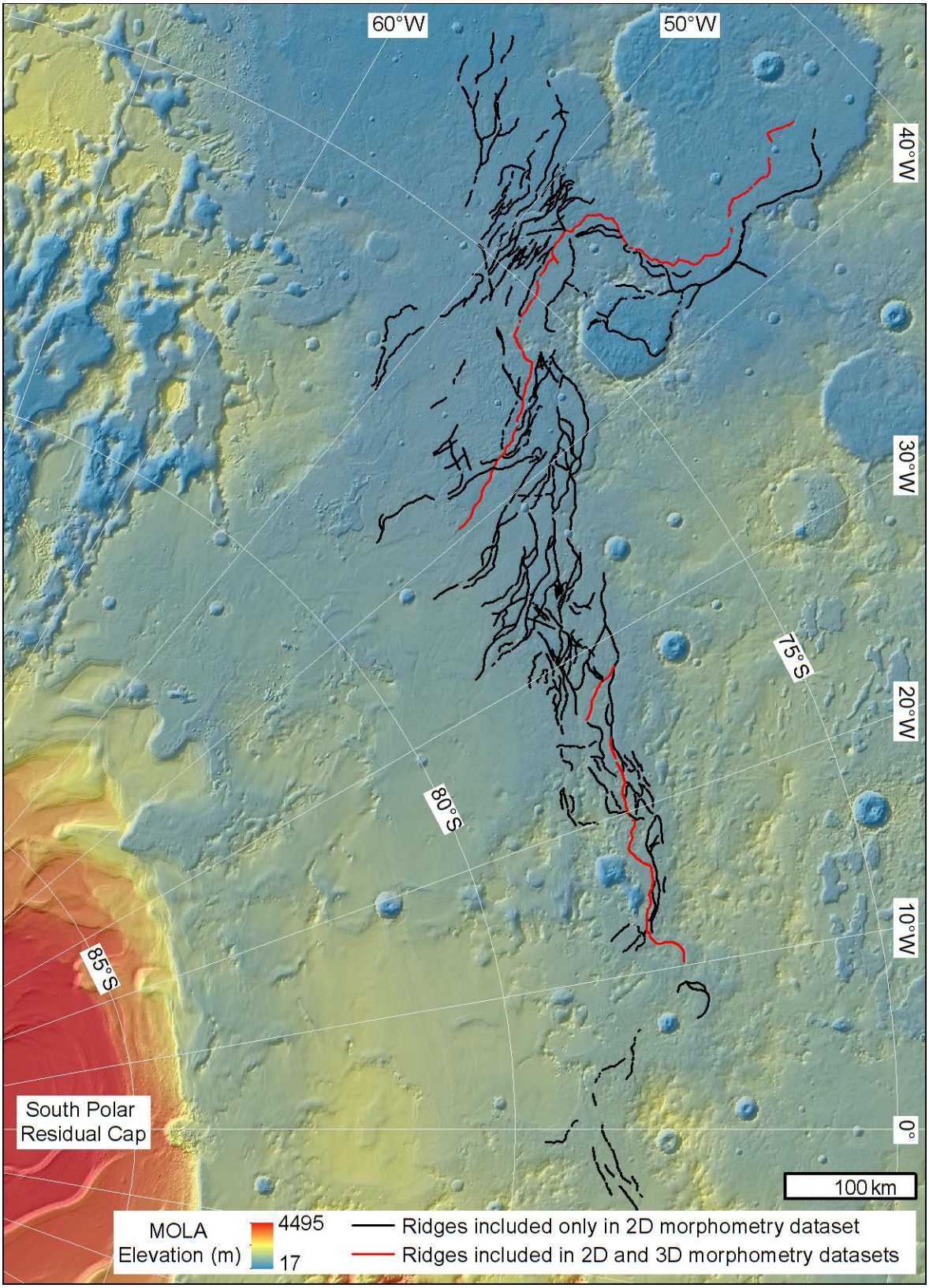

Figure 5.4. Map of the Dorsa Argentea eskers measured by Butcher et al. (2016). MOLA elevation map overlain on hillshade map showing the Dorsa Argentea ridges for which Butcher et al. (2016) measured 2D morphometries (both red and black ridges) and 3D morphometries (red ridges only). Redrawn from Butcher et al. (2016). See Table 5.1 for data products.

5.7. Comparisons with Eskers on Earth

In Chapter 7, I also compare the morphometries of eskers on Mars with 2D planform morphometries of large samples of eskers in Canada (Storrar et al., 2013, 2014a), and to a new dataset comprising 2D and 3D morphometries of eskers in SW Finland (Storrar and Jones, unpublished). The dataset for SW Finland, which was obtained by Storrar and Jones (unpublished) in parallel with this thesis, is the first large dataset comprising systematic measurements of heights and widths of eskers to be obtained for eskers on Earth, and is used here with permission. What follows is a brief summary of these datasets.

5.7.1. Canada, Earth

In Chapter 7, I compare the 2D planform morphometries of eskers on Mars to those obtained by Storrar et al. (2014a) for > 20,000 individual esker segments in Canada, Earth (Figure 5.5). The Canadian eskers were deposited during the early Holocene deglaciation of the Laurentide Ice Sheet ~16.8–7 calibrated kyr before present (cal kyr BP; Dyke et al., 2003; Storrar et al., 2014a, 2014b). Storrar et al. (2014a) extracted 2D esker morphometries (including segment and system length, sinuosity, and continuity) for eskers throughout Canada from the 1:5,000,000 scale map of esker crests (Figure 5.5) produced by Storrar et al. (2013), which covers an area of ~10 million km^2. Storrar et al. (2013) digitised the Canadian eskers onto a basemap that comprised 678 Landsat images (Landsat 7 Enhanced Thematic Mapper Plus and Landsat 5 Thematic Mapper images) with horizontal resolutions of 15–30 m, and a contextual DEM with an approximate horizontal resolution of ~1 km, which they generated from the USGS Global 30 Arc-Second Elevation Dataset (GTOPO30; Storrar et al., 2013). I measured 2D morphometries for the Phlegra Montes and NW Tempe Terra eskers via the same method (see Section 5.4.1) as was used by Storrar et al. (2014a) for the Canadian eskers. Butcher et al. (2016) used the same method to obtain 2D morphometries for the Dorsa Argentea on Mars (see Section 5.6).

5.7.2. SW Finland, Earth

In Chapter 7, I also compare 3D morphometries of eskers on Mars to those of eskers in SW Finland (Figure 5.6; Storrar and Jones, unpublished). For completeness, I also compare eskers on Mars to the 2D morphometries of the same eskers. However, this dataset is currently limited to 2D morphometries of individual segments; esker system morphometries are not yet available. The eskers measured by Storrar and Jones formed beneath an ice stream flowing NW–SE (Punkari, 1994, 1997; Kleman et al., 1997; Stroeven et al., 2016) at the SE margins of the Fennoscandian ice sheet as it retreated across SW Finland between the onset of the Younger Dryas stadial (Donner, 1978; Rainio et al., 1995; Stroeven et al., 2016), a

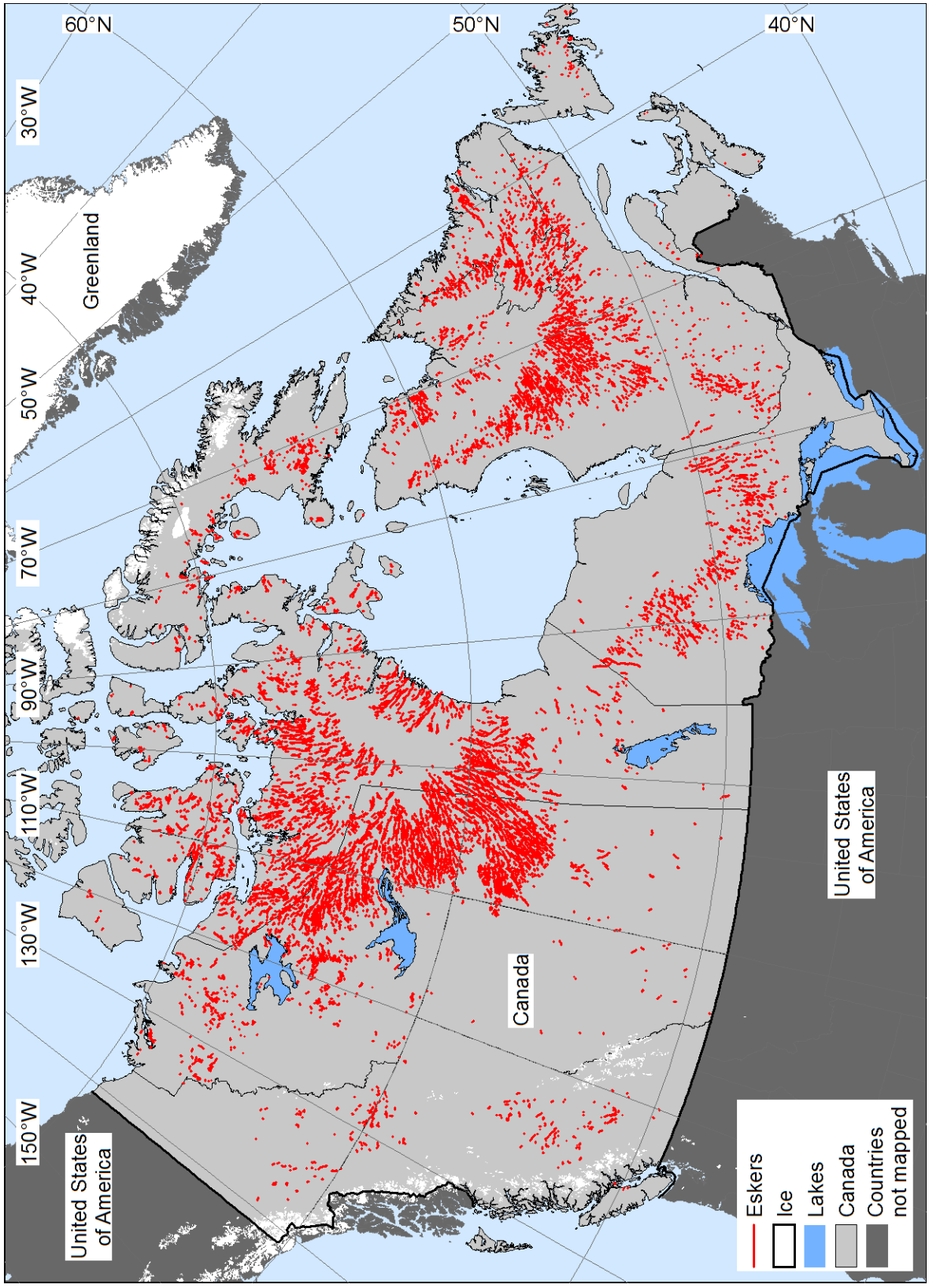

Figure 5.5. Map of eskers in Canada, Earth with which I compare 2D morphometries of eskers on Mars. > 20,000 eskers (red lines) mapped by Storrar et al. (2013) and measured by Storrar et al. (2014a). Redrawn from Storrar et al. (2013). See Table 5.1 for a list of data products.

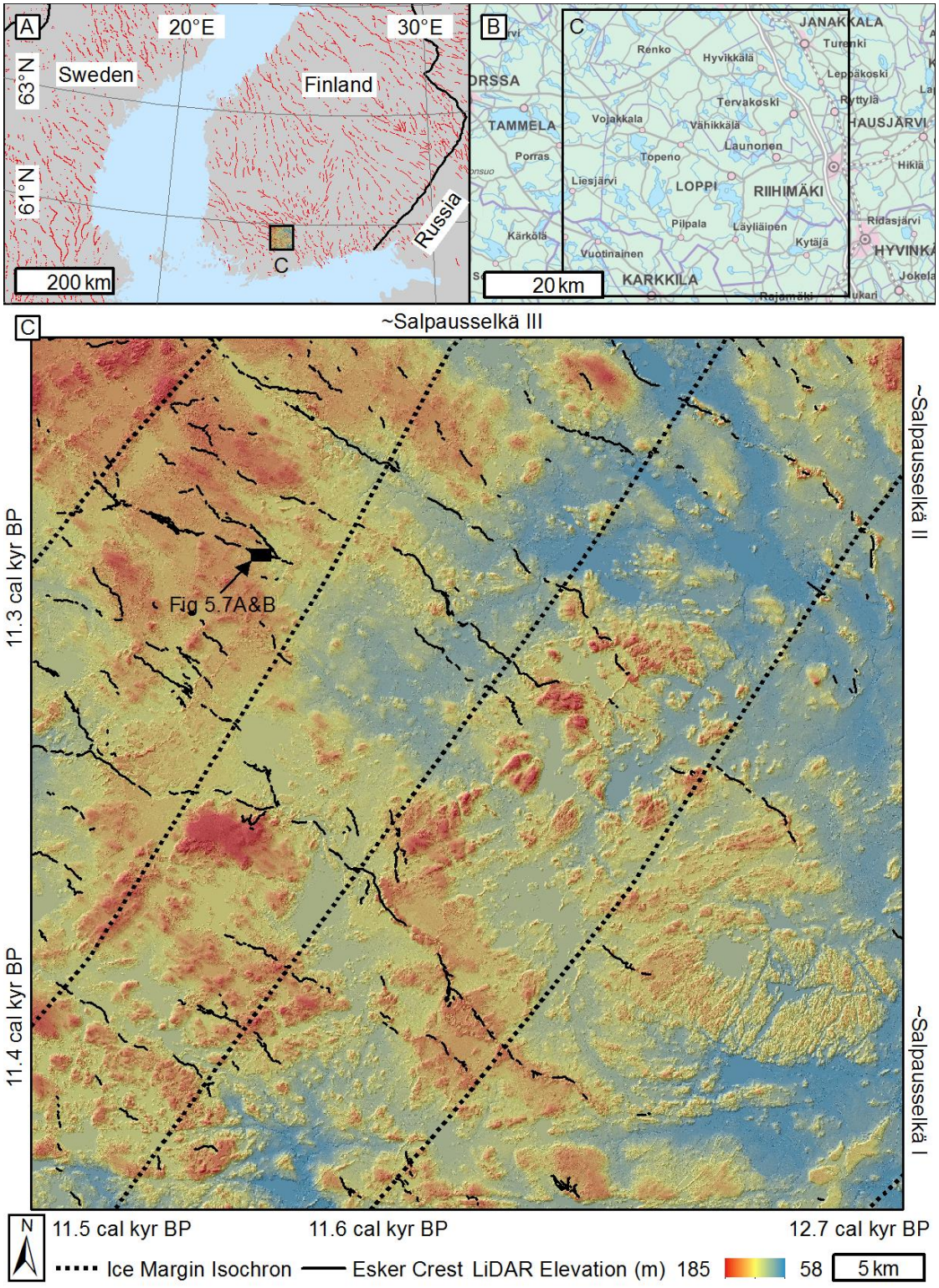

Figure 5.6. Map of eskers in SW Finland with which I compare the 2D and 3D morphometries of eskers on Mars. (A) Context map of esker crestlines (red lines) compiled by Stroeven et al. (2016) for SE Fennoscandia. Black box shows the location of the study site of Storrar and Jones (unpublished). (B) Regional context map showing location (black box) of the study site of Storrar and Jones (unpublished). (C) LiDAR elevation map showing crestlines of eskers measured by Storrar and Jones (unpublished). They sampled 3D morphometries every ~10 m along these crestlines. Black dotted lines show ice margin isochrons from Stroeven et al. (2016). Approximate positions of the isochron-parallel Salpausselkä I–III ice marginal complexes are also labelled. See Table 5.1 for a list of data products.

cold period ~12.9-11.6 cal kyr BP (Rasmussen et al., 2014; Stroeven et al., 2016) that punctuated the overall retreat of the Northern Hemisphere ice sheets following the Last Glacial Maximum (26.5–20 cal kyr BP; Clark et al., 2009), and the Preboreal oscillation, a cold event ~11.4 cal kyr BP (Rasmussen et al., 2014) that disrupted general climate warming in the early Holocene (Figure 5.6C). The SE terminus of the Fennoscandian ice sheet formed the margin of the 349,400 km^2 (Jakobsson et al., 2007), ice-dammed Baltic Ice Lake until ~11.62 cal kyr BP (Stroeven et al., 2015), when catastrophic drainage of 18% of its area lowered the lake level by 25 m to the contemporaneous level of the North Sea, forming the Yoldia Sea in the present Baltic Sea basin (e.g., Donner, 1978; Björck, 1995; Jakobsson et al., 2007).

Storrar and Jones (unpublished) obtained 2D and 3D measurements of eskers (including segment length and sinuosity, width, and height) for a 2305 km^2 site (centred on 24.36°E, 60.75°N) in SW Finland. Their basemap data comprised a mosaic of 64 6 × 6 km, gridded Light Detection and Ranging (LiDAR) DEM tiles with 2 m/pixel horizontal resolution, and hillshade and slope maps generated from this DEM mosaic. They imported these data into ArcGIS in their native transverse Mercator projection (TM35FIN), based on the European Terrestrial Reference System 1989 datum.

Storrar and Jones (unpublished) obtained 2D measurements via the same method used in the present study (Storrar et al., 2014a; Butcher et al., 2016). Owing to the labour intensive nature of the 3D point classification method described in Section 5.4.2 and their objective to obtain measurements for a large sample size, Storrar and Jones (unpublished) adopted an alternative semi-automated 2D plan-view delineation method (summarised below) to classify the left base, right base and crest points for cross-sectional transects.

They manually digitised three lines for each esker segment within the SW Finland site on to a slope map generated from the DEM: (1) the crestline of the segment (from which the 2D morphometries were extracted), (2) the break in slope at the base of the right flank, and (3) the break in slope at the base of the left flank. They closed the ends of the left and right flank lines at the end of each segment to generate a segment-encompassing polygon. They then used a Python script[7] to generate equidistant transects that extended between the digitised flank base lines and were oriented perpendicular to the digitised crestlines, with transects spaced at 10 m intervals along each ridge (with slight increases in sample spacing around tight bends, and avoiding areas modified by e.g., roads and quarries). The end points of these

[7] Script by Andrew Jones adapted from one by Mateus Ferreira.

transects were taken as the left base and right base points of the ridge. Therefore, the length of a given transect was taken as the ridge width in that location. Next, the script extracted elevation values from the DEM along each transect and classified the point of maximum elevation as the crest point. For consistency with measurements obtained in the present study, I used the elevations of the left base, right base, and crest points classified by Storrar and Jones to calculate ridge height according to Equation 5.4[8]. The raw dataset generated by Storrar and Jones comprised 27,412 individual transects, covering 853 individual esker segments.

Prior to analysis, I undertook pre-processing of the 3D morphometry dataset to ensure consistency with the sampling strategy used for the martian eskers (Section 5.4.3). I undertook visual inspection of all 27,412 transects and excluded any transects that deviated significantly from ridge-perpendicular (i.e., in areas where smoothing had not removed digitisation noise in the paths of the crestlines). Similarities in the distances over which the ends of ridge segments tapered between the Phlegra Montes and NW Tempe Terra eskers, and the eskers in SW Finland meant that it was suitable to apply the same exclusion distance from segment ends to remove unrepresentative transects within tapered end zones. Thus, I excluded transects within 40 m of the ends of each segment for the SW Finland eskers, consistent with the sampling strategy in Section 5.4.3. Finally, I excluded all transects from the SW Finland site with heights < 0.3 m, since I found measurements of ridges below this height to be unreliable as it is similar to the scale of local topographic undulations. The filtered dataset comprised a sample size of 20,269 (74% of the raw transects).

I then computed the width-height ratios and average cross-sectional slopes from the widths and heights of the sampled transects, according to Equations 5.7 and 5.8 respectively.

It should be noted that, prior to undertaking comparisons between the martian eskers and the eskers in SW Finland, I undertook blind repeat measurement experiments in collaboration with Storrar and Jones to ensure that the validity of comparisons would not be affected by the different methods used to classify ridge crest, left base, and right base points (Figures 5.7 and 5.8). Briefly, I obtained blind repeat measurements for a 500 m long portion of an esker in SW Finland (n = 47; Figure 5.7) using the manual 3D point classification method described in Section 5.4.2, while Storrar and Jones obtained blind repeat measurements

[8] In the raw dataset provided by Storrar and Jones, esker height had been calculated by subtracting the minimum elevation along a given transect from the elevation of the crest point for that transect. I performed height recalculations in consultation with Storrar. I undertook visual inspection of several transects in topographic profile and found that Equation 5.4 returned heights that were more representative of the true ridge height than the original values.

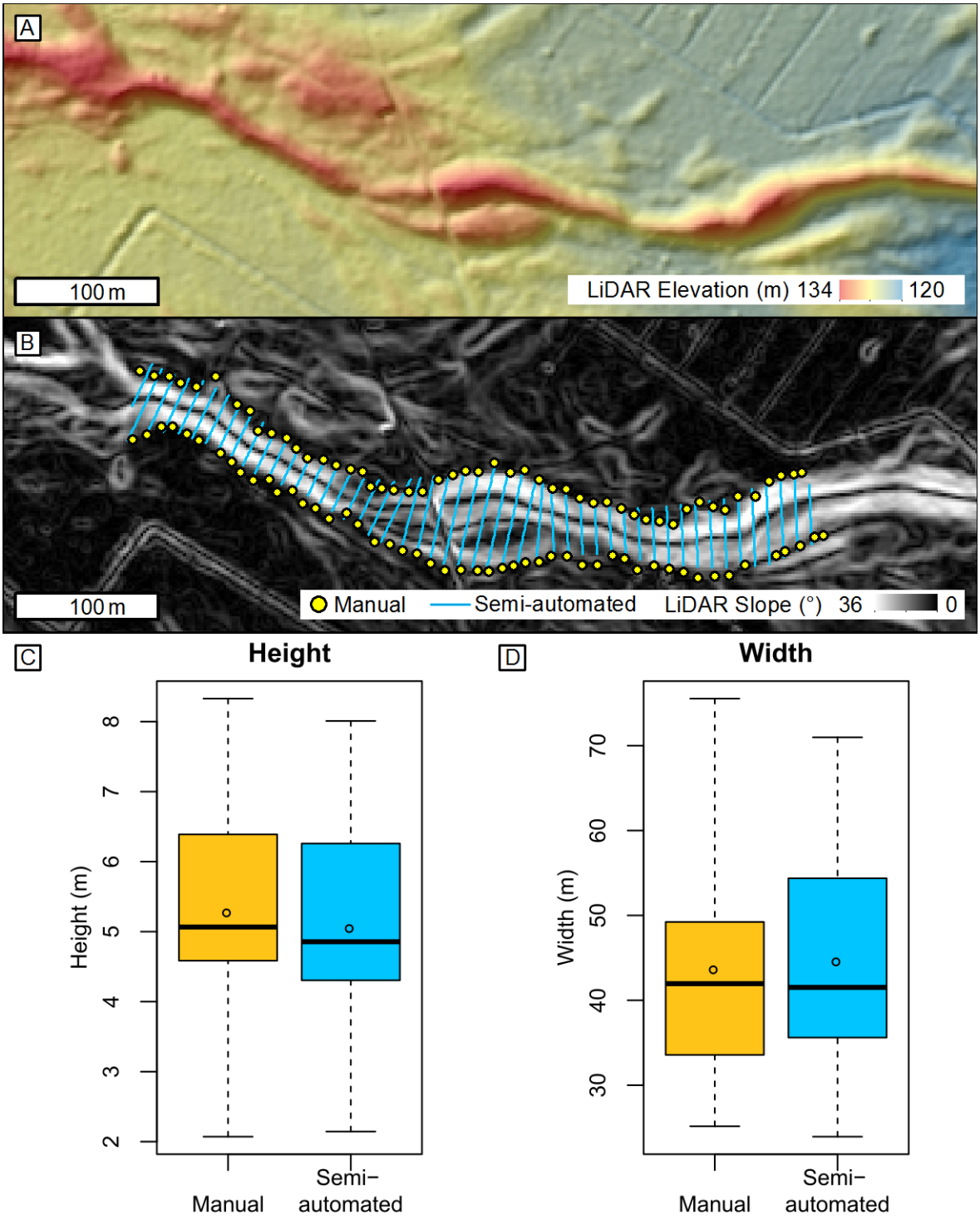

Figure 5.7. Experimental blind repeat measurements of an esker in SW Finland (A) LiDAR DEM overlain on hillshade model of the portion of the esker segment (extent in Figure 5.7A) for which I undertook blind repeat measurements in collaboration with Storrar and Jones (extent in Figure 5.6C). (B) Slope map derived from the LiDAR DEM (same extent as panel A) showing blind repeat measurements from the manual and semi-automated (Storrar and Jones) methods. (C) Boxplot comparing repeat height measurements (n = 47) for samples shown in panel B. (D) Boxplot comparing repeat width measurements (n = 47) for samples shown in panel B. In panels C and D boxes represent interquartile range, whiskers represent maximum and minimum, solid lines represent the median, and points represent the mean. See Table 5.1 for list of data products.

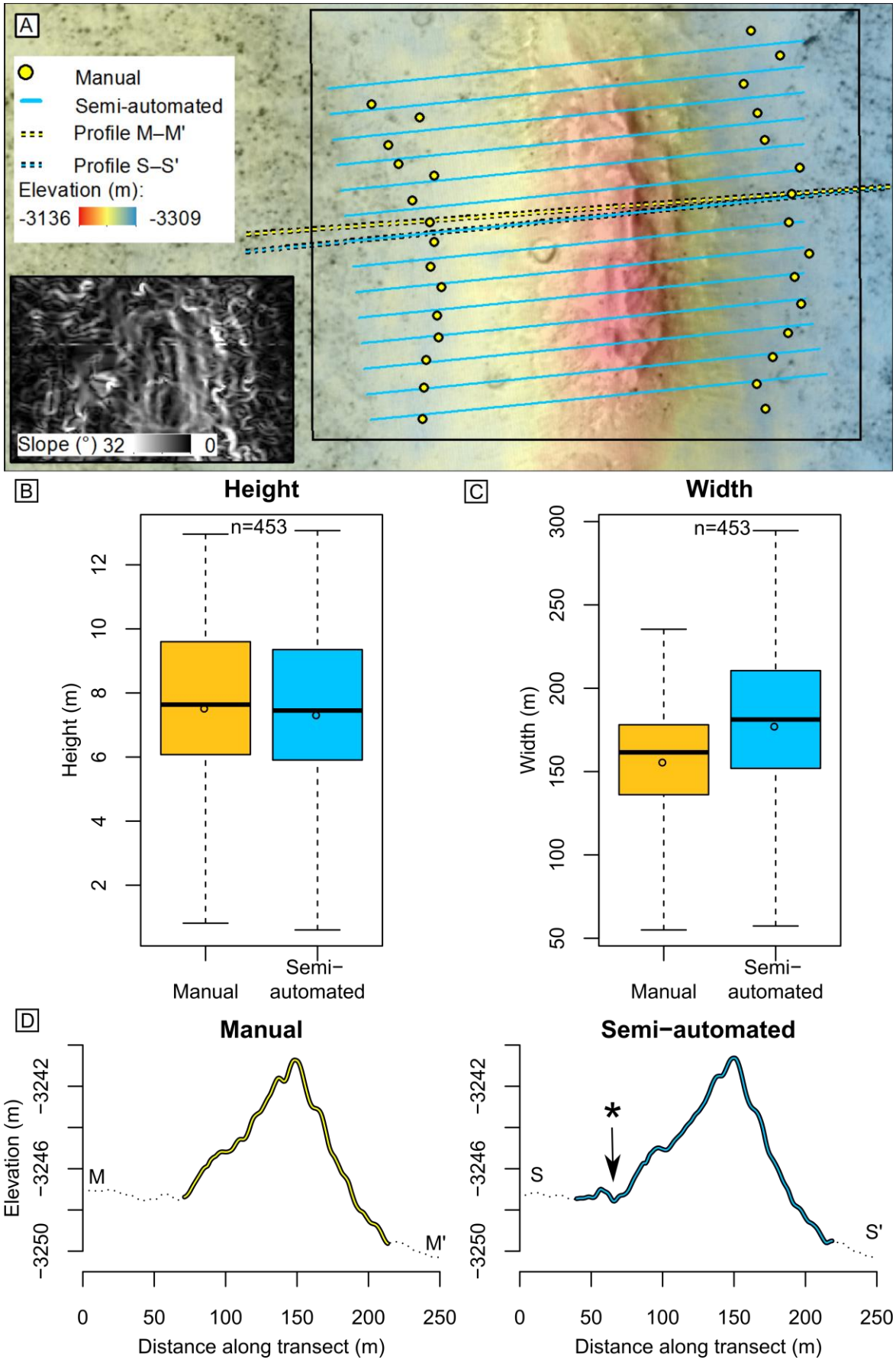

Figure 5.8. Experimental blind repeat measurements of the Phlegra Montes esker complex, Mars (A) Examples of repeat measurements for which the semi-automated 2D plan-view delineation method consistently overestimates ridge width as a result of challenges in identifying the ridge margins due to noise in the slope (caption continues on next page)

(caption continued from previous page) map (inset). Dashed lines show locations of profiles M–M' and S–S' (panel D). (B) Boxplot comparing 453 repeat height measurements from the manual and semi-automated methods for the Phlegra Montes esker complex. (C) Boxplot comparing 453 repeat width measurements from the manual and semi-automated methods for the Phlegra Montes esker complex. In panels B and C boxes represent interquartile range, whiskers represent maximum and minimum, solid lines represent the median, and points represent the mean. (D) Cross-sectional topographic profiles of transects M–M' and S–S' (locations in panel A) showing that the major break in slope is more easily identified in topographic profile, resulting in more accurate identification of the ridge margins by the manual 3D point classification method. Solid lines show the extent of the transect within the ridge margins as classified by the manual (blue) and semi-automated (yellow) methods. Dotted lines show the adjacent topography beyond the ridge margins. The asterisk on profile S–S' indicates the location where the left base point would be classified under the manual 3D point classification method. See Table 5.1 for data products.

(n = 453) over the entire Phlegra Montes esker system on Mars using the semi-automated 2D planform delineation method outlined above. Repeat measurements over the full Phlegra Montes esker complex were made possible by the efficiency of the semi-automated method, whereas the labour intensity of the manual method precluded complete coverage of sampled eskers in SW Finland.

I then compared the repeat measurements to the original datasets. For the repeat measurements of the eskers in SW Finland, I found that the semi-automated plan-view delineation method provided effective replication of the more rigorous but labour-intensive manual 3D point classification method (Figure 5.8), with typical discrepancies between width and height measurements of < 10%, and no statistically significant difference in these quantities between the datasets.

In contrast, I found that the semi-automated 2D planform delineation method failed to replicate adequately the manual 3D point classification measurements for the Phlegra Montes esker complex (Figure 5.8). Percentage discrepancies > 20% affected 43% of repeat width measurements for the eskers in Phlegra Montes and resulted in a statistically significant difference in median width between the datasets. Discrepancies > 20% affected 11% of height measurements but did not exert sufficient influence on the overall distributions to generate a statistically significant difference in median heights between the semi-automated and manual methods. Visual inspection of the base point classifications for the Phlegra Montes esker complex highlighted that these discrepancies arose from difficulties in identifying the break in slope at the base of the ridges via the semi-automated 2D planform delineation method for the Phlegra Montes site (Figure 5.8). Subtle breaks in slope (arising from low ridge flank slopes) at the base of ridge segments in the Phlegra Montes esker complex combined with noise in the DEM inhibited confident digitisation of the ridge baselines using the slope map (and indeed the hillshade and aspect maps and

orthorectified images) alone (Figure 5.8A, inset). When repeat transects are compared in topographic profile (Figure 5.8D), it is clear that the manual 3D point classification method more effectively captures the true break in slope demarcating the base of the ridge. Well-defined breaks in slope at the base of the eskers in SW Finland combined with low DEM noise (e.g., Figure 5.7B) mean that these challenges do not affect measurements obtained by Storrar and Jones (unpublished) using the semi-automated 2D planform delineation method for SW Finland.

The above findings show that, rather than compromising their validity, the differences in approach to measuring 3D esker morphometries for Earth and Mars likely enhance the quality of comparisons undertaken in Chapter 7. The semi-automated 2D planform delineation and manual 3D point classification methods were the optimal approaches for the sites to which they were applied. The efficient semi-automated planform delineation method, which does not require inspection of individual transects in topographic profile or manual identification of crest and base points, permitted collection of accurate measurements for a large sample of eskers in SW Finland, enhancing the statistical significance of comparisons. The more rigorous but labour-intensive manual 3D point classification method permitted accurate identification of ridge base points for the Phlegra Montes site despite subtle breaks in slope at the base of the ridges and DEM noise which made the semi-automated 2D planform delineation method ineffective for this site. Given the short (~17 km) length of the NW Tempe Terra esker, I also opted to apply the manual approach for this ridge.

CHAPTER 6

MORPHOMETRY OF A GLACIER-LINKED ESKER IN NW TEMPE TERRA, MARS, AND IMPLICATIONS FOR MELTWATER DRAINAGE DYNAMICS

6.1. Background

In this chapter, I use the 3D morphometry of the newly-identified glacier-linked esker in NW Tempe Terra (Chapter 4; Butcher et al., 2017) to develop a conceptual model for the dynamics of the subglacial meltwater drainage episode that formed it.

Eskers on Earth are widely used for reconstructing the hydrological and dynamic evolution of glaciers and ice sheets. In planform, esker distribution and orientation can be used to reconstruct patterns of deglaciation (e.g., Boulton et al., 2001; Kleman et al., 1997; Stroeven et al., 2016) and hydrological potential gradients at the former bed of their parent ice body (e.g., Shreve, 1985a, 1985b) which can, in turn, be used to infer variations in ice surface slope and ice flow direction (e.g., Shreve, 1985b; Bernhardt et al., 2013). If a syn-depositional ice marginal position is known, such ice surface slope reconstructions can be used to approximate the surface topography of the parent ice body (Shreve, 1985b), as demonstrated by Bernhardt et al. (2013) for ancient candidate eskers in southern Argyre Planitia, Mars.

Assuming limited post-depositional modification, esker morphology and sedimentology can also provide insights into the temporal evolution of meltwater drainage dynamics under changing meltwater and sediment supply regimes (e.g., Shreve, 1985a; Burke et al., 2008, 2010; Storrar et al., 2014b; Burke et al., 2012b; Perkins et al., 2013; Burke et al., 2015). Detailed reconstructions of the dynamics of esker-forming melt events on Earth can be

achieved via field studies of the structure and calibre of esker interior sediments (accessed both via logging at exposures and geophysical surveying techniques; e.g., Banerjee and McDonald, 1975; Brennand, 1994, 2000; Burke et al., 2008, 2010; Cummings et al., 2011; Burke et al., 2012b; Perkins et al., 2013; Burke et al., 2015; Perkins et al., 2016). Unlike eskers on Earth, candidate eskers on Mars are currently inaccessible via all but orbital remote sensing techniques. Observations of relationships between the interior sedimentology (and hence detailed formation dynamics) and macro-scale morphology of eskers on Earth hold promising potential for understanding the dynamics of esker-forming drainage events on Mars, where metre-scale morphometric observations are enabled by new high-resolution remote sensing datasets, but sub-metre-scale sedimentological observations are not currently possible.

6.2. Aims

In this chapter, I present the first systematic, metre-scale characterisation of the 3D morphometry of an esker on Mars. I characterise both the 2D and 3D morphometries of the glacier-linked esker in NW Tempe Terra, including length, continuity, sinuosity, height, width, width-height ratio, and average cross-sectional slope. In the following chapter, I compare these morphometries to similar measurements of the glacier-linked esker complex in Phlegra Montes (this thesis), to the ancient Dorsa Argentea eskers (Butcher et al., 2016), and to eskers in Canada (Storrar et al., 2014a) and SW Finland (Storrar and Jones, unpublished), Earth. The focus of the present chapter is on the implications of the 3D morphometry of the NW Tempe Terra esker for the spatiotemporal dynamics of the meltwater drainage event that formed it. Based on insights from the 3D measurements of the esker, I explore the hypothesis that it is in fact a composite esker formation comprising two 'stacked' ridge members. Based on observations of relationships between the morphology and interior sedimentary properties of eskers on Earth, and associated inferences about the processes that influence these relationships (e.g., Burke et al., 2015), I develop a conceptual model for the multi-phase subglacial sediment-discharge dynamics that could explain formation of the stacked esker formation in NW Tempe Terra. I propose that the morphology of the esker records spatiotemporal variations in meltwater discharge, sediment supply, and/or accommodation space within the parent drainage conduit. To my knowledge, this constitutes the first example of an attempt to reconstruct the multi-phase dynamics of an esker-forming drainage episode (or episodes) on Mars. I present morphometric distributions for the individual ridge members and for morphological subzones along those ridge members, which I compare to the morphometries of eskers on Earth and Mars in Chapter 7.

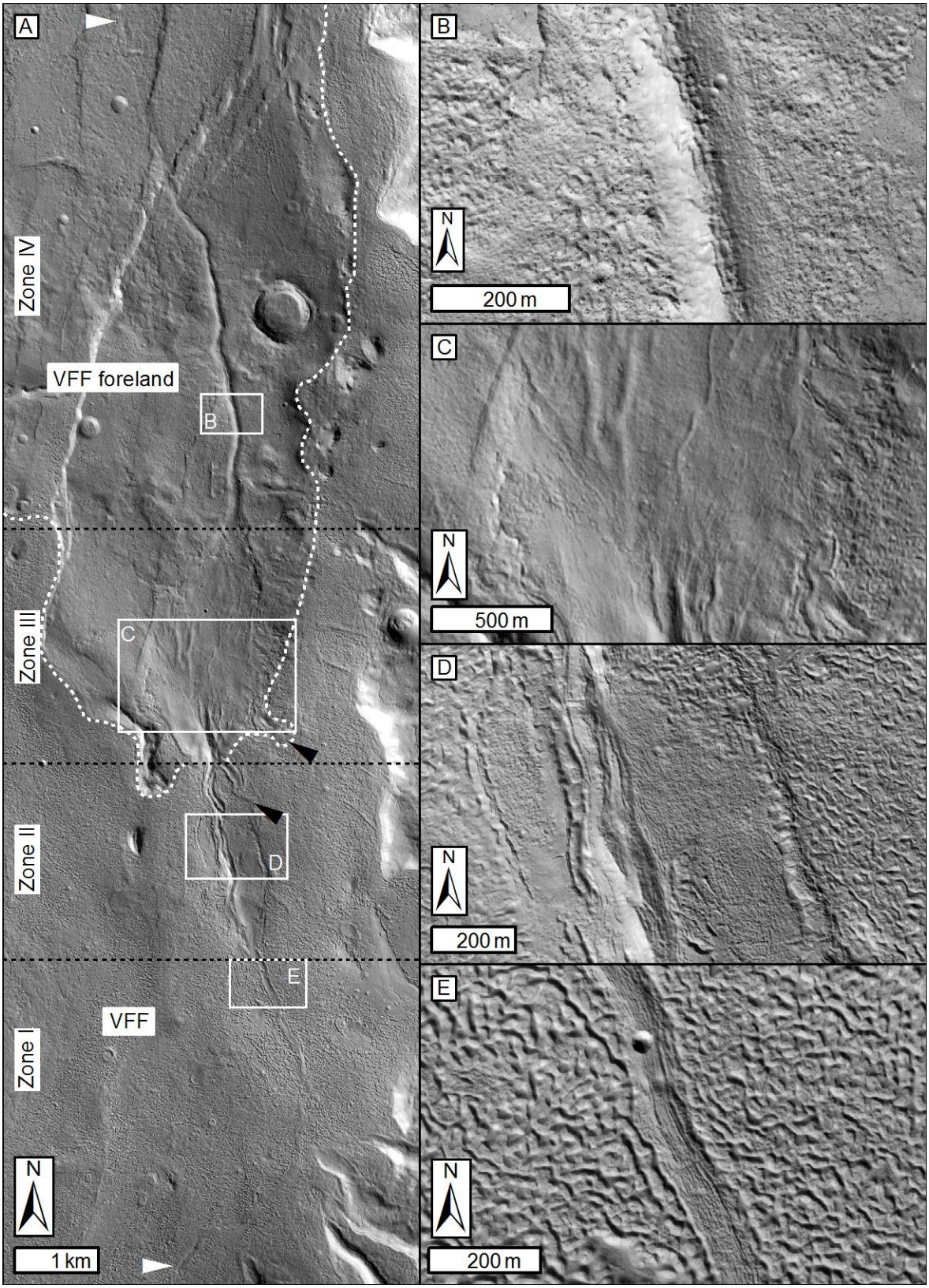

Figure 6.1. Morphological zones along the glacier-linked esker in NW Tempe Terra. (A) CTX image mosaic of the VFF-linked esker (white arrows mark southern and northernmost visible extent, and black arrows mark heads of two possible tributary eskers) in NW Tempe Terra (Chapter 4, this thesis; Butcher et al., 2017) which emerges from its parent viscous flow feature (VFF; white dotted line is present terminus), with morphological zones I-IV delineated (black dotted lines), and showing extents of panels B–E, which show portions of: (B) zone IV. (C) zone III, (D) zone II, and (E) zone I. Panels B, D, and E, are orthorectified HiRISE images, and panel C is a CTX image. See Table 6.1 for list of image products.

6.3. Data and Methods

The reader is referred to Chapter 5 for a description of the methods used to measure the 2D and 3D morphometries of the glacier-linked esker in NW Tempe Terra. I undertook post-processing of the raw morphometry data during analysis, which I describe in Section 6.5.1.3.

6.4. Morphometry of the NW Tempe Terra Esker

6.4.1. Planform Morphology

The planform morphology of the NW Tempe Terra esker is described in detail in Chapter 4. To summarise, the esker comprises a single major system and two short (possible tributary) ridges that merge with its eastern flank. In Chapter 4, I defined four morphological zones along the NW Tempe Terra esker (Figure 6.1): zone I (0–5 km), a sinuous, low-relief, textured band comprising ridges and troughs within the surface of the remnant parent glacier (Figure 6.1E); zone II (5–7.6 km), a ~150 m wide, sharp- to multi-crested ridge atop a broader 500–1500 m wide ridge with the lower portions of its gently-sloping margins mantled by remnant glacier materials of unknown thickness (Figure 6.1D); zone III (7.6–10.7 km), a round-crested, 1300 m wide portion of the ridge that extends ~3 km northward into the glacier foreland from the glacier terminus (Figure 6.1C); and zone IV (10.7–15 km), a 150–200 m wide sharp-crested ridge that extends a further ~4.3 km into the glacier foreland and becomes fragmented and topographically indistinct at its northernmost end (Figure 6.1B).

Table 6.1. List of data products used in Chapter 6.

Instrument or Source	Image/Product ID	Figure
Context Camera[1]	Mosaic[2] generated from images: B21_017807_2262_XN_46N083W, P05_002907_2258_XN_45N083W, P15_007021_2276_XN_47N082W, P18_008168_2279_XI_47N082W[3]	6.1A, C; 6.2A; 6.5B; 6.6B; 6.7A; 6.8A; 6.10C–D, F–H
High Resolution Imaging Science Experiment[4]	ESP_049573_2265 (orthorectified)[2]	6.1B, D–E; 6.7B; 6.10B.
	Digital elevation model[2] generated from images ESP_049573_2265 and ESP_49639_2265[5]	6.8B–I, 6.9
	Hillshade model generated from DEM[2]	6.9

[1] (Malin et al., 2007)
[2] Generated by F. E. G. Butcher
[3] Arizona State University http://viewer.mars.asu.edu/viewer/ctx#T=0
[4] (McEwen et al., 2007)
[5] The University of Arizona https://hirise.lpl.arizona.edu/

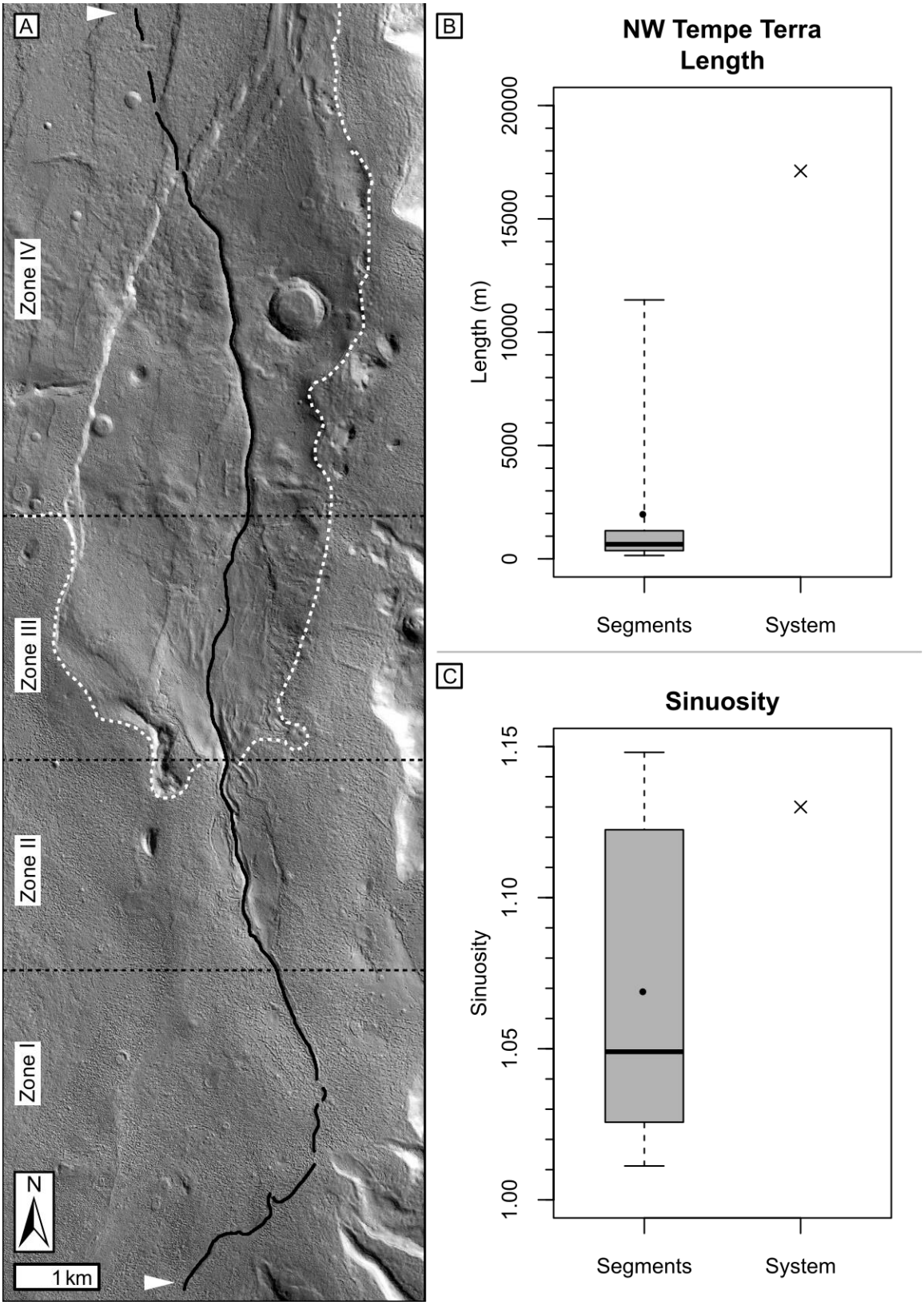

Figure 6.2. Crestline map and 2D morphometries for the NW Tempe Terra esker. (A) Crestline map on CTX image mosaic (Table 6.1) of the NW Tempe Terra esker (continuous black lines represent segments, which comprise a single ridge system that originates and terminates at the white arrows), with morphological zones I-IV delineated by black dotted lines. White dotted line is present ice terminus. (B) Boxplot showing the distribution of segment lengths and the length of the whole system (cross). (C) Boxplot showing the distribution of segment sinuosities, and the sinuosity of the whole system (cross). In panels B and C, boxes represent interquartile range, whiskers represent maximum and minimum, solid lines represent the median and points represent the mean.

6.4.2. Planform Morphometry

The NW Tempe Terra esker is a single esker system comprising up to 8 individual segments. Individual segments have lengths in the range 149 m–11.4 km, while the esker system has an interpolated length of 17.1 km (Table 6.2, Figure 6.2A–B). I emphasise that this is a minimum estimate of system length, since it is possible that the esker extends further beneath the remnant glacier materials beyond the southernmost visible trace of the textured band. Gaps between ridge segments comprise 1045 m of the length of the system, giving a system continuity of 0.94 (Table 6.2). This may be an underestimation of the true continuity since four of the mapped segments are entirely surrounded by remnant glacier materials within zone I (Figure 6.2A); hence, apparent gaps between these segments may be due to superposition of underlying ridge connections by remnant glacier materials, rather than true gaps. The sinuosity of individual ridge segments along the NW Tempe Terra esker ranges between 1.01 and 1.15, with a median of 1.05 (Table 6.2, Figure 6.2C). The esker system has a sinuosity of 1.13.

Table 6.2. Descriptive statistics for 2D morphometries of the NW Tempe Terra esker.

	Segment Length	**Segment Sinuosity**	**Mapped Length**	**System Length**	**Continuity**	**System Sinuosity**
N	8	8	1	1	1	1
Total	16,066 m	N/A	16,066 m	17,111 m	0.94	1.13
Minimum	149 m	1.01				
Maximum	11,424 m	1.15				
Quartile 1	363 m	1.03				
Quartile 3	989 m	1.11				
Median	644 m	1.05				
Mean	2008 m	1.07				
St. Dev	3835 m	0.06				

6.4.3. Raw Height and Width

As explained in Chapter 5, I excluded segments in zone I (textured band) from analyses of the 3D geometry of the NW Tempe Terra esker since their heights approach or are below the vertical precision of the DEM, and the geometry of the esker is almost entirely obscured by superposing glacier materials in this zone.

Descriptive statistics for the raw height and width measurements of the NW Tempe Terra esker are displayed in Table 6.3. In zones II-IV, the raw height of the NW Tempe Terra esker ranges between 1–54 m, with a median height of 14 m (Figure 6.3A). Transects in zone III

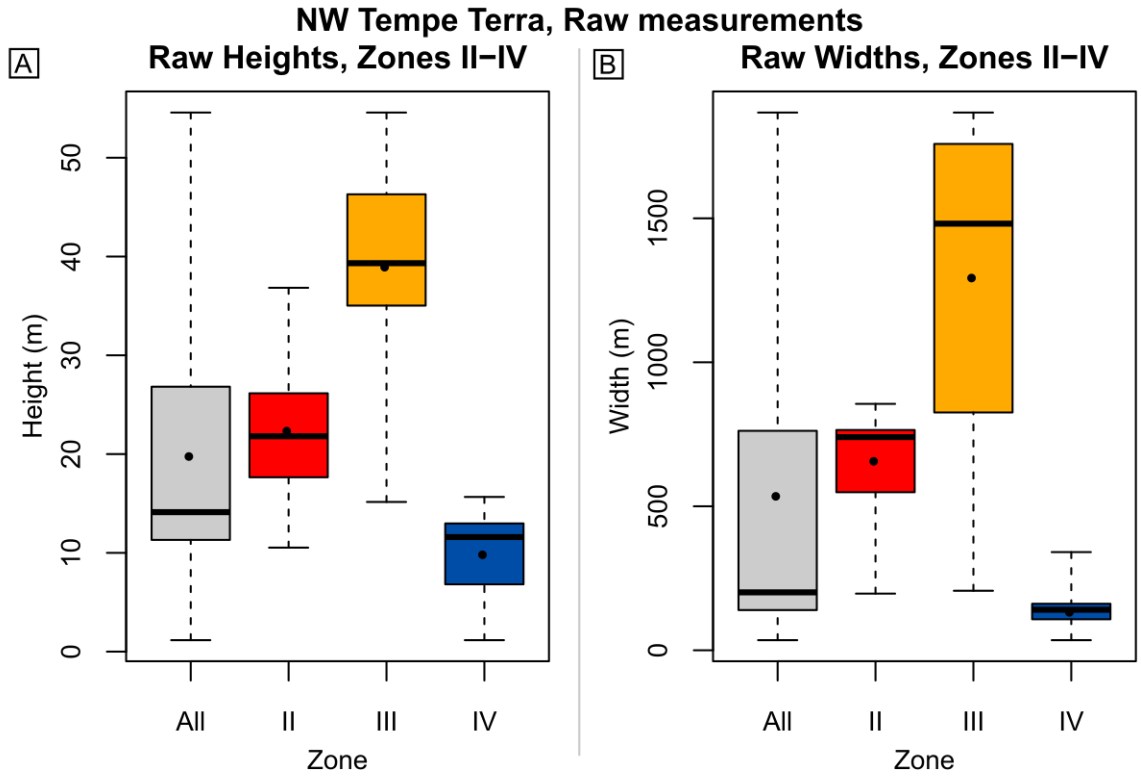

Figure 6.3. Distributions of raw heights and widths along the NW Tempe Terra esker. (A) Boxplots of ridge height, categorised by morphological zone (II–IV, see e.g., Figure 6.1). (B) Boxplots of ridge widths categorised by morphological zone (II-IV). In both panels, boxes represent the interquartile range, whiskers represent maximum and minimum, solid lines represent the medians, and points represent the means.

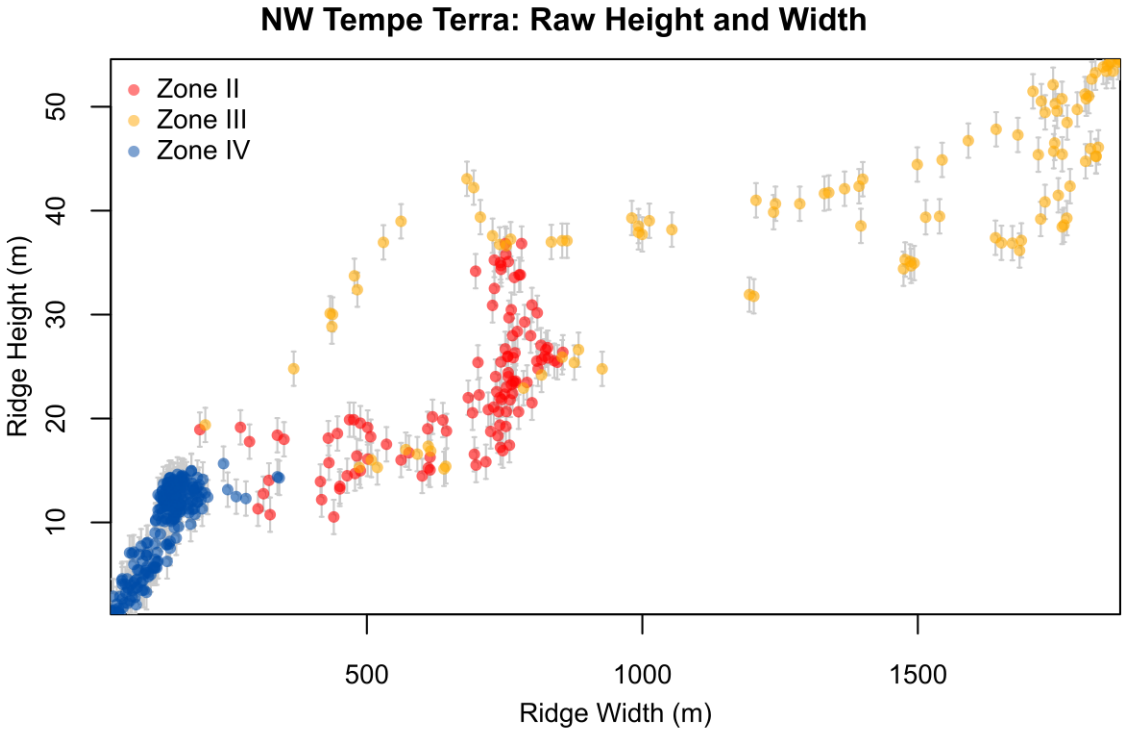

Figure 6.4. Scatterplot of raw height and width measurements for zones II–IV of the NW Tempe Terra esker. Measurements are categorised by zone. Zones II and III have complex width-height relationships which I explore further in Section 6.5.

Table 6.3. Descriptive statistics for raw height and width measurements of the NW Tempe Terra esker, and morphological zones II–IV.

	Height	Width		Height	Width
All transects			**Zone III**		
N	457	457	N	108	108
Minimum	1 m	35 m	Minimum	15 m	207 m
Maximum	55 m	1867 m	Maximum	55 m	1868 m
Range	53 m	1832 m	Range	39 m	1661 m
Quartile 1	11 m	140 m	Quartile 1	35 m	830 m
Quartile 3	27 m	762 m	Quartile 3	46 m	1757 m
Median	14 m	201 m	Median	39 m	1482 m
Mean	20 m	539 m	Mean	39 m	1297 m
St. Dev.	14 m	539 m	St. Dev.	11 m	503 m
Skewness	0.93	1.22	Skewness	-0.66	-0.47
Kurtosis	2.85	3.33	Kurtosis	2.88	1.71
Zone II			**Zone IV**		
N	112	112	N	237	237
Minimum	11 m	197 m	Minimum	1 m	35 m
Maximum	37 m	856 m	Maximum	16 m	341 m
Range	26 m	659 m	Range	15 m	306 m
Quartile 1	18 m	555 m	Quartile 1	7 m	108 m
Quartile 3	26 m	765 m	Quartile 3	13 m	162 m
Median	22 m	740 m	Median	12 m	141 m
Mean	22 m	661 m	Mean	10 m	136 m
St. Dev.	7 m	159 m	St. Dev.	4 m	47 m
Skewness	0.43	-1.09	Skewness	-0.78	0.47
Kurtosis	2.46	3.03	Kurtosis	2.25	5.27

have the greatest heights, with a median height of 39 m. This is nearly twice the median height of transects in zone II (22 m), and more than three times the median height of transects in zone IV (12 m; Figure 6.3A).

The width of the NW Tempe Terra esker has a range of 35–1876 m, with a median width of 201 m (Figure 6.3B). Zone III is the widest portion of the ridge, with a median width of 1482 m, while zone IV is the narrowest (median = 141 m). Zone II has widths in the range 197–856 m (median = 661 m,), falling largely within the first quartile of zone III widths (Figure 6.3B).

When plotted together, the height and width measurements for the NW Tempe Terra esker are positively correlated but exhibit complex trends (Figure 6.4). Zone IV measurements

appear to follow a relatively simple linear trend, while the zone II and III measurements exhibit multiple complex groupings.

6.5. Analysis

6.5.1. A Stacked Esker Formation?

In Section 6.4.3, I presented the complex height-width relationships of the NW Tempe Terra esker. In this section, I analyse these height-width relationships, and suggest that they represent the compound geometries of a composite esker formation comprising two 'stacked' ridge members deposited under a dynamic, multi-phase regime of esker sedimentation. Within this analysis, I explore the geometries of the individual members of the stacked formation, providing modified geometry distributions from which I then calculate width-height ratios and average cross-sectional slopes. I explore the implications of this model for the dynamics of esker formation in Section 6.6.

In order to simplify analyses of the relationships represented by each of the groupings in the raw height-width scatterplot (Figure 6.4), subsequent analyses exclude transects covering the transitions between the morphological zones (crosses in Figure 6.5A, n = 43) defined in Chapter 4 (Butcher et al., 2017) since their morphometries are not representative of the typical height-width relationships of the individual morphological zones.

6.5.1.1. Definition of Morphological Subzones and their Morphometric Signatures

The six groupings of the height-width scatterplot (Figure 6.6) for the NW Tempe Terra esker illustrate morphometric complexity below the scale of the morphological zones described in Chapter 4 (Butcher et al., 2017). As illustrated in Figure 6.6, each grouping is related to a group of spatially-associated transects. Five of the groupings describe distinctive morphological *subzones* (IIa–b and IIIa–c) within the larger morphological zones II and III that were defined in Chapter 4 (Butcher et al., 2017). The sixth grouping represents all transects within zone IV as defined in Chapter 4 (Butcher et al., 2017). Subzones IIa and IIIc follow similar height-width trends, while in subzones IIIa and IIIb, the ridge is significantly taller for a given width. This difference is particularly marked in the width range ~500–1000 m and diminishes toward width values of ~1250 m. Subzone IIb exhibits no correlation between height and width; transects in this subzone cluster in a relatively narrow width range (697–825 m), but their heights (in the range 17–37 m) bridge the gap between transects with similar widths in subzones IIa and IIIc, and IIIa and IIIb (Figure 6.6). Each subzone has a distinctive morphology (Figures 6.7 and 6.8) that, I suggest, can explain the different trends described by each grouping in the raw height-width scatterplot (Figure 6.6).

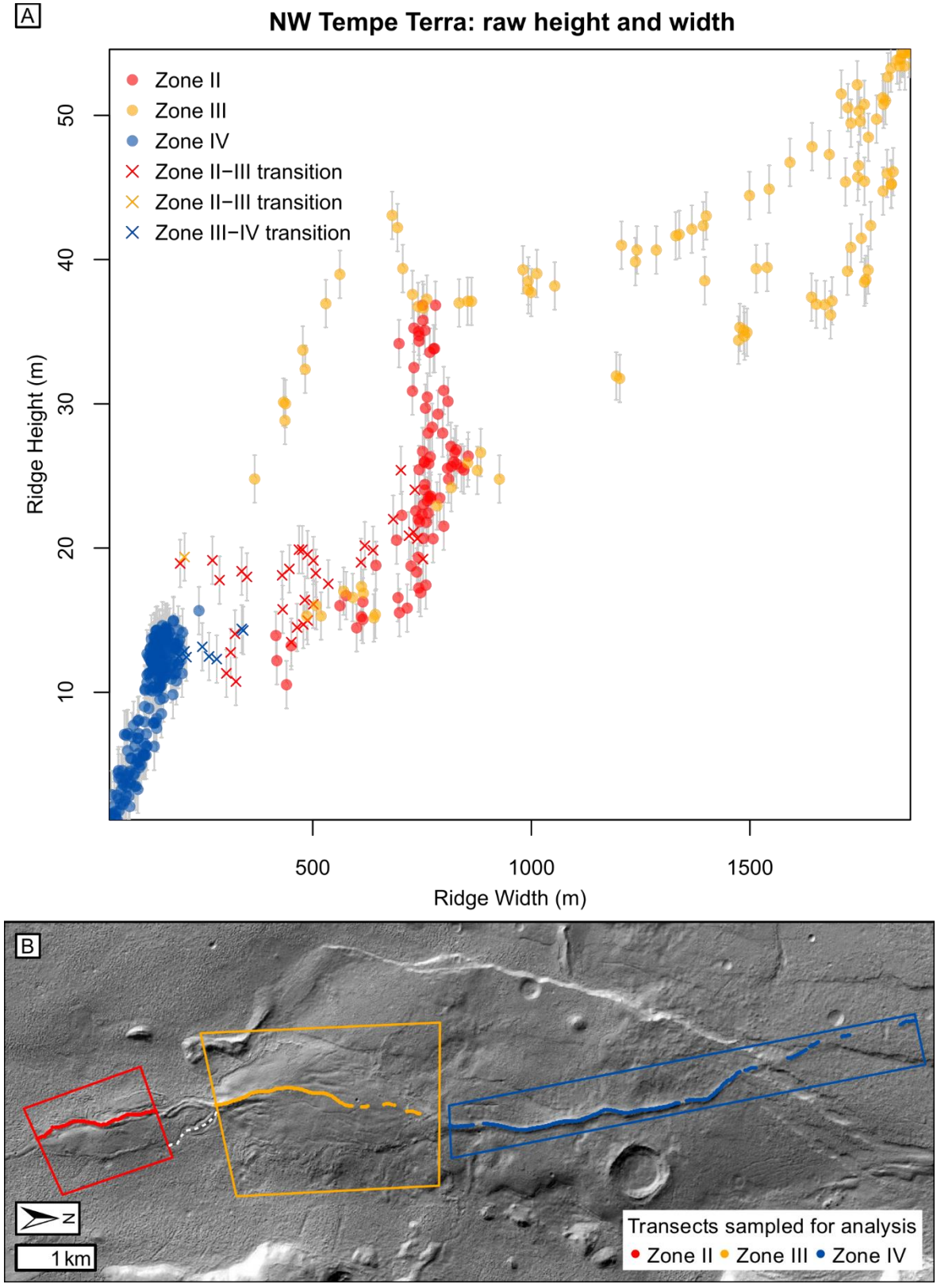

Figure 6.5. Exclusion of transects covering zone transitions along the NW Tempe Terra. (A) Scatterplot of raw height and width measurements highlighting measurements covering transitions between zones (crosses) that are excluded from subsequent analyses. (B) CTX image (Table 6.1) showing locations of transects sampled for further analyses (points, with colours corresponding to those in panel A). Boxes represent along-ridge extents over which morphological zones II–IV are sampled. The zone II–III exclusion zone extends along the portion of the ridge that is flanked by a possible subparallel tributary (white dotted line), which obscures the eastern ridge margin across the zone II–III transition.

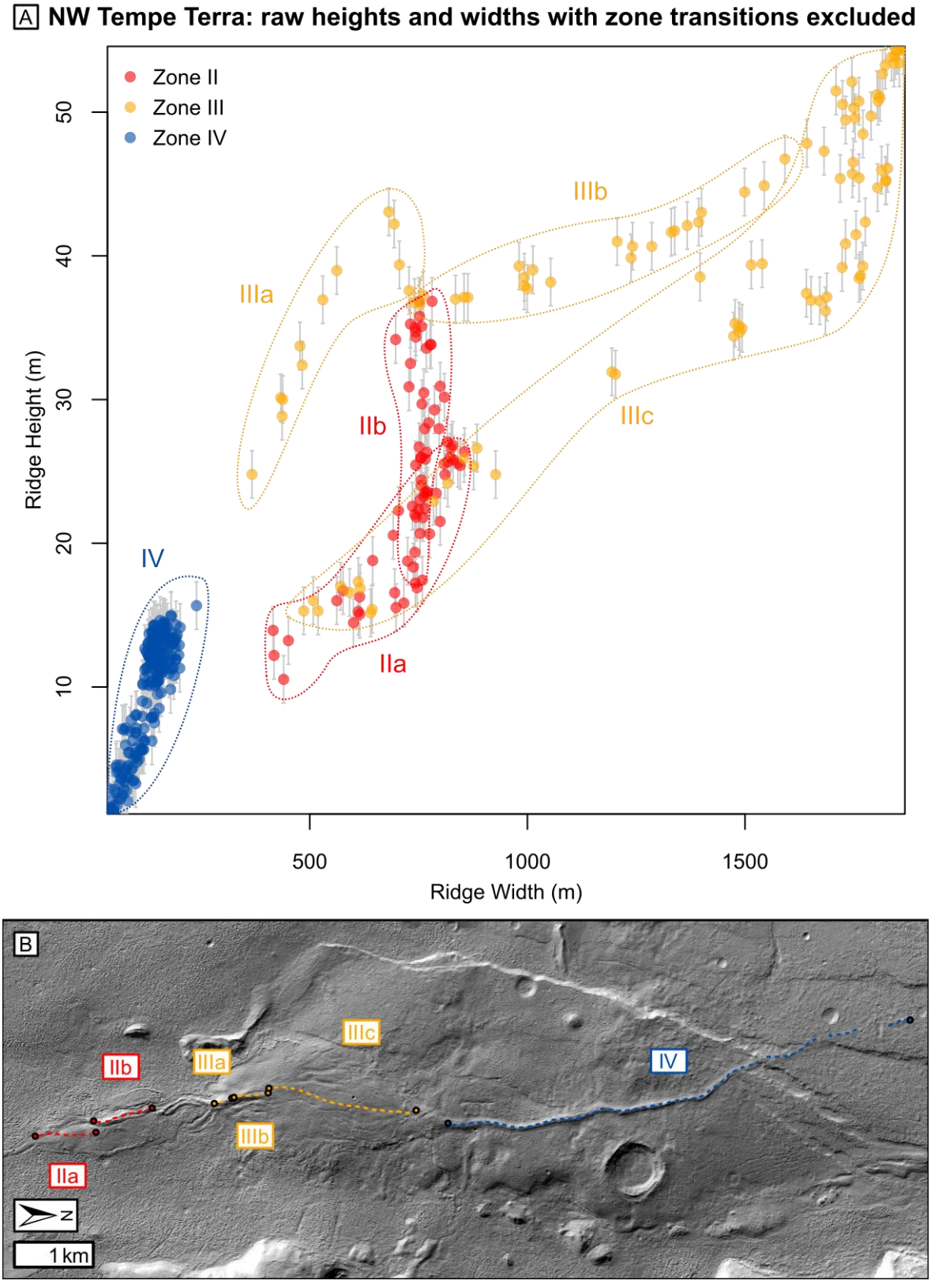

Figure 6.6. Morphometric definition of subzones along the NW Tempe Terra esker. (A) Scatterplot of raw height-width measurements for the NW Tempe Terra esker (excluding zone transitions highlighted in Figure 6.5) with groupings of spatially-associated points grouped into subzones IIa–b, IIIa–c, and IV (dashed loops), the extents of which are shown in (B). (B) A CTX image (Table 6.1) mosaic of zones II–IV of the NW Tempe Terra esker with points joined by dashed lines representing the morphological subzones represented by each grouping of the scatterplot in panel A.

Subzones IIa and IIb are located within zone II of the esker, which I described as multi-crested in Chapter 4 (Butcher et al., 2017). In subzone IIa, the ridge is characterised by a broad, rounded central crest, and a second parallel, less distinct crest part way down its gently-sloping western flank (Figures 6.7B and 6.8I). The crests are separated by a 100–200 m wide, 2–5 m deep, flat-bottomed trough (Figure 6.8I) which itself is partially infilled by a small proto-ridge (Figure 6.8H) towards the northern boundary of the subzone and the transition to subzone IIb.

The broad, gently-sloping flanks of subzone IIa continue into subzone IIb, but the crest of the ridge is instead characterised by a narrow, more steep-sided central prominence atop the broader ridge (Figure 6.8F–G), with a sharp crest that transitions to two sharp parallel crests that are separated by a 50–60 m wide, ~5 m deep, v-shaped trough (Figure 6.8F). The depth of this inter-crest trough is less than the height of the central prominence in which it occurs. Qualitatively, the central prominence in subzone IIb appears to be continuous with the proto-ridge that occupies the northern end of the inter-crest trough in subzone IIa (Figures 6.7B and 6.8H). The sharp to multi-crested central prominence continues to the zone II–III transition, but I exclude its northernmost portions from quantitative analyses owing to significant obscuration of the ridge flanks by both remnant glacier materials and the possible tributary ridge (Chapter 4; Butcher et al., 2017) that appears to run parallel with the main ridge before merging with its easternmost flank at the zone II–III transition (Figure 6.5B).

Subzone IIIa is a short subzone at the southernmost end of zone III. It is morphologically similar to subzone IIb (i.e., comprising broad lower flanks and a central prominence), except that the central prominence is more pronounced and characterised by a single sharp crest (Figures 6.7B and 6.8E). The crest of the central prominence gradually becomes lower, wider, and more rounded (Figure 6.8D) into subzone IIIb, eventually grading into the surface of the broader ridge (Figure 6.7) at the northernmost end of subzone IIIb. Visually, the terminus of the central prominence in subzone IIIb is indistinct, but the topography of its lowering and widening terminal zone approximates a fan-like shape (Figure 6.7B). The surface of this fan-shaped section is characterised by multiple narrow, divergent troughs (Figure 6.7A).

Subzone IIIc is characterised by the relatively simple, wide, round crest morphology (Figure 6.8B–C) that typifies zone III as described in Chapter 4 (Butcher et al., 2017). It narrows and lowers toward its northern end and transitions gradationally into the narrow, sharp-crested zone IV ridge (Figure 6.8B) which crosses the floor of the rift valley in the proglacial zone, becoming fragmented at its northernmost end (Figure 6.2A). Like subzone IIIc, the

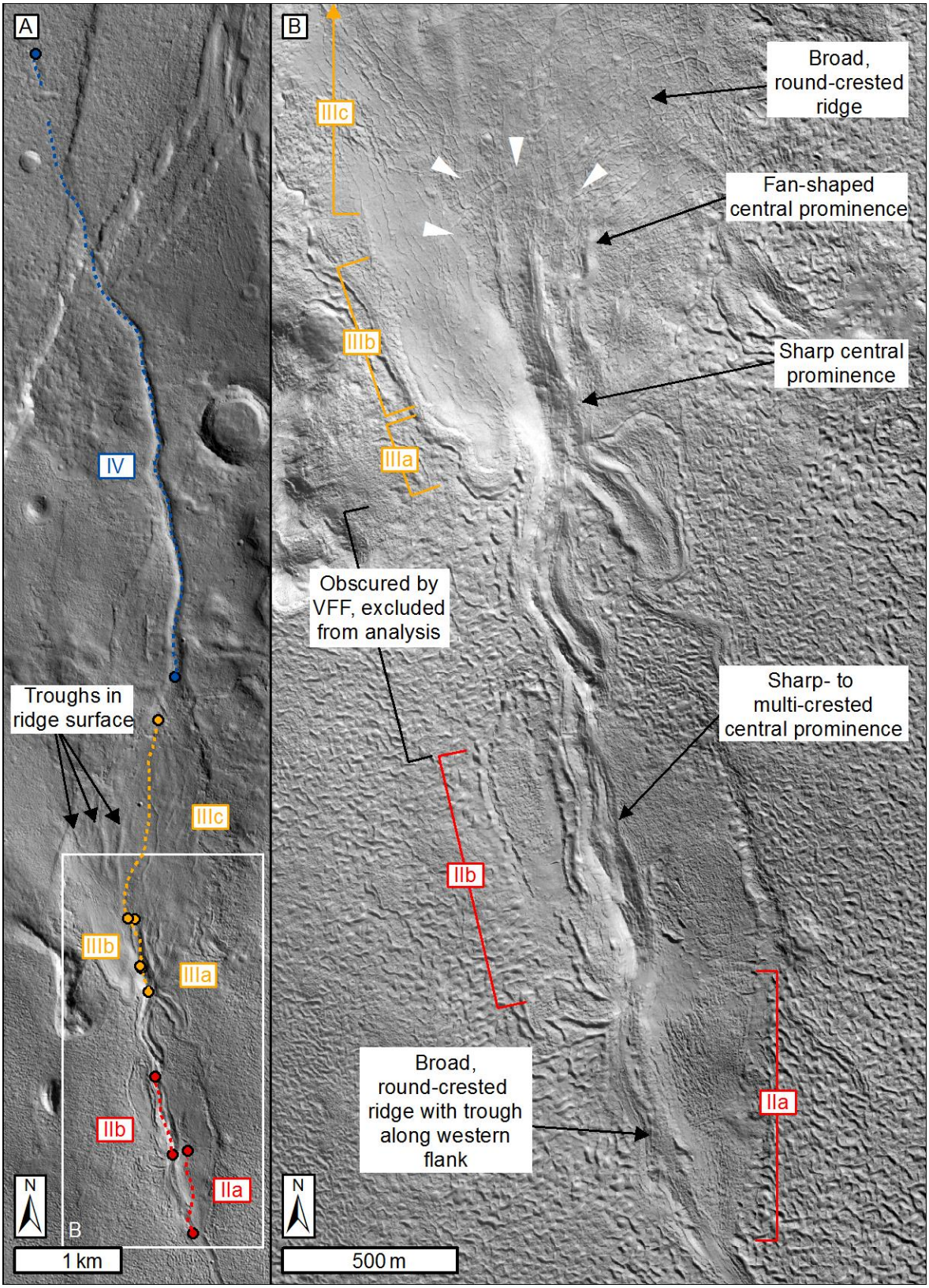

Figure 6.7. Morphological subzones of the NW Tempe Terra esker in context (A) CTX image mosaic showing extents of subzones (points joined by dotted lines), and extent of panel B, orthorectified HiRISE image of subzones IIa–b, IIIa and the southern portion of subzone IIIb. White arrows indicate the location where the fan-shaped portion of the upper member ridge becomes topographically indistinct. See Table 6.1 for list of data products.

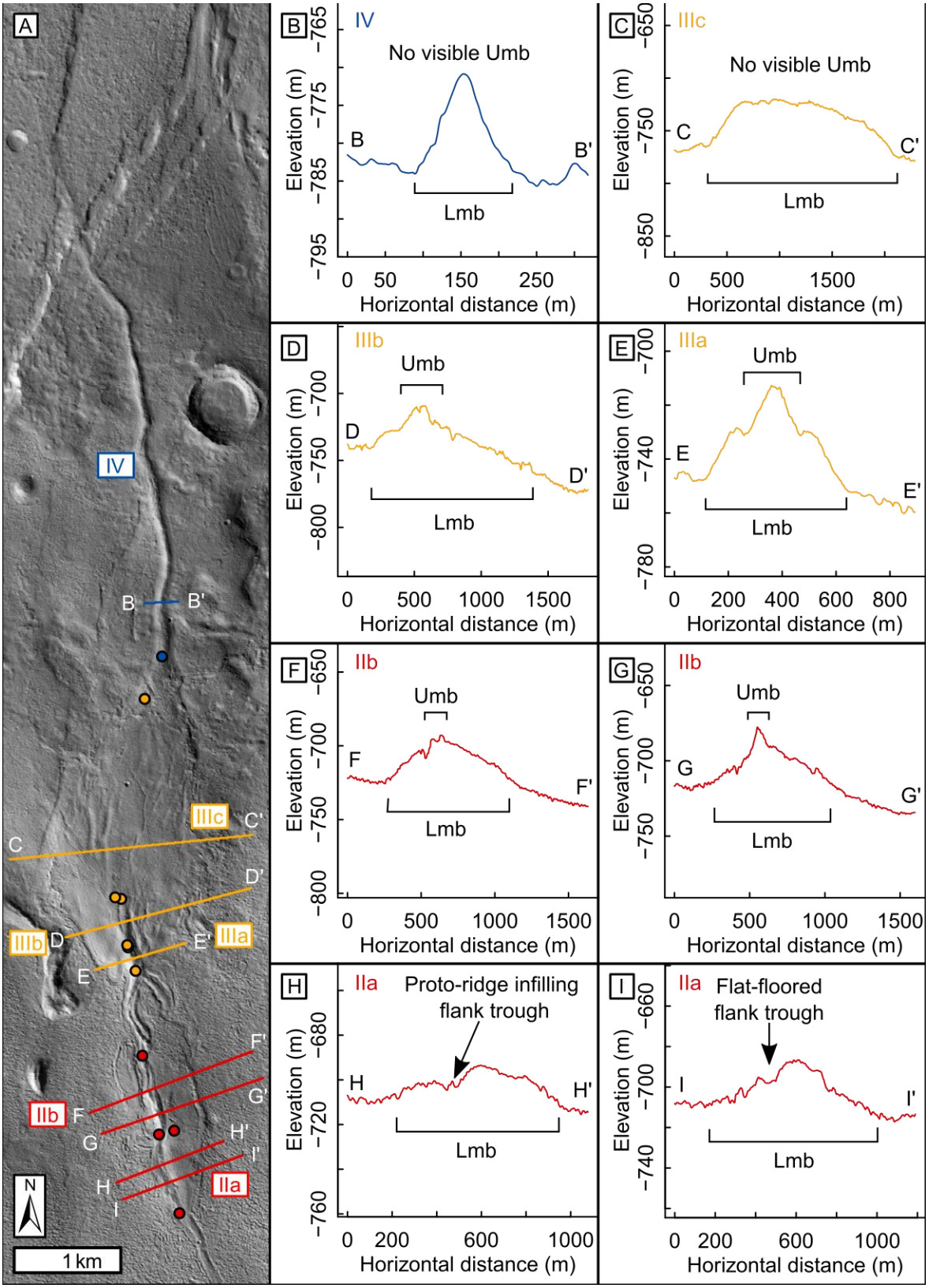

Figure 6.8. Topographic profiles showing characteristics of subzones along the NW Tempe Terra esker. (A) CTX image mosaic (Table 6.1; points show extents of labelled subzones), showing locations of HiRISE topographic profiles (Table 6.1): (B) B–B', showing the sharp crested portion of the ridge in zone IV where there is no visible upper member ridge; (C) C–C' showing the wide, round crest characteristic of subzone IIIc, where there is no visible upper member ridge; (D) D–D' showing the wide lower member (Lmb) ridge superposed by the low, fan-shaped terminus of the upper member ridge (Umb) in subzone IIIb; (E) E–E' showing the wide lower member ridge (caption continues on next page)

(caption continued from previous page) superposed by a prominent sharp-crested portion of the upper member in subzone IIIa; (F) F–F' showing a multi-crested portion of the upper member in subzone IIb, atop the wider, round-crested Lmb; (G) G–G' showing a sharp-crested portion of the upper member in subzone IIb, atop the wider, round-crested Lmb; (H) H–H' showing the wide, round-crested ridge in subzone IIa, at the location where the upper member ridge appears to originate as a proto-ridge occupying a trough on the western flank; and (I) I–I' showing the wide, round-crested ridge in subzone IIa with a flat-floored trough in its western flank. All topographic profiles are displayed at ten times vertical exaggeration.

portion of the ridge in zone IV exhibits no evidence for a distinct central prominence, and its heights and widths cluster in a single grouping of the scatterplot (Figure 6.6). This sharp-crested ridge (Figure 6.8) is similar in width to both the central prominence in subzones IIb and IIIa (Figure 6.8D–G), and to the inter-crest trough in subzone IIa (Figure 6.8H–I).

6.5.1.2. Stacked Esker Hypothesis

The observations of the morphological subzones described above lead me to propose that zones II and III of the NW Tempe Terra esker comprise two stacked esker ridges (Figure 6.9) that formed either under a changing sediment-discharge regime within a single, multi-phase esker-forming melt event, or during two temporally distinct meltwater events. I propose that the relatively steep-sided central prominence in subzones IIb and IIIa (Figures 6.7B and 6.8E–G) and its fan-shaped terminus in subzone IIIb (Figures 6.7B and 6.8D) were deposited under a different deposition regime after formation of the much wider, underlying, round-crested ridge. Following this hypothesis, I propose that the ridge in subzone IIa was not originally multi-crested, and that the multi-crested morphology is inherited from post-depositional erosion of an inter-crest trough part way down the gently-sloping western flank of an existing round-crested ridge. I propose that this erosion was driven by channelised meltwater supplying the narrower, secondary, superposed ridge in subzone IIb, with which the trough is aligned. Consequently, the origination of the superposed ridge as a proto-ridge infilling the northernmost portion of the flank trough in subzone IIa could represent the location of a transition from erosional to depositional drainage within the subglacial meltwater conduit. I therefore propose that the heights recorded in groupings IIb, IIIa and IIIb of the raw height-width scatterplot (Figure 6.10E) represent the composite height of a stacked esker *formation* comprising two esker *members* in the northern portion of zone II and the southern portion of zone III: a broad underlying ridge that is continuous with the subzone IIIc and zone IV portions of the ridge, which I term the *lower member* (Lmb) ridge, and a narrower secondary ridge (the *upper member*, Umb) that superposes it in subzones IIb, IIIa, and IIIb.

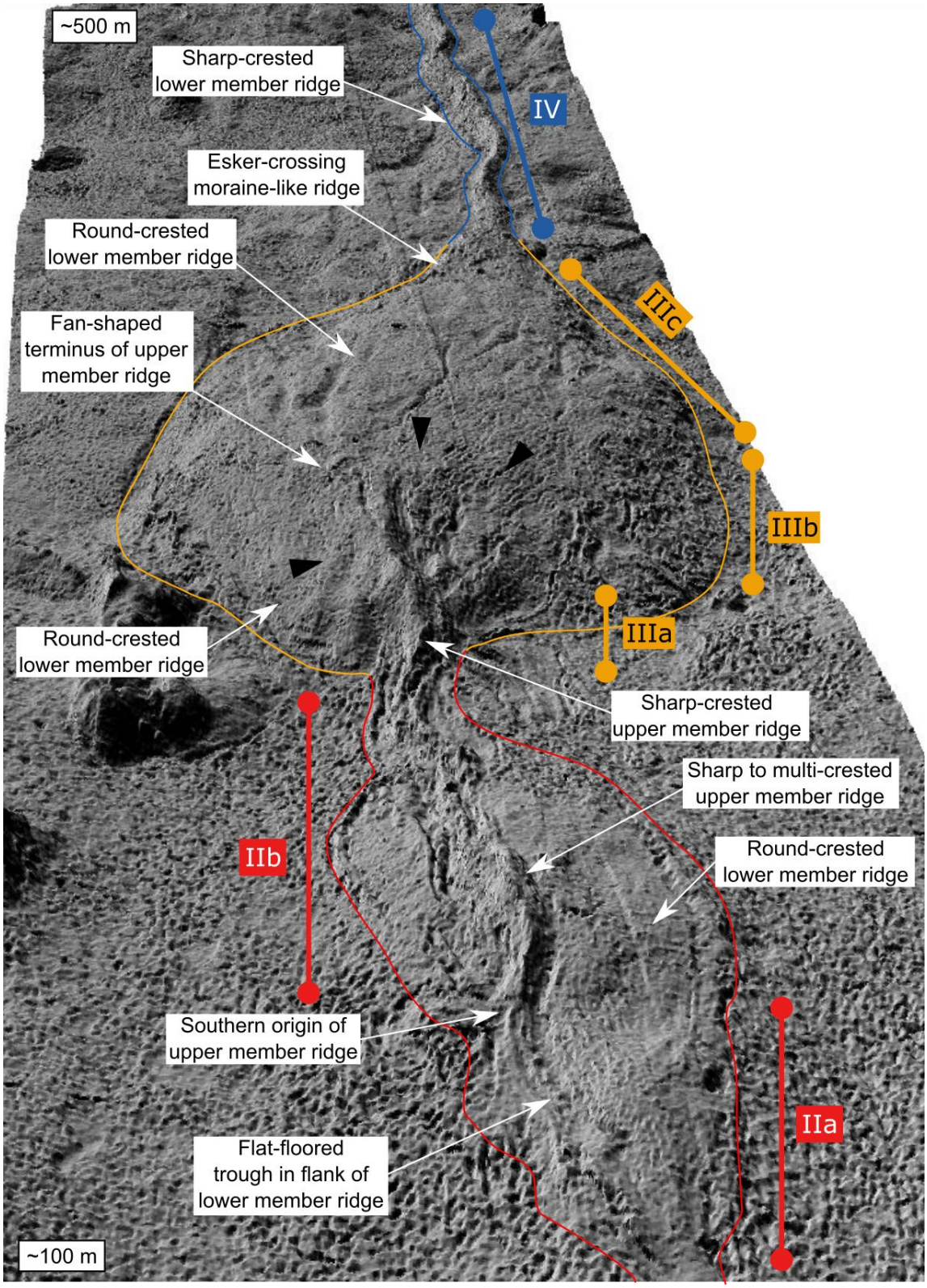

Figure 6.9. Oblique 3D view of the NW Tempe Terra esker showing stacked morphology. Hillshade model draped on DEM (five times vertical exaggeration) looking northward from southern end of subzone IIa. Thin lines are margins of esker. Thick dot-ended lines show extents of individual morphological subzones. Key morphologies are labelled, and black arrows indicate the margins of the fan-like terminus of the upper member ridge. The lower member ridge extends northward of this point (into subzones IIIc and IV) with no evidence of a morphologically-distinct upper member ridge. The zone IV ridge extends beyond the upper margin of the image. Pitted texture of foreground surface adjacent to esker is real topography of pitted surface of the remnant parent glacier, which terminates at the zone II–III transition.

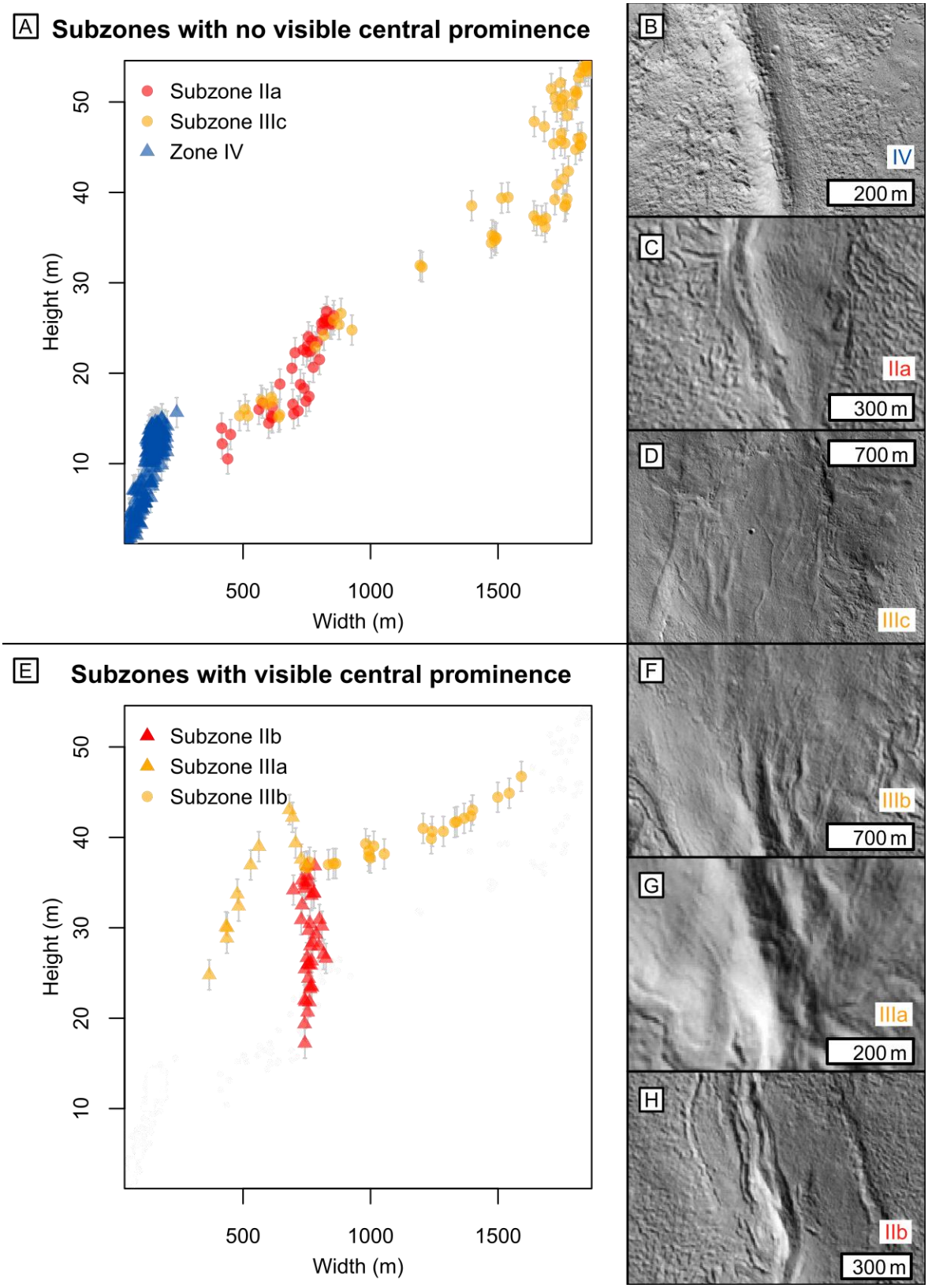

Figure 6.10. Scatterplots of raw heights and widths of the NW Tempe Terra esker in subzones with and without central prominence. (A) Scatterplot of raw ridge height and width for subzones IIa, IIIc, and zone IV (shown in panels B–D), where the ridge has no visible central prominence. (B) HiRISE image of portion of zone IV. (C) CTX image of subzone IIa. (D) CTX image of subzone IIIC. (E) Scatterplot of raw ridge height and width for subzones IIb, IIIa, and IIIb (shown in panels F–H), where the ridge has a visible central prominence. (F) CTX image of subzone IIIb. (G) CTX image of subzone IIIa. (H) CTX image of subzone IIb. See Table 6.1 for a list of data products.

6.5.1.3. Tests of the Stacked Esker Hypothesis

In order to explore the hypothesis outlined in Section 6.5.1.2 that the NW Tempe Terra esker is a stacked formation comprising an earlier lower member and a later upper member ridge, I first made predictions about the height-width trends that would be observed if the signals of the upper and lower member ridges were separated. The lower member ridge comprises two portions where there is no evidence for a superposed ridge (subzone IIIc and zone IV). The portion in subzone IIIc has a simple round-crested morphology, while the portion in zone IV has a simple, sharp-crested morphology. I used the morphometries of these portions of the ridge as reference morphometries, upon which I based my predictions for the height-width trends of the separated upper and lower member ridges in the stacked subzones which approximate similar morphologies to the portions in zone IV and IIIc, respectively. Thus, my predictions were based on the underlying assumption that portions of martian esker ridges with similar crest morphologies have similar morphometric relationships (in this case, between height and width).

Under the stacked esker hypothesis, the flat-floored trough of the lower member ridge in subzone IIa formed via erosion into the surface of the lower member ridge by meltwater supplying sediment to the upper member ridge down-conduit (beginning as the proto-ridge that occupies the northern end of this trough). Since this hypothesised secondary erosion occurred part way down the flank of the lower member ridge I suggest that the height of the central crest of the ridge in this subzone is representative of the original height of the lower member ridge, which would have been round-crested prior to incision of the flank trough. This is supported by the similarity in the raw height-width trend between this subzone and the round-crested portion of the lower member ridge in subzone IIIc. Thus, the lower member ridge in subzone IIa can also be used for reference morphometries of round-crested ridge portions, in particular in the lower range of widths and heights to which the subzone IIIc ridge does not extend.

My predictions are as follows. If the stacked esker hypothesis is correct, subtracting the height of the upper member ridge from the total height of the ridge formation in subzones IIb, IIIa, and IIIb should return height-width trends for the lower member ridge in these subzones that align approximately with the reference trends of the lower member ridge in subzones IIa and IIIc (Figure 6.11A), where the ridge has a similar broad morphology, but with no evidence of a secondary superposing ridge (Figure 6.10A, C–D).

The approximate visual similarity in width and morphology between the upper member ridge in subzones IIb and IIIa (Figures 6.7B and 6.8D–G, and 6.10G–H), and the sharp-crested

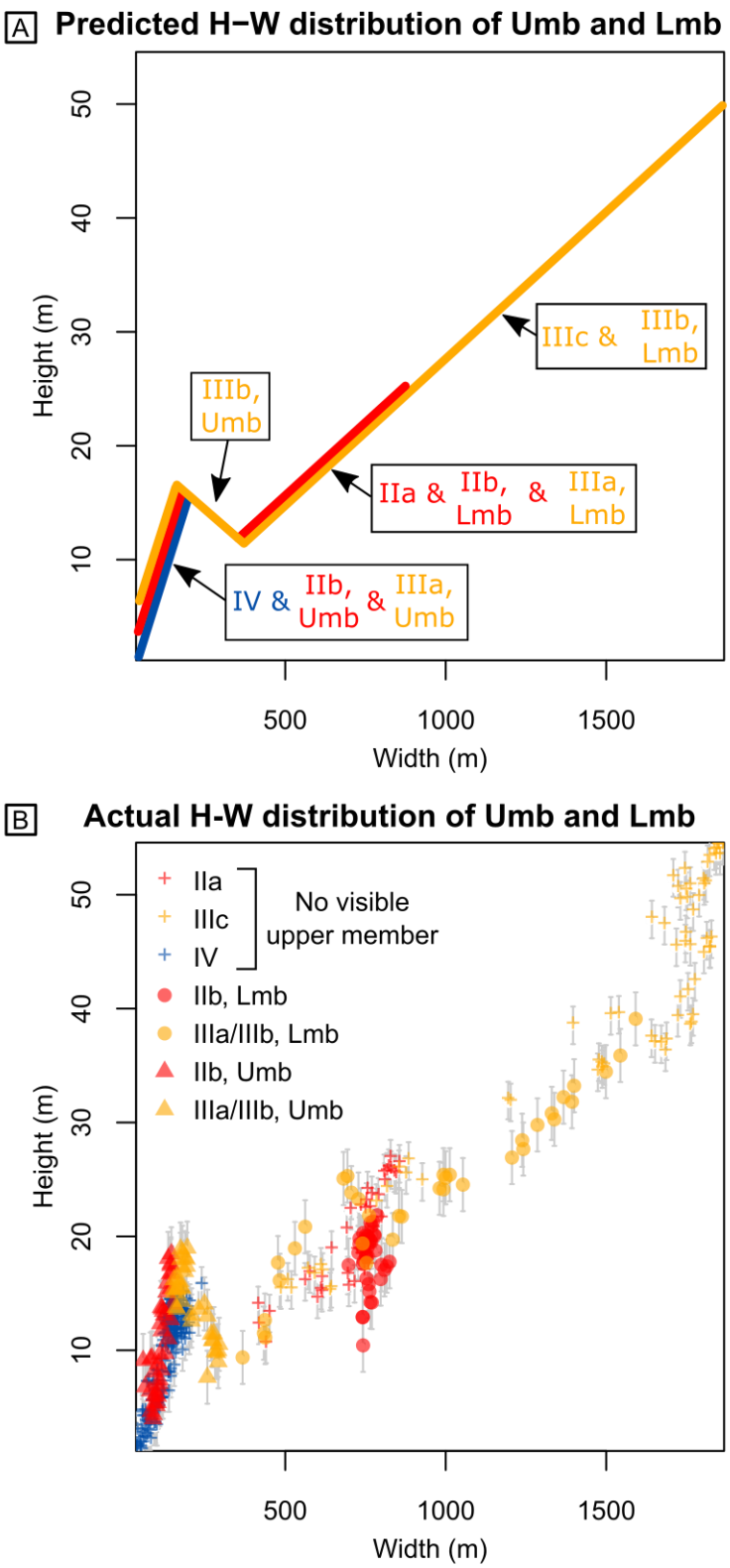

Figure 6.11. Predicted and actual height-width relationships for the upper and lower member ridges of the NW Tempe Terra esker formation. (A) Schematic showing predicted trends of height and width measurements of the upper and lower member ridges of the NW Tempe Terra esker formation. Predictions are based on trends for subzones with similar crest morphologies, but no visible upper member ridge (Figure 6.10A). Colours represent zones, and labels indicate predicted positions of subzones in the scatterplot. (B) Actual distribution of upper (triangles) and lower (points) members of the ridge relative to subzones where there is no visible upper member ridge (crosses). Colours represent zones.

portion of the lower member ridge in zone IV (Figure 6.10B), where there is no evidence for a superposed ridge, also leads me to predict that height and width measurements of the upper member ridge would follow a similar trend to those of the lower member ridge in zone IV (Figures 6.10A and 6.11A).

Finally, since the fan-shaped terminus of the upper member in subzone IIIb extends from the tallest point of the upper member in subzone IIIa and lowers and widens northward to grade into the broader lower member ridge in subzone IIIc, I predict that its height and width will follow negative trend connecting the high height-width end of grouping IV to the low height-width end of grouping IIa in the raw height-width scatterplot (Figure 6.11A).

If all of the above predictions are correct, the complex groupings of the raw height-width scatterplot in Figure 6.10 should effectively collapse onto the reference trends described by the portions of the ridge with no evidence of a superposed ridge, as illustrated in Figure 6.11.

To test my predictions, I extracted height and width measurements for the upper member ridge in subzones IIb, IIIa, and IIIb according to the same point classification method and using the same transects as for the raw measurements, with the key difference that I classified the base points of the central prominence rather than the base points of the full ridge formation. I subtracted the height of the upper member ridge from the raw height measurements in these subzones, to give the approximate height of the lower member ridge. I then replotted the height-width scatterplot with the upper and lower members separated (Figure 6.11B) to test whether they followed the trends predicted in Section 6.5.1.2 (Figure 6.11A), i.e., that the lower member in subzones IIb, IIIa, and IIIb approximates a similar trend to groupings IIa and IIIc of the height-width scatterplot, and that the upper member approximates a similar trend to grouping IV of the scatterplot. The uncertainty in height measurements of the constituent upper and lower members is compounded by subtraction of the height of the upper member ridge from that of the lower member ridge. The calculated uncertainty in ridge height for measurements of the constituent upper and lower member ridges was 2.33 m (Appendix A). The uncertainty in width remains the same as that for raw width measurements (Section 5.5).

The scatterplot in Figure 6.11B illustrates that, when subdivided into the upper and lower members described in Section 6.5.1.2, the complexity of height-width relationships for the NW Tempe Terra esker is significantly reduced. As predicted, the upper groupings (IIb, IIIa, and IIIb) of the raw height-width scatterplot (Figure 6.10A) collapse onto the existing reference trends described by portions of the ridge with similar crest morphologies where

there is no visible upper member ridge (groupings IIa, IIIc, and IV; Figure 6.10B). The dimensions of the round-crested lower member ridge in subzones IIb, IIIa, and IIIb (circular points in Figure 6.11B) fall along a similar trend to those of the round-crested portions of the lower member ridge in subzones IIa and IIIc (red and yellow crosses in Figure 6.11B, respectively) where there is no visible upper member ridge. Similarly, the dimensions of the sharp- to multi-crested upper member in subzones IIb and IIIa (triangles that follow a positive trend in Figure 6.11B) occupy a similar space to those of the sharp-crested ridge in zone IV (blue crosses in Figure 6.11B). The fan-shaped portion of the upper member in subzone IIIb (yellow triangles that follow a negative trend in Figure 6.11B) follows a transitional negative trend between the upper range of zone IV dimensions and the lower range of subzone IIa dimensions. Thus, visually, the dimensions of the constituent lower and upper members of the NW Tempe Terra esker formation follow the predicted trends (Figure 6.11A), supporting the hypothesis that it represents a stacked esker formation.

I now test the similarity between the predicted (Figure 6.11A) and observed (Figure 6.11B) trends statistically, both by comparing linear fits (Figure 6.12A and D; Table 6.4), and by undertaking statistical tests for difference (Table 6.5; Figure 6.12).

I modelled the predicted trends (black dotted lines in Figures 6.12A and D) by producing linear fits for the reference trends described by the sharp-crested (zone IV) and round-crested (subzones IIa and IIIc) portions of the NW Tempe Terra esker where there is no distinct upper member ridge (crosses in Figures 6.12A and D). The observed trends (black dashed lines in Figures 6.12A and D) are described by the constituent sharp- to multi-crested upper member (triangles in Figure 6.12D) and round-crested lower member ridges in subzones IIb, IIIa, and IIIb (circular points in Figure 6.12A). Given that the fan-shaped upper member ridge in subzone IIIb has a transitional morphology for which a reference trend is not available (i.e., it is not morphologically comparable to that of any of the portions of the ridge where no stacking is observed), this subzone is excluded from these statistical analyses.

Skewness and kurtosis values combined with Shapiro-Wilk tests for normality (p-value < 0.01 means variable is not normally distributed) determined that height and width measurements for all samples used to model observed and predicted trends were not normally distributed (Table 6.4). Therefore, I tested the strength of height-width correlations for each sample using non-parametric Spearman's rank correlation tests because non-normality of the samples combined with the fact that neither height nor width represent an independent variable meant that the core assumptions of regression modelling were not satisfied. The Spearman's rho value returned by this test can range between -1 and +1, with

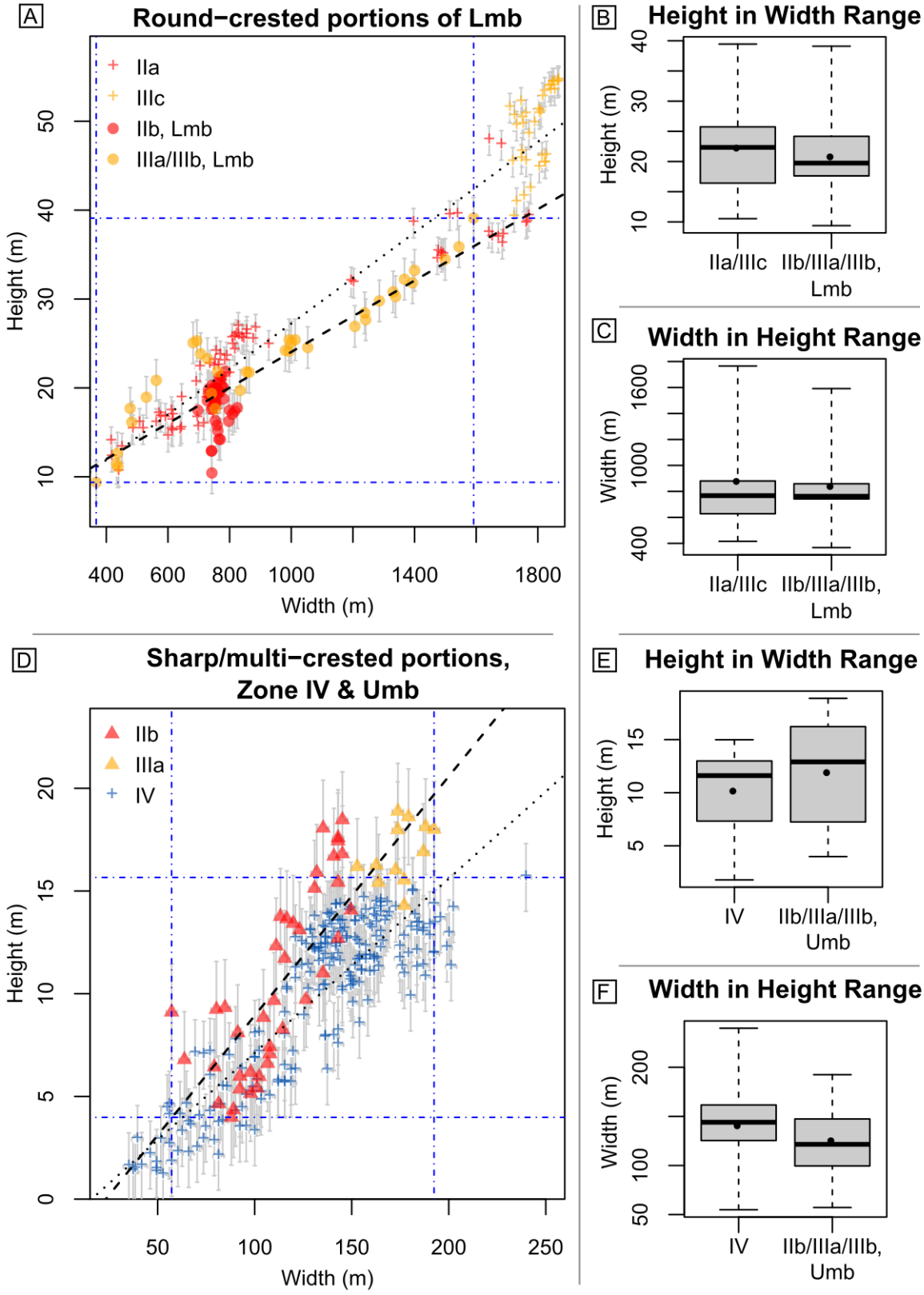

Figure 6.12. Tests for difference between predicted and observed height-width distributions for the upper and lower member ridges in stacked subzones of the NW Tempe Terra esker formation. (A) Scatterplot showing predicted (black dotted line) and observed (black dashed line) height-width trends for measurements of the lower member ridge in stacked subzones IIb, IIIa and IIIb (circular points). Crosses are measurements of round-crested portions of the ridge in subzones IIa and IIIc where no upper member ridge is observed, from which the predicted trend was derived. Blue dot-dash lines show height ranges (horizontal lines) and width ranges (vertical lines) over which tests for (caption continues on next page)

(caption continued from previous page) difference were undertaken for ridge widths and heights, respectively. (B) Boxplot showing distributions of predicted (column 1) and observed (column 2) heights of the round-crested lower member ridge in subzones IIb, IIIa, and IIIb, within the width range (vertical blue dot-dash lines in A) occupied by both the predictive (crosses in A) and observed (circular points in A) measurements. (C) Boxplot showing distributions of predicted (column 1) and observed (column 2) widths of the round-crested lower member ridge in subzones IIb, IIIa, and IIIb, within the height range (horizontal blue dot-dash lines in A) occupied by both the predictive (crosses in A) and observed (circular points in A) measurements. (D) Scatterplot showing predicted (black dotted line) and observed (black dashed line) height-width trends for measurements of the upper member ridge (triangles) in stacked subzones IIb, and IIIa. Crosses are measurements of the sharp-crested portion of the ridge in zone IV, where no upper member ridge is observed, from which the predicted trend was derived. Blue dot-dash lines show height ranges (horizontal lines) and width ranges (vertical lines) over which tests for difference were undertaken for ridge widths and heights, respectively. (E) Boxplot showing distributions of predicted (column 1) and observed (column 2) heights of the sharp- to multi-crested upper member ridge in subzones IIb and IIIa, within the width range (vertical blue dot-dash lines in A) occupied by both the predictive (crosses in D) and observed (triangles in D) measurements. In all boxplots (panels B, C, E, and F), boxes represent the interquartile range, whiskers represent maximum and minimum, solid lines represent the medians, and points represent the means.

Table 6.4. Predictive and observed height-width correlation statistics and linear fits for the lower and upper members of the stacked portions of the NW Tempe Terra esker. Predictive fits are based on height and width measurements of portions of the ridge in the stated subzones with no visible upper member ridge, but which have similar crest morphologies to the lower (i.e., round-crested) or upper (i.e., sharp- to multi-crested) member ridges in stacked subzones. Observed fits refer to height and width measurements of the constituent lower and upper member ridges in the stated subzones.

	Predictive		**Observed**	
	Height	**Width**	**Height**	**Width**
Round-crested lower member	**Subzones IIa and IIIc**		**Subzones IIb, IIIa, and IIIb, lower member**	
N	109	109	76	76
Skewness	0.13	-0.04	0.78	1.11
Kurtosis	1.55	1.23	3.64	3.92
Shaprio-Wilk p-value	< 0.01	< 0.01	< 0.01	< 0.01
Spearman's rank rho	0.96		0.88	
Spearman's rank p-value	< 0.01		< 0.01	
Linear fit	$H = 0.03\ W + 1.66$		$H = 0.02\ W + 3.96$	
Sharp- to multi-crested upper member	**Zone IV**		**Subzones IIb and IIIa, upper member**	
N	229	229	52	52
Skewness	-0.73	-0.50	-0.15	0.18
Kurtosis	2.17	2.67	1.57	2.13
Shaprio-Wilk p-value	< 0.01	< 0.01	< 0.01	< 0.01
Spearman's rank rho	0.87		0.84	
Spearman's rank p-value	< 0.01		< 0.01	
Linear fit	$H = 0.09\ W - 1.35$		$H = 0.12\ W - 2.71$	

Table 6.5. Wilcoxon tests for difference between predictive and observed heights and widths for the lower and upper members of the stacked portions of the NW Tempe Terra esker. Predictive samples are based on height and width measurements of portions of the ridge in the stated subzones with no visible upper member ridge, but which have similar crest morphologies to the lower (i.e., round-crested) or upper (i.e., sharp- to multi-crested) member ridges in stacked subzones. Observed samples refer to height and width measurements of the constituent lower and upper member ridges in the stated subzones. Predictive and observed heights are sampled only in the width range over which the two samples overlap (vertical blue dot-dash lines in Figures 6.12 A and D), and predictive and observed widths are sampled only in the height range over which the two samples overlap (horizontal blue dot-dash lines in Figures 6.12A and D). See Figure 6.12 for comparative scatterplots and boxplots of sampled measurements.

	Heights	
	Predictive	**Observed**
Round-crested lower member	**Subzones IIa and IIIc**	**Subzones IIb, IIIa, and IIIb, lower member**
N	63	76
Shapiro-Wilk p-value	< 0.01	< 0.01
Wilcoxon p-value	0.42	
Sharp- to multi-crested upper member	**Zone IV**	**Subzones IIb and IIIa, upper member**
N	207	52
Shapiro-Wilk p-value	< 0.01	< 0.01
Wilcoxon p-value	< 0.01	
	Widths	
	Predictive	**Observed**
Round-crested lower member	**Subzones IIa and IIIc**	**Subzones IIb, IIIa, and IIIb, lower member**
N	68	76
Shapiro-Wilk p-value	< 0.01	< 0.01
Wilcoxon p-value	0.84	
Sharp- to multi-crested upper member	**Zone IV**	**Subzones IIb and IIIa, upper member**
N	201	52
Shapiro-Wilk p-value	< 0.01	0.22
Wilcoxon p-value	< 0.01	

the former representing a perfect negative correlation, and the latter representing a perfect positive correlation, though it should be noted that these correlations are not necessarily monotonic. An accompanying Spearman's rank p-value < 0.01 indicates statistical significance of the Spearman's rho value.

I performed statistical tests for difference between predictive and observed trends for width and height variables individually. I performed tests for difference in heights for

measurements within the ranges where ridge widths overlapped (range shown by vertical blue dot-dash lines in Figures 6.12A and D), and tests for difference in widths within the range where heights overlapped (range shown by horizontal blue dot-dash lines in Figure 6.12A and D). This avoided skewing of the comparison by differences in the centroids of the full samples along the height-width trends.

Shapiro-Wilk tests indicating non-normal distributions for all samples (see Table 6.5) determined that non-parametric Wilcoxon tests (where a Wilcoxon p-value < 0.01 suggests a statistically significant difference between sample medians) were suitable for all comparisons. It should be noted that this approach is appropriate only for comparing samples with trends that do not intersect towards the centre of their distributions, so for the datasets shown here this approach is appropriate.

The height-width relationship for the round-crested portion of the NW Tempe Terra esker in subzones IIa and IIIc, which I used to predict the trend described by the round-crested lower member ridge in subzones IIb, IIIa, and IIIb, is best described by a linear fit with the equation:

$$H = 0.03W + 1.66 \quad \textbf{6.1}$$

where *H* is ridge height and *W* is ridge width. The observed height-width relationship for the round-crested lower member ridge in subzones IIb, IIIa, and IIIb is best described by a linear fit with an equation that—considering the magnitude of measurement uncertainties—is very similar to Equation 6.1:

$$H = 0.02W + 3.96 \quad \textbf{6.2}$$

It should be noted that the points in subzone IIb (Lmb) that appear to have heights ~2–5 m below the general trend for the lower member (Figure 6.11B) represent locations where the upper member sits within a ~2–5 m deep trough in the surface of the lower member; hence, the relatively low heights of these points can be explained by underestimation of the true height of the lower member in these locations.

While the round-crested ridge in subzones IIa and IIIc approximates a slightly steeper linear trend than the lower member ridge in subzones IIb, IIIa and IIIb, this does not result in a statistically significant difference in ridge height over the width range occupied by both sets of measurements, or a statistically significant difference in ridge width over the height range occupied by both sets of measurements (Wilcoxon p-values both > 0.05; Figures 6.12A–C, Table 6.5).

The height-width relationship for the sharp-crested portion of the NW Tempe Terra esker in zone IV, which I used to predict the trends described by the sharp- to multi-crested upper member ridge in subzone IIb, and the sharp-crested upper member ridge in subzone IIIa (Figure 6.12), is best described by a linear fit with the equation:

$$H = 0.09W - 1.35 \quad \textbf{6.3}$$

Considering the magnitude of measurement uncertainties (Section 5.5) this is not highly dissimilar from the linear fit that best describes the combined measurements of the sharp- to multi-crested upper member ridge in subzones IIb and IIIa:

$$H = 0.12W - 2.71 \quad \textbf{6.4}$$

However, there is a statistically significant difference in both height and width between the upper member in subzones IIb and IIIa, and the sharp-crested portion of the ridge in zone IV; non-parametric Wilcoxon tests return p-values of <0.01 for both sampled heights and widths (Table 6.5, Figures 6.12D–F). The sharp-crested ridge in zone IV is typically lower and wider than the upper member ridge in subzones IIb and IIIa (Figures 6.12D–F). However, I suggest that this does not provide a strong challenge to the stacked esker hypothesis; there are two primary reasons why the distributions of the sharp-crested portion of the ridge in zone IV and the sharp- to multi-crested upper member ridge in subzones IIb and IIIa may be expected to vary slightly from one another. Firstly, the upper member ridge incorporates both sharp-crested and multi-crested morphologies in subzone IIb, whereas the zone IV ridge is entirely sharp-crested. Secondly, there is evidence for a difference in degradation state between the upper member ridge in subzones IIb and IIIa, and the zone IV ridge. The crest of the ridge in zone IV is densely pitted. This pitting, which I have previously (Chapter 4; Butcher et al., 2017) attributed to sublimation loss of ice that was trapped within the esker during deposition, means that the ridge lacks a crisp crestline observable in either CTX or HiRISE images. This contrasts with the relatively pristine crests of the upper member in subzones IIb and IIIa, which lack pitting and are clearly traceable in HiRISE images. I therefore suggest that the difference in height and width between the upper member of subzones IIb and IIIa, and zone IV, might result from differences in the degradation state of the ridge crests; sublimation loss at the ridge crest could simultaneously lower ridge height and increase ridge width by promoting downslope-mobilisation of ridge sediments. More advanced degradation of the ridge crest in zone IV is consistent with its more distal position from the ice terminus (hence probable earlier exposure), and its continuation from the lower member ridge, which I propose formed prior to the upper member ridge.

In summary, I find that the replotted height-width trends support the hypothesis that the NW Tempe Terra esker is a composite esker comprising a wide, round-crested lower member ridge that transitions into a sharp-crested ridge in zone IV, and a narrower, sharp-crested to multi-crested upper member ridge that superposes the broad, round-crested portions of the primary ridge in zones II and III. The northern terminus of the upper member ridge has a fan-shaped morphology that is transitional between the sharp- to multi-crested morphology of the upper member ridge and the round-crested portions of the lower member ridge. The individual members of the NW Tempe Terra esker formation therefore follow two dominant trends, which appear to be controlled by crest morphology. Thus, I argue that the raw height and width distributions presented for the NW Tempe Terra esker in Section 6.4.3 represent the composite geometries of a stacked esker formation comprising upper and lower ridge members.

I discuss the possible implications of this stacked morphology for the dynamics of esker formation in Section 6.6. In Section 6.5.2, I present modified 3D morphometry distributions for the NW Tempe Terra esker, with the raw geometries subdivided into those of their constituent ridge members, and crest morphologies. Given the similarities in height and width between subzones IIa and IIIc, and the lower member in subzones IIb, IIIa, and IIIb, I combine these measurements into a single group representing all round-crested portions of the NW Tempe Terra esker formation in subsequent analyses. I take a cautious approach and continue to treat the upper member ridge in subzones IIb and IIIa, and the sharp-crested ridge in zone IV, separately owing to statistically significant—if subtle—differences in their height-width relationships, and differences in crest morphology. I also treat the fan-shaped terminus of the upper ridge member in subzone IIIb separately owing to the transitional nature of its morphometry, and lack of analogous morphologies in other portions of the ridge.

6.5.2. 3D Morphometry Distributions for Constituent Members and Crest Morphologies of the Stacked NW Tempe Terra Esker Formation

The 3D morphometry distributions for the upper and lower ridge members of the NW Tempe Terra esker formation, categorised into subzones that share similar crest morphologies, are displayed in Figure 6.13, and descriptive statistics are displayed in Table 6.6.

6.5.2.1. Height and Width

The lower member of the NW Tempe Terra esker comprises two wide, round-crested, lozenge-shaped components in zones II and III, and a somewhat degraded sharp-crested component in zone IV that becomes fragmented and less distinct towards the northern

terminus of the esker. The round-crested components of the lower ridge member in zones II and III range in width between 367 m and 1867 m, with a median width of 809 m (Figure 6.13B). The heights of these sections vary between 9 m and 55 m, with a median height of 24 m (Figure 6.13A). The sharp-crested portion of the ridge in zone IV is significantly lower and narrower than the round-crested portions of the ridge in zones II and I, with widths in the range 35–240 m (median = 140 m) and heights in the range 1–16 m (median = 11 m; Figure 6.13A–B). The upper member in subzones IIb and IIIa has widths in the range 57–192 m (median = 122 m; Figure 6.13B) and heights in the range 4–19 m (median = 13 m; Figure 6.13A). The upper member in subzones IIb and IIIa is morphometrically similar to the sharp-crested portion of the lower member ridge in zone IV, having widths in the range 57–192 m (median = 122 m), and heights in the range 4 m–19 m (median = 13 m; Figure 6.13A–B). The fan-shaped terminus of the upper member ranges in width between 152 m and 294 m (median = 239 m; Figure 6.13B), and in height between 8 m and 19 m (median = 13 m; Figure 6.13A).

6.5.2.2. Width-Height Ratio and Average Cross-Sectional Slope

The width-height ratios of the individual members of the NW Tempe Terra esker range from 6 (subzones IIb and IIIa, upper member) to 71 (subzones IIa–IIIc, lower member; Figure 6.13C). The round-crested lower member ridge in subzones IIa–IIIc has a significantly higher width-height ratio than both the sharp-crested portion of the lower member (zone IV), and the upper member ridge (subzones IIb–IIIb). Its width-height ratio ranges between 27 and 71, with a median ratio of 38 (Figure 6.13C). This translates to low average cross-sectional slopes in the range 2–4° (median = 3°) for the round-crested portions of the lower member ridge (Figure 6.13D).

As discussed in Section 6.5.1.3, for a given width, the upper member in subzones IIb and IIIa is somewhat taller than the sharp-crested portion of the ridge zone IV. It has width-height ratios in the range 6–22, with a median ratio of 11 compared to width-height ratios in the range 10–45 for zone IV, which has a median ratio of 14 (Figure 6.13C). The highly positively skewed (skewness = 2.2) and leptokurtic (kurtosis = 9.2) distribution of width-height ratios for zone IV (Table 6.6) can be explained by the increasingly degraded appearance of the ridge towards its fragmented northern terminus where the ridge segments become lower relative to their widths, consistent with an increasing exposure age with distance from the glacier margin. These width-height ratios translate to average cross sectional slopes in the range 3–12° (median = 8°) for the sharp-crested portion of the lower

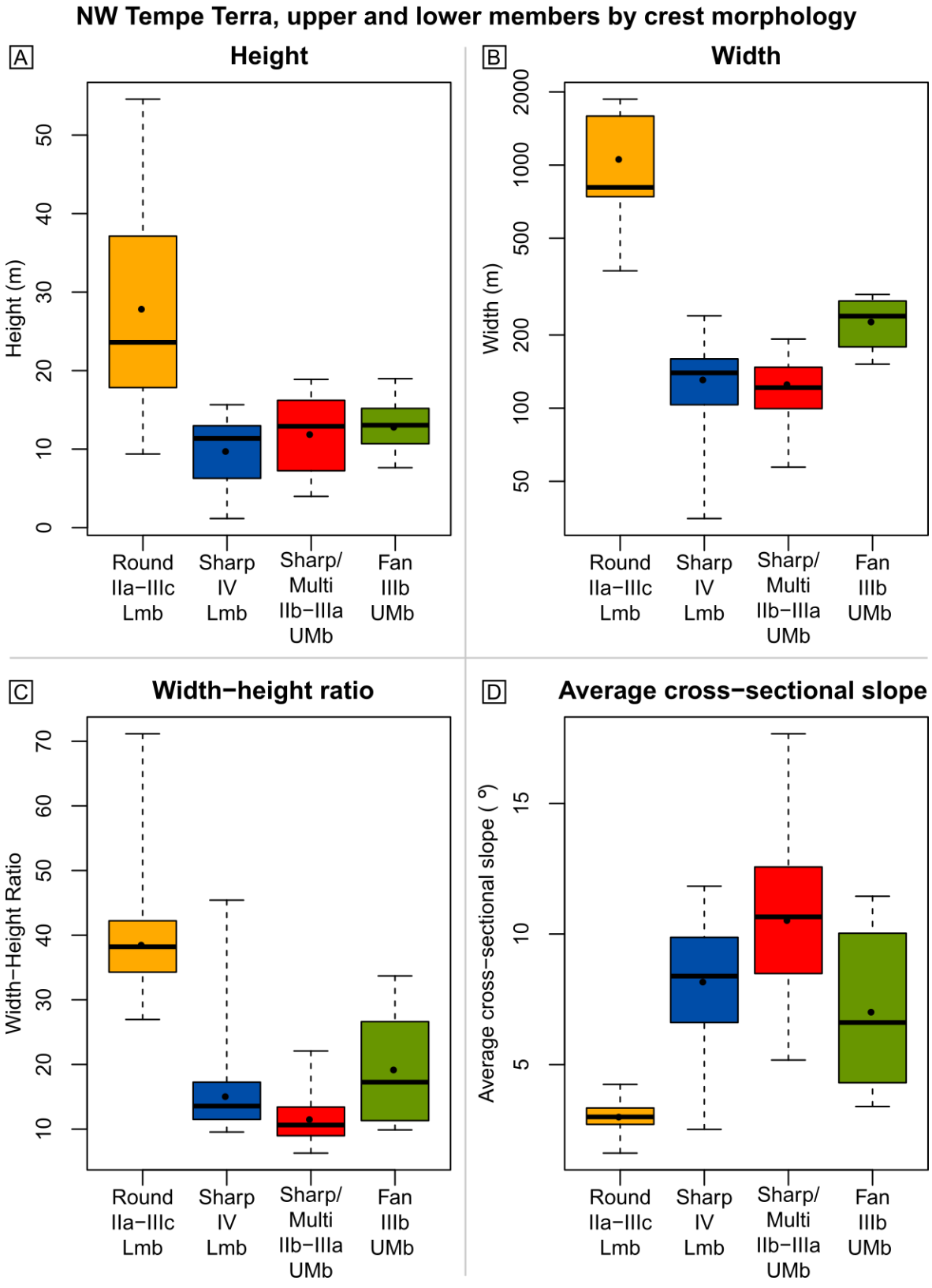

Figure 6.13. Boxplots showing the 3D morphometries of the upper and lower member ridges of the NW Tempe Terra esker formation, categorised by subzone and crest morphology. (A) Height. (B) Width. Note logarithmic scale. (C) Width-height ratio. (D) Average cross-sectional slope. In all boxplots, boxes represent the interquartile range, whiskers represent maximum and minimum, solid lines represent the medians, and points represent the means.

Table 6.6. Descriptive statistics for 3D morphometries of constituent upper and lower members of the NW Tempe Terra esker formation, grouped by subzones with similar crest morphologies. Upper and lower member ridges are included separately within the grouping 'all'. See Table 6.3 for composite heights and widths in stacked zones.

	Height	Width	Width-height ratio	Average cross-sectional slope
All (upper and lower member ridges separated)				
N	490	490	490	490
Minimum	2 m	35 m	6	2°
Maximum	18 m	1867 m	71	18°
Range	16 m	1832 m	65	16°
Quartile 1	3 m	133 m	12	3°
Quartile 3	9 m	756 m	36	9°
Median	6 m	173 m	18	6°
Mean	6 m	489 m	24	6°
Standard Deviation	3 m	537 m	13	3°
Skewness	0.37	1.38	0.52	0.37
Kurtosis	1.96	3.67	2.01	1.96
Subzones IIa–IIIc, lower member (round-crested)				
N	185	185	185	185
Minimum	9 m	367 m	27	2°
Maximum	55 m	1867 m	71	4°
Range	45 m	1500 m	44	3°
Quartile 1	18 m	741 m	34	3°
Quartile 3	37 m	1592 m	42	3°
Median	24 m	809 m	38	3°
Mean	28 m	1066 m	39	3°
Standard Deviation	13 m	474 m	6	0°
Skewness	0.76	0.55	1.28	0.15
Kurtosis	2.28	1.70	7.61	3.55
Subzones IIb and IIIa, upper member (sharp- to multi-crested)				
N	52	52	52	52
Minimum	4 m	57 m	6	5°
Maximum	19 m	192 m	22	18°
Range	15 m	135 m	15	12°
Quartile 1	7 m	100 m	9	9°
Quartile 3	16 m	146 m	13	13°
Median	13 m	122 m	11	11°
Mean	12 m	126 m	12	11°
Standard Deviation	5 m	35 m	4	3°
Skewness	-0.15	0.18	1.08	-0.08
Kurtosis	1.57	2.13	3.32	2.51

Table 6.6 continues on next page

Table 6.6 (continued from previous page)

	Height	Width	Width-height ratio	Average cross-sectional slope
Subzone IIIb, upper member (fan-shaped)				
N	24	24	24	24
Minimum	8 m	151 m	10	3°
Maximum	19 m	294 m	34	11°
Range	11 m	142 m	24	8°
Quartile 1	11 m	179 m	11	4°
Quartile 3	15 m	275 m	26	10°
Median	13 m	239 m	17	7°
Mean	13 m	228 m	19	7°
Standard Deviation	3 m	52 m	8	3°
Skewness	0.23	-0.18	0.29	0.25
Kurtosis	2.36	1.44	1.61	1.43
Zone IV (sharp-crested)				
N	229	229	229	229
Minimum	1 m	35 m	10	3°
Maximum	16 m	240 m	45	12°
Range	15 m	205 m	36	9°
Quartile 1	6 m	103 m	11	7°
Quartile 3	13 m	159 m	17	10°
Median	11 m	140 m	14	8°
Mean	10 m	132 m	15	8°
Standard Deviation	4 m	41 m	6	2°
Skewness	-0.73	-0.50	2.22	-0.52
Kurtosis	2.17	2.67	9.23	2.57

member in zone IV, and slopes in the range 5–18° (median = 11°) for the upper member in subzones IIb and IIIa (Figure 6.13D).

The fan-shaped terminus of the upper member in subzone IIIb has width-height ratios in the range 10–34, with a median ratio of 17. This range of ratios extends from the second quartile of width-height ratios for the upper member ridge in subzones IIb and IIIa, and the second quartile of the width-height ratios for the round-crested portions of the lower member ridge in subzones IIa–IIIc (Figure 6.13C), consistent with the fan-shaped terminus representing a transition from a sharp-crested to round-crested morphology. These width-height ratios translate to average cross-sectional slopes in the range 3–11° (median = 7°; Figure 6.13).

6.6. Discussion

6.6.1. Sediment-Discharge Dynamics and the Morphology of Eskers on Earth.

In Section 6.5.1, I presented tests of the hypothesis that the NW Tempe Terra esker is a stacked esker formation comprising upper member and lower member ridges. I found that the ridge comprises a round-crested lower member ridge in zones II–III that transitions to a sharp-crested ridge in zone IV, and a narrower multi-crested to sharp-crested upper ridge that superposes the lower member ridge in zones II and III. The upper member ridge has a fan-shaped terminus that grades into the surface of the underlying ridge in zone III. In this section, I propose that this composite morphology reflects at least two phases of esker deposition within a subglacial meltwater conduit, either during the same meltwater drainage episode, or during two distinct drainage episodes (Figure 6.15).

In Chapter 4 (see also Butcher et al., 2017), I suggested that the broad-scale transitions in crest morphology between zones I and IV of the NW Tempe Terra esker are consistent with the progression of esker morphology that Shreve (1985a) predicted as an esker-forming meltwater conduit approaches, ascends, and then descends an undulation in the bed. Shreve's theory states that the morphology of the resulting esker deposit will transition from sharp-crested on level bedslopes, to multi-crested on gradual upslope reaches, to broad-crested on steep upslope reaches, and back to sharp-crested on downslope reaches in the lee of a bedslope undulation (See Section 4.5.1). However, numerous field studies (e.g., Banerjee and McDonald, 1975; Brennand, 1994; Burke et al., 2008, 2010, 2012b, 2015; Perkins et al., 2016) have shown that macro-scale esker morphology is intimately linked also to sediment-discharge dynamics that complicate conduit evolution beyond Shreve's bedslope-morphology model (Shreve, 1985a).

Detailed insights into the sedimentary architecture of eskers on Earth have shown that they are composite landforms generated by progressive sedimentation as a conduit enlarges and migrates (laterally, longitudinally, and vertically). The timescale over which this occurs is a topic of significant debate, but there is evidence that eskers can form over timescales ranging between days and millennia (e.g., Banerjee and McDonald, 1975; Aylsworth and Shilts, 1989; Clark and Walder, 1994; Brennand, 1994, 2000; Hooke and Fastook, 2007; Burke et al., 2008, 2010; Cummings et al., 2011; Storrar et al., 2014b, 2014a). Typical estimates of flow depths associated with esker formation, and thus conduit heights (assuming channel full conditions), are on the order of just a few metres (McDonald and Vincent, 1972; Banerjee and McDonald, 1975; Clark and Walder, 1994; Burke et al., 2010), although some estimates range up to 25 m (Brennand, 1994). Thus, a scenario whereby the NW Tempe

Terra esker was deposited in a steady-state subglacial conduit with the same shape and dimensions as the final landform, as is assumed by Shreve's (1985a) model, is probably an oversimplification. Given the new morphometric insights in the present chapter, which suggest that the NW Tempe Terra ridge is indeed a composite landform comprising two stacked ridges with distinct crest morphologies, I modify my initial hypothesis (Chapter 4) for the controls upon the crest morphology of the esker, and instead argue that dynamic sediment-discharge processes appear to provide a better explanation of the new observations presented here.

On Earth, ridge enlargements along eskers, akin to the broad, tall, round-crested lower member ridge in zones II and III of the NW Tempe Terra esker, have been found to comprise sedimentary macroforms (Figure 6.14). Macroforms represent large depocentres with complex sedimentary architectures recording upflow, downflow, vertical and lateral accretion (e.g., Brennand, 1994, 2000; Burke et al., 2008, 2010, 2012b, 2015; Perkins et al., 2016). Where sediment supply is abundant and flow power high, deposition of bedforms such as dunes or antidunes on the conduit floor can partially (or completely) obstruct the flow of conduit-confined meltwater (e.g., Brennand, 1994; Burke et al., 2008, 2010, 2012b, 2015). Focussing of meltwater flow via this mechanism drives an increase in hydraulic pressure and flow power, promoting vertical, lateral, and/or longitudinal conduit expansion over and/or around the macroform via conduit wall and roof melting (e.g., Brennand, 1994; Burke et al., 2008, 2010, 2012b, 2015). In turn, this conduit enlargement (which can promote cavity formation on the stoss and lee sides of the bedform), results in a reduction in flow power, encouraging deposition and growth of macroforms via upflow, downflow, lateral, and/or vertical aggradation (Figure 6.14, column 1). This forms a positive feedback of conduit migration and macroform growth (Brennand, 1994; Burke et al., 2015), and results in formation of enlarged ridge morphologies (e.g., Burke et al., 2015).

In contrast, narrow, sharp-crested to round-crested portions of eskers typically lack the complex ridge morphologies associated with macroforms (Figure 6.14, column 2). They have been found to have relatively simple sedimentary architectures comprising tabular or arched beds (e.g., Brennand, 1994, 2000; Burke et al., 2012b, 2008, 2010, 2015). This contrast has been attributed to differences in sediment supply and flow power during formation of sharp-crested portions of eskers and macroform-dominated ridge enlargements (Burke et al., 2015). Whereas ridge enlargements have been associated with regimes of abundant sediment supply, narrow portions of eskers have been associated with regimes of moderate or limited sediment supply (Burke et al., 2015). Under scenarios of moderate

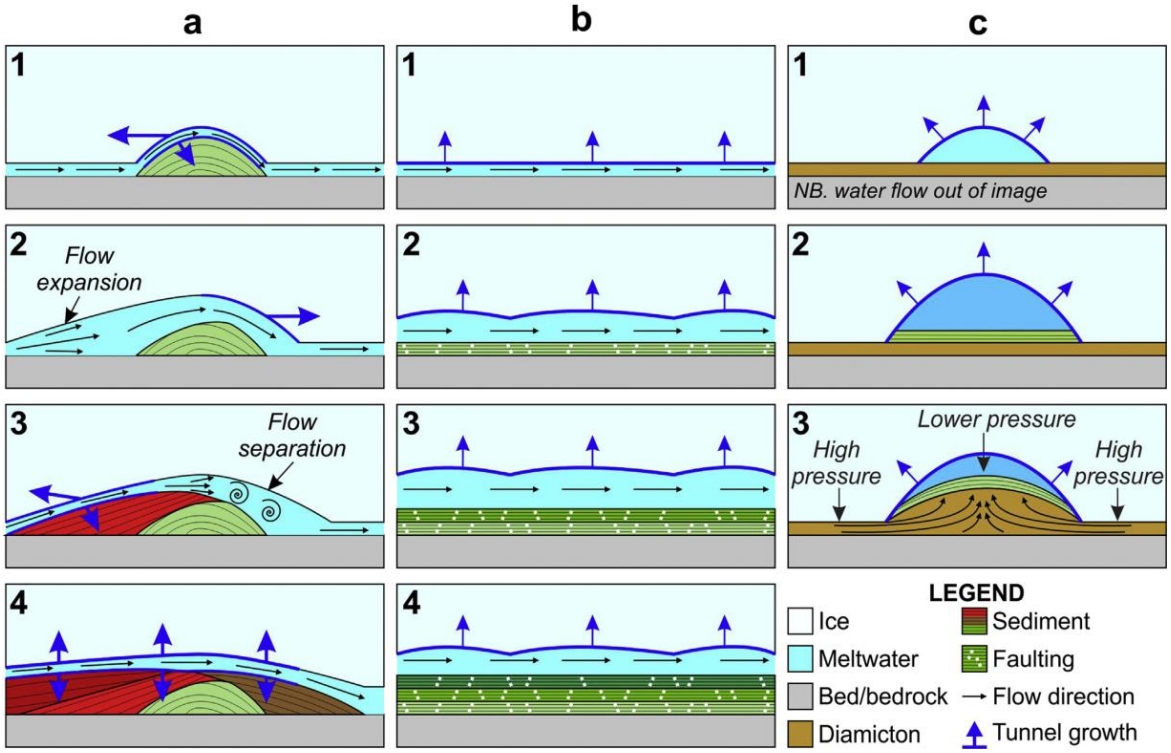

Figure 6.14. Theoretical evolution of an esker-forming drainage conduit under different sediment supply and flow power regimes. Columns a–c are different sediment supply and flow power scenarios, and rows 1–4 show temporal evolution of conduit under those scenarios. Column a is for high sediment supply and high flow conditions. Column b is for limited sediment supply and high flow power. Column c is for limited sediment supply accompanied by a drop in meltwater discharge in row 3. See text for explanation. From Burke et al. (2015).

sediment supply, deposition along the conduit is more evenly distributed, resulting in deposition of quasi-continuous tabular beds and uniform conduit growth that is not strongly influenced by sedimentation (Figure 6.14, column 2; Banerjee and McDonald, 1975; Brennand, 2000; Burke et al., 2015). A lack of conduit obstruction prevents the need for cavity formation or conduit migration, such that conduit growth is largely controlled by discharge and is dominated by vertical roof melting. This results in formation of narrow, sharp-crested to round-crested eskers. Under scenarios of strongly limited sediment supply, conduit growth is controlled almost exclusively by meltwater discharge, and sedimentation within the conduit is very low or absent. Reductions in discharge can occur on shorter timescales than the conduit can shrink to compensate for a reduction in hydraulic pressure. This results in a steep pressure gradient between the bed and the conduit, and can cause deformation of bed sediments into the conduit to equilibrate the pressure difference (Figure 6.14, column 3). Burke et al. (2015) propose that this mechanism can explain why narrow eskers with arched beds commonly contain a substantial core of diamicton, or even bedrock.

By extension, reductions in sediment supply associated with development of macroforms at up-conduit depocentres (e.g., Brennand, 1994; Burke et al., 2015) have been invoked to

explain transitions from wide, complex ridge enlargements to relatively simple, narrow, sharp-to-round-crested ridge morphologies along eskers on Earth (Burke et al., 2015).

Multi-crested eskers on Earth, similar to the multi-crested portion of the upper member ridge in zone II of the NW Tempe Terra esker, have been attributed to either exploitation of structural weaknesses (e.g., fractures) and/or flow divergence around ice blocks under high flow power conditions (Burke et al., 2012b; Perkins et al., 2016), or formation of eskers in englacial conduits and subsequent let-down and loss of an internal ice core (Price, 1966).

6.6.2. Multi-Phase Dynamics of Esker Formation in NW Tempe Terra, Mars?

Figure 6.15 illustrates two possible conceptual models for multi-phase dynamics that could explain the stacked morphology of the esker formation in NW Tempe Terra. These models are informed by the morpho-sedimentary associations observed along eskers on Earth, as summarised above. Under both formation models, the proposed dynamics of the formation of the lower member ridge (Section 6.6.2.1) are the same. The models diverge in their temporal placement of the formation of the upper member ridge (Section 6.6.2.2). Model A (Figure 6.15) considers the upper and lower member ridges to have formed under a changing sediment-discharge regime during at least two phases of a single esker-forming drainage episode, while model B (Figure 6.15) considers the upper member to have formed during a second, distinct drainage episode following significant retreat of the ice terminus across zone IV of the lower member ridge.

It must be emphasised that Perkins et al. (2013) demonstrated that geomorphic-inversion techniques alone can be unreliable for inferring esker-formation environments and dynamics on Earth. They suggest that integration of contextual geomorphic and stratigraphic reconstructions, and detailed morpho-sedimentary analyses, are required for confident reconstruction of esker formation processes. My analyses of the NW Tempe Terra esker include geomorphic mapping, stratigraphic reconstruction (Chapter 4; Butcher et al., 2017), and detailed metre-scale morphometric analyses, but a lack of sedimentary insight is unavoidable given limitations in accessibility and data resolution. It is not yet possible to undertake field studies to probe the sedimentary properties and architecture of eskers on Mars. Thus, while geomorphic inversion is an essential technique for reconstructing the formation of landforms on Mars, it should not be undertaken in isolation from detailed consultation of the morpho-sedimentary relationships of analogous eskers on Earth. I emphasise that the formation models presented below provide two possible explanations of the stacked morphology of the NW Tempe Terra esker, but that these scenarios are by no means exhaustive.

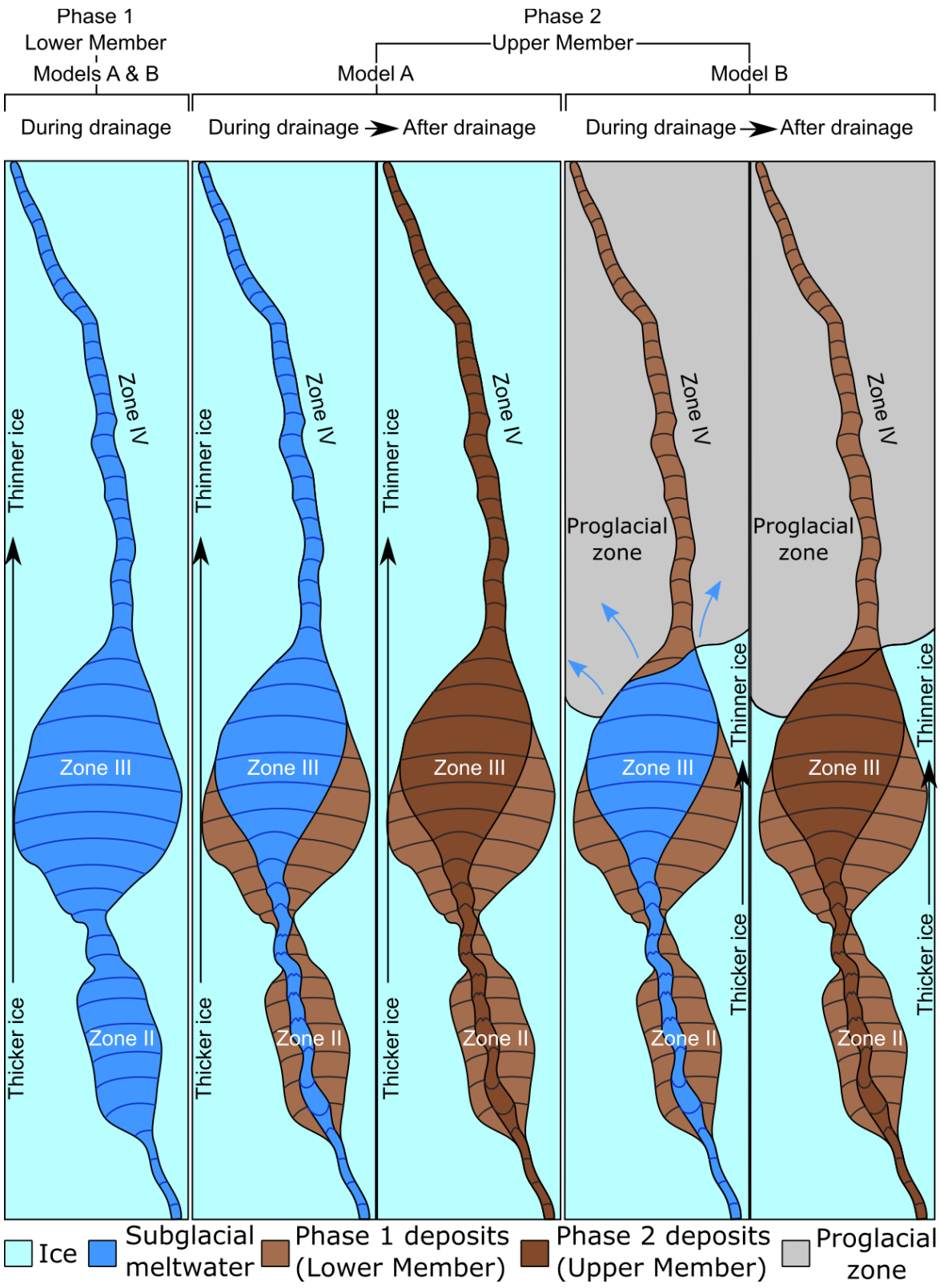

Figure 6.15. Schematic showing two possible models for the formation of the stacked esker morphology in NW Tempe Terra, Mars. Models A and B diverge in their temporal placement of upper member ridge formation. In model A (panels 2 and 3) the upper member ridge formed during a second phase of flow within the same melt episode during which the lower member ridge was deposited (panel 1). Model B (panels 4 and 5) places upper member ridge formation during a distinct melt episode, following ice terminus retreat to the location of the esker-transverse moraine-like ridge (Chapter 4; Butcher et al., 2017). I do not speculate on dynamics of ridge formation to the south (zone I), since this is largely obscured by remnant VFF materials. See text for full description of model.

6.6.2.1. Formation of the Lower Member Ridge

The lower member ridge comprises two broad, round-crested, lozenge-shaped portions in zones II and III, the northernmost of which (in zone III) progressively lowers and narrows towards its transition to the narrow, sharp-crested ridge in zone IV (Figures 6.7 and 6.8). The northern portion of zone II, approaching the zone II-III transition, is obscured by remnant LDA materials, so I interpolate interpretations across this portion of the ridge. The ridge is almost entirely obscured by remnant LDA materials in zone I, so I do not speculate on the dynamics of ridge formation in this zone.

I propose that the lower member ridge formed under high discharge and high sediment supply conditions. Meltwater flowing along the conduit was laden with sediment, promoting rapid, non-uniform deposition along the conduit. Deposition became focussed at two depocentres: one located in zone II, and one in zone III. Constriction or obstruction of the conduit by the deposited sediment increased meltwater flow power and promoted vertical, lateral and longitudinal migration of the conduit. Resultant cavity formation reduced the flow power, encouraging further deposition and initiating a positive feedback of ridge growth and conduit enlargement. The tapered margins and gradual lowering of the broad, round-crested portion of the ridge towards the zone III-IV transition (Figure 6.1) is consistent with streamlining of esker sediments, and possibly the conduit itself in the lee cavity of the zone III sedimentary depocentre (Figure 6.14; Burke et al., 2015).

Sediment accumulation in the large zone II and III depocentres reduced sediment availability down-conduit. This meant that conduit growth in zone IV was predominantly controlled by discharge, rather than sedimentation-driven changes in accommodation space, resulting in uniform conduit growth. Thus, here, the conduit adopted a relatively narrow (Figure 6.15), sharp-crested geometry. There is no evidence for deformation of the bed lateral to the ridge in zone IV, so I suggest that the esker accumulated via gradual accretion under moderate sediment supply conditions, rather than pressure-driven deformation of surrounding bed materials under a sediment-starved regime (see Section 6.6).

6.6.2.2. Formation of the Upper Member Ridge

Following Burke's (2015) sediment-discharge model, I suggest that the sharp-to-multi-crested upper member of the NW Tempe Terra esker formed within a narrow meltwater conduit that passed along the flank and crest of the lower member ridge under hydraulic pressure in zones II and III.

I propose two possible conceptual models for the formation of the upper member ridge (Figure 6.15). However, before I describe these models, I first discuss some pertinent aspects of the morphology of the upper member ridge that may provide insight into its formation.

The southernmost end of the upper member ridge in zone II originates in the northern portion of a flat-floored trough of similar width that crosses the lower member ridge part way down its western flank (Figures 6.8B and 6.8H–I). The alignment, similarity in width, and physical association of this trough with the upper member ridge, and its flat-floored morphology are consistent with its origin as a meltwater-incised trough (akin to a Nye channel; e.g., Weertman, 1972; Walder and Hallet, 1979). I suggest that the trough formed in a portion of the conduit that fed the upper member ridge, where the flow of meltwater was erosive. The trough crosses a topographic high in the underlying lower member ridge, which is consistent with Shreve's (1985a) prediction that topographic undulations in the bed (in this case, the upper surface of the lower member ridge) focus lines of hydraulic equipotential at their peaks, resulting in increased flow power within the meltwater conduit such that non-deposition, or even erosion, can occur (see Figure 4.9). The southern end of the upper member ridge in zone II would therefore represent the location where this erosive regime transitioned to a depositional regime on the lee slope of the peak.

Unlike the sharp-crested portion of the lower member ridge in zone IV, portions of the upper member ridge are located within a shallow (~2–5 m deep) trough (e.g., Figure 6.8F). Thus, a scenario whereby the parent meltwater conduit was strongly sediment starved, and the upper member ridge primarily comprises sediment scavenged from the lower member ridge that was squeezed into the conduit following a sudden reduction in conduit pressure, is plausible. However, it is also possible that this trough represents a period of erosive flow prior to the onset of deposition of the upper member ridge under a moderate sediment supply regime. Given that detailed sedimentary insights into the genesis of esker sediments are not yet possible on Mars, discriminating between the moderate sediment supply and sediment starved scenarios is not possible. Hence, I suggest that either mechanism is plausible, but do not speculate further on which sediment supply regime could have prevailed.

I also suggest that, consistent with observations of multi-crested portions of eskers on Earth (Burke et al., 2012b; Perkins et al., 2016), the multi-crested portion of the upper member ridge represents a location where high flow power forced meltwater into structural weaknesses in the overlying ice. I argue that the location of portions of the multi-crested ridge within a shallow trough in the surface of the lower member ridge is inconsistent with the alternative explanation that the multi-crested morphology was inherited from the loss of

an internal ice core following esker let-down from an englacial or a supraglacial position (Price, 1966). This trough, and that from which the upper member ridge emerges in subzone IIa, both provide strong evidence for direct interaction of meltwater with the surface of the lower member ridge within a subglacial conduit. The exploitation of structural weaknesses by pressurised subglacial meltwater may suggest that mechanical conduit erosion was an important process in formation of the upper member ridge. This could imply that discharge may have varied on timescales that were shorter than those over which the conduit could adjust via wall melting, during a catastrophic drainage event.

I now present two conceptual models for the formation of the upper member ridge, which differ from one another in their temporal placement of its formation relative to that of the lower member ridge (Figure 6.15). Model A places formation of the upper member ridge during the late stages of the same drainage episode that formed the lower member ridge, while model B places its formation during a second, distinct drainage episode following retreat of the glacier terminus across zone IV. The main justification for invoking a distinct drainage episode in model B is to provide an alternative explanation for why the stacked morphology is only observed in zones II and III and is not observed in zone IV.

6.6.2.2.1. Model A: Late-Stage Formation during a Single, Multi-Phase Drainage Episode

As discussed in Section 6.6.2.2, Burke et al. (2015) suggest that narrow eskers tend to form under moderate-to-low sediment supply conditions. Thus, in model A, I propose that the upper member ridge was deposited during the same melt episode as the lower member ridge, as sediment supply and/or meltwater discharge waned. Under these conditions, the conduit in zone II shrank to equilibrate hydraulic pressure within the conduit with ice overburden pressure, and flow became focussed along the relatively narrow path of the upper member ridge (Figure 6.15, 2nd panel). Such conduit shrinkage under waning flow has been proposed to explain narrowing of depositional pathways along eskers on Earth (Shaw, 1983; Burke et al., 2012b). Conduit shrinkage maintained hydraulic pressure, forcing meltwater to ascend the lower member ridge in zone II, where it may have exploited structural weaknesses in the conduit roof in the location of the multi-crested portion.

As the conduit approached thinner ice towards the terminus, the tendency for pressure-driven conduit closure under waning discharge reduced. This meant that the conduit retained its breadth in the northern portion of zone III despite waning discharge and/or sediment supply (Figure 6.15, 2nd panel). As meltwater passed into the broader conduit in zone III, flow power reduced, and sediment dispersed over the surface of the underlying ridge, resulting in the fan-shaped deposit at the terminus of the upper member ridge. Sedimentation may have

continued down-flow of the fan-shaped deposit (Figure 6.15, 3rd panel), but a lack of change in conduit geometry approaching the terminus means that late-stage sedimentation was indistinct from the earlier stages and there was no notable vertical transition in the morphology of the ridge crest.

6.6.2.2.2. Model B: Formation during a Second, Temporally-Distinct Melt Episode

I present model B, which places formation of the upper-member ridge during a temporally distinct drainage episode following retreat of the glacier terminus across zone IV (Figure 6.15, 4th panel), as an alternative explanation for the transition from a stacked to a single ridge morphology northward of zone III of the NW Tempe Terra esker.

Under this scenario, the upper member ridge formed when the glacier terminus was located close to the fan-shaped terminus of the upper member ridge (Figure 6.15, 4th panel), possibly at the location of the transverse ridge that crosses the esker crest at the zone III-IV transition, which I have previously interpreted as a recessional moraine (Chapter 4, this thesis; Butcher et al., 2017). The second melt episode re-established a meltwater pathway over the lower member ridge in zones II and III. I do not speculate as to whether the conduit had partially or completely shut down in the intervening time between the two melt episodes, or the period of time over which terminus retreat may have occurred. The multi-crested morphology of the upper member ridge in zone II suggests that this may have been a high flow power event that exploited structural weaknesses in the conduit roof (Burke et al., 2012b; Perkins et al., 2016). The relatively uniform, narrow morphology of the upper member ridge also suggests that sediment supply was lower during this melt episode, preventing non-uniform conduit enlargement, and allowing development of a narrow conduit atop the lower member ridge (Figure 6.15, 4th panel).

Proximal to the ice margin, subglacial meltwater conduits commonly expand into larger portals. While the fan-shaped terminus of the upper member ridge becomes topographically indistinct at the northernmost end of subzone IIIb, visual inspection of the surface of the lower member ridge in subzone IIIc highlights that longitudinal troughs appear to emanate from the fan-shaped terminus of the upper member ridge (Figure 6.7A). I suggest that, if the glacier terminus was located at the zone III-IV boundary, the fan-shaped terminus of the upper member ridge and the longitudinal troughs that extend from it represent the dissipation of flow and dispersal of sedimentation across the western flank of the lower member ridge as the conduit approached the terminal portal (Figure 6.15, 4th panel).

6.6.3. Spatiotemporal Nature of Esker Deposition in NW Tempe Terra

I now consider the implications of the morphometric observations of the NW Tempe Terra esker for the spatiotemporal nature of esker deposition in this location. The spatiotemporal nature of esker deposition on Earth is the topic of ongoing debate (e.g., Shreve, 1985a; Hooke and Fastook, 2007; Brennand, 1994, 2000; Burke et al., 2008, 2010; Cummings et al., 2011; Storrar et al., 2014a; Perkins et al., 2016). The formation of some terrestrial eskers has been associated with high-magnitude drainage episodes (i.e., glacial outburst floods) over timescales of just a few days (Burke et al., 2008, 2010; Storrar et al., 2015). Some workers theorise that eskers can form synchronously within continuous, steady-state drainage conduits extending over the full length of the resulting esker deposits (e.g., Brennand, 1994, 2000; Burke et al., 2012b, 2010, 2008; Perkins et al., 2016), while others suggest that time-transgressive headward aggradation behind a retreating ice margin over interannual timescales provides a better explanation of their formation (e.g., Banerjee and McDonald, 1975; Aylsworth and Shilts, 1989; Clark and Walder, 1994; Cummings et al., 2011; Storrar et al., 2014b, 2014a). In reality, it is likely that both mechanisms have prevailed in different locations on Earth, but the dominant mechanism is poorly constrained.

Detailed field studies of esker sediments and internal architecture have been instrumental in discriminating between synchronous and time-transgressive deposition regimes for eskers on Earth. Storrar et al. (2014a) hypothesised that relationships between esker length and sinuosity, both of which can be measured using remote sensing techniques, could provide insights into the proximity of esker deposition to a receding ice margin, but this hypothesis remains to be tested with field observations. Thus, the current inaccessibility of eskers on Mars by all but orbital remote sensing techniques severely inhibits the possibility of constraining with confidence whether the formation of individual eskers on Mars was synchronous or time-transgressive.

My observations of NW Tempe Terra esker provide ambiguous evidence for the spatiotemporal nature of esker deposition. Model A is a single pipe model and, in this regard, is most consistent with synchronous deposition along the full length of the conduit during one or more catastrophic drainage episodes. The lack of a depositional fan at the northernmost terminus of the lower member ridge is most consistent with synchronous formation during a short, high-magnitude drainage event than with time-transgressive formation (e.g., Burke et al., 2012b). Similarly, evidence for ascent of bed slopes and possibly exploitation of structural weaknesses in the conduit roof during formation of the

sharp-to-multi-crested upper member ridge, provides evidence for rapid-onset, high flow-power drainage (e.g., Burke et al., 2010, 2012b; Perkins et al., 2016).

The nature of model B, which invokes two distinct phases of esker aggradation at a retreating ice margin is inherently time-transgressive. Unless meltwater drainage was quasi-continuous throughout this terminus retreat, model B requires two distinct melt episodes. However, it should be noted that under model B the individual ridge members could effectively have formed synchronously during their respective drainage episodes.

6.6.4. Implications for Environmental Controls on Melting

Formation of the NW Tempe Terra esker during a single, multi-phase drainage episode (model A) is more consistent than model B with the hypothesis that late-Amazonian esker-forming melt events were driven by transient geothermal heating of the basal ice (Gallagher and Balme, 2015; Butcher et al., 2017; Chapter 5, this thesis). The occurrence of two distinct geothermal events under model B seems less likely than a single event under model A, but cannot be ruled out. On Earth, the formation of eskers, and indeed subglacial meltwater conduits, is typically associated with a component of supraglacial melt input to the bed (e.g., via moulins or crevasses). I find no substantive evidence for a component of supraglacial meltwater in the formation of the NW Tempe Terra esker. Thus, I conservatively suggest that meltwater was supplied solely by basal melting under cold, late-Amazonian climate conditions but emphasise that the physical conditions that could permit formation of subglacial eskers on Mars without a component of supraglacial meltwater input is an important area of future research.

The hypothesis of esker formation during a transient melt episode that punctuated a long-term cold-based thermal regime could be considered a challenge for the high sediment-supply regime invoked to explain morphological transitions along the lower member ridge (Section 6.6.2.1). Typically, cold-based glaciers are associated with extremely low rates of sliding and erosion at their beds, although sliding and erosion may not be insignificant when integrated over long timescales (Shreve, 1984; Echelmeyer and Wang, 1987; Dyke, 1993; Cuffey et al., 2000; Waller, 2001; Atkins et al., 2002; Lloyd Davies et al., 2009; C. A. Smith et al., 2009). However, weakened bedrock in tectonic settings is a source of abundant sediment to the surfaces and beds of glaciers on Earth (Hallet et al., 1996). Therefore, the steep-sided scarps that bound the tectonic rift valley that hosts the NW Tempe Terra esker could plausibly have provided a ready supply of sediment to the glacier bed in the absence of long-term sediment production via glacier sliding. Furthermore, high strain rates

associated with flow convergence of glacial ice at the base of the rift-bounding fault scarps (Chapter 4, this thesis; Butcher et al., 2017) could have induced strong stress gradients at the bed that encouraged mechanical erosion at rates above those associated with cold-based glaciers in non-convergent settings on Earth (e.g., Cuffey et al., 2000)

6.7. Conclusions

This chapter presents the first metre-scale characterisation of a late-Amazonian-aged glacier-linked esker in NW Tempe Terra, Mars. It also constitutes the first attempt to reconstruct the multi-phase dynamics of esker formation on Mars and demonstrates the potential power of detailed morphometric analyses for providing insight into the nature and dynamics of esker-forming melt events. Such insights are important for informing modelling experiments that aim to constrain the environmental drivers of esker-forming meltwater generation on Mars.

In the case of Mars, direct sedimentary insights are not yet possible, so reconstructions of esker-formation dynamics via the morphometric inversion approach used here must be undertaken with caution, and with reference to morpho-sedimentary associations observed along analogous landforms on Earth. Based on the analyses presented here, and considering the limitations described above, I draw the following key conclusions regarding the morphometry and possible formation dynamics of the NW Tempe Terra esker:

- The NW Tempe Terra esker comprises two stacked esker ridges: a lower member ridge comprising broad, round-crested portions in zones II and III that transition to a narrow sharp-crested morphology in zone IV; and a narrow, sharp- to multi-crested upper member ridge that crosses the flanks of the lower member ridge in zones II and III, and terminates in a fan-shaped deposit in zone III.
- When the geometries of the upper and lower member ridges of the NW Tempe Terra esker are plotted separately. Sharp- to multi-crested portions of the upper and lower member ridges follow similar height-width relationships. Slight differences between their relationships may result from variations in degradation state arising from differences in exposure ages of these ridge portions from the parent glacier. Similarly, all broad, round-crested portions of the lower member ridge adhere to a consistent height-width trend. This suggests that the morphometries of ridge portions with similar crest morphologies may be governed by primary formation processes.
- Morphological transitions along the lower member ridge, and between the lower and upper member ridges may be explained by spatiotemporal variations in sediment supply and discharge during esker formation (e.g., Burke et al., 2015).

- I interpret the enlarged, round-crested portions of the lower member ridge as sedimentary depocentres formed under high meltwater discharge and/or sediment supply conditions that encouraged a positive feedback of sediment accumulation and conduit enlargement (Burke et al., 2015). Depocentre growth limited sediment supply downflow, and gradual sediment accumulation meant that conduit growth was more uniform (Burke et al., 2015), explaining the transition to a relatively narrow, sharp-crested morphology along the lower member ridge.
- The stacked esker morphology suggests esker deposition during at least two phases of sedimentation, either within a single episode of subglacial drainage, or two distinct drainage episodes.
- If the upper member ridge formed during the same drainage episode as the lower member ridge (model A), a reduction in sediment supply and/or discharge in the waning stages of meltwater drainage could explain the stacked esker morphology. This encouraged conduit shrinkage (Shaw, 1983; Burke et al., 2012b) beneath relatively thick ice in zone II and at the entry to zone III, and more gradual sediment accumulation allowed drainage to establish a consistent flow path over the underlying lower member ridge. At the entry to zone II, flow was erosive (Shreve, 1985a), forming a Nye channel-like trough within the surface of the lower member ridge. A depositional regime prevailed downflow, forming the sharp- to multi-crested upper member ridge. As the conduit passed into thinner ice towards the terminus, the tendency for conduit shrinkage under waning discharge reduced, and the conduit retained its enlarged form in the northern portion of zone III, and its narrow form in zone IV. As meltwater entered zone III, it dispersed across the surface of the lower member ridge, forming the fan-shaped terminus of the upper member ridge. Beyond the fan-shaped portion, deposited sediments are morphometrically indistinct from the lower member ridge.
- An alternative model (model B) is that the upper member ridge, for which there is no distinct morphometric signature northward of the fan-shaped terminus at the entry to zone III, was deposited during a distinct drainage episode following a period of retreat of the glacier terminus, possibly to the location of the esker-transverse moraine-like ridge that crosses the esker at the zone III-IV transition (Butcher et al., 2017; Chapter 4, this thesis). Under this scenario, renewed drainage re-established a flow path over the lower member ridge, but lower sediment supply and/or lower meltwater discharge meant that the conduit did not undergo such significant enlargement and migration as during formation of the lower member ridge. The

conduit opened out into a portal approaching the glacier terminus, in which the fan-shaped terminus of the upper member ridge was deposited.

- Evidence for synchronous or time-transgressive deposition of the NW Tempe Terra esker is ambiguous. However, ascent of bedslopes, a lack of fan morphology at the terminus of the ridge in zone IV, and evidence for exploitation of structural weaknesses in the conduit roof during formation of the multi-crested portion of the upper member ridge are most consistent with catastrophic drainage under hydraulic pressure, and synchronous deposition along the individual ridge members. I suggest that model A, in which I propose that the upper member ridge formed during the waning stages of the same drainage episode that formed the lower member ridge, is more consistent with the hypothesis that basal melting was driven by geothermal heating because it does not require more than one melt event.
- The novel morphometric approach presented in this chapter demonstrates the potential for: (a) the use of reference morphometries to predict the morphometric relationships along portions of esker-like sinuous ridges on Mars that have similar crest morphologies, and therefore to test for esker origins of those sinuous ridges if these relationships are indeed process-controlled; and (b) deciphering the implications of complex morphometric signatures for the dynamics of esker-forming meltwater drainage on both Mars and Earth.

CHAPTER 7

MORPHOMETRIES OF ESKERS ON MARS AND COMPARISONS TO TERRESTRIAL ANALOGUES

7.1. Attribution

This chapter reports on morphometric analyses of candidate eskers on Mars, and comparisons to eskers on Earth. The morphometry datasets for the candidate eskers in Phlegra Montes and NW Tempe Terra, Mars are original datasets. The 2D and 3D morphometry datasets for the south polar Dorsa Argentea eskers on Mars were made by Butcher et al. (2016); this publication was developed from work submitted to a previous degree, but I perform additional analyses for the purposes of the present study. The 2D and 3D morphometry datasets for the eskers in SW Finland, Earth were made by Storrar and Jones (unpublished) in parallel with the preparation of this thesis, and are used here with their kind permission. The 2D morphometry dataset for eskers in Canada was made by Storrar et al. (2013, 2014a) and is also used here with their kind permission. All data sources used in the present study are included in Table 7.1.

7.2. Background

As landforms that are identifiable using orbital remote sensing techniques, eskers hold significant potential for informing insights into the distribution and nature of wet-based glaciation on Mars. In the absence of ground-based observations, morphometric analyses are vital tools for discriminating between esker-like sinuous ridges with different origins on Mars. Sinuous ridges with similar morphologies to eskers (e.g., Banks et al., 2009; Burr et al., 2009; Chapter 8, this thesis) can form via numerous non-glacial mechanisms, including fluvial (e.g., inverted fluvial channels; Burr et al., 2009), tectonic (e.g., wrinkle ridges; Watters, 1988), volcanic (e.g., exhumed dikes and lava flows, including esker-like ice-confined lava flows; Mathews, 1958; Carr et al., 1977; Smellie and Skilling, 1994; Lescinsky and Fink, 2000; Pedersen et al., 2010; Hungerford et al., 2014), and aeolian (e.g., dunes;

Banks et al., 2009) processes. As I will discuss further in Chapter 8, this can complicate confident identification of eskers on Mars, as demonstrated by decades of debate surrounding the origins of the ancient south polar Dorsa Argentea eskers (Howard, 1981; Parker et al., 1986; Tanaka and Scott, 1987; Ruff and Greeley, 1990; Kargel, 1993; Tanaka and Kolb, 2001; Metzger, 1992; Kargel and Strom, 1992; Head, 2000a, 2000b; Head and Hallet, 2001a, 2001b; Head and Pratt, 2001; Tanaka et al., 2014b; Kress and Head, 2015; Butcher et al., 2016). Characterisation of the morphometries of sinuous ridges for which we have a relatively high level of confidence of esker origins, such as the eskers associated with extant parent glaciers in Phlegra Montes (Gallagher and Balme, 2015) and NW Tempe Terra (Butcher et al., 2017; Chapter 4, this thesis), will provide vital reference morphometries against which measurements of other sinuous ridges (including those for which formation mechanisms may be more ambiguous) can be compared during tests of landform origins.

Comparisons with terrestrial analogues are also insightful for probing the origins of landforms on Mars. Butcher et al. (2016) found striking similarities between the Dorsa Argentea eskers and the first large sample of 2D morphometries for eskers on Earth, which were measured by Storrar et al. (2013, 2014a) for > 20,000 eskers in Canada. However, as highlighted by Howard (1981), the potential for 3D morphometric comparisons of eskers on Earth and Mars has been limited by a lack of extensive 3D measurements of eskers on Earth. Previously, published 3D morphometries of eskers on Earth were mainly limited to generalised field descriptions and measurements along individual esker ridges, with no large-scale databases of measurements over large areas or on a range of scales. The first large-scale database (> 20,000) of 3D morphometries for eskers on Earth was compiled by Storrar and Jones (unpublished) for a 2305 km^2 site in southwest Finland (Chapter 5) in parallel with the preparation of this thesis, providing new opportunities for high-resolution 3D comparisons to terrestrial analogue landforms.

As demonstrated in Chapter 6, the morphometries of eskers can provide insight into the nature and dynamics of the meltwater events that formed them. They can also be used to constrain parameters within numerical models aiming to simulate the environmental drivers of esker-forming glacial melt events. For example, the morphometries of the ancient Dorsa Argentea eskers near Mars' south pole, have been used to constrain parameters for coupled global climate and glacial flow modelling experiments that aim to reconstruct the climatic conditions under which they formed (Scanlon et al., 2018).

7.3. Aims

In this chapter, I present the first metre-scale characterisation of the glacier-linked esker in Phlegra Montes (162.96°E, 32.68°N; Figure 7.1) that was identified in a 6 m/pixel CTX image by Gallagher and Balme (2015). As described in Chapter 5, 25 cm/pixel HiRISE stereo-pair images released since their study provide complete coverage and allow high-resolution morphometric analyses using a 1 m/pixel DEM derived from those images. As performed for the glacier-linked esker in NW Tempe Terra in Chapter 6, I characterise both 2D and 3D morphometries including length, continuity, sinuosity, height, width, aspect ratio, and average cross-sectional slopes for the Phlegra Montes esker.

I then perform comparative analyses of the 2D and 3D morphometries of the late-Amazonian-aged glacier-linked eskers in Phlegra Montes (this chapter) and NW Tempe Terra (Chapter 6) with those of the early-Hesperian-aged Dorsa Argentea eskers for which Butcher et al. (2016) compiled a database of 2D and 3D morphometries (see Chapter 5). No such database is currently available for the ancient eskers in southern Argyre Planitia.

I then exploit the new opportunities afforded by the measurements of Storrar et al. (2014a) and Storrar and Jones (unpublished) for comparisons of 2D and 3D morphometries of eskers on Mars and Earth. I compare the 2D and 3D morphometries of the martian eskers to the 2D morphometries of eskers in Canada (Storrar et al., 2014a) and SW Finland (Storrar and Jones, unpublished), and to the new 3D measurements of eskers in SW Finland (Storrar and Jones, unpublished).

In undertaking these analyses, I aim to constrain reference morphometries against which landforms of more ambiguous origin can be compared. Of particular interest are possible relationships between the morphometry and crest morphology of eskers on Mars, which could be used in tests of the esker hypothesis for landforms with similar crest morphologies elsewhere, and the effect of landform age upon variations in these relationships.

7.4. Data and Methods

The reader is referred to Chapter 5 for a description of the methods used to measure the 2D and 3D morphometries of the glacier-linked esker in Phlegra Montes, and those used by Butcher et al. (2016), Storrar et al. (2013, 2014a), and Storrar and Jones (unpublished) to measure the morphometries of the Dorsa Argentea eskers, the Canadian eskers, and eskers in SW Finland, respectively. I reported the new measurements of the 2D and 3D morphometries of the glacier-linked esker in NW Tempe Terra in Chapter 6. The analyses

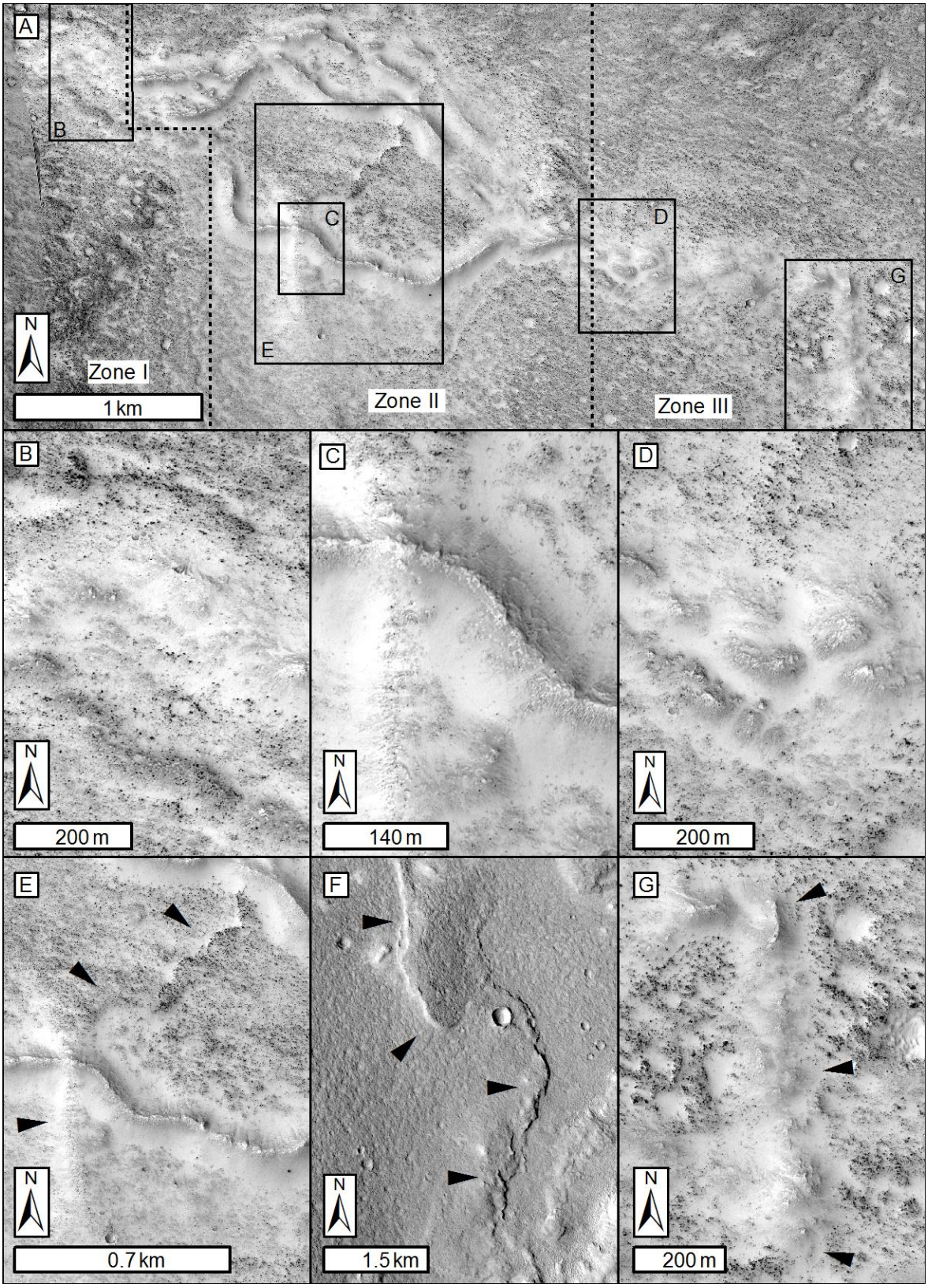

Figure 7.1. Morphology of the Phlegra Montes esker complex revealed by HiRISE images. (A) Orthorectified HiRISE image of the Phlegra Montes esker complex showing morphological zones I–III (dotted lines are zone transitions), and extents of panels A–E and (G) containing the same HiRISE image. (B) Portion of zone I. (C) Portion of zone II. (D) Portion of zone III. (E) Valley-transverse ridge (black arrows) that Gallagher and Balme (2015) interpret as a moraine, but I suggest resembles a tectonic wrinkle ridge e.g., (F) CTX image (centred on 163.29°E, 32.32°N) of a nearby wrinkle ridge (black arrows). (G) A moraine-like ridge (black arrows) at the terminus of the esker complex. See Table 7.1 for a list of data products.

Table 7.1. List of data products used in Chapter 7.

Instrument or Source	Image/Product ID	Figure	Table
Context Camera[1]	Mosaic[2] generated from images: B05_011706_2116_XN_31N198W G20_026224_2116_XN_31N196W G23_027279_2132_XN_33N198W P18_007935_2132_XN_33N197W P22_009583_2132_XN_33N197W P22_009794_2155_XI_35N198W[3]	7.1A, 7.2A–B	-
	G02_019143_2141_XN_34N196W[3]	7.1F	-
High Resolution Imaging Science Experiment[4]	ESP_044804_2130 (orthorectified)[2]	7.1A–E, 7.1G, 7.2A–B, 7.11F	-
	ESP_044316_2130 (orthorectified)[2]	-	-
	ESP_044105_2130[5]	7.1A, 7.2A–B	-
	ESP_049573_2265 (orthorectified)[2]	7.11D–E	-
	ESP_049639_2265 (orthorectified)[2]	-	-
	DEM[2] generated from images ESP_044316_2130 and ESP_044804_2130[5]	7.2C–D, 7.11C	-
	DEM[2] generated from images ESP_049573_2265 and ESP_49639_2265[5]	7.11A–B	-
Storrar et al. (2014)	2D morphometry dataset of eskers in Canada[6]	7.7	7.5
Personal communication	2D and 3D morphometries of putative eskers in the Dorsa Argentea formation[7]	7.7, 7.8, 7.9	7.5, 7.6, 7.7
	2D and 3D morphometries of eskers in SW Finland[8]	7.7, 7.8, 7.9, 7.10A	7.5, 7.6, 7.7

[1](Malin et al., 2007)
[2] Generated by F. E G. Butcher
[3]Arizona State University http://viewer.mars.asu.edu/viewer/ctx#T=0
[4](McEwen et al., 2007)
[5]The University of Arizona https://hirise.lpl.arizona.edu/
[6] Accessed on 01/11/2018 at: www.sciencedirect.com/science/article/pii/S0277379115301141#ec2
[7] Butcher et al. (2016); data available from the author
[8]Storrar and Jones (unpublished); data provided by R.D. Storrar and processed by F. E. G. Butcher

described in Chapter 6 revealed that the NW Tempe Terra esker is probably a composite esker formation comprising two stacked esker ridges. The comparisons in the present chapter refer to the separated morphometries lower member and upper member ridges described in Chapter 6.

7.5. Results: Morphometry of the Phlegra Montes Esker Complex, Mars

7.5.1. Planform Morphology

The glacier-linked esker complex in Phlegra Montes is ~4.5 km long and up to ~1.4 km wide, and comprises multiple round- to sharp-crested ridge segments. The ridge complex separates into two distinct subparallel networks ~1 km from the westernmost end of the complex (Figure 7.1), which rapidly diverge to a lateral separation of ~300 m (Gallagher and Balme, 2015). The branches re-converge ~2.6 km from the westernmost end of the complex, which extends a further 1.9 km to the ESE. In this distal zone, its morphology is dominated by multiple elongate hillocks resembling esker beads (e.g., Banerjee and McDonald, 1975; Gorrell and Shaw, 1991; Gallagher and Balme, 2015).

Building upon the morphological description by Gallagher and Balme (2015), I qualitatively define three morphological zones along the Phlegra Montes esker complex based on HiRISE images released after the publication of Gallagher and Balme (2015; Figure 7.1). The boundaries between morphological zones coincide approximately with the locations where the northern and southern networks diverge and re-converge.

Zone I comprises the glacier-proximal (easternmost) end of the ridge complex; it extends ~500 m westward from the glacier-proximal end of the northern ridge network, and ~1 km westward of the glacier-proximal end of the southern ridge network (Figure 7.1A). Ridges within this zone are relatively low and either poorly developed or heavily degraded, typically lacking distinct crests (Figure 7.1B). The lowest ridges within this zone have a speckled appearance in the HiRISE images consistent with shadows of decimetre-scale boulders on their flanks and crests, which also cover the surrounding glacier foreland (Figure 7.1A–B).

The divergence of the two major ridge networks coincides approximately with a transition in morphology at the start of zone II (Figure 7.1A). Within this ~1.6 km-long zone, the ridges have more prominent, relatively continuous crests (Figure 7.1C). They have higher albedos than the surrounding bounder-rich plains and lack the dense speckling that characterises zone I ridges. While some boulders are visible on the ridge flanks, they are not as dense as in zone I.

As described by Gallagher and Balme (2015), the confluence of the northern and southern ridge networks coincides with a transition in ridge morphology in the westernmost portion of the ridge complex, which I define as the zone II–zone III transition (Figure 7.1A). Zone III is ~1.9 km long and comprises a single ~150–200 m wide corridor of discontinuous, round-crested, elongate hills (Figure 7.1D). These hills lack consistent orientation and alignment. As a result, I was cautious in grouping zone III hills into ridge systems, or classifying them as continuations of ridge systems from zone II for the purposes of 2D morphometry measurements (Chapter 5).

The Phlegra Montes eskers ascend topographic undulations, including a sinuous, low-relief esker-transverse ridge in zone II (Figure 7.1E), which Gallagher and Balme (2015) posit to be an ice-marginal formation. I find that, despite insights from the HiRISE images released since their study, such an origin remains tentative, owing to similarities in form to (and possible alignment with) wrinkle ridges in the surrounding area which suggest a possible origin as a pre-glacial tectonic fault structure (e.g., Figure 7.1F). Using the HiRISE images, I do however identify a second, previously unreported esker-transverse ridge, at the glacier-distal end of zone III (Figure 7.1G). The ~850 m long, ~150–180 m wide, N–S oriented ridge abuts the westernmost (i.e., glacier-distal) terminus of the Phlegra Montes esker complex, which does not cross it. At its northernmost end, it has a ~150 m long arcuate crest, whereas its central and southern portions are characterised by rounded hummocks. The ridge has a similar high albedo to the zone II and III esker ridges, and I suggest that it represents a terminal moraine, possibly comprising reworked esker sediments.

7.5.2. 2D Morphometries

Descriptive statistics for the planform morphometries of ridges in the Phlegra Montes esker complex are displayed in Table 7.2. The Phlegra Montes esker complex comprises 38 individual esker segments (Figure 7.2A). Ridge segments range in length from 14 m to 2430 m, and are typically hundreds of metres long (median L_s = 114 m; Figure 7.3A). The total length of ridge segments within the Phlegra Montes esker complex is 11.918 km.

According to my conservative groupings, these segments form 22 discontinuous ridge systems (Figure 7.2A) with a total length of 12.6 km; 12 systems comprise a single segment, 7 systems comprise 2 segments, 2 systems comprise 3 segments, and one system comprises 6 segments. Gaps between related segments comprise 682 m of the total length of ridge systems. The lengths of individual ridge system lengths range from 102 m to 2.67 km, with a median system length of 318 m (Figure 7.3A). System continuity varies between 0.74 and 1 (Figure 7.3C). The median continuity of ridge systems is 1, although this could result from

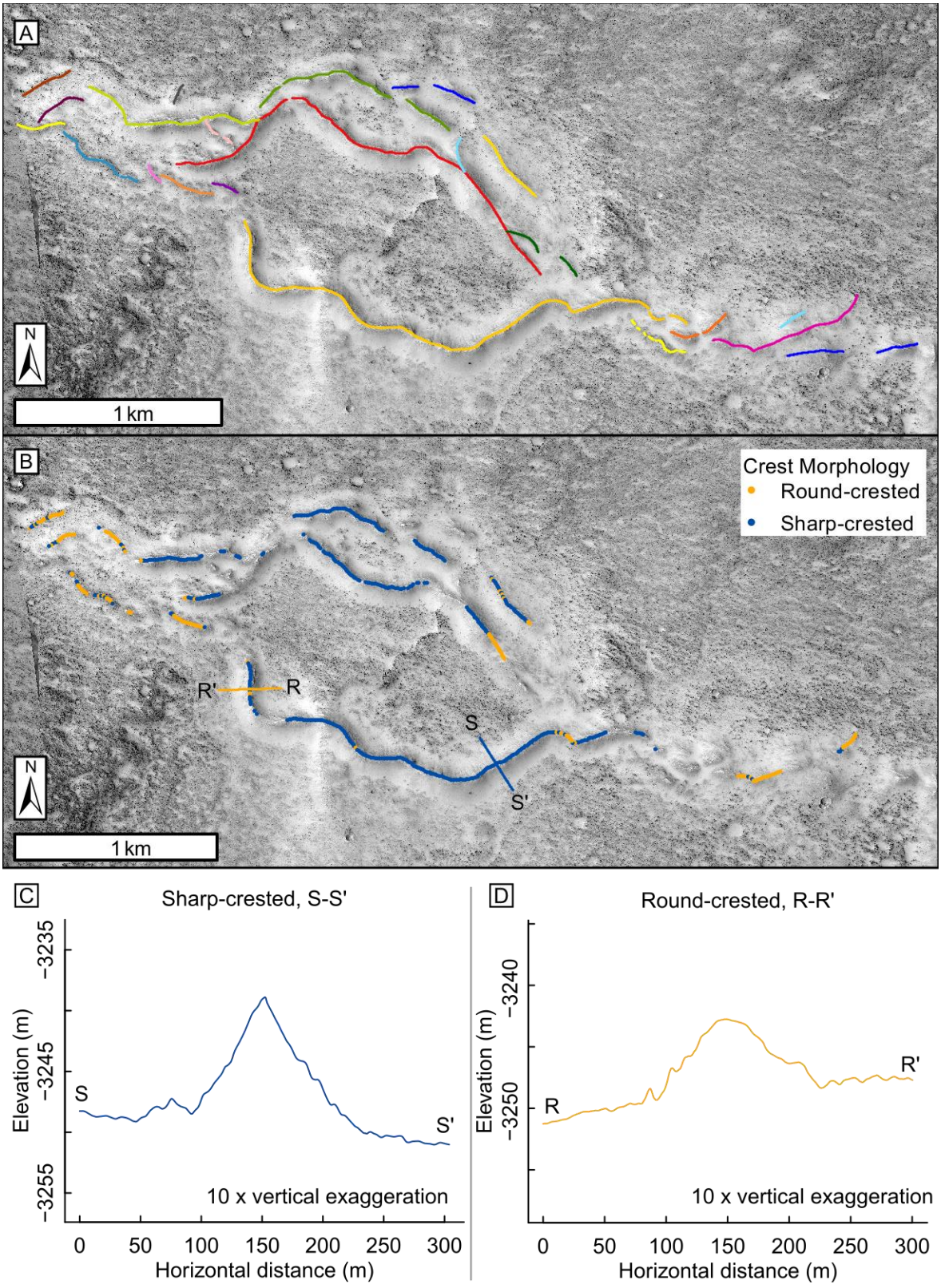

Figure 7.2. System and crest morphology classifications for the Phlegra Montes esker complex. (A) Crestline map of the Phlegra Montes esker complex showing cautious classifications of related ridge segments (unbroken lines) into ridge systems (colours). (B) 3D morphometry sample locations classified by crest morphology, showing locations of transects for: (C) cross-sectional topographic profile (with ten times vertical exaggeration) S–S', classified as sharp crested, and (D) cross-sectional topographic profile R–R' (with ten times vertical exaggeration), classified as round crested. See Table 7.1 for list of data products, and Section 5.4 for an explanation of sampling strategy.

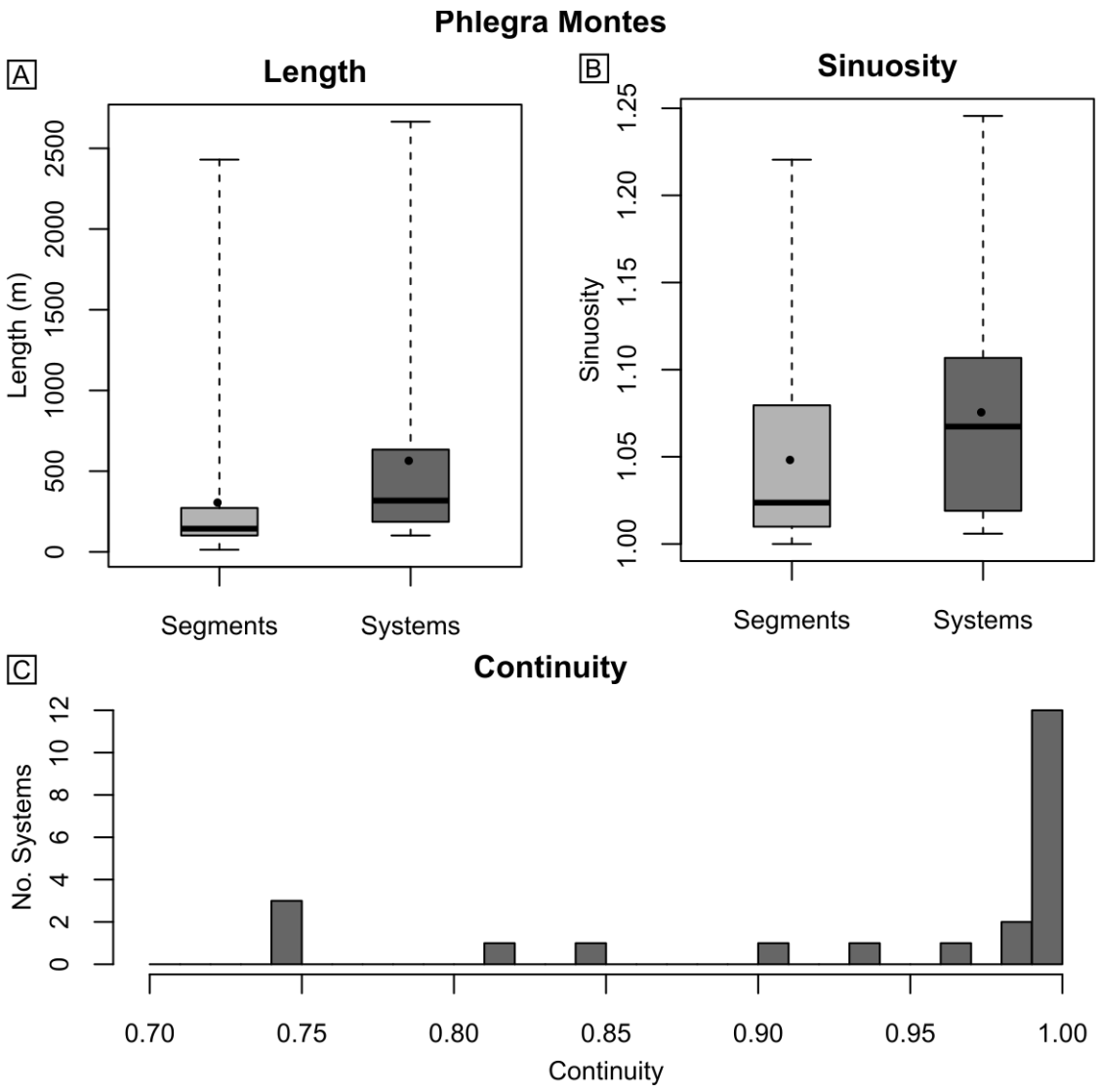

Figure 7.3. Distributions of 2D morphometries of the Phlegra Montes esker. (A) Boxplot showing the lengths of segments and systems. (B) Boxplot showing the sinuosity of segments and systems. (C) Histogram (bin width = 0.01) of the continuity of ridge systems. In panels A and B, boxes represent interquartile range, whiskers represent maximum and minimum, solid lines represent the median, and points represent the mean.

Table 7.2. Descriptive statistics for 2D morphometries of the Phlegra Montes esker complex.

	Segment Length	Mapped Length	System Length	Continuity	Segment Sinuosity	System Sinuosity
N	38	22	22	22	38	22
Total	11,918 m	11,918 m	12,600 m	N/A	N/A	N/A
Minimum	14 m	102 m	102 m	0.74	1	1.01
Maximum	2430 m	2613 m	2665 m	1	1.22	1.25
Quartile 1	102 m	188 m	199 m	0.91	1.01	1.02
Quartile 3	270 m	466 m	592 m	1	1.08	1.11
Median	114 m	281 m	318 m	1	1.02	1.07
Mean	314 m	542 m	573 m	0.94	1.05	1.08
St. Dev.	466 m	663 m	673 m	0.095	0.052	0.067

my cautious approach to grouping individual segments into longer ridge systems. The sinuosity of segments in the Phlegra Montes esker complex varies between 1 and 1.22, while system sinuosity varies between 1.01 and 1.25 (Figure 7.3B). Segments have a median sinuosity of 1.02, while systems have a median sinuosity of 1.07 (Figure 7.3B).

7.5.3. Cross-Sectional Crest Morphology

When viewed in topographic profile, the cross-sectional transects of the Phlegra Montes eskers can be categorised as either the sharp-crested (i.e., approximating a triangle; Figure 7.2C), or round-crested (i.e., approximating a half pipe; Figure 7.2D) morphological subtypes defined by Perkins et al. (2016). A majority (76%) of transects have sharp-crested morphologies; round-crested ridges dominate in zones I and III, while sharp-crested subtypes dominate in zone II (Figure 7.2B). In zone II, rare round-crest morphologies typically persist for just 10–20 m (and in one case, 150 m) along the ridges before their crests transition back to sharp morphologies (Figure 7.2B). These round-crested sections are typically lower than adjacent sharp-crested portions of the ridges.

7.5.4. Height and Width

The height and width distributions for the Phlegra Montes eskers are displayed in Figure 7.4. Descriptive statistics are displayed in Table 7.1. The ridges range in height from < 1 m to 13 m, with a median height of 7 m. As illustrated in Figure 7.4B, ridge heights exhibit a bimodal distribution, which can be explained by differences in height between sharp- and round-crested morphologies. Sharp crested ridge portions have a median height of 8 m (ranging between 1 m and 13 m), while round-crested portions have a significantly lower median height of 2 m (ranging between 0.5 m and 7 m; Figure 7.4A).

In contrast, the widths of the Phlegra Montes ridges do not exhibit a bimodal distribution (Figure 7.4D). Sharp- and round-crested ridge portions have a similar range of widths (sharp = 185 m, round = 183 m; Figure 7.4C). While the median width of round-crested portions (102 m) is 59 m less than that of sharp-crested portions (161 m), the greater abundance of sharp-crested transects, and spread over a similar range of values, means that the round-crested transects do not have a significant effect on the shape of the width distribution in Figure 7.4D.

Plotted together (Figure 7.5), ridge height and width cluster by crest morphological type (Figure 7.5A) and by zone (Figure 7.5B). Width and height are positively correlated for both sharp-crested and round-crested transects (Table 7.4). Round-crested transects have a stronger positive correlation (Spearman's rho = 0.88, p-value < 0.01) than sharp-crested

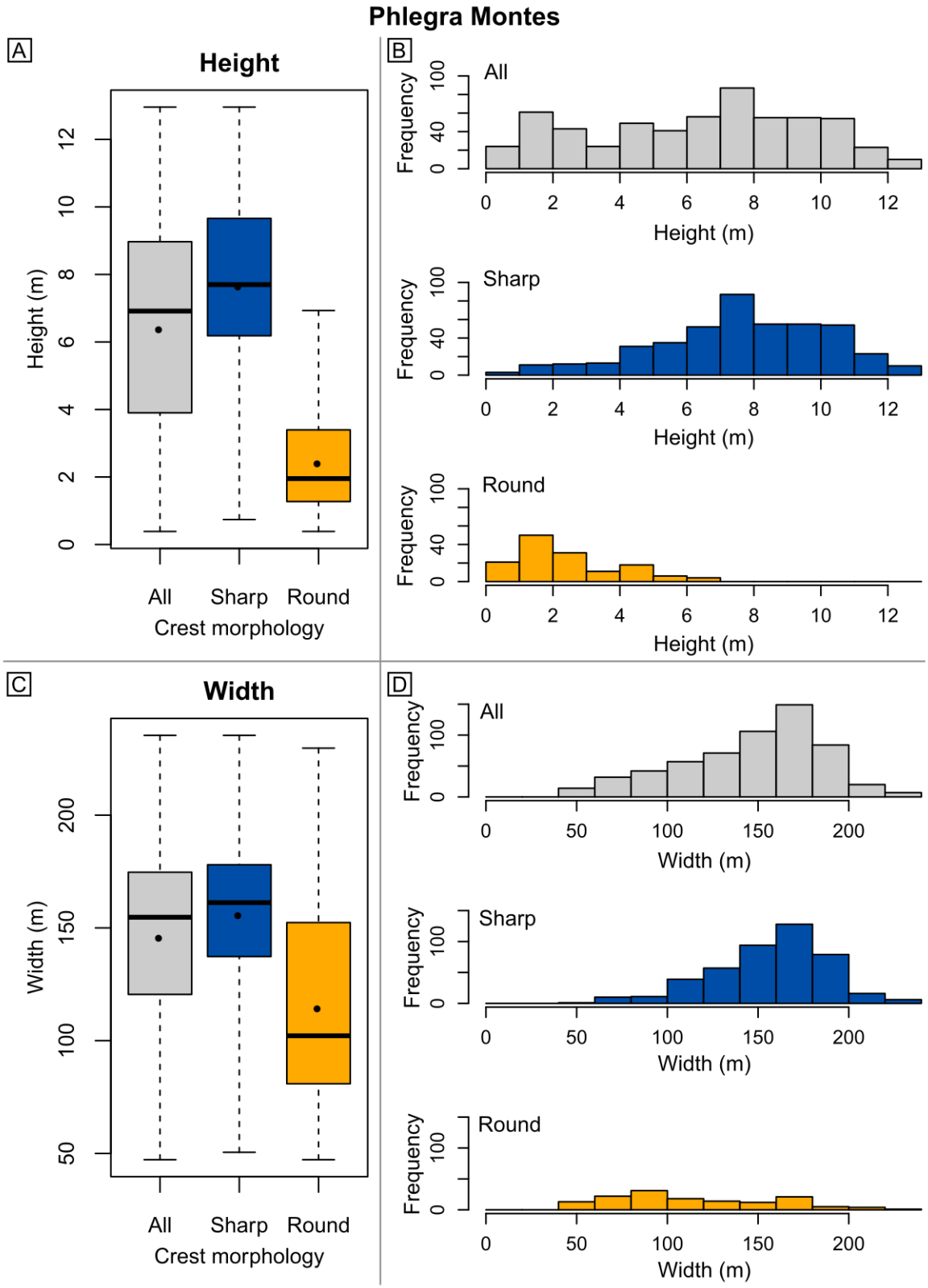

Figure 7.4. Distributions of heights and widths of ridges in the Phlegra Montes esker complex. (A) Boxplot of ridge heights categorised by crest morphology. (B) Histograms of ridge heights (bin width = 1 m), categorised by crest morphology. (C) Boxplot of ridge widths categorised by crest morphology. (D) Histograms of ridge widths (bin width = 20 m), categorised by crest morphology. In panels A and C, boxes represent interquartile range, whiskers represent maximum and minimum, solid lines represent the medians, and points represent the means.

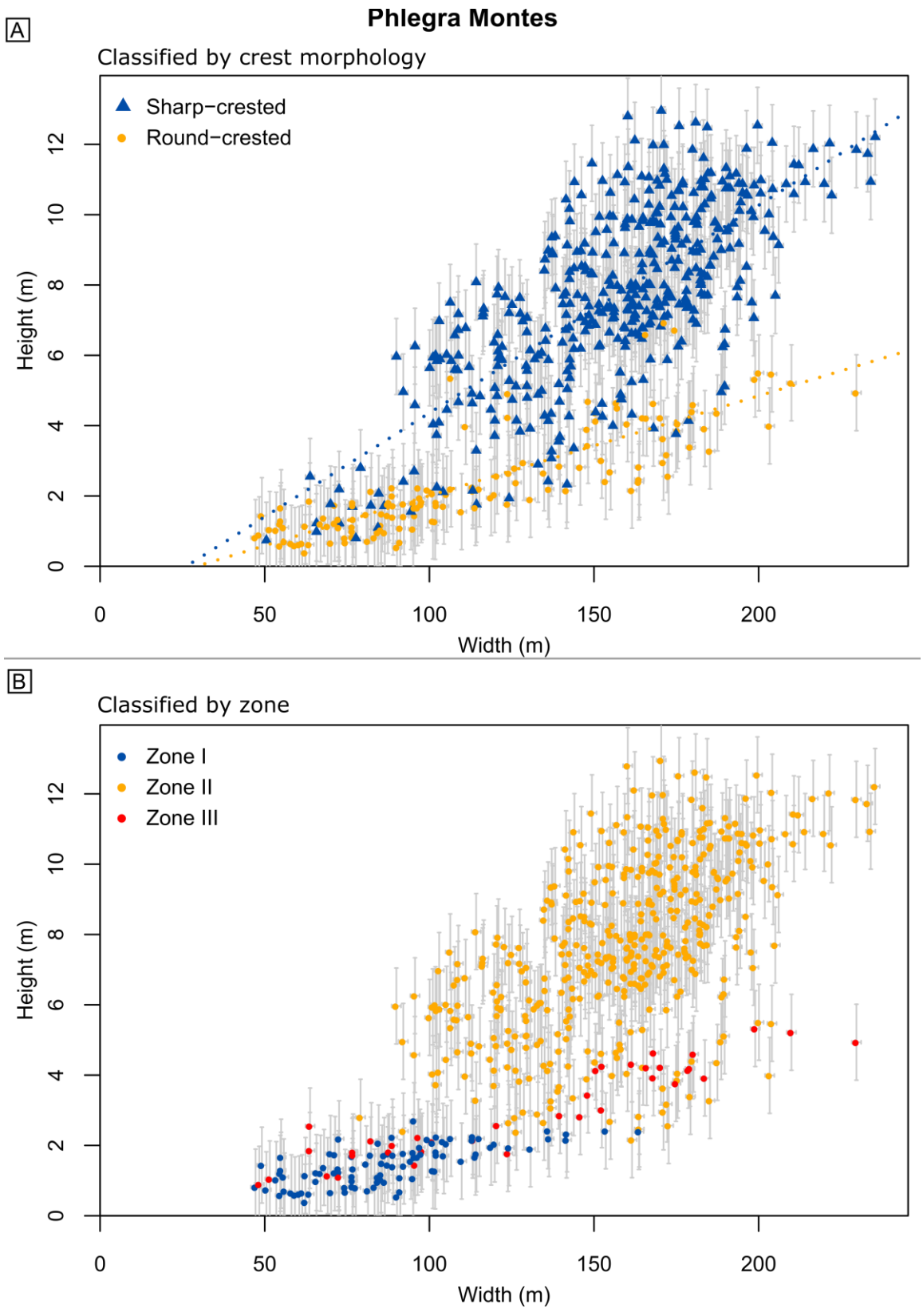

Figure 7.5. Scatterplots of ridge height and width for the Phlegra Montes esker complex. Scatterplots of ridge height and width categorised by: (A) crest morphology (dotted lines show linear fits) for sharp (blue) and round (yellow) crest morphologies (see Table 7.4), and (B) by zone (see Section 7.5.1).

Table 7.3. Descriptive statistics for 3D morphometries of sharp- and round-crested portions of the Phlegra Montes esker complex.

	Height	Width	Width-height ratio	Average cross-sectional slope
All transects				
N	582	582	582	582
Minimum	0.5 m	47 m	13	0.7°
Maximum	13 m	235 m	167	9°
Range	13 m	188 m	154	8°
Quartile 1	4 m	121 m	18	3°
Quartile 3	9 m	175 m	39	6°
Interquartile Range	5 m	54 m	21	3°
Median	7 m	155 m	22	5°
Mean	6 m	146 m	31	5°
Standard Deviation	3 m	39 m	21	2°
Sharp-crested				
N	441	441	441	441
Minimum	1 m	50 m	13	1°
Maximum	13 m	235 m	97	9°
Range	12 m	185 m	85	8°
Quartile 1	6 m	137 m	17	5°
Quartile 3	10 m	178 m	24	7°
Interquartile Range	3 m	41 m	6	2°
Median	8 m	161 m	20	6°
Mean	8 m	156 m	23	6°
Standard Deviation	3 m	32 m	10	1°
Round-crested				
N	141	141	141	141
Minimum	0.5 m	47 m	20	0.7°
Maximum	7 m	230 m	167	6°
Range	7 m	182 m	147	5°
Quartile 1	1 m	81 m	43	2°
Quartile 3	3 m	152 m	66	3°
Interquartile Range	2 m	72 m	23	1°
Median	2 m	102 m	52	2°
Mean	2 m	115 m	58	2°
Standard Deviation	2 m	44 m	24	1°

Table 7.4. Relationships between ridge height and width for sharp- and round-crested portions of the Phlegra Montes esker complex. Relationships are described separately for sharp-crested and round-crested portions of the Phlegra Montes esker complex. Skewness and kurtosis values, combined with Shapiro-Wilk tests (p-value < 0.01 means variable is not normally distributed) determine that height and width for both sharp- and round-crested transects are not normally distributed, hence I use the non-parametric Spearman's rank correlation test to describe relationships between ridge height and width.

	Height	Width
Sharp-crested		
N	441	441
Skewness	-0.43	-0.54
Kurtosis	2.83	3.30
Shapiro-Wilk p-value	< 0.01	< 0.01
Normally distributed?	No	No
Spearman's rank rho	0.69	
Spearman's rank p-value	< 0.01	
Linear fit	$H = 0.06\ W - 1.55$	
Round-crested		
N	141	141
Skewness	0.94	0.49
Kurtosis	3.09	2.15
Shapiro-Wilk p-value	< 0.01	< 0.01
Normally distributed?	No	No
Spearman's rank rho	0.88	
Spearman's rank p-value	< 0.01	
Linear fit	$H = 0.03\ W - 0.83$	

segments (Spearman's rho = 0.69, p-value < 0.01). These relationships are best described by linear fits (Figure 7.5; Table 7.4). Sharp-crested portions of the ridges tend towards greater heights for a given width than round-crested portions, being approximately twice as tall as round-crested portions of similar widths.

7.5.5. Width-Height Ratio and Average Cross-Sectional Slope

Taken together, the Phlegra Montes eskers are typically 22 times wider than they are tall (Table 7.3). Sharp-crested portions have width-height ratios in the range 13–97, with a median ratio of 20, while round-crested portions have ratios in the range 20–167, with a median ratio of 53 (twice that of sharp-crested portions; Figure 7.6).

Sharp-crested transects have higher average cross-sectional slopes in the range 1–9°, with a median of 6°, while round-crested transects have average cross-sectional slopes in the range

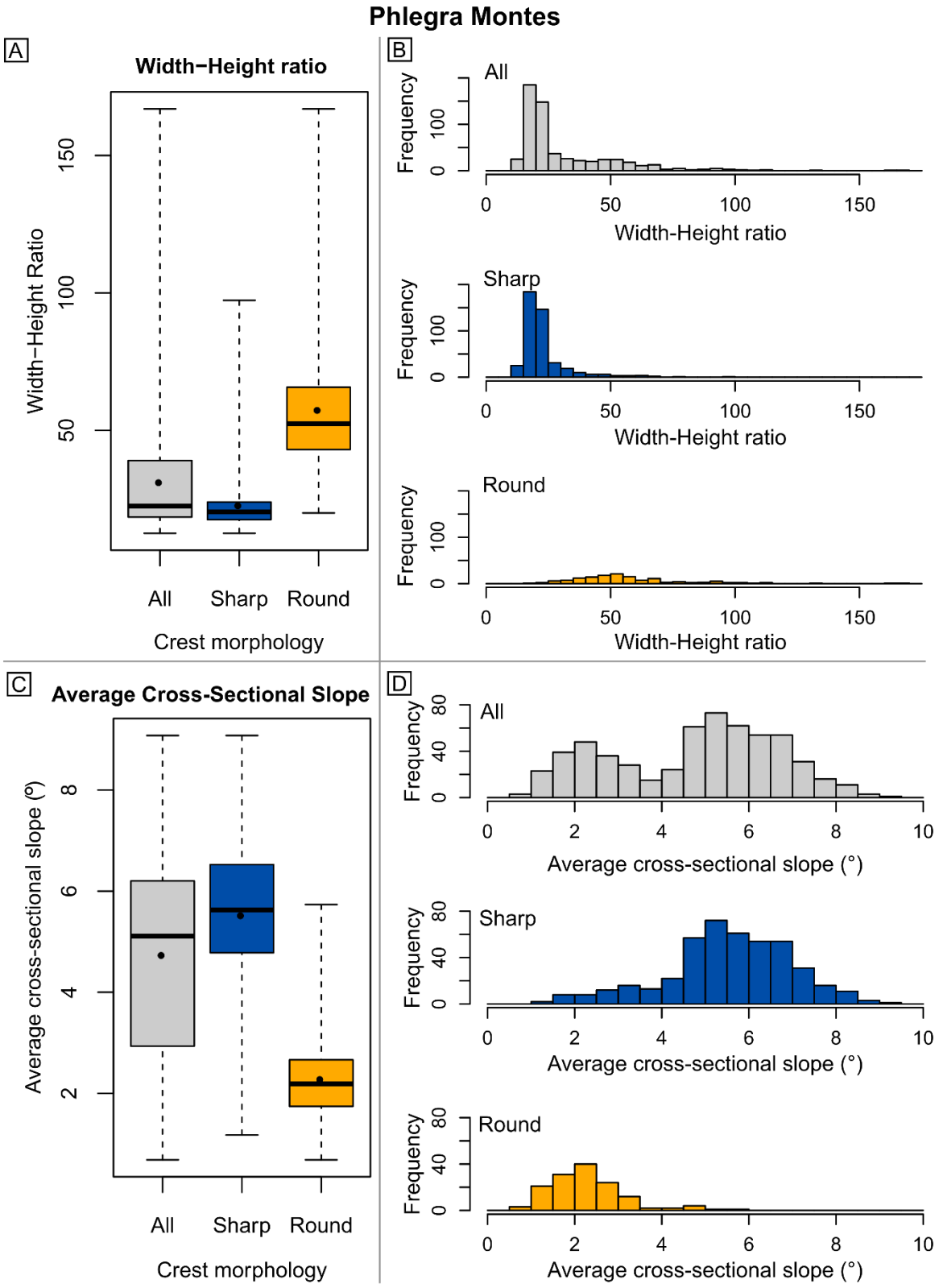

Figure 7.6. Width-height ratios and average cross-sectional slopes for ridges in the Phlegra Montes esker complex. (A) Boxplot of ridge width-height ratios categorised by crest morphology. (B) Histograms of ridge width-height ratios (bin width = 5), categorised by crest morphology. (C) Boxplot of average cross-sectional slopes categorised by crest morphology. (D) Histograms of average cross-sectional slopes (bin width = 0.5°), categorised by crest morphology. In panels A and C, boxes represent interquartile range, whiskers represent maximum and minimum, solid lines represent the median, and points represent the mean.

< 1–6°, with a median of 2°, resulting in bimodality in the distribution of average cross-sectional slopes (Figure 7.6).

7.6. Analysis: Comparisons of Eskers on Mars and Earth

7.6.1. Comparison of Eskers on Mars

In the following section, I compare the 2D plan-view and 3D morphometries of the Phlegra Montes and NW Tempe Terra eskers (Chapter 6), both with one another, and with measurements (Butcher et al., 2016) of the ancient south polar Dorsa Argentea eskers on Mars (see Chapter 5). All comparisons with the esker in NW Tempe Terra are based on the individual morphometry distributions for the lower and upper members of the NW Tempe Terra esker formation presented in Chapter 6.

As described in Chapter 5, I emphasise that the resolutions of the image and digital elevation model basemaps available for the Dorsa Argentea (~8 m/pixel CTX images and 115 m/pixel DEM) mean that Dorsa Argentea ridges with widths less than three times the pixel size of the DEM (~345 m, i.e., with similar width scales to the Phlegra Montes and NW Tempe Terra eskers) were undetectable within the DEM used by Butcher et al. (2016). Therefore, Butcher et al. (2016) restricted 2D planform morphometry measurements of the Dorsa Argentea ridges to ridge systems > 10 km in length, and the 3D measurements to the four largest ridges in the population. This unavoidable, resolution-driven sampling bias for the Dorsa Argentea dataset means that comparisons with absolute geometries of the smaller Phlegra Montes and NW Tempe Terra eskers are not, in themselves, informative. However, given that the Phlegra Montes and NW Tempe Terra eskers exhibit strong relationships between ridge height and width, comparing their width-height ratio and average cross-sectional slopes to the Dorsa Argentea could provide insight into the similarities and differences between the different ridge populations.

It should also be noted that, while Butcher et al. (2016) presented geometry distributions for sharp-crested and broad-crested eskers, here I do not subdivide the Dorsa Argentea distributions by crest morphological type for the present analyses due to improvements in the classification criteria in the present study; following Bernhardt et al. (2013), Butcher et al. (2016) categorised broad-crested transects as those for which the point-to-point cross-sectional slope was lower than 1° for more than 345 m about the crest point, and sharp-crested transects as those where the slope exceeded this empirical threshold. In the present study, I adopted the improved classification scheme of Perkins et al. (2016), which, while qualitative, takes into account both the concavity of the flank slopes and the shape of the

crest in classifying eskers as sharp-crested (approximating a triangle) or round-crested (approximating a half pipe). Hence, the crest morphology classifications by Butcher et al. (2016) for the Dorsa Argentea are not directly comparable to those performed in the present study for the Phlegra Montes and NW Tempe Terra eskers. Consequently, I undertake comparisons with the 3D morphometries of all Dorsa Argentea transects without morphological subdivision.

7.6.1.1. 2D morphometries

The Phlegra Montes and NW Tempe Terra eskers both comprise segments with length scales of hundreds to thousands of metres, which form discontinuous esker systems with lengths of up to 2.7 km for Phlegra Montes, and a single system of length 17.1 km in NW Tempe Terra (Figure 7.7B). The maximum length of the Phlegra Montes esker systems falls below the minimum length (10 km) of Dorsa Argentea esker systems sampled by Butcher et al. (2016), but the system length of the NW Tempe Terra esker falls within the second quartile of system lengths for the sampled Dorsa Argentea eskers (i.e., systems > 10 km; Figure 7.7B).

The Phlegra Montes, NW Tempe Terra and Dorsa Argentea eskers have similar sinuosity, both for individual segments and systems. The Phlegra Montes and Dorsa Argentea eskers both have median segment sinuosity of 1.02 (Figure 7.7C), and median system sinuosity of 1.07 (Figure 7.7D). The NW Tempe Terra esker is only slightly more sinuous, having a median segment sinuosity of 1.05 and a system sinuosity of 1.13. The maximum segment sinuosity of the Phlegra Montes and NW Tempe Terra eskers varies by just 0.07 (max sinuosity = 1.15 and 1.22, respectively; Figure 7.7C).

Like the Dorsa Argentea (Butcher et al., 2016), the Phlegra Montes and Tempe Terra eskers have a low degree of fragmentation; both have continuity values of 0.94, which are comparable to the continuity of 0.91 measured for the Dorsa Argentea ridges (Table 7.5). It should be noted that conservative grouping of segments into related ridge systems probably results in overestimation of continuity for the Phlegra Montes esker, while obscuration of the ridge by remnant glacial materials in zone I of the NW Tempe Terra esker could, in contrast, result in underestimation of its true continuity (I assumed that disappearance of the trace of the ridge beneath the mantling LDA materials represented a break between segments, but it is possible that the ridge is continuous beneath these mantled portions). Thus, the Phlegra Montes and NW Tempe Terra eskers probably bracket representative continuity values for mid-latitude eskers on Mars. That they share median continuity values suggests that the continuity estimates are robust.

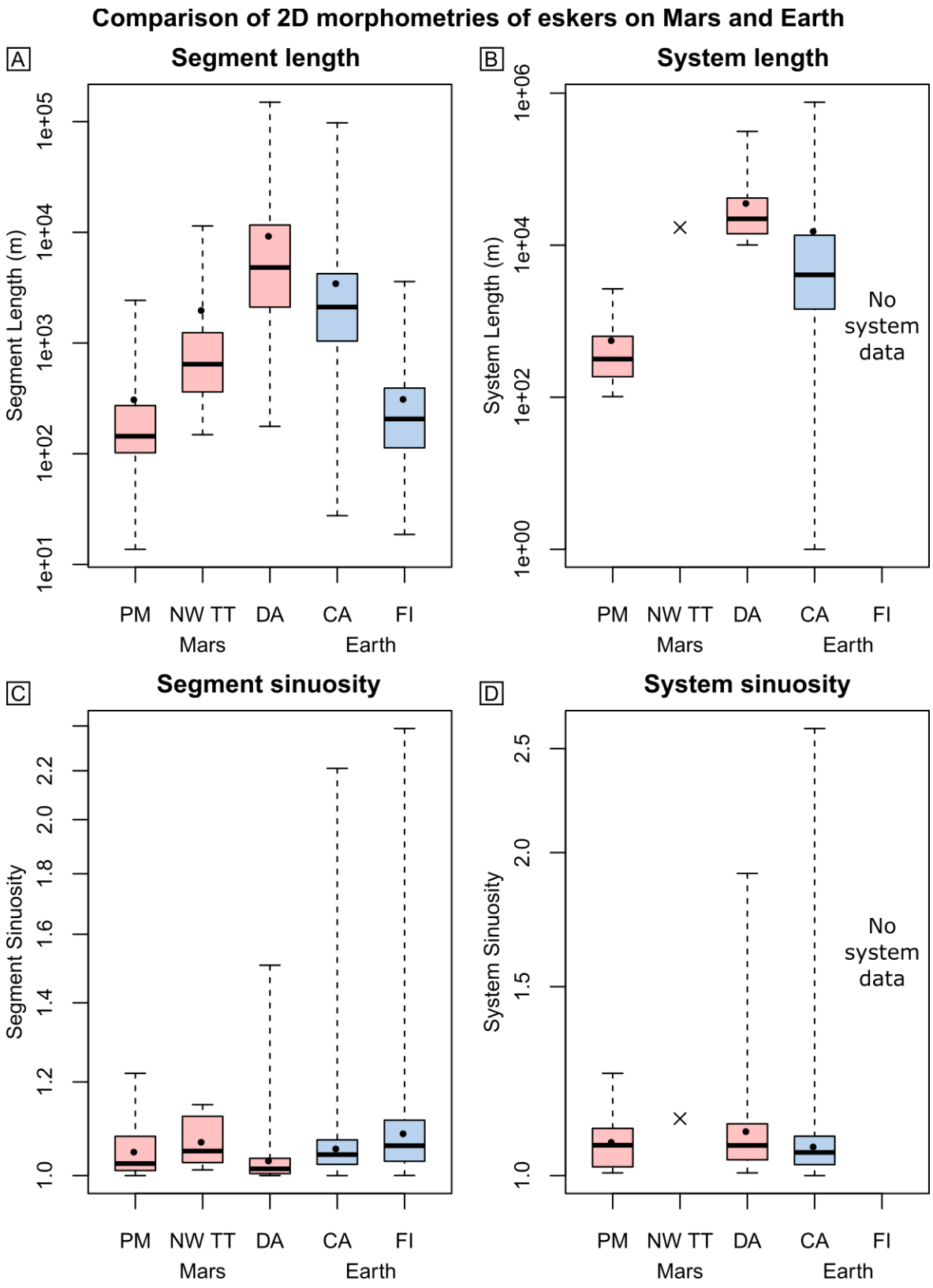

Figure 7.7. Comparisons of distributions of 2D morphometries of eskers on Mars and Earth. Boxplots showing (A) segment lengths, (B) system lengths, (C) segment sinuosity, and (D) system sinuosity of putative eskers in: Phlegra Montes (PM), NW Tempe Terra (NW TT) and the Dorsa Argentea Formation (DA; data from Butcher et al., 2016), Mars (pink); and Canada (CA; data from Storrar et al., 2014a) and SW Finland (FI, segment morphometries only; from Storrar and Jones, unpublished), Earth (light blue). In all boxplots, boxes represent the interquartile range, whiskers represent maximum and minimum, solid lines represent the medians, and points represent the means. Note logarithmic axes. Crosses (panels B and D) represent values for the single ridge system in NW Tempe Terra. See Table 7.1 for data products.

Table 7.5. Comparison of descriptive statistics for 2D morphometries of eskers on Mars and Earth. Data for the Dorsa Argentea are from Butcher et al. (2016). Data for Canadian eskers are from Storrar et al. (2014a), with updated sample sizes (Storrar, personal communication). Data for SW Finland eskers are from Storrar and Jones (unpublished). Data for system morphometries are not yet available for the SW Finland site.

	Mars			Earth	
	Phlegra Montes	**NW Tempe Terra**	**Dorsa Argentea[1]**	**Canada[2]**	**SW Finland[3]**
Segment length					
N	38	8	720	20,712[4]	853
Mean (km)	0.314	2.008	9.4	3.5	0.316
Median (km)	0.114	0.644	4.8	2.1	0.206
Maximum (km)	2.43	11.424	149.8	97.5	3.592
System length					
N	22	1	260	7027[4]	-
Mean (km)	0.573	17.111	36.5	15.6	-
Median (km)	0.318	-	22.2	4.1	-
Maximum (km)	2.665	-	313.9	760	-
Segment sinuosity					
N	38	8	720	20,712[4]	853
Mean	1.05	1.05	1.04	1.06	1.09
Median	1.02	1.07	1.02	1.04	1.06
Maximum	1.22	1.15	1.75	2.21	2.39
System sinuosity					
N	22	1	260	7027[4]	-
Mean	1.08	1.13	1.10	1.08	-
Median	1.07	-	1.07	1.06	-
Maximum	1.25	-	1.91	2.62	-
Continuity					
N	22	1	260.00	7027[4]	
Mean	0.94	0.94	0.91	0.65	-
Median	1	-	0.94	-	-

[1] Butcher et al. (2016) [2] Storrar et al. (2014a) [3] Storrar and Jones (unpublished)
[4] Updated from Storrar et al. (2014a; personal communication)

7.6.1.2. 3D morphometries

As illustrated in Figure 7.8, the ridge members of the NW Tempe Terra esker formation are typically taller (median height = 13 m; Figure 7.8A) and wider (median width = 173 m; Figure 7.8B) than the Phlegra Montes esker complex (median height = 7 m, median width = 155 m). However, the eskers have comparable median width-height ratios (Phlegra Montes = 22; NW Tempe Terra = 18; Figure 7.8C), and median average cross-sectional slopes (Phlegra Montes = 6°; NW Tempe Terra = 6°; Figure 7.8D). As illustrated in Figure 7.8B, all measured widths for the Phlegra Montes esker are below the width detection limit for the Dorsa Argentea measurements (Butcher et al., 2016) such that a comparison of their absolute geometries is not meaningful. However, in general, the Phlegra Montes and NW Tempe Terra eskers are significantly taller relative to their widths (Figure 7.8C), and thus have steeper average cross-sectional slopes (Figure 7.8D) than the largest Dorsa Argentea ridges (median width-height ratio = 75; median average cross-sectional slope = 2°).

Figure 7.9 compares the distributions of the 3D morphometries of the sharp-crested and round-crested portions of the Phlegra Montes esker and the morphological subtypes of the upper and lower members of the NW Tempe Terra esker formation (see Chapter 6). It illustrates similarities between the morphometries of portions of the eskers with similar crest morphologies. In general, the sharp-crested portions of the NW Tempe Terra (subzones IIb and IIIa, upper member, and zone IV) and Phlegra Montes eskers have comparable absolute widths (Figure 7.9B) and heights (Figure 7.9A), but these portions of the Phlegra Montes esker are typically wider relative to their heights (Figure 7.9C) than those of the NW Tempe Terra esker, having a median average cross-sectional slope of 6°, compared to 8° and 11° for zone IV and the upper member (subzones IIb and IIIa; see Chapter 6) of the NW Tempe Terra esker, respectively (Figure 7.9D).

The round-crested portion of the NW Tempe Terra esker (subzones IIa–IIIc, lower member; see Chapter 6) is significantly taller and wider than the round-crested portions of the Phlegra Montes esker (Figure 7.9C); its median height (24 m) is 12 times greater, and its median width (809 m; Figure 7.9D) is 8 times greater than the round-crested portions of the Phlegra Montes esker (median height = 2 m, median width = 102 m). Despite significant differences in absolute heights and widths, the round-crested portions of the Phlegra Montes and NW Tempe Terra eskers have remarkably similar height-width relationships (Figure 7.9C–D), as illustrated by the linear fits in Figure 7.10B (Table 7.7). While the round-crested portions of the Phlegra Montes esker have a higher median width-height ratio (52) and slightly lower median average cross-sectional slopes (2°) than the round-crested portion of the NW Tempe

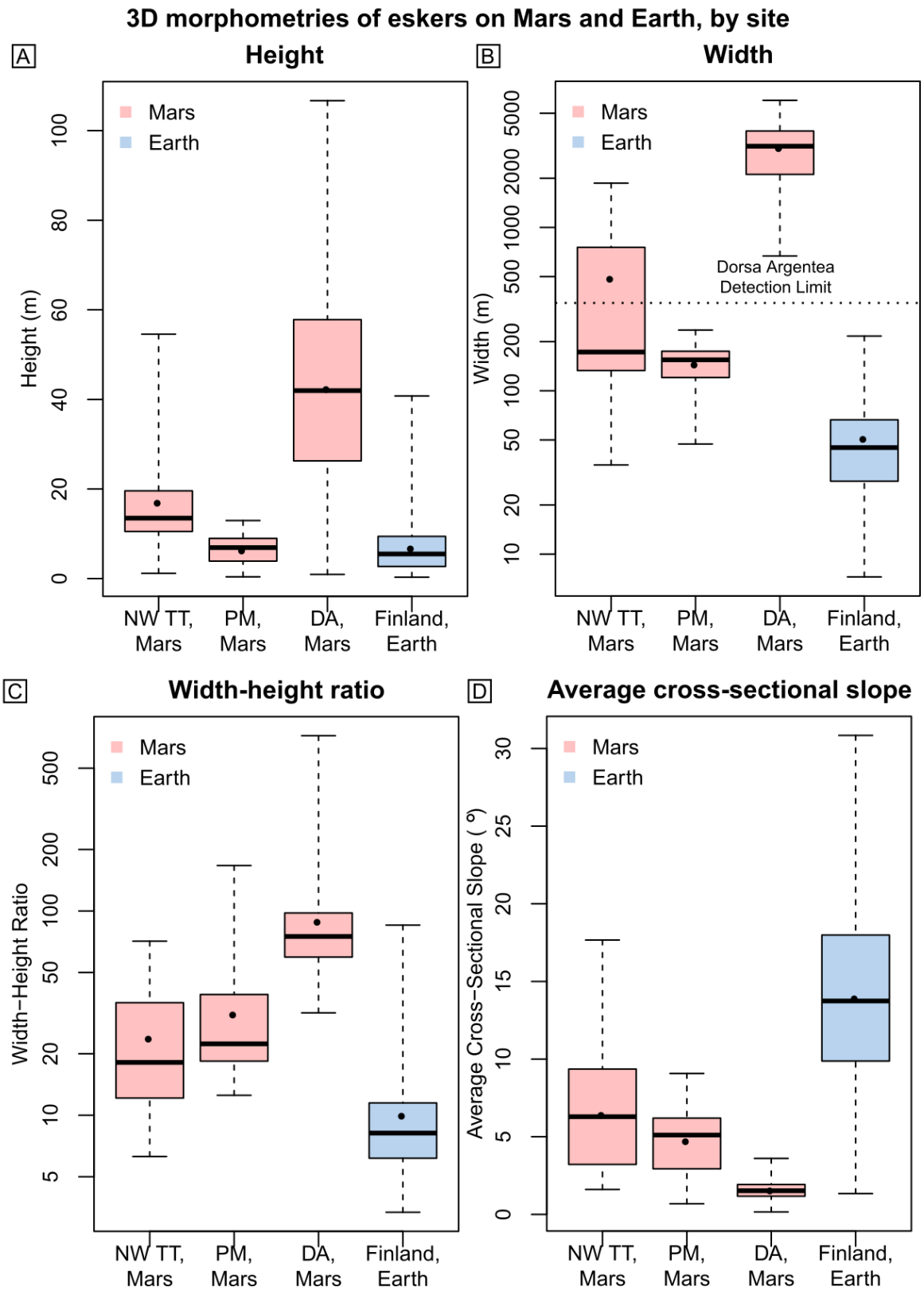

Figure 7.8. Comparisons of distributions of 3D morphometries of eskers on Mars on Earth, grouped by site. Boxplots showing distributions of (A) height, (B) width, (C) width-height ratio, and (D) average cross-sectional slope, for eskers in NW Tempe Terra (NW TT), Phlegra Montes (PM), and the Dorsa Argentea Formation (DA; data from Butcher et al., 2016), Mars (pink), and SW Finland (Storrar and Jones, unpublished), Earth (light blue). Morphometries of the NW Tempe Terra esker are with upper and lower ridge members separated (see Figure 6.3 for composite heights and widths). In all boxplots, boxes represent the interquartile range, whiskers represent maximum and minimum, solid lines represent the medians, and points represent the means. Note logarithmic axes in panels B and C.

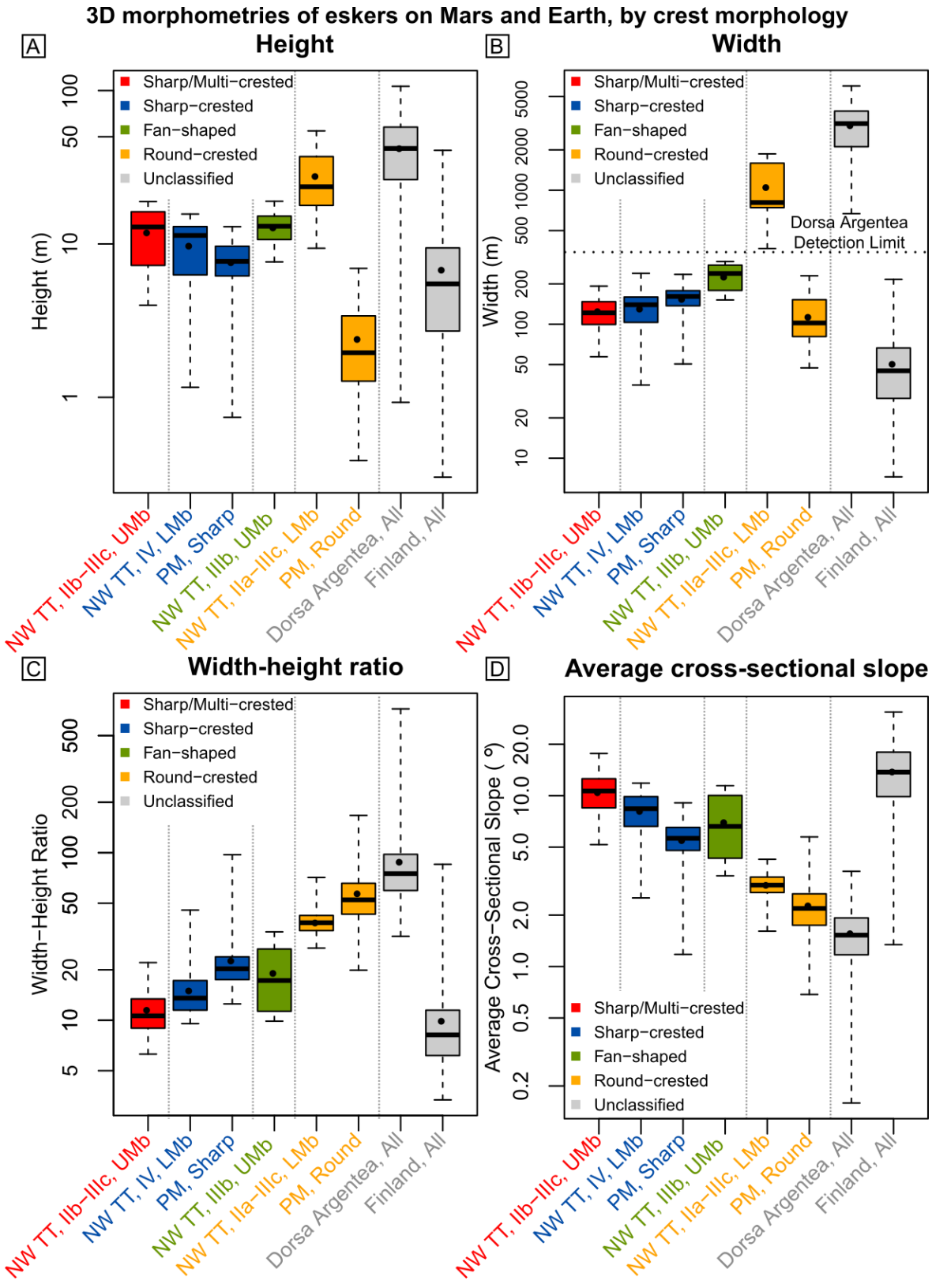

Figure 7.9. Comparisons of distributions of 3D morphometries of eskers on Mars on Earth, grouped by crest morphology. Boxplots showing distributions of (A) height, (B) width, (C) width-height ratio, and (D) average cross-sectional slope, for morphological subtypes (colours) of eskers in NW Tempe Terra (NW TT), Phlegra Montes (PM), and the Dorsa Argentea Formation (DA; data from Butcher et al., 2016), Mars (pink), and SW Finland (Storrar and Jones, unpublished), Earth (light blue). NW TT measurements are categorised by morphological subzones of the upper member (Umb) and lower member (Lmb) ridges described in Chapter 6. Boxes are interquartile ranges, whiskers represent maxima and minima, solid lines represent the medians, and points represent the means. Note logarithmic axes in all panels.

Table 7.6. 3D morphometry statistics for eskers on Mars and Earth, by site and crest morphology. NW Tempe Terra upper (Umb) and lower (Lmb) member ridges (see Chapter 6) included separately (see Table 6.3 for composite stacked heights and widths). Dorsa Argentea and SW Finland measurements from Butcher et al. (2016) and Storrar and Jones (unpublished), respectively.

	Phlegra Montes			NW Tempe Terra				Dorsa Argentea[2]	SW Finland[3]
Subzone	-			-	IV, Lmb	IIb–IIIa, Umb	IIa–IIIc, Lmb	IIIb, Umb	-	-
Crest type	**All**	**Sharp**	**Round**	**All[1]**	**Sharp**	**Sharp/multi**	**Round**	**Fan-shaped**	**All**	**All**
N	582	441	141	490	229	52	185	24	211	20,269
Height (m)										
Minimum	0.5	0.7	0.5	1	1	4	9	8	1	0.30
Maximum	13	13	7	55	16	19	55	19	107	41
Quartile 1	4	6	1	11	6	7	18	11	26	3
Quartile 3	9	10	3	20	13	16	37	15	58	9
Median	7	8	2	13	11	13	24	13	42	5
Mean	6	8	2	17	10	12	28	13	42	7
St. Dev.	3	3	2	12	4	5	13	3	21	5
Width (m)										
Minimum	47	50	47	35	35	57	367	152	669	7.3
Maximum	235	235	230	1867	240	192	1867	294	5999	216
Quartile 1	121	137	81	133	103	100	741	179	2112	28
Quartile 3	175	178	152	756	159	146	1592	275	3893	67
Median	155	161	102	173	140	122	809	239	3143	45
Mean	146	156	115	489	132	126	1066	228	3083	51
St. Dev.	39	32	44	537	41	35	474	52	1203	30

Table 7.6 continues on next page.

Table 7.6 continued from previous page

	Phlegra Montes				NW Tempe Terra				Dorsa Argentea[2]	SW Finland[3]
Subzone		-		-	IV, Lmb	IIb/IIIa, Umb	IIa–IIIc, Lmb	IIIb, Umb	-	-
Crest type	**All**	**Sharp**	**Round**	**All[1]**	**Sharp**	**Sharp/multi**	**Round**	**Fan-shaped**	**All**	**All**
N	582	441	141	490	229	52	185	24	211	20,269
Width-Height ratio										
Minimum	13	13	20	6	10	6	27	10	32	3
Maximum	167	97	167	71	45	22	71	34	721	85
Quartile 1	18	17	43	12	11	9	34	11	59	6
Quartile 3	39	24	66	36	17	13	42	26	98	11
Median	22	20	52	18	14	11	38	17	75	8
Mean	31	23	58	24	15	12	39	19	89	10
St. Dev.	21	10	24	13	6	4	6	8	69	6
Average cross-sectional slope (°)										
Minimum	0.7	1	0.7	2	3	5	2	3	0.2	1
Maximum	9	9	6	18	12	18	4	11	4	31
Quartile 1	3	5	2	3	7	9	3	4	1	10
Quartile 3	6	7	3	9	10	13	3	10	2	18
Median	5	6	2	6	8	11	3	7	2	14
Mean	45	6	2	6	8	11	3	7	2	14
St. Dev.	2	1	1	3	2	3	0.4	3	0.6	5

[1] NW Tempe Terra measurements in column 5 (‘All’) are with upper and lower member ridges separated. See Table 6.3 for composite stacked heights and widths.

[2] Data from Butcher et al. (2016)

[3] Data from Storrar and Jones (unpublished)

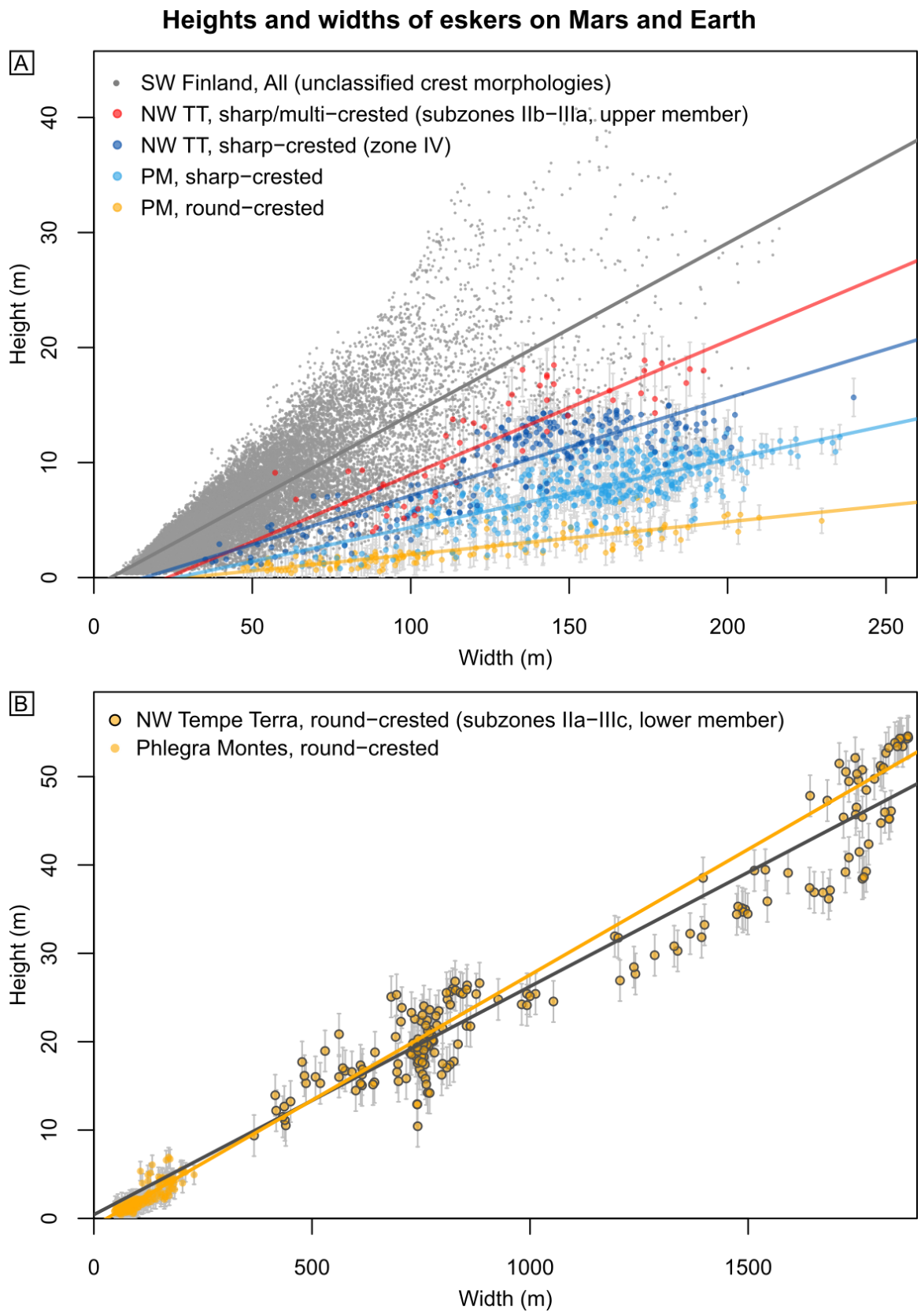

Figure 7.10. Scatterplots of height versus width for eskers on Mars, and comparison to eskers in SW Finland, Earth. Scatterplot comparing height-width trends for sharp-/multi-crested portions of the NW Tempe Terra esker, with those of sharp-crested and round-crested portions of the Phlegra Montes esker, and eskers in SW Finland (data from Storrar and Jones, unpublished; see Table 7.1). (B) Scatterplot comparing height-width trends for round-crested portions of the Phlegra Montes esker, and the round-crested lower member of the NW Tempe Terra esker. Lines in both panels are linear fits for each grouping (see Table 7.7).

Table 7.7. Correlation statistics and linear fits for eskers on Mars and Earth, categorised by crest morphology. Skewness, kurtosis, and Shapiro-Wilk (SW-test; for small samples) or Kolmogorov-Smirnov (KS-test; for large samples) tests for normality (p-values > 0.01 suggest normal distribution) determined whether a non-parametric Spearman's rank, or a parametric Pearson's correlation test, was suitable for correlation testing. *H* is height and *W* is width.

	Phlegra Montes				**NW Tempe Terra**						**Dorsa Argentea[1]**		**SW Finland[2]**	
Subzone	-				**IV, Lmb**		**IIb/IIIa, Umb**		**IIa–IIIc, Lmb**		-		-	
Crest type	**Sharp**		**Round**		**Sharp**		**Sharp/multi**		**Round**		**All**		**All**	
Variable	***H***	***W***	***H***	***W***	***H***	***W***	***H***	***W***	***H***	***W***	***H***	***W***	***H***	***W***
N	441	441	141	141	229	229	52	52	185	185	211	211	20269	20269
Skewness	-0.43	-0.54	0.94	0.45	-0.73	-0.50	-0.15	0.18	0.76	0.55	0.31	0.14	1.51	1.30
Kurtosis	2.83	3.30	3.09	2.15	2.17	2.67	1.57	2.13	2.28	1.70	2.79	2.37	6.21	5.17
SW test p-value	< 0.01	< 0.01	< 0.01	< 0.01	< 0.01	< 0.01	< 0.01	0.22	< 0.01	< 0.01	0.02	0.01	-	-
KS-test p-value	-	-	-	-	-	-	-	-	-	-	-	-	<0.01	<0.01
Spearman's rank rho	0.69		0.88		0.76		0.86		0.91		-		0.87	
Spearman's rank p-value	< 0.01		< 0.01		< 0.01		< 0.01		< 0.01		-		< 0.01	
Pearson's coefficient	-		-		-				-		0.77		-	
Pearson's p-value	-		-		-				-		< 0.01		-	
Linear fit (*H*=)	0.06*W*−1.55		0.03*W*−0.83		0.08*W*−1.35		0.12*W*−2.71		0.03*W*+0.43		0.01*W*+1.47		0.15*W*−0.79	

[1] Derived from data from Butcher et al. (2016). See Table 7.1 for list of data products.
[2] Derived from data from Storrar and Jones (unpublished). See Table 7.1 for list of data products.

Terra esker (median width-height ratio = 38, median average cross-sectional slope = 3°), the ranges of these variables for the NW Tempe Terra esker fall entirely within those of the round-crested portions of the Phlegra Montes esker (Figure 7.9C–D).

It should be noted that, although the typical morphometries of the Phlegra Montes and NW Tempe Terra eskers are not comparable to those of the largest Dorsa Argentea eskers measured by Butcher et al. (2016), the round-crested portion of the lower member ridge of the NW Tempe Terra esker has widths that are above the detection limit imposed by the available DEM resolution for the Dorsa Argentea (Figure 7.9B). Therefore, it is possible to draw a meaningful comparison for this portion of the sample. The widths of the round-crested portion of the lower member of the NW Tempe Terra esker (Figure 7.9B) fall largely within the lower quartile of widths of the four largest Dorsa Argentea ridges, while its heights (Figure 7.9A) fall within the first, second and third quartiles of those of the Dorsa Argentea ridges. The round-crested portion of the NW Tempe Terra esker has average cross-sectional slopes (Figure 7.9D) that span the third and fourth quartiles of those of the four largest Dorsa Argentea ridges.

The fan-shaped terminus of the upper member in subzone IIIb of the NW Tempe Terra esker has width-height ratios and average cross-sectional slopes that are intermediate between the distributions of these morphometries for sharp-crested and round-crested portions of the Phlegra Montes and NW Tempe Terra eskers (Figure 7.9C–D).

7.6.2. Comparison with Eskers in Canada and SW Finland, Earth.

In the following sections, I compare the morphometries of the Phlegra Montes and NW Tempe Terra eskers to the 2D planform morphometries of > 20,000 esker segments in Canada (see Section 5.7.1; Storrar et al., 2014a) and the 2D and 3D morphometries of ~70 km of esker segments in SW Finland (see Section 5.7.2; Storrar and Jones, unpublished). The large 3D esker morphometry dataset (comprising > 20,000 individual transects) is the first of its kind and was compiled by Storrar and Jones (unpublished) in parallel with the development of this thesis (see Chapter 5). At the time of writing, 2D measurements of the eskers in SW Finland were available only for esker segments, and 2D morphometries of esker systems and classifications of crest morphologies were not yet available. However visual inspection of the study site shows that sharp esker crest morphologies are dominant.

7.6.2.1. 2D Morphometries

As shown in Table 7.5 and Figure 7.7, the Canadian eskers mapped by Storrar et al. (2013) and measured by Storrar et al. (2014a) have segment lengths in the range 27 m–97.53 km

(median = 2114 m; Figure 7.7A), and form systems with an average continuity of 0.65, and lengths of up to 760 km (median = 4076 m; Figure 7.7B). Individual esker segments in SW Finland are typically shorter than their Canadian counterparts, having a maximum segment length (3.59 km) that falls within the third quartile of Canadian esker segment lengths, and a median segment length (206 m, IQR = 279 m) that falls within the first quartile of segment lengths of the Canadian eskers (Figure 7.7A). This may be partly attributable to the differences in sampling area between the two mapping studies (Canada = 10 million km^2, Figure 5.5; SW Finland = 2305 km^2, Figure 5.6).

Esker segments in SW Finland and Canada have very similar sinuosity (Figure 7.7C). Individual segments in Canada have sinuosities in the range 1–2.21 (median = 1.04), while those in SW Finland have sinuosities in the range 1–2.39 (median = 1.06). Esker systems in Canada have sinuosities in the range 1–2.62 (median = 1.06; Figure 7.7D; Storrar et al., 2014a); system measurements are not yet available for SW Finland.

Whereas individual segments of the Dorsa Argentea eskers measured by Butcher et al. (2016) occupy (and exceed) the upper range of segment lengths of the Canadian eskers, the shorter Phlegra Montes and NW Tempe Terra eskers largely fall within the lower range (i.e., first and second quartiles) of segment lengths of the Canadian eskers (Figure 7.7A). The median and interquartile range of segment lengths of both the Phlegra Montes (median = 114 m, IQR = 168 m) and NW Tempe Terra (median = 2.43 km, IQR = 626 m) eskers fall within the first quartile of segment lengths of the Canadian eskers. The Phlegra Montes esker segments (lengths in the range 14–2430 m, median = 144 m) are very similar in length to the SW Finland esker segments (lengths in the range 19–3592 m, median = 206 m; Figure 7.7A). While most of the NW Tempe Terra esker segments fall within the upper range of segment lengths of the SW Finland eskers, the main segment is 7.83 km longer than the longest segment measured in SW Finland. However, considering that individual esker segments in Canada can extend for up to ~100 km (Storrar et al., 2014a), in relative terms, the NW Tempe Terra esker can be considered to have segment lengths that are similar to the eskers of SW Finland.

Like the Dorsa Argentea (Butcher et al., 2016), the Phlegra Montes and NW Tempe Terra eskers have very similar sinuosity to the eskers of Canada and SW Finland (Figure 7.7C–D); the martian eskers and the Canadian and Finnish eskers all have median segment and system sinuosity in the range 1.02–1.07. The maximum sinuosity measured for the martian eskers is notably lower than the maximum sinuosities (> 2) of the Canadian and Finnish eskers (Table 7.5; Figure 7.7C–D).

The Phlegra Montes and NW Tempe Terra eskers are consistent with the Dorsa Argentea eskers in having lower degrees of fragmentation (i.e., higher continuity values) than the Canadian eskers (Table 7.5). Butcher et al. (2016) suggest that this difference could be an outcome both of post-depositional erosion rates on Mars that are orders of magnitude lower than on Earth (Carr and Head, 2010), and differences in the spatiotemporal nature of esker deposition. I discuss the implications of the new insights into eskers in Mars' mid latitudes for the spatiotemporal dynamics of esker formation on Mars in Section 7.7.1.

7.6.2.2. 3D Morphometries

As shown in Table 7.6, and Figures 7.8A and 7.9A, the eskers of SW Finland measured by Storrar and Jones (unpublished) range in height between < 1 m and 41 m. Their height distribution is highly positively skewed and leptokurtic (skewness = 1.51, kurtosis = 6.21; Table 7.7), with a median height of 6 m (Figure 7.8A). Similarly, the eskers have highly positively skewed, leptokurtic width distributions (skewness = 1.30, kurtosis = 5.17; Table 7.7) in the range 7–216 m, with a median width of 45 m (Figure 7.8B). The width-height ratios of the eskers in SW Finland range between 3 and 85, with a median of 8 (Figure 7.8C), leading to average cross-sectional slopes in the range 1–31°, and median average cross-sectional slopes of 14° (Figure 7.8D). Esker height in SW Finland is strongly correlated with width (Spearman's rank rho = 0.87, p-value < 0.01, n = 20,269; Table 7.7); this relationship is best described by a linear fit with the equation:

$$H = 0.15W - 0.79 \quad \textbf{7.1}$$

where H is height and W is width (Table 7.7; Figure 7.10A), though the variance of height for a given width increases significantly towards higher values of width (Figure 7.10A).

The height distribution of the SW Finland eskers is similar to the Phlegra Montes esker complex (Figure 7.8A; Table 7.6). The first, second, and third quartiles of their distributions are virtually indistinguishable (SW Finland median height = 6 m, IQR = 7 m; Phlegra Montes median height = 7 m, IQR = 5 m; Figure 7.8A), though the maximum height of the eskers in SW Finland (41 m) is 3 times greater than that of the Phlegra Montes esker (13 m; Figure 7.8A). The heights of the Phlegra Montes esker fall entirely within the range of heights of eskers in SW Finland. When subdivided by morphological type (Figure 7.9A), the heights of sharp-crested portions of the Phlegra Montes esker typically span the upper third and lower fourth quartiles of the eskers in SW Finland, while the typical heights of round-crested portions span the upper first and lower second quartiles (Figure 7.9A). The individual members of the NW Tempe Terra esker are taller than the typical heights of eskers in SW

Finland (Figure 7.8A). While 92% of transects along the individual members of the NW Tempe Terra esker have heights within the range of esker heights in SW Finland, all but the first quartile fall within or exceed the fourth quartile of heights of the Finnish eskers (Figure 7.7A). When measurements of the NW Tempe Terra esker formation are categorised by morphological type (Figure 7.9) and ridge member (see Chapter 6), the sharp-crested to multi-crested upper member (subzones IIb and IIIa), and the sharp-crested portion of the lower member (zone IV), are most morphometrically similar to the eskers of SW Finland, while heights of the round-crested lower member (subzones IIa–IIIc) occupy the upper range of Finnish esker heights. In general, however, the Phlegra Montes and NW Tempe Terra eskers have comparable heights to the eskers of SW Finland eskers (Figures 7.8A and 7.9A; Butcher et al., 2016). The Dorsa Argentea are significantly taller than the Finnish eskers, having a median height (42 m) that is similar to the maximum height of the Finnish eskers (41 m).

While still comparable, the widths of the eskers on Mars are more dissimilar to the eskers in SW Finland than their heights. The widths of the sharp- and multi-crested portions of the NW Tempe Terra esker (subzones IIb and IIIa, upper member; and the lower member in zone IV), and both the sharp- and round-crested portions of the Phlegra Montes esker, largely fall within the upper quartile of widths of the SW Finland eskers (Figure 7.9B), indicating that the Mars eskers are typically wider than those in SW Finland. The median widths of these esker portions (in the range 102–161 m; Table 7.6) are two to four times the median width of the eskers in SW Finland (median width = 45 m). The widths of the round-crested lower member of the NW Tempe Terra esker (in the range 367–1867 m) are far greater than the maximum width (216 m) recorded by Storrar and Jones for eskers in SW Finland (Figure 7.9B).

The height-width relationships of the eskers on Mars and Earth are illustrated in Figures 7.8, 7.9C, and 7.10, and summarised in Table 7.7. Butcher et al. (2016) observed that the Dorsa Argentea have significantly greater width-height ratios than is typical of eskers on Earth. This is supported by the new 3D measurements of eskers in SW Finland and is also consistent with the new measurements of the Phlegra Montes and NW Tempe Terra eskers on Mars (e.g., Figure 7.8C). However, the width-height ratios, and by extension, the average cross-sectional slopes, of the Phlegra Montes and NW Tempe Terra eskers are more similar to the SW Finland eskers than the Dorsa Argentea (Figure 7.8C–D). Whereas the median width-height ratio of the Dorsa Argentea (75) approaches the maximum ratio (85) recorded for the SW Finland eskers, the width-height ratios of the different morphological subtypes of the

Phlegra Montes and NW Tempe Terra eskers fall largely within the upper quartile of ratios recorded for the SW Finland eskers (Figure 7.9C). This means that the average cross-sectional slopes of the Phlegra Montes (up to 9°) and NW Tempe Terra (up to 18°) eskers approach more similar values to eskers on Earth (SW Finland average cross section slopes fall in the range 1–31°) than those recorded for the Dorsa Argentea (maximum average cross-sectional slope ~4°; Figures 7.8D and 7.9D). The average cross-sectional slopes of the Phlegra Montes and NW Tempe Terra eskers fall largely within the first quartile of those of the SW Finland eskers.

7.7. Discussion

Prior to the present study, morphometric analyses of eskers on Mars were limited to samples of the populations of large eskers in the Dorsa Argentea Formation (Kress and Head, 2015; Butcher et al., 2016) and southern Argyre Planitia (Banks et al., 2009; Bernhardt et al., 2013). These eskers record extensive basal melting of ancient ice sheets during the early Hesperian (~3.48 Ga and ~3.6 Ga ago, respectively; Kress and Head, 2015; Bernhardt et al., 2013), and detailed measurements were only made for the largest ridges within these populations. The new measurements of the late-Amazonian-aged Phlegra Montes and NW Tempe Terra eskers presented here expand the range of ages and glaciological contexts for which morphometric observations of eskers on Mars are available. The Phlegra Montes and NW Tempe Terra eskers formed more recently (~110–150 Ma, up to 1 Ga; Gallagher and Balme, 2015; Butcher et al., 2017), and as a result of more spatially-limited (valley glacier or ice cap style) basal melting, than the more ancient Argyre Planitia and Dorsa Argentea eskers (Head and Pratt, 2001; Hiesinger and Head, 2002; Banks et al., 2009; Bernhardt et al., 2013; Fastook et al., 2012; Kress and Head, 2015; Butcher et al., 2016; Scanlon et al., 2018).

7.7.1. 2D Morphometries

7.7.1.1. Length

Together, the segment lengths of the Dorsa Argentea, Phlegra Montes, and NW Tempe Terra eskers (Section 7.5) span the full range of esker segment lengths observed on Earth (Figure 7.7A). Thus, the new measurements show that, while rarer, esker-forming melt events on Mars have occurred over a similar range of spatial scales to those that have occurred on Earth, ranging from extensive basal melting that formed eskers with length scales of up to hundreds of kilometres beneath large ice sheets, to more spatially-limited basal melting that formed eskers with length scales of 100s metres to tens of kilometres beneath valley glaciers and/or small ice caps. The smaller and more spatially-restricted nature of the Phlegra Montes and NW Tempe Terra eskers is consistent with the general cooling and drying of Mars'

climate that is widely thought to have occurred between the late Noachian and Amazonian; late-Amazonian environmental conditions on Mars are thought to have been less conducive to meltwater production than those of the Noachian and early Hesperian (e.g., Carr and Head, 2010; Fastook et al., 2012). However, I emphasise that the small number of esker-like ridge populations on Mars for which the esker-hypothesis has been tested robustly means that the observed reduction in the spatial scale of esker deposition over time is limited by the statistics of small numbers.

7.7.1.2. Sinuosity

My observations that the Phlegra Montes and NW Tempe Terra eskers have similar sinuosities to typical eskers on Earth (Figure 7.7C–D; Table 7.5) is consistent with sinuosity measurements of the Dorsa Argentea eskers (Kress and Head, 2015; Butcher et al., 2016). Although the typical sinuosities of eskers on Earth and Mars are similar, the maximum sinuosities of eskers on Mars are consistently lower than the maximum sinuosity of eskers in Canada and SW Finland (Figure 7.7C–D; Table 7.5). Storrar et al. (Storrar et al., 2014a) suggested that sinuosity is related to hydraulic pressure within an esker-forming conduit; straighter eskers form under greater hydraulic pressure than more sinuous eskers. This could suggest that eskers on Mars formed entirely within pressurised subglacial meltwater conduits. In contrast, it is likely that the large 2D morphometry datasets of eskers in Canada (Storrar et al., 2014a) and SW Finland (Storrar and Jones, unpublished) sample some eskers that formed under lower pressures in en-glacial and/or supraglacial drainage systems, which may explain the greater maximum sinuosity recorded in these samples.

7.7.1.3. Continuity

The very low degree of fragmentation of the Phlegra Montes and NW Tempe Terra eskers compared with that of eskers on Earth (Table 7.5) is also consistent with observations of the Dorsa Argentea and southern Argyre Planitia eskers (e.g., Metzger, 1992; Kress and Head, 2015; Butcher et al., 2016). Previous workers have suggested that the high continuity of eskers on Mars may result from a combination of low post-depositional erosion rates under Mars' cold, hyper-arid climate conditions and thin atmosphere (Banks et al., 2009; Bernhardt et al., 2013; Kress and Head, 2015; Butcher et al., 2016), and synchronous deposition along continuous conduits with lengths similar to those of the resulting landforms, rather than gradual (time-transgressive) growth of eskers within shorter conduits close to the glacier terminus that extended headward at the retreating margin of the parent glacier (Head and Pratt, 2001; Butcher et al., 2016). While the great lengths (up to 100s km) of the Dorsa Argentea pose a challenge to the hypothesis of synchronous formation (Butcher et al., 2016),

esker systems in Phlegra Montes and NW Tempe Terra are within the length range of eskers for which synchronous deposition has been inferred on Earth (Figure 7.7B). For example, the Chasm esker in British Columbia, Canada, is ~32 km long, with individual segments up to 15 km long, has a system sinuosity of 1.06, and is thought to have been deposited synchronously during a glacial outburst flood (Burke et al., 2012b). Discriminating between synchronous and time-transgressive modes of esker formation on Earth relies on detailed field studies of their internal sediments and architecture (e.g., Banerjee and McDonald, 1975; Gorrell and Shaw, 1991; Brennand, 1994, 2000; Mäkinen, 2003; Burke et al., 2008, 2010; Cummings et al., 2011; Burke et al., 2012b; Perkins et al., 2013; Burke et al., 2015; Perkins et al., 2016). In the absence of detailed insights into the internal sedimentary architecture of eskers on Mars, discriminating between these spatiotemporal regimes is challenging.

7.7.2. 3D Morphometries

The new 3D measurements of the Phlegra Montes and NW Tempe Terra eskers illustrate that these eskers are more similar to terrestrial eskers in their heights, widths, width-height ratios and average cross-sectional slopes (Figures 7.8 and 7.9) than the Dorsa Argentea eskers, which were previously the only eskers on Mars for which a systematic 3D morphometric survey had been undertaken (Butcher et al., 2016). The present study provides the first comparison to 3D measurements of a large sample of eskers on Earth, which were made for the first time by Storrar and Jones (unpublished) in parallel with this thesis. These data were not available for the morphometric study of Butcher et al. (2016), and meaningful comparisons to eskers on Earth for the Dorsa Argentea eskers continue to be limited by the coarse (~115 m) horizontal resolution of the topographic data available for this site. The present study exploits 1–2 m/pixel HiRISE DEMs at the Phlegra Montes and NW Tempe Terra sites. This is comparable to the 2 m resolution DEMs used by Storrar and Jones (unpublished) for SW Finland (see Section 5.7.2). The morphometric comparisons of the Phlegra Montes and NW Tempe Terra eskers with eskers in SW Finland presented here are therefore not limited by differences in data resolution.

I find that the Phlegra Montes and NW Tempe Terra eskers typically have larger width-height ratios than terrestrial eskers (Figure 7.8C), in agreement with observations of the Dorsa Argentea and Argyre Planitia eskers (e.g., Banks et al., 2009; Bernhardt et al., 2013; Butcher et al., 2016). Butcher et al. (2016) reported width-height ratios for the Dorsa Argentea that were larger than all but the widest terrestrial eskers (e.g., Banerjee and McDonald, 1975; Shreve, 1985a; Storrar and Jones, unpublished), and low side slopes of < 4°. I find that round-crested portions of the Phlegra Montes and NW Tempe Terra eskers

have width-height ratios and average cross-sectional slopes that approach those of the Dorsa Argentea, while sharp-crested to multi-crested portions approach values that are more typical of terrestrial eskers (Figure 7.9C–D).

As described in Section 7.6.1.2, the round-crested portions of the Phlegra Montes and NW Tempe Terra eskers have remarkably similar height width relationships and thus width-height ratios and average cross-sectional slopes (Figures 7.9C–D and 7.10B; Table 7.7), despite significant differences in their absolute widths and heights (Figure 7.9A–B). This similarity between two spatially-separated esker complexes suggests that there may be a primary formation control upon the morphometry of eskers with similar crest morphologies on Mars. If this is the case, height-width relationships of round-crested sinuous ridges elsewhere on Mars could be compared to the relationships presented here in tests for esker origins of those landforms. Given the similar range of widths occupied by sharp- and round-crested portions of the Phlegra Montes esker, it is possible that the height-width relationship observed for round-crested portions of this esker are the product of degradation from previously sharp-crested ridges, rather than a product of primary controls upon esker morphometry. However, I suggest that this is unlikely because, under the crest morphology classification criteria used, round-crested portions approximate half-pipes (having convex flank slopes) in topographic cross-section, while sharp-crested portions approximate triangles and often have concave flank slopes (e.g., Figures 7.2 and 7.11). It is difficult to reconcile the convex flanks of round-crested sections with mass wasting and/or creep relaxation of a previously sharp-crested ridge with planar to concave flank slopes.

Unlike the round-crested portions discussed above, I have identified variations in height-width relationships between sharp-crested and sharp- to multi-crested portions of the Phlegra Montes and NW Tempe Terra eskers (Figure 7.10A; Table 7.7). In the discussion that follows, I develop upon the hypothesis presented in Chapter 6 that these differences arise from variations in degradation state between sharp-crested and sharp- to multi-crested portions of the eskers with different exposure ages. I suggest that the lack of observed difference in height-width relationships of the round-crested ridge portions between the Phlegra Montes and NW Tempe Terra eskers could be explained by the lower average slopes of portions with round-crested morphologies, and thus their lower susceptibility to mass wasting of their flanks.

In Chapter 6, I suggested that the slightly lower gradient of the height-width relationship for the sharp-crested ridge portion in zone IV of the NW Tempe Terra esker compared to that of the sharp- to multi-crested upper member ridge in subzones IIb and IIIa could be explained

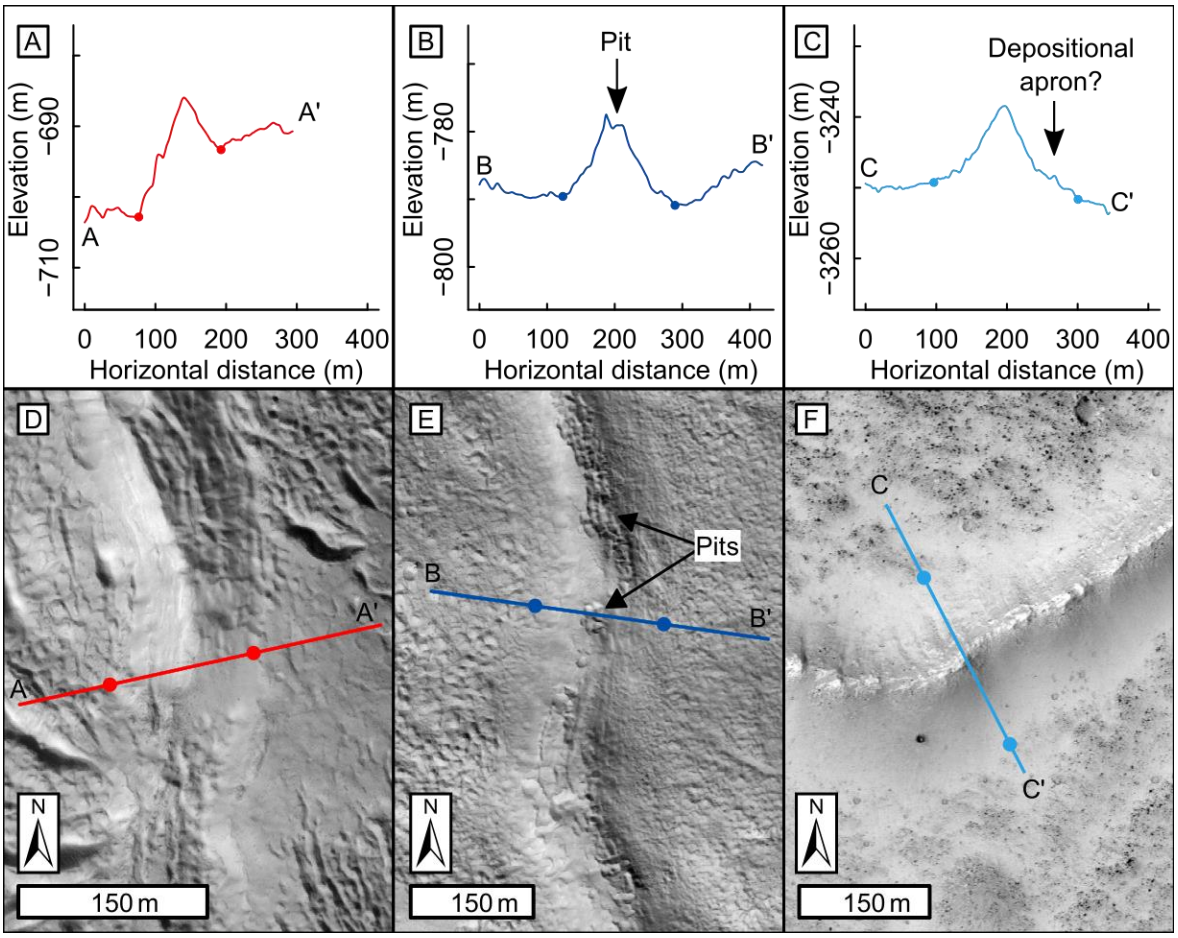

Figure 7.11. Differences in degradation state of sharp-crested portions between the Phlegra Montes and NW Tempe Terra eskers. Topographic profiles in panels (A)–(C) are from HiRISE DEMS (see Table 7.1 for data products) and panels D–F show profile locations (coloured lines) in context (orthorectified HiRISE images; Table 7.1). Coloured points in all panels mark the locations of the classified base points of the ridges. (A) Topographic profile A–A' showing the pristine nature of the crest of the sharp- to multi-crested upper member ridge in subzone IIb of the NW Tempe Terra esker, and the well-defined break in slope at its base. (B) Topographic profile B–B' showing the influence of pervasive sublimation pits (Chapter 4; Butcher et al., 2017) upon the height of the sharp-crested portion of the NW Tempe Terra esker in zone IV, but the well-defined nature of the break in slope at the base of the ridge (with some evidence for deposition of mass-wasted materials at the foot of the ridge's eastern flank). (C) Topographic profile C–C' showing the pristine nature of the crest in some sharp-crested portions of the Phlegra Montes esker, but the weak definition of the break in slope at the ridge base, which I attribute to mass wasting of the ridge flanks and deposition of this material in aprons at the base of the ridge. (D) HiRISE image of a sharp-crested portion of the upper member ridge in subzone IIb of the NW Tempe Terra esker, showing profile A–A'(panel A) in context. (E) HiRISE image of a portion of the sharp-crested portion of the NW Tempe Terra esker in zone IV, showing profile B–B' (panel B) in context. (F) HiRISE image of a sharp-crested portion of the Phlegra Montes esker showing topographic profile C–C' (panel C) in context.

by more advanced volatile loss and hence flank mass wasting in zone IV, which is located further from the present glacier terminus (and therefore has an older exposure age) than the upper member ridge in subzones IIb and IIIb. There is a visible difference in degradation state between the upper member ridge in subzones IIa-IIIa, which has a pristine crestline and is proximal to the present glacier terminus (Figure 7.11A and D), and the heavily pitted (Figure 7.11E), glacier-distal portion of the ridge in zone IV. I attributed the pitted texture of the zone IV ridge to loss of interstitial ice within esker sediments since its exposure from beneath the parent glacier (Chapter 4; Butcher et al., 2017). Therefore, I suggested that the difference in degradation state between the two ridge portions could reflect earlier exposure of the zone IV ridge as the glacier margin retreated southward, and hence earlier onset of volatile loss from its interior.

The new measurements presented here show that sharp-crested portions of the Phlegra Montes esker have lower-gradient height-width relationships than either the zone IV or subzone IIb and IIIa portions of the NW Tempe Terra esker. Sharp-crested portions of the Phlegra Montes esker have relatively gradual and indistinct breaks in slope at their bases (Figure 7.11C) compared to those of the NW Tempe Terra esker (Figure 7.11A–B), and have possible topographic signatures of depositional aprons on their lower flanks (Figure 7.11C). This suggests more advanced mass wasting and/or creep relaxation of the flank slopes of the sharp-crested portions of the Phlegra Montes esker, which is in agreement with the differences in the estimated minimum ages for the eskers (Gallagher and Balme, 2015; Butcher et al., 2017) between the two sites. Gallagher and Balme (2015) calculated an impact crater retention age of 150 Myr for the parent glacier of the Phlegra Montes esker complex. The esker complex is located ~36 km beyond the present glacier terminus (see Figure 3.11A), so this age estimate (which may record the last major activity of the glacier surface) is probably an underestimation of the formation and exposure age of the esker complex itself. In contrast, the NW Tempe Terra esker remains in partial contact with its parent glacier, for which I calculated an impact crater retention age of 110 Myr (Chapter 4; Butcher et al., 2017). Although the uncertainties associated with impact crater dating of planetary surfaces (particularly young surfaces with small surface areas) are larger than the difference between the estimated ages of the two esker complexes (Hartmann, 2005) it is likely that the NW Tempe Terra esker is indeed younger, owing to its proximity to (and only partial exposure from) its parent glacier (see Figure 4.2). Hence, more advanced mass wasting and/or creep relaxation of the flank slopes of the Phlegra Montes esker, and a lower-gradient height-width relationship is to be expected. However, it should be noted that sharp-crested portions of the

Phlegra Montes esker have pristine crestlines similar to those of subzones IIb and IIIa of the NW Tempe Terra esker, which has a steeper height-width relationship. This could be difficult to explain under the flank degradation model. The sharpness of esker crests may be expected to soften as mass wasting of flank slopes advances and the ridges lower and widen.

I tentatively suggest that a lack of evidence for volatile loss (i.e., pitted morphologies) from the Phlegra Montes esker could provide an explanation for preservation of pristine sharp crestlines at this site, despite evidence for more advanced degradation of its flank slopes. There are multiple possible explanations for differences in the propensity for volatile preservation between eskers at different sites. These explanations include, but are not limited to, differences in ice content within eskers and differences in the porosity of esker sediments. If the differences in width-height ratio between sharp-crested portions of the NW Tempe Terra and Phlegra Montes eskers are indeed explained by differences in exposure age and degradation state, this would suggest that volatile loss is a more effective driver of crestline softening than wastage and/or relaxation of the ridge flanks.

However, given the lack of apparent crestline degradation of sharp-crested portions of the Phlegra Montes esker, I cannot rule out an alternative primary formation control upon the difference in width-height ratios (Figures 7.9C and 7.1A) between sharp-crested portions of the Phlegra Montes and NW Tempe Terra eskers.

Identifications of new candidate eskers on Mars would facilitate tests of such relationships, and should be accompanied by classifications of crest degradation state and approximations of exposure age where possible. In the case of glacier-linked eskers, the crater-retention age of the parent glacier (Gallagher and Balme, 2015; Butcher et al., 2017), and the distance of the esker from the glacier margin may provide sufficient first-order estimates of relative exposure ages. The large size and spatially extensive distribution (Figure 5.4) of the Dorsa Argentea eskers has allowed approximations of their age (~3.48 Ga) via buffered impact crater counting techniques (Kress and Head, 2015). Age approximations may be more difficult to obtain for candidate eskers that are neither associated with a parent ice deposit, nor are sufficiently large to obtain reliable impact crater statistics for the ridges themselves, and would instead rely on detailed geomorphic and stratigraphic mapping of the surrounding region and analyses of impact crater size-frequency distributions of geomorphic units that envelope esker formation in the stratigraphy.

Considering the above discussion, I propose that the differences in width-height ratio between eskers on Earth and Mars could be a product of differences in age, and thus

degradation state. Alternatively, the consistently higher width-height ratios of eskers on Mars relative to eskers on Earth could reflect differences in the fundamental controls upon esker formation, such as the influence of gravity upon the size and shape of subglacial meltwater conduits and the dynamics of esker-forming meltwater drainage.

7.8. Conclusions

This chapter presents the first metre-scale characterisation of late-Amazonian-aged glacier-linked eskers in Phlegra Montes (Gallagher and Balme, 2015) and NW Tempe Terra (Chapter 4, this thesis; Butcher et al., 2017), Mars, and comparisons to the 2D and 3D morphometries of eskers on Earth. The primary aim of this study was to characterise the 2D and 3D morphometric signatures of the two mid-latitude glacier-linked eskers identified to date, and their morphological subtypes, to aid future identification of candidate eskers elsewhere on Mars. I draw the following key conclusions from the morphometric analyses and comparisons to terrestrial analogues:

- The Phlegra Montes and NW Tempe Terra eskers are shorter in length than typical ridges comprising the ancient Dorsa Argentea esker complex and extend the range of length scales of eskers identified on Mars to date.
- When combined with the Dorsa Argentea, the new measurements of the Phlegra Montes and NW Tempe Terra eskers show that martian eskers extend over the full range of length scales of eskers observed on Earth. This suggests that, though rarer on Mars, wet-based glaciation has occurred on a similar range of spatial scales on Earth and Mars. While the Dorsa Argentea represent extensive basal melting of a large, ancient, south polar ice sheet (Head and Pratt, 2001; Hiesinger and Head, 2002; Banks et al., 2009; Bernhardt et al., 2013; Fastook et al., 2012; Kress and Head, 2015; Butcher et al., 2016; Scanlon et al., 2018), the Phlegra Montes and NW Tempe Terra eskers represent more recent and spatially-limited wet-based valley or ice-cap-style glaciation. This is consistent with the broad trend of climate cooling and drying that is widely thought to have occurred between the late Noachian and early Amazonian (Chapter 1; e.g., Carr and Head, 2010).
- The Phlegra Montes and NW Tempe Terra eskers have extremely low sinuosities that are consistent with those observed for both the Dorsa Argentea eskers on Mars (Kress and Head, 2015; Butcher et al., 2016) and eskers in Canada (Storrar et al., 2014a) and SW Finland (Storrar and Jones, unpublished) on Earth. Low sinuosities are consistent with esker formation under hydraulic pressure in subglacial meltwater conduits.

- Consistent with previous observations of eskers on Mars (Metzger, 1992; Banks et al., 2009; Bernhardt et al., 2013; Kress and Head, 2015; Butcher et al., 2016), the Phlegra Montes and NW Tempe Terra eskers have significantly higher continuities (> 90%) than is typical for eskers on Earth. This may arise from lower rates of post-depositional erosion on Mars, or synchronous esker deposition (as opposed to time-transgressive headward landform growth at a retreating ice margin), or a combination of both.
- Unlike the Dorsa Argentea, which occupy (and extend beyond) the upper range of heights and widths of eskers on Earth, the heights and widths of the Phlegra Montes and NW Tempe Terra eskers approach values that are more typical of eskers on Earth. The widest, tallest, round-crested portions of the NW Tempe Terra esker approach the dimensions of the Dorsa Argentea, Mars. The narrower, sharp-crested portions of the NW Tempe Terra esker and those of the Phlegra Montes esker are more similar in cross-sectional scale to eskers in SW Finland, Earth.
- Sharp-crested portions of the Phlegra Montes and NW Tempe Terra eskers tend to have lower width-height ratios (i.e., steeper side slopes) than round-crested sections.
- Although the round-crested portions of the NW Tempe Terra esker have greater absolute heights and widths than the round-crested portions of the Phlegra Montes esker, their height-width relationships follow similar trends, which may imply a primary formation control upon the geometries of round-crested eskers on Mars. Thus, these relationships could be used as reference morphometries against which those of round-crested sinuous ridges elsewhere on Mars can be compared in tests of the esker hypothesis.
- The height-width relationships of the sharp-crested portions of the NW Tempe Terra and Phlegra Montes eskers are less similar to one another than the round-crested portions. In Phlegra Montes, they follow a somewhat lower-gradient height-width trend (i.e., higher width-height ratios and lower average cross-sectional slopes) than in NW Tempe Terra. I suggest that this may also be explained by variations in exposure age, and thus the degradation state between the Phlegra Montes and NW Tempe Terra eskers. I suggest that sharp-crested portions (with their steeper average cross-sectional slopes) are more susceptible to lowering of their flanks via mass wasting than round-crested portions, for which I do not observe such a difference between the Phlegra Montes and NW Tempe Terra eskers.
- The height-width relationships observed for sharp-crested portions of the NW Tempe Terra and Phlegra Montes eskers could be used as reference morphometries in tests

of the esker hypothesis for sharp-crested sinuous ridges elsewhere on Mars, but such tests should take into account the possible effects of landform exposure ages and evidence for mass wasting and/or crest degradation upon observed morphometries and those of the reference landforms.

- Consistent with previous observations of the Dorsa Argentea eskers (e.g., Banks et al., 2009; Bernhardt et al., 2013; Butcher et al., 2016), I find that the Phlegra Montes and NW Tempe Terra eskers are wider relative to their heights (and thus have lower average cross-sectional slopes) than typical eskers on Earth. It is possible that this is a product of differences in age between esker populations on Earth and Mars, but could also be explained by differences in the parameters that governed their formation, such as the effect of gravity on conduit growth and meltwater discharge.

CHAPTER 8

A CAUTIONARY TALE FROM CHUKHUNG CRATER, MARS: AMBIGUOUS ORIGINS OF GLACIER-LINKED SINUOUS RIDGES

8.1. Attribution

Digital elevation models that are used for this study were derived from both CTX and HiRISE images by D. Mayer and E. Kite (Mayer and Kite, 2016; see Table 8.1), and are used with their kind permission.

8.2. Background

Chapters 6–7 contain analyses of sinuous ridges associated with existing mid-latitude viscous flow features (VFFs) on Mars. The ridges are interpreted as late-Amazonian-aged eskers associated with extant remnants of their parent glaciers (Chapters 3 and 4; Gallagher and Balme, 2015; Butcher et al., 2017). The locations of the Phlegra Montes and NW Tempe Terra eskers within tectonic rift/graben valleys supports the hypothesis that localised geothermal heating, possibly accompanied by viscous strain heating within the basal ice, was a prerequisite for the production of esker-forming glacial meltwater under cold late-Amazonian climate conditions (Chapters 3 and 4; Gallagher and Balme, 2015; Butcher et al., 2017). In order to test this hypothesis further, it is necessary to search for additional candidate eskers associated with late-Amazonian-aged VFF, and to explore whether their geologic settings are consistent with geothermal controls on the production of esker-forming meltwater. In this chapter, I begin this process by presenting Chukhung crater in central Tempe Terra (Figure 8.1) as a new site of interest in the search for glacier-linked

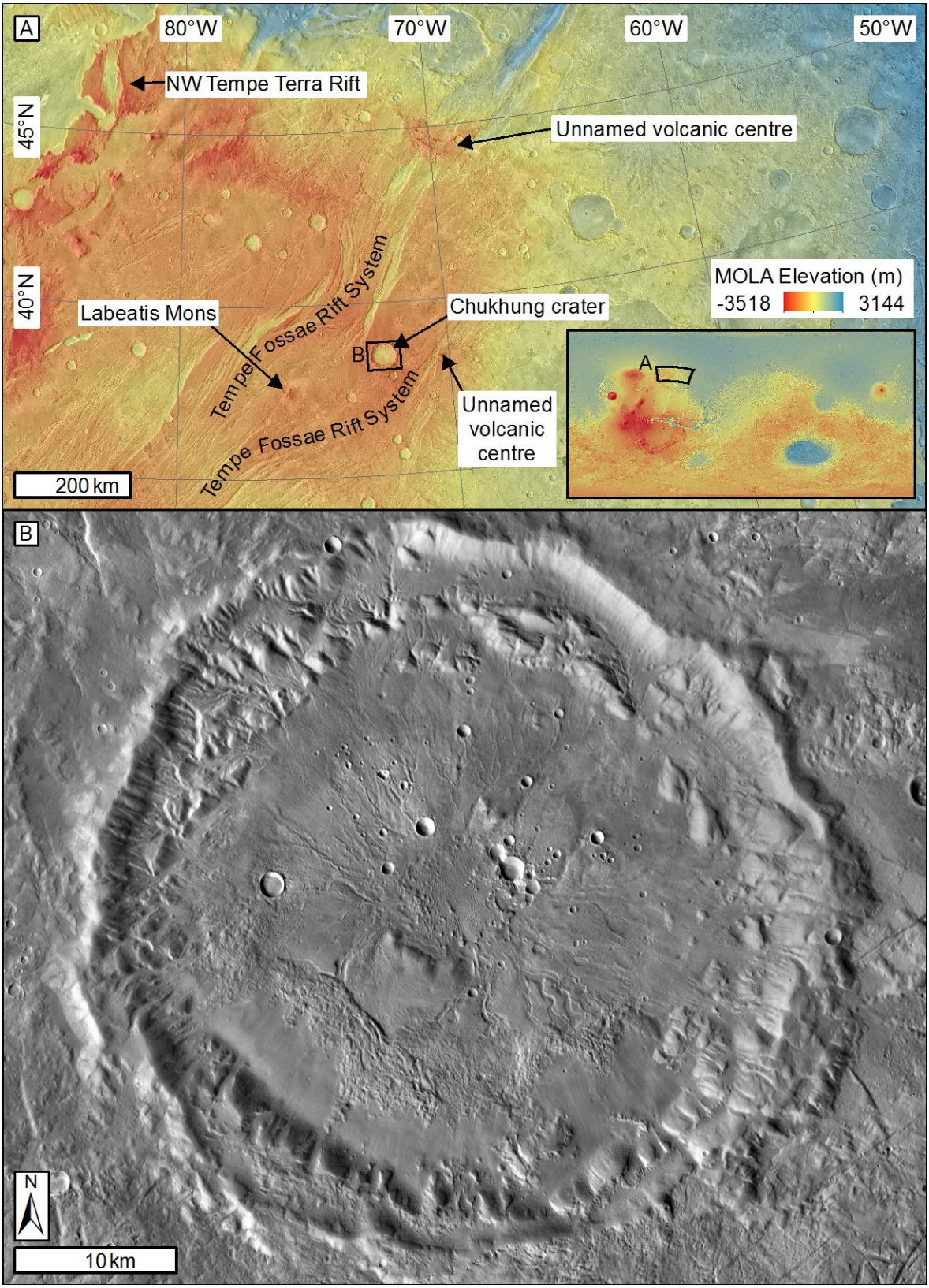

Figure 8.1. Location of Chukhung crater, Tempe Terra, Mars. (A) THEMIS daytime infrared image mosaic overlain by colourised MOLA elevation data of central Tempe Terra (location shown in the inset global MOLA elevation map), showing the location of Chukhung Crater relative to the NW Tempe Terra rift mapped in Chapter 4 (Butcher et al., 2017), and major fault branches and volcanic centres of the Tempe Fossae rift system. (B) CTX image mosaic of Chukhung crater. Extent shown in panel A. See Table 8.1 for list of data products.

eskers on Mars[9]. Chukhung crater hosts sinuous ridges associated with VFFs, which have a number of esker-like characteristics. However, it also hosts landforms interpreted as inverted palaeochannel landforms. As I will discuss, the co-existence of the VFF-linked sinuous ridges with inverted palaeochannels casts doubt on the origin of the VFF-linked ridges as eskers because of the issue of convergence of form (whereby different processes form landforms with similar morphologies) between inverted palaeochannels and eskers (e.g., Burr et al., 2009). Inverted palaeochannels (Figure 8.2) are ridges that preserve former fluvial channels in positive relief; they form when channel-fill deposits develop greater resistance to erosion than the adjacent valley floor and/or sides, and are exhumed as a result of more rapid erosion of those neighbouring materials (Figure 8.3; Maizels, 1987; Pain and Oilier, 1995; Williams et al., 2013, 2007). Unlike eskers, their formation does not require glaciation or glacial meltwater. Inverted palaeochannel and esker hypotheses have been at the forefront of debate regarding the origins of sinuous ridges in many locations on Mars (e.g., Howard, 1981; Tanaka and Kolb, 2001; Banks et al., 2009; Burr et al., 2009). Most notable in the context of the present study are the debates surrounding the origin of the south polar Dorsa Argentea (Howard, 1981; Parker et al., 1986; Tanaka and Scott, 1987; Ruff and Greeley, 1990; Kargel and Strom, 1992; Metzger, 1992; Kargel, 1993; Head, 2000a, 2000b; Head and Hallet, 2001a, 2001b; Head and Pratt, 2001; Tanaka and Kolb, 2001; Tanaka et al., 2014a; Kress and Head, 2015; Butcher et al., 2016), which are now generally (though not unanimously, see e.g., Tanaka et al., 2014a) thought to be ancient eskers, and the equatorial Aeolis Dorsa (Nussbaumer et al., 2003; Nussbaumer, 2005; Burr et al., 2009; Zimbelman and Griffin, 2010; Lefort et al., 2012; Williams et al., 2013; Kite et al., 2015; Cardenas et al., 2018), which are generally thought to be inverted palaeochannels. Chukhung crater provides a pertinent demonstration of the challenges for the confident interpretation of sinuous ridges on Mars as eskers, which result from similarities in form between eskers and inverted palaeochannels.

Confidence in a proposed formation mechanism for a given sinuous ridge on Mars can be greatly enhanced when that sinuous ridge is located within a wider landsystem that is geomorphically consistent with the proposed mechanism (Pain et al., 2007; Burr et al., 2009; Gallagher and Balme, 2015; Butcher et al., 2017). In the cases of the glacier-linked candidate eskers in Phlegra Montes (Chapters 3 and 7; Gallagher and Balme, 2015) and NW

[9] The esker hypothesis for sinuous ridges in Chukhung crater was previously discussed by E. Lakdawalla in two online blog posts for the Planetary Society available at: http://www.planetary.org/blogs/emily-lakdawalla/2010/2822.html and http://www.planetary.org/blogs/emily-lakdawalla/2011/2879.html (last accessed 24/01/2019).

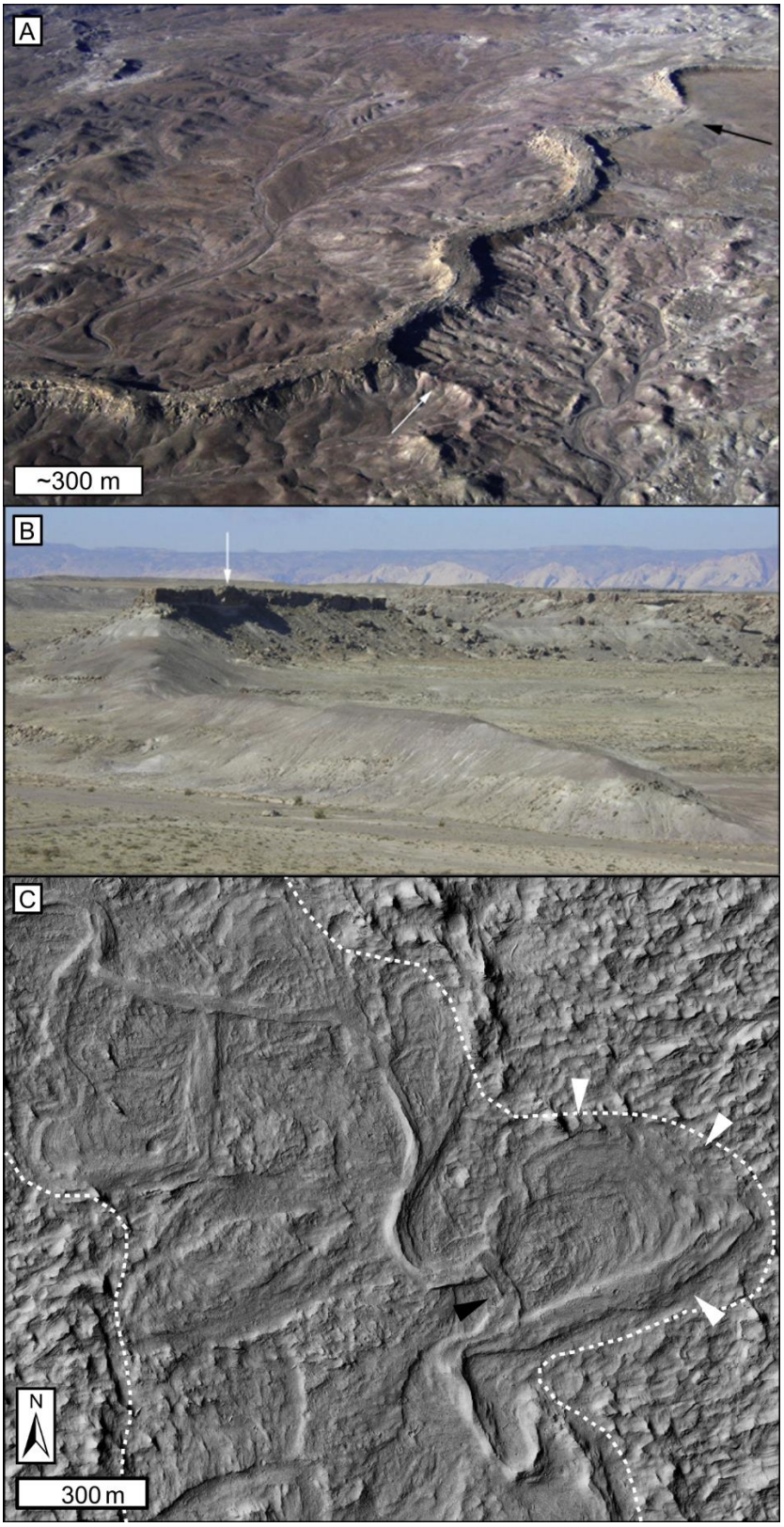

Figure 8.2. Inverted palaeochannels on Earth and Mars. (A) Oblique aerial photo of a flat-topped inverted palaeochannel near Green River, Utah, with a round-crested tributary ridge (white arrow). Modern drainage has eroded a ridge gap (black arrow). Adapted from Williams et al. (2009). (B) A portion of the same inverted palaeochannel system as in panel A, where the flat-topped capping materials (white arrow) have been eroded to form a round to sharp-crested ridge. Adapted from Williams et al. (2009). (C) HiRISE image (Table 8.1) of putative inverted palaeochannels in Aeolis Dorsa, Mars with evidence for migration (white arrows) of a meander across a flood plain (bounded by dotted white lines), and its subsequent cut-off by a channel at its neck (black arrow). After Cardenas et al. (2018).

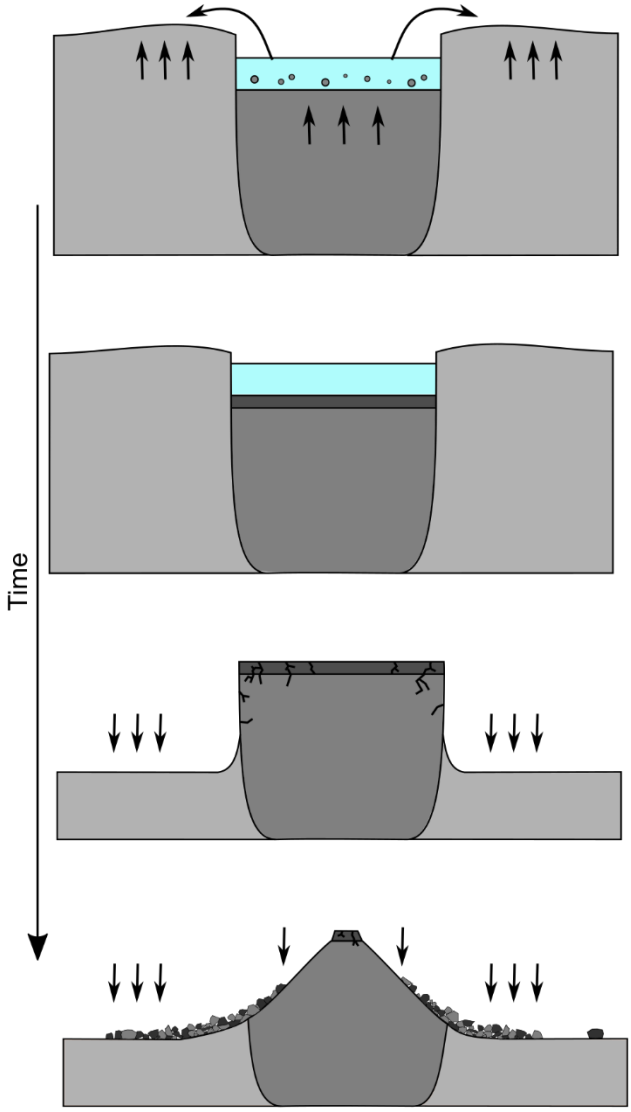

Figure 8.3. Schematic of inverted palaeochannel formation. Initially, sediment aggrades within an active fluvial channel, and on surrounding flood plains. The floor of the channel becomes more resistant to erosion than the surroundings, for example by deposition of coarse sediment or lava, or by chemical induration (either during or after the cessation of fluvial activity within the channel). Regional erosion promotes deflation of less resistant materials surrounding the channel sediments, exhuming them to form a ridge called an inverted palaeochannel. Eventual weakening and/or undermining of the resistant surface of the inverted palaeochannel can promote mass wasting of the ridge flanks, retreat of the lateral margins of the resistant surface materials, and a transition in ridge cross-sectional morphology.

Tempe Terra (Chapters 4 and 6; Butcher et al., 2017), associations with VFFs and other landforms with possible glacial origins (see Chapters 3 and 4), bolsters confidence in their origins as eskers. In contrast, the lack of preservation of a parent glacier or other glaciogenic landforms in the vicinity of the ancient sinuous ridges in the Dorsa Argentea Formation provided a strong challenge to their origins as eskers, and fuelled debate over their origins that has spanned several decades (e.g., Howard, 1981; Tanaka and Kolb, 2001; Butcher et al., 2016, and references therein). In presenting the case study of VFF-linked sinuous ridges in Chukhung crater, I aim to demonstrate that, even when sinuous ridges are associated with

VFFs or other ice-rich deposits, the challenges presented by their similarity in form to inverted palaeochannels of non-glacial origin often remain, particularly if VFF-linked sinuous ridges coexist with landforms that are also consistent with inverted palaeochannel origins. Thus, Chukhung crater provides a cautionary tale that should be considered during the search for eskers elsewhere on Mars.

8.2.1. The Esker vs. Inverted Palaeochannel Problem

Previous studies exploring the origins of sinuous ridges at several sites on Mars have commonly converged on a debate between their origins as either eskers or inverted palaeochannels (e.g., Tanaka and Kolb, 2001; Burr et al., 2009; Banks et al., 2009). On Earth, inverted palaeochannels are commonly found in arid environments (e.g., Oman, Australia, Utah, and the Atacama Desert; Maizels, 1987; Pain and Oilier, 1995; Williams et al., 2007, 2013; Lefort et al., 2012), and topographic inversion has been driven by aeolian deflation of the landscape, often with a contribution from fluvial erosion (Figure 8.3). Greater resistance of channel fill materials has been attributed to two dominant mechanisms: (1) chemical induration of channel fill materials, for example due to alteration by groundwater (e.g., Pain and Oilier, 1995; Williams et al., 2013), and (2) armouring by emplacement of resistant materials (e.g., coarse-grained fluvial deposits; Pain and Oilier, 1995; Williams et al., 2013, 2007).

Inverted palaeochannels are thought to be common landforms on Mars. For example, recent mapping by Davis et al. (2016) identified extensive networks of inverted palaeochannels within ancient, Noachian-aged terrains in Arabia Terra which, in many cases, extend from the highland valley networks (e.g., Hynek et al., 2010). An inverted palaeochannel origin for sinuous ridges on Mars is often more easily diagnosed than an esker origin. In many locations, topographic inversion not only exhumes a single channel, but also other features that represent migration of that channel across a flood plain, including inverted point and scroll bars (e.g., Maizels, 1987; Williams et al., 2007; Burr et al., 2009; Cardenas et al., 2018). Such migration features are not commonly observed in association with eskers on Earth because if a subglacial conduit migrates laterally, deposits that trace former conduit locations are often (though not invariably) eroded by the basal ice that surrounds the active channel. Thus, observation of such features in association with a sinuous ridge can improve confidence in an inverted palaeochannel origin.

The ‘esker vs. inverted palaeochannel problem’ is most acute in the case of sinuous ridges that are not associated with corroborating evidence for channel migration across a flood

plain. There are many possible reasons why such features may be absent in the vicinity of an inverted palaeochannel, including preferential induration and/or preservation of a single channel, or a lack of migration of the original channel (e.g., Williams et al., 2013). In exploring the origins of sinuous ridges on Mars, previous workers have appealed to several other characteristics of those ridges to favour either an inverted palaeochannel or an esker origin, including: (1) ridge crest morphology, (2) relationship of the ridge with the path of steepest topographic descent, (3) 3D ridge morphometry, and (4) ridge sinuosity. However, there are several caveats for the use of these criteria for distinguishing between eskers and inverted palaeochannels on Mars.

8.2.2. Chukhung Crater: A Case Study

In this study, I demonstrate some of the challenges that remain for the identification of eskers on Mars in the context of VFF-linked sinuous ridges in Chukhung crater. In this location, several challenges for esker identification converge. The VFF-linked sinuous ridges in Chukhung crater have many esker-like characteristics but the caveats concerning the criteria that are commonly invoked to support esker hypotheses must be given careful consideration. Additionally, mapping of both glaciated and unglaciated portions of Chukhung crater reveal that there are numerous sinuous ridges in Chukhung crater that do not emerge from VFFs or glaciated portions of the crater, and which have landform associations that are more consistent with inverted palaeochannel origins.

Chukhung crater (38.48°N, 72.5°W) is a ~45 km diameter, ~2300 m deep impact crater in central Tempe Terra (Figure 8.1). It is within the same physiographic region as the study site explored in Chapter 4, being located ~600 km from the tectonic rift hosting the NW Tempe Terra esker (Figure 8.1A). Chukhung crater is located between major grabens within the southwestern segment of the Tempe Fossae rift system (Hauber and Kronberg, 2001), and ~150 km ENE of the central construct of Labeatis Mons. Labeatis Mons is a large (~200 km diameter) late-Hesperian-aged (3.51 Ga; Hauber and Kronberg, 2001) volcano that formed during late-stage rifting in Tempe Fossae, and was probably active after major rifting ceased (Hauber and Kronberg, 2001; Hauber et al., 2010). A second, smaller volcanic construct is located within a swarm of grabens ~70 km east of Chukhung crater (Figure 8.1A).

If the sinuous ridges in Chukhung crater are eskers, their spatial association with the major grabens and volcanic edifices of the Tempe Fossae rift system would provide additional support to the hypothesis at the core of this thesis: that geothermal heat was a prerequisite for localised, geologically recent, wet-based glaciation in Mars' mid latitudes. However, for

the VFF-linked sinuous ridges in Chukhung crater, I suggest that the hypothesis that they are non-glacial inverted palaeochannels cannot be excluded given the present state of knowledge.

8.3. Aims

In this chapter, I present a geomorphic map of Chukhung crater and explore hypotheses for the formation of its interior units and landforms. In particular, I explore the origins of sinuous ridges that occupy two different portions of the crater floor: (1) sinuous ridges on the southern portion of the crater floor that are spatially associated with VFFs, and (2) sinuous ridges that extend across the northern portion of the crater floor where there is no discernible evidence for past glaciation. I first consider the hypotheses that: (1) the VFF-linked ridges on the southern portion of the crater floor are eskers, and (2) that the sinuous ridges on the northern portion of the crater floor are inverted palaeochannels of non-glacial origin. I then discuss the alternative hypotheses for the origins of the sinuous ridges: that both populations of sinuous ridges in Chukhung crater are eskers, or that both populations are inverted palaeochannels which pre-date the present glaciation of Chukhung crater. I highlight challenges that remain for the esker hypothesis despite spatial association of the southern sinuous ridges with existing VFFs (i.e., candidate parent glaciers). Finally, I consider the implications of sinuous ridges for the history of liquid water in Chukhung crater, and the implications of this case study for the ongoing search for glacier-linked eskers on Mars.

8.4. Data and Methods

8.4.1. Observations and Mapping

I produced a geomorphic map of the interior of Chukhung crater using a basemap comprising ~6 m/pixel CTX images (Table 8.1), which provided complete coverage of the mapping area (Figure 8.4). I supplemented analyses with seven HiRISE images (six of 25 cm/pixel, and one of 50 cm/pixel horizontal resolution), which provided partial coverage of the mapping area (Figure 8.4; Table 8.1). I integrated these image data with: (1) a single 75 m/pixel HRSC digital elevation model (DEM), which provided complete coverage of the mapping area (Figure 8.4; Table 8.1); (2) a 24 m/pixel DEM derived from two CTX images by Mayer and Kite (2016) using NASA Ames Stereo Pipeline software, which provided coverage of the western two-thirds of the mapping area; and (3) a 1 m/pixel HiRISE DEM generated by the same authors (Mayer and Kite, 2016), which provided coverage of a portion of the central crater floor (See Table 8.1 for a complete list of data products, and Figure 8.4 for data coverage). To minimise cartographic distortion, I digitised the map in a sinusoidal projection

Table 8.1. List of data products used in Chapter 8.

Instrument or Source	Image/Product ID	Figure
Mars Orbiter Laser Altimeter[1]	Global Elevation Model 463 m (MEGDR)[2]	8.1A and Inset
Thermal Emission Imaging System[3–4]	THEMIS-IR Day Global Mosaic 100m v12[2]	8.1A
Context Camera[5]	Mosaic[6] generated from images: P04_002577_2186_XN_38N072W, P02_002010_2188_XN_38N072W, G23_027037_2183_XN_38N072W, P02_001799_2187_XN_38N072W, G19_025626_2167_XN_36N071W, F23_044773_2196_XN_39N072W, D21_035397_2180_XN_38N072W, G20_026193_2183_XN_38N071W[7]	8.1B, 8.4, 8.5, 8.6A–O, 8.9, 8.10A, 8.10C, 8.11A, 8.11C, 8.11F, 8.12A–B, 8.13, 8.16A–C, 8.18A
	Digital elevation model[8] generated from images: B20_017477_2187 and G01_018545_2187	8.7, 8.8, 8.18B–E
High Resolution Imaging Science Experiment[9]`	ESP_017477_2190[10]	-
	ESP_023503_2185[10]	8.10D
	ESP_035397_2185[10]	8.11E
	ESP_037164_2190[10]	-
	ESP_043296_2190[10]	-
	ESP_048887_2190[10]	-
	PSP_010322_1740[10]	8.2
	Digital elevation model[8] generated from images: ESP_017477_2190 and ESP_018545_2190	8.7, 8.8
	Orthorectified image[8] generated from images: ESP_017477_2190 and ESP_018545_2190	8.1A–B, 8.1D, 8.1F, 8.10B–C
High Resolution Stereo Camera[11–12]	h1462_0000.da4.52[13]	8.7, 8.8

Table 8.1 continues on next page

Table 8.1 continued from previous page

Instrument or Source	Image/Product ID	Figure
National Land Service of Finland[14]	Light Detection and Ranging DEM mosaic[15] generated from 8 x 8 grid 6 x 6 km tiles[14]. Tile codes for corners of grid: L4224B, L4242H, L4213A, L4231G	8.17A, 8.17C–D
	Hillshade model generated from DEM[15]	8.17A
Natural Earth[16]	1:10 million physical vector shapefiles	8.17A–B (Insets)
	1:10 million cultural vector shapefiles	8.17A–B (Insets)
Utah Automated Geographic Reference Center[17]	5 m Auto-Correlated DEM from 1 m GSD Orthophotography (NAIP2006). Tile code: 12SWJ600000	8.17E–F
	1 m GSD Orthophotograph (NAIP2006). Tile codes q2732_se_NAIP2006 and q2832_ne_NAIP2006	8.17B
Personal Communication	Crestline map of eskers in Fennoscandia[18]	8.17A (Inset)

[1](Smith et al., 2001)
[2] United States Geological Survey Planetary GIS Web Server: http://webgis.wr.usgs.gov/pigwad/down/mars_dl.htm
[3] (Christensen et al., 2004)
[4] (Edwards et al., 2011)
[5] (Malin et al., 2007)
[6] Generated by F. E. G. Butcher
[7] Arizona State University http://viewer.mars.asu.edu/viewer/ctx#T=0
[8] (Mayer and Kite, 2016)
[9] (McEwen et al., 2007)
[10] The University of Arizona https://hirise.lpl.arizona.edu/
[11] (Neukum et al., 2004)
[12] (Jaumann et al., 2007)
[13] Freie Universität Berlin: http://maps.planet.fu-berlin.de/
[14] Available at https://tiedostopalvelu.maanmittauslaitos.fi/tp/kartta?lang=en, accessed 12/07/2018.
[15] Generated by R. D. Storrar (see Chapter 5)
[16] Available at: www.naturalearthdata.com, accessed 12/07/2018.
[17] Available at: https://gis.utah.gov/data/elevation-and-terrain/, accessed 18/12/2018
[18] Stroeven et al. (2016); data provided by C. Hättestrand (personal communication)

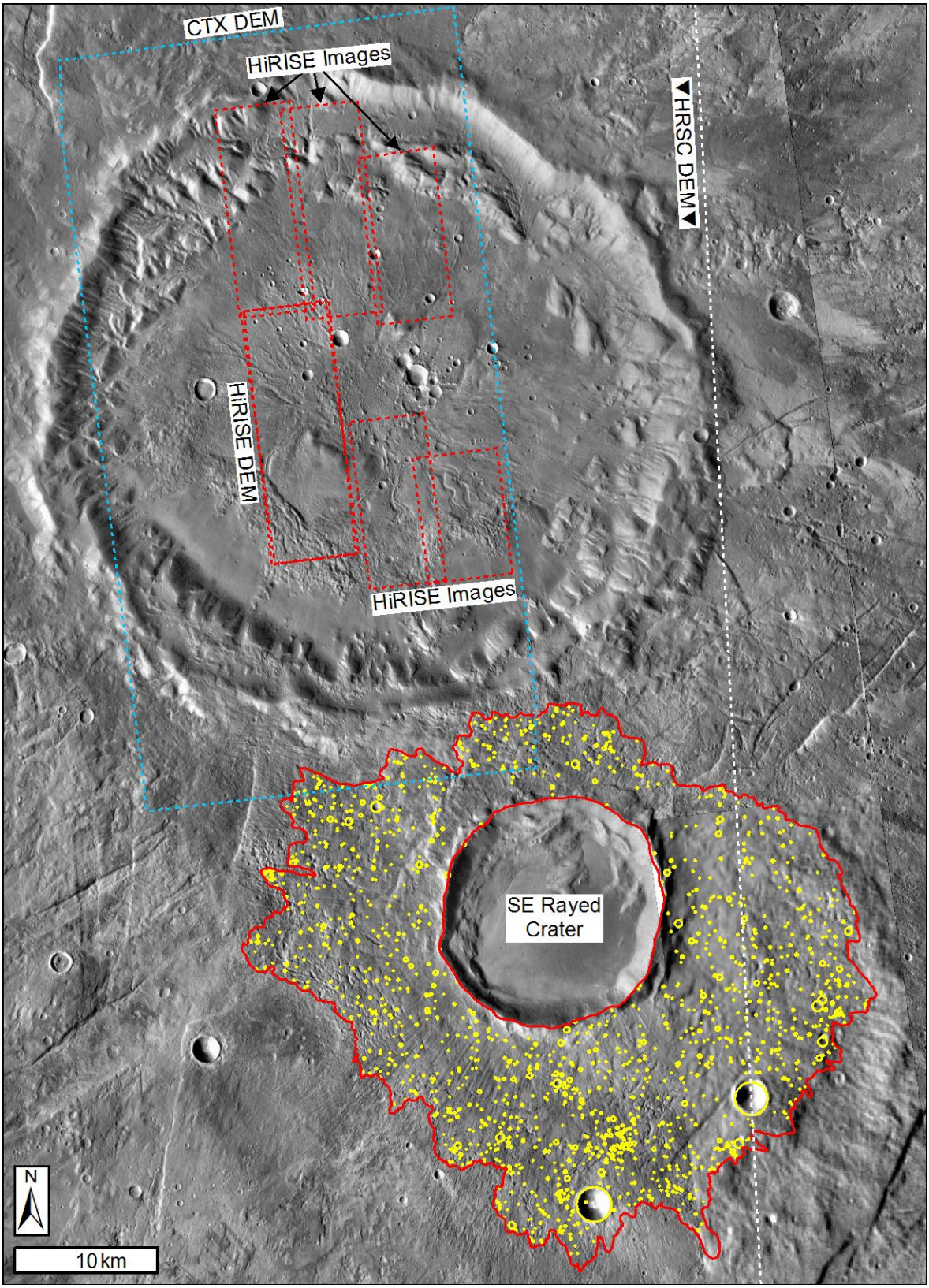

Figure 8.4. Data coverage of Chukhung crater and the rayed impact crater to the SE. The CTX image basemap provided complete coverage of the study area. Dashed boxes show extents of: 7 HiRISE images (red), including a stereo pair from which Mayer and Kite (2016) produced a digital elevation model (DEM); the CTX DEM (blue) from Mayer and Kite (2016); and the HRSC DEM (white dashed line shows easternmost extent). The solid red line shows the area of the impact ejecta of the SE rayed crater for which I obtained impact crater size-frequency statistics. Yellow circles are counted impact craters with diameters > 70 m. See Table 8.1 for data products.

centred on 72.5°W using ESRI ArcGIS 10.1 software. I identified map units on the basis of visual similarities in their surface morphologies. I identified contacts between map units on the basis of changes in surface morphology and/or differences in unit emplacement ages evidenced by superposition relationships. In order to visualise relationships between mapped units, I also viewed the orthorectified CTX image from oblique viewing angles in ESRI ArcScene 10.1, using elevation values extracted from the CTX DEM.

8.4.2. Age Estimations from Impact Crater Size-Frequency Distributions

I measured size-frequency distributions of impact craters in order to estimate: (1) an approximate envelope for the age of Chukhung crater itself, and (2) the minimum age of the last major phase of VFF-surface modification within Chukhung crater. I used the same method as is described in Chapter 4 (see also Gallagher and Balme, 2015), using the *CraterTools* add-in for ArcGIS (Kneissl et al., 2011), and measuring craters on the CTX image basemap.

I identified potential for a significant influence of secondary impact craters upon the size-frequency distributions of measured impact craters. The rayed ejecta of a ~15 km diameter impact crater to the SE of Chukhung crater (hereafter termed the SE rayed crater) superposes the southeastern rim of Chukhung, indicating that it formed after Chukhung crater. It is possible that material that was ejected from the SE rayed crater (or the impactor itself) formed secondary impact craters on its ejecta blanket and in the vicinity of the VFFs in Chukhung crater. Therefore, I performed spatial randomness analyses (Michael et al., 2012) on the measured impact crater populations to assess the influence of secondary craters on the reliability of modelled age estimates. Using the randomness analysis tool in *CraterStats2*, I produced 3000 random spatial distributions of a crater population with the same characteristics as the measured population. Following Michael et al. (2012), I then compared the mean second closest neighbour distance (M2CND) of the measured population (for various ranges of impact crater diameters) to those of the simulated populations (over the same diameter range). For impact crater diameter ranges in which the true M2CND fell within one standard deviation of the mean simulated M2CND, I considered crater distributions to be spatially random. In contrast, for impact crater diameter ranges in which the true M2CND deviated from the mean simulated M2CND by more than one standard deviation, I considered impact craters to be non-randomly distributed. Where this was true, I considered contamination of the impact crater population by secondary impact craters to be important and approached interpretation of modelled ages with caution. Secondary impact craters have the effect of artificially increasing the modelled age of the affected surface.

Spatially heterogeneous resurfacing processes can also cause spatial clustering. In contrast to secondary cratering, resurfacing destroys impact craters, resulting in underestimation of model ages from impact crater size-frequency distributions.

8.4.2.1. Estimation of the Age of Chukhung Crater

The ejecta blanket of Chukhung crater is thin and indistinct. This suggests that model age determination for Chukhung crater based upon the size-frequency distribution of impact craters on its ejecta blanket would be affected by impact craters in the underlying surface and would be unreliable. Therefore, in order to constrain an approximate envelope for the age of Chukhung crater itself, I compared the estimated age of the geologic unit upon which it is superposed (early-Hesperian volcanic unit, eHv; Tanaka et al., 2014b) with new measurements of the size-frequency distribution of impact craters on the better-preserved ejecta blanket of the SE rayed crater that superposes portions of the southeastern rim of Chukhung crater (Figure 8.4). The age estimate for the early-Hesperian volcanic unit by Tanaka et al. (2014b) is based upon the size-frequency distribution of impact craters on a key reference surface centred on 105.96°W, 41.92°S (Icaria Planum; Tanaka et al., 2014a). I measured all undeformed impact craters of diameter (D) ≥ 70 m on the surface of the ejecta blanket of the superposing rayed impact crater to the southeast of Chukhung crater (Figure 8.4). The decametre-scale relief of the topography of this rayed impact ejecta made identification of impact craters with D < 70 m unreliable.

8.4.2.2. Estimation of Impact Crater Retention Age of VFFs

I also analysed the size-frequency distribution of impact craters on the surface of VFFs within Chukhung crater to obtain a minimum age estimate for the termination of the last major modification of the VFF surfaces. I measured all undeformed impact craters of $D \geq 50$ m. Impact craters with diameters of $D < 50$ m could not be distinguished reliably from pits on the VFF surfaces.

8.5. Observations

An enlarged version of the geomorphic map of Chukhung crater (Figure 8.5) is provided in Appendix B. Chukhung is ~45 km in diameter and ~2300 m deep. It hosts multiple crater wall terraces, and a ~10.7 km diameter central floor pit (Robbins and Hynek, 2012) with a maximum depth of 225 m (Figures 8.5 and 8.7). The rim of Chukhung crater's central pit has variable topographic expression (Figures 8.7 and 8.8). A ~2 km wide portion of the NE margin of the central pit is defined by a prominent rim element, which protrudes up to 100 m above the upper level of the crater floor to the NE (Figure 8.7C). In contrast, a ~6 km wide

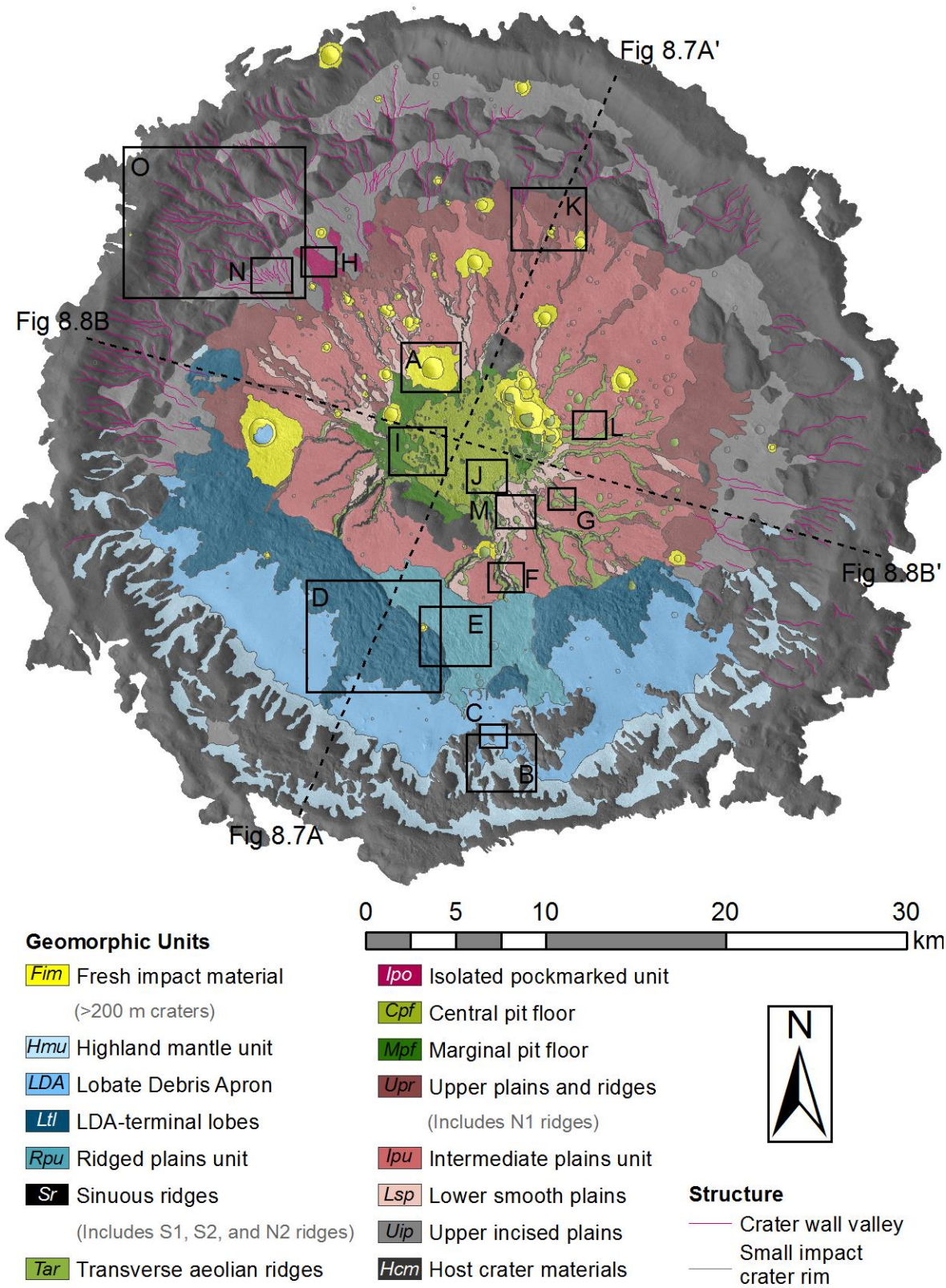

Figure 8.5. Geomorphic map of Chukhung crater. Boxes show extents of panels in Figure 8.6, and dashed lines show locations of profiles A–A' and B–B' in Figure 8.7 and Figure 8.8, respectively. Map overlain on CTX image mosaic (Table 8.1). See Appendix B for enlarged map.

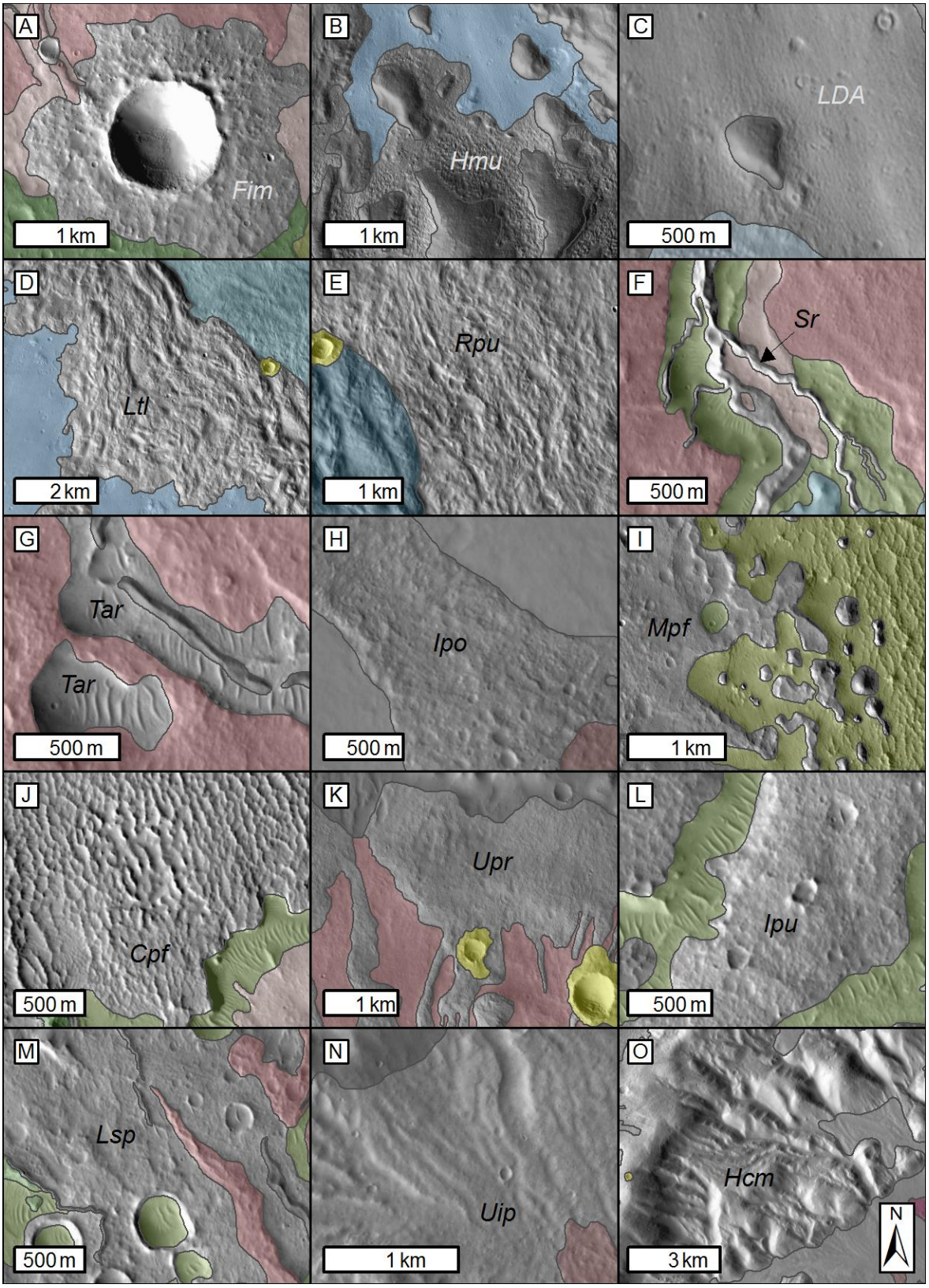

Figure 8.6. CTX images of geomorphic units in Chukhung crater. For clarity, contextual units are coloured, but the subject unit of each panel is not. See Figure 8.5 for extents and unit colour key. (A) Fresh impact material, Fim. (B) Highland mantle unit, Hmu. (C) Lobate Debris Apron, LDA. (D) LDA-terminal lobes, Ltl. (E) Ridged plains unit, Rpu. (F) Sinuous ridges, Sr. (G) Transverse aeolian ridges, Tar. (H) Isolated pockmarked unit, Ipo. (I) Marginal pit floor unit, Mpf. (J) Central pit floor, Cpf. (K) Upper plains and ridges unit, Upr. (L) Intermediate plains unit, Ipu. (M) Lower smooth plains, Lsp. (N) Upper incised plains, Uip. (O) Host crater materials, Hcm. See Table 8.1 for data products.

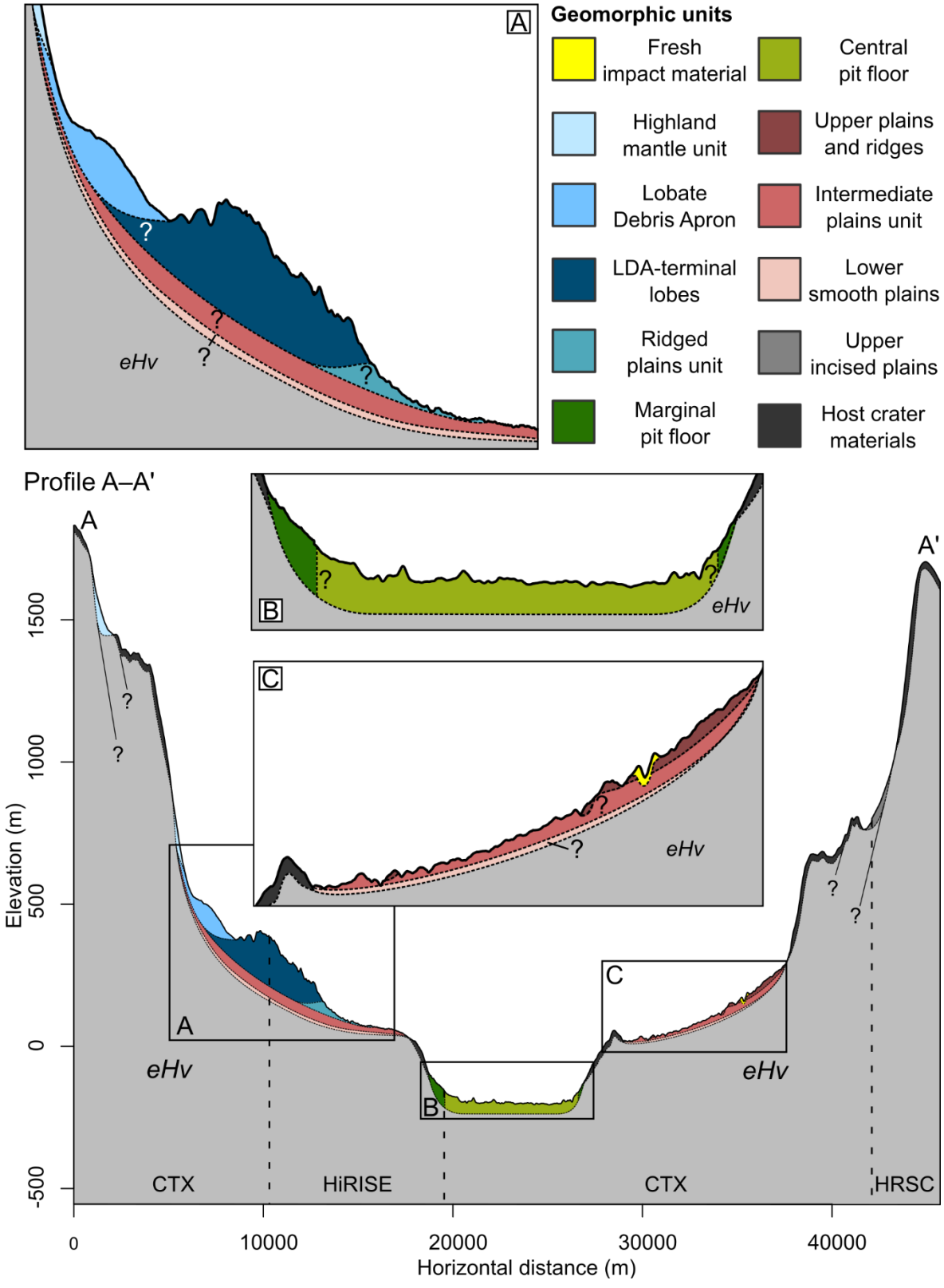

Figure 8.7. Schematic cross-section A–A', showing inferred stratigraphic relationships between mapped units in Chukhung crater. Location of profile A–A' is shown in Figure 8.5. The upper solid line is topography from CTX, HiRISE, and HRSC DEMs at 15 times vertical exaggeration (DEM extents shown by vertical dashed lines; see Table 8.1 for data products), and all contacts below this line have inferred depths and profiles. Boxes show extents of enlarged inset views A, B and C. eHv is the early-Hesperian volcanic unit (Tanaka et al., 2014b). In this topographic profile, Chukhung crater's central pit has well-defined margins.

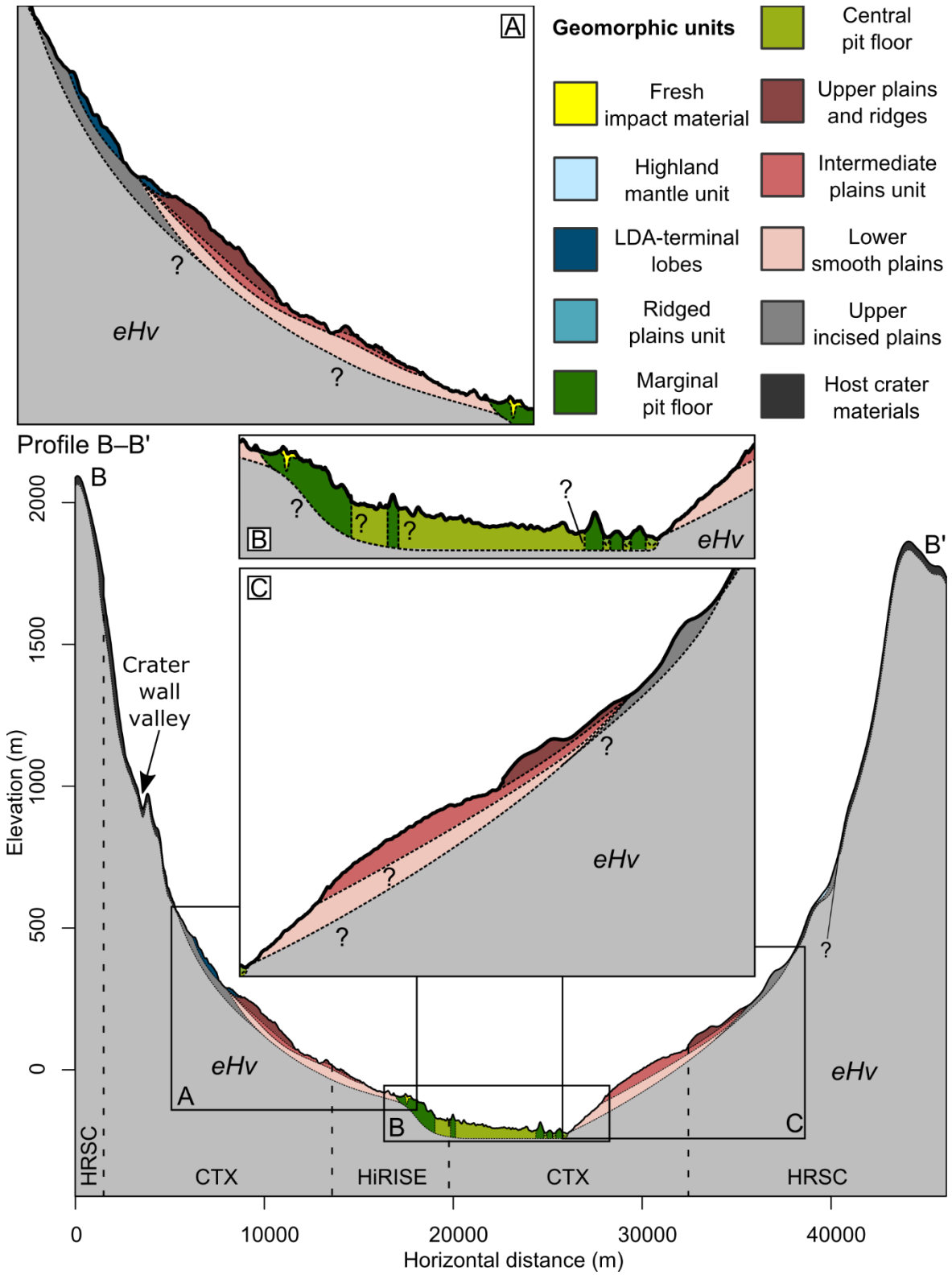

Figure 8.8. Schematic cross-section B–B', showing inferred stratigraphic relationships between mapped units in Chukhung crater. Location of profile B–B' is shown in Figure 8.5. The upper solid line is topography from CTX, HiRISE, and HRSC DEMs at 15 times vertical exaggeration (DEM extents shown by vertical dashed lines; see Table 8.1 for data products), and all contacts below this line have inferred depths and profiles. Boxes show extents of enlarged inset views A, B and C. eHv is the early-Hesperian volcanic unit (Tanaka et al., 2014b). This profile illustrates that the NW margin of Chukhung crater's central pit is poorly-defined, and that the NW portion of the crater floor has a broadly concave topographic profile from the base of the crater wall to the centre of the crater.

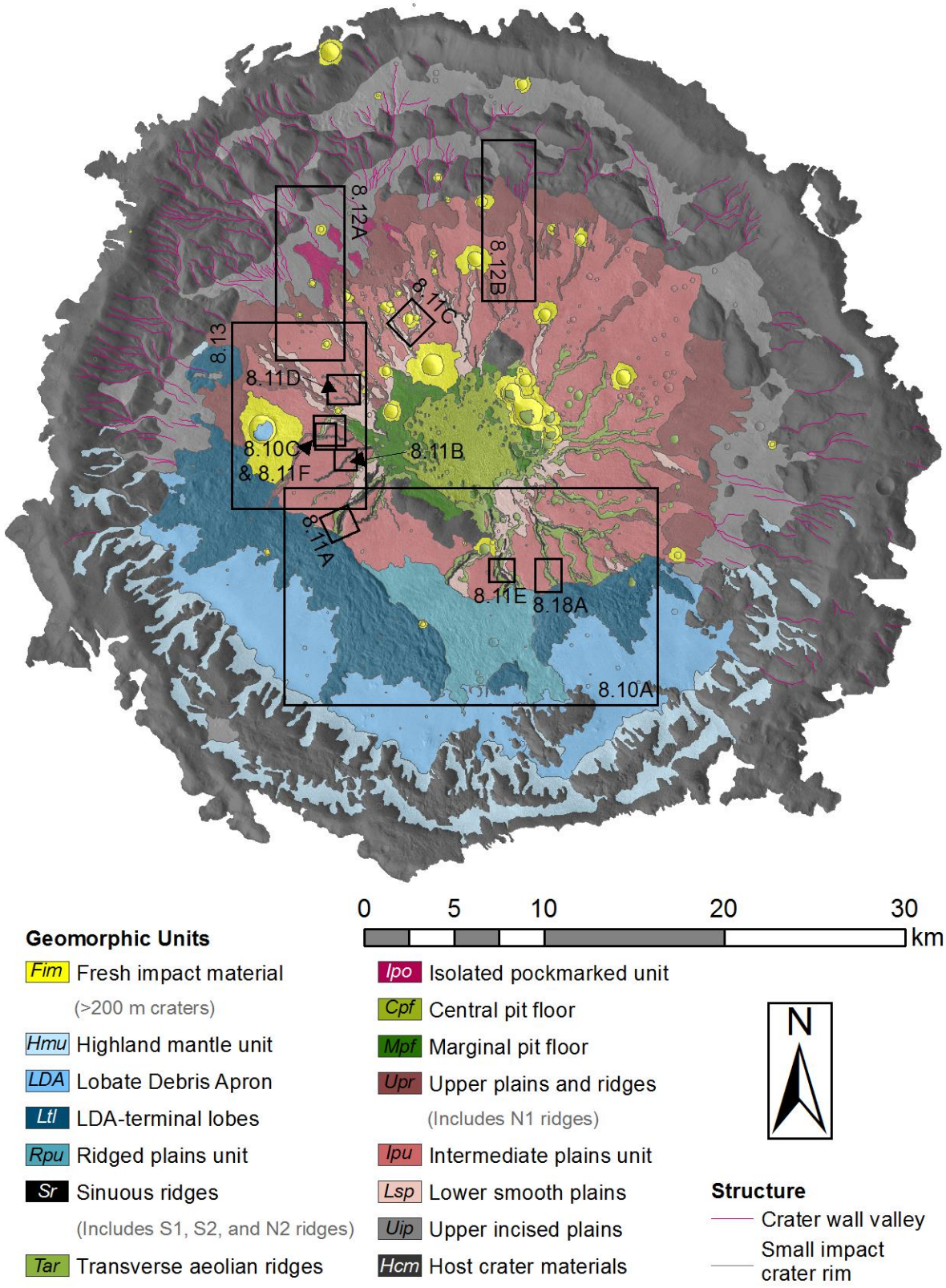

Figure 8.9. Geomorphic map of Chukhung crater showing extents of subsequent figures. See Appendix B for enlarged map.

portion of the SW margin of the central pit is defined by a steep, rounded scarp that grades into the crater floor above, with no evidence of a rim element that protrudes above the elevation of the upper level of the crater floor (Figure 8.7). The S–NE portion of the margin of the central pit is also bounded by a rounded scarp, but appears to have been heavily modified by post-impact processes (Figures 8.5 and 8.8). The N–W portion of the margin of the central pit is topographically indistinct and is not marked by either a scarp or a rim element; a topographic profile from the crater rim to the floor of the central pit has a broadly concave profile (Figure 8.8). The floor of Chukhung crater appears to have undergone significant post-impact modification. It hosts various geomorphic units (Figures 8.5–8.8), which I describe in detail here.

8.5.1. Lobate Debris Aprons and Highland Mantle Units

Pitted and lineated deposits consistent with lobate debris apron (LDA) type VFFs (e.g., Squyres, 1979; Head et al., 2010) extend up to 5 km across the floor of Chukhung crater from the W–SE portions of the crater wall (Figures 8.5, 8.6C, 8.7, 8.8, and 8.10A). Topographic profiles oriented from their headward to their terminal margins are predominantly convex-up (Figure 8.7), though in some areas, they are concave. At their headward margins, LDA surfaces transition gradationally to a highland mantle (Hmu), similar to that which I observed in NW Tempe Terra in Chapter 4 (Butcher et al., 2017), which infills topographic lows in the southern crater wall, including wide (hundreds of metres), low-sinuosity, theatre-headed crater wall valleys, and the upper surfaces of crater wall terraces (Figures 8.5, 8.6B, 8.7, and 8.8). I find no evidence for similar ice-rich LDA or highland mantle deposits on the northern or eastern portions of the crater floor or wall (Figures 8.5, 8.7, and 8.8).

8.5.2. LDA-Terminal Lobes and Ridged Plains Units

The termini of LDA in Tempe Terra are bounded by prominent lobate ridges (LDA-terminal lobes, Ltl) comprising hummocky deposits and concentric parallel ridges (Figures 8.5, 8.6D, and 8.10A). The lobes are oriented parallel to—and extend 2–5 km across the southern crater floor from—the LDA termini (Figures 8.5, 8.7, and 8.10A). LDA materials infill topographic depressions in the upper margins of the LDA-terminal lobes (Figure 8.10), whereas the steep lobe-frontal margins have tens of metres (up to ~100 m) of relief (Figures 8.5, 8.6D, 8.7, and 8.10A). Two ~2 km wide gaps exist in the lobate deposits at the termini of the north-facing LDA (Figures 8.5 and 8.10A). In these zones, the LDA termini transition to low-relief hummocky plains (Figures 8.6E, 8.7, and 8.10A) comprising heterogeneous undulatory

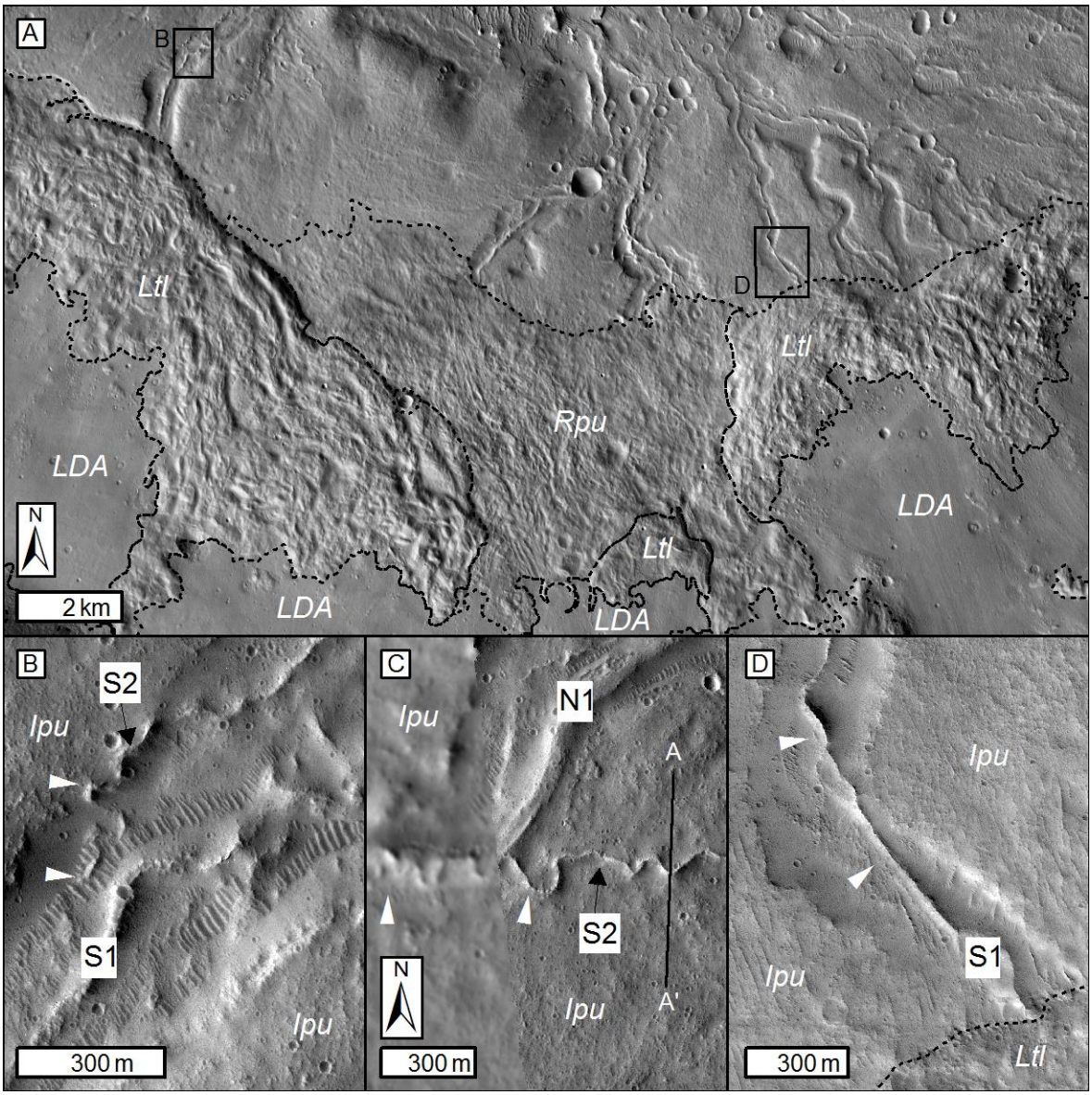

Figure 8.10. Landform associations and sinuous ridges on the southern floor of Chukhung crater. (A) CTX image mosaic showing the LDA-terminal lobes (Ltl) that bound the LDA termini, the Ridged plains unit (Rpu) that occupies a gap in the Ltl, and the emergence of several of the southern sinuous ridges from beneath these units. Black boxes show the extents of panels (B) and (D). (B) HiRISE image showing a sharp-crested S2-type ridge that ascends the wall of a crater floor valley (between white arrows) which is occupied by an S1-type sinuous ridge. (C) HiRISE and CTX images showing a sharp-crested S2-type ridge that superposes the flat-topped crest of the SW branch of the N1-type ridge in Figure 8.13 (between white arrows) and ascends out of the crater floor valley and onto the adjacent intermediate plains (Ipu). Extent in Figure 8.9. (D) HiRISE image showing a sharp-crested S1-type ridge that emerges from beneath LDA-terminal lobe (Ltl) materials and appears to ascend the wall of the crater floor valley that it occupies (between white arrows).

forms that superpose numerous parallel, NNW-oriented lineations with lengths of hundreds of metres (Figure 8.6E). The LDA-terminal lobes and ridged plains units are located only on the southern and western portions of the crater floor, and do not occur on the northern or eastern floor (Figure 8.5).

8.5.3. Southern Sinuous Ridges and Crater-Floor Valleys

The southern floor of Chukhung crater hosts 16 sinuous ridge systems (Figures 8.10 and 8.11A, B, E and F), five of which emerge from beneath the LDA-terminal lobes and ridged plains units (e.g., Figures 8.10A and D, and 8.11A). They extend several kilometres towards the margins of the crater's central pit. Superposition relationships (e.g., Figure 8.11E) suggest that at least two stratigraphically-distinct sets of sinuous ridges exist on the southern crater floor: a stratigraphically-lower set of ridges (hereafter referred to as S1 ridges; Figure 8.11A), and a stratigraphically-higher set of ridges (hereafter referred to as S2 ridges; Figure 8.11B). The S1 ridges (n = 7) have lengths in the range 1480–4050 m (median = 2380 m) and sinuosities in the range 1.05–1.19 (median = 1.08, mean = 1.10), whereas the S2 ridges (n = 9) have lengths in the range 25–4050 m (median = 647 m) and sinuosities in the range 1.00–1.63 (median = 1.11, mean = 1.16). Thus, although ridge sets S1 and S2 have similar median sinuosities, the sinuosities of the younger S2 ridges are more variable, and extend up to significantly higher values than the S1 ridges.

The S1 ridges are predominantly sharp- or round-crested, but ~40% of S1 ridges also have flat-topped sections. The S1 ridge with HiRISE DEM coverage (Figure 8.11A) has a typical height of ~10–20 m, and width of ~150–300 m, with a width-height ratio of ~10–20, and average cross-sectional slopes of ~8–15°. The S2 ridges are sharp-crested. Those with HiRISE DEM coverage (e.g., Figure 8.11B) have typical heights of ~7–10 m, and widths of ~100–150 m, with width-height ratios of ~10–14 and average cross-sectional slopes of ~8–10°.

The S1 ridges occupy broad crater floor valleys (with widths of hundreds of metres and depths of tens of metres; e.g., Figures 8.6F, 8.10 and 8.11A) that extend across the intermediate plains unit (Ipu; Figures 8.5, 8.6L, and 8.11A). The intermediate plains unit is crater-concentric and dominates the crater floor (Figure 8.5). In contrast to the S1 ridges, the S2 ridges do not conform to the crater floor valleys. Four S2 ridges ascend the walls of those valleys and cross onto the adjacent plateaus of the intermediate plains unit (Figures 8.10B–C and 8.11B) and one crosses the intermediate plains without interacting with a crater floor valley. Five S2 ridges superpose S1 ridges, tracking along their crests or crossing over them

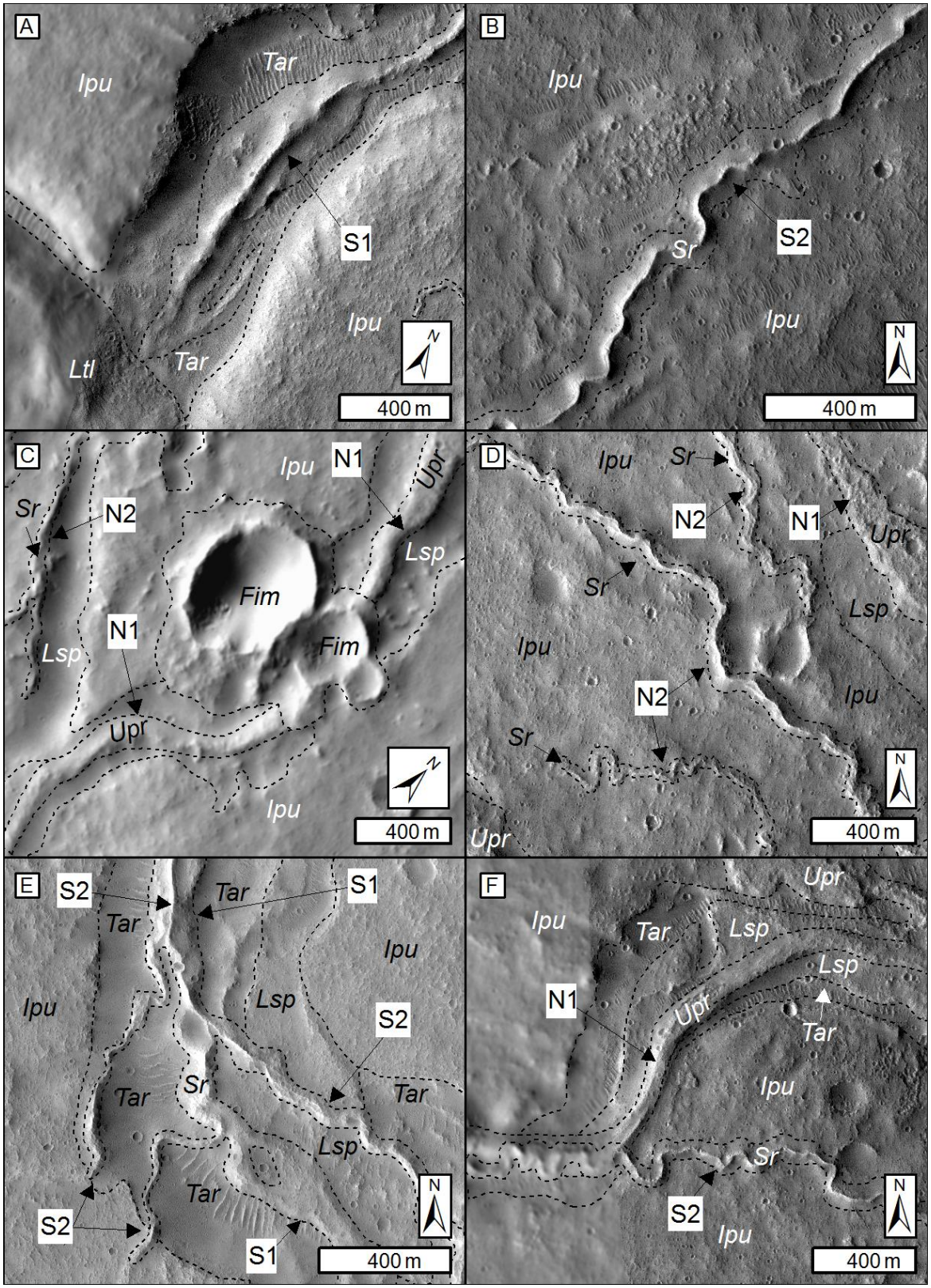

Figure 8.11. Sinuous ridges in Chukhung crater. (A) Sharp- to round-crested S1-type sinuous ridge within a valley on the southern floor of Chukhung crater. (B) Sharp-crested S2-type sinuous ridge crossing a plateau on the southern crater floor. (C) Flat-topped to round-crested N1 sinuous ridge within a valley on the northern portion of the crater floor. It is disrupted by fresh impact material. (D) Sharp-crested N2-type sinuous ridges crossing plains on the northern portion of the crater floor. (E) Dendritic network of sharp-crested S2-type ridges that descend into a valley on the southern portion of the crater floor and superpose the flat-topped crest of an S1-type sinuous ridge on the valley floor. (F) Sharp-crested S2-type ridge that superposes the flat-topped crest of an N1-type ridge on the western (caption continues on next page)

(caption continued from previous page) portion of the crater floor. The S2 ridge crosses onto a plateau to the east of the valley hosting the N1 type ridge. Extents in Figure 8.9. Panels A–B and D–F are HiRISE images. Panel C and a portion of panel F are CTX images. See Figure 8.5 for unit abbreviations and Table 8.1 for data products.

(Figure 8.11E). In two locations, S2 ridge systems form quasi-dendritic networks (Figures 8.5 and 8.11E). There is at least one location where an S1 ridge does not appear to follow the central axis of its host valley, but the ridge does not cross out of the valley in this location (Figure 8.10D).

The valleys within which the S1 sinuous ridges are located are consistently deeper than the height of the sinuous ridges and have visually distinct walls. Nine similar crater floor valleys on the SE and E floor of Chukhung crater do not emerge from beneath the termini of the LDA-terminal lobes or ridged plains units (Figure 8.5). The heads of these valleys commonly emerge from beneath sinuous, finger-like extensions of a smooth plains unit (upper plains and ridges, Usp) that superposes the intermediate plains unit upslope (Figures 8.5, 8.6K, 8.7 and 8.8). Sinuous ridges are uncommon within the valleys on the SE and E floor but are not absent.

The downslope termini of the southern crater floor valleys are indistinct; they open out onto a smooth plains unit (lower smooth plains, Lsp) that extends from the lower margins of the intermediate plains unit, to the margins of the central pit (Figures 8.5 and 8.6M). Lower smooth plains materials are exposed in some portions of the valley floors themselves, but the valley floors are largely obscured by subparallel, valley-transverse curvilinear ridges (Figure 8.6G) that are consistent with transverse aeolian ridges (TARs; e.g., Balme et al., 2008). TARs also occur on the floors of many small impact craters on the southern and eastern floor of Chukhung crater (Figures 8.5 and 8.6G). Where they coexist with sinuous ridges, TARs superpose the flanks and crests of those ridges.

8.5.4. Northern Sinuous Ridges and Crater Floor Valleys

The northern portion of the floor of Chukhung crater also hosts assemblages of sinuous ridges and valleys. As on the southern floor, valleys occur within intermediate plains unit materials, and expose lower smooth plains materials on their floors (Figures 8.9 and 8.11C).

However, in this portion of the crater floor, the valley walls are less visually distinct (being more easily identifiable in topographic profiles than in images), and the surrounding intermediate plains unit has a more rugged and degraded appearance than on the southern floor (Figures 8.12A and 8.13).

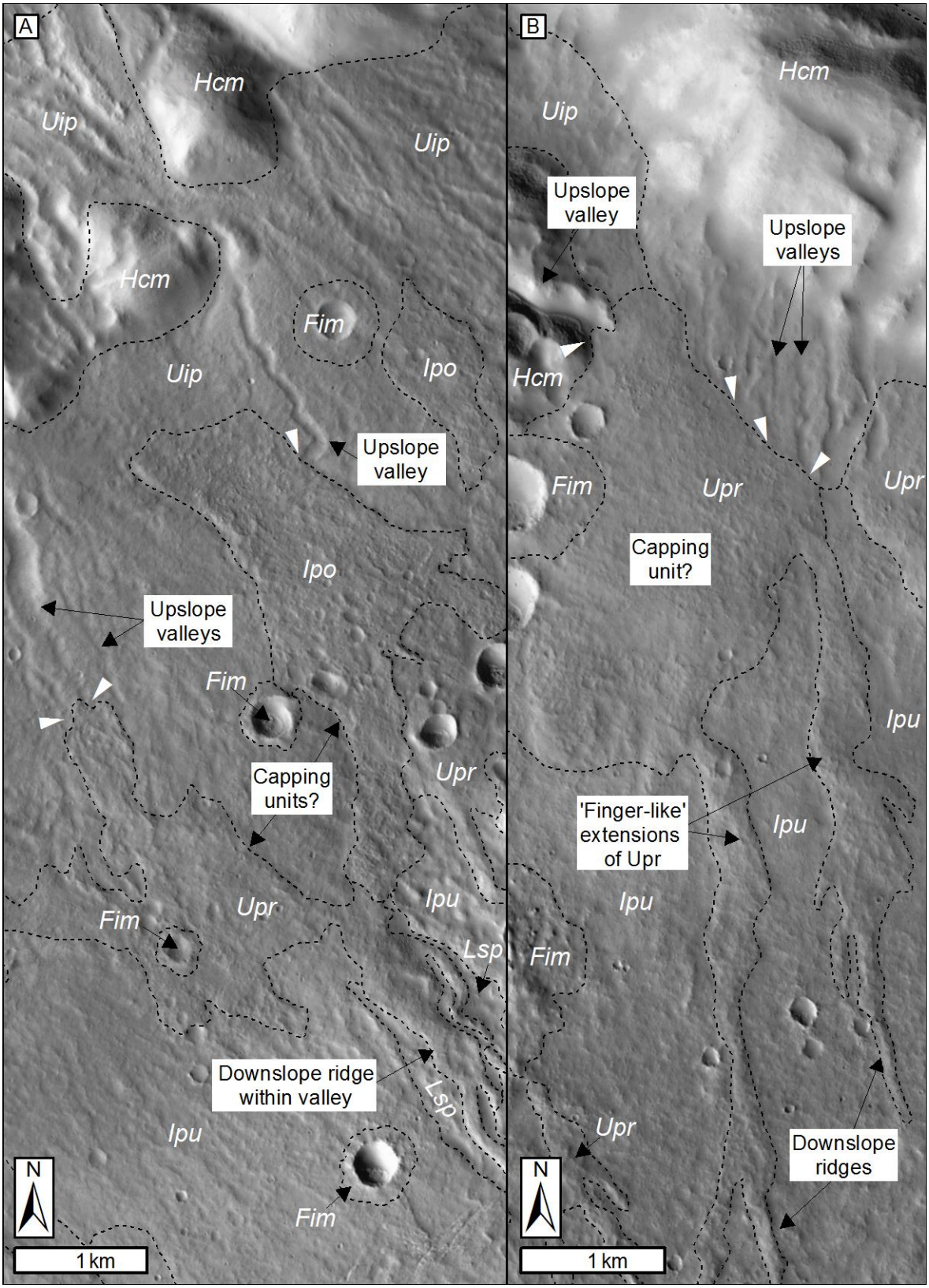

Figure 8.12. Relationships between upslope valleys and downslope sinuous ridges in the northern portion of Chukhung crater. (A) CTX image mosaic showing valleys within the Upper incised plains units that are superposed (white arrows) by the upslope margins of the Upper plains and ridges (Upr) and Isolated pockmarked units (Ipo). Associated sinuous ridges extend downslope from the Upr. (B) CTX image mosaic showing crater wall valleys that are superposed by the Upr unit, and finger-like extensions of the downslope margins of the Upr unit that transition into sinuous ridges downslope. Extents and unit abbreviations in Figure 8.9. See Table 8.1 for data products.

Some of the northern crater floor valleys appear to be longitudinally discontinuous, though ejecta of numerous superposed impact craters commonly obscure their relationships to down-slope valley portions (Figures 8.5 and 8.6C). Unlike in the southern portion of the crater, the floors of these valleys are unobscured by TARs. Similarly to the valleys on the southeastern and eastern portion of the crater floor that are not associated with LDA-terminal lobes or ridged plains units, the valleys on the northern floor of Chukhung crater commonly emerge from beneath sinuous, finger-like extensions of a smooth upper plains unit (upper plains and ridges unit, Upr; Figures 8.5, 8.6K, 8.12). On the northern floor, many—though not all—of these finger-like features are continuous or aligned with sinuous ridge systems (hereafter referred to as N1 ridges, n = 18; Figures 8.11C, 8.12, and 8.13), whose paths appear largely to conform to the axes of the valleys within which they occur (Figure 8.11C). Approximately 20% of the sinuous ridges that extend from the upper plains and ridges unit are not clearly associated with crater floor valleys (Figure 8.12B).

The N1 ridges have lengths of ~0.15–7.5 m and low sinuosities in the range 1.00–1.17 (median and mean = 1.05). The N1 ridges have more variable crest morphologies (including sharp-crested, round-crested, multi-crested, and flat-topped) and more rugged surface textures than other sinuous ridge features in Chuhkung crater (Figures 8.12 and 8.13). They have variable topographic expression, ranging from prominent ridges to low-relief features. In locations with high-resolution HiRISE DEM (Figure 8.11F) coverage and medium-resolution CTX DEM coverage, prominent ridge portions have heights of ~5–20 m, and widths of ~150–1100 m, with width-height ratios of ~15–60, and average cross-sectional slopes of 2–7°.

A notable N1-type sinuous ridge network occurs on the WNW portion of the crater floor (Figure 8.13). It has a flat-topped to multi-crested morphology, and a complex network morphology. It has multiple branches that extend from the upper plains unit to the NW, and another branch that emerges from beneath the LDA-terminal lobe unit to the SW and merges with the NW branch close to the margins of the crater's central pit (Figure 8.13). The portion of the upper plains and ridges unit from which it emerges appears to be layered (Figure 8.13, white arrows). Two of the NW branches appear to form an anabranching network morphology, but close inspection suggests that one branch may superpose the other, and that the branches could be at different stratigraphic levels (Figure 8.13, inset). The SW branch that emerges from the LDA-terminal lobe is superposed by an S2 sinuous ridge (Figures 8.11F and 8.13), which cuts west-to-east across the valley, weaving along a ~600 m portion

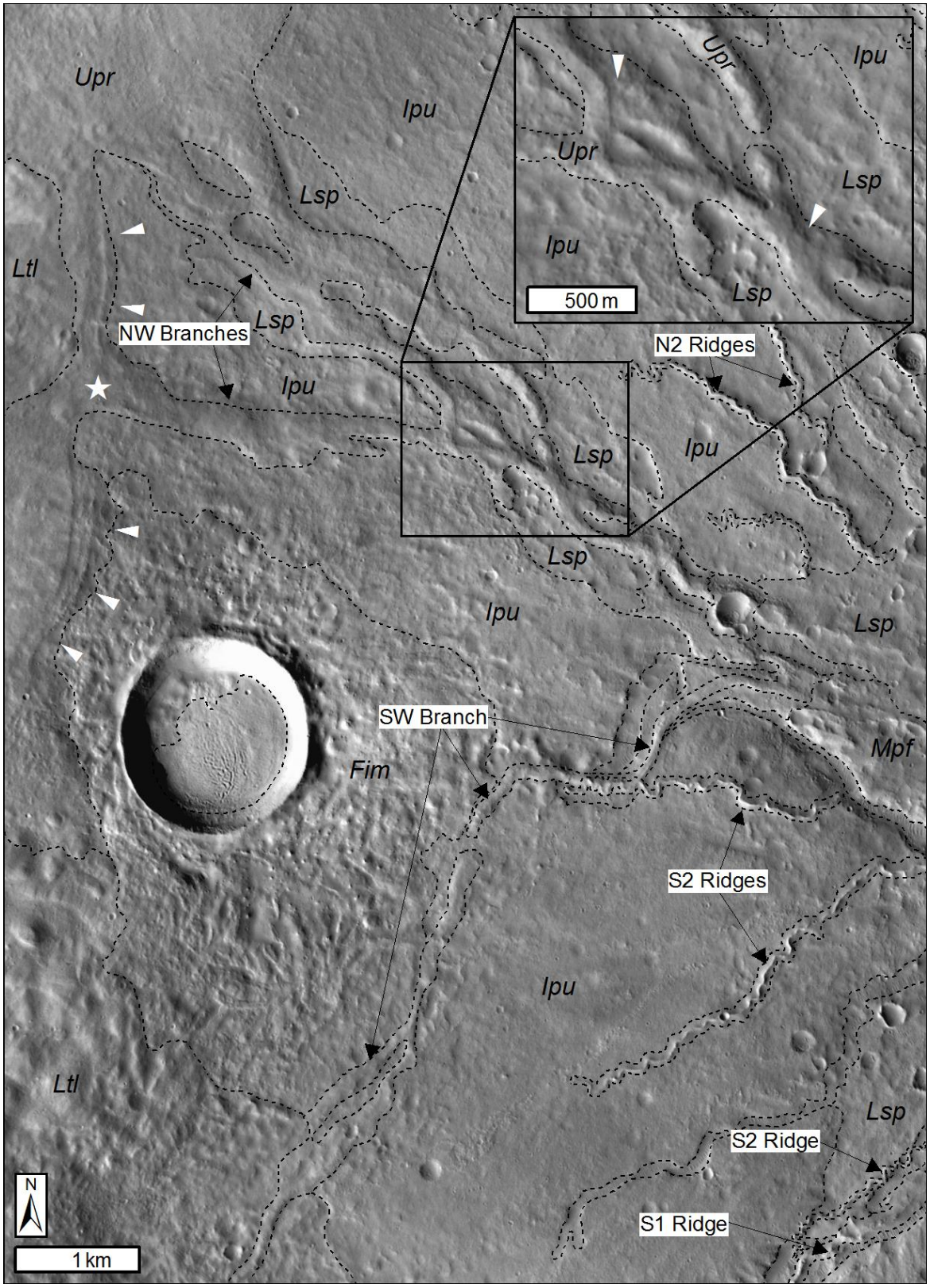

Figure 8.13. A prominent N1-type sinuous ridge on the NW floor of Chukhung crater. Key units labelled (see Figure 8.5 for abbreviations). Plains-forming Upr materials appear to host internal layering (white arrows) where one of the NW branches emerges (white star). The NW branches may represent an anastomosing channel network, but subtle differences in the elevations of the surfaces of crossing ridges (white arrows in inset) may instead indicate that they represent migratory channel systems at different stratigraphic levels. The SW branch emerges from the LDA-terminal ridge unit and is superposed by an S2-type ridge on the SW portion of the crater floor. The NW and SW branches converge where they grade into materials of the marginal pit floor unit. CTX image mosaic (Table 8.1).

of the crest of the N1 ridge before extending eastward across the adjacent intermediate plains unit.

Eleven sharp-crested, high-sinuosity ridge systems (hereafter referred to as N2 ridges) with very similar typical heights, widths, width-height ratios and average cross-sectional slopes to the S2 ridges on the southern portion of the crater floor, also occur on the northern portion of the floor of Chukhung crater (Figures 8.5 and 8.11D). They have sinuosities in the range 1.03–2.12 (median = 1.3, mean = 1.3), similar to the S2 ridges but extending to a higher maximum sinuosity. One example comprises two branches that extend along a valley network which emerges from beneath a finger-like extension of the upper plains and ridges unit (to the NE of the box demarcating the extent of Figure 8.6A in Figure 8.5). None of the N2 ridge systems appear to ascend valley walls or cross the crests of N1 type ridges.

In many locations, the relationship between the northern sinuous ridges and deposits in the central pit are obscured by small impact craters. However, where they can be traced to its margins, they appear to grade into deposits within the central pit.

8.5.5. Central Pit Units

As described in Section 8.5, the N–W margins of Chukhung crater's central pit lack topographic expression, and topographic profiles from the upper level of the crater floor to the centre of the central pit are broadly concave (Figure 8.8). Two of the major sinuous ridge networks that extend across the NW portion of the floor of Chukhung crater appear to transition into a smooth unit that occupies the inner margins of the central pit (marginal pit floor unit, Mpf; Figures 8.5, 8.6I, 8.13). This unit extends unbroken from the northern margin of the central pit, westward around its margins, to the base of the scarp that defines the southwestern margin of the central pit (Figure 8.5). The marginal pit floor unit occurs on a general slope towards the SE (Figure 8.8), but well-preserved portions of its surface have flat tops (Figure 8.6I).

The eastern margins of the marginal pit floor unit are abrupt, and have tens of metres of relief (Figures 8.6I and 8.8). Numerous outlying flat-topped and rounded mesas of marginal pit floor materials occur to the east of the margins of the main deposit, their spatial density reducing towards the centre of the central pit (Figures 8. 5 and 8.6I). Similar mesas also occur around the NE, W and S margins of the floor of the central pit, and at the terminus of one S1 ridge in the southern sinuous ridge population (Figure 8.5).

The mesas of the marginal pit floor are surrounded by the unit that dominates the central portion of the floor of Chukhung's central pit. The central pit floor (Cpf) unit is ~30 m lower

in elevation than the marginal pit floor and hosts a high density of variably-oriented ridges in highly interconnected networks (Figure 8.6J). These ridges are morphologically consistent with networks of interconnected TARs (e.g., Balme et al., 2008). The SE margin of the central pit floor unit is marked by a steep, ~20–30 m high scarp (Figure 8.6J), which suggests that the unit is lithified. This scarp forms the wall of a ~400 m wide trench that separates the central pit floor unit from the SE wall of the central pit. The floor of this trench is occupied by numerous subparallel, trench-transverse TARs (Figure 8.6J).

8.5.6. Crater Wall Valleys and Upper Incised Plains

All portions of the wall of Chukhung crater that are not superposed by the LDA or highland mantle units host high densities of sinuous, dendritic, kilometre-scale valley networks (Figures 8.5 and 8.6O). These valley networks are considerably smaller in scale than the regional, 100 km scale, Noachian-aged valley networks discussed in Chapter 2. Many of valleys in Chukhung crater incise smooth plains deposits (upper incised plains, Uip; Figures 8.5, 8.6N, and 8.12) that occupy topographic lows in the crater wall (e.g., crater wall terraces), and in places, extend several kilometres from the foot of the crater wall to the upper margins of the upper plains and ridges unit (Figure 8.12A). The upper plains and ridges unit overlies the upper incised plains unit (Figures 8.7 and 8.12). In some locations, valleys within the upper incised plains are aligned with sinuous ridges and valleys that extend from the downslope margins of the upper plains and ridges unit (Figures 8.5 and 8.12). This relationship is particularly distinct where isolated patches of rough, pockmarked material (Isolated pockmarked unit, Ipo; Figures 8.6H and 8.12A) superpose both the upper incised plains and the upper plains and ridges units (Figure 8.12A).

8.5.7. Impact Crater Retention Ages

8.5.7.1. Age Estimation for Chukhung Crater

Chukhung crater is located within the early-Hesperian volcanic (eHv) unit, defined by Tanaka et al. (2014b) as regionally-sourced flood lavas. Impact crater size frequency distributions return a best-fit model age of 3.59 Ga for the eHv unit (Tanaka et al., 2014a), providing a maximum bounding age in the early Hesperian for Chukhung crater.

The size-frequency distribution of impact craters superposed upon the impact ejecta blanket of the SE rayed crater, which superposes the SE rim of Chukhung crater (Figure 8.4), is displayed in Figure 8.14. In total, I counted 1457 impact craters with $D \geq 70$ m over the superposed impact ejecta (8.63×10^2 km^2; Figures 8.4 and 8.14), 1436 of which fall along isochrons defined by Hartmann and Neukum (2001). D(70–150 m) impact craters (n = 1187)

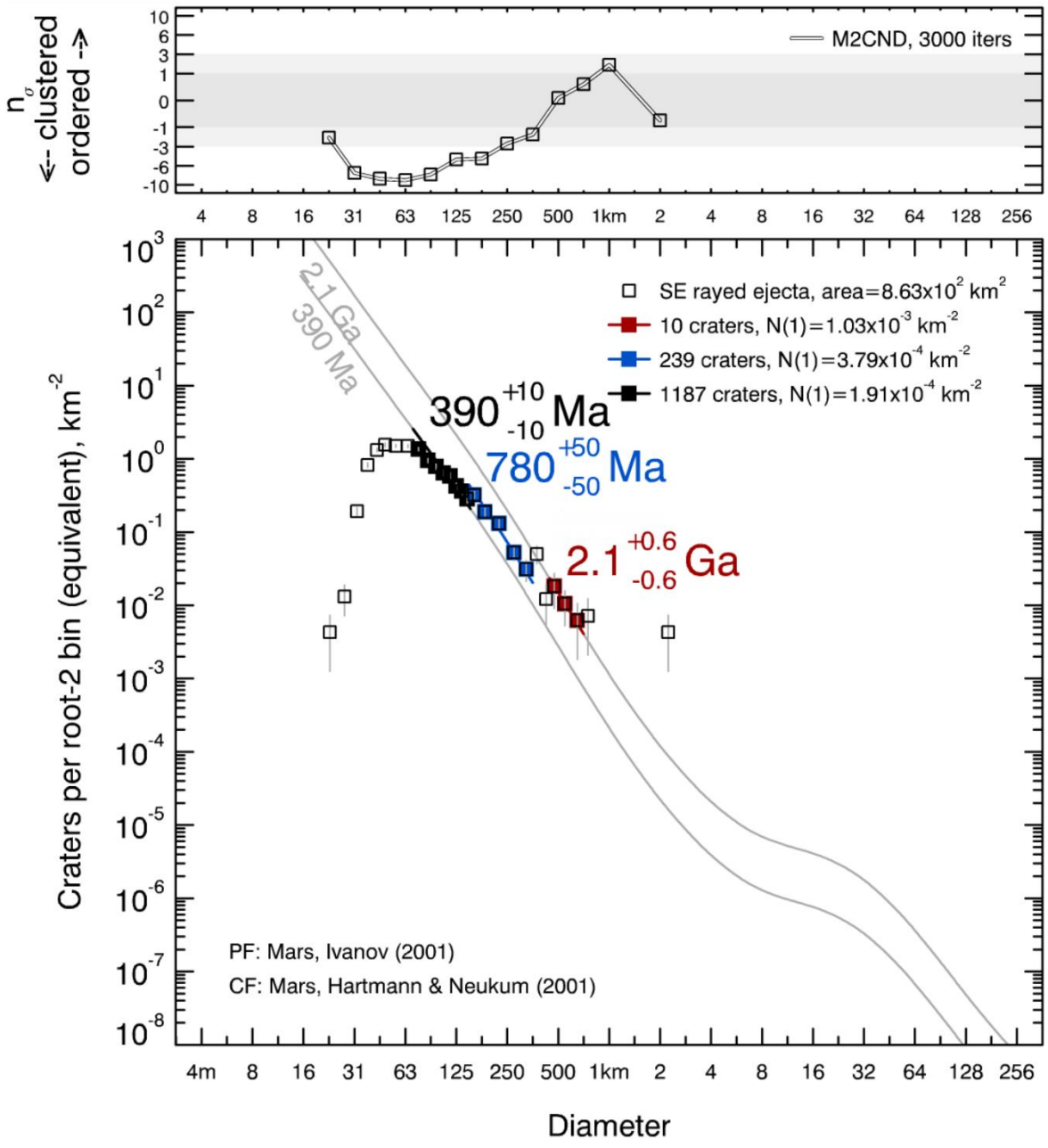

Figure 8.14. Impact crater size-frequency distribution for the ejecta blanket of the SE rayed impact crater. The lower axes are a log incremental plot (Hartmann, 2005) showing best-fit ages that follow three isochrons. Modelled ages are based upon the Ivanov (2001) production function and the Hartmann and Neukum (2001) chronology function. The count area and locations of counted craters are displayed in Figure 8.4. The roll-off for diameters < 70 m represents the lower limit for reliable detection of impact craters. The upper axes show the results of spatial randomness analyses (Michael et al., 2012); the y-axis represents the number of standard deviations by which the M2CND of 3000 simulated impact crater populations deviates from the M2CND of the real impact crater population. Points within the grey region show that impact craters in the real population (and within the associated diameter bin) approach a spatially random distribution with increasing diameter. Points below the grey region show that impact craters in the real population (and within the associated diameter bin) are spatially clustered, possibly indicating the presence of secondary impact craters or the occurrence of heterogeneous resurfacing.

follow the 390 ± 10 Ma isochron, *D*(150 m–350 m) impact craters (n = 239) follow the 780 ± 50 Ma isochron, and *D*(450 m–700 m) impact craters (n = 10) follow the 2.1 ± 0.6 Ga isochron. I use the best-fit age (2.1 ± 0.6 Ga) derived from *D*(450 m–700 m) impact craters as a conservative estimate of the impact crater retention age of the superposed impact ejecta blanket. Spatial randomness analyses (Figure 8.14) of measured craters suggest that *D*(450 m–700 m) craters, from which this age estimate was obtained, are spatially random, and therefore that their size-frequency distribution is unlikely to have been strongly influenced by resurfacing and/or secondary cratering processes. However, I emphasise that this best-fit age is derived from a small sample of impact craters (n = 10). Combined with the small count area (Warner et al., 2015), this introduces significant uncertainty in the 2.1 ± 0.6 Ga age estimate. Spatial randomness analyses show clustering of *D*(70 m–350 m) impact craters that were used to derive fits to the 390 Ma and 780 Ma isochrons; thus, these fits may reflect resurfacing and/or secondary impact cratering events during the mid Amazonian. Considering these impact crater size-frequency analyses and the age of the eHv unit within which Chukhung crater is located (Tanaka et al., 2014a), Chukhung crater probably formed ~3.6–2.1 Ga, between the early Hesperian and early Amazonian.

8.5.7.2. LDA Impact Crater Retention Age

I measured 309 impact craters on all LDAs within Chukhung crater (1.25×10^2 km^2; Figure 8.15), 133 of which fall along the Hartmann and Neukum (2001) isochrons. *D*(50–90 m) impact craters (n = 274) follow the 84 ± 7 Ma isochron, while *D*(150–300 m) impact craters (n = 10) follow the 330 ± 90 Ma isochron. However, spatial randomness analyses suggest that the true M2CNDs (see Section 8.4.2) of *D*(50–200 m) impact craters fall ~0.5–1.5 standard deviations below those simulated for similar impact crater populations with spatially random distributions. Thus, spatial clustering of impact craters could make both modelled best-fit age estimates unreliable. Additionally, dependence upon impact craters with $D < 100$ m was unavoidable, potentially introducing a factor of ten uncertainty in the 84 ± 7 Ma fit (Hartmann, 2005). It should also be noted that the minimum age estimate for the LDAs (330 ± 90 Ma) relies upon a small sample of impact craters (n = 10), introducing additional uncertainty into this estimate. These uncertainties are unavoidable and necessitate caution in interpretation of the ages of LDAs in Chukhung crater. However, the key result, that the LDAs are young relative to the age of Chukhung crater itself, remains.

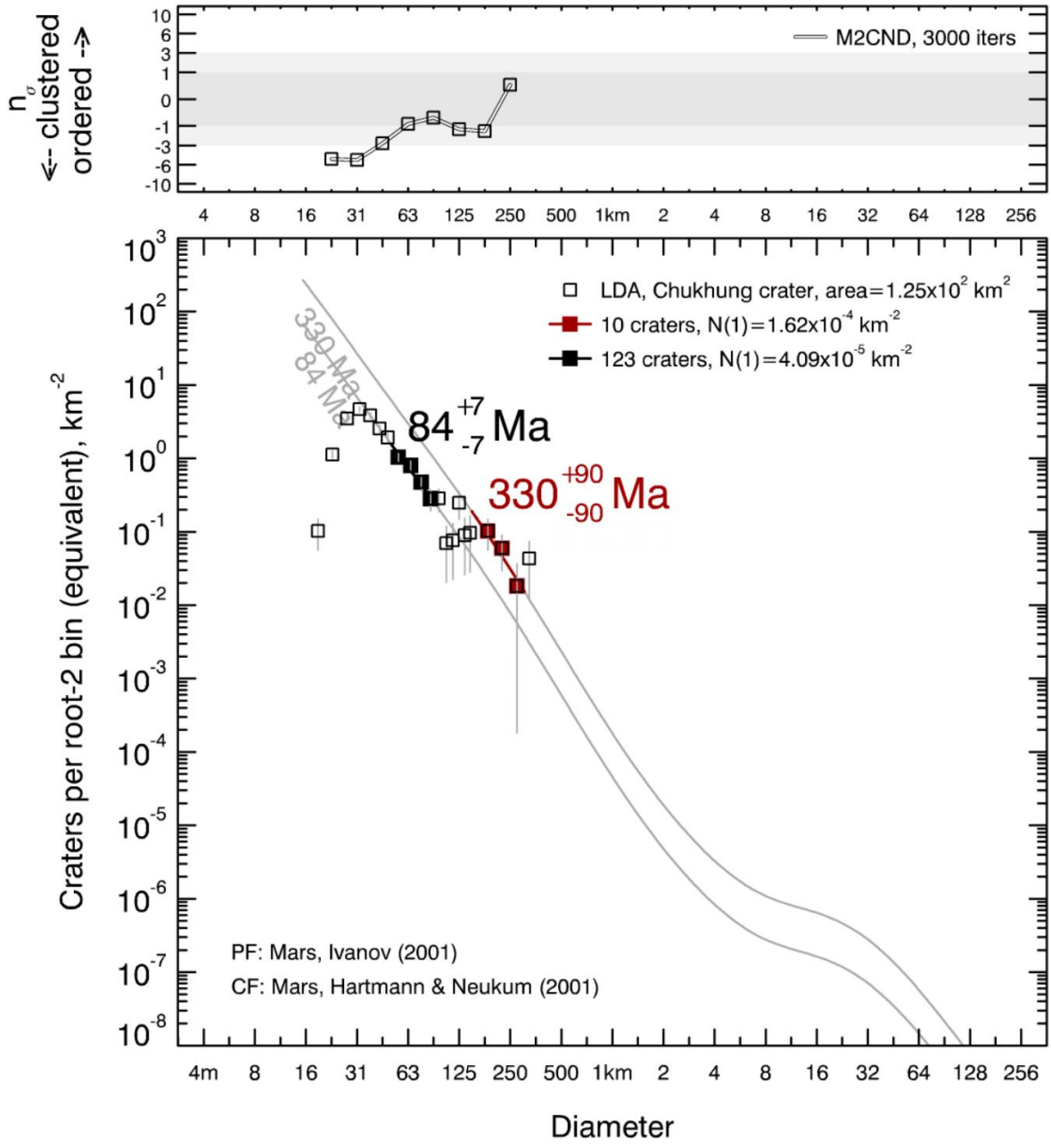

Figure 8.15. Impact crater size-frequency distribution for LDA in Chukhung crater. The lower axes are a log incremental plot (Hartmann, 2005) showing best-fit ages that follow two isochrons. Modelled ages are based upon the Ivanov (2001) production function and the Hartmann and Neukum (2001) chronology function. The roll-off for diameters < 50 m represents the lower limit for reliable detection of impact craters. The upper axes show the results of spatial randomness analyses (Michael et al., 2012); the y-axis represents the number of standard deviations by which the M2CND of 3000 simulated impact crater populations deviates from the M2CND of the real impact crater population. Points within the grey region show that impact craters in the real population (and within the associated diameter bin) approach a spatially random distribution. Points below the grey region show that impact craters in the real population (and within the associated diameter bin) are spatially clustered, possibly indicating the presence of secondary impact craters or the occurrence of resurfacing.

8.6. Discussion

The floor of Chukhung crater has undergone significant post-impact modification. In the discussion that follows, I present evidence that post-impact processes within Chukhung crater included ancient subaerial fluvial activity, and more recent glaciation. I first consider the hypothesis that landform assemblages in the southern portion of Chukhung crater, including the LDA-terminal lobes, ridged plains units, and the southern sinuous ridges were formed by glaciation, and that the southern sinuous ridges are eskers (Section 8.6.2). I then consider evidence for non-glacial (i.e., subaerial) fluvial processes recorded in landform assemblages in the northern portion of Chukhung crater (Section 8.6.1). In Section 8.6.2, I return to discussion of the southern sinuous ridges and consider the challenges for the esker hypothesis in the context of evidence for protracted pre-glacial fluvial activity in Chukhung crater, and consider the alternative hypothesis that all sinuous ridges in Chukhung crater are inverted palaeochannels. Finally, I review the challenges that remain for discriminating eskers from inverted palaeochannels on Mars (Section 8.6.2) in the context of my observations from Chukhung crater.

8.6.1. Fluvial Activity and the Inverted Palaeochannel Hypothesis

Central pit craters on Mars commonly host valley networks and other landforms of fluvial origin (e.g., alluvial fans and palaeolake deposits) that have been attributed to localised precipitation and/or snowmelt during the Hesperian or Amazonian (Peel and Fassett, 2013). These valley networks commonly occur on the floors of central pit craters and on the crater walls. In some central pit craters, crater wall valleys are continuous with crater floor valleys. Peel and Fassett (2013) identified Chukhung crater as hosting such valley networks, and noted that several of those valleys are topographically inverted. My observations of the northern portion of Chukhung crater are in agreement with those of Peel and Fassett (2013).

The ubiquitous occurrence of dendritic valley networks on the unglaciated portions of the walls of Chukhung crater (Figure 8.5) is consistent with subaerial fluvial drainage from a distributed source of liquid water, such as precipitation as rain or snowmelt (Peel and Fassett, 2013). Given the continuity of crater wall valleys with valleys in the upper incised plains unit, and the tendency of this unit to infill topographic lows, I interpret the upper incised plains as comprising subaerial fluvial deposits. The alignment of several valleys within the upper incised plains with finger-like extensions from the downslope margins of the upper plains and ridges unit (Figure 8.12) leads me to propose that the upper plains and ridges unit comprises resistant materials (indurated and/or coarse-grained). These were deposited atop the upper incised plains and within the crater floor valleys downslope, and promoted

topographic inversion of channels downslope to form inverted palaeochannels. Visible layering within portions of the upper plains and ridges unit (Figure 8.13), and their associations with crater floor valleys, are consistent with their origins as fluvial deposits.

The occurrence of many of the northern sinuous ridges within negative-relief crater floor valleys suggests that the sinuous ridges probably represent valley-interior channels or channel belts (e.g., Cardenas et al., 2018), and that these interior deposits were exhumed by removal of more susceptible materials on the valley floors. Sinuous ridges that appear to cross one another, possibly at different stratigraphic levels, along the major sinuous ridge network on the NW floor of Chukhung crater (Figure 8.13) suggest that topographically inverted palaeochannels on the northern floor might represent resistant remnants of migratory channel systems (e.g., Williams et al., 2007). The rugged texture of the intermediate plains unit in the northern portion of Chukhung crater, and the visual subtlety of the valley walls, suggests that significant regional deflation may have accompanied channel exhumation, but that this deflation was insufficient to completely erase the original valleys within which the fluvial channels occurred.

The isolated pocked capping unit shows similar relationships with upslope valleys and downslope sinuous ridges to those that I have observed with the upper plains and ridges unit (Figure 8.6H). However, the limited, discontinuous extent of the isolated pocked capping unit leads me to suggest that this unit did not play a significant role in the broad-scale topographic inversion of the crater floor (e.g., as a resistant capping unit). Its pockmarked texture, patchy distribution, and lack of clear source within the crater leads me to suggest that it may be an airfall deposit, but its limited extent means its origins are difficult to constrain with confidence and I do not speculate further.

Peel and Fassett (2013) noted common relationships between valley networks and sedimentary deposits within central floor pit craters on Mars, which they interpreted as fluvial or lacustrine in origin. Given that several of the northern sinuous ridges grade into the marginal pit floor unit (e.g., Figure 8.13), I propose that this unit represents erosional remnants of lithified fluvial or lacustrine deposits that were transported to Chukhung crater's central pit by fluvial valley networks. The surfaces of well-preserved portions of this unit, and associated mesas, are flat-topped, and could reflect equipotential surface levels of a former palaeolake. Alternatively, the marginal pit floor unit could represent highly eroded remnants of alluvial fan deposits, which may be more consistent with the general slope of this unit towards the SE (Figure 8.8). I suggest that the marginal pit unit previously provided more extensive coverage of the floor of the central pit. Evidence supporting this suggestion

includes: (a) the termination of this unit in a steep valley-distal scarp with relief of tens of metres (Figure 8.6I); (b) the existence of several isolated mesas of marginal pit floor materials beyond this scarp, and around N and E margins of the central pit (Figure 8.5); and (c) significant evidence for aeolian modification of valley-distal materials on the central pit floor (in the central pit floor unit; Figure 8.6J), suggesting that materials in this location have been heavily modified, and possibly removed. I propose that aeolian erosion has promoted retreat of the valley-distal scarp of the marginal pit floor unit, with some remnants preserved as outlying mesas, and that the central pit floor unit has become exposed by the removal of this material. Preferential preservation of fluvial deposits within the marginal pit floor unit close to the termini of the northern sinuous ridges (Figures 8.7 and 8.8) is consistent with the deposition of coarse-grained sediments proximal to the contributory valley networks. Deposition of susceptible, fine-grained sediments in valley-distal positions close to the centre of the central pit would explain preferential aeolian modification and retreat of the marginal pit floor unit from this location. The ~30 m deep trench along the SE margin of the central pit floor (Figure 8.6J) unit suggests that post-impact deposits of at least 30 m thickness remain on the floor of the central pit beyond the margins of the marginal pit floor unit, and that headward erosion of these central pit floor unit materials toward the NW has also occurred, but not to the same extent as the marginal pit floor unit.

8.6.2. Glaciation and the Esker Hypothesis

Landform relationships on the northern wall and floor of Chukhung crater (including association of the northern sinuous ridges with upslope valleys and a possible capping unit, and evidence for migration of ridge-forming flows) are most consistent with the origins of the northern sinuous ridges as inverted palaeochannels. Given the lack of evidence for past or present glaciation or ice-rich mantling of the northern wall or floor of Chukhung crater, I argue that the hypothesis that the northern sinuous ridges are inverted palaeochannels is considerably more likely than the alternative hypothesis that they are eskers.

In contrast, the southern portion of Chukhung crater is glacierised in the present day. The surfaces of many portions of the LDA are convex-up in topographic profile, and may retain a substantial ice content in their interiors. However, concave longitudinal topographic profiles along some portions of the LDA, and the highly tortuous LDA termini (as opposed to smooth, lobate termini) imply that the LDA have probably undergone significant downwasting (probably via sublimation) and retreat since glacial maximum.

I suggest that the LDA-terminal lobes that consistently bound LDA deposits on the southern floor may represent moraines deposited by the LDA. Hummocks and arcuate ridges within the LDA-terminal lobes are morphologically similar to hummocky moraines on Earth, which commonly contain substantial ice cores (e.g., Hambrey et al., 1997; Krüger and Kjær, 2000). In their global survey of martian impact craters using THEMIS daytime infrared images (100–233 m/pixel resolution), Robbins and Hynek (2012) categorised these deposits as crater wall slump deposits formed by mass wasting of the crater wall or rim. I suggest that the higher-resolution CTX and HiRISE images, and topographic data analysed in the present study support a moraine interpretation because: (a) the lobes are consistently spatially associated with LDA, and (b) I find insufficient evidence for a source region (e.g., consistently spatially-associated crater wall alcoves, depressions in the elevation of the crater rim, or topographic asymmetry between the northern and southern crater walls) for a slump event of the magnitude implied by the extensive and voluminous nature of the LDA-terminal lobes. Thus, I suggest that the LDA in Chukhung crater previously extended at least to the northernmost margins of the LDA-terminal lobe unit.

8.6.2.1. LDA Crater Retention Ages

The majority of *D*(40–90 m) impact craters on LDAs in Chukhung crater have bowl-shaped morphologies, while *D*(150–300 m) impact craters have 'ring-mold' morphologies (Kress and Head, 2008; Baker and Carter, 2019a) that have been attributed to modification of impact craters by deposition and modification of ice-rich dust mantle atop LDA surfaces (Baker and Carter, 2019a). Thus, the best-fit age of 78 ± 4 Ma derived from *D*(40–90 m) impact craters (dominated by bowl-shaped morphologies) probably reflects an episode of LDA resurfacing by the deposition of a mantling deposit during the late Amazonian, while the best-fit age of 330 ± 90 Ma derived from *D*(150–300 m) impact craters (dominated by ring-mold morphologies) probably reflects the minimum age of the LDA in Chukhung crater, which falls in the mid to late Amazonian.

Considering the uncertainties associated with age estimations from impact crater size-frequency statistics, including those arising from small count areas (e.g., Warner et al., 2015) and an unavoidable dependence on impact craters with small diameters (e.g., Hartmann, 2005), the best-fit model ages that I have identified for LDA in Chukhung crater can be considered as broadly consistent with those obtained for the parent VFF of the candidate eskers in NW Tempe Terra (110 ± 10 Ma ; Chapter 4; Butcher et al., 2017) and Phlegra Montes (150 ± 20 Ma; Gallagher and Balme, 2015).

8.6.2.2. Glacial Modification of Impact Ejecta in the Ridged Plains Unit

The origin of the ridged plains unit is ambiguous. This unit lacks the decametre-scale undulations within the LDA-terminal lobes, but its spatial association with other glacigenic units (Figure 8.10A) leads me to suggest that it could represent a ground moraine deposited by the LDAs. However, the ridged plains unit hosts numerous subparallel lineations that align with rays within ejecta of the SE rayed impact crater located ~10 km from Chukhung crater (Figure 8.16). The northern margin of the ridged plains unit is ~24 km from the NW rim of the SE rayed crater, which is comparable to the ~25 km distance between its SE rim and the SE margins of its distal ejecta blanket. Thus, I suggest that the lineations within the ridged plains unit could comprise distal ejecta from that impact, which clearly postdates the Chukhung-forming impact (see Section 8.4.2.1.). A lack of evidence for ejecta or similar lineations on nearby LDAs or LDA-terminal lobes suggests that the ejecta was emplaced prior to the most recent glaciation. However, lineations in distal ejecta SE of the parent impact crater (Figure 8.16C) are significantly more pristine than the lineations in the ridged plains unit (Figure 8.16B) within Chukhung crater. In some locations within Chukhung crater, the lineations are superposed by materials with morphologies that are similar to (but lower relief than) those within the LDA-terminal lobes. Thus, I suggest that the ridged plains unit may represent distal rayed ejecta from the SE rayed crater, but that this impact ejecta may have undergone modification and partial burial by ground moraines during subsequent glaciation.

8.6.2.3. Southern Sinuous Ridges and the Esker Hypothesis

Given the spatial association of the southern (S1 and S2) sinuous ridges with the LDA (i.e., putative debris-covered glaciers) and possible glacigenic deposits in the LDA-terminal lobe and ridged plains units (Figure 8.10), I present arguments that could support their origins as eskers formed during one or more phase(s) of wet-based glaciation on the southern floor of Chukhung crater.

Most notable among the esker-like characteristics of the southern sinuous ridges, aside from their associations with glacigenic deposits, are: (a) their ascent of valley walls and topographic divides (e.g., Figure 8.10B–D); (b) similarities between their crest morphologies and those of eskers on Earth (e.g., Shreve, 1985a; Perkins et al., 2016), being dominated by sharp-crested morphologies, but also having round-crested and flat-topped portions (e.g., Figures 8.10B–D and 8.11A–B); and (c) similarities between their typical morphometries and those of martian sinuous ridges for which we are confident of an esker origin (Chapters 3-7; Gallagher and Balme, 2015; Butcher et al., 2017).

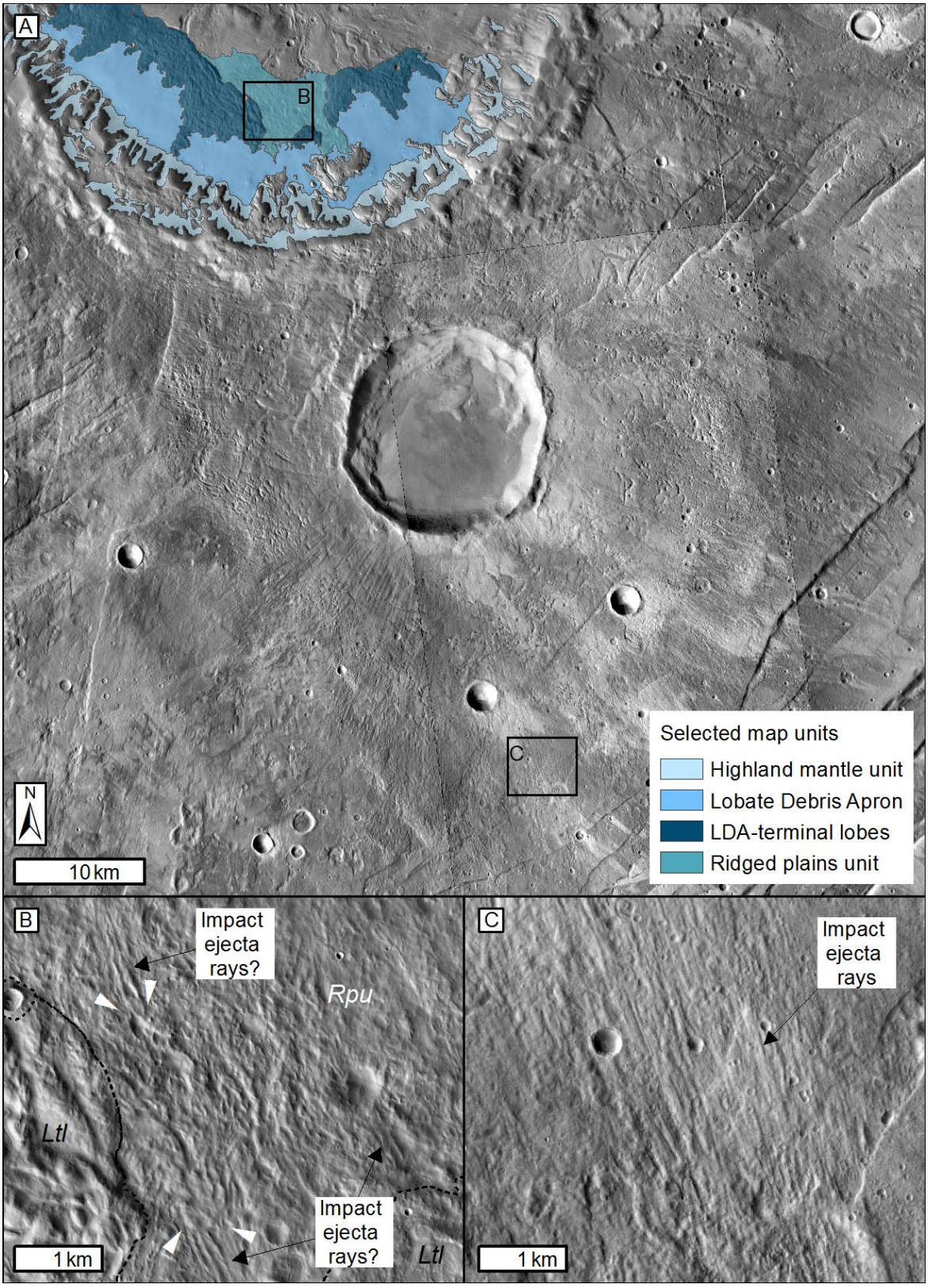

Figure 8.16. Evidence for glacial modification of rayed impact ejecta in Chukhung crater. (A) CTX image mosaic (Table 8.1) showing the rayed impact crater SE of, and inferred glacial and glacigenic units within, Chukhung crater, and the extents of panels: (B) possible ejecta from the SE rayed impact crater within the Ridged plains unit (Rpu) that appears to have been overprinted (white arrows) by materials that grade texturally into the LDA-terminal lobes (Ltl); and (C) rayed ejecta on the opposite side of the impact ejecta blanket but at a similar distance from the parent crater rim to panel B, showing rays that are relatively morphologically pristine. This difference suggests that rayed ejecta within Chukhung crater has been modified by processes that haven't occurred elsewhere on the ejecta blanket (i.e., glaciation).

Eskers are ice-contact landforms, and ascent of bedslopes is consistent with their formation in pressurised subglacial conduits (e.g., Shreve, 1972). While subglacial drainage generally converges towards broad topographic lows, spatial variations in ice overburden pressure resulting from variations in ice thickness modify the direction of steepest hydraulic potential gradient. Thus, as explained in Chapter 4, routing of subglacial meltwater can deviate from the direction of steepest topographic slope. This could explain why many S1 ridges do not appear to conform to the axes of the crater floor valleys, and in some cases, ascend valley walls and cross adjacent plains (e.g., Shreve, 1972, 1985a).

Qualitatively, the crest morphologies of the S1 and S2 ridges are strikingly similar to those of eskers on Earth, being dominated by distinct sharp crests. Preliminary measurements of the geometries of representative portions of the southern ridges (Section 8.5.3) demonstrate that they have similar morphometries to the mid-latitude VFF-linked sinuous ridges in Phlegra Montes (Chapter 7; Gallagher and Balme, 2015) and NW Tempe Terra (Chapters 4 and 6; Butcher et al., 2017), for which we are confident of esker origins. Their typical heights (S1 ridges have heights of ~10–20 m, and S2 ridges have heights of ~7–10 m) are comparable to the median heights of similar sharp-crested portions of the VFF-linked eskers in Phlegra Montes (median = 7.7 m; Chapter 7, this thesis) and NW Tempe Terra (median = 12.9 m; Chapter 6, this thesis). Similarly, their widths (S1 ridges are typically ~150–300 m wide and S2 ridges are typically ~100–150 m wide) are comparable to sharp-crested portions of the Phlegra Montes (median width = ~161 m) and NW Tempe Terra (median width = ~122 m) candidate eskers. This results in typical width-height ratios (~10–20 for S1 ridges and ~10–14 for S2 ridges) and average cross-sectional slopes (~8–15° for S1 ridges and ~8–10° for S2 ridges) for the southern sinuous ridges in Chukhung crater that are similar to those of sharp-crested portions of the Phlegra Montes (median width-height ratio = 20 and median average cross-sectional slope = 5.6°) and NW Tempe Terra (median width-height ratio = 10.6 and median average cross-sectional slope = 10.6°) candidate eskers (Chapter 7, this thesis).

The southern sinuous ridges emerge from beneath the LDA-terminal lobe and ridged plains units, which I have interpreted as moraines (Figure 8.10A and D). Thus, if the southern sinuous ridges are eskers, glaciers previously extended up to ~15 km across the crater floor, towards the margins of the crater's central pit. One or more episodes of basal melting and esker formation were followed by glacier retreat then readvance to form the moraine deposits that superpose the heads of the sinuous ridges (LDA-terminal lobes and ridged plains deposits). Moraines on Earth that are as voluminous and extensive as the LDA-terminal

lobes in Chukhung crater typically require meltwater to form. The transition from esker-forming to moraine-forming subglacial conditions could have arisen via collapse of an efficient network of subglacial drainage conduits as a result of waning meltwater discharge towards the end of glacier retreat, and a transition to a relatively inefficient distributed drainage system comprising linked cavities and/or thin films of subglacial meltwater (e.g., Kamb, 1987). The less efficient nature of such drainage systems on Earth results in higher basal water pressures and more rapid basal sliding of the overlying ice (Kamb, 1987), which encourages more pervasive deformation of bed sediments. Hence, a collapse of a channelised, esker-forming drainage system during glacier retreat could have encouraged glacier readvance and deformation of sediments to form moraines at the present termini of the VFFs.

The esker interpretation is dependent upon my interpretation of the ridged plains unit as glacially-modified impact ejecta (Section 8.6.2.2), and the LDA-terminal lobes as moraines. If the ridged plains unit comprises impact ejecta over which glaciers did not subsequently advance, and/or the LDA-terminal lobes are crater wall-slump deposits (Robbins and Hynek, 2012), these units instead represent a temporal discontinuity between formation of the sinuous ridges that they superpose, and formation of the LDA that they underlie.

Eskers on Earth are commonly associated with tunnel valleys that form during subglacial drainage (e.g., Kehew et al., 2012). It is possible that the valleys with which the southern sinuous ridges are associated are tunnel valleys. However, I find little additional evidence other than the association of some of the valleys with esker-like sinuous ridges to challenge the hypothesis of Peel and Fassett (2013) that they are subaerial fluvial valleys of Hesperian or Amazonian age. While eskers on Earth do cross topographic undulations and ascend bedslopes, they commonly occur within broader topographic lows (Shreve, 1972). Thus, if the southern sinuous ridges are eskers, subglacial drainage pathways may have routed along pre-existing fluvial valleys, but hydraulic potential gradients could have driven local deviations in the pathways of those eskers from the path of steepest topographic slope.

8.6.3. Challenges for the Esker Hypothesis for VFF-Linked Sinuous Ridges

Having summarised evidence for extensive fluvial activity and topographic inversion in the northern portions of Chukhung crater (Section 8.6.1), which lack associated evidence for glaciation, I now return to discussion of the origins of the sinuous ridges and valley networks associated with glacial deposits in the southern portion of Chukhung crater. I consider the challenges for the esker hypothesis, and the alternative hypothesis that all sinuous ridges in Chukhung crater are inverted palaeochannels.

As explained in Section 8.2, confidence in inferences about the origins of any landform on a planetary surface is heavily reliant upon the consistency of this mechanism with the broader landsystem within which it is located. In the case of inverted palaeochannels, a contextually consistent landsystem may be one comprising evidence for extensive erosion and landscape deflation (e.g., Davis et al., 2016; Zimbelman and Griffin, 2010) and/or association with other landforms that corroborate a subaerial fluvial origin, such as fluvial valley networks that exhibit alignment or continuity relationships with the sinuous ridges in question (e.g., Maizels, 1987; Pain and Oilier, 1995; Davis et al., 2016), and/or evidence for channel migration (e.g., point and scroll bars, or crossing ridges at different stratigraphic levels; Maizels, 1987; Williams et al., 2007; Burr et al., 2009; Cardenas et al., 2018). In the case of eskers, a contextually consistent landsystem may be one comprising other glacigenic landforms, such as moraines, and/or the presence of a candidate parent ice deposit, as is the case for the eskers in Phlegra Montes and NW Tempe Terra (Chapters 3-7; Gallagher and Balme, 2015; Butcher et al., 2017).

In locations where sinuous ridges are associated with landforms that are consistent with either an esker or an inverted palaeochannel origin, and there is no corroborating contextual evidence for the alternative origin, as is the case for the candidate VFF-linked eskers in Phlegra Montes and NW Tempe Terra, the formation mechanism may be inferred with relative confidence. However, in Chukhung crater, landforms that are contextually consistent with both esker and inverted palaeochannel origins coexist in close proximity.

The highland mantle, LDA, LDA-terminal lobes, and ridged plains units present difficulties for interpreting the pre-glacial history of the southern portion of Chukhung crater. They obscure topographic lows in the crater wall and the intermediate-to-upper elevations of the southern crater floor. It is in these locations on the northern portion of the crater floor that the landform associations providing strongest evidence for origins of the northern sinuous ridges as inverted palaeochannels (e.g., associations with crater wall valley networks, and a possible capping unit) are found (Figure 8.5). The near-ubiquitous distribution of valley networks on all unmantled portions of the crater walls suggests that the highland mantle unit may obscure similar valley networks on the southern crater wall. Thus, it is possible that despite their associations with glacial deposits, the southern sinuous ridges in Chukhung crater are also inverted palaeochannels that pre-date this glaciation. The SW branch of the major sinuous ridge network on the NW portion of the crater floor emerges from beneath an LDA-terminal lobe on the SW floor, demonstrating that the LDAs do obscure ridges interpreted as inverted palaeochannels in some locations.

In circumstances where contextual landsystems are consistent with both esker and inverted palaeochannel origins for sinuous ridges on Mars, it is necessary to appeal to characteristics of the ridges themselves to explore possible formation mechanisms. In the sections that follow, I consider each of the esker-like characteristics of the southern sinuous ridges in Chukhung crater in more detail, and highlight the caveats of using these characteristics to exclude an inverted palaeochannel origin for the esker-like sinuous ridges in Chukhung crater.

8.6.3.1. Crest Morphology

The southern sinuous ridges in Chukhung crater share morphological similarities with eskers on Earth, being predominantly sharp-crested. Several workers have invoked comparisons to typical crest morphologies of either eskers or inverted palaeochannels to favour one or other interpretation of their formation mechanism (e.g., Kargel and Strom, 1992; Pain et al., 2007; Burr et al., 2009). These arguments are based on an informal understanding that inverted palaeochannels are typically flat-topped, and eskers are more often characterised by one or more sharp or rounded medial crests.

However, on Earth, neither morphology is unique to inverted palaeochannels or eskers (Figure 8.17). Although inverted palaeochannels on Earth are predominantly flat-topped (Pain et al., 2007; Williams et al., 2007), they can host a diverse range of additional morphologies (Williams et al., 2013) that are similar to those observed along eskers (e.g., Shreve, 1985a; Perkins et al., 2016) including: round-crested, sharp-crested (termed pinnacle by Williams et al., 2013), and multi-crested (double ridge and ridge-bounded trough subtypes described by Williams et al. 2013) sections, and sections that retain negative relief troughs (Maizels, 1987; Pain and Oilier, 1995; Williams et al., 2007). Flat-topped morphologies have also been observed along eskers on Earth (Perkins et al., 2016; Kargel and Strom, 1992), and are largely thought to be associated with esker deposition within open, ice-walled channels, or within subglacial conduits at atmospheric pressure (i.e., under non-channel-full conditions; e.g., Burke et al., 2012b; Perkins et al., 2016). Therefore, distinguishing between eskers and inverted palaeochannels on Mars based on their crest morphologies alone represents an oversimplification. Indeed, 40% of the S1 ridges in southern Chukhung crater exhibit transitions from sharp-crested to flat-crested reaches.

I therefore argue that the predominance of sharp-crest morphologies along the southern sinuous ridges in Chukhung crater is not uniquely indicative of an esker origin, despite striking visual similarities to typical eskers on Earth. Furthermore, I note that there are several examples of sinuous ridges on the northern floor of Chukhung crater (the N2 ridges;

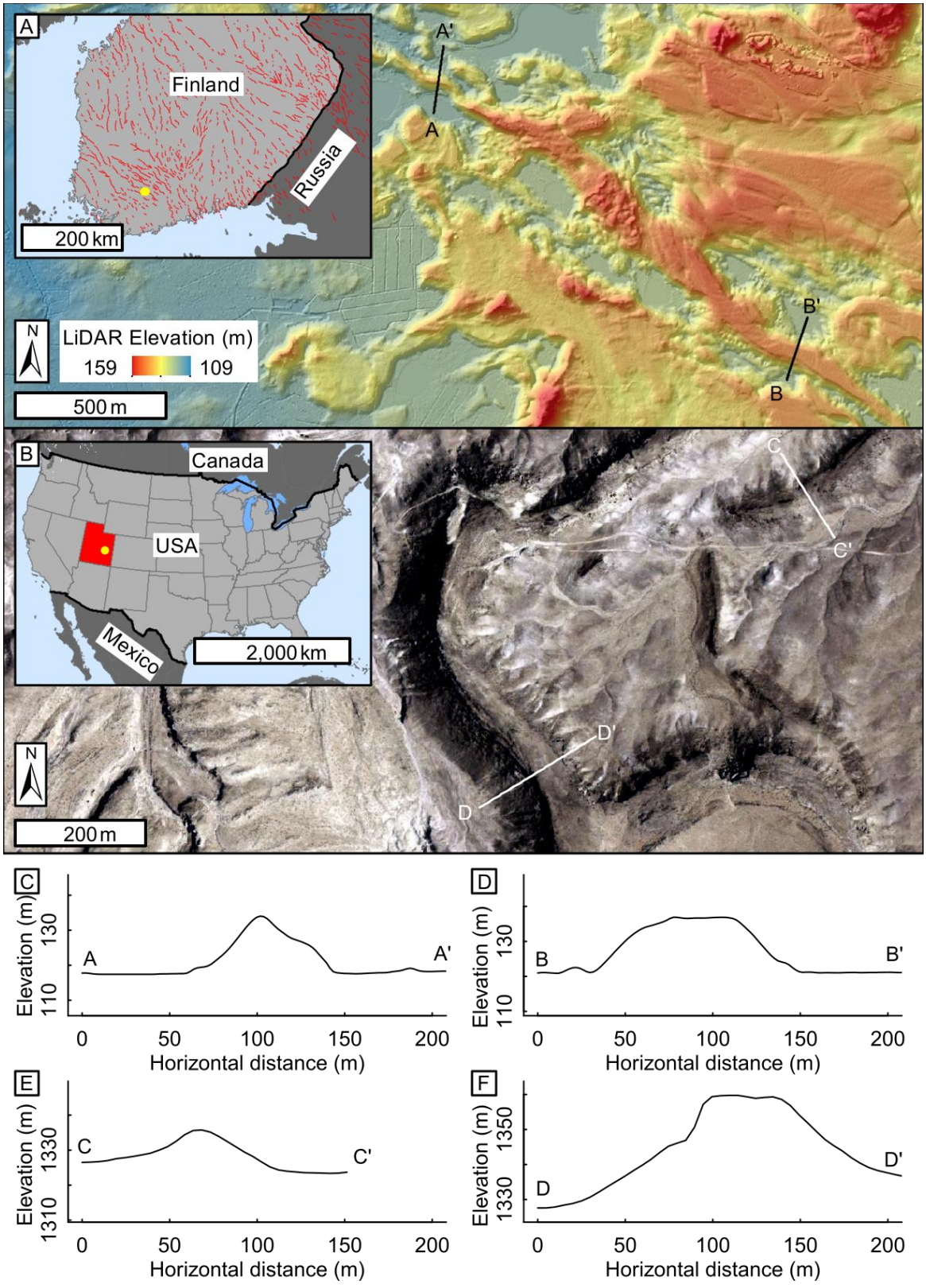

Figure 8.17. Morphological similarities between eskers and inverted palaeochannels on Earth. (A) LiDAR DEM of an esker in SW Finland showing locations of cross-sectional topographic profiles (at 2 m horizontal resolution) A–A' (panel C, a sharp-crested portion) and B–B' (panel D, a flat-topped portion). Location is shown by yellow point in inset map, in which red lines are esker crestlines compiled by Stroeven et al. (2016). (B) Aerial orthophoto of inverted palaeochannels in Utah (location shown by yellow point in inset map) showing locations of cross-sectional topographic profiles (at 5 m horizontal resolution) C–C' (panel E, a sharp- to round-crested portion) and D–D' (panel F, a flat-topped portion). See Table 8.1 for data products.

Figure 8.11D) that have very similar morphologies and morphometries to high-sinuosity, sharp-crested S2 ridges on the southern floor (Figure 8.11B), including some that extend from the downslope ends of N1 ridges. There is no evidence for either past or present glaciation of the northern portion of Chukhung crater. Thus, the existence of morphologically similar sinuous ridges on the northern floor of Chukhung crater calls into question the hypothesis that the S2 ridges on the southern crater floor are eskers. This observation corroborates an additional challenge to the esker hypothesis; aside from the sinuous ridges, there is no additional evidence for glaciation of the portion of the southern crater floor beyond the LDA-terminal lobes and ridged plains unit. Hence, it is possible that glaciers never advanced past the northern margins of the LDA-terminal lobe and ridged plains units, and that the association of the southern sinuous ridges with the termini of these units is simply a product of glacier advance over pre-existing inverted palaeochannels.

8.6.3.2. Ascent of Bedslopes

A characteristic that is often invoked to support esker origins for sinuous ridges on Mars is ascent of bedslopes by the ridges (e.g., Head and Hallet, 2001a, 2001b; Head, 2000b, 2000a; Banks et al., 2009; Burr et al., 2009; Butcher et al., 2016, 2017), as I observe for sinuous ridges in southern Chukhung crater. Under hydraulic pressure within confined subglacial conduits, subglacial meltwater follows the hydraulic gradient, which is controlled primarily by ice surface slope, rather than bed topography (Shreve, 1972, 1985a). Thus, the paths of eskers commonly deviate from the steepest topographic slope or even ascend topography. This contrasts markedly with subaerial rivers, whose path invariably follows the steepest topographic gradient under gravity. As a result, evidence for ascent of bedslopes necessarily casts doubt upon inverted palaeochannel interpretations for sinuous ridges on Mars.

However, recent studies have demonstrated that the inverted palaeochannel hypothesis cannot be ruled out by observations of ascent of bedslopes by sinuous ridges (Lefort et al., 2012; Williams et al., 2013). The upper surface of an inverted palaeochannel does not necessarily preserve the slope of the original channel bed, owing to spatial variations in induration or armouring, and post-exhumation modification (Lefort et al., 2012; Williams et al., 2013). Lefort et al. (2012) suggested that apparent slope ascent by inverted palaeochannels could be an artefact of several geologic processes that could occur after the cessation of channel flow, including: (1) differential modification of the topography of the channel floor (i.e., the upper surface of the exhumed ridge) before and/or after exhumation, (2) exhumation of multiple generations palaeochannels at different stratigraphic levels, (3) differential erosion of the surrounding region (e.g., due to spatial variations in induration),

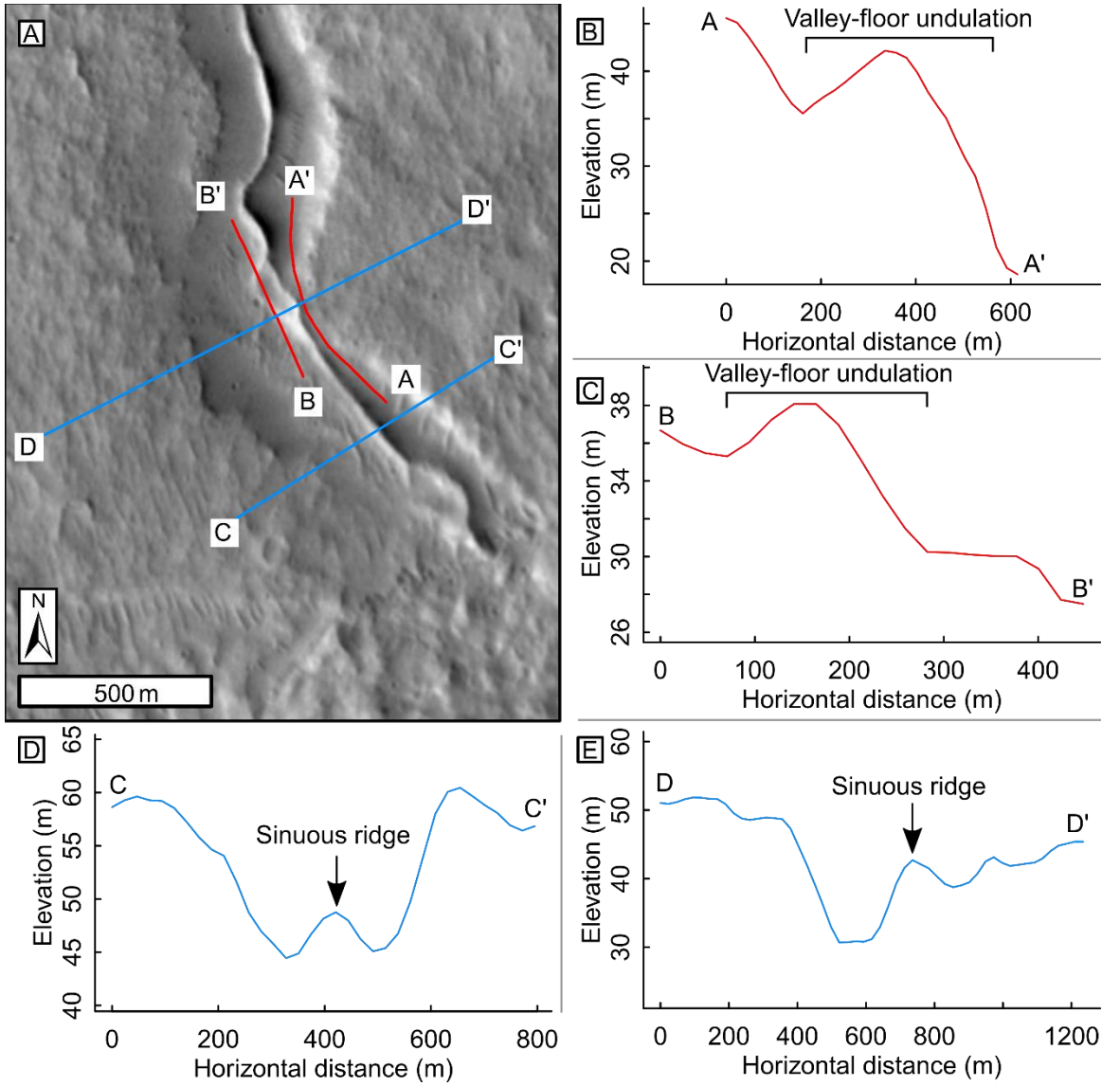

Figure 8.18. The possible role of differential erosion in the ascent of present-day bedslopes by sinuous ridges in Chukhung crater. (A) CTX image of an S1-type sinuous ridge in southern Chukhung crater that appears to ascend ~7 m up the wall of the valley it occupies, showing the locations of topographic profiles (obtained from the CTX DEM; Table 8.1) in subsequent panels. (B) Topographic profile A–A' showing the ~7 m along-ridge undulation in the present-day topography of the valley to the east of the sinuous ridge in panel A. (C) Topographic profile B–B' showing the along-ridge undulation in the present-day topography to the west of the sinuous ridge in panel A. (D) Valley-transverse topographic profile C–C' showing the sinuous ridge where it occupies the lowest point within the valley, upslope of the topographic undulation in panels B and C. (E) Valley-transverse topographic profile D–D' showing the sinuous ridge where it appears to be 'perched' part way up the valley wall. It should be noted that the width sinuous ridge approaches the 24 cm/pixel horizontal resolution of the CTX DEM available for this location.

(4) differential settling and/or compaction of materials underlying the ridge, (5) tectonic deformation, and/or (6) igneous intrusions into the substrate.

In Chukhung crater, I observe several locations where apparent ascent of bedslopes by the southern sinuous ridges may be due to the processes described by Lefort et al. (2012), rather than their origins as eskers. For example, it is possible that the appearance of a ~7 m ascent

of a valley wall by the S1 type ridge in Figure 8.18A–C is an outcome of differential erosion of valley-fill materials surrounding the ridge during exhumation. The base of the eastern flank of the ridge is ~10 m higher in elevation than the western flank near to the peak of the along-valley undulation (Figure 8.18E), and the crest of the ridge is lower in elevation than the top of the valley wall. Hence, it is possible that material has been preferentially eroded from the valley floor to the west of the ridge, and that valley floor-filling materials to the east of the ridge have been preferentially preserved. Preferential preservation of materials to the east of the ridge could occur, for example, as a result of greater resistance of materials deposited on the interior bend of a fluvial channel, or sheltering (e.g., from aeolian erosion) of the narrow corridor between the ridge and the valley wall. As such, if the sinuous ridge is an inverted palaeochannel, the present bedslope of the valley (Figure 8.18B–C) may not preserve the palaeoslope during subaerial drainage, giving the impression of ascent of topography by the flow that formed the sinuous ridge.

The sharp-crested S2-type sinuous ridge that superposes the flat-topped S1-type sinuous ridge in Figure 8.11E could represent a location where differential erosion and/or compaction of inverted palaeochannels at different stratigraphic levels gives the impression of ascent of bedslopes by the stratigraphically-higher sinuous ridges. The similar relationship between the S2 ridge and the SW branch of the major N1 ridge in Figure 8.11F could also result from exhumation of inverted palaeochannels at different stratigraphic levels. If the S2 sinuous ridges are inverted palaeochannels, their paths across plateaus adjacent to the crater floor valleys may suggest that subaerial fluvial activity and channel inversion was not isolated to the crater floor valleys, but that fluvial activity and subsequent landscape deflation also occurred in the plains regions intervening these valleys. I discuss this possibility further in Section 8.6.4.

8.6.3.3. 3D Morphometry

The southern sinuous ridges in Chukhung crater have typical heights, widths, width-height ratios and average cross-sectional slopes that are comparable to those of the VFF-linked eskers in Phlegra Montes and NW Tempe Terra (Table 7.6; Chapters 4–7). This suggests that they could share a common formation mechanism. However, the southern sinuous ridges also show morphometric similarities to the sinuous ridges on the northern floor of Chukhung crater, for which I have inferred an inverted palaeochannel origin with relative confidence. Additionally, there is limited existing knowledge on the morphometries of inverted palaeochannels on Earth, or of sinuous ridges on Mars for which there is general consensus for an inverted palaeochannel origin. The same is true for eskers; the new measurements of

the 3D morphometries of eskers in SW Finland by Storrar and Jones (unpublished; Chapter 7, this thesis) comprise the first large database of the 3D morphometries of terrestrial eskers. Thus, it is not yet known whether inverted channels and eskers have distinct morphometric signatures that can be used to diagnose an esker origin.

8.6.3.4. Sinuosity

Several workers have invoked differences in typical sinuosities between eskers and rivers on Earth to distinguish between esker and inverted palaeochannel origins for sinuous ridges on Mars (e.g., Metzger, 1992; Kargel, 1993; Banks et al., 2009; Burr et al., 2009; Williams et al., 2013; Kress and Head, 2015; Butcher et al., 2016). In general, eskers on Earth typically have low sinuosities, with median values < 1.1 (e.g., Storrar et al., 2014a, their Figures 3 and 13; Figure 7.7 and Table 7.8, this thesis), while meandering rivers typically have sinuosities >1.3 (Schumm, 1963). In this regard, some of the S2 sinuous ridges in southern Chukhung crater are somewhat atypical of eskers on Earth; having a median sinuosity of 1.11, and a maximum sinuosity of 1.63, while the S1 sinuous ridges have sinuosities (median = 1.08, maximum = 1.19) that are more similar to those that are typical of eskers.

However, specific ranges of sinuosity values are by no means unique to either eskers or inverted palaeochannels on Earth, and overlap in sinuosity occurs for features that deviate from the typical values. For example some eskers in Canada (Storrar et al., 2014a) and SW Finland (Storrar and Jones, unpublished), have sinuosities significantly in excess of 1.3, ranging up to 2.62 for esker systems in Canada (Storrar et al., 2014a; see also Figure 7.5 and Table 7.7, this thesis.). This is higher than the maximum sinuosity of the S2 ridges (1.63). Similarly, many rivers have sinuosity lower than 1.3; indeed, Maizels (1987) found that four of the five inverted palaeochannel systems for which they measured sinuosity in western Sharqiya, Wahiba, Oman, had sinuosity values < 1.1, similar to typical values recorded for eskers in Canada (Storrar et al., 2014a) and SW Finland (Storrar and Jones, unpublished; see Chapter 7). This illustrates that sinuosity characteristics are non-unique for eskers and inverted palaeochannels and cannot be used reliably to distinguish between these formation mechanisms.

8.6.4. Origins of Sinuous Ridges and Palaeoenvironmental Implications

The origins of the southern sinuous ridges are ambiguous; there is evidence to support both esker and inverted palaeochannel origins. I suggest that, despite their association with glacigenic deposits and extant VFFs, there are reasons to doubt the hypothesis that the southern sinuous ridges in Chukhung crater are eskers. Esker-like characteristics of the

ridges (such as sharp crest morphologies, ascent of bedslopes, and morphometric similarities to sinuous ridges elsewhere for which we are confident of esker origins) are not necessarily unique to eskers and could also be explained by an inverted palaeochannel hypothesis. The associations of the southern sinuous ridges with non-glacial units mapped in Chukhung crater are consistent with those of the northern sinuous ridges. I am confident of inverted palaeochannel origins for the northern sinuous ridges, given their associations with valleys on the crater walls, and relationships to a possible capping unit (upper plains and ridges unit), and evidence for extensive erosion and landscape deflation. Hence, I suggest that it is entirely possible that the southern ridges in Chukhung crater are also inverted palaeochannels, rather than eskers recording wet-based glaciation in southern Chukhung crater.

If all sinuous ridges in Chukhung crater are inverted palaeochannels, they probably comprise topographically-inverted channel fills that were deposited during subaerial fluvial drainage. Drainage of water from a distributed source (such as precipitation or snowmelt) occurred on all portions of the crater wall, forming valley networks on the crater walls and floor. Superposition of sinuous ridges in Chukhung crater suggests that there were at least two phases of fluvial drainage, the first of which was focussed within the existing valleys on the crater floor, and the second of which was not confined to these valleys (Figure 8.19). The earlier phase of drainage contributed to deposition of fluvial materials within the central floor pit of Chukhung crater, which may have hosted a lake at that time.

That the S1 and N1 ridges typically conform to crater floor valleys, while S2 and N2 ridges do not, suggests that the crater floor valleys became infilled, for example by aggradation of channel overbank deposits, and that fluvial deposition also occurred on the intervening plains prior to a second phase of fluvial incision recorded by the S2 and N2 ridges (Figure 8.19). The plains materials were then removed by regional deflation, followed by the underlying valley-filling materials, exposing resistant channel fills from both the first and second drainage episodes, and re-exposing the crater floor valleys in negative relief. Abundant TARs within the southern intermediate plains support extensive erosion and mobilisation of sand-sized material across the southern floor. However, the better preservation of the walls of the crater floor valleys on the southern floor, and the more rugged surface of the intermediate plains unit on the northern floor, suggests that regional deflation may have been weaker in the south and stronger in the north.

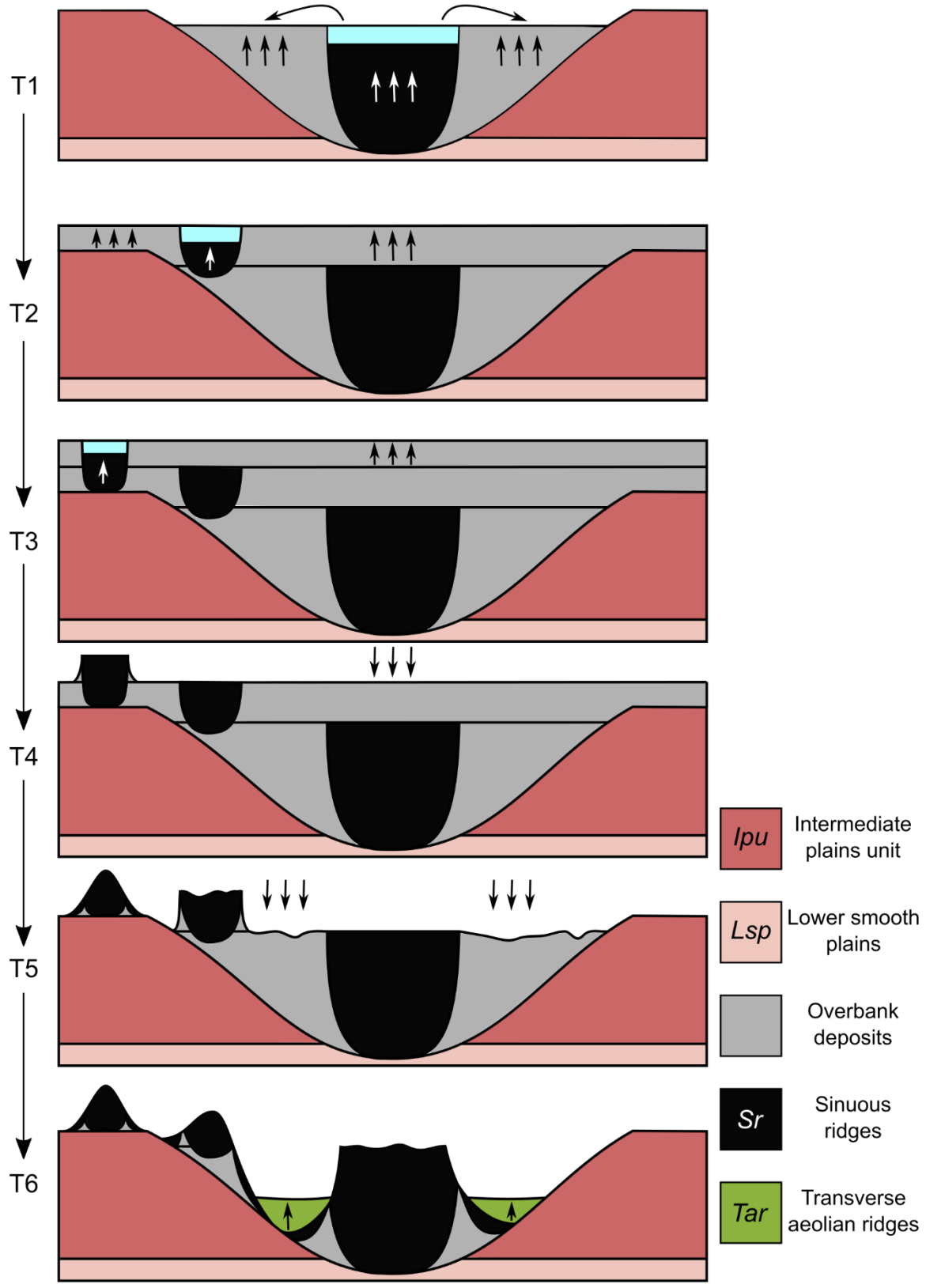

Figure 8.19. Schematic illustrating a model for the formation of the southern sinuous ridges in Chukhung crater under the inverted palaeochannel hypothesis. This model could explain their apparent ascent of valley sides, location on plateaus above valleys, and the predominance of sharp-crested morphologies amongst stratigraphically-higher (S2) sinuous ridges, compared to the more common occurrence of flat-topped morphologies among stratigraphically lower (S1) ridges. At T1, fluvial activity within crater floor valleys promotes aggradation of channel-fill and overbank deposits within the valleys. As the valleys infill, overbank deposits begin to aggrade on the plateaus adjacent (caption continues on next page)

(caption continued from previous page) to the valleys (at T2), and drainage channels, which are no longer controlled by the topography of the buried valleys, migrate laterally, forming channel-fill deposits that are situated above the sides of the buried valley (T2), and on the adjacent plains (T3). Fluvial activity ceases and regional erosion begins to preferentially remove less-resistant overbank deposits, exhuming more resistant channel-fill deposits as ridges. The youngest, stratigraphically higher channel fills are exhumed first (T4 and T5) and begin to degrade. Mass wasting of their flanks and degradation of their resistant surfaces promotes a transition from flat-topped to sharp-crested morphologies. Inverted palaeochannels that formed above buried valley walls protect underlying valley-fill deposits, and mass-wasting of their flanks produces sharp crest morphologies and the appearance that the ridges are perched on the valley sides. The oldest channel-fills in the valley bottom are exhumed last (T6) and are more likely to retain flat-topped morphologies due to their more recent exhumation than stratigraphically-higher ridges. On the southern crater floor, aeolian processes deposit transverse aeolian ridges within the valleys, possibly comprising materials sourced from the eroded valley-fill or plains deposits, or the sinuous ridges themselves.

Earlier exposure (and therefore more advanced erosion) of stratigraphically-higher sinuous ridges (S2 and N2 ridges) on the plains above the crater floor valleys and part way up the valley walls could explain their predominantly sharp-crested morphologies (see Figure 8.3), while more recent exposure of stratigraphically lower valley-floor ridges could explain why flat-topped morphologies are more common among S1 and N1 ridges. As illustrated in Figure 8.19, over time, undermining and/or removal of resistant channel-fill materials following ridge exhumation could have promoted mass wasting of the ridge flanks, and retreat of the lateral margins of the resistant capping materials, driving a transition from flat-topped to sharp-crested ridge morphologies. Thus, differences in crest morphology could represent differences in degradation state, rather than formation mechanism. A caveat of this model is that production of sharp crest morphologies via ridge degradation could also be expected to result in greater fragmentation of sharp-crested ridges compared to flat-topped ridges. Qualitative observations suggest that this is not the case, and all ridges have a high level of continuity despite differences in crest morphology. Future quantitative analyses of the sinuous ridges in Chukhung crater should include tests for relationships between ridge continuity and crest morphology.

Although stratigraphic relationships between valleys in the incised plains unit and plains-forming materials of the upper plains and ridges unit provide evidence for emplacement of a fluvial capping unit on the northern floor of Chukhung crater, I suggest that induration and/or lithification of channel fill sediments may be required to explain the extensive preservation of sinuous ridges at different stratigraphic levels on the southern floor of Chukhung crater, unless emplacement of capping materials was recurrent. Inverted palaeochannels on Earth are typically lithified, comprising sandstones and mudstones formed by compaction of unconsolidated channel fills via burial (e.g., Williams et al., 2007; R. M. E. Williams et al., 2009). Inverted palaeochannels elsewhere on Mars are commonly

associated with remnants of overburden materials with hundreds of metres of thickness (e.g., Kite et al., 2015), which provide evidence for such burial. Evidence for at least tens of metres of erosion of materials within the central pit of Chukhung crater suggest that significant thicknesses of material have been removed, and TARs on the intermediate plains and within crater floor valleys suggest mobilisation of material throughout Chukhung crater. However, the depth to which the portions of the crater floor outside of the central pit was buried remains uncertain, and there is a lack of clear sediment sink to account for removal of material in volumes sufficient to exhume channel-fill deposits at multiple stratigraphic levels.

Notable differences in sinuosity between the older (S1 and N1) and younger (S2 and N2) ridges suggest that hydraulic conditions of subaerial drainage may have varied through time within Chukhung crater. Maizels (1987) invoked increased grain size of entrained sediments, and increases in peak flow depths and velocities to explain the decrease in sinuosity between stratigraphically-lower (i.e., older, with sinuosities of > 1.7) and stratigraphically-higher (i.e., younger, with sinuosities of ~1.03) inverted palaeochannels in Oman. I therefore suggest that the increase in sinuosity between older and younger sinuous ridges in Chukhung crater, which is of a similar magnitude but opposite sense (i.e., an increase in sinuosity rather than a decrease) to that observed by Maizels (1987), could have arisen from reductions in sediment grain size, flow depths and velocities towards later drainage events. Factors that could have promoted such a transition include: reductions in the slope of the crater wall and floor due to relaxation and/or infilling of crater topography, reductions in sediment supply and/or flow power under drying climate conditions, or even an increase in hydraulic base level (e.g., the depth of a lake in the central pit) associated with a transition towards wetter climate conditions.

Multi-phase subaerial drainage in Chukhung crater is consistent with the interpretations of Peel and Fassett (2013) that many central pit craters on Mars probably experienced protracted fluvial activity during the Hesperian or Amazonian. The age envelope that I have obtained for Chukhung crater, which places its formation between the early Hesperian and early Amazonian (~3.6–2.1 Ga; Section 8.5.7.1), is consistent with the observations of Peel and Fassett (2013), and the occurrence of fluvial activity in Chukhung crater after the period of major valley network formation on Mars (e.g., Fassett and Head, 2008b; Hynek et al., 2010). Thus, regardless of whether they are eskers or inverted channels, the sinuous ridges, and associated valley networks, in Chukhung crater represent protracted and/or episodic periods of unusually wet conditions between the early Hesperian and mid Amazonian (i.e.,

between the formation of Chukhung crater and the formation of VFFs within it), despite the general cooling and drying that is widely thought to have occurred during this time (see Chapter 2).

While the sinuous ridges that emerge from glacigenic deposits on the southern crater floor of Chukhung crater are remarkably esker-like, I argue that it is also possible that they formed via a similar mechanism to sinuous ridges in the northern portion of Chukhung crater, as inverted palaeochannels. The unusually voluminous and extensive nature of the LDA-terminal lobes (which I interpret as moraines) provides some support for former wet-based glaciation in Chukhung crater. However, aside from the esker-like properties of the southern sinuous ridges, I find no additional evidence that valley or ridge-forming fluvial activity in Chukhung crater persisted into the mid to late Amazonian or overlapped temporally with glaciation of the southern portion of the crater wall or floor. Hence, there is considerable reason to doubt that mid- to late-Amazonian glaciation of Chukhung crater was wet-based. However, it should be noted that if the southern sinuous ridges are eskers, and/or if the LDA-terminal lobes are moraines, Chukhung crater's location within an extensive tectonic rift system is consistent with the hypothesis at the core of this thesis: that elevated geothermal heat flux was a pre-requisite for wet-based glaciation on Mars (Chapters 3-4; Gallagher and Balme, 2015; Butcher et al., 2017). However, this rift system and associated volcanic constructs are thought to have ceased major activity during the late Hesperian (Hauber and Kronberg, 2001; Hauber et al., 2010). Thus, further investigation of the tectonic and volcanic history of the region surrounding Chukhung crater would be required to corroborate a geothermal control upon mid- to late-Amazonian glacial melting in this location.

8.7. Potential Insights from Morphometric Analyses

In Chapters 6 and 7, I demonstrated that eskers on Mars with similar crest morphologies might exhibit similar height-width relationships. In the case of the glacier-linked esker in NW Tempe Terra, I effectively predicted the height-width relationships of portions of the ridge based on reference relationships exhibited by other portions of the ridge with similar crest morphologies. Additionally, in Chapter 7, I found a consistent height-width relationship between round-crested portions of the glacier-linked eskers in Phlegra Montes and NW Tempe Terra, and suggested that small variations in height-width relationships between sharp-crested portions of these eskers could result from differences in exposure age and thus degradation state.

These observations suggest that primary formation processes (including the physics of subglacial drainage and sedimentation) exerted a primary control on the morphometries of

eskers on Mars. However, no systematic, high-resolution analyses of the 3D morphometries of inverted palaeochannels on either Earth or Mars have been undertaken to date. Thus, it is not yet possible to conclude whether such relationships are uniquely esker-like, or even that they are more typical of eskers than inverted palaeochannels. However, the greater importance of secondary modification processes (including induration, burial, exhumation, and erosion) in the formation of inverted palaeochannels suggests that their morphometries will be far more heterogeneous, less strongly related to crest morphology, and therefore less predictable than those of eskers. Thus, if future systematic morphometric analyses of the sinuous ridges in Chukhung crater reveal similar morphometric relationships to those identified for the glacier-linked eskers in Phlegra Montes and NW Tempe Terra (with accompanying consideration of possible exposure ages and degradation states discussed in Chapters 6 and 7), confidence in an esker interpretation for their origins could improve.

Changes in ridge morphometry along the ridge length could provide additional evidence. For example, previous workers assessing the esker hypothesis for sinuous ridges on Mars have developed tests for variations in the heights and crest morphologies of sinuous ridges that were predicted by Shreve (1985a) based on the theory of subglacial drainage as an esker approaches, ascends, crosses, and subsequently descends a topographic undulation (see Figure 4.9; Banks et al., 2009; Butcher et al., 2016). Butcher et al. (2016) found statistically significant relationships between ridge height and bedslope for the south polar Dorsa Argentea on Mars, supporting the widely-held view that they are ancient eskers. However, such height-bedslope relationships are deemed to be esker-like mainly on the basis of glacial theory and the method has not been validated against eskers on Earth. In fact, Perkins et al. (2016) suggested that the esker morphometry-bedslope relationships that were predicted by Shreve (1985a) are not consistently observed along eskers on Earth. Additionally, it is not known if this relationship is unique to eskers, or if it also occurs along inverted palaeochannels, which can also ascend present-day slopes (e.g., Lefort et al., 2012). In contrast to eskers, there is no existing theory for the occurrence of such relationships along inverted palaeochannels. However, given the present state of knowledge, identification of such relationships for sinuous ridges on Mars cannot be considered to be entirely diagnostic of esker origins as has been suggested by some workers (e.g., Pain et al., 2007), and an absence of these relationships cannot be considered to rule out an esker origin.

Systematic measurements of the morphometries of a large sample of inverted palaeochannels on Earth and Mars could greatly enhance the potential for diagnostic morphometric tests of esker hypothesis for sinuous ridges on Mars. Comparisons between the typical

morphometries of large samples of eskers (such as those presented in Chapters 6 and 7) and inverted channels on both Earth and Mars could enhance confidence in one or other hypothesis for a given sinuous ridge, provided that population analyses identify statistically significant differences between those typical morphometries. Additionally, tests for height-bedslope relationships along both eskers and inverted channels on Earth and Mars would permit validation of the height-bedslope method used in tests of the esker hypothesis for the Argyre Planitia and Dorsa Argentea eskers by Banks et al. (2009) and Butcher et al. (2016). The method would be validated if the predicted height-bedslope relationship is observed along eskers and if inverted channels exhibit dissimilar behaviours in this parameter space to eskers. In combination with similarities in absolute geometries, observations of process-controlled morphometric relationships (including relationships between crest morphology and height-width trends identified in Chapters 6 and 7, and height-bedslope relationships described above), would greatly enhance confidence in the esker hypothesis for sinuous ridges on Mars if those relationships are validated against observations of eskers and inverted channels on Earth.

8.8. Conclusions

Chukhung crater provides a valuable case study highlighting challenges that remain for the identification of eskers on Mars. The definitive identification of eskers on Mars is complicated by similarities in form between eskers and inverted palaeochannels. Confidence that a sinuous ridge on Mars is an esker can be significantly improved if that sinuous ridge is associated with extant ice deposits such as VFFs, and there is no associated evidence for deflation or topographic inversion in the surrounding landscape. However, in locations such as Chukhung crater, coexistence of landsystems that are consistent with both esker and inverted palaeochannel origins in close proximity complicates definitive interpretation of VFF-linked sinuous ridges as eskers. Sinuous ridges in Chukhung crater that emerge from glacigenic deposits have several characteristics that are commonly considered to be esker-like including sharp crest morphologies, and paths that do not follow the steepest topographic slope and occasionally ascend topography. However, I emphasise that many of the properties that are commonly invoked to support an esker origin for sinuous ridges on Mars are non-unique to eskers and could also be explained under the alternative hypothesis that they are inverted palaeochannels. I find insufficient evidence to suggest that the VFF-linked sinuous ridges in southern Chukhung crater formed via a different mechanism to sinuous ridges in northern Chukhung crater. In the northern portion of the crater floor, there is no evidence for past or present glaciation, and association of the sinuous ridges with crater

wall valleys and evidence for landscape deflation leads me to conclude with confidence that the northern sinuous ridges are inverted palaeochannels. I conclude that it is more likely that the VFF-linked sinuous ridges in southern Chukhung crater formed via the same mechanism, as inverted palaeochannels recording multiple phases of pre-glacial subaerial fluvial activity, than that they are eskers formed under wet-based glaciation during the mid to late Amazonian.

If the sinuous ridges are inverted palaeochannels, they provide evidence for multiple prolonged episodes of distributed, possibly precipitation-driven, subaerial fluvial activity and sedimentary aggradation between the early Hesperian and mid Amazonian. Thus, Chukhung crater or the wider central Tempe Terra region probably experienced climate conditions that were unusually warm and wet compared to the generally cold and dry climate conditions that are thought to have prevailed during that time period.

If the southern sinuous ridges are eskers, their location in a tectonic rift zone is consistent with geothermal controls on basal melting of their parent glaciers, but further analyses of the regional tectonic history are required to assess the likelihood that elevated geothermal heat flux persisted into the period during which Chukhung crater was glacierised.

This study highlights the requirement to expand and compare observations of large samples of eskers and inverted palaeochannels on Earth and Mars, in order to perform direct comparisons of their morphometries, and to search for unique characteristics that can be used to diagnose esker or inverted palaeochannel origins from orbital remote sensing data. If all sinuous ridges in Chukhung crater are inverted palaeochannels, they provide an optimum opportunity to explore the processes leading to morphological and morphometric diversity among inverted palaeochannels on Mars. If Chukhung crater hosts both inverted channels and eskers, it provides an optimum opportunity to compare sinuous ridges of different origins that have been subjected to broadly similar conditions since the formation (or exposure) of the youngest ridge population.

CHAPTER 9

SYNTHESIS

9.1. Attribution

In this chapter, I draw together new insights presented in this thesis and consider their implications for the broader understanding of Mars' environmental and glaciological history. In doing so, I discuss work to which I contributed in parallel with the preparation of this thesis. In Section 9.2, I describe numerical modelling experiments performed by N. S. Arnold for the journal article published in *Journal of Geophysical Research: Planets*, of which I am lead author (Butcher et al., 2017). In Section 9.4, I discuss the evolving view of wet-based glaciation on Mars, including the results of a journal article published in *Geomorphology* (Conway et al., 2018a), of which I am second author. These results develop on a study published in *Geological Society of London Special Publication 467* (de Haas et al., 2017), of which I am third author.

9.2. Environmental and Glaciological Drivers of Basal Melting

9.2.1. Requisite Geothermal Heat Flux and the Role of Strain Heating

The observations presented in this thesis are in agreement with the hypothesis of Gallagher and Balme (2015) that elevated geothermal heat flux was a key driver of basal melting of glaciers in Mars' mid latitudes during the mid to late Amazonian. Strain heating caused by ice convergence within steep-sided valleys (Chapter 4), and possibly impact crater (Chapter 8) settings could have supplemented geothermal heating in promoting basal melting.

My discovery of the glacier-linked esker in NW Tempe Terra (Chapter 4; Butcher et al., 2017) prompted us to explore quantitatively, the possible combinations of environmental and glaciological parameters (including mean annual surface temperature, geothermal heat flux, ice thickness, and driving stress) that could permit basal melting of glaciers on Mars under cold climate conditions (Figure 9.1; Butcher et al., 2017; modelling experiments performed by co-author N. S. Arnold). Using a 1D numerical model of heat flow through

glacial ice, the temperature at the glacier bed was calculated by comparing possible rates of geothermal and viscous strain heating of the basal ice with the rate of heat loss to the ice surface. Following Cassanelli et al. (2015), the calculations assumed a linear temperature profile through the ice. Glaciers on Earth commonly have non-linear temperature/depth profiles modified by ice flow and the advection of cold ice from higher altitudes (Cuffey and Paterson, 2010), but these effects are probably negligible on Mars owing to slow ice flow and an extremely weak dependence of surface temperatures on altitude (Butcher et al., 2017).

The temperature of the basal ice was calculated according to:

$$dT = \frac{H_i Q}{k_T} \quad \textbf{9.1}$$

where dT is the difference between the mean annual surface temperature (varied between 190–230 K, compared to ~190 K in the present day) and the temperature of the basal ice (K), H_i is ice thickness (varied between 500–1500 m), k_T is thermal conductivity of the ice (assumed to be 2.5 W m^{-1} K^{-1} following Cassanelli et al. 2015), and Q is basal heating (W m^{-2}), equal to geothermal heat flux (varied between 0.02–0.1 W m^{-2}) plus internal strain heating (Butcher et al., 2017).

The initial experiments considered only geothermal heating as a heat input to the basal ice (Figure 9.1A). In subsequent experiments (Figure 9.1B–D), volumetric strain heating was included as an additional heat input, with the assumption that strain heating only within the lowest 10% of the ice thickness affects the basal temperature. Strain heating has been ignored as a potential heat source in previous modelling studies (Cassanelli et al., 2015). Volumetric strain heating was calculated according to:

$$P = 2A_T {\sigma_{xz}}^4 \quad \textbf{9.2}$$

where A_T is the temperature-dependent flow rate factor for clean ice (s^{-1} Pa^{-3}; Cuffey and Paterson, 2010) and σ_{xz} is shear stress (Pa). A range of basal driving (shear) stress conditions (20–100 kPa; calculated as $\rho g h \tan \alpha$, where ρ is ice density, g is gravity, h is depth within the ice, and α is ice surface slope) was calculated by varying ice surface slope (~0.1–3.5°) with ice thickness. The present surface slope of viscous flow features (VFFs) in the NW Tempe Terra rift (Chapter 4) is ~2–2.5°.

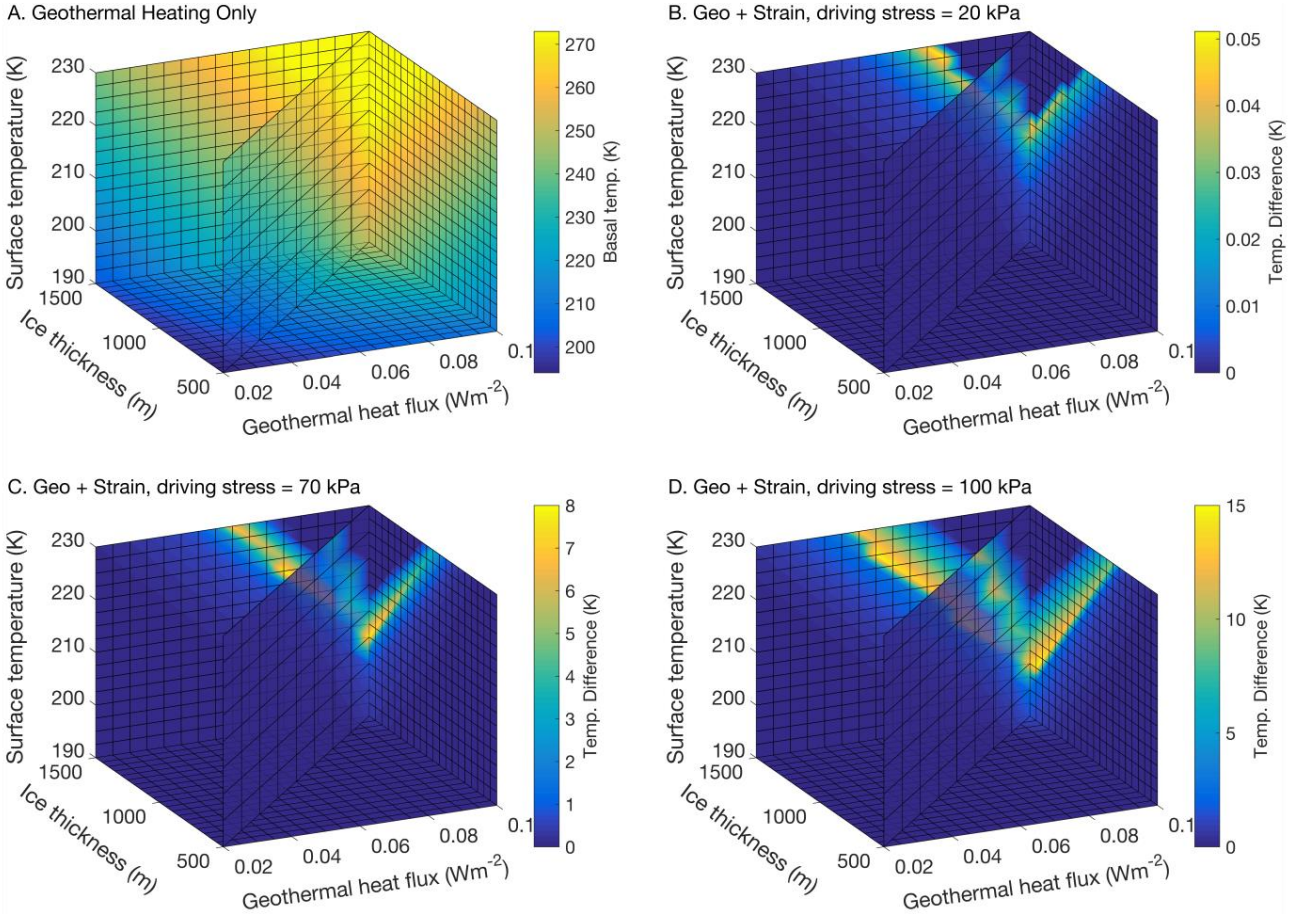

Figure 9.1. Constraints on environmental and glaciological requirements for basal melting from a 1D numerical model. 3D projections of calculated basal temperatures for a range of ice thicknesses, geothermal heat fluxes, mean annual surface temperatures, and driving stresses. (A) Basal temperatures for geothermal heating only from Equation 9.1 (B–D) Temperature change relative to conditions in panel A induced by strain heating from Equation 9.2 for driving stresses of 20 kPa (panel B), 70 kPa (panel C), and 100 kPa (panel D). The diagonal axes show a plane through the parameter space. The top-right-hand corners of panels B–D are already at 273 K, so no temperature change occurs. From Butcher et al. (2017).

To estimate basal temperature for each scenario, an initial basal temperature was calculated using Equation 9.1. This informed estimations of A_T (from Cuffey and Paterson, 2010 p. 75), which were then inserted into Equation 9.2 to calculate P in the lowest 10% of the ice thickness. P was integrated over this depth to obtain basal strain heating in W m^{-2}. Adding strain heating to geothermal heating, new basal temperatures were extracted from Equation 9.1 along with new A_T values, and this process iterated until basal temperatures stabilised or reached 273 K (Butcher et al., 2017).

The experiments aimed to constrain a first-order estimate of the most conservative environmental scenario required for basal melting. Hence, it was assumed that neither debris cover (which reduces heat loss to the glacier surface, warming the basal ice), nor impurities (e.g., salts, which lower the melting point of ice) were present. There remains considerable uncertainty over the effect of impurities upon the rheology of ice on both Earth and Mars (e.g., Parsons et al., 2011); hence the value of A_T pertaining to clean terrestrial ice was used.

Assuming that geothermal heat is the only source of heat to the basal ice (Figure 9.1A), warm mean annual surface temperatures (> 215 K), thick ice (> 1100 m), and high geothermal heat flux (80 mW m^{-2}) are required to induce temperatures approaching 273 K (Butcher et al., 2017). These conditions seem unlikely for the late Amazonian, although such locally high geothermal heat flux relative to the martian global average (23–27 mW m^{-2}; Plesa et al., 2016) may be plausible in the vicinity of, for example, a near-surface magmatic dike (Wilson and Head, 2002; Cassanelli et al., 2015).

Experiments incorporating strain heating for the first time, however, showed a greatly expanded range of environmental conditions over which basal melting of VFFs could occur (Figure 9.1B-D; Butcher et al., 2017). Basal temperatures approach 273 K for mean annual surface temperatures > 205 K, ice thicknesses > 900 m, or geothermal heat fluxes > 50 mW m^{-2}, given local driving stresses of 100 kPa (Figure 9.1D). Strain heating provided up to 50 mW m^{-2} of additional heating, warming the basal ice by a further 14.5 K and approximately halving the requisite geothermal anomaly that would be required in the absence of strain heating (Butcher et al., 2017). The maximum warming effect of strain heating increased to 18.5 K when A_T was doubled (simulating softer ice), and decreased to 11.1 K when A_T was halved (simulating harder ice). Thus, even considering uncertainty over the rheological effect of impurities on VFFs (e.g., Parsons et al., 2011), strain heating could have made a significant contribution to warming of basal ice (Butcher et al., 2017).

The contribution of strain heating to warming of basal ice increases highly non-linearly with temperature because A_T increases by three orders of magnitude between 220–270 K and driving stress is raised to the fourth power in Equation 9.2. While average driving stresses calculated for bulk VFFs on Mars (~20–35 kPa; Karlsson et al., 2015) are low compared to typical terrestrial glaciers (~50–200 kPa; Cuffey and Paterson, 2010), it is highly likely that localised variations in ice thickness and surface slope induce large local-scale deviations from these average driving stresses. It is entirely plausible that basal driving stresses approaching those that are more typical of terrestrial values (i.e., 70–100 kPa; Figure 9.1C–D) could occur in areas of locally thick ice and/or steep slopes that encourage ice flow convergence. Considering the geomorphic evidence presented in this thesis, including the location of the parent glaciers of candidate eskers within (Chapters 3 and 4) or near (Chapter 8) tectonic rifts, and in association with steep topography, I consider such conditions to be plausible for mid-latitude VFFs during the mid to late Amazonian. Thus, as discussed in Chapter 4, the potential influence of strain heating upon basal melting of glaciers on Mars should not be ignored.

9.2.2. The Role of Melting Point Depression by Salts

The experiments described above do not consider the potential influence of salts (which are abundant on Mars' surface; Hecht et al., 2009) in depressing the melting temperature beneath glacial ice. Orosei et al. (2018) suggested that their discovery (during the preparation of this thesis) of radar evidence for a possible present-day subglacial lake or water-saturated sediments beneath Mars' south polar ice cap could be explained by salts, albeit beneath 1.5 km thick ice at different (polar) latitudes to the mid-latitude locations treated in the present thesis. By extension, it is possible that salts also influenced the occurrence and distribution of wet-based glaciation across Mars' surface in the past.

Recent modelling experiments are, however, in agreement with the hypothesis at the core of this thesis, that geothermal heat was, and continues to be, a prerequisite for wet-based glaciation during the Amazonian. Sori and Bramson (2019) found that salts in any viable concentration could not permit basal melting of Mars' south polar cap in the absence of greatly elevated geothermal heat flux. Given a present-day mean annual surface temperature of 162 K at the south pole, a 20% dust fraction within the polar cap, and > 50 mass percent of perchlorate salts within its basal ice, they found that an elevated geothermal heat flux of > 72 mW m^{-2} is required for present-day basal melting of the south polar cap (Sori and Bramson, 2019). In the absence of salts, > 204 mW m^{-2} of geothermal heating is required for basal melting (Sori and Bramson, 2019). They found that such geothermal heat fluxes could

have been induced by a ~5–6 km diameter magma chamber emplaced at a crustal depth within 6–8 km of the base of the south polar cap during the last 1 Myr (Sori and Bramson, 2019). While it is possible that locally strong strain heating could be induced by small-scale topography at the base of the south polar cap, I suggest that the low slope of the ice surface, its negligible flow rate, and lack of confining topography (and hence probably a weak tendency for flow convergence) means that strain heating is less influential than geothermal heat flux in permitting basal melting of the south polar ice cap than it may have been for valley and crater glaciers in Mars' mid latitudes. Nonetheless, the strong temperature dependence of strain heating justifies further investigation of its involvement within the south polar cap.

9.2.3. Glacier-Linked Eskers and Late Amazonian Climate Conditions

Although a systematic global survey dedicated to the identification of candidate glacier-linked eskers on Mars has not yet been undertaken, the current state of knowledge pertaining to the geomorphology of VFFs and their forelands suggests that such eskers are probably rare. Thus, basal melting of VFFs in Phlegra Montes (Gallagher and Balme, 2015) and NW Tempe Terra (Chapter 4; Butcher et al., 2017) was probably driven by localised phenomena rather than global-scale, hemispheric, or zonal-scale climate changes. This is supported by remarkable similarity in the geologic settings of these glaciers, within tectonic rift/graben valleys in regions that could plausibly have experienced elevated geothermal heat flux into the late Amazonian (Chapter 4). If early- to mid-Amazonian-aged glacier-linked sinuous ridges of more ambiguous origin in Chukhung crater (Chapter 8) are eskers, the location of their host crater between major fault branches of the Tempe Fossae fault system is also broadly consistent with geothermal rather than climatic drivers of basal melting.

Given the present state of knowledge I cannot, however, rule out some involvement of climatic variations in driving rare, localised occurrences of wet-based glaciation on Mars during the mid to late Amazonian. The numerical modelling experiments described in Section 9.2.1 demonstrate that some degree of climate warming is required to explain basal melting within the range of geothermal heat flux, ice thickness, and strain heating parameters that were explored (Butcher et al., 2017). Considering the magnitude of geothermal heat flux anomalies in regions experiencing near-surface magmatism and/or hydrothermal circulation on Earth (e.g., 150-2000 mW m-1 in Yellowstone, USA; R. B. Smith et al., 2009), it is possible that geothermal heat flux far exceeded the parameter range explored in our models. However, taking a cautious approach to the magnitude of geothermal heating on Mars during the Amazonian, our models suggest that local or regional climate warming of at least 15 K

(from ~190 K mean annual temperature in Mars' mid latitudes at present) is required to explain basal melting, and ~25 K is required in the absence of strain heating (Butcher et al., 2017). The magnitude of mean annual surface temperature fluctuations associated with cyclic excursions to higher spin-axis obliquity during the Amazonian are thought to have had magnitudes of < 10 K for Mars' mid latitudes, with the greatest warming effects (of tens of K) having occurred in the polar regions (Fanale et al., 1986; François et al., 1990). Thus, a small amount of additional climate warming beyond that provided by obliquity-driven climate changes may have been required to explain the production of meltwater beneath mid-latitude glaciers during the mid to late Amazonian.

In Chapter 8, I demonstrated that esker-like glacier-linked sinuous ridges in Chukhung crater have ambiguous origins, and that associated landscape evidence could suggest that they are inverted palaeochannels comprising deposits of subaerial flows of liquid water. Such origins would be consistent with the conclusions of Peel and Fassett (2013), that some Amazonian-aged central pit craters on Mars host evidence for prolonged episodes of subaerial fluvial activity and sedimentary aggradation during the early to mid Amazonian. The climate changes required to permit such subaerial flows, which appear to have been sourced from distributed precipitation and/or snowmelt (Chapter 8; Peel and Fassett, 2013) are, as yet, unexplained. However, it should be noted that these early- to mid- Amazonian valley-forming climates probably occurred prior to the occurrences wet-based glaciation in Phlegra Montes and NW Tempe Terra ~110–150 Ma (Gallagher and Balme, 2015; Peel and Fassett, 2013; Butcher et al., 2017), and thus are unlikely to account for the formation of eskers in those locations. However, given evidence for the cyclic nature of climate changes on Mars during the Amazonian (Chapters 2 and 3), it is possible that mechanisms driving climate changes associated with river and esker formation were similar, if separated in time.

9.3. The Utility of Martian Eskers

In Chapter 6, I demonstrated the potential utility of systematic morphometric analyses for reconstructing the spatiotemporal dynamics of esker-forming meltwater drainage events on Mars. Such reconstructions will be essential for informing future modelling experiments aiming to constrain in more detail the environmental and glaciological drivers of wet-based glaciation on Mars, including the possible magnitude and duration of meltwater flows. In both Chapters 6 and 7, I identified possible relationships between the crest morphologies and morphometries of glacier-linked eskers which, in combination with considerations of landform exposure age and degradation state, could be used as reference morphometries for tests of the esker hypothesis for sinuous ridges of more ambiguous origin (e.g., in Chukhung

crater, Chapter 8) elsewhere on Mars. As demonstrated in Chapter 8, the origins of sinuous ridge landforms on Mars can be ambiguous despite association with an extant parent glacier if those glaciers co-exist with landforms that are also consistent with alternative non-glacial (e.g., inverted palaeochannel) origins for the sinuous ridges.

As discussed in Chapters 2, Mars' climate has become colder and more arid, and its geothermal heat flux has waned over the course of its geological history. Thus, identification of geologically young eskers associated with late-Amazonian-aged glaciers on Mars suggests that wet-based glaciation could have been more common and spatially extensive earlier in Mars' history. Consequently, it is possible that eskers dating from earlier periods of Mars' geological history (including those with smaller spatial scales and extents than the ancient Dorsa Argentea and Argyre Planitia eskers; see Chapter 3) are relatively common landforms at various latitudes across Mars' surface. However, confidence in interpretations of sinuous ridges as eskers is reduced in the absence of a preserved parent glacier. Constraining the range of morphometries, and possible process-related morphometric relationships exhibited by those glacier-linked sinuous ridges for which we are relatively confident of esker origins (e.g., Chapters 6 and 7) is therefore essential for developing robust tests of the esker hypothesis for esker-like sinuous ridges of more ambiguous origins (e.g., Chapter 8) elsewhere on Mars.

9.3.1. Eskers as Potential Proxies for Geothermal Heat Flux Variations

The evolving understanding of recent (Hubbard et al., 2011; Gallagher and Balme, 2015; Butcher et al., 2017; this thesis), and possibly present-day (Orosei et al., 2018; Sori and Bramson, 2019) wet-based glaciation on Mars raises interesting potential for understanding the broader geological evolution of the planet. If above-average geothermal heat flux is indeed a prerequisite for basal melting during the Amazonian, landforms produced by wet-based glaciers (such as eskers) could provide useful proxies for understanding spatiotemporal variations in planetary heat flux. Aside from landforms produced by eruptive volcanism and tectonism, extensive ice deposits including VFFs are probably the most sensitive features to variations in geothermal heat flux (including those induced by possible subsurface magmatism that does not manifest as eruptions or faulting at the surface) that are observable on Mars' surface using remote sensing techniques. As explained in Chapter 3, existing estimates of Mars' geothermal heat flux are derived from numerical models with numerous simplifying assumptions (McGovern et al., 2002; Montési and Zuber, 2003; McGovern et al., 2004; Plesa et al., 2016). The InSight lander landed in Elysium Planitia (135.0°E, 4.5°N, ~2250 km SW of Phlegra Montes) on 26th November 2018. At the time of

writing, preparations were underway to deploy the subsurface heat flow probe onboard the lander, which will take the first direct measurement of Mars' geothermal heat flux. This measurement will provide essential ground-truth for Mars' geothermal heat flux, but will be for a single location and representative only of the present day. Therefore, geomorphic proxies for spatiotemporal variations in Mars' geothermal heat flux, such as landforms produced by geothermally-controlled wet-based glaciation, will remain essential for understanding heat-producing processes (such as magmatism and hydrothermal circulation) that have occurred in Mars' subsurface. As discussed in Chapter 4, insights from glacier-linked eskers suggest that late-Amazonian geothermal activity may not have been isolated to the interiors of the large volcanic provinces as predicted by simplified models, and that Mars' recent magmatic and/or hydrothermal history could be more diverse and complex than previously thought.

9.4. Wet-Based Glaciation and Landscape Evolution on Amazonian Mars

Eskers are indicative of glacial melting, but wet-based glaciers do not invariably produce eskers. Eskers do not form in subglacial environments in which meltwater discharge is insufficient to promote formation of channelised drainage systems (comprising well-integrated, efficient conduits in which eskers are deposited) of adequate size, or where the availability of esker-forming sediments at the bed is strongly limited. Thus, if glaciers elsewhere on Mars did produce meltwater, but in volumes smaller than those required for channelisation of subglacial drainage or in areas with insufficient sediment, eskers would not have formed.

In a study to which I contributed (as second author) in parallel with the preparation of this thesis (Conway et al., 2018a), we identified evidence for an episode of relatively extensive production of small (i.e., non-esker-forming) volumes of subglacial meltwater in numerous glacierised impact craters on Mars ~5–10 Ma. We quantified the amount and rate of erosion of the glaciated walls of eleven young (ranging from ~0.5 Myr–1.8 Gyr old) impact craters across Mars' mid latitudes for which HiRISE DEMs were available. These crater walls host arcuate moraine-like ridges similar to those that bound glacier-like forms (see Chapter 3; Hubbard et al., 2011; Souness and Hubbard, 2012), and/or extend above the surfaces of crater-interior VFFs (e.g., Figure 9.2A–B). We identified remarkably consistent associations between these arcuate ridges and thick deposits of smooth, lineated, and/or polygonised material upslope (Figure 9.2B–C), which is sometimes termed pasted-on terrain, and planed-off, rough (texturally-altered) bedrock that is invariably present above the upslope margins of this pasted-on terrain (Figure 9.2B-D; Conway et al., 2018a). This geomorphic

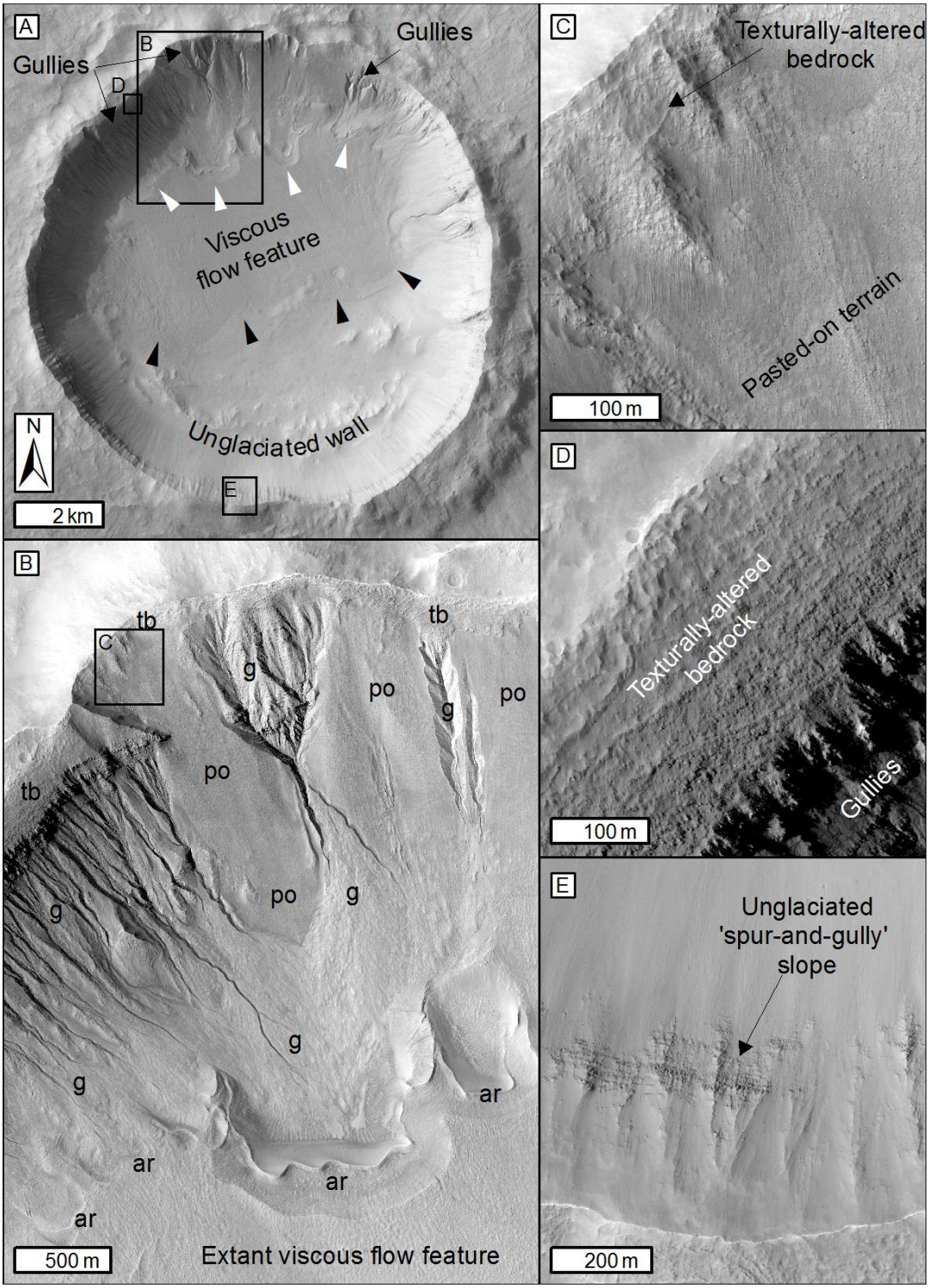

Figure 9.2. A landform assemblage of possible wet-based glaciation and subsequent gully formation in Niquero Crater, Mars. (A) CTX image P03_002383_1417 of Niquero crater (38.77°S, 193.99°E) which hosts a VFF (black arrows are VFF margins) with arcuate moraine-like ridges (white arrows, 'ar' in panel B) forming spatulate depressions at its upslope margins, gullies ('g' in panel B) incising 'pasted-on terrain' ('po' in panel B) and depositing aprons of material upslope of the arcuate ridges, and texturally-altered bedrock('tb' in panel B) upslope of the pasted-on terrain. Black boxes show extents of panels B, D and E. (B) Detail of the landform assemblage described for panel A and the extent of panel C (black box). (C) Pasted-on terrain downslope of texturally-altered bedrock. (D) Texturally-altered bedrock upslope of a closely-spaced gullies which postdate and have backfilled the depressions bounded by arcuate ridges downslope. (E) The relatively pristine 'spur-and-gully' morphology of the facing crater wall, where there is no evidence for past glaciation. Panels B–E are HiRISE image ESP_030021_1410. Based on Conway et al. (2018).

assemblage contrasts consistently with portions of facing crater walls (Figure 9.2E), which host no evidence for either past or present glaciation and have relatively pristine 'spur and gully' rim morphologies that are typical of young impact craters (Conway et al., 2018a).

We quantified the slopes of the texturally-altered bedrock (e.g., Figure 9.2D) and compared them with those of unglaciated impact crater walls (often within the same impact crater, e.g., Figure 9.2E) to estimate the excess retreat of the texturally-altered bedrock relative to that of relatively pristine impact crater walls. Following Levy et al. (2016; see Section 3.6.2), we compared these crater wall retreat rates with estimates of the duration of the last glacial epoch (Fastook and Head, 2014) to quantify erosion rates that have occurred on impact crater walls hosting texturally altered bedrock (Conway et al., 2018a).

Our calculated erosion rates (of up to ~10^2 m Myr^{-1}) are similar to rates of erosion beneath wet-based glaciers on Earth (e.g., Hallet et al., 1996; Geirsdóttir et al., 2007), suggesting that the glaciers that formed the arcuate ridges and eroded the texturally-altered bedrock could have been wet-based. Following this interpretation, the pasted-on terrain could comprise till deposits sourced from wet-based glacial erosion of the upper crater walls (Conway et al., 2018a). The absence of proglacial fluvial valleys associated with the studied landform assemblages but abundant evidence for glaciotectonic deformation associated with the arcuate moraine-like ridges led us to suggest that liquid water, if involved, was in small volumes and existed as pressurised pore water within basal sediments that were confined by ground ice in the surroundings (Conway et al., 2018a).

This possible episode of wet-based glaciation, which was remarkably temporally consistent across studied impact craters (~5–10 Ma), occurred more recently than the localised esker-forming melt events in Phlegra Montes and NW Tempe Terra ~110–150 Ma (Conway et al., 2018a).

If glacial meltwater was involved in lowering slopes of texturally-altered bedrock and/or the formation of associated glacial landforms, the extensive distribution of this geomorphic assemblage (which is widespread beyond those impact craters for which HiRISE DEMs were available) is potentially problematic for the hypothesis that elevated geothermal heat flux (which probably occurred only on local or regional scales during the Amazonian) was a prerequisite for geologically-recent wet-based glaciation. Formation of this landform assemblage across many regions of Mars' mid latitudes probably requires spatially-extensive increases in atmospheric temperatures beyond those induced by cyclic variations in planetary spin-axis obliquity (Conway et al., 2018a). In combination with the climatic requirements

for formation of late-Amazonian-aged glacier-linked eskers (Section 9.2.3), streamlined glacial bedforms in Greg crater (Hubbard et al., 2011), and possibly even landforms suggestive of periglacial freeze-thaw processes beyond the VFFs discussed in this thesis (e.g., Balme et al., 2013), these findings are problematic for current models of environmental change in Mars' mid latitudes during the Amazonian, and warrant further investigation.

The occurrence of widespread wet-based glaciation within mid-latitude impact craters could, however, help to explain a morphometric peculiarity of another group of late Amazonian-aged mid-latitude landforms on Mars: gullies (e.g., Figure 9.2A-B; de Haas et al., 2017). Gullies commonly incise crater walls on Mars. They comprise an erosional source alcove, a transportation channel, and a depositional apron (e.g., Malin and Edgett, 2000). Gullies are a topic of high-profile debate owing to the possible involvement of geologically-recent subaerial flows of liquid water in their formation (see Chapter 2). In an earlier study (de Haas et al., 2017), we found that the size of gully alcoves is remarkably consistent regardless of the age of the host craters whose walls or interior deposits they incise. Given that impact events are expected to have generated steep slopes in impact craters throughout Mars' history, this suggests that some spatially-extensive process erased older gullies, which would be expected to have larger alcoves than younger gullies (de Haas et al., 2017). In gullied craters with evidence of past or present glaciation (e.g., arcuate ridges and/or extant VFFs), we identified evidence that multiple generations of alcoves had been partially erased by glacial erosion, and that this glaciation effectively reset those crater walls to allow a new cycle of gully incision. Hence, gullies in older impact craters are not larger than those in very young impact craters because older generations of gullies have been erased (de Haas et al., 2017).

The magnitude of glacial erosion quantified from our slope measurements of texturally-altered bedrock within gullied and glacierised impact craters (many of which also host gullies; Conway et al., 2018a) is sufficient to completely erase older generations of gullies, supporting the model of cyclic gully incision and removal described above (de Haas et al., 2017). These insights provide tantalising evidence for the involvement of wet-based glaciation at the intersection of glacier, moraine, and gully-forming processes on Mars. They suggest that the nature of wet-based glaciation could have been more diverse than the esker-forming drainage events discussed in the present thesis, and that wet-based glaciation could have exerted a more widespread influence on the evolution of Mars' contemporary geomorphic record than previously thought. Given the probability that Mars' climate was generally extremely cold during the Amazonian, it is possible that small-volume basal

meltwater production, such as that invoked by Conway et al. (2018a), was more common (and widespread) than relatively high-volume basal meltwater production associated with esker formation, and that the eskers discussed in this thesis represent only the highest magnitude discharges of basal meltwater that occurred during the Amazonian. This highlights the requirement to re-evaluate the potential involvement of meltwater in the broader evolution of Amazonian-aged landscapes on Mars.

9.5. Implications for Ancient Environments on Mars

As discussed in Chapter 1, the nature of Mars' ancient climate is a topic of significant debate. Considering the model that Mars underwent a general cooling and drying trend between the Noachian and Amazonian (e.g., Carr and Head, 2010), evidence for geologically recent wet-based glaciation discussed in this thesis suggests that it could have been an important phenomenon under comparatively warm climate conditions and higher geothermal heat flux in Mars' ancient past. If strain heating did indeed contribute to warming of glacier beds (Section 9.2.1), it seems entirely plausible that basal melting could occur more extensively during the Noachian, when global average geothermal heat flux (see Chapter 3; Montési and Zuber, 2003; McGovern et al., 2004; Solomon et al., 2005) approached the 50 mW m^{-2} threshold identified in our 1D modelling experiments (Section 9.2.1) and probably far exceeded it in volcanic regions and proximal to impact craters. Conservative (cold and dry) endmember scenarios for Mars' Noachian climate conditions invoke transient melting of ice deposits to explain formation of the large valley networks in the southern highlands (Wordsworth et al., 2013, 2015), and formation of the extensive Dorsa Argentea and Argyre Planitia eskers (e.g., Fastook et al., 2012; Scanlon et al., 2018). This demonstrates the potential importance of wet-based glaciation not only in shaping Mars' recent geomorphic record (Section 9.4), but also that for its ancient past.

9.6. Implications for Life and Human Exploration

Liquid water is essential for life as we know it. Subglacial environments are of significant interest in the search for past and present microbial life on Mars (e.g., Skidmore et al., 2000). Aside from the ready supply of water ice in these environments, glaciers on Mars shield their beds from intense and harmful radiation at Mars' surface. Thus, if microbial life did emerge on Mars, the beds of glaciers could have provided habitable niches for that life. Evidence for geologically recent meltwater production in subglacial environments presented in this thesis enhances this habitability potential.

Exploration of Mars' surface will continue to rely on data returned from robotic spacecraft, landers and rovers for many years to come. However, there is growing potential for future

crewed exploration of Mars' surface by humans on landed missions. Debris-covered glaciers in Mars' mid latitudes are perhaps the most promising targets for in situ water ice resource utilisation by such missions, which will probably be unable to transport all requisite water resources from Earth (Hoffman et al., 2017). Consequently, it is necessary to identify targets of scientific interest that are within accessible distances of these glaciers (Baker and Carter, 2019b). The eskers discussed in this thesis could provide such targets. Direct sampling of glacial ice in search of microbial life should be supplemented by analyses of the mechanisms of meltwater productions that could have facilitated habitability. The analyses in Chapter 6 suggest that the glacier-linked esker in NW Tempe Terra could have a complex sedimentary architecture recording detailed dynamics of a subglacial drainage event, and could therefore provide such insights. Its morphology is most consistent with one or more high-magnitude catastrophic drainage events, so I do not predict that biosignatures could be well preserved within the esker sediments. However, esker-forming conduits drain meltwater from relatively low-energy environments in surrounding regions of a glacier bed, which could have greater biosignature preservation potential than eskers themselves.

The glacier-linked eskers in both Phlegra Montes and NW Tempe Terra are strong candidates for crewed exploration. I suggest that the low-relief plains into which the Phlegra Montes esker extends (Chapter 3) could provide a less hazardous site for entry, descent and landing of a crewed mission than the steep-sided rift valley hosting the esker in NW Tempe Terra (Chapter 4). On the other hand, the location of the Phlegra Montes esker ~36 km from its parent glacier, and evidence for boulder-rich plains in the intervening glacier foreland (Chapter 7) could make essential water ice resources inaccessible from this site. I suggest that the extensive, high-relief moraine-like ridge complex that separates debris-covered glaciers from candidate eskers in Chukhung crater (Chapter 8) could also limit accessibility of water-ice resources from locations of key exploration targets. In this regard, the NW Tempe Terra esker (which is only partially exposed from its parent glacier and is not associated with boulder-rich plains) could provide the best target for future crewed exploration among the sites analysed in this thesis.

CHAPTER 10

CONCLUSIONS AND FUTURE WORK

10.1. Conclusions

This thesis presents new insights into the distribution, dynamics, and possible environmental drivers of geologically-recent basal melting of debris-covered glaciers (viscous flow features; VFF) in Mars' mid latitudes. Previously, indicative evidence identified for past basal melting of these debris-covered glaciers was restricted to a single esker complex associated with a ~150 Myr old debris-covered glacier in Phlegra Montes (Gallagher and Balme, 2015).

In Chapter 4, I presented the discovery of a second glacier-linked esker, which emerges from a ~110 Myr old debris-covered glacier in the NW Tempe Terra region of Mars' northern mid latitudes. This demonstrates that at least two existing mid-latitude glaciers of broadly similar age underwent basal melting (albeit in transient episodes) during the late Amazonian despite extremely cold, hyper-arid climate conditions that are thought to have prevailed throughout the Amazonian.

That the parent glaciers of the two Amazonian-aged mid-latitude glacier-linked eskers identified to date both occupy similar tectonic graben/rift valleys suggests that geothermal heat was a prerequisite for rare, localised occurrences of esker-forming wet-based glaciation during the late Amazonian (Chapter 4). If correct, this would suggest that geothermal activity (e.g., due to magmatism and/or hydrothermal circulation) persisted into the late Amazonian in NW Tempe Terra and Phlegra Montes, extending the period for which such activity has been inferred for these regions. Evidence for geologically-recent tectonic activity proximal to the rift valley hosting the glacier-linked esker in NW Tempe Terra demonstrates that late-stage geothermal activity in the vicinity of the parent glacier is plausible.

Strain heating has not previously been considered as an important driver of heat production within mid-latitude debris-covered glaciers on Mars. Incorporation of strain heating into a

1D numerical model of heat flow through glacial ice for the first time (Chapter 9) shows that strain heating could have contributed up to 50% of the basal heat required to melt the basal ice, greatly expanding the range of conditions under which basal melting could occur. Strain heating exhibits a highly non-linear relationship to ice temperature and basal shear stress. Therefore, it probably supplemented warming of glacier beds in settings where geothermal heat flux raised basal ice temperatures and/or bounding topography encouraged convergence of ice flow. Steep-sided tectonic rift/graben valleys (Chapters 3 and 4), and impact craters within tectonised regions (Chapter 8) could have provided such settings. However, increases in mean annual surface temperatures with magnitudes greater than those thought to have been induced by cyclic increases in planetary spin-axis obliquity alone might also be required to explain the occurrence of wet-based glaciation during the Amazonian. Hence, glacier-linked eskers associated with existing Amazonian-aged glaciers in Mars' mid latitudes suggest that Mars' recent climatic and geothermal evolution was complex, and that there were probably local, and perhaps short duration, excursions from the extremely cold, hyper-arid conditions predicted by global climate models.

In Chapter 8, I presented the first in-depth analyses of sinuous ridges in Chukhung crater, central Tempe Terra. While sinuous ridges in the southern portion of Chukhung crater have many esker-like characteristics and are associated with extant (~330 Myr old) debris-covered glaciers, they have more ambiguous origins than those in Phlegra Montes and NW Tempe Terra. The sinuous ridges and associated glaciers in the southern portion of Chukhung crater coexist with an older, Hesperian- to Amazonian-aged landscape that hosts landforms consistent with the alternative hypothesis that the southern sinuous ridges are inverted palaeochannels. A key challenge for the esker hypothesis lies in the morphological similarity between the glacier-linked sinuous ridges in southern Chukhung crater and sinuous ridges in the northern portion of Chukhung crater where there is no evidence for either past or present glaciation. The sinuous ridges in northern Chukhung crater are instead associated with fluvial valley networks and possibly a capping unit, which suggest that they are inverted palaeochannels recording prolonged periods of distributed (i.e., probably precipitation and/or snowmelt-fed) subaerial fluvial runoff. Thus, morphological similarity with these sinuous ridges and those associated with glaciers in southern Chukhung crater necessarily casts doubt over the origins of the glacier-linked sinuous ridges as eskers. On the other hand, a challenge for the inverted palaeochannel hypothesis lies in the volume of material that would need to have been removed from Chukhung crater to exhume of channel fill deposits at multiple stratigraphic levels, and the absence of a clear sediment sink for this

material. If the glacier-linked sinuous ridges in Chukhung crater are eskers, the location of the crater between major fault branches of the Tempe Fossae rift system is broadly consistent with the hypothesis that above-average geothermal heat flux was required for wet-based glaciation during the Amazonian. If they are inverted palaeochannels, they provide evidence for prolonged, possibly episodic overland flow, valley incision, and sedimentary aggradation within Chukhung crater since its formation between the early Hesperian and early Amazonian. Thus, regardless of whether sinuous ridges in Chukhung crater are eskers or inverted palaeochannels, their formation required environmental conditions that were atypical of Mars after the Noachian and are as yet unexplained by the general model of long-term cooling and drying of Mars climate after the Noachian-Hesperian transition.

This thesis also presents the first systematic, metre-scale morphometric characterisation of eskers anywhere on Mars (Chapters 5–7). Previous systematic measurements of eskers on Mars were limited to the large, early-Hesperian-aged Dorsa Argentea and Argyre Planitia eskers and used topographic data with spatial resolutions of hundreds of metres (Banks et al., 2009; Bernhardt et al., 2013; Butcher et al., 2016). The new measurements for the smaller, late-Amazonian-aged glacier-linked eskers in Phlegra Montes and NW Tempe Terra expand the range of landform ages and scales for which the morphometries of eskers on Mars are known.

The morphometry of the glacier-linked esker in NW Tempe Terra suggests that it comprises two stacked ridge members recording complex spatiotemporal variations in sediment-discharge dynamics along a pressurised esker-forming subglacial meltwater conduit (Chapter 6). An initial phase of drainage characterised by high discharge and sediment supply formed the lower of the stacked ridge members, while a later phase of reduced discharge and/or sediment supply (probably within the same drainage event, but possibly within a temporally distinct event following a period of ice margin retreat) formed the superposed upper member ridge. Different portions of the esker with similar crest morphologies have remarkably similar morphometric relationships, some small differences between which could be explained by increases in exposure age, and hence degradation state, with distance from the present glacier terminus. These similarities also exist between portions of the glacier-linked eskers in NW Tempe Terra and Phlegra Montes with similar crest morphologies (Chapter 7). This suggests that the morphometries of eskers on Mars could be governed by glacio-hydrological controls during the primary formation process. In combination with considerations of esker exposure age and degradation state, such process-controlled relationships (if validated, see Section 10.2.3) could thus be used to test for esker

origins of sinuous ridges elsewhere on Mars. The glacier-linked eskers in NW Tempe Terra and Phlegra Montes are more similar in scale and 3D morphometry to typical eskers on Earth than the Dorsa Argentea and Argyre Planitia eskers (Chapter 7). However, all eskers on Mars measured to date tend towards greater width-height ratios, and therefore lower cross-sectional slopes than typical eskers on Earth. This could result from differences in landform age and hence degradation state, or could instead be explained by more fundamental differences between Earth and Mars in the parameters governing the growth of subglacial meltwater conduits and the morphometries of eskers deposited within them, and should be explored further (Section 10.2.3).

The presence of eskers in Phlegra Montes and NW Tempe Terra (Chapters 3 and 4) indicates that their parent glaciers produced liquid water at their beds and has important implications beyond reconstructions of environmental change on Mars. Subglacial environments, which are protected from harmful radiation at the surface are of significant interest in the search for past or present microbial life on Mars (e.g., Skidmore et al., 2000), and evidence for the availability of liquid water in these environments further enhances their habitability potential. Glacier-linked eskers, which probably contain complex sedimentary records of the dynamics of the glacial melt events that formed them (e.g., Chapter 6) could provide important exploration targets for future crewed missions to Mars, which are likely to rely upon in situ water ice resources from mid-latitude debris-covered glaciers within their exploration zones (e.g., Hoffman et al., 2017; Baker and Carter, 2019b).

10.2. Future Work

I identify several avenues for future research that could develop upon the insights provided by this thesis, including: (1) a systematic survey for candidate glacier-linked eskers throughout Mars' mid latitudes, (2) systematic morphometric analyses to test the origins of glacier-linked sinuous ridges in Chukhung crater further, (3) development and validation of diagnostic morphometric tests of esker origins for sinuous ridges on Mars, and (4) 3D glacier flow modelling to constrain in more detail the requisite conditions for basal melting of glaciers on Mars.

10.2.1. Systematic Survey for Candidate Glacier-Linked Eskers

To date, no systematic survey has been undertaken in search of candidate eskers associated with VFFs in Mars' mid latitudes. Such a survey, which could be guided by existing catalogues of mid-latitude VFFs (Souness et al., 2012; Levy et al., 2014), would improve understanding of how frequently (or rarely) VFFs underwent basal melting, and allow

assessment of the geological settings in which wet-based glaciation occurred during the Amazonian. I expect eskers associated with VFFs to be rare, but I have observed at least two additional candidate eskers associated with VFFs that occupy grabens in a preliminary survey of the wider Tempe Terra region. If few further examples are identified during the survey, this would not compromise its scientific importance; an absence of eskers beyond those already observed would have similarly important implications for drivers of basal melting at known esker locations. If additional eskers are found, their spatial distributions, spatial densities, and geologic settings will allow further scrutiny of the possible environmental and glaciological controls on the distribution of wet-based glaciation during the Amazonian.

10.2.2. Morphometric Analyses of Sinuous Ridges in Chukhung Crater

The logical next step for testing the origins of glacier-linked sinuous ridges in Chukhung crater is to undertake similar morphometric analyses to those performed for the glacier-linked eskers in Phlegra Montes and NW Tempe Terra in order to assess whether they exhibit similarities, both in their absolute morphometries and in possible process-driven morphometric relationships, with those landforms.

10.2.3. Esker Identification: Development and Validation of Morphometric Tests

I identify several priorities for additional development and validation of morphometric techniques which could greatly improve confidence in tests of the esker hypothesis for sinuous ridges on Mars. Currently, understanding of 'esker-like' morphometric relationships is based largely on theory of subglacial meltwater drainage (e.g., Shreve, 1985a) and localised empirical field studies (e.g., Perkins et al., 2016), and are not strongly grounded in morphometric observations along large samples of eskers on Earth. Therefore, I suggest that the possible existence of process-driven morphometric relationships identified for eskers on Mars should be validated against a large sample of systematic observations of eskers on Earth such as that collected by Storrar and Jones (unpublished) during the preparation of this thesis (see Chapter 5). These relationships include: (1) associations between crest morphology and esker height-width relationships (e.g., Chapters 6 and 7); (2) relationships between ridge height and along-ridge bedslope (see Section 8.7; Butcher et al., 2016); and (3) relationships between exposure ages, degradation states, and flank slopes. These analyses could be supplemented with targeted field studies analysing relationships between morphometry and sedimentary architecture (such as those performed by Burke et al., 2015 and; Perkins et al., 2016) to assess whether any observed relationships are indeed process-driven. Additionally, it would be beneficial to make theoretical predictions of possible

differences between the morphometries of eskers on Earth and Mars that could arise from differences in governing parameters such as gravity and atmospheric pressure. This could be achieved, for example, by incorporating Mars-like parameters into the recent numerical model by Beaud et al. (2018) of morphodynamics in esker-forming subglacial meltwater conduits. A priority for such a study would be to identify possible explanations for consistently higher width-height ratios observed for putative eskers on Mars compared with eskers on Earth (e.g., Chapters 6 and 7; Banks et al., 2009; Butcher et al., 2016).

The utility of morphometric analyses for testing the esker hypothesis for sinuous ridges on Mars would be enhanced by the availability of systematic, high-resolution measurements of inverted palaeochannels on both Earth and Mars. While the influence of secondary induration, burial and exhumation processes probably results in highly variable, and possibly random morphometric relationships along inverted palaeochannels, comparisons with the growing number of measurements of eskers on both Earth and Mars will improve understanding of the morphometric similarities and differences between these landform types. In particular, these measurements could be used to assess the degree of overlap between typical morphometries of esker and inverted palaeochannel populations on Earth and Mars, and to validate whether morphometric relationships observed along eskers are uniquely esker-like (and therefore indicative of esker origins), or whether they could also be explained under the inverted palaeochannel hypothesis. If inverted channels do indeed have random or near-random morphometric relationships, but relationships along eskers are process-driven (and therefore non-random), observations of similar esker-like relationships along a given sinuous ridge on Mars would greatly enhance confidence in the esker hypothesis for that landform.

10.2.4. 3D Glacier Flow Modelling

I am currently undertaking new 3D glacier flow modelling experiments to constrain the environmental requirements for basal melting of glaciers on Mars using the state of the art Ice Sheet System Model (ISSM; Larour et al., 2012). These experiments develop upon the first-order constraints provided by the 1D thermal modelling experiments discussed in Section 9.2. Initially simulating ice sheet-style glaciation (following the model of Fastook et al., 2014 and; Baker and Head, 2015; see Chapter 3) over a domain covering the southern Phlegra Montes region and terminating at the location of the glacier-linked esker complex (with basal topography from the 463 m/pixel gridded MOLA DEM; Figure 10.1A), I am performing experiments that perturb mean annual surface temperature and geothermal heat

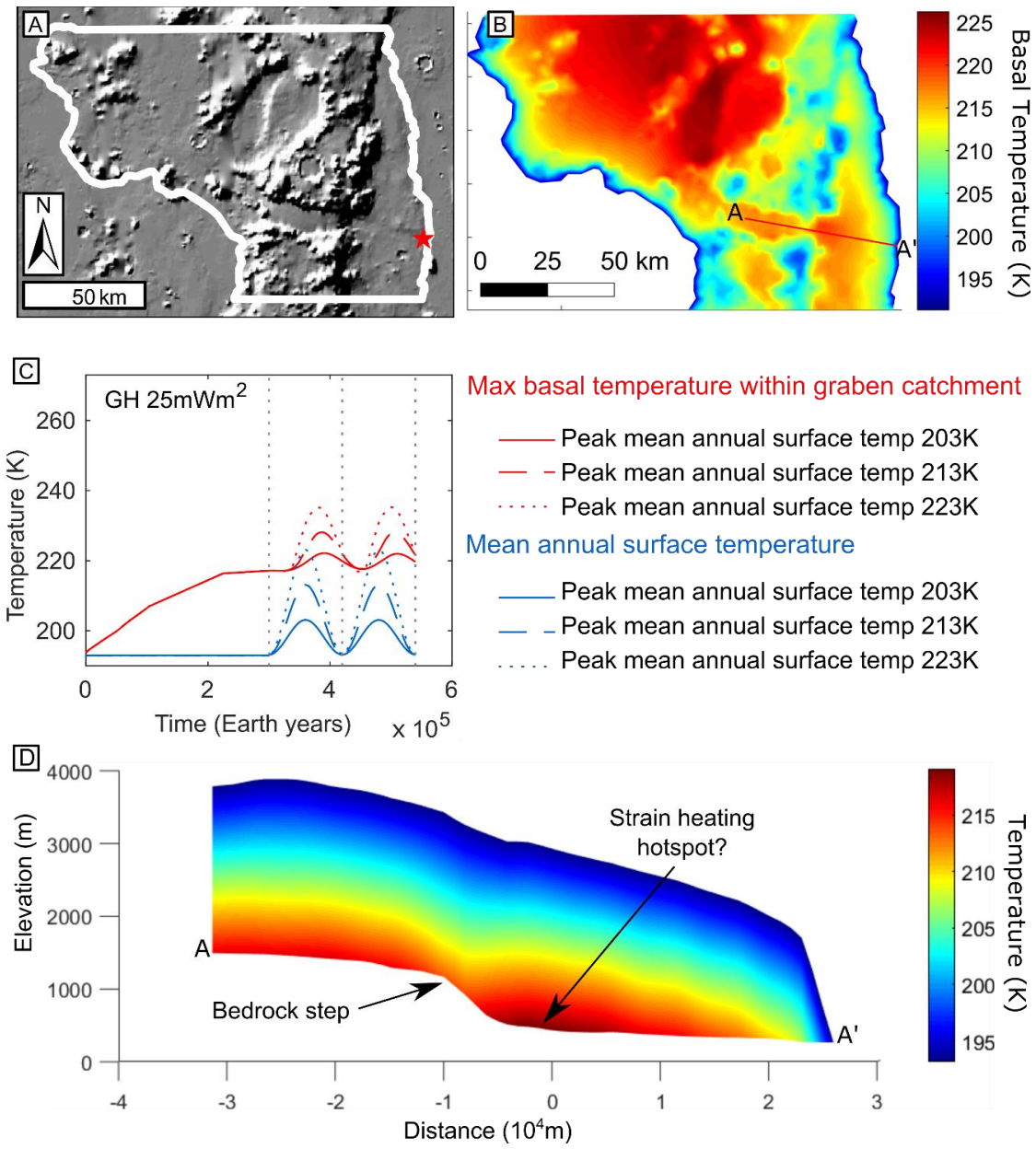

Figure 10.1. Preliminary 3D glacial flow modelling in Phlegra Montes using the Ice Sheet System Model. (A) MOLA hillshade map showing the ice sheet domain (white line), which terminates at the glacier-linked esker (red star) in southern Phlegra Montes. (B) A map of basal temperature over the domain for an ice sheet grown to steady state for 300 kyr under constant regional geothermal heat flux of 25 mW m^{-2}, mean annual surface temperature of 193 K, and a glacier mass balance of 12 mm yr^{-1} (reducing to 0 mm yr^{-1} in a narrow zone approaching the ice margin) followed by two cyclic, 120 kyr-period climate perturbations in which mean annual surface temperature increased to 203 K and regional mass balance decreased to 0 mm yr^{-1}. (C) Mean annual surface temperature and associated maximum basal temperature within the ice divide surrounding the graben that presently hosts the parent glacier of esker complex. Temperatures are for the same experiment as in panel B (solid lines), and for two additional experiments perturbing mean annual surface temperature to peaks of 213 K (dashed lines) and 223 K (dotted lines). (D) A cross section through the simulated ice sheet for profile A–A' in panel B showing the possible influence of flow convergence (and hence strain heating) on elevating basal temperature down-glacier of a bedrock step that separates the Phlegra Montes esker complex from the present-day terminus of its parent glacier. Meltwater morphologies observed by Gallagher and Balme (2015) occur down-flow of this step, so it is possible that flow convergence was an important stimulus of basal melting in this location (under warmer mean annual surface temperatures and/or geothermal heat flux conditions than those shown here), and that meltwater was not produced up-glacier of the bedrock step.

flux for ice sheets grown to steady state under a range of initial mean annual surface temperature and geothermal heat flux conditions. Current experiments simulate cyclic variations in mean annual surface temperature for various spatially uniform geothermal heat fluxes (e.g., Figure 10.1B–D). Future experiments will: simulate transient increases in geothermal heat flux within and near to the graben hosting the parent glacier of the esker; simulate the combined effects of both mean annual surface temperature and geothermal heat flux variations on basal temperatures; and explore the influence of other factors such as mass balance and ice rheology upon the requirements for basal melting. These experiments will provide new constraints of the magnitude of climatic and geothermal heat flux variations (at least transiently and on local scales) required to explain geomorphic evidence for wet-based glaciation in Mars' geologically recent past.

The NASA InSight lander is anticipated to return new insights into geothermal processes occurring in Mars' subsurface and will provide essential ground truth for existing estimates of Mars' geothermal heat flux. If Amazonian wet-based glaciation was indeed geothermally controlled, future constraints on requisite geothermal heat fluxes for esker formation could provide crucial spatiotemporal context for the single point measurement returned from the InSight mission. Therefore, future studies of eskers on Mars could help to advance understanding not only of past glaciological and climatological processes, but also of processes that have occurred deeper in Mars' subsurface, beyond the realms that are visible to current orbital remote sensing missions.

APPENDIX A

DERIVATION OF MEASUREMENT UNCERTAINTIES REPORTED IN TABLE 5.2

A.1. Calculation of Measurement Uncertainties

I propagated uncertainties[10] for measurements of the glacier-linked eskers in NW Tempe Terra and Phlegra Montes based on experimentally-derived quantification of errors combined with calculated uncertainties arising from the the precisions of the DEMs and the magnitude of vertical noise within the HiRISE DEMs (see Sections 5.5.3 and 5.5.4, respectively). I found uncertainties arising from distortion by the map projection to be insignificant for both sites (Section 5.5.2). This approach follows that of Butcher et al. (2016).

A.1.1. Segment Lengths

I quantified error arising from the accuracy with which I digitised segment crestlines by re-digitising the longest and shortest ridge segments, plus a segment of intermediate length at each site three times in ArcMap, without referring to crestlines digitised previously. I then calculated the standard error of the digitised line lengths of each segment and took the mean of these standard errors as the uncertainty in segment length (δL_S).

The uncertainty in segment length was ± 1.27 m for Phlegra Montes and ± 5.48 m for NW Tempe Terra. The uncertainty for the NW Tempe Terra site was larger than that for Phlegra Montes largely because the broad, indistinct nature of the ridge crest in zone III of the ridge introduced larger deviations from the originally digitised crestline.

[10] Uncertainty propagation followed: Harvard University Department of Physics Instructional Physics Laboratory, 2007, Physical Sciences 2: A Summary of Error Propagation [Online], available at: http://ipl.physics.harvard.edu/wp-uploads/2014/01/ps2_fa13_err.pdf (last accessed 07/02/2019).

A.1.2. Path Lengths

I quantified the uncertainty in path lengths (δP_S) from the repeat crestlines digitised during quantification of uncertainty in segment length (Section A.1.1), taking mean of the standard errors for the three path length measurements for each of the segments.

The uncertainty in path length was ± 1.23 m for Phlegra Montes and ±1.55 m for NW Tempe Terra.

A.1.3. Mapped Lengths

I calculated the uncertainty in mapped ridge length by propagating the error in segment lengths (Section A.1.1) from which mapped ridge length is derived. I based the propagation upon the 8 segments that comprise the single ridge system in NW Tempe Terra, and the 6 segments that comprise the system with the greatest number of segments in Phlegra Montes.

Phlegra Montes:

Segment length error = ± 1.27 m

$$\delta L_m = \pm\sqrt{6 \times 1.27^2} = \pm 3.11\ m$$

NW Tempe Terra:

Segment length error = ± 5.48 m

$$\delta L_m = \pm\sqrt{8 \times 5.48^2} = \pm 15.50\ m$$

A.1.4. System Lengths

The errors in linearly-interpolated distance between ridge gaps due to projection distortion were negligible for both the Phlegra Montes and NW Tempe Terra sites. Hence, I estimated the uncertainties in system length (δL_i) for each site to be equivalent to those of mapped ridge length above (Section A.1.3).

A.1.5. System Continuities

I calculated the uncertainty in ridge continuity (δC) from the uncertainties in mapped ridge lengths and system lengths. For the Phlegra Montes site, I based this calculation on the ridge system with the greatest number of segments (6).

Phlegra Montes:

Mapped length: 242.66 ± 3.11 m

System length: 327.09 ± 3.11 m

Continuity: 0.74

$$\delta C = \pm 0.74 \times \sqrt{\left(\frac{3.11}{242.66}\right)^2 + \left(\frac{3.11}{327.09}\right)^2} = \pm 0.012$$

NW Tempe Terra:

Mapped length: 16066.13 ± 15.50 m

System length: 17111.41 ± 15.50 m

Continuity: 0.94

$$\delta C = \pm 0.94 \times \sqrt{\left(\frac{15.50}{16066.13}\right)^2 + \left(\frac{15.50}{17111.41}\right)^2} = \pm\, 0.001$$

A.1.6. Segment Sinuosities

I calculated the uncertainty in segment sinuosity (δS_s) by propagating the uncertainties in segment path lengths (Section A.1.2) and segment lengths (Section A.1.1) calculated above. I based the calculation upon the shortest segment at each site.

Phlegra Montes:

Segment length: 13.70 ± 1.27 m

Path length: 13.70 ± 1.23 m

$$\delta S_s = \pm \frac{13.70}{13.70} \times \sqrt{\left(\frac{1.27}{13.70}\right)^2 + \left(\frac{1.23}{13.70}\right)^2} = \pm\, 0.13$$

NW Tempe Terra:

Segment length: 148.96 ± 5.48 m

Path length: 135.34 ± 1.55 m

Continuity: 0.94

$$\delta S_S = \pm \frac{148.69}{135.34} \times \sqrt{\left(\frac{5.48}{148.69}\right)^2 + \left(\frac{1.55}{135.34}\right)^2} = \pm\, 0.04$$

A.1.7. System Sinuosities

I calculated the uncertainty in system sinuosity by propagating uncertainties in system lengths and system path lengths. Since the effect uncertainty is greater as a proportion of shorter ridges compared to longer ridges, I quantified the uncertainty based on the shortest system at each site. For Phlegra Montes, this system comprised a single segment so I calculated uncertainty in the same manner as segment sinuosity.

System length: 102.02 ± 3.11 m

Path length: 100.11 ± 1.23 m

$$\delta S_i = \pm \frac{102.02}{100.11} \times \sqrt{\left(\frac{3.11}{102.02}\right)^2 + \left(\frac{1.23}{100.11}\right)^2} = \pm\, 0.03$$

For the NW Tempe Terra site, I converted the uncertainty in error in segment path length to a percentage of the shortest segment length and applied this percentage to calculate the uncertainty in the path length the full system δP_i as follows:

Segment length (shortest segment): 148.69 ± 5.48 m

Path length (shortest segment): 135.34 ± 1.55 m

$$\frac{1.55\ m}{135.34\ m} \times 100 = 1.15\ \%$$

System length: 17,111.41 ± 15.5 m

System path length: 15,108.69 ± 1.15 %

Uncertainty in system path length$= \frac{15{,}108.69 \times 1.15}{100} = \pm 173.75\ m$

$$\delta S_i = \pm \frac{17111.41}{15108.69} \times \sqrt{\left(\frac{15.5}{17111.41}\right)^2 + \left(\frac{173.75}{15108.69}\right)^2} = \pm 0.01$$

A.1.8. Ridge Base Elevations

I calculated the uncertainty in ridge base elevation (δZ_{base}) from the vertical magnitude of DEM noise calculated for each site (± 0.889 m for Phlegra Montes and ± 1.343 for NW Tempe Terra; Section 5.5.4), since the magnitudes of these uncertainties were greater than those introduced by the vertical precision of the DEMs (Section 5.5.3).

Phlegra Montes:

$$\delta Z_{base} = \pm \frac{\sqrt{0.889^2 + 0.889^2}}{2} = \pm 0.629\ m$$

NW Tempe Terra:

$$\delta Z_{base} = \pm \frac{\sqrt{1.343^2 + 1.343^2}}{2} = \pm 0.950\ m$$

A.1.9. Ridge Heights

As for ridge base elevations, I calculated the uncertainty in ridge height (δH) taking the uncertainty in the elevation of the crest points (δZ_{crest}) as equivalent to the vertical magnitudes of noise in the DEMs, since these exceeded the uncertainty introduced by the vertical precisions of the DEMs.

Phlegra Montes:

δZ_{crest} = ± 0.889 m

δZ_{base} = ± 0.629 m

$$\delta H = \pm\sqrt{0.889\,m^2 + 0.629\,m^2} = \pm 1.09\,m$$

NW Tempe Terra:

$\delta Z_{crest} = \pm$ 1.343 m

$\delta Z_{base} = \pm$ 0.950 m

$$\delta H = \pm\sqrt{1.343^2 + 0.950^2} = \pm\,1.65\,m$$

A.1.10. Ridge Widths

I calculated the uncertainty in ridge widths by taking the uncertainty in the along-transect distances of the left and right base points as equivalent to the horizontal resolution of the DEMs (1 m/pixel for Phlegra Montes and 2 m/pixel for NW Tempe Terra).

Phlegra Montes:

$$\delta W = \pm\sqrt{1^2 + 1^2} = \pm\,1.41\,m$$

NW Tempe Terra:

$$\delta \mathrm{W} = \pm\sqrt{2^2 + 2^2} = \pm\,2.83\,m$$

A.1.11. Width-Height Ratio

I calculated the uncertainty in width-height ratios for the esker complex in Phlegra Montes based on the errors in ridge height and width, using the transects with the median width-height ratios (22.33).

Phlegra Montes:

$$\delta A_{W:H} = \pm\sqrt{\left(\frac{1.41}{169.191}\right)^2 + \left(\frac{1.08}{7.5753}\right)^2} = \pm\,14.3\,\%$$

$$\delta A_{W:H} = \frac{22.33 \times 14.3}{100} = \pm\ 3.19$$

The reported width-height ratios for the esker in NW Tempe Terra are for the individual upper and lower member ridges comprising the stacked esker formation (Chapter 6). I calculated the uncertainty in width-height ratios considering the uncertainty in the heights of the constituent upper and lower member ridges. The uncertainty in the heights of the constituent ridge members is propagated from the uncertainty in height according to:

$$\delta A_{W:H} = \pm\sqrt{1.65^2 + 1.65^2} = \pm\,2.33\,m$$

I then used this uncertainty to calculate that for the width-height ratios of the constituent ridge members for the transect with the median width-height ratio (18.14) according to:

$$\delta A_{W:H} = \sqrt{\left(\frac{2.83}{153.99}\right)^2 + \left(\frac{2.33}{8.51}\right)^2} = \pm\ 27.4\%$$

$$\delta A_{W:H} = \frac{18.14 \times 27.4}{100} = \pm 4.97$$

A.1.12. Average Cross-Sectional Slope

I quantified the uncertainty in average cross-sectional slope ($\delta\theta_{CS}$) for the same representative transects as those for which I calculated uncertainties in width-height ratios. For Phlegra Montes, the height of the representative transect was 7.58 m and its width was 169.19 m.

Phlegra Montes:

$$\delta H = \pm 1.08\, m$$

$$\delta W = \pm 1.41\, m$$

$$\frac{\delta W}{2} = 0.705\, m$$

$$\delta \frac{H}{0.5W} = \left(\frac{7.5753}{0.5 \times 169.191}\right) \times \sqrt{\left(\frac{1.08}{7.5753}\right)^2 + \left(\frac{0.705}{0.5 \times 169.191}\right)^2} = \pm 0.0128$$

$$Maximum\ slope = \tan^{-1}\left[\left(\frac{7.5753}{0.5 \times 169.191}\right) + 0.0128\right] = 5.84°$$

$$Minimum\ slope = \tan^{-1}\left[\left(\frac{7.5753}{0.5 \times 169.191}\right) - 0.0128\right] = 4.39°$$

$$\delta\theta_{CS} = \pm 5.84° - 4.39° = 1.45°$$

As with the width-height ratios for NW Tempe Terra, average cross-sectional slopes for this site are reported for the constituent upper and lower ridge members. Thus, the uncertainty is based on the uncertainty in height for the individual ridge members as calculated in Section A.1.11, and the same representative transect as I used to calculate the uncertainty in width-height ratio. This transect had a height of 8.51 m and a width of 153.99 m.

NW Tempe Terra:

$$\delta H = \pm 2.33\, m$$

$$\delta W = \pm 2.83\, m$$

$$\frac{\delta W}{2} = 1.415\, m$$

$$\delta\frac{H}{0.5W} = \left(\frac{8.51\,m}{0.5\times 153.99\,m}\right)\times\sqrt{\left(\frac{2.33\,m}{8.51\,m}\right)^2+\left(\frac{1.415\,m}{0.5\times 153.99\,m}\right)^2} = \pm 0.03033$$

$$Maximum\ slope = \tan^{-1}\left[\left(\frac{8.51\,m}{0.5\times 153.99\,m}\right)+0.03033\right] = 8.02°$$

$$Minimum\ slope = \tan^{-1}\left[\left(\frac{8.51\,m}{0.5\times 153.99\,m}\right)-0.03033\right] = 4.59°$$

$$\delta\theta_{CS} = \pm 8.02° - 4.59° = \pm\,3.43°$$

APPENDIX B

GEOMORPHIC MAP OF CHUKHUNG CRATER, CENTRAL TEMPE TERRA, MARS

B.1. Geomorphic Map of Chukhung Crater

What follows is an enlarged version of the geomorphic map of Chukhung crater discussed in Chapter 8.

APPENDIX B

Geomorphic map of Chukhung crater, central Tempe Terra, Mars

Frances E. G. Butcher

Geomorphic Units

- *Fim* Fresh impact material (>200 m craters)
- *Hmu* Highland mantle unit
- *LDA* Lobate Debris Apron
- *Ltl* LDA-terminal lobes
- *Rpu* Ridged plains unit
- *Sr* Sinuous ridges (Includes S1, S2, and N2 ridges)
- *Tar* Transverse aeolian ridges
- *Ipo* Isolated pockmarked unit
- *Cpf* Central pit floor
- *Mpf* Marginal pit floor
- *Upr* Upper plains and ridges (Includes N1 ridges)
- *Ipu* Intermediate plains unit
- *Lsp* Lower smooth plains
- *Uip* Upper incised plains
- *Hcm* Host crater materials

Structure

- Crater wall valley
- Small impact crater rim

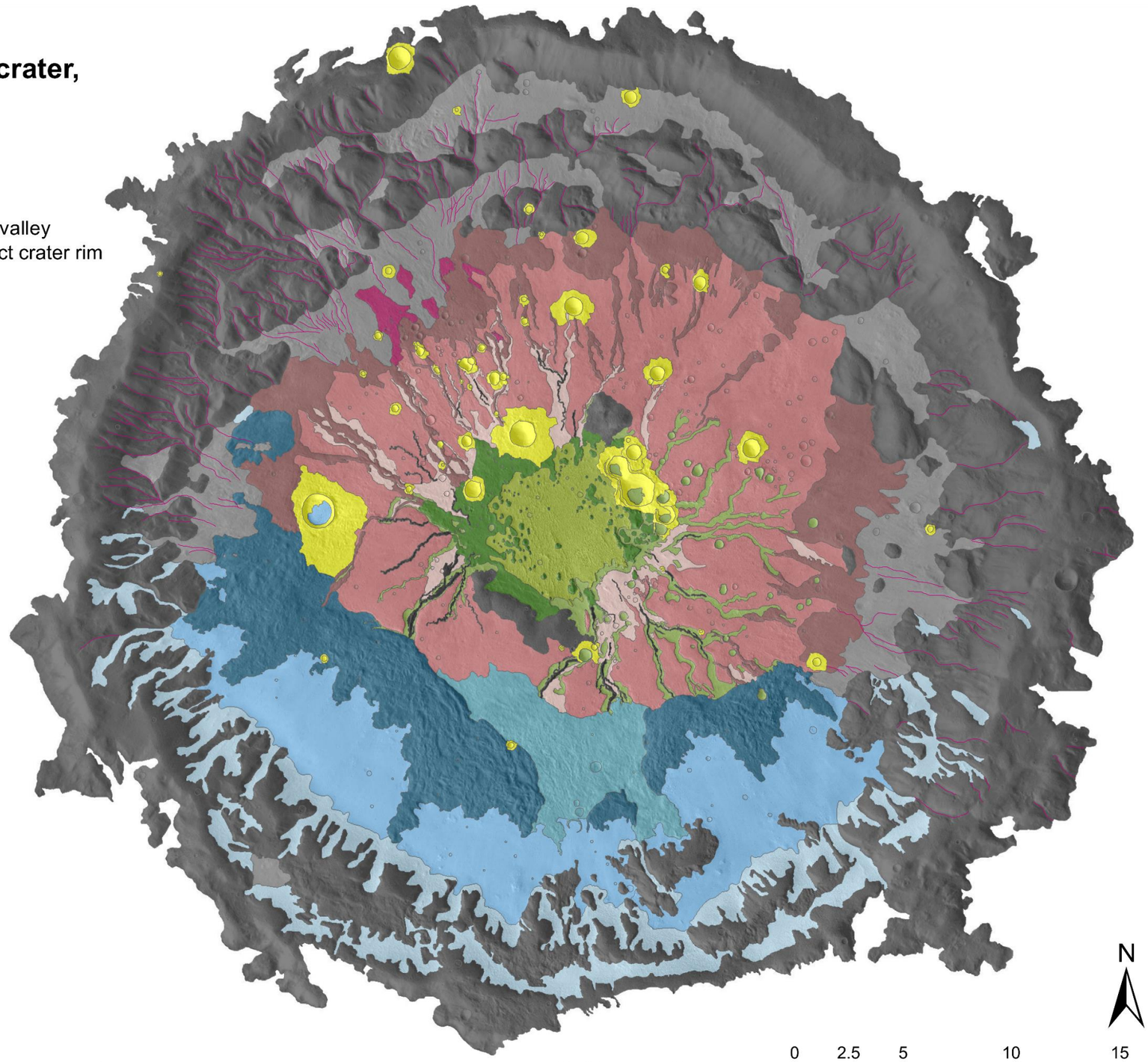

Coordinate system information

Projection: Sinusoidal
Central meridian: 72.5°W
Sphere radius: 3396.190 km

Basemap image data

Context Camera images
Downloaded from: http://viewer.mars.asu.edu/viewer/ctx#T=0

Map centred on 72.5°W, 38.46°N

N

0 2.5 5 10 15 km

REFERENCES

Adeli, S., Hauber, E., Kleinhans, M., Le Deit, L., Platz, T., Fawdon, P., Jaumann, R., 2016. Amazonian-aged fluvial system and associated ice-related features in Terra Cimmeria, Mars. Icarus 277, 286–299. https://doi.org/10.1016/j.icarus.2016.05.020

Anderson, R.S., Anderson, S.P., 2010. Geomorphology: the mechanics and chemistry of landscapes. Cambridge University Press, Cambridge.

Appéré, T., Schmitt, B., Langevin, Y., Douté, S., Pommerol, A., Forget, F., Spiga, A., Gondet, B., Bibring, J.-P., 2011. Winter and spring evolution of northern seasonal deposits on Mars from OMEGA on Mars Express. J. Geophys. Res. Planets 116, E05001. https://doi.org/10.1029/2010JE003762

Arfstrom, J., Hartmann, W.K., 2005. Martian flow features, moraine-like ridges, and gullies: Terrestrial analogs and interrelationships. Icarus 174, 321–335. https://doi.org/10.1016/j.icarus.2004.05.026

Atkins, C.B., Barrett, P.J., Hicock, S.R., 2002. Cold glaciers erode and deposit: Evidence from Allan Hills, Antarctica. Geology 30, 659–662. https://doi.org/10.1130/0091-7613(2002)030<0659:CGEADE>2.0.CO;2

Aylsworth, J.M., Shilts, W.W., 1989. Bedforms of the Keewatin Ice Sheet, Canada. Sediment. Geol. 62, 407–428. https://doi.org/10.1016/0037-0738(89)90129-2

Baker, D.M.H., Carter, L.M., 2019a. Probing supraglacial debris on Mars 2: Crater morphology. Icarus 319, 264–280. https://doi.org/10.1016/j.icarus.2018.09.009

Baker, D.M.H., Carter, L.M., 2019b. Probing supraglacial debris on Mars 1: Sources, thickness, and stratigraphy. Icarus 319, 745–769. https://doi.org/10.1016/j.icarus.2018.09.001

Baker, D.M.H., Head, J.W., 2015. Extensive Middle Amazonian mantling of debris aprons and plains in Deuteronilus Mensae, Mars: Implications for the record of mid-latitude glaciation. Icarus 260, 269–288. https://doi.org/10.1016/j.icarus.2015.06.036

Baker, D.M.H., Head, J.W., Marchant, D.R., 2010. Flow patterns of lobate debris aprons and lineated valley fill north of Ismeniae Fossae, Mars: Evidence for extensive mid-latitude glaciation in the Late Amazonian. Icarus 207, 186–209. https://doi.org/10.1016/j.icarus.2009.11.017

Baker, V.R., 2014. Terrestrial analogs, planetary geology, and the nature of geological reasoning. Planet. Space Sci., Planetary Geology Field Symposium, Kitakyushu, Japan, 2011: Planetary Geology and Terrestrial Analogs 95, 5–10. https://doi.org/10.1016/j.pss.2012.10.008

Baker, V.R., 1996. Hypotheses and Geomorphological Reasoning, in: Rhoads, B.L., Thorn, L.H. (Eds.), The Scientific Nature of Geomorphology: Proceedings of the 27th Binghampton Symposium in Geomorphology Held 27-29 September 1996. John Wiley & Sons, Chichester, pp. 57–85.

Balme, M., Berman, D.C., Bourke, M.C., Zimbelman, J.R., 2008. Transverse Aeolian Ridges (TARs) on Mars. Geomorphology 101, 703–720. https://doi.org/10.1016/j.geomorph.2008.03.011

Balme, M., Mangold, N., Baratoux, D., Costard, F., Gosselin, M., Masson, P., Pinet, P., Neukum, G., 2006. Orientation and distribution of recent gullies in the southern hemisphere of Mars: Observations from High Resolution Stereo Camera/Mars Express (HRSC/MEX) and Mars Orbiter Camera/Mars Global Surveyor (MOC/MGS) data. J. Geophys. Res. Planets 111, E05001. https://doi.org/10.1029/2005JE002607

Balme, M.R., Gallagher, C.J., Hauber, E., 2013. Morphological evidence for geologically young thaw of ice on Mars: A review of recent studies using high-resolution imaging data. Prog. Phys. Geogr. 37, 289–324. https://doi.org/10.1177/0309133313477123

Bamber, J.L., Griggs, J.A., Hurkmans, R.T.W.L., Dowdeswell, J.A., Gogineni, S.P., Howat, I., Mouginot, J., Paden, J., Palmer, S., Rignot, E., Steinhage, D., 2013. A new bed elevation dataset for Greenland. The Cryosphere 7, 499–510. https://doi.org/10.5194/tc-7-499-2013

Banerjee, I., McDonald, B.C., 1975. Nature of Esker Sedimentation. Glacifluvial Glacilacustrine Sediment. Soc. Econ. Paleontol. Mineral. Spec. Publ. 23, 304–320.

Banks, M.E., Lang, N.P., Kargel, J.S., McEwen, A.S., Baker, V.R., Grant, J.A., Pelletier, J.D., Strom, R.G., 2009. An analysis of sinuous ridges in the southern Argyre Planitia, Mars using HiRISE and CTX images and MOLA data. J. Geophys. Res. Planets 114, E09003. https://doi.org/10.1029/2008JE003244

Beaud, F., Flowers, G.E., Venditti, J.G., 2018. Modeling Sediment Transport in Ice-Walled Subglacial Channels and Its Implications for Esker Formation and Proglacial Sediment Yields. J. Geophys. Res. Earth Surf. 123, 3206–3227. https://doi.org/10.1029/2018JF004779

Benn, D.I., Evans, D.J.A., 2010. Glaciers & Glaciation, Second Edition. ed. Hodder Education, London.

Benn, D.I., Thompson, S., Gulley, J., Mertes, J., Luckman, A., Nicholson, L., 2017. Structure and evolution of the drainage system of a Himalayan debris-covered glacier, and its relationship with patterns of mass loss. The Cryosphere 11, 2247–2264. https://doi.org/10.5194/tc-11-2247-2017

Berman, D.C., Crown, D.A., Joseph, E.C.S., 2012. Constraints on the formation and modification of lobate debris aprons through categorized crater counts. Lunar Planet. Sci. Conf. XLIII Abstract #1593.

Bernhardt, H., Hiesinger, H., Reiss, D., Ivanov, M., Erkeling, G., 2013. Putative eskers and new insights into glacio-fluvial depositional settings in southern Argyre Planitia, Mars. Planet. Space Sci. 85, 261–278. https://doi.org/10.1016/j.pss.2013.06.022

Bibring, J.-P., Langevin, Y., Gendrin, A., Gondet, B., Poulet, F., Berthé, M., Soufflot, A., Arvidson, R., Mangold, N., Mustard, J., Drossart, P., the OMEGA team, 2005. Mars Surface Diversity as Revealed by the OMEGA/Mars Express Observations. Science 307, 1576–1581. https://doi.org/10.1126/science.1108806

Bibring, J.P., Langevin, Y., Poulet, F., Gendrin, A., Gondet, B., Berthé, M., Soufflot, A., Drossart, P., Combes, M., Bellucci, G., Moroz, V., Mangold, N., Schmitt, B., the OMEGA team, 2004. Perennial water ice identified in the south polar cap of Mars. Nature 428, 627–630. https://doi.org/doi:10.1038/nature02461

Bingham, R.G., Hubbard, A.L., Nienow, P.W., Sharp, M.J., 2008. An investigation into the mechanisms controlling seasonal speedup events at a High Arctic glacier. J. Geophys. Res. Earth Surf. 113, F02006. https://doi.org/10.1029/2007JF000832

Bingham, R.G., Nienow, P.W., Sharp, M.J., Boon, S., 2005. Subglacial drainage processes at a High Arctic polythermal valley glacier. J. Glaciol. 51, 15–24. https://doi.org/doi:10.3189/172756505781829520

Björck, S., 1995. A review of the history of the Baltic Sea, 13.0-8.0 ka BP. Quat. Int. 27, 19–40. https://doi.org/10.1016/1040-6182(94)00057-C

Boulton, G.S., Dongelmans, P., Punkari, M., Broadgate, M., 2001. Palaeoglaciology of an ice sheet through a glacial cycle: the European ice sheet through the Weichselian. Quat. Sci. Rev. 20, 591–625. https://doi.org/10.1016/S0277-3791(00)00160-8

Boynton, W.V., Feldman, W.C., Squyres, S.W., Prettyman, T.H., Brückner, J., Evans, L.G., Reedy, R.C., Starr, R., Arnold, J.R., Drake, D.M., Englert, P. a. J., Metzger, A.E., Mitrofanov, I., Trombka, J.I., d'Uston, C., Wänke, H., Gasnault, O., Hamara, D.K., Janes, D.M., Marcialis, R.L., Maurice, S., Mikheeva, I., Taylor, G.J., Tokar, R., Shinohara, C., 2002. Distribution of Hydrogen in the Near Surface of Mars: Evidence for Subsurface Ice Deposits. Science 297, 81–85. https://doi.org/10.1126/science.1073722

Bramson, A.M., Byrne, S., Putzig, N.E., Sutton, S., Plaut, J.J., Brothers, T.C., Holt, J.W., 2015. Widespread excess ice in Arcadia Planitia, Mars. Geophys. Res. Lett. 42, 6566–6574. https://doi.org/10.1002/2015GL064844

Brennand, T.A., 2000. Deglacial meltwater drainage and glaciodynamics: inferences from Laurentide eskers, Canada. Geomorphology 32, 263–293. https://doi.org/10.1016/S0169-555X(99)00100-2

Brennand, T.A., 1994. Macroforms, large bedforms and rhythmic sedimentary sequences in subglacial eskers, south-central Ontario: implications for esker genesis and meltwater regime. Sediment. Geol. 91, 9–55. https://doi.org/10.1016/0037-0738(94)90122-8

Brough, S., Hubbard, B., Hubbard, A., 2019. Area and volume of mid-latitude glacier-like forms on Mars. Earth Planet. Sci. Lett. 507, 10–20. https://doi.org/10.1016/j.epsl.2018.11.031

Brough, S., Hubbard, B., Hubbard, A., 2016. Former extent of glacier-like forms on Mars. Icarus 274, 37–49. https://doi.org/10.1016/j.icarus.2016.03.006

Brough, S., Hubbard, B., Souness, C., Grindrod, P.M., Davis, J., 2015. Landscapes of polyphase glaciation: eastern Hellas Planitia, Mars. J. Maps 1–13. https://doi.org/10.1080/17445647.2015.1047907

Burke, M.J., Brennand, T.A., Perkins, A.J., 2012a. Evolution of the subglacial hydrologic system beneath the rapidly decaying Cordilleran Ice Sheet caused by ice-dammed lake drainage: implications for meltwater-induced ice acceleration. Quat. Sci. Rev. 50, 125–140. https://doi.org/10.1016/j.quascirev.2012.07.005

Burke, M.J., Brennand, T.A., Perkins, A.J., 2012b. Transient subglacial hydrology of a thin ice sheet: insights from the Chasm esker, British Columbia, Canada. Quat. Sci. Rev. 58, 30–55. https://doi.org/10.1016/j.quascirev.2012.09.004

Burke, M.J., Brennand, T.A., Sjogren, D.B., 2015. The role of sediment supply in esker formation and ice tunnel evolution. Quat. Sci. Rev. 115, 50–77. https://doi.org/10.1016/j.quascirev.2015.02.017

Burke, M.J., Woodward, J., Russell, A.J., Fleisher, P.J., Bailey, P.K., 2010. The sedimentary architecture of outburst flood eskers: A comparison of ground-penetrating radar data from Bering Glacier, Alaska and Skeiðarárjökull, Iceland. Geol. Soc. Am. Bull. 122, 1637–1645. https://doi.org/10.1130/B30008.1

Burke, M.J., Woodward, J., Russell, A.J., Fleisher, P.J., Bailey, P.K., 2008. Controls on the sedimentary architecture of a single event englacial esker: Skeiðarárjökull, Iceland. Quat. Sci. Rev. 27, 1829–1847. https://doi.org/10.1016/j.quascirev.2008.06.012

Burr, D.M., Enga, M.-T., Williams, R.M.E., Zimbelman, J.R., Howard, A.D., Brennand, T.A., 2009. Pervasive aqueous paleoflow features in the Aeolis/Zephyria Plana region, Mars. Icarus 200, 52–76. https://doi.org/10.1016/j.icarus.2008.10.014

Butcher, F.E.G., Balme, M.R., Gallagher, C., Arnold, N.S., Conway, S.J., Hagermann, A., Lewis, S.R., 2017. Recent Basal Melting of a Mid-Latitude Glacier on Mars. J. Geophys. Res. Planets 122, 2445–2468. https://doi.org/10.1002/2017JE005434

Butcher, F.E.G., Balme, M.R., Gallagher, C., Arnold, N.S., Conway, S.J., Storrar, R.D., Hagermann, A., Lewis, S.R., 2018. Evidence for Recent Wet-Based Crater Glaciation in Tempe Terra, Mars. Lunar Planet. Sci. Conf. XLIX Abstract #1498.

Butcher, F.E.G., Conway, S.J., Arnold, N.S., 2016. Are the Dorsa Argentea on Mars eskers? Icarus 275, 65–84. https://doi.org/10.1016/j.icarus.2016.03.028

Butler, B.J., Muhleman, D.O., Slade, M.A., 1993. Mercury: full-disk radar images and the detection and stability of ice at the North Pole. J. Geophys. Res. Planets 98, 15003–15023. https://doi.org/10.1029/93JE01581

Byrne, S., Dundas, C.M., Kennedy, M.R., Mellon, M.T., McEwen, A.S., Cull, S.C., Daubar, I.J., Shean, D.E., Seelos, K.D., Murchie, S.L., Cantor, B.A., Arvidson, R.E., Edgett, K.S., Reufer, A., Thomas, N., Harrison, T.N., Posiolova, L.V., Seelos, F.P., 2009. Distribution of Mid-Latitude Ground Ice on Mars from New Impact Craters. Science 325, 1674–1676. https://doi.org/10.1126/science.1175307

Byrne, S., Ingersoll, A.P., 2003. Martian climatic events on timescales of centuries: Evidence from feature morphology in the residual south polar ice cap. Geophys. Res. Lett. 30, 1696. https://doi.org/10.1029/2003GL017597

Cardenas, B.T., Mohrig, D., Goudge, T.A., 2018. Fluvial stratigraphy of valley fills at Aeolis Dorsa, Mars: Evidence for base-level fluctuations controlled by a downstream water body. Geol. Soc. Am. Bull. 130, 484–498. https://doi.org/10.1130/B31567.1

Carr, M.H., 2007. The Surface of Mars, Cambridge Planetary Science. Cambridge University Press, Cambridge. https://doi.org/10.1017/CBO9780511536007

Carr, M.H., 2001. Mars Global Surveyor observations of Martian fretted terrain. J. Geophys. Res. Planets 106, 23571–23593. https://doi.org/10.1029/2000JE001316

Carr, M.H., 1973. Volcanism on Mars. J. Geophys. Res. 78, 4049–4062. https://doi.org/10.1029/JB078i020p04049

Carr, M.H., Greeley, R., Blasius, K.R., Guest, J.E., Murray, J.B., 1977. Some Martian volcanic features as viewed from the Viking orbiters. J. Geophys. Res. 82, 3985–4015. https://doi.org/10.1029/JS082i028p03985

Carr, M.H., Head, J.W., 2015. Martian surface/near-surface water inventory: Sources, sinks, and changes with time. Geophys. Res. Lett. 42, 726–732. https://doi.org/10.1002/2014GL062464

Carr, M.H., Head, J.W., 2010. Geologic history of Mars. Earth Planet. Sci. Lett. 294, 185–203. https://doi.org/10.1016/j.epsl.2009.06.042

Carr, M.H., Schaber, G.G., 1977. Martian permafrost features. J. Geophys. Res. 82, 4039–4054. https://doi.org/10.1029/JS082i028p04039

Cassanelli, J.P., Head, J.W., Fastook, J.L., 2015. Sources of water for the outflow channels on Mars: Implications of the Late Noachian “icy highlands” model for melting and groundwater recharge on the Tharsis rise. Planet. Space Sci. 108, 54–65. https://doi.org/10.1016/j.pss.2015.01.002

Christensen, P.R., 2003. Formation of recent martian gullies through melting of extensive water-rich snow deposits. Nature 422, 45–48. https://doi.org/10.1038/nature01436

Christensen, P.R., Jakosky, B.M., Kieffer, H.H., Malin, M.C., McSween Jr, H.Y., Nealson, K., Mehall, G.L., Silverman, S.H., Ferry, S., Caplinger, M., Ravine, M., 2004. The Thermal Emission Imaging System (THEMIS) for the Mars 2001 Odyssey Mission. Space Sci. Rev. 110, 85–130. https://doi.org/doi:10.1023/B:SPAC.0000021008.16305.94

Clark, P.U., Dyke, A.S., Shakun, J.D., Carlson, A.E., Clark, J., Wohlfarth, B., Mitrovica, J.X., Hostetler, S.W., McCabe, A.M., 2009. The Last Glacial Maximum. Science 325, 710–714. https://doi.org/10.1126/science.1172873

Clark, P.U., Walder, J.S., 1994. Subglacial Drainage, Eskers, and Deforming Beds Beneath the Laurentide and Eurasian Ice Sheets. Geol. Soc. Am. Bull. 106, 304–314. https://doi.org/10.1130/0016-7606(1994)106<0304:SDEADB>2.3.CO;2

Clifford, S.M., 1993. A model for the hydrologic and climatic behavior of water on Mars. J. Geophys. Res. Planets 98, 10,973-11,016. https://doi.org/10.1029/93JE00225

Clifford, S.M., 1991. The role of thermal vapor diffusion in the subsurface hydrologic evolution of Mars. Geophys. Res. Lett. 18, 2055–2058. https://doi.org/10.1029/91GL02469

Clifford, S.M., Lasue, J., Heggy, E., Boisson, J., McGovern, P., Max, M.D., 2010. Depth of the Martian cryosphere: Revised estimates and implications for the existence and detection of subpermafrost groundwater. J. Geophys. Res. Planets 115, E07001. https://doi.org/10.1029/2009JE003462

Clifford, S.M., Parker, T.J., 2001. The Evolution of the Martian Hydrosphere: Implications for the Fate of a Primordial Ocean and the Current State of the Northern Plains. Icarus 154, 40–79. https://doi.org/10.1006/icar.2001.6671

Conway, S.J., Balme, M.R., 2014. Decameter thick remnant glacial ice deposits on Mars. Geophys. Res. Lett. 41, 5402–5409. https://doi.org/10.1002/2014GL060314

Conway, S.J., Butcher, F.E.G., de Haas, T., Deijns, A.A.J., Grindrod, P.M., Davis, J.M., 2018a. Glacial and gully erosion on Mars: A terrestrial perspective. Geomorphology 318, 26–57. https://doi.org/10.1016/j.geomorph.2018.05.019

Conway, S.J., de Haas, T., Harrison, T.N., 2018b. Martian gullies: a comprehensive review of observations, mechanisms and insights from Earth analogues. Geol. Soc. Lond. Spec. Publ. 467, 7–66. https://doi.org/10.1144/SP467.14

Craddock, R.A., Howard, A.D., 2002. The case for rainfall on a warm, wet early Mars. J. Geophys. Res. Planets 107, 5111. https://doi.org/10.1029/2001JE001505

Craddock, R.A., Maxwell, T.A., Howard, A.D., 1997. Crater morphometry and modification in the Sinus Sabaeus and Margaritifer Sinus regions of Mars. J. Geophys. Res. Planets 102, 13321–13340. https://doi.org/10.1029/97JE01084

Crown, D.A., Pierce, T.L., McElfresh, S.B.Z., Mest, S.C., 2002. Debris Aprons in the Eastern Hellas Region of Mars: Implications for Styles and Rates of Highland Degradation. Lunar Planet. Sci. Conf. XXXIII Abstract #1642.

Cuffey, K.M., Conway, H., Gades, A.M., Hallet, B., Lorrain, R., Severinghaus, J.P., Steig, E.J., Vaughn, B., White, J.W.C., 2000. Entrainment at cold glacier beds. Geology 28, 351–354. https://doi.org/10.1130/0091-7613(2000)28<351:EACGB>2.0.CO;2

Cuffey, K.M., Paterson, W.S.B., 2010. The Physics of Glaciers, 4th ed. Elsevier Science, Oxford.

Cummings, D.I., Gorrell, G., Guilbault, J.-P., Hunter, J.A., Logan, C., Ponomarenko, D., André, J.-M.P., Pullan, S.E., Russell, H.A.J., Sharpe, D.R., 2011. Sequence stratigraphy of a glaciated basin fill, with a focus on esker sedimentation. Geol. Soc. Am. Bull. 123, 1478–1496. https://doi.org/10.1130/B30273.1

Davis, J.M., 2017. The Geology of Ancient Fluvial and Lacustrine Systems in Arabia Terra and Melas Chasma, Mars (PhD Thesis). University College London, London.

Davis, J.M., Balme, M., Grindrod, P.M., Williams, R.M.E., Gupta, S., 2016. Extensive Noachian fluvial systems in Arabia Terra: Implications for early Martian climate. Geology 44, 847–850. https://doi.org/10.1130/G38247.1

de Haas, T., Conway, S.J., Butcher, F.E.G., Levy, J.S., Grindrod, P.M., Goudge, T.A., Balme, M.R., 2017. Time will tell: temporal evolution of Martian gullies and palaeoclimatic implications. Geol. Soc. Lond. Spec. Publ. 467, 165–186. https://doi.org/10.1144/SP467.1

Di Achille, G., Hynek, B.M., 2010. Ancient ocean on Mars supported by global distribution of deltas and valleys. Nat. Geosci. 3, 459–463. https://doi.org/10.1038/ngeo891

Dickson, J.L., Fassett, C.I., Head, J.W., 2009. Amazonian-aged fluvial valley systems in a climatic microenvironment on Mars: Melting of ice deposits on the interior of Lyot Crater. Geophys. Res. Lett. 36, L08201. https://doi.org/10.1029/2009GL037472

Dickson, J.L., Head, J.W., Fassett, C.I., 2012. Patterns of accumulation and flow of ice in the mid-latitudes of Mars during the Amazonian. Icarus 219, 723–732. https://doi.org/10.1016/j.icarus.2012.03.010

Dickson, J.L., Head, J.W., Marchant, D.R., 2010. Kilometer-thick ice accumulation and glaciation in the northern mid-latitudes of Mars: Evidence for crater-filling events in the Late Amazonian at the Phlegra Montes. Earth Planet. Sci. Lett. 294, 332–342. https://doi.org/10.1016/j.epsl.2009.08.031

Dickson, J.L., Head, J.W., Marchant, D.R., 2008. Late Amazonian glaciation at the dichotomy boundary on Mars: Evidence for glacial thickness maxima and multiple glacial phases. Geology 36, 411–414. https://doi.org/10.1130/G24382A.1

Donner, J., 1978. The dating of the levels of the Baltic Ice Lake and the Salpausselkä moraines in South Finland. Comment. Phys.-Math. 48, 11–38.

Dowdeswell, J.A., Ottesen, D., 2016. Eskers formed at the beds of modern surge-type tidewater glaciers in Spitsbergen. Geol. Soc. Lond. Mem. 46, 83–84. https://doi.org/10.1144/M46.70

Dundas, C.M., Bramson, A.M., Ojha, L., Wray, J.J., Mellon, M.T., Byrne, S., McEwen, A.S., Putzig, N.E., Viola, D., Sutton, S., Clark, E., Holt, J.W., 2018. Exposed subsurface ice sheets in the Martian mid-latitudes. Science 359, 199–201. https://doi.org/10.1126/science.aao1619

Dundas, C.M., McEwen, A.S., Chojnacki, M., Milazzo, M.P., Byrne, S., McElwaine, J.N., Urso, A., 2017. Granular flows at recurring slope lineae on Mars indicate a limited role for liquid water. Nat. Geosci. 10, 903–908. https://doi.org/10.1038/s41561-017-0012-5

Dundas, C.M., McEwen, A.S., Diniega, S., Byrne, S., Martinez-Alonso, S., 2010. New and recent gully activity on Mars as seen by HiRISE. Geophys. Res. Lett. 37, L07202. https://doi.org/10.1029/2009GL041351

Dyke, A.S., 1993. Landscapes of cold-centred Late Wisconsinan ice caps, Arctic Canada. Prog. Phys. Geogr. 17, 223–247. https://doi.org/10.1177/030913339301700208

Dyke, A.S., Moore, A., Robertson, L., 2003. Deglaciation of North America. Geol. Surv. Can. Open File 1574, 2 sheets; 1 CD-ROM. https://doi.org/10.4095/214399

Echelmeyer, K., Wang, Z., 1987. Direct Observation of Basal Sliding and Deformation of Basal Drift at Sub-Freezing Temperatures. J. Glaciol. 33, 83–98. https://doi.org/10.3189/S0022143000005396

Edwards, C.S., Nowicki, K.J., Christensen, P.R., Hill, J., Gorelick, N., Murray, K., 2011. Mosaicking of global planetary image datasets: 1. Techniques and data processing for Thermal Emission Imaging System (THEMIS) multi-spectral data. J. Geophys. Res. Planets 116, E10008. https://doi.org/10.1029/2010JE003755

Ehlmann, B.L., Mustard, J.F., Murchie, S.L., Bibring, J.-P., Meunier, A., Fraeman, A.A., Langevin, Y., 2011. Subsurface water and clay mineral formation during the early history of Mars. Nature 479, 53–60. https://doi.org/10.1038/nature10582

El-Maarry, M.R., Dohm, J.M., Michael, G., Thomas, N., Maruyama, S., 2013. Morphology and evolution of the ejecta of Hale crater in Argyre basin, Mars: Results from high resolution mapping. Icarus 226, 905–922. https://doi.org/10.1016/j.icarus.2013.07.014

Eyles, N. (Ed.), 1983. Glacial Geology: An Introduction for Engineers and Earth Scientists, 1st Edition. ed. Pergamon-Elsevier, Oxford. https://doi.org/10.1016/C2009-0-14654-8

Eyles, N., Rogerson, R.J., 1978. A framework for the investigation of medial moraine formation: Austerdalsbreen, Norway, and Berendon Glacier, British Columbia, Canada. J. Glaciol. 20, 99–113. https://doi.org/10.3189/S0022143000021249

Fanale, F.P., 1976. Martian volatiles: Their degassing history and geochemical fate. Icarus 28, 179–202. https://doi.org/10.1016/0019-1035(76)90032-4

Fanale, F.P., Salvail, J.R., Zent, A.P., Postawko, S.E., 1986. Global distribution and migration of subsurface ice on Mars. Icarus 67, 1–18. https://doi.org/10.1016/0019-1035(86)90170-3

Farmer, C.B., Doms, P.E., 1979. Global seasonal variation of water vapor on Mars and the implications for permafrost. J. Geophys. Res. Solid Earth 84, 2881–2888. https://doi.org/10.1029/JB084iB06p02881

Fassett, C.I., Dickson, J.L., Head, J.W., Levy, J.S., Marchant, D.R., 2010. Supraglacial and proglacial valleys on Amazonian Mars. Icarus 208, 86–100. https://doi.org/10.1016/j.icarus.2010.02.021

Fassett, C.I., Head, J.W., 2008a. Valley network-fed, open-basin lakes on Mars: Distribution and implications for Noachian surface and subsurface hydrology. Icarus 198, 37–56. https://doi.org/10.1016/j.icarus.2008.06.016

Fassett, C.I., Head, J.W., 2008b. The timing of martian valley network activity: Constraints from buffered crater counting. Icarus 195, 61–89. https://doi.org/10.1016/j.icarus.2007.12.009

Fassett, C.I., Levy, J.S., Dickson, J.L., Head, J.W., 2014. An extended period of episodic northern mid-latitude glaciation on Mars during the Middle to Late Amazonian: Implications for long-term obliquity history. Geology 42, 763–766. https://doi.org/10.1130/G35798.1

Fastook, J.L., Head, J.W., 2015. Glaciation in the Late Noachian Icy Highlands: Ice accumulation, distribution, flow rates, basal melting, and top-down melting rates and patterns. Planet. Space Sci. 106, 82–98. https://doi.org/10.1016/j.pss.2014.11.028

Fastook, J.L., Head, J.W., 2014. Amazonian mid- to high-latitude glaciation on Mars: Supply-limited ice sources, ice accumulation patterns, and concentric crater fill glacial flow and ice sequestration. Planet. Space Sci. 91, 60–76. https://doi.org/10.1016/j.pss.2013.12.002

Fastook, J.L., Head, J.W., Deutsch, A.N., 2019. Glaciation on Mercury: Accumulation and flow of ice in permanently shadowed circum-polar crater interiors. Icarus 317, 81–93. https://doi.org/10.1016/j.icarus.2018.07.004

Fastook, J.L., Head, J.W., Marchant, D.R., 2014. Formation of lobate debris aprons on Mars: Assessment of regional ice sheet collapse and debris-cover armoring. Icarus 228, 54–63. https://doi.org/10.1016/j.icarus.2013.09.025

Fastook, J.L., Head, J.W., Marchant, D.R., Forget, F., 2008. Tropical mountain glaciers on Mars: Altitude-dependence of ice accumulation, accumulation conditions, formation times, glacier dynamics, and implications for planetary spin-axis/orbital history. Icarus 198, 305–317. https://doi.org/10.1016/j.icarus.2008.08.008

Fastook, J.L., Head, J.W., Marchant, D.R., Forget, F., Madeleine, J.-B., 2012. Early Mars climate near the Noachian–Hesperian boundary: Independent evidence for cold conditions from basal melting of the south polar ice sheet (Dorsa Argentea Formation) and implications for valley network formation. Icarus 219, 25–40. https://doi.org/10.1016/j.icarus.2012.02.013

Fawdon, P., Gupta, S., Davis, J.M., Warner, N.H., Adler, J.B., Balme, M.R., Bell, J.F., Grindrod, P.M., Sefton-Nash, E., 2018. The Hypanis Valles delta: The last highstand of a sea on early Mars? Earth Planet. Sci. Lett. 500, 225–241. https://doi.org/10.1016/j.epsl.2018.07.040

Feldman, W.C., Prettyman, T.H., Maurice, S., Plaut, J.J., Bish, D.L., Vaniman, D.T., Mellon, M.T., Metzger, A.E., Squyres, S.W., Karunatillake, S., Boynton, W.V., Elphic, R.C., Funsten, H.O., Lawrence, D.J., Tokar, R.L., 2004. Global distribution of near-surface hydrogen on Mars. J. Geophys. Res. Planets 109, E09006. https://doi.org/10.1029/2003JE002160

Fernàndez, M., Banda, E., 1990. Geothermal anomalies in the Valles-Penedes Graben Master Fault: Convection through the Horst as a possible mechanism. J. Geophys. Res. Solid Earth 95, 4887–4894. https://doi.org/10.1029/JB095iB04p04887

Forget, F., Haberle, R.M., Montmessin, F., Levrard, B., Head, J.W., 2006. Formation of Glaciers on Mars by Atmospheric Precipitation at High Obliquity. Science 311, 368–371. https://doi.org/10.1126/science.1120335

François, L.M., Walker, J.C.G., Kuhn, W.R., 1990. A numerical simulation of climate changes during the obliquity cycle on Mars. J. Geophys. Res. Solid Earth 95, 14761–14778. https://doi.org/10.1029/JB095iB09p14761

Frey, H.V., 2003. Buried Impact Basins and The Earliest History of Mars. Sixth Int. Conf. Mars Abstract #3104.

Gallagher, C., Balme, M., 2015. Eskers in a complete, wet-based glacial system in the Phlegra Montes region, Mars. Earth Planet. Sci. Lett. 431, 96–109. https://doi.org/10.1016/j.epsl.2015.09.023

Geirsdóttir, Á., Miller, G.H., Andrews, J.T., 2007. Glaciation, erosion, and landscape evolution of Iceland. J. Geodyn. 43, 170–186. https://doi.org/10.1016/j.jog.2006.09.017

Ghatan, G.J., Head, J.W., III, 2004. Regional drainage of meltwater beneath a Hesperian-aged south circumpolar ice sheet on Mars. J. Geophys. Res. 109, E07006. https://doi.org/10.1029/2003JE002196

Goldspiel, J.M., Squyres, S.W., 2000. Groundwater Sapping and Valley Formation on Mars. Icarus 148, 176–192. https://doi.org/10.1006/icar.2000.6465

Goodsell, B., Hambrey, M.J., Glasser, N.F., 2005. Debris transport in a temperate valley glacier: Haut Glacier d'Arolla, Valais, Switzerland. J. Glaciol. 51, 139–146. https://doi.org/10.3189/172756505781829647

Gorrell, G., Shaw, J., 1991. Deposition in an esker, bead and fan complex, Lanark, Ontario, Canada. Sediment. Geol. 72, 285–314. https://doi.org/10.1016/0037-0738(91)90016-7

Goudge, T.A., Fassett, C.I., Head, J.W., Mustard, J.F., Aureli, K.L., 2016. Insights into surface runoff on early Mars from paleolake basin morphology and stratigraphy. Geology 44, 419–422. https://doi.org/10.1130/G37734.1

Grimm, R.E., Harrison, K.P., Stillman, D.E., 2014. Water budgets of martian recurring slope lineae. Icarus 233, 316–327. https://doi.org/10.1016/j.icarus.2013.11.013

Grott, M., Morschhauser, A., Breuer, D., Hauber, E., 2011. Volcanic outgassing of CO2 and H2O on Mars. Earth Planet. Sci. Lett. 308, 391–400. https://doi.org/10.1016/j.epsl.2011.06.014

Gulick, V.C., Baker, V.R., 1990. Origin and evolution of valleys on Martian volcanoes. J. Geophys. Res. Solid Earth 95, 14325–14344. https://doi.org/10.1029/JB095iB09p14325

Haberle, R.M., McKay, C.P., Schaeffer, J., Cabrol, N.A., Grin, E.A., Zent, A.P., Quinn, R., 2001. On the possibility of liquid water on present-day Mars. J. Geophys. Res. Planets 106, 23317–23326. https://doi.org/10.1029/2000JE001360

Hallet, B., Hunter, L., Bogen, J., 1996. Rates of erosion and sediment evacuation by glaciers: A review of field data and their implications. Glob. Planet. Change 12, 213–235. https://doi.org/10.1016/0921-8181(95)00021-6

Hambrey, M.J., Huddart, D., Bennett, M.R., Glasser, N.F., 1997. Genesis of 'hummocky moraines' by thrusting in glacier ice: evidence from Svalbard and Britain. J. Geol. Soc. 154, 623–632. https://doi.org/10.1144/gsjgs.154.4.0623

Harrison, T.N., Osinski, G.R., Tornabene, L.L., Jones, E., 2015. Global documentation of gullies with the Mars Reconnaissance Orbiter Context Camera and implications for their formation. Icarus 252, 236–254. https://doi.org/10.1016/j.icarus.2015.01.022

Hartmann, W.K., 2005. Martian cratering 8: Isochron refinement and the chronology of Mars. Icarus 174, 294–320. https://doi.org/10.1016/j.icarus.2004.11.023

Hartmann, W.K., 1977. Relative crater production rates on planets. Icarus 31, 260–276. https://doi.org/10.1016/0019-1035(77)90037-9

Hartmann, W.K., Ansan, V., Berman, D.C., Mangold, N., Forget, F., 2014. Comprehensive analysis of glaciated martian crater Greg. Icarus 228, 96–120. https://doi.org/10.1016/j.icarus.2013.09.016

Hartmann, W.K., Neukum, G., 2001. Cratering Chronology and the Evolution of Mars. Space Sci. Rev. 96, 165–194. https://doi.org/10.1023/A:1011945222010

Hauber, E., Brož, P., Jagert, F., Jodłowski, P., Platz, T., 2011. Very recent and wide-spread basaltic volcanism on Mars. Geophys. Res. Lett. 38, L10201. https://doi.org/10.1029/2011GL047310

Hauber, E., Gasselt, S. van, Chapman, M.G., Neukum, G., 2008. Geomorphic evidence for former lobate debris aprons at low latitudes on Mars: Indicators of the Martian paleoclimate. J. Geophys. Res. Planets 113, E02007. https://doi.org/10.1029/2007JE002897

Hauber, E., Grott, M., Kronberg, P., 2010. Martian rifts: Structural geology and geophysics. Earth Planet. Sci. Lett. 294, 393–410. https://doi.org/10.1016/j.epsl.2009.11.005

Hauber, E., Kronberg, P., 2001. Tempe Fossae, Mars: A planetary analogon to a terrestrial continental rift? J. Geophys. Res. Planets 106, 20587–20602. https://doi.org/10.1029/2000JE001346

Hauber, E., Platz, T., Reiss, D., Deit, L.L., Kleinhans, M.G., Marra, W.A., Haas, T. de, Carbonneau, P., 2013. Asynchronous formation of Hesperian and Amazonian-aged deltas on Mars and implications for climate. J. Geophys. Res. Planets 118, 1529–1544. https://doi.org/10.1002/jgre.20107

Hauber, E., van Gasselt, S., Ivanov, B., Werner, S., Head, J.W., Neukum, G., Jaumann, R., Greeley, R., Mitchell, K.L., Muller, P., The HRSC Co-Investigator Team, 2005. Discovery of a flank caldera and very young glacial activity at Hecates Tholus, Mars. Nature 434, 356–361. https://doi.org/10.1038/nature03423

Hayne, P.O., Paige, D.A., Schofield, J.T., Kass, D.M., Kleinböhl, A., Heavens, N.G., McCleese, D.J., 2012. Carbon dioxide snow clouds on Mars: South polar winter observations by the Mars Climate Sounder. J. Geophys. Res. Planets 117, E08014. https://doi.org/10.1029/2011JE004040

Head, J.W., 2000a. Tests for Ancient Polar Deposits on Mars: Morphology and Topographic Relationships of Esker-like Sinuous Ridges (Dorsa Argentea) Using MOLA Data. Lunar Planet. Sci. Conf. XXXI Abstract #1117.

Head, J.W., 2000b. Tests for Ancient Polar Deposits on Mars: Origin of Esker-like Sinuous Ridges (Dorsa Argentea) Using MOLA Data. Lunar Planet. Sci. Conf. XXXI Abstract #1116.

Head, J.W., Hallet, B., 2001a. Origin of Sinuous Ridges in the Dorsa Argentea Formation: New Observations and Tests of the Esker Hypothesis. Lunar Planet. Sci. Conf. XXXII Abstract #1373.

Head, J.W., Hallet, B., 2001b. Origin of Sinuous Ridges in the Dorsa Argentea Formation: Additional Criteria for Tests of the Esker Hypothesis. Lunar Planet. Sci. Conf. XXXII Abstract #1366.

Head, J.W., Marchant, D.R., 2003. Cold-based mountain glaciers on Mars: Western Arsia Mons. Geology 31, 641–644. https://doi.org/10.1130/0091-7613(2003)031<0641:CMGOMW>2.0.CO;2

Head, J.W., Marchant, D.R., Agnew, M.C., Fassett, C.I., Kreslavsky, M.A., 2006. Extensive valley glacier deposits in the northern mid-latitudes of Mars: Evidence for Late Amazonian obliquity-driven climate change. Earth Planet. Sci. Lett. 241, 663–671. https://doi.org/10.1016/j.epsl.2005.11.016

Head, J.W., Marchant, D.R., Dickson, J.L., Kress, A.M., Baker, D.M., 2010. Northern mid-latitude glaciation in the Late Amazonian period of Mars: Criteria for the recognition of debris-covered glacier and valley glacier landsystem deposits. Earth Planet. Sci. Lett. 294, 306–320. https://doi.org/10.1016/j.epsl.2009.06.041

Head, J.W., Marchant, D.R., Kreslavsky, M.A., 2008. Formation of gullies on Mars: Link to recent climate history and insolation microenvironments implicate surface water flow origin. Proc. Natl. Acad. Sci. U. S. A. 105, 13258–13263. https://doi.org/10.1073/pnas.0803760105

Head, J.W., Mustard, J.F., Kreslavsky, M.A., Milliken, R.E., Marchant, D.R., 2003. Recent ice ages on Mars. Nature 426, 797–802. https://doi.org/10.1038/nature02114

Head, J.W., Neukum, G., Jaumann, R., Hiesinger, H., Hauber, E., Carr, M., Masson, P., Foing, B., Hoffmann, H., Kreslavsky, M., Werner, S., Milkovich, S., van Gasselt, S., The HRSC Co-Investigator Team, 2005. Tropical to mid-latitude snow and ice accumulation, flow and glaciation on Mars. Nature 434, 346–351. https://doi.org/10.1038/nature03359

Head, J.W., Pratt, S., 2001. Extensive Hesperian-aged south polar ice sheet on Mars: Evidence for massive melting and retreat, and lateral flow and ponding of meltwater. J. Geophys. Res. Planets 106, 12275–12299. https://doi.org/10.1029/2000JE001359

Hecht, M.H., Kounaves, S.P., Quinn, R.C., West, S.J., Young, S.M.M., Ming, D.W., Catling, D.C., Clark, B.C., Boynton, W.V., Hoffman, J., DeFlores, L.P., Gospodinova, K., Kapit, J., Smith, P.H., 2009. Detection of Perchlorate and the Soluble Chemistry of Martian Soil at the Phoenix Lander Site. Science 325, 64–67. https://doi.org/10.1126/science.1172466

Hepburn, A., Ng, F., Livingstone, S.J., Hubbard, B., 2018. Polyphase mid-latitude glaciation on Mars evidenced by dating of superimposed lobate debris aprons. EGU Gen. Assem. 20, 1087.

Hess, S.L., Henry, R.M., Leovy, C.B., Ryan, J.A., Tillman, J.E., 1977. Meteorological results from the surface of Mars: Viking 1 and 2. J. Geophys. Res. 82, 4559–4574. https://doi.org/10.1029/JS082i028p04559

Hiesinger, H., Head, J.W., 2002. Topography and morphology of the Argyre Basin, Mars: implications for its geologic and hydrologic history. Planet. Space Sci. 50, 939–981. https://doi.org/10.1016/S0032-0633(02)00054-5

Hoffman, S.J., Andrews, A., Joosten, B.K., Watts, K., 2017. A water rich mars surface mission scenario. 2017 IEEE Aerosp. Conf. 1–21. https://doi.org/10.1109/AERO.2017.7943911

Holt, J.W., Safaeinili, A., Plaut, J.J., Head, J.W., Phillips, R.J., Seu, R., Kempf, S.D., Choudhary, P., Young, D.A., Putzig, N.E., Biccari, D., Gim, Y., 2008. Radar Sounding Evidence for Buried Glaciers in the Southern Mid-Latitudes of Mars. Science 322, 1235–1238. https://doi.org/10.1126/science.1164246

Hooke, R.L., Fastook, J., 2007. Thermal conditions at the bed of the Laurentide ice sheet in Maine during deglaciation: implications for esker formation. J. Glaciol. 53, 646–658. https://doi.org/10.3189/002214307784409243

Howard, A.D., 1981. Etched plains and braided ridges of the south polar region of Mars: Features produced by basal melting of ground ice? Rep. Planet. Geol. Program 1981 Natl. Aeronaut. Space Adm. Tech. Memo. 84211, 286–288.

Howard, A.D., Moore, J.M., Irwin, R.P., 2005. An intense terminal epoch of widespread fluvial activity on early Mars: 1. Valley network incision and associated deposits. J. Geophys. Res. Planets 110, E12S14. https://doi.org/10.1029/2005JE002459

Hubbard, B., Milliken, R.E., Kargel, J.S., Limaye, A., Souness, C., 2011. Geomorphological characterisation and interpretation of a mid-latitude glacier-like form: Hellas Planitia, Mars. Icarus 211, 330–346. https://doi.org/10.1016/j.icarus.2010.10.021

Hubbard, B., Souness, C., Brough, S., 2014. Glacier-like forms on Mars. The Cryosphere 8, 2047–2061. https://doi.org/10.5194/tc-8-2047-2014

Hungerford, J.D.G., Edwards, B.R., Skilling, I.P., Cameron, B.I., 2014. Evolution of a subglacial basaltic lava flow field: Tennena volcanic center, Mount Edziza volcanic complex, British Columbia, Canada. J. Volcanol. Geotherm. Res. 272, 39–58. https://doi.org/10.1016/j.jvolgeores.2013.09.012

Hynek, B.M., Beach, M., Hoke, M.R.T., 2010. Updated global map of Martian valley networks and implications for climate and hydrologic processes. J. Geophys. Res. Planets 115, E09008. https://doi.org/10.1029/2009JE003548

Imbrie, J., Boyle, E.A., Clemens, S.C., Duffy, A., Howard, W.R., Kukla, G., Kutzbach, J., Martinson, D.G., McIntyre, A., Mix, A.C., Molfino, B., Morley, J.J., Peterson, L.C., Pisias, N.G., Prell, W.L., Raymo, M.E., Shackleton, N.J., Toggweiler, J.R., 1992. On the Structure and Origin of Major Glaciation Cycles 1. Linear Responses to Milankovitch Forcing. Paleoceanography 7, 701–738. https://doi.org/10.1029/92PA02253

Irwin, R.P., Howard, A.D., Craddock, R.A., Moore, J.M., 2005. An intense terminal epoch of widespread fluvial activity on early Mars: 2. Increased runoff and paleolake development. J. Geophys. Res. Planets 110, E12S15. https://doi.org/10.1029/2005JE002460

Ivanov, B.A., 2001. Mars/Moon Cratering Rate Ratio Estimates. Space Sci. Rev. 96, 87–104. https://doi.org/10.1023/A:1011941121102

Jakobsson, M., Björck, S., Alm, G., Andrén, T., Lindeberg, G., Svensson, N.-O., 2007. Reconstructing the Younger Dryas ice dammed lake in the Baltic Basin: Bathymetry, area and volume. Glob. Planet. Change 57, 355–370. https://doi.org/10.1016/j.gloplacha.2007.01.006

Jakosky, B.M., 1983. Comment on ‘Mars residual north polar cap: Earth-based spectroscopic confirmation of water ice as a major constituent and evidence for hydrated minerals’ by Roger N. Clark and Thomas B. McCord. J. Geophys. Res. Solid Earth 88, 4329–4330. https://doi.org/10.1029/JB088iB05p04329

Jakosky, Bruce M., Haberle, R.M., 1992. The seasonal behavior of water on Mars, in: Kieffer, H.H., Jakosky, B. M., Snyder, C.W., Matthews, M.S. (Eds.), Mars. The University of Arizona Press, Tuscon, pp. 969–1016.

James, P.B., Kieffer, Hugh H., Paige, D.A., 1992. The seasonal cycle of carbon dioxide on Mars, in: Kieffer, H. H., Jakosky, B.M., Snyder, C.W., Matthews, M.S. (Eds.), Mars. The University of Arizona Press, Tuscon, pp. 934–968.

Jaumann, R., Neukum, G., Behnke, T., Duxbury, T.C., Eichentopf, K., Flohrer, J., Gasselt, S. v., Giese, B., Gwinner, K., Hauber, E., Hoffmann, H., Hoffmeister, A., Köhler, U., Matz, K.-D., McCord, T.B., Mertens, V., Oberst, J., Pischel, R., Reiss, D., Ress, E., Roatsch, T., Saiger, P., Scholten, F., Schwarz, G., Stephan, K., Wählisch, M., 2007. The high-resolution stereo camera (HRSC) experiment on Mars Express: Instrument aspects and experiment conduct from interplanetary cruise through the nominal mission. Planet. Space Sci. 55, 928–952. https://doi.org/10.1016/j.pss.2006.12.003

Jawin, E.R., Head, J.W., Marchant, D.R., 2018. Transient post-glacial processes on Mars: Geomorphologic evidence for a paraglacial period. Icarus 309, 187–206. https://doi.org/10.1016/j.icarus.2018.01.026

Jones, A.P., McEwen, A.S., Tornabene, L.L., Baker, V.R., Melosh, H.J., Berman, D.C., 2011. A geomorphic analysis of Hale crater, Mars: The effects of impact into ice-rich crust. Icarus 211, 259–272. https://doi.org/10.1016/j.icarus.2010.10.014

Jordan, T.A., Ferraccioli, F., Vaughan, D.G., Holt, J.W., Corr, H., Blankenship, D.D., Diehl, T.M., 2010. Aerogravity evidence for major crustal thinning under the Pine Island Glacier region (West Antarctica). Geol. Soc. Am. Bull. 122, 714–726. https://doi.org/10.1130/B26417.1

Kadish, S.J., Head, J.W., Fastook, J.L., Marchant, D.R., 2014. Middle to Late Amazonian tropical mountain glaciers on Mars: The ages of the Tharsis Montes fan-shaped deposits. Planet. Space Sci. 91, 52–59. https://doi.org/10.1016/j.pss.2013.12.005

Kadish, S.J., Head, J.W., Parsons, R.L., Marchant, D.R., 2008. The Ascraeus Mons fan-shaped deposit: Volcano–ice interactions and the climatic implications of cold-based tropical mountain glaciation. Icarus 197, 84–109. https://doi.org/10.1016/j.icarus.2008.03.019

Kamb, B., 1987. Glacier surge mechanism based on linked cavity configuration of the basal water conduit system. J. Geophys. Res. Solid Earth 92, 9083–9100. https://doi.org/10.1029/JB092iB09p09083

Kargel, J.S., 1993. Geomorphic processes in the Argyre-Dorsa Argentea region of Mars. Lunar Planet. Sci. Conf. XXIV Abstract #1378.

Kargel, J.S., Strom, R.G., 1992. Ancient glaciation on Mars. Geology 20, 3–7. https://doi.org/10.1130/0091-7613(1992)020<0003:AGOM>2.3.CO;2

Kargel, J.S., Strom, R.G., 1991. Terrestrial Glacial Eskers: Analogs for Martian Sinuous Ridges. Lunar Planet. Sci. Conf. XXII 683–684.

Karlsson, N.B., Schmidt, L.S., Hvidberg, C.S., 2015. Volume of Martian midlatitude glaciers from radar observations and ice flow modeling. Geophys. Res. Lett. 42, 2627–2633. https://doi.org/10.1002/2015GL063219

Kavanaugh, J.L., Clarke, G.K.C., 2001. Abrupt glacier motion and reorganisation of basal shear stress following the establishment of a connected drainage system. J. Glaciol. 47, 472–480. https://doi.org/doi:10.3189/172756501781831972

Kehew, A.E., Piotrowski, J.A., Jørgensen, F., 2012. Tunnel valleys: Concepts and controversies — A review. Earth-Sci. Rev. 113, 33–58. https://doi.org/10.1016/j.earscirev.2012.02.002

Kieffer, H., 1970. Interpretation of the Martian polar cap spectra. J. Geophys. Res. 75, 510–514. https://doi.org/10.1029/JC075i003p00510

Kirk, R.L., Howington-Kraus, E., Rosiek, M.R., Anderson, J.A., Archinal, B.A., Becker, K.J., Cook, D.A., Galuszka, D.M., Geissler, P.E., Hare, T.M., Holmberg, I.M., Keszthelyi, L.P., Redding, B.L., Delamere, W.A., Gallagher, D., Chapel, J.D., Eliason, E.M., King, R., McEwen, A.S., 2008. Ultrahigh resolution topographic mapping of Mars with MRO HiRISE stereo images: Meter-scale slopes of candidate Phoenix landing sites. J. Geophys. Res. Planets 113, E00A24. https://doi.org/10.1029/2007JE003000

Kite, E.S., Howard, A.D., Lucas, A.S., Armstrong, J.C., Aharonson, O., Lamb, M.P., 2015. Stratigraphy of Aeolis Dorsa, Mars: Stratigraphic context of the great river deposits. Icarus 253, 223–242. https://doi.org/10.1016/j.icarus.2015.03.007

Kleman, J., Hättestrand, C., Borgström, I., Stroeven, A., 1997. Fennoscandian palaeoglaciology reconstructed using a glacial geological inversion model. J. Glaciol. 43, 283–299. https://doi.org/10.3189/S0022143000003233

Kneissl, T., Reiss, D., van Gasselt, S., Neukum, G., 2010. Distribution and orientation of northern-hemisphere gullies on Mars from the evaluation of HRSC and MOC-NA data. Earth Planet. Sci. Lett. 294, 357–367. https://doi.org/10.1016/j.epsl.2009.05.018

Kneissl, T., van Gasselt, S., Neukum, G., 2011. Map-projection-independent crater size-frequency determination in GIS environments—New software tool for ArcGIS. Planet. Space Sci. 59, 1243–1254. https://doi.org/10.1016/j.pss.2010.03.015

Kochel, R.C., Peake, R.T., 1984. Quantification of waste morphology in Martian fretted terrain. J. Geophys. Res. Solid Earth 89, C336–C350. https://doi.org/10.1029/JB089iS01p0C336

Komar, P.D., 1979. Comparisons of the hydraulics of water flows in Martian outflow channels with flows of similar scale on Earth. Icarus 37, 156–181. https://doi.org/10.1016/0019-1035(79)90123-4

Kostama, V.-P., Kreslavsky, M.A., Head, J.W., 2006. Recent high-latitude icy mantle in the northern plains of Mars: Characteristics and ages of emplacement. Geophys. Res. Lett. 33, L11201. https://doi.org/10.1029/2006GL025946

Kreslavsky, M.A., Head, J.W., 2002. Mars: Nature and evolution of young latitude-dependent water-ice-rich mantle. Geophys. Res. Lett. 29, 1719. https://doi.org/10.1029/2002GL015392

Kress, A.M., Head, J.W., 2015. Late Noachian and early Hesperian ridge systems in the south circumpolar Dorsa Argentea Formation, Mars: Evidence for two stages of melting of an extensive late Noachian ice sheet. Planet. Space Sci. 109–110, 1–20. https://doi.org/10.1016/j.pss.2014.11.025

Kress, A.M., Head, J.W., 2008. Ring-mold craters in lineated valley fill and lobate debris aprons on Mars: Evidence for subsurface glacial ice. Geophys. Res. Lett. 35, L23206. https://doi.org/10.1029/2008GL035501

Krüger, J., Kjær, K.H., 2000. De-icing progression of ice-cored moraines in a humid, subpolar climate, Kötlujökull, Iceland. The Holocene 10, 737–747. https://doi.org/10.1191/09596830094980

Langevin, Y., Poulet, F., Bibring, J.-P., Schmitt, B., Douté, S., Gondet, B., 2005. Summer Evolution of the North Polar Cap of Mars as Observed by OMEGA/Mars Express. Science 307, 1581–1584. https://doi.org/10.1126/science.1109438

Larour, E., Seroussi, H., Morlighem, M., Rignot, E., 2012. Continental scale, high order, high spatial resolution, ice sheet modeling using the Ice Sheet System Model (ISSM). J. Geophys. Res. Earth Surf. 117, F01022. https://doi.org/10.1029/2011JF002140

Laskar, J., Correia, A.C.M., Gastineau, M., Joutel, F., Levrard, B., Robutel, P., 2004. Long term evolution and chaotic diffusion of the insolation quantities of Mars. Icarus 170, 343–364. https://doi.org/10.1016/j.icarus.2004.04.005

Laskar, J., Joutel, F., Robutel, P., 1993. Stabilization of the Earth's obliquity by the Moon. Nature 361, 615–617. https://doi.org/10.1038/361615a0

Lasue, J., Clifford, S.M., Conway, S.J., Mangold, N., Butcher, F.E.G., 2019. The Hydrology of Mars Including a Potential Cryosphere, in: Filiberto, J., Schwenzer, S.P. (Eds.), Volatiles in the Martian Crust. Elsevier, pp. 185–246. https://doi.org/10.1016/B978-0-12-804191-8.00007-6

Lasue, J., Mangold, N., Hauber, E., Clifford, S., Feldman, W., Gasnault, O., Grima, C., Maurice, S., Mousis, O., 2013. Quantitative Assessments of the Martian Hydrosphere. Space Sci. Rev. 174, 155–212. https://doi.org/10.1007/s11214-012-9946-5

Lefort, A., Burr, D.M., Beyer, R.A., Howard, A.D., 2012. Inverted fluvial features in the Aeolis-Zephyria Plana, western Medusae Fossae Formation, Mars: Evidence for post-formation modification. J. Geophys. Res. Planets 117, E03007. https://doi.org/10.1029/2011JE004008

Leighton, R.B., Horowitz, N.H., Murray, B.C., Sharp, R.P., Herriman, A.H., Young, A.T., Smith, B.A., Davies, M.E., Leovy, C.B., 1969. Mariner 6 and 7 Television Pictures: Preliminary Analysis. Science 166, 49–67. https://doi.org/10.1126/science.166.3901.49

Leighton, R.B., Murray, B.C., 1966. Behavior of Carbon Dioxide and Other Volatiles on Mars. Science 153, 136–144. https://doi.org/10.1126/science.153.3732.136

Lenaerts, J.T.M., Vizcaino, M., Fyke, J., Kampenhout, L., Broeke, M.R., 2016. Present-day and future Antarctic ice sheet climate and surface mass balance in the Community Earth System Model. Clim. Dyn. 1–15. https://doi.org/10.1007/s00382-015-2907-4

Leovy, C.B., 1973. Exchange of water vapor between the atmosphere and surface of Mars. Icarus 18, 120–125. https://doi.org/10.1016/0019-1035(73)90178-4

Lescinsky, D.T., Fink, J.H., 2000. Lava and ice interaction at stratovolcanoes: Use of characteristic features to determine past glacial extents and future volcanic hazards. J. Geophys. Res. Solid Earth 105, 23711–23726. https://doi.org/10.1029/2000JB900214

Levrard, B., Forget, F., Montmessin, F., Laskar, J., 2007. Recent formation and evolution of northern Martian polar layered deposits as inferred from a Global Climate Model. J. Geophys. Res. Planets 112, E06012. https://doi.org/10.1029/2006JE002772

Levrard, B., Forget, F., Montmessin, F., Laskar, J., 2004. Recent ice-rich deposits formed at high latitudes on Mars by sublimation of unstable equatorial ice during low obliquity. Nature 431, 1072–1075. https://doi.org/10.1038/nature03055

Levy, J.S., Fassett, C.I., Head, J.W., 2016. Enhanced erosion rates on Mars during Amazonian glaciation. Icarus 264, 213–219. https://doi.org/10.1016/j.icarus.2015.09.037

Levy, J.S., Fassett, C.I., Head, J.W., Schwartz, C., Watters, J.L., 2014. Sequestered glacial ice contribution to the global Martian water budget: Geometric constraints on the volume of remnant, midlatitude debris-covered glaciers. J. Geophys. Res. Planets 119, 2188–2196. https://doi.org/10.1002/2014JE004685

Levy, J.S., Head, J.W., Marchant, D.R., 2010a. Concentric crater fill in the northern mid-latitudes of Mars: Formation processes and relationships to similar landforms of glacial origin. Icarus 209, 390–404. https://doi.org/10.1016/j.icarus.2010.03.036

Levy, J.S., Head, J.W., Marchant, D.R., 2009. Concentric crater fill in Utopia Planitia: History and interaction between glacial "brain terrain" and periglacial mantle processes. Icarus 202, 462–476. https://doi.org/10.1016/j.icarus.2009.02.018

Levy, J.S., Head, J.W., Marchant, D.R., 2007. Lineated valley fill and lobate debris apron stratigraphy in Nilosyrtis Mensae, Mars: Evidence for phases of glacial modification of the dichotomy boundary. J. Geophys. Res. Planets 112, E08004. https://doi.org/10.1029/2006JE002852

Levy, J.S., Marchant, D.R., Head, J.W., 2010b. Thermal contraction crack polygons on Mars: A synthesis from HiRISE, Phoenix, and terrestrial analog studies. Icarus 206, 229–252. https://doi.org/10.1016/j.icarus.2009.09.005

Lloyd Davies, M.T., Atkins, C.B., van der Meer, J.J.M., Barrett, P.J., Hicock, S.R., 2009. Evidence for cold-based glacial activity in the Allan Hills, Antarctica. Quat. Sci. Rev. 28, 3124–3137. https://doi.org/10.1016/j.quascirev.2009.08.002

Longhi, J., 2006. Phase equilibrium in the system CO2-H2O: Application to Mars. J. Geophys. Res. Planets 111, E06011. https://doi.org/10.1029/2005JE002552

Lucchitta, B.K., 1984. Ice and debris in the Fretted Terrain, Mars. J. Geophys. Res. Solid Earth 89, B409–B418. https://doi.org/10.1029/JB089iS02p0B409

Lucchitta, B.K., 1981. Mars and Earth: Comparison of cold-climate features. Icarus 45, 264–303. https://doi.org/10.1016/0019-1035(81)90035-X

Madeleine, J.-B., Forget, F., Head, J.W., Levrard, B., Montmessin, F., Millour, E., 2009. Amazonian northern mid-latitude glaciation on Mars: A proposed climate scenario. Icarus 203, 390–405. https://doi.org/10.1016/j.icarus.2009.04.037

Maizels, J.K., 1987. Plio-Pleistocene raised channel systems of the western Sharqiya (Wahiba), Oman. Geol. Soc. Lond. Spec. Publ. 35, 31–50. https://doi.org/10.1144/GSL.SP.1987.035.01.04

Mäkinen, J., 2003. Time-transgressive deposits of repeated depositional sequences within interlobate glaciofluvial (esker) sediments in Köyliö, SW Finland. Sedimentology 50, 327–360. https://doi.org/10.1046/j.1365-3091.2003.00557.x

Malin, M.C., Bell, J.F., Cantor, B.A., Caplinger, M.A., Calvin, W.M., Clancy, R.T., Edgett, K.S., Edwards, L., Haberle, R.M., James, P.B., Lee, S.W., Ravine, M.A., Thomas, P.C., Wolff, M.J., 2007. Context Camera Investigation on board the Mars Reconnaissance Orbiter. J. Geophys. Res. Planets 112, E05S04. https://doi.org/10.1029/2006JE002808

Malin, M.C., Edgett, K.S., 2003. Evidence for Persistent Flow and Aqueous Sedimentation on Early Mars. Science 302, 1931–1934. https://doi.org/10.1126/science.1090544

Malin, M.C., Edgett, K.S., 2000. Evidence for Recent Groundwater Seepage and Surface Runoff on Mars. Science 288, 2330–2335. https://doi.org/10.1126/science.288.5475.2330

Mangold, N., 2003. Geomorphic analysis of lobate debris aprons on Mars at Mars Orbiter Camera scale: Evidence for ice sublimation initiated by fractures. J. Geophys. Res. Planets 108, 8021. https://doi.org/10.1029/2002JE001885

Mangold, N., Ansan, V., 2006. Detailed study of an hydrological system of valleys, a delta and lakes in the Southwest Thaumasia region, Mars. Icarus 180, 75–87. https://doi.org/10.1016/j.icarus.2005.08.017

Mangold, N., Maurice, S., Feldman, W.C., Costard, F., Forget, F., 2004a. Spatial relationships between patterned ground and ground ice detected by the Neutron

Spectrometer on Mars. J. Geophys. Res. Planets 109, E08001. https://doi.org/10.1029/2004JE002235

Mangold, N., Quantin, C., Ansan, V., Delacourt, C., Allemand, P., 2004b. Evidence for Precipitation on Mars from Dendritic Valleys in the Valles Marineris Area. Science 305, 78–81. https://doi.org/10.1126/science.1097549

Maslin, M., Seidov, D., Lowe, J., 2001. Synthesis of the Nature and Causes of Rapid Climate Transitions During the Quaternary, in: Seidov, D., Haupt, B.J., Maslin, M. (Eds.), The Oceans and Rapid Climate Change: Past, Present and Future. American Geophysical Union, pp. 9–52.

Masursky, H., Boyce, J.M., Dial, A.L., Schaber, G.G., Strobell, M.E., 1977. Classification and time of formation of Martian channels based on Viking data. J. Geophys. Res. 82, 4016–4038. https://doi.org/10.1029/JS082i028p04016

Mathews, W.H., 1958. Geology of the Mount Garibaldi map-area, Southwestern British Columbia Part II: Geomorphology and Quaternary volcanic rocks. Geol. Soc. Am. Bull. 69, 179–198. https://doi.org/10.1130/0016-7606(1958)69[179:GOTMGM]2.0.CO;2

Mayer, D.P., Kite, E.S., 2016. An Integrated Workflow for Producing Digital Terrain Models of Mars from CTX and HiRISE Stereo Data Using the NASA Ames Stereo Pipeline. Lunar Planet. Sci. Conf. XLVII Abstract #1241.

McDonald, B.C., Vincent, J.S., 1972. Fluvial sedimentary structures formed experimentally in a pipe, and their implications for interpretation of subglacial sedimentary environments. Geological Survey of Canada Paper 72–27.

McEwen, A.S., Eliason, E.M., Bergstrom, J.W., Bridges, N.T., Hansen, C.J., Delamere, W.A., Grant, J.A., Gulick, V.C., Herkenhoff, K.E., Keszthelyi, L., Kirk, R.L., Mellon, M.T., Squyres, S.W., Thomas, N., Weitz, C.M., 2007. Mars Reconnaissance Orbiter's High Resolution Imaging Science Experiment (HiRISE). J. Geophys. Res. 112, E05S02. https://doi.org/10.1029/2005JE002605

McEwen, A.S., Ojha, L., Dundas, C.M., Mattson, S.S., Byrne, S., Wray, J.J., Cull, S.C., Murchie, S.L., Thomas, N., Gulick, V.C., 2011. Seasonal Flows on Warm Martian Slopes. Science 333, 740–743. https://doi.org/10.1126/science.1204816

McGovern, P.J., Solomon, S.C., Smith, D.E., Zuber, M.T., Simons, M., Wieczorek, M.A., Phillips, R.J., Neumann, G.A., Aharonson, O., Head, J.W., 2004. Correction to "Localized

gravity/topography admittance and correlation spectra on Mars: Implications for regional and global evolution." J. Geophys. Res. Planets 109, E07007. https://doi.org/10.1029/2004JE002286

McGovern, P.J., Solomon, S.C., Smith, D.E., Zuber, M.T., Simons, M., Wieczorek, M.A., Phillips, R.J., Neumann, G.A., Aharonson, O., Head, J.W., 2002. Localized gravity/topography admittance and correlation spectra on Mars: Implications for regional and global evolution. J. Geophys. Res. Planets 107, 19-1-19–25. https://doi.org/10.1029/2002JE001854

Mège, D., Masson, P., 1996. A plume tectonics model for the Tharsis province, Mars. Planet. Space Sci. 44, 1499–1546. https://doi.org/10.1016/S0032-0633(96)00113-4

Mellon, M.T., Arvidson, R.E., Sizemore, H.G., Searls, M.L., Blaney, D.L., Cull, S., Hecht, M.H., Heet, T.L., Keller, H.U., Lemmon, M.T., Markiewicz, W.J., Ming, D.W., Morris, R.V., Pike, W.T., Zent, A.P., 2009. Ground ice at the Phoenix Landing Site: Stability state and origin. J. Geophys. Res. Planets 114, E00E07. https://doi.org/10.1029/2009JE003417

Mellon, M.T., Jakosky, B.M., 1995. The distribution and behavior of Martian ground ice during past and present epochs. J. Geophys. Res. Planets 100, 11781–11799. https://doi.org/10.1029/95JE01027

Mellon, M.T., Jakosky, B.M., 1993. Geographic variations in the thermal and diffusive stability of ground ice on Mars. J. Geophys. Res. Planets 98, 3345–3364. https://doi.org/10.1029/92JE02355

Mellon, M.T., Phillips, R.J., 2001. Recent gullies on Mars and the source of liquid water. J. Geophys. Res. Planets 106, 23165–23179. https://doi.org/10.1029/2000JE001424

Metzger, S.M., 1992. The Eskers of New York State: Formation Process Implications and Esker-like Features on the Planet Mars. Lunar Planet. Sci. Conf. XXIII Abstract #1448.

Michael, G.G., 2013. Planetary surface dating from crater size–frequency distribution measurements: Multiple resurfacing episodes and differential isochron fitting. Icarus 226, 885–890. https://doi.org/10.1016/j.icarus.2013.07.004

Michael, G.G., Neukum, G., 2010. Planetary surface dating from crater size–frequency distribution measurements: Partial resurfacing events and statistical age uncertainty. Earth Planet. Sci. Lett., Mars Express after 6 Years in Orbit: Mars Geology from Three-Dimensional Mapping by the High Resolution Stereo Camera (HRSC) Experiment 294, 223–229. https://doi.org/10.1016/j.epsl.2009.12.041

Michael, G.G., Platz, T., Kneissl, T., Schmedemann, N., 2012. Planetary surface dating from crater size–frequency distribution measurements: Spatial randomness and clustering. Icarus 218, 169–177. https://doi.org/10.1016/j.icarus.2011.11.033

Milliken, R.E., Mustard, J.F., Goldsby, D.L., 2003. Viscous flow features on the surface of Mars: Observations from high-resolution Mars Orbiter Camera (MOC) images. J. Geophys. Res. Planets 108, 5057. https://doi.org/10.1029/2002JE002005

Montési, L.G.J., Zuber, M.T., 2003. Clues to the lithospheric structure of Mars from wrinkle ridge sets and localization instability. J. Geophys. Res. Planets 108, 5048. https://doi.org/10.1029/2002JE001974

Moore, J.M., Howard, A.D., 2005. Large alluvial fans on Mars. J. Geophys. Res. Planets 110. https://doi.org/10.1029/2004JE002352

Mouginot, J., Pommerol, A., Kofman, W., Beck, P., Schmitt, B., Herique, A., Grima, C., Safaeinili, A., Plaut, J.J., 2010. The 3–5 MHz global reflectivity map of Mars by MARSIS/Mars Express: Implications for the current inventory of subsurface H2O. Icarus 210, 612–625. https://doi.org/10.1016/j.icarus.2010.07.003

Mustard, J.F., Cooper, C.D., Rifkin, M.K., 2001. Evidence for recent climate change on Mars from the identification of youthful near-surface ground ice. Nature 412, 411–414. https://doi.org/doi:10.1038/35086515

Mutch, T.A., Arvidson, R.E., Binder, A.B., Guinness, E.A., Morris, E.C., 1977. The geology of the Viking Lander 2 site. J. Geophys. Res. 82, 4452–4467. https://doi.org/10.1029/JS082i028p04452

Neukum, G., Jaumann, R., Hoffmann, H., Hauber, E., Head, J.W., Basilevsky, A.T., Ivanov, B.A., Werner, S.C., van Gasselt, S., Murray, J.B., McCord, T., The HRSC Co-Investigator Team, 2004a. Recent and episodic volcanic and glacial activity on Mars revealed by the High Resolution Stereo Camera. Nature 432, 971–979. https://doi.org/10.1038/nature03231

Neukum, G., Jaumann, R., the HRSC Co-Investigator and Experiment Team, 2004b. HRSC: The high resolution stereo camera of Mars Express, in: Wilson, A. (Ed.), Mars Express: The Scientific Payload, European Space Agency Special Publication 1240. pp. 17–35.

Niles, P.B., Catling, D.C., Berger, G., Chassefière, E., Ehlmann, B.L., Michalski, J.R., Morris, R., Ruff, S.W., Sutter, B., 2013. Geochemistry of Carbonates on Mars: Implications

for Climate History and Nature of Aqueous Environments. Space Sci. Rev. 174, 301–328. https://doi.org/10.1007/s11214-012-9940-y

Nussbaumer, J., 2005. Extent and further characteristics of form glaciated terrain in Elysium Planitia, Mars. Lunar Planet. Sci. Conf. XXXVI Abstract #1949.

Nussbaumer, J., Jaumann, R., Hauber, E., 2003. Evidence for a Surging Ice-Sheet in Elysium Planitia, Mars. Sixth Int. Conf. Mars Abstract #3018.

Nyquist, L.E., Bogard, D.D., Shih, C.-Y., Greshake, A., Stöffler, D., Eugster, O., 2001. Ages and Geologic Histories of Martian Meteorites. Space Sci. Rev. 96, 105–164. https://doi.org/10.1023/A:1011993105172

Ojha, L., Wilhelm, M.B., Murchie, S.L., McEwen, A.S., Wray, J.J., Hanley, J., Massé, M., Chojnacki, M., 2015. Corrigendum: Spectral evidence for hydrated salts in recurring slope lineae on Mars. Nat. Geosci. 8, 704–709. https://doi.org/10.1038/ngeo2584

Okubo, C.H., 2010. Structural geology of Amazonian-aged layered sedimentary deposits in southwest Candor Chasma, Mars. Icarus 207, 210–225. https://doi.org/10.1016/j.icarus.2009.11.012

Orosei, R., Lauro, S.E., Pettinelli, E., Cicchetti, A., Coradini, M., Cosciotti, B., Paolo, F.D., Flamini, E., Mattei, E., Pajola, M., Soldovieri, F., Cartacci, M., Cassenti, F., Frigeri, A., Giuppi, S., Martufi, R., Masdea, A., Mitri, G., Nenna, C., Noschese, R., Restano, M., Seu, R., 2018. Radar evidence of subglacial liquid water on Mars. Science eaar7268. https://doi.org/10.1126/science.aar7268

Paige, D.A., Bachman, J.E., Keegan, K.D., 1994. Thermal and albedo mapping of the polar regions of Mars using Viking thermal mapper observations: 1. North polar region. J. Geophys. Res. Planets 99, 25959–25991. https://doi.org/10.1029/93JE03428

Pain, C.F., Clarke, J.D.A., Thomas, M., 2007. Inversion of relief on Mars. Icarus, Deep Impact Mission to Comet 9P/Tempel 1, Part 2 190, 478–491. https://doi.org/10.1016/j.icarus.2007.03.017

Pain, C.F., Oilier, C.D., 1995. Inversion of relief — a component of landscape evolution. Geomorphology 12, 151–165. https://doi.org/10.1016/0169-555X(94)00084-5

Parker, T.J., Pieri, D.C., Saunders, R.S., 1986. Morphology and distribution of sinuous ridges in central and southern Argyre. Natl. Aeronaut. Space Adm. Tech. Memo. 88383, 468–470.

Parker, T.J., Saunders, R.S., Schneeberger, D.M., 1989. Transitional morphology in West Deuteronilus Mensae, Mars: Implications for modification of the lowland/upland boundary. Icarus 82, 111–145. https://doi.org/10.1016/0019-1035(89)90027-4

Parsons, R.A., Nimmo, F., Miyamoto, H., 2011. Constraints on martian lobate debris apron evolution and rheology from numerical modeling of ice flow. Icarus 214, 246–257. https://doi.org/10.1016/j.icarus.2011.04.014

Pedersen, G.B.M., Head, J.W., Wilson, L., 2010. Formation, erosion and exposure of Early Amazonian dikes, dike swarms and possible subglacial eruptions in the Elysium Rise/Utopia Basin Region, Mars. Earth Planet. Sci. Lett. 294, 424–439. https://doi.org/10.1016/j.epsl.2009.08.010

Peel, S.E., Fassett, C.I., 2013. Valleys in pit craters on Mars: Characteristics, distribution, and formation mechanisms. Icarus 225, 272–282. https://doi.org/10.1016/j.icarus.2013.03.031

Perkins, A.J., Brennand, T.A., Burke, M.J., 2016. Towards a morphogenetic classification of eskers: Implications for modelling ice sheet hydrology. Quat. Sci. Rev. 134, 19–38. https://doi.org/10.1016/j.quascirev.2015.12.015

Perkins, A.J., Brennand, T.A., Burke, M.J., 2013. Genesis of an esker-like ridge over the southern Fraser Plateau, British Columbia: Implications for paleo-ice sheet reconstruction based on geomorphic inversion. Geomorphology 190, 27–39. https://doi.org/10.1016/j.geomorph.2013.02.005

Petersen, E.I., Holt, J.W., Levy, J.S., 2018. High Ice Purity of Martian Lobate Debris Aprons at the Regional Scale: Evidence From an Orbital Radar Sounding Survey in Deuteronilus and Protonilus Mensae. Geophys. Res. Lett. 45, 11,595-11,604. https://doi.org/10.1029/2018GL079759

Phillips, R.J., Zuber, M.T., Solomon, S.C., Golombek, M.P., Jakosky, B.M., Banerdt, W.B., Smith, D.E., Williams, R.M.E., Hynek, B.M., Aharonson, O., Hauck, S.A., 2001. Ancient Geodynamics and Global-Scale Hydrology on Mars. Science 291, 2587–2591. https://doi.org/10.1126/science.1058701

Pierce, T.L., Crown, D.A., 2003. Morphologic and topographic analyses of debris aprons in the eastern Hellas region, Mars. Icarus 163, 46–65. https://doi.org/10.1016/S0019-1035(03)00046-0

Pilorget, C., Forget, F., 2016. Formation of gullies on Mars by debris flows triggered by CO2 sublimation. Nat. Geosci. 9, 65–69. https://doi.org/10.1038/ngeo2619

Piqueux, S., Kleinböhl, A., Hayne, P.O., Kass, D.M., Schofield, J.T., McCleese, D.J., 2015. Variability of the martian seasonal CO2 cap extent over eight Mars Years. Icarus, Dynamic Mars 251, 164–180. https://doi.org/10.1016/j.icarus.2014.10.045

Plaut, J.J., Picardi, G., Safaeinili, A., Ivanov, A.B., Milkovich, S.M., Cicchetti, A., Kofman, W., Mouginot, J., Farrell, W.M., Phillips, R.J., Clifford, S.M., Frigeri, A., Orosei, R., Federico, C., Williams, I.P., Gurnett, D.A., Nielsen, E., Hagfors, T., Heggy, E., Stofan, E.R., Plettemeier, D., Watters, T.R., Leuschen, C.J., Edenhofer, P., 2007. Subsurface Radar Sounding of the South Polar Layered Deposits of Mars. Science 316, 92–95. https://doi.org/10.1126/science.1139672

Plaut, J.J., Safaeinili, A., Holt, J.W., Phillips, R.J., Head, J.W., Seu, R., Putzig, N.E., Frigeri, A., 2009. Radar evidence for ice in lobate debris aprons in the mid-northern latitudes of Mars. Geophys. Res. Lett. 36, L02203. https://doi.org/10.1029/2008GL036379

Plesa, A.-C., Grott, M., Tosi, N., Breuer, D., Spohn, T., Wieczorek, M.A., 2016. How large are present-day heat flux variations across the surface of Mars? J. Geophys. Res. Planets 121, 2386–2403. https://doi.org/10.1002/2016JE005126

Plescia, J.B., 2003. Cerberus Fossae, Elysium, Mars: a source for lava and water. Icarus 164, 79–95. https://doi.org/10.1016/S0019-1035(03)00139-8

Plescia, J.B., 1981. The Tempe volcanic province of Mars and comparisons with the Snake River Plains of Idaho. Icarus 45, 586–601. https://doi.org/10.1016/0019-1035(81)90024-5

Pollack, J.B., Kasting, J.F., Richardson, S.M., Poliakoff, K., 1987. The case for a wet, warm climate on early Mars. Icarus 71, 203–224. https://doi.org/10.1016/0019-1035(87)90147-3

Price, R.J., 1966. Eskers near the Casement Glacier, Alaska, Geografiska Annaler. Series A, Physical Geography 48, 111–125. https://doi.org/10.2307/520521

Punkari, M., 1997. Glacial and glaciofluvial deposits in the interlobate areas of the Scandinavian ice sheet. Quat. Sci. Rev. 16, 741–753. https://doi.org/10.1016/S0277-3791(97)00020-6

Punkari, M., 1994. Function of the ice streams in the Scandinavian ice sheet: analyses of glacial geological data from southwestern Finland. Earth Environ. Sci. Trans. R. Soc. Edinb. 85, 283–302. https://doi.org/10.1017/S0263593300002054

Putzig, N.E., Mellon, M.T., 2007. Apparent thermal inertia and the surface heterogeneity of Mars. Icarus 191, 68–94. https://doi.org/10.1016/j.icarus.2007.05.013

R Development Core Team, 2008. R: A language and environment for statistical computing. R Foundation for Statistical Computing, Vienna, Austria.

Rainio, H., Saarnisto, M., Ekman, I., 1995. Younger Dryas end moraines in Finland and NW Russia. Quat. Int. 28, 179–192. https://doi.org/10.1016/1040-6182(95)00051-J

Rasmussen, S.O., Bigler, M., Blockley, S.P., Blunier, T., Buchardt, S.L., Clausen, H.B., Cvijanovic, I., Dahl-Jensen, D., Johnsen, S.J., Fischer, H., Gkinis, V., Guillevic, M., Hoek, W.Z., Lowe, J.J., Pedro, J.B., Popp, T., Seierstad, I.K., Steffensen, J.P., Svensson, A.M., Vallelonga, P., Vinther, B.M., Walker, M.J.C., Wheatley, J.J., Winstrup, M., 2014. A stratigraphic framework for abrupt climatic changes during the Last Glacial period based on three synchronized Greenland ice-core records: refining and extending the INTIMATE event stratigraphy. Quat. Sci. Rev. 106, 14–28. https://doi.org/10.1016/j.quascirev.2014.09.007

Read, P.L., Lewis, S.R., Mulholland, D.P., 2015. The physics of Martian weather and climate: a review. Rep. Prog. Phys. 78, 125901. https://doi.org/10.1088/0034-4885/78/12/125901

Robbins, S.J., Hynek, B.M., 2012. A new global database of Mars impact craters ≥1 km: 2. Global crater properties and regional variations of the simple-to-complex transition diameter. J. Geophys. Res. Planets 117, E06001. https://doi.org/10.1029/2011JE003967

Rodriguez, J.A.P., Fairén, A.G., Tanaka, K.L., Zarroca, M., Linares, R., Platz, T., Komatsu, G., Miyamoto, H., Kargel, J.S., Yan, J., Gulick, V., Higuchi, K., Baker, V.R., Glines, N., 2016. Tsunami waves extensively resurfaced the shorelines of an early Martian ocean. Sci. Rep. 6, 25106. https://doi.org/10.1038/srep25106

Rossbacher, L.A., Judson, S., 1981. Ground ice on Mars: Inventory, distribution, and resulting landforms. Icarus 45, 39–59. https://doi.org/10.1016/0019-1035(81)90005-1

Ruddiman, W.F., Raymo, M.E., Martinson, D.G., Clement, B.M., Backman, J., 1989. Pleistocene Evolution: Northern Hemisphere Ice Sheets and North Atlantic Ocean. Paleoceanography 4, 353–412. https://doi.org/10.1029/PA004i004p00353

Ruff, S.W., Greeley, R., 1990. Sinuous Ridges of the South Polar Region, Mars: Possible Origins. Lunar Planet. Sci. Conf. XXI Abstract #1532.

Scanlon, K.E., Head, J.W., Fastook, J.L., Wordsworth, R.D., 2018. The Dorsa Argentea Formation and the Noachian-Hesperian climate transition. Icarus 299, 339–363. https://doi.org/10.1016/j.icarus.2017.07.031

Scanlon, K.E., Head, J.W., Marchant, D.R., 2015. Volcanism-induced, local wet-based glacial conditions recorded in the Late Amazonian Arsia Mons tropical mountain glacier deposits. Icarus 250, 18–31. https://doi.org/10.1016/j.icarus.2014.11.016

Scanlon, K.E., Head, J.W., Wilson, L., Marchant, D.R., 2014. Volcano–ice interactions in the Arsia Mons tropical mountain glacier deposits. Icarus 237, 315–339. https://doi.org/10.1016/j.icarus.2014.04.024

Schmidt, F., Andrieu, F., Costard, F., Kocifaj, M., Meresescu, A.G., 2017. Formation of recurring slope lineae on Mars by rarefied gas-triggered granular flows. Nat. Geosci. 10, 270–273. https://doi.org/10.1038/ngeo2917

Schon, S.C., Head, J.W., Fassett, C.I., 2012. Recent high-latitude resurfacing by a climate-related latitude-dependent mantle: Constraining age of emplacement from counts of small craters. Planet. Space Sci. 69, 49–61. https://doi.org/10.1016/j.pss.2012.03.015

Schon, S.C., Head, J.W., Milliken, R.E., 2009. A recent ice age on Mars: Evidence for climate oscillations from regional layering in mid-latitude mantling deposits. Geophys. Res. Lett. 36, L15202. https://doi.org/10.1029/2009GL038554

Schorghofer, N., 2008. Temperature response of Mars to Milankovitch cycles. Geophys. Res. Lett. 35, L18201. https://doi.org/10.1029/2008GL034954

Schorghofer, N., Aharonson, O., 2005. Stability and exchange of subsurface ice on Mars. J. Geophys. Res. Planets 110, E05003. https://doi.org/10.1029/2004JE002350

Schroeder, D.M., Blankenship, D.D., Young, D.A., Quartini, E., 2014. Evidence for elevated and spatially variable geothermal flux beneath the West Antarctic Ice Sheet. Proc. Natl. Acad. Sci. 111, 9070–9072. https://doi.org/10.1073/pnas.1405184111

Schumm, S.A., 1963. Sinuosity of Alluvial Rivers on the Great Plains. Geol. Soc. Am. Bull. 74, 1089–1100. https://doi.org/10.1130/0016-7606(1963)74[1089:SOAROT]2.0.CO;2

Scott, D.H., Dohm, J.M., 1990a. Chronology and global distribution of fault and ridge systems on Mars. Proc. Lunar Planet. Sci. Conf. 20, 487–501.

Scott, D.H., Dohm, J.M., 1990b. Faults and ridges - Historical development in Tempe Terra and Ulysses Patera regions of Mars. Proc. Lunar Planet. Sci. Conf. 20, 503–513.

Segura, T.L., Toon, O.B., Colaprete, A., Zahnle, K., 2002. Environmental Effects of Large Impacts on Mars. Science 298, 1977–1980. https://doi.org/10.1126/science.1073586

Seibert, N.M., Kargel, J.S., 2001. Small-scale Martian polygonal terrain: Implications for liquid surface water. Geophys. Res. Lett. 28, 899–902. https://doi.org/10.1029/2000GL012093

Sharp, R.P., 1980. Geomorphological Processes on Terrestrial Planetary Surfaces. Annu. Rev. Earth Planet. Sci. 8, 231–261. https://doi.org/10.1146/annurev.ea.08.050180.001311

Sharp, R.P., 1973a. Mars: Fretted and chaotic terrains. J. Geophys. Res. 78, 4073–4083. https://doi.org/10.1029/JB078i020p04073

Sharp, R.P., 1973b. Mars: South polar pits and etched terrain. J. Geophys. Res. 78, 4222–4230. https://doi.org/10.1029/JB078i020p04222

Shaw, J., 1983. Drumlin Formation Related to Inverted Melt-Water Erosional Marks. J. Glaciol. 29, 461–479. https://doi.org/10.3189/S0022143000030367

Shean, D.E., 2010. Candidate ice-rich material within equatorial craters on Mars. Geophys. Res. Lett. 37, L24202. https://doi.org/10.1029/2010GL045181

Shean, D.E., Alexandrov, O., Moratto, Z.M., Smith, B.E., Joughin, I.R., Porter, C., Morin, P., 2016. An automated, open-source pipeline for mass production of digital elevation models (DEMs) from very-high-resolution commercial stereo satellite imagery. ISPRS J. Photogramm. Remote Sens. 116, 101–117. https://doi.org/10.1016/j.isprsjprs.2016.03.012

Shean, D.E., Head, J.W., Fastook, J.L., Marchant, D.R., 2007. Recent glaciation at high elevations on Arsia Mons, Mars: Implications for the formation and evolution of large tropical mountain glaciers. J. Geophys. Res. Planets 112, E03004. https://doi.org/10.1029/2006JE002761

Shean, D.E., Head, J.W., Marchant, D.R., 2005. Origin and evolution of a cold-based tropical mountain glacier on Mars: The Pavonis Mons fan-shaped deposit. J. Geophys. Res. Planets 110, E05001. https://doi.org/10.1029/2004JE002360

Shreve, R.L., 1985a. Esker characteristics in terms of glacier physics, Katahdin esker system, Maine. Geol. Soc. Am. Bull. 96, 639–646. https://doi.org/10.1130/0016-7606(1985)96<639:ECITOG>2.0.CO;2

Shreve, R.L., 1985b. Late Wisconsin ice-surface profile calculated from esker paths and types, Katahdin esker system, maine. Quat. Res. 23, 27–37. https://doi.org/10.1016/0033-5894(85)90069-9

Shreve, R.L., 1984. Glacier sliding at subfreezing temperatures. J. Glaciol. 30, 341–347.

Shreve, R.L., 1972. Movement of water in glaciers. J. Glaciol. 11, 205–214. https://doi.org/doi: 10.3189/S002214300002219X

Skidmore, M.L., Foght, J.M., Sharp, M.J., 2000. Microbial Life beneath a High Arctic Glacier. Appl. Environ. Microbiol. 66, 3214–3220. https://doi.org/10.1128/AEM.66.8.3214-3220.2000

Smellie, J.L., Skilling, I.P., 1994. Products of subglacial volcanic eruptions under different ice thicknesses: two examples from Antarctica. Sediment. Geol. 91, 115–129. https://doi.org/10.1016/0037-0738(94)90125-2

Smith, C.A., Lowell, T.V., Caffee, M.W., 2009. Lateglacial and Holocene cosmogenic surface exposure age glacial chronology and geomorphological evidence for the presence of cold-based glaciers at Nevado Sajama, Bolivia. J. Quat. Sci. 24, 360–372. https://doi.org/10.1002/jqs.1239

Smith, D.E., Zuber, M.T., Frey, H.V., Garvin, J.B., Head, J.W., Muhleman, D.O., Pettengill, G.H., Phillips, R.J., Solomon, S.C., Zwally, H.J., Banerdt, W.B., Duxbury, T.C., Golombek, M.P., Lemoine, F.G., Neumann, G.A., Rowlands, D.D., Aharonson, O., Ford, P.G., Ivanov, A.B., Johnson, C.L., McGovern, P.J., Abshire, J.B., Afzal, R.S., Sun, X., 2001. Mars Orbiter Laser Altimeter: Experiment summary after the first year of global mapping of Mars. J. Geophys. Res. Planets 106, 23689–23722. https://doi.org/10.1029/2000JE001364

Smith, I.B., Putzig, N.E., Holt, J.W., Phillips, R.J., 2016. An ice age recorded in the polar deposits of Mars. Science 352, 1075–1078. https://doi.org/10.1126/science.aad6968

Smith, R.B., Jordan, M., Steinberger, B., Puskas, C.M., Farrell, J., Waite, G.P., Husen, S., Chang, W.-L., O'Connell, R., 2009. Geodynamics of the Yellowstone hotspot and mantle plume: Seismic and GPS imaging, kinematics, and mantle flow. J. Volcanol. Geotherm. Res. 188, 26–56. https://doi.org/10.1016/j.jvolgeores.2009.08.020

Solomon, S.C., Aharonson, O., Aurnou, J.M., Banerdt, W.B., Carr, M.H., Dombard, A.J., Frey, H.V., Golombek, M.P., Hauck, S.A., Head, J.W., Jakosky, B.M., Johnson, C.L., McGovern, P.J., Neumann, G.A., Phillips, R.J., Smith, D.E., Zuber, M.T., 2005. New

Perspectives on Ancient Mars. Science 307, 1214–1220. https://doi.org/10.1126/science.1101812

Sori, M., Bramson, A.M., 2019. A Story of Water, Ice and Fire on Mars: Conditions for Generating Liquid Water under the South Polar Layered Deposits. Lunar Planet. Sci. Conf. L Abstract #1073.

Souness, C., Hubbard, B., 2012. Mid-latitude glaciation on Mars. Prog. Phys. Geogr. 36, 238–261. https://doi.org/10.1177/0309133312436570

Souness, C., Hubbard, B., Milliken, R.E., Quincey, D., 2012. An inventory and population-scale analysis of martian glacier-like forms. Icarus 217, 243–255. https://doi.org/10.1016/j.icarus.2011.10.020

Souness, C.J., Hubbard, B., 2013. An alternative interpretation of late Amazonian ice flow: Protonilus Mensae, Mars. Icarus 225, 495–505. https://doi.org/10.1016/j.icarus.2013.03.030

Squyres, S.W., 1979. The distribution of lobate debris aprons and similar flows on Mars. J. Geophys. Res. Solid Earth 84, 8087–8096. https://doi.org/10.1029/JB084iB14p08087

Squyres, S.W., 1978. Martian Fretted Terrain: Flow of Erosional Debris. Icarus 34, 600–613. https://doi.org/10.1016/0019-1035(78)90048-9

Squyres, S.W., Carr, M.H., 1986. Geomorphic evidence for the distribution of ground ice on Mars. Science 231, 249–252. https://doi.org/10.1126/science.231.4735.249

Squyres, S.W., Clifford, S.M., Kuzmin, R.O., Zimbelman, J.R., Costard, F.M., 1992. Ice in the Martian regolith, in: Kieffer, H.H., Jakosky, B.M., Snyder, C., Matthews, M.S. (Eds.), Mars. University of Arizona Press, Tuscan, pp. 523–554.

Stern, S.A., Bagenal, F., Ennico, K., Gladstone, G.R., Grundy, W.M., McKinnon, W.B., Moore, J.M., Olkin, C.B., Spencer, J.R., Weaver, H.A., Young, L.A., Andert, T., Andrews, J., Banks, M., Bauer, B., Bauman, J., Barnouin, O.S., Bedini, P., Beisser, K., Beyer, R.A., Bhaskaran, S., Binzel, R.P., Birath, E., Bird, M., Bogan, D.J., Bowman, A., Bray, V.J., Brozovic, M., Bryan, C., Buckley, M.R., Buie, M.W., Buratti, B.J., Bushman, S.S., Calloway, A., Carcich, B., Cheng, A.F., Conard, S., Conrad, C.A., Cook, J.C., Cruikshank, D.P., Custodio, O.S., Ore, C.M.D., Deboy, C., Dischner, Z.J.B., Dumont, P., Earle, A.M., Elliott, H.A., Ercol, J., Ernst, C.M., Finley, T., Flanigan, S.H., Fountain, G., Freeze, M.J., Greathouse, T., Green, J.L., Guo, Y., Hahn, M., Hamilton, D.P., Hamilton, S.A., Hanley, J., Harch, A., Hart, H.M., Hersman, C.B., Hill, A., Hill, M.E., Hinson, D.P., Holdridge, M.E.,

Horanyi, M., Howard, A.D., Howett, C.J.A., Jackman, C., Jacobson, R.A., Jennings, D.E., Kammer, J.A., Kang, H.K., Kaufmann, D.E., Kollmann, P., Krimigis, S.M., Kusnierkiewicz, D., Lauer, T.R., Lee, J.E., Lindstrom, K.L., Linscott, I.R., Lisse, C.M., Lunsford, A.W., Mallder, V.A., Martin, N., McComas, D.J., McNutt, R.L., Mehoke, D., Mehoke, T., Melin, E.D., Mutchler, M., Nelson, D., Nimmo, F., Nunez, J.I., Ocampo, A., Owen, W.M., Paetzold, M., Page, B., Parker, A.H., Parker, J.W., Pelletier, F., Peterson, J., Pinkine, N., Piquette, M., Porter, S.B., Protopapa, S., Redfern, J., Reitsema, H.J., Reuter, D.C., Roberts, J.H., Robbins, S.J., Rogers, G., Rose, D., Runyon, K., Retherford, K.D., Ryschkewitsch, M.G., Schenk, P., Schindhelm, E., Sepan, B., Showalter, M.R., Singer, K.N., Soluri, M., Stanbridge, D., Steffl, A.J., Strobel, D.F., Stryk, T., Summers, M.E., Szalay, J.R., Tapley, M., Taylor, A., Taylor, H., Throop, H.B., Tsang, C.C.C., Tyler, G.L., Umurhan, O.M., Verbiscer, A.J., Versteeg, M.H., Vincent, M., Webbert, R., Weidner, S., Weigle, G.E., White, O.L., Whittenburg, K., Williams, B.G., Williams, K., Williams, S., Woods, W.W., Zangari, A.M., Zirnstein, E., 2015. The Pluto system: Initial results from its exploration by New Horizons. Science 350, aad1815. https://doi.org/10.1126/science.aad1815

Stillman, D.E., Michaels, T.I., Grimm, R.E., Hanley, J., 2016. Observations and modeling of northern mid-latitude recurring slope lineae (RSL) suggest recharge by a present-day martian briny aquifer. Icarus 265, 125–138. https://doi.org/10.1016/j.icarus.2015.10.007

Stillman, D.E., Michaels, T.I., Grimm, R.E., Harrison, K.P., 2014. New observations of martian southern mid-latitude recurring slope lineae (RSL) imply formation by freshwater subsurface flows. Icarus 233, 328–341. https://doi.org/10.1016/j.icarus.2014.01.017

Storrar, R.D., Evans, D.J.A., Stokes, C.R., Ewertowski, M., 2015. Controls on the location, morphology and evolution of complex esker systems at decadal timescales, Breiðamerkurjökull, southeast Iceland. Earth Surf. Process. Landf. 40, 1421–1438. https://doi.org/10.1002/esp.3725

Storrar, R.D., Stokes, C.R., Evans, D.J.A., 2014a. Morphometry and pattern of a large sample (>20,000) of Canadian eskers and implications for subglacial drainage beneath ice sheets. Quat. Sci. Rev. 105, 1–25. https://doi.org/10.1016/j.quascirev.2014.09.013

Storrar, R.D., Stokes, C.R., Evans, D.J.A., 2014b. Increased channelization of subglacial drainage during deglaciation of the Laurentide Ice Sheet. Geology 42, 239–242. https://doi.org/10.1130/G35092.1

Storrar, R.D., Stokes, C.R., Evans, D.J.A., 2013. A map of large Canadian eskers from Landsat satellite imagery. J. Maps 9, 456–473. https://doi.org/10.1080/17445647.2013.815591

Stroeven, A.P., Hättestrand, C., Kleman, J., Heyman, J., Fabel, D., Fredin, O., Goodfellow, B.W., Harbor, J.M., Jansen, J.D., Olsen, L., Caffee, M.W., Fink, D., Lundqvist, J., Rosqvist, G.C., Strömberg, B., Jansson, K.N., 2016. Deglaciation of Fennoscandia. Quat. Sci. Rev. 147, 91–121. https://doi.org/10.1016/j.quascirev.2015.09.016

Stroeven, A.P., Heyman, J., Fabel, D., Björck, S., Caffee, M.W., Fredin, O., Harbor, J.M., 2015. A new Scandinavian reference 10Be production rate. Quat. Geochronol. 29, 104–115. https://doi.org/10.1016/j.quageo.2015.06.011

Stuurman, C.M., Osinski, G.R., Holt, J.W., Levy, J.S., Brothers, T.C., Kerrigan, M., Campbell, B.A., 2016. SHARAD detection and characterization of subsurface water ice deposits in Utopia Planitia, Mars. Geophys. Res. Lett. 43, 9484–9491. https://doi.org/10.1002/2016GL070138

Tanaka, K.L., 1990. Tectonic history of the Alba Patera-Ceraunius Fossae region of Mars. Proc. Lunar Planet. Sci. Conf. 20, 515–523.

Tanaka, K.L., Kolb, E.J., 2001. Geologic History of the Polar Regions of Mars Based on Mars Global Surveyor Data I. Noachian and Hesperian Periods. Icarus 154, 3–21. https://doi.org/10.1006/icar.2001.6675

Tanaka, K.L., Scott, D.H., 1987. Geologic map of the polar regions of Mars,U.S Geological Survey Miscellaneous Investigations Series Map 1-1802-C, scale 1:15,000,000.

Tanaka, K.L., Skinner, J.A., Dohm, J.M., Irwin III, R.P., Kolb, E.J., Fortezzo, C.M., Platz, T., Michael, G.G., Hare, T., 2014a. Geologic map of Mars, Pamphlet to accompany Scientific Investigations Map 3292. US Geological Survey.

Tanaka, K.L., Skinner, J.A., Dohm, J.M., Irwin III, R.P., Kolb, E.J., Fortezzo, C.M., Platz, T., Michael, G.G., Hare, T., 2014b. Geologic Map of Mars, US Geologic Survey Scientific Investigations Map 3292, scale 1:20,000,000, with 43 p. pamphlet.

Taylor, J., Teanby, N.A., Wookey, J., 2013. Estimates of seismic activity in the Cerberus Fossae region of Mars. J. Geophys. Res. Planets 118, 2570–2581. https://doi.org/10.1002/2013JE004469

van Gasselt, S., Hauber, E., Neukum, G., 2010. Lineated valley fill at the Martian dichotomy boundary: Nature and history of degradation. J. Geophys. Res. Planets 115, E08003. https://doi.org/10.1029/2009JE003336

van Gasselt, S., Hauber, E., Rossi, A.-P., Dumke, A., Orosei, R., Neukum, G., 2011. Periglacial geomorphology and landscape evolution of the Tempe Terra region, Mars, in: Balme, M.R., Bargery, A.S., Gallagher, C.J., Gupta, S. (Eds.), Martian Geomorphology. Geological Society, London, Special Publications, 356. pp. 43–67, doi: 10.1144/SP356.4.

Vere, D.M., Benn, D.I., 1989. Structure and Debris Characteristics of Medial Moraines in Jotunheimen, Norway: Implications for Moraine Classification. J. Glaciol. 35, 276–280. https://doi.org/10.1017/S0022143000004615

Walder, J., Hallet, B., 1979. Geometry of Former Subglacial Water Channels and Cavities. J. Glaciol. 23, 335–346. https://doi.org/10.1017/S0022143000029944

Waller, R.I., 2001. The influence of basal processes on the dynamic behaviour of cold-based glaciers. Quat. Int. 86, 117–128. https://doi.org/10.1016/S1040-6182(01)00054-4

Warner, N.H., Gupta, S., Calef, F., Grindrod, P., Boll, N., Goddard, K., 2015. Minimum effective area for high resolution crater counting of martian terrains. Icarus 245, 198–240. https://doi.org/10.1016/j.icarus.2014.09.024

Watters, T.R., 1988. Wrinkle ridge assemblages on the terrestrial planets. J. Geophys. Res. Solid Earth 93, 10236–10254. https://doi.org/10.1029/JB093iB09p10236

Weertman, J., 1972. General theory of water flow at the base of a glacier or ice sheet. Rev. Geophys. 10, 287–333. https://doi.org/10.1029/RG010i001p00287

Weiss, D.K., Head, J.W., 2017. Evidence for stabilization of the ice-cemented cryosphere in earlier martian history: Implications for the current abundance of groundwater at depth on Mars. Icarus 288, 120–147. https://doi.org/10.1016/j.icarus.2017.01.018

Werner, S.C., 2009. The global martian volcanic evolutionary history. Icarus 201, 44–68. https://doi.org/10.1016/j.icarus.2008.12.019

Whiteway, J.A., Komguem, L., Dickinson, C., Cook, C., Illnicki, M., Seabrook, J., Popovici, V., Duck, T.J., Davy, R., Taylor, P.A., Pathak, J., Fisher, D., Carswell, A.I., Daly, M., Hipkin, V., Zent, A.P., Hecht, M.H., Wood, S.E., Tamppari, L.K., Renno, N., Moores, J.E., Lemmon, M.T., Daerden, F., Smith, P.H., 2009. Mars Water-Ice Clouds and Precipitation. Science 325, 68–70. https://doi.org/10.1126/science.1172344

Williams, K.E., Toon, O.B., Heldmann, J.L., Mellon, M.T., 2009. Ancient melting of mid-latitude snowpacks on Mars as a water source for gullies. Icarus 200, 418–425. https://doi.org/10.1016/j.icarus.2008.12.013

Williams, R.M.E., Chidsey Jr, T.C., Eby, D.E., 2007. Exhumed paleochannels in central Utah—Analogs for raised curvilinear features on Mars, in: Hylland, M.D., Clark, D.L., Chidsey, T.C. (Eds.), Central Utah - Diverse Geology of a Dynamic Landscape, Utah Geological Association Publication.

Williams, R.M.E., Irwin, R.P., Burr, D.M., Harrison, T., McClelland, P., 2013. Variability in martian sinuous ridge form: Case study of Aeolis Serpens in the Aeolis Dorsa, Mars, and insight from the Mirackina paleoriver, South Australia. Icarus 225, 308–324. https://doi.org/10.1016/j.icarus.2013.03.016

Williams, R.M.E., Irwin, R.P., Zimbelman, J.R., 2009. Evaluation of paleohydrologic models for terrestrial inverted channels: Implications for application to martian sinuous ridges. Geomorphology 107, 300–315. https://doi.org/10.1016/j.geomorph.2008.12.015

Wilson, L., Head, J.W., 2002. Heat transfer and melting in subglacial basaltic volcanic eruptions: implications for volcanic deposit morphology and meltwater volumes, in: Smellie, J.L., Chapman, M.G. (Eds.), Volcano-Ice Interaction on Earth and Mars. Geological Society, London, Special Publications, 202. pp. 5–26.

Wilson, S.A., Howard, A.D., Moore, J.M., Grant, J.A., 2016. A cold-wet middle-latitude environment on Mars during the Hesperian-Amazonian transition: Evidence from northern Arabia valleys and paleolakes. J. Geophys. Res. Planets 121, 1667–1694. https://doi.org/10.1002/2016JE005052

Wordsworth, R., Forget, F., Millour, E., Head, J.W., Madeleine, J.-B., Charnay, B., 2013. Global modelling of the early martian climate under a denser CO2 atmosphere: Water cycle and ice evolution. Icarus 222, 1–19. https://doi.org/10.1016/j.icarus.2012.09.036

Wordsworth, R.D., 2016. The Climate of Early Mars. Annu. Rev. Earth Planet. Sci. 44, 381–408. https://doi.org/10.1146/annurev-earth-060115-012355

Wordsworth, R.D., Kerber, L., Pierrehumbert, R.T., Forget, F., Head, J.W., 2015. Comparison of "warm and wet" and "cold and icy" scenarios for early Mars in a 3-D climate model. J. Geophys. Res. Planets 120, 1201–1219. https://doi.org/10.1002/2015JE004787

Zimbelman, J.R., Griffin, L.J., 2010. HiRISE images of yardangs and sinuous ridges in the lower member of the Medusae Fossae Formation, Mars. Icarus 205, 198–210. https://doi.org/10.1016/j.icarus.2009.04.003

Zuber, M.T., Smith, D.E., Solomon, S.C., Abshire, J.B., Afzal, R.S., Aharonson, O., Fishbaugh, K., Ford, P.G., Frey, H.V., Garvin, J.B., Head, J.W., Ivanov, A.B., Johnson, C.L., Muhleman, D.O., Neumann, G.A., Pettengill, G.H., Phillips, R.J., Sun, X., Zwally, H.J., Banerdt, W.B., Duxbury, T.C., 1998. Observations of the North Polar Region of Mars from the Mars Orbiter Laser Altimeter. Science 282, 2053–2060. https://doi.org/10.1126/science.282.5396.2053

Zurek, R.W., Barnes, J.R., Haberle, R.M., Pollack, J.B., Tillman, J.E., Leovy, C.B., 1992. The Dynamics of the Atmosphere of Mars, in: Kieffer, H.H., Jakosky, B.M., Snyder, C.W., Matthews, M.S. (Eds.), Dynamics of the Atmosphere of Mars. The University of Arizona Press, Tuscon, pp. 835–933.